Physics of the Solid State, Vol. 42, No. 7, 2000, pp. 1187–1191. Translated from Fizika Tverdogo Tela, Vol. 42, No. 7, 2000, pp. 1153–1157.

METALS AND SUPERCONDUCTORS

Features of Electrical Conductivity in an Incommensurate Phase of Graphite Intercalation Compound $C_{10}HNO_3$

A. M. Ziatdinov

Institute of Chemistry, Far East Division, Russian Academy of Sciences, pr. Stoletiya Vladivostoka 159, Vladivostok, 690022 Russia

e-mail: chemi@online.ru

Received October 25, 1999

Abstract—Electrical conductivity and conduction-electron spin resonance (CESR) have been studied in stage-2 acceptor α-graphite–nitric acid intercalation compound $C_{10}HNO_3$. It is found that the electrical conductivity σ_c along the *c* axis in the structurally incommensurate phase of this compound is temperature independent, whereas the electrical conductivity σ_a along carbon layers exhibits "metallic" temperature behavior. Analysis of the temperature dependences of σ_c, σ_a, and the CESR linewidth demonstrates that, in the incommensurate phase of the graphite intercalation compound, the electrical conductivity along the *c* axis is realized through a nonband mechanism—the transfer of free charge carriers along thin high-conductivity channels shunting the carbon layers adjacent to the intercalate. © *2000 MAIK "Nauka/Interperiodica".*

1. INTRODUCTION

The structure of graphite intercalation compounds is formed by alternating sequence of *n* hexagonal graphite layers (*n* is the stage index) and a layer of "guest" atoms or molecules (intercalate). By intercalating different chemical species into graphite and varying their concentration, it is possible to change the sign and concentration of free charge carriers in the carbon network of materials and, consequently, their electric, magnetic, and other properties [1, 2]. The electrical conductivity is one of the most extensively studied properties of graphite intercalation compounds. This is explained primarily by three remarkable features found in acceptor graphite intercalation compounds: (1) the high conductivity σ_a in the basal plane, which in some compounds is comparable to the conductivity of copper at room temperature [1, 3]; (2) the large ratio between σ_a and the electrical conductivity σ_c along the *c* axis (σ_a/σ_c), which, for the majority of compounds, is as great as ~10^5 [1, 4–6]; and (3) the metallic type of the temperature dependence of σ_c for compounds with the small stage index (as a rule, at $n \le 3$) [1, 5–7]. The last feature of electrical conductivity in acceptor graphite intercalation compounds has attracted the particular attention, because the magnitude of σ_c in these conductors is several ten times smaller than the fundamental critical value of *n*-type conductivity, below which, according to the Ioffe–Regel criterion [8], the conduction electrons are localized. Moreover, it is difficult to relate this feature of the conductivity σ_c to the fact that its values lying in the range from 0.1 to 10 Ω^{-1} cm^{-1} [1, 4–7], according to the Drude classical formula, correspond to the electron mean free paths of less than 1 Å, which is almost one order of magnitude smaller than the typical distances between carbon layers adjacent to the intercalate in the acceptor graphite intercalation compounds [1, 2]. At present, the universally accepted theory of the σ_c conductivity in these compounds is absent. In the literature, the features of the σ_c conductivity, including those mentioned above, are explained within mutually exclusive models that postulate either nonband [6, 9–14] or band [15–17] mechanisms of conductivity. In this respect, the search and investigations into the new features of the σ_c conductivity in acceptor graphite intercalation compounds can provide a deeper insight into its nature and are important steps in the development of the theory of free charge carrier transfer along the *c* axis in these synthetic conductors.

In the present work, we studied the stage-2 acceptor α-graphite intercalation compound $C_{10}HNO_3$ and found a new feature of the σ_c conductivity. This feature resides in the fact that σ_c in the structurally incommensurate phase is temperature independent, whereas the electrical conductivity σ_a has "metallic" temperature behavior. The structurally incommensurate phase in $C_{10}HNO_3$ is formed at a temperature below $T_c \sim 250$ K due to the crystallization of two-dimensional liquidlike HNO_3 layers and remains stable down to the "lock-in" transition at $T_{l-i} \sim 210$ K [18, 19].

2. EXPERIMENTAL TECHNIQUE

All highly oriented pyrolytic graphite plates used for the synthesis of stage-2 α-graphite–nitric acid intercalation compound $C_{10}HNO_3$ were cut from the same graphite bar with the conductivity in the basal plane $\sigma_a = (1.2 \pm 0.2) \times 10^4$ Ω^{-1} cm^{-1} and had the shape of a rectangular parallelepiped with sizes: width (l) × height

1063-7834/00/4207-1187$20.00

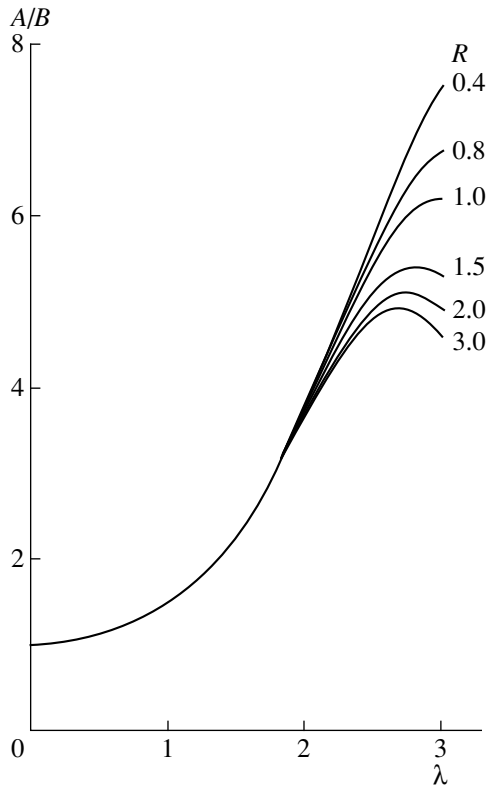

Fig. 1. Dependences of the asymmetry parameter A/B of the first derivative of the ESR absorption line on $\lambda = l/\delta$ (l is the plate thickness, and δ is the skin layer depth) for different ratios $R = (T_D/T_2)^{1/2}$ (T_D is the time of spin diffusion through the skin layer δ and T_2 is the spin-lattice relaxation time).

(h) × thickness (d), where $l \times h$ is the area of the basal face. The sizes of plates were determined accurate to within $\sim 5 \times 10^{-4}$ cm. The $C_{10}HNO_3$ compound was synthesized in "fuming" nitric acid with the density ρ = 1.565 g/cm^3. The graphite intercalation compound was identified by x-ray diffraction analysis on a DRON-3.0 diffractometer (CuK_α radiation).

The conductivity σ_a of the $C_{10}HNO_3$ samples was measured by the contactless induction technique using a setup similar to that described in [20]. In this technique, the electrical conductivity of a conductor is determined from comparison of the changes in the inductance of a measuring cell after alternately bringing the studied and reference conductor plates into the cell.

The conductivity σ_c was also measured using the contactless technique. This technique is based on the fact known from the theory of conduction-electron spin resonance (CESR) [21, 22] that, for samples with sizes of an order of the skin layer, the asymmetry parameter A/B of the first derivative of the CESR absorption line (the ratio between the peak intensities of its more intense wing A and the less intense wing B) does not depend on the diffusion rate of current carriers (Fig. 1). The ratio A/B for these samples is determined only by their electrical conductivity and the microwave field frequency of a spectrometer. Since the plates of the acceptor graphite intercalation compound exhibit a large anisotropy of electrical conductivity, the contribution from regions adjacent to the basal faces to the CESR signal can be ignored [22, 23]. Therefore, at the known frequency of a microwave field, the conductivity σ_c can be uniquely determined from the A/B ratio of the CESR signal of the acceptor graphite intercalation compound plate with the sizes $l/\delta_c \le 2$ (δ_c is the skin layer thickness determined by σ_c) using the nomographic chart depicted in Fig. 1. Both techniques used for measuring the electrical conductivity are free of a number of disadvantages that are characteristic of contact techniques for measuring the electrical conductivity (problems associated with contacts, stray currents, etc.). The conductivities σ_a and σ_c were measured accurate to $\sim 10^5$ and $\sim 0.1\ \Omega^{-1}\ \text{cm}^{-1}$, respectively.

In order to evaluate the collision relaxation times of current carriers in different phases of $C_{10}HNO_3$, the widths of the CESR signals were also measured in the ESR experiments carried out in order to determine the σ_c conductivity. The CESR signals of the $C_{10}HNO_3$ plates were recorded on an ESR-231 spectrometer (Germany) working in the X band.

The temperature dependences of the σ_a and σ_c conductivities were measured in the range 77–300 K with the use of the $C_{10}HNO_3$ plates of geometric sizes $0.4 \times 0.4 \times 0.02$ and $0.04 \times 0.4 \times 0.02$ cm, respectively. In all the experiments, the temperature was changed by controlling the rate and the temperature of a gaseous nitrogen stream flowing through a quartz Dewar vessel. The accuracies of the measurement and maintenance of the temperature were equal to ~0.5 K and ~1 K/h, respectively.

3. RESULTS

Figure 2 demonstrates the experimental dependences of the electrical conductivity for the $C_{10}HNO_3$ graphite intercalation compound in the temperature range covering the range of its incommensurate phase. It is seen from the figure that, as the temperature decreases, the σ_a conductivity increases irrespective of the aggregate state of the intercalate and the structural modification of its crystalline phase. Outside the temperature range of the incommensurate phase, the σ_c conductivity also exhibits metallic temperature behavior. In the structurally incommensurate phase of the studied compound, within the limits of experimental error, σ_c does not depend on the temperature. Upon crystallization (melting) of the subsystem of intercalated molecules, both conductivities under consideration increase (decrease) jumpwise. The qualitative character of the temperature dependences of the σ_c and

σ_a conductivities does not depend on the direction of changes in the temperature and the number of thermocycling of the $C_{10}HNO_3$ plate in the range involving the temperature range of the incommensurate phase.

At room temperature, the CESR signal of the $C_{10}HNO_3$ graphite intercalation compound is characterized by the following parameters: $g_{\|} = 2.0023 \pm 0.0002$, $g_{\perp} = 2.0028 \pm 0.0002$, $\Delta H_{\|} = (0.38 \pm 0.02) \times 10^{-4}$ T, and $\Delta H_{\perp} = (0.36 \pm 0.02) \times 10^{-4}$ T. Here, $g_{\|}$ ($\Delta H_{\|}$) and $g_{\perp}$ ($\Delta H_{\perp}$) are the g tensor components (the half-widths of the A peak) of the CESR signal at the external constant magnetic field $\mathbf{H}_0$ aligned along and perpendicular to the c axis. The crystallization of the intercalate brings about the broadening of the CESR signal by a factor of two or three. The direction of the axial symmetry of the spectrum and the values of the g tensor do not depend on the aggregate state of the intercalate subsystem.

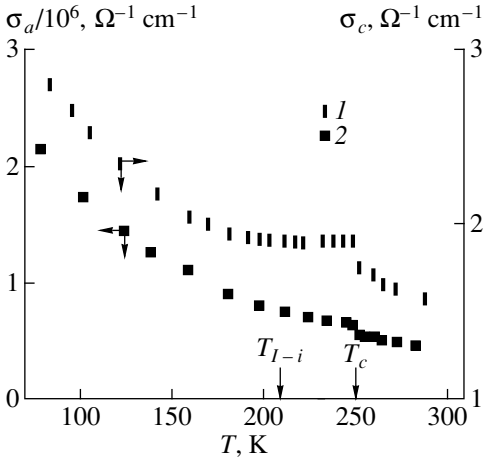

Fig. 2. Temperature dependences of (*1*) σ_c and (*2*) σ_a conductivities for the $C_{10}HNO_3$ graphite intercalation compound plates.

4. DISCUSSION

Within the theory of nonband transfer of free charge carriers along the c axis in the acceptor graphite intercalation compounds [6, 9–14], the metallic type of the temperature dependence of the σ_c conductivity for low-stage compounds ($n \le 3$) is associated with the fact that, at all temperatures, the σ_c conductivity is predominantly provided by the mechanism of charge transfer through very thin high-conductivity paths (channels) shunting the nearest carbon layers separated by the intercalate. According to Suzuki *et al.* [14], the contribution of this mechanism to the σ_c conductivity is defined by the relationship

$$\sigma_c = \frac{16e^2}{\hbar^3} m^* d_I V_0^2 \left(\frac{N_c}{\Gamma}\right), \qquad (1)$$

where V_0 is the matrix element of the scattering potential, N_c is the number of conducting channels per unit cell, m^* is the effective mass of current carriers in the basal plane, d_I is the distance between the nearest graphite layers separated by the intercalate, e is the electronic charge, $\hbar$ is the Planck constant, and $\Gamma/\hbar$ is the sum of relaxation rates of current carriers in the basal plane due to phonon and impurity scattering: $\Gamma = \Gamma_{ph} + \Gamma_I$. At high temperatures, $\Gamma/\hbar$ with a high accuracy can be taken to be equal to the relaxation rate of current carriers in the basal plane $\Gamma_a/\hbar$ related to σ_a [13, 14].

In the framework of the band model [15–17], it is supposed that the σ_c conductivity is associated with a weak overlap of wave functions for the states of current carriers in the nearest carbon layers separated by the intercalate. In this case [15, 17],

$$\sigma_c \propto \frac{e^2}{\hbar} d_I \left(\frac{B^2}{\Gamma}\right), \qquad (2)$$

where B is the resonance integral relating the states of current carriers in the carbon layers adjacent to the intercalate, and the other designations are the same as in relationship (1). From a comparison of the electrical conductivity anisotropy in a number of graphite intercalation compounds, it was found that [15, 17]

$$B \propto \exp(-d_I/d_0),$$

where $d_0 = 0.71$ Å.

If the temperature variations in d_I and V_0 are neglected, it is seen from relationships (1) and (2) that σ_c can remain constant in a certain temperature range in the presence of the temperature dependence of Γ ($\propto\Gamma_a$) and, hence, σ_a only in the case when the temperature variations in Γ and B^2 (in the band model) or Γ and N_c (in the nonband model) are mutually compensated in this temperature range. Within the band model of the σ_c conductivity in graphite intercalation compounds, it is impossible to propose a physically reasonable mechanism providing such temperature variations in Γ and B that are required for the constancy of σ_c. At the same time, for the nonband model of the σ_c conductivity in graphite intercalation compounds through thin high-conductivity channels, it is easy to explain why, in some phases of graphite intercalation compounds, the ratio N_c/Γ determining σ_c [see relationship (1)] can be temperature independent. Actually, this can stem from the high concentration of structural defects N_d in these phases when the value of $\Gamma/\hbar$, to a first approximation, is determined only by the scattering of current carriers by defects; i.e., $\Gamma/\hbar \cong \Gamma_I/\hbar \propto N_d$. Since, according to the nonband concepts [6, 9–14], $N_c \propto N_d$, it is evident that, in phases of graphite intercalation compounds with a high content of defects, the N_c/Γ ratio and, hence, σ_c [see relationship (1)] can be temperature independent. Taking into consideration that $\sigma_a \propto (N_d)^{-1}$, from the

foregoing it follows that the independence of σ_c from the temperature in the presence of the temperature dependence of σ_a in the incommensurate phase of $C_{10}HNO_3$ can be explained by the fact that the incommensurate crystallization of the intercalate leads to the formation of new structural defects whose concentration decreases with a decrease in the temperature. Note that the assumption on the more defective $C_{10}HNO_3$ structure in the solid intercalate phase is indirectly corroborated by the broadening of the CESR signal by a factor of two or three upon crystallization of intercalate.

New defects in the crystalline phase of the intercalate subsystem can arise from its domain structure. For example, the solid intercalate phase can involve a set of several types of two-dimensional orientational domains whose boundaries (walls) form a particular type of structural defects inherent in this phase. In principle, these defects can be responsible for the appearance of new thin conducting channels along the *c* axis upon crystallization of intercalate. However, it should be believed that this concerns not all the channels, because the appearance of similar defects upon phase transition can explain only the jump of σ_c and (at their sufficiently high concentration) the temperature independence of σ_c below the transition temperature. On the other hand, the appearance of these defects cannot explain the "metallic" temperature behavior of the σ_a conductivity in the solid intercalate phase, since there are no data indicating that their concentration depends on the temperature. At the same time, it is known that, in addition to the orientational domains, modulated phases of crystals can involve wide domain walls separating translational domains ("strip domains"), as well as structural solitons whose concentration decreases as the temperature of the "lock-in" transition is approached [24, 25]. According to the x-ray structural data for $C_{10}HNO_3$ [19], analogous structural imperfections can occur in this graphite intercalation compound below the crystallization temperature of the intercalate. The quasi-elastic neutron scattering investigation of $C_{10}HNO_3$ [26] confirms this conclusion and, moreover, suggests a decrease in the concentration of "strip domains" as the temperature of the "lock-in" transition is approached. Consequently, if, in the incommensurate phase of the $C_{10}HNO_3$ graphite intercalate compound, $\Gamma_{ph} \gg \Gamma_I$, and a part of high-conductivity channels arising upon crystallization of the intercalate is associated with the "strip domains" or structural solitons in the intercalate layers, a decrease in their concentration as the temperature of the "lock-in" transition is approached can be responsible for an increase in σ_a at constant σ_c. Furthermore, as follows from the aforesaid, in general, in certain phases of the graphite intercalation compounds, the "metallic" temperature behavior of σ_a can be determined by the structural ordering in the intercalate subsystem, rather than by a decrease in the amplitude of atomic thermal vibrations in the carbon and intercalate layers.

The crystallization of the intercalate subsystem in $C_{10}HNO_3$ also leads to the change in its electronic structure [27] and, as a consequence, to an increase in the density of states at the Fermi level [28]. The latter fact suggests that the jumpwise increase in σ_a upon crystallization of intercalate in this graphite intercalation compound (Fig. 2) can be attributed to an increase in the concentration of current carriers whose contribution exceeds the expected decrease in the conductivity due to a decrease in the mobility of current carriers (owing to an increase in the defect concentration).

Until recently, the problem concerning the search and investigations into possible features of the electrical conductivity in the incommensurate phases of acceptor graphite intercalation compounds was not considered in the literature. However, analysis of the available data demonstrates that, among the graphite intercalation compounds, for which the temperature dependence of σ_c was studied, several compounds exhibit structurally incommensurate phases. These are the acceptor stage-3, stage-4, and stage-6 $SbCl_5$ graphite intercalation compounds [29], in which the intercalate subsystem at $T \approx 210$ K undergoes a phase transition to a structurally incommensurate state [30]. For all these graphite intercalation compounds, the magnitude of the temperature coefficient of electrical conductivity upon the phase transition to the structurally incommensurate state sharply decreases down to small value and, for stage-3 and stage-4 compounds, is virtually zero over a wide range of temperatures below the transition point. These facts suggest that the temperature invariance of σ_c, found in the incommensurate phase of $C_{10}HNO_3$, can be the feature inherent in all the structurally incommensurate phases of acceptor graphite intercalation compounds.

In closing, let us evaluate the concentration of thin high-conductivity channels in the incommensurate phase of $C_{10}HNO_3$ immediately after the crystallization of the intercalate by using relationship (1). For this purpose, we will ignore the possible difference between Γ and Γ_a and assume that Γ_a can be calculated from the known Drude relationship $\sigma_a = Ne^2/(\Gamma_a/\hbar)m^*$ (where N is the concentration of current carriers). Then, the following parameters are substituted in relationship (1): $\sigma_c = 1.9\ \Omega^{-1}\ cm^{-1}$, $\sigma_a = 8 \times 10^5\ \Omega^{-1}\ cm^{-1}$, $V_0 = (2–3) \times 10^{-2}$ eV [11, 13, 14], $N = 1.02 \times 10^{21}\ cm^{-3}$ [31], $d_I = 7.80$ Å, and $m^* = (0.06–0.32)m_0$ [32, 33–37] (where m_0 is the mass of free electron). As a result, we have $N_I = (1.1–65) \times 10^{-5}$. (The σ_c, σ_a, and d_I values used for the calculation of N_I were determined by the author. The V_0 and m^* values for the nitric acid–intercalated graphite compound are not known. Therefore, the minimum and maximum values of these parameters for other acceptor graphite intercalation compounds available in the literature were chosen for the evaluation of N_I.) It should be mentioned that, according to the Suzuki estimates for stage-2 $MoCl_5$-intercalated graphite compound [14],

$N_I \sim 5 \times 10^{-5}$. As can be seen, despite a different intercalate nature, the value of N_I for this graphite intercalation compound falls in the range evaluated for the incommensurate phase of $C_{10}HNO_3$.

Thus, the data on the electrical conductivity in the $C_{10}HNO_3$ graphite intercalation compound and their analysis led to the conclusion that the σ_c conductivity in the structurally incommensurate phase of this compound has a nonband nature. The transfer of free charge carriers along the *c* axis in this phase can occur through the mechanism of the charge transport along thin high-conductivity channels shunting the carbon layers adjacent to the intercalate.

ACKNOWLEDGMENTS

I am grateful to my colleagues N.M. Mishchenko and V.V. Sereda for assistance in the temperature measurements of electrical conductivity, L.B. Nepomnyashchiĭ (Grafit Research Institute, Moscow) for supplying graphite samples, and Prof. K. Sugihara (Nihon University, Chiba, Japan) for his interest in this work and helpful remarks.

This work was supported by the Russian Foundation for Basic Research, project no. 97-03-33346.

REFERENCES

1. M. S. Dresselhaus and G. Dresselhaus, Adv. Phys. **30** (2), 139 (1981).
2. S. A. Solin and H. Zabel, Adv. Phys. **37** (2), 87 (1988).
3. G. M. T. Foley, C. Zeller, E. R. Falardeau, and F. L. Vogel, Solid State Commun. **24**, 371 (1977).
4. A. R. Ubbelohde, Proc. R. Soc. London, Ser. A **327**, 289 (1972).
5. A. R. Ubbelohde, Synth. Met. **1**, 13 (1979).
6. D. T. Morelli and C. Uher, Phys. Rev. B **27**, 2477 (1983).
7. E. McRae and J. F. Mareche, J. Mater. Res. **3** (1), 75 (1988).
8. A. F. Ioffe and A. R. Regel, Prog. Semicond. **4**, 237 (1960).
9. K. Sugihara, Phys. Rev. B **29**, 5872 (1984).
10. S. Shimamura, Synth. Met. **12** (1–2), 365 (1985).
11. K. Sugihara, Phys. Rev. B **37**, 4752 (1988).
12. K. Matsubara, K. Sugihara, and T. Tsuzuku, Phys. Rev. B **41**, 969 (1990).
13. K. Sugihara, J. Phys. Soc. Jpn. **62**, 624 (1993).
14. M. Suzuki, C. Lee, I. S. Suzuki, *et al.*, Phys. Rev. B **54**, 17128 (1996).
15. R. S. Markiewicz, Solid State Commun. **57** (4), 237 (1986).
16. H. Zaleski and W. R. Datars, Phys. Rev. B **35**, 7690 (1987).
17. R. S. Markiewicz, Phys. Rev. B **37**, 6453 (1988).
18. D. E. Nixon, G. S. Parry, and A. R. Ubbelohde, Proc. R. Soc. London, Ser. A **291**, 324 (1966).
19. E. J. Samuelsen, R. Moret, H. Fuzellier, *et al.*, Phys. Rev. B **32**, 417 (1985).
20. L. A. Pendrys, C. Zeller, and F. L. Vogel, J. Mater. Sci. **15**, 2103 (1980).
21. H. Kodera, J. Phys. Soc. Jpn. **28**, 89 (1970).
22. M. Saint-Jean and E. McRae, Phys. Rev. B **43**, 3969 (1991).
23. A. M. Ziatdinov and N. M. Mishchenko, Solid State Commun. **97**, 1085 (1996).
24. R. A. Cowley and A. J. Bruce, J. Phys. C **11**, 3577 (1978).
25. P. Bak, Rep. Prog. Phys. **45**, 587 (1982).
26. F. Batallan, I. Rosenman, A. Magerl, and H. Fuzellier, Phys. Rev. B **32**, 4810 (1985).
27. A. M. Ziatdinov and Yu. M. Nikolenko, Fiz. Tverd. Tela (S.-Peterburg) **35**, 2259 (1993) [Phys. Solid State **35**, 1122 (1993)].
28. A. M. Ziatdinov and N. M. Mishchenko, in *Science and Technology of Carbon, Ext. Abstracts, France, Strasbourg, 1998*, Ed. by Eurocarbon Group, Vol. I, p. 775.
29. C. Uher and D. T. Morelli, Mat. Res. Soc. **20**, 163 (1983).
30. H. Homma and R. Clarke, Phys. Rev. B **31**, 5865 (1985).
31. F. L. Vogel, H. Fuzellier, C. Zeller, and E. J. McRae, Carbon **17**, 255 (1979).
32. E. Méndez, T. C. Chieu, N. Kambe, and M. S. Dresselhaus, Solid State Commun. **33**, 837 (1980).
33. W. R. Datars, P. K. Ummat, H. Aoki, and S. Uji, Phys. Rev. B **48**, 18174 (1993).
34. V. A. Kulbachinskii, S. G. Ionov, S. A. Lapin, *et al.*, Mol. Cryst. Liq. Cryst. **245**, 31 (1994).
35. V. A. Kulbachinskii, S. G. Ionov, S. A. Lapin, and V. V. Avdeev, J. Phys. (Paris) **2**, 1941 (1992).
36. G. Wang, P. K. Ummat, and W. R. Datars, Phys. Rev. B **47**, 3864 (1993).
37. T. R. Chien, D. Marchesan, P. K. Ummat, and W. R. Datars, J. Phys.: Condens. Mater **6**, 3031 (1994).

Translated by O. Borovik-Romanova

Physics of the Solid State, Vol. 42, No. 7, 2000, pp. 1192–1195. Translated from Fizika Tverdogo Tela, Vol. 42, No. 7, 2000, pp. 1158–1160.

METALS AND SUPERCONDUCTORS

Evaluation of the Influence of Dissolved Hydrogen on Mechanical Properties of Palladium

Yu. K. Tovbin and E. V. Votyakov

State Scientific Center of the Russian Federation, Karpov Research Institute of Physical Chemistry, ul. Vorontsovo Pole 10, Moscow, 103064 Russia

e-mail: tovbin@cc.nifhi.ac.ru

Received December 7, 1999

Abstract—Based on the averaged atomic model and experimental data on the variations in the unit cell parameter and thermodynamic characteristics of the Pd–H binary alloy (the enthalpy of sublimation of palladium, hydrogen sorption, and phase separation in the Pd–H system), the variation in the shear modulus of palladium is estimated as a function of the concentration of dissolved hydrogen. The bulk compression and Young's moduli are also evaluated. The model provides a qualitative agreement with the available data on mechanical moduli. *© 2000 MAIK "Nauka/Interperiodica".*

In the hydrogen–palladium system, the local concentration of interstitial hydrogen θ_H can vary over a wide range from zero to one hydrogen atom per metal atom [1–4]. The interstitial hydrogen causes the local deformation of the lattice and, as a consequence, the variation in mechanical properties of the metal. This fact is important for palladium membranes, in which a large concentration gradient of hydrogen can be realized. In addition, the phase state of the metal can change at temperatures below $T \sim 565$ K: the α and β phases are formed at a low and high content of interstitial hydrogen, respectively. It is assumed that the variation in mechanical properties is responsible for the presence of the hysteresis-type effects in flow characteristics of membranes, irreproducibility of the experimental data, and an increase in the hydrogen embrittlement of palladium [1–4]. A strong influence of interstitial hydrogen on the mechanical, sorption, and transport properties of palladium membranes is confirmed by numerous investigations [1–4]. However, these measurements were nonsystematic. Specifically, the experimental data on the influence of the concentration of interstitial hydrogen on the mechanical properties of palladium are actually unavailable. In this work, we proposed a method for theoretically evaluating the influence of dissolved hydrogen concentration on the mechanical properties of palladium. The method is based on the thermodynamic characteristics and concentration dependence of the unit cell parameter for the Pd–H alloy.

The mechanical moduli of a solid can be expressed in terms of elastic constants, which are related to the potentials of interatomic interactions [5, 6]. The potential energy of the system can be represented in the form: $U = U_{MM} + U_{MH} + U_{HH}$, where the first term describes the metal–metal interactions, the second term accounts for the metal–hydrogen interactions, and the third term characterizes the hydrogen–hydrogen interactions. Although the question regarding the form of potential functions for interstitials in metals was repeatedly discussed in the literature [7–12], it is still an open question. For this reason, in order to perform qualitative evaluations, we introduce the following simplifications.

(i) The contribution of vacancies in the metal lattice can be neglected at relatively low temperatures [5].

(ii) We assume that the pair interactions of all the components are described by the Lennard-Jones potential: $\varphi_{ij}(r_{ij}) = 4\varepsilon_{ij}[(\sigma_{ij}/r_{ij})^{12} - (\sigma_{ij}/r_{ij})^6]$, where ε_{ij} and σ_{ij} are the parameters of the corresponding pair interaction potentials. Summarizing the contributions of the interactions between atoms *ij* over the lattice, we obtain the modified pair Lennard-Jones potential, which can be written as $\varphi_{ij}(r_{ij}) = 4\varepsilon_{ij}[S_{12}^{ij}(\sigma_{ij}/r_{ij})^{12} - S_6^{ij}(\sigma_{ij}/r_{ij})^6]$, where $S_{12,6}^{ij}$ allow for contributions from the second nearest neighbors and more distant ones of the atoms [13].

(iii) We use the mean values of the unit cell parameter for the face-centered cubic (fcc) metal and reduce the problem to the effective "single-atom" lattice by assuming that hydrogen atoms make the averaged contribution to the potential curve describing the palladium–palladium interactions.

The potential energy of the system, which is accounted for by the palladium atom (located in the

1063-7834/00/4207-1192$20.00

site f), can be written as

$$U_f = z_f\varepsilon_{\text{eff}} = \sum_{q\in z_f}\varphi_{\text{MM}}(r_{fg}) + \sum_{h\in z_f}\theta_h^{\text{H}}\varphi_{\text{MH}}(r_{fh}) + \sum_{h\in z_f}\sum_{g\in z_h}\theta_{hg}^{\text{HH}}\varphi_{\text{HH}}(r_{hg})/2, \quad (1)$$

where z_f nearest neighbors in the metal lattice surrounding the site f are numbered by the g index in the first summand, z_h nearest neighbors in the interstices surrounding the site f are numbered by the h index in the second and third summands, z_f nearest interstices surrounding the interstice h (for the fcc structure, $z_h = z_f/2$) are numbered by the g index in the last summand, and ε_{eff} is the effective metal–metal potential.

Averaging the local distributions of hydrogen atoms in the neighborhood of the labeled metal atom, we introduce the mean concentrations of hydrogen $\theta_{\text{H}} = \sum_{h\in z_f}\theta_h^{\text{H}}/z_f$. In this case, the second summand in (1) can be written as $z_h\theta_{\text{H}}\varphi_{\text{MH}}(r_{fh})$, and the third summand can be rewritten as $z_f z_h\theta_{\text{HH}}\varphi_{\text{HH}}(r_{hg})/2$. Here, θ_{hg}^{HH} is the probability of occurring the hydrogen atoms in the neighboring interstices. The functional relation $\theta_{\text{HH}}(\theta_{\text{H}})$ is known in concrete approximations. These are the Bethe (quasi-chemical) approximation, which takes into account the short-range correlation effects, and the Gorsky–Bragg–Williams (GBW) (mean-field) approximation, which does not take into account these correlations [14, 15]. With allowance made for the aforesaid, we have

$$\varepsilon_{\text{eff}} = 4(\varepsilon_{\text{MM}}\Psi_{\text{MM}} + \theta_{\text{H}}\varepsilon_{\text{MH}}\Psi_{\text{MH}}/2 + z_h\theta_{\text{HH}}\varepsilon_{\text{HH}}\Psi_{\text{HH}}/2), \quad (2)$$

where $\Psi_{ij} = S_{12}^{ij}(\sigma_{ij}/r_{ij})^{12} - S_6^{ij}(\sigma_{ij}/r_{ij})^6$. The functions $S_{12,6}^{ij}$ for atoms ij = MH (index 1) and HH (index 2) take the form: $S_{n,m}^{1,2} = 1 + d_{n,m}^{1,2}t_{\text{HH}}$, where $t_{\text{HH}} = \theta_{hg}^{\text{HH}}/\theta_{\text{HH}}$, $d_6^1 = 0.07$, $d_6^2 = 0.2$, $d_{12}^1 = 0.002$, and $d_{12}^2 = 0.011$ (for a pair of atoms ij = MM, $S_{12}^{\text{MM}} = 1.011$ and $S_6^{\text{MM}} = 1.20$). The minimum of potential (2) corresponds to the distance between the neighboring palladium atoms $r_{\min}(\theta_{\text{H}})$, which depends on the hydrogen concentration.

The fcc structure of the Pd–H solid solution has three independent elastic constants C_{11}, C_{12}, and C_{44}. Reducing our consideration to the isotropic model of the structure, we found that the relation between the shear modulus and elastic constants is given by the formula $C_s = C_{44}$ [6]. The elastic constants, in turn, can be expressed through the coefficient of elasticity M of the metal–metal bonds as $C_{11} = 2M/r_{\min}(\theta_{\text{H}})$ and $C_{12} = C_{44} = M/r_{\min}(\theta_{\text{H}})$, where M (under the assumption that palladium atoms can be displaced in any direction with equal probability) is described by the parameters of the interparticle potential (2) as $M = 48z_f\varepsilon_{\text{eff}}(\theta_{\text{H}})/[r_{\min}(\theta_{\text{H}})]^2$.

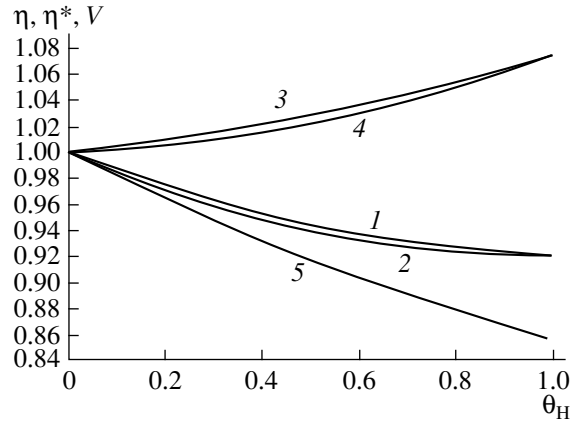

Concentration dependences of the relative change in the shear modulus $\eta(\theta_{\text{H}})$ for (*1*, *2*) the equilibrium state of the system, (*3*, *4*) the nonequilibrium state of the system $\eta^*(\theta_{\text{H}})$, and (*5*) the relative change in the volume per palladium atom $V(\theta_{\text{H}})$ at 300 K. Curves *1* and *3* are calculated in the Bethe approximation, and curves *2* and *4*, in the GBW approximation.

In order to evaluate the influence of the concentration of interstitial hydrogen, we consider the ratio $\eta(\theta_{\text{H}}) = G_s(\theta_{\text{H}})/G_s(\theta_{\text{H}} = 0) = \varepsilon_{\text{eff}}(\theta_{\text{H}})V/\varepsilon_{\text{eff}}(\theta_{\text{H}} = 0)$, where $V(\theta_{\text{H}}) = [r_{\min}(\theta_{\text{H}} = 0)/r_{\min}(\theta_{\text{H}})]^3$. Let us estimate all the energy parameters ε_{ij} in equation (2) from the available data on the enthalpies of the corresponding processes. The $r_{\min}(\theta_{\text{H}})$ dependence is considered to be known from independent experimental measurements.

The ε_{MM} parameter can be determined from the data on sublimation of pure palladium $\Delta H_{\text{subl}} = z_f\varepsilon_{\text{MM}}$ ($\Delta H_{\text{subl}} \approx 90$ kcal/mol; however, there are rather large discrepancies in the available data: 93 [16], 89 [17], 85 [12], and even 110 [18] kcal/mol). The ε_{MH} parameter is related to the dissolution (sorption) of the hydrogen atoms in a pure metal with the formation of the α phase. The experimental value of enthalpy for this process is equal to approximately 4.62 kcal/mol [19] ($\Delta H_{\text{sor}} = z_h\varepsilon_{\text{MH}}$). The phase separation of the alloy, followed by the formation of the two-phase α–β system, occurs at equilibrium conditions with an increase in the hydrogen concentration. In terms of thermodynamics, this process can be treated [19] as the reaction: $2/\{\theta_{\min}(\beta) - \theta_{\max}(\alpha)\}\text{PdH}_\beta = 2/\{\theta_{\min}(\beta) - \theta_{\max}(\alpha)\}\text{PdH}_\alpha + H_2$ with the enthalpy of reaction $\Delta H_R = 9.4$–9.8 kcal/mol. The two-phase region is located between $\theta_{\max}(\alpha)$ and $\theta_{\min}(\beta)$. In the case of the pair potential of interatomic interaction, by analogy with [20], it is possible to derive the heat of sorption under conditions of phase separation $\Delta H_R = z_f\varepsilon_{\text{HH}}/2$. Let us use this relationship to estimate the ε_{HH} quantity.

According to [19], the following estimates of the changes in the unit cell parameter $r_{min}(\theta_H)$ at $0 \le \theta_H \le 1$ are obtained for different phases: $r_{min}(\theta_H) = 0.3890 + 0.05\theta_H$ nm for the α phase and $r_{min}(\theta_H) = 0.3915 + 0.018\theta_H$ nm for the β phase. The $r_{min}(\theta_H)$ quantity for the two-phase region was calculated with due regard for the "lever" rule. The ratio of the specific volumes $V(\theta_H)$ (per palladium atom) for the complete saturation of the metal by hydrogen is 0.863.

The figure shows the concentration dependences of V (curve *5*) and η, which are calculated in the Bethe (curve *1*) and GBW (curve *2*) approximations.

The proposed model also allows us to estimate the shear modulus in the case of nonequilibrium states of isolated local regions of the α phase, in which palladium cannot transform into the β phase because of the external compression [8]. By assuming $V \sim 1$, we have $\eta^*(\theta_H) \approx \varepsilon_{eff}(\theta_H)/\varepsilon_{eff}(\theta_H = 0)$. The dependences $\eta^*(\theta_H)$ are also presented in the figure. The η^* and η curves variously change with respect to the line $\eta = 1$ with an increase in the interstitial hydrogen concentration. In other words, the shear modulus for a nonequilibrium state can differ drastically from its equilibrium value. For the complete saturation of the α phase by hydrogen in the compressed state, $\eta^*(1) = 1.075$.

Within the model considered, the bulk compression and Young's moduli are directly proportional to the shear modulus. The bulk compression modulus, according to [6], can be expressed in the form $G_c(\theta_H) = 4M/3r_{min}(\theta_H) = 4G_s(\theta_H)/3$, and the Young modulus $H(\theta_H)$ is determined by the standard expression [21]: $H(\theta_H) = 9G_c(\theta_H)G_s(\theta_H)/[3G_c(\theta_H) + G_s(\theta_H)] = 2.4G_s(\theta_H)$.

The model proposed qualitatively agrees with the very scarce reliable experimental data on the influence of dissolved hydrogen on the mechanical moduli. The model adequately predicts a decrease in the Young and shear moduli upon saturation of the metal by hydrogen over a wide concentration range. At low hydrogen concentrations, the model gives a linear decrease in the Young modulus, as it was found in [22]. Specifically, up to $\theta_H \sim 0.014$, the Young modulus decreases by 0.65 (in the Bethe approximation) and 0.70% (in the GBW approximation), whereas the experiment [22] gives the decrease by 1.1%. For $\theta_H = 0.63$, the model predicts a decrease in the shear modulus by 6.3 (in the Bethe approximation) and 7.0% (in the GBW approximation), whereas the experiment [23] gives the decrease of 4%. Moreover, the estimates obtained in the GBW approximation at $\theta_H \sim 0.6$ in [24] led these authors to the conclusion that, at high hydrogen concentrations, when the effects of interactions between interstitial atoms become significant, the increase in the dynamic Young modulus in the Pd–H system should reach 8%. With the proviso that the dynamic character of the Young modulus stems from the nonequilibrium state of the metal, this conclusion is in a good agreement with an increase in η^* by 7.4%.

Thus, the model proposed permits one to establish the interrelation between independent experimental data and gives reasonable estimates for the mechanical moduli without invoking additional fitting parameters. In the framework of this model, we can discard the direct use of the experimental dependence $r_{min}(\theta_H)$. Then, by varying the parameters σ_{MH} and σ_{HH}, we can quantitatively describe the $r_{min}(\theta_H)$ dependence and improve agreement between the model and the experimental values of mechanical moduli. However, in order to obtain the completely self-consistent parameters for the potentials of the model, the phase separation curve in the phase diagram of the Pd–H system should be preliminarily described.

ACKNOWLEDGMENTS

This work was supported by the Russian Foundation for Basic Research, project no. 97-03-33197a.

REFERENCES

1. *Hydrogen in Metals*, Ed. by G. Alefeld and J. Voekl (Springer-Verlag, New York, 1978; Mir, Moscow, 1981), Vols. I and II.
2. *Interaction of Hydrogen with Metals*, Ed. by A. P. Zakharov (Nauka, Moscow, 1987).
3. *Metals and Alloys As Membrane Catalysts*, Ed. by V. M. Gryaznov and E. I. Klabunovskiĭ (Nauka, Moscow, 1981).
4. P. V. Gel'd, R. A. Ryabov, and L. P. Mokhracheva, *Hydrogen and Physical Properties of Metals and Alloys* (Nauka, Moscow, 1985).
5. A. M. Kosevich, *Physical Mechanics of Real Crystals* (Naukova Dumka, Kiev, 1981).
6. G. Leibfried, in *Handbuch der Physik*, Ed. by S. Flugge (Springer-Verlag, Berlin, 1955; Fizmatgiz, Moscow, 1963), Vol. 7, Part 1.
7. H. Brodowsky, Ber. Bunsen–Ges. Phys. Chem. **72**, 1055 (1968).
8. A. G. Khachaturyan, *The Theory of Phase Transformations and the Structure of Solid Solutions* (Nauka, Moscow, 1974).
9. F. Wagner, in *Hydrogen in Metals*, Ed. by G. Alefeld and J. Voekl (Springer-Verlag, New York, 1978; Mir, Moscow, 1981), Vol. 1, p. 16.
10. O. P. Burmistrova, N. I. Kulikov, and N. D. Potekhina, in *Interaction of Hydrogen with Metals*, Ed. by A. P. Zakharov (Nauka, Moscow, 1987), p. 5.
11. N. I. Kulikov, in *Interaction of Hydrogen with Metals*, Ed. by A. P. Zakharov (Nauka, Moscow, 1987), p. 61.
12. M. A. Shtremel', *Strength of Alloys* (Mosk. Inst. Stali i Splavov, Moscow, 1999), Chap. 1, p. 383.
13. V. M. Danilenko, *Models of Real Crystals* (Naukova Dumka, Kiev, 1983).
14. M. A. Krivoglaz and A. A. Smirnov, *The Theory of Order–Disorder in Alloys* (Fizmatgiz, Moscow, 1958; Macdonald, London, 1964).

15. Yu. K. Tovbin, *The Theory of Physicochemical Processes at the Gas–Solid Interface* (Nauka, Moscow, 1990).
16. *Handbook of Chemist* (Khimiya, Leningrad, 1971), Vol. 1.
17. *Handbook of Elements. Physical Properties* (Metallurgiya, Moscow, 1976), Chap. 1.
18. G. S. Zhdanov, *Crystal Physics* (Mosk. Gos. Univ., Moscow, 1961; Oliver and Boyd, Edinburgh, 1965).
19. E. Wicke and H. Brodowsky, in *Hydrogen in Metals*, Ed. by G. Alefeld and J. Voekl (Springer-Verlag, New York, 1978; Mir, Moscow, 1981), Vol. 2, p. 91.
20. R. H. van Dongen and J. C. P. Broeckhaff, Surf. Sci. **18**, 462 (1969).
21. L. D. Landau and E. M. Lifshitz, *Course of Theoretical Physics. Vol. 7. Theory of Elasticity* (Nauka, Moscow, 1982; Pergamon Press, New York, 1986).
22. R. J. Farrago and R. B. McLellan, J. Phys. Chem. Solids **39**, 781 (1978).
23. J. M. Rove, J. Phys. F **8**, L7 (1978).
24. L. I. Smirnov and V. A. Gol'tsov, Fiz. Met. Metalloved. **84** (6), 47 (1997).

Translated by N. Korovin

Physics of the Solid State, Vol. 42, No. 7, 2000, pp. 1196–1198. Translated from Fizika Tverdogo Tela, Vol. 42, No. 7, 2000, pp. 1161–1163.

METALS AND SUPERCONDUCTORS

Investigation of the Electronic Structure of the Fe–Si Systems by X-ray Photoelectron Spectroscopy

I. N. Shabanova, N. S. Terebova, and V. I. Kormilets

Physicotechnical Institute, Ural Division, Russian Academy of Sciences, ul. Kirova 132, Izhevsk, 426001 Russia

e-mail: xps@fti.udmurtia.su

Received December 16, 1999

Abstract—The paper reports the results of investigations of the valence bands for the Fe–Si alloys containing 50 and 25 at. % Si and the alloys at a metalloid content of 2–20 at. %. The x-ray photoelectron spectra of the valence bands are compared with the band calculations of the total and partial densities of states for the stoichiometric alloys by the tight-binding linearized muffin-tin orbital method. © *2000 MAIK "Nauka/Interperiodica".*

1. INTRODUCTION

Fe–Si alloys, by virtue of a great variety of physical properties, have been extensively used in various fields of modern technology [1, 2]. The electronic structure of alloys, which is eventually responsible for their characteristics, still remains unclear.

The purpose of the present work was to investigate the electronic structure of the Fe–Si alloys at a silicon content of 2–50 at. % and to elucidate how the variation in the number of silicon atoms surrounding the iron atom affects the participation of the Fe *d* electrons in the Fe–Si bond.

In this work, we studied the Fe–Si system at a metalloid content below 20 at. % and samples containing 25 and 50 at. % Si. The last two samples represent the ordered compounds with the stoichiometric compositions Fe_3Si and FeSi, respectively.

2. EXPERIMENTAL TECHNIQUE

The x-ray photoelectron spectra (XPS) were recorded on an x-ray magnetic spectrometer [3]. The influence of the technique of cleaning the surface of impurities on the silicon content in a near-surface layer was investigated in [4]. The applied technique included heating, etching by argon ions with an energy of 500 eV, and mechanical cleaning in a spectrometer chamber. It was demonstrated that ion etching to a depth of 150 Å decreases the silicon line intensity related to the total intensity of the iron and silicon lines (proportional to the silicon content on the sample surface) by 20–30% compared to the samples mechanically cleaned under vacuum. In order to obtain a clean surface of samples, the mechanical cleaning of the samples was carried out immediately in the spectrometer chamber. This treatment did not change the surface composition. The mechanical cleaning was performed with a device that provided the removal of surface layers of the sample with a tungsten brush. The absence of contamination on the sample surface was checked against the x-ray photoelectron spectra of the Fe2*p*, O1*s*, and C1*s* core levels. In order to improve the spectral resolution and contrast range, we used the procedure described in [4]. As a result, the contrast range of a fine structure in the spectra of the valence bands was improved to a large extent. The band calculations of the total and partial densities of states (DOS) for the components of the alloys of stoichiometric compositions were carried out by the tight-binding linearized muffin-tin orbital (TBLMTO) method.

The samples were prepared by alloying the iron ingots (99.99% pure) and silicon single crystals (at least 99.99% pure) in a vacuum furnace.

3. RESULTS AND DISCUSSION

As was shown earlier [5], in the case of hybridization of the *d*(Fe) and *p*(X) electrons, the form of the alloy valence band reflects the Fe *d* electron density distribution, because the photoionization cross-section of the *d* electrons is several tens of times greater than that of the *p* electrons. In this case, the structure of the *p* electron density distribution of the second component manifests itself in the form of the alloy valence band; i.e., the structure of the alloy valence band is similar to the structure of the valence band of the second component.

Let us consider the FeSi alloy (Fig. 1). A comparison of the calculations of the total and partial densities of the *d* and *p* states and the x-ray photoelectron spectra of the valence bands of FeSi shows a good agreement in the position and relative intensity of maxima in the curves of fine structure. The exception is the region near E_f. In this region, the higher intensity in the *d* DOS

1063-7834/00/4207-1196$20.00 © 2000 MAIK "Nauka/Interperiodica"

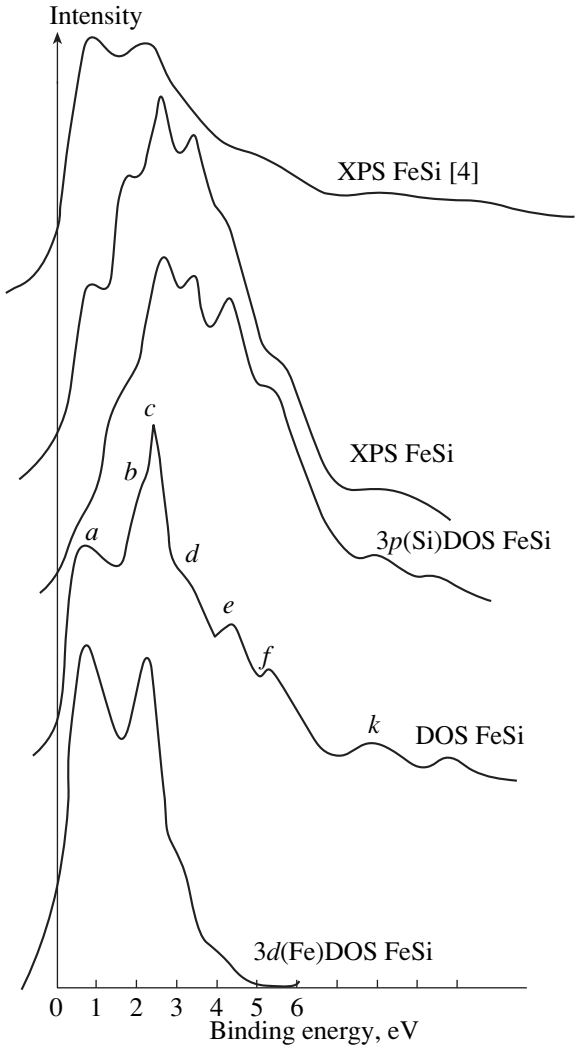

Fig. 1. X-ray photoelectron spectra of the valence bands of the FeSi alloy and the results of the TBLMTO calculations of the total and partial densities of states for the alloy.

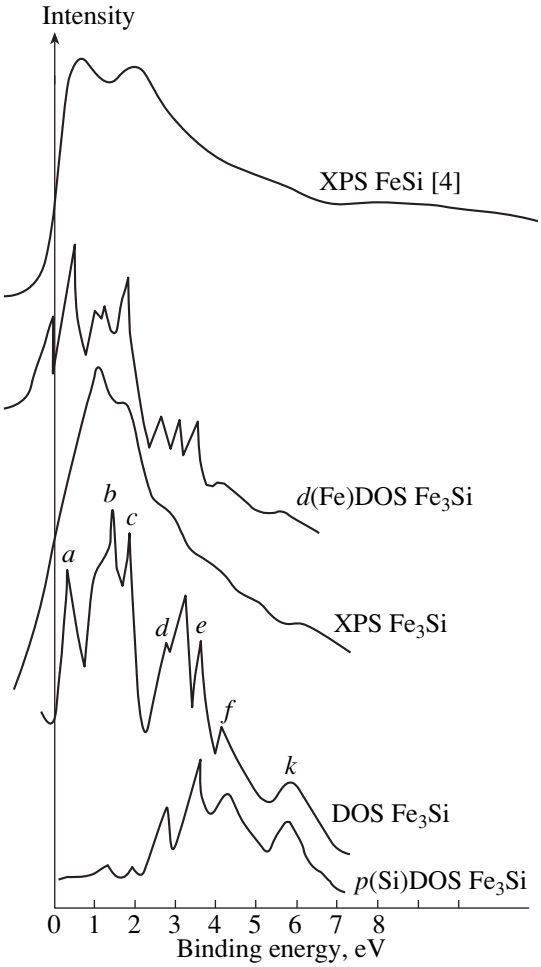

Fig. 2. X-ray photoelectron spectra of the valence bands of the Fe_3Si alloy and the results of the TBLMTO calculations of the total and partial densities of states for the alloy.

and in the total DOS indicates that, in addition to the hybridization of the *d* and *p* states, there is a contribution of the Fe *d* states not involved in the Fe–Si bond. It is our opinion that the difference between the x-ray photoelectron spectrum of the FeSi valence band and the spectrum obtained in [6] stems from the difference in methods of cleaning the sample surface.

Note that the theoretical calculation suggests the presence of the energy gap of width 0.1 eV. Since the contribution of the Fe *d* electrons to the density of states at the valence band top and conduction band bottom is dominant, the energy gap in the valence band of FeSi appears as the result of splitting the Fe *d* band into two subbands. The fact that the structure of the valence band spectrum is consistent with the band calculations of the partial densities of the *d*(Fe) and *p*(Si) states indicates their substantial hybridization upon the formation of the Fe–Si bond. This is also evidenced by the appearance of the energy gap in the *d* states, which are characteristic of silicon. This is apparently due to the fact that the Fe–Si interatomic distance in the FeSi cubic structure (2.24 Å) is considerably less than that between identical atoms Fe–Fe (2.75 Å) and Si–Si (2.27 Å).

For the Fe_3Si alloy (Fig. 2), the curves of band calculations and the x-ray photoelectron spectra of the valence band change in their structure. The intensity maximum is shifted to E_f by 1–1.3 eV. A fine structure in the band calculations of the total density of states agrees closely with the experimental spectrum of the valence band. We compared these curves with calculations of the partial densities of the *d*(Fe) and *p*(Si) states in Fe_3Si. It is seen that the contribution of the Fe *d* electrons, which do not participate in the Fe–Si bond, remains dominant in the vicinity of E_f (maxima *a*, *b*, and *c*). This leads to the shift of maxima in the curves

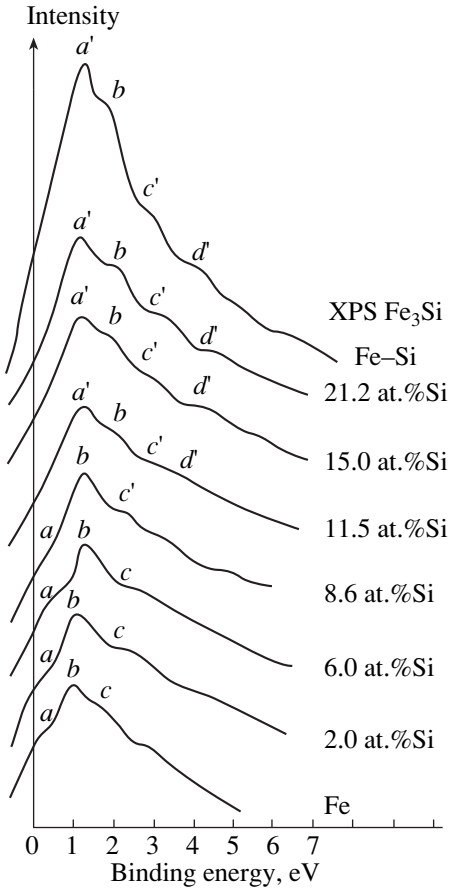

Fig. 3. X-ray photoelectron spectra of the valence bands of the Fe–Si alloys.

of densities of states toward the E_f region. A considerable weakening of the hybridization of the *d*(Fe) and *p*(Si) states can be explained by the increase in the Fe–Si distance (2.43 Å) compared to the FeSi alloy.

With a further decrease in the silicon content in the Fe–Si system (21.2, 20.0, 15.0, and 11.5 at. %), the valence band structure remains similar to the structure of the experimental spectrum of the valence band for Fe_3Si (Fig. 3). This is apparently caused by the fact that the number of silicon atoms surrounding the iron atoms remains unchanged. The structure of the valence band spectra drastically changes with a decrease in the silicon content below 10 at. %. For these systems, the structure of valence bands resembles the valence band spectrum of pure iron. In this case, the hybridization of the *d*(Fe) and *p*(Si) states is not observed, and the Fe–Si bond is realized solely through the hybridization of the *p* states of iron and the *p* states of silicon.

Thus, the *d* electrons of iron atoms can participate in the hybridized bond only provided that a certain number of atoms of the second component (Si) are involved in the environment of the iron atom. This number is defined by the spatial overlapping of the wave functions of valence electrons belonging to both components of the alloy. This constraint is met at a silicon content of more than 10 at. %, when three silicon atom are included in the environment of the iron atom.

REFERENCES

1. P. V. Gel'd and R. A. Sidorenko, *Silicides of Transition Metals of the Fourth Period* (Metallurgiya, Moscow, 1971).
2. G. V. Samsonov and I. M. Vinitskiĭ, *Handbook of Refractory Compounds* (Metallurgiya, Moscow, 1976; Plenum Press, New York, 1980).
3. I. N. Shabanova, V. P. Sapozhnikov, and V. Ya. Bayankin, Prib. Tekh. Éksp., No. 5, 38 (1975).
4. E. P. Elsukov, L. V. Dobysheva, and I. N. Shabanova, Izv. Akad. Nauk SSSR, Met., No. 3, 170 (1988).
5. I. N. Shabanova, Fiz. Met. Metalloved. **79** (6), 79 (1995).
6. V. R. Galahov, E. Z. Kurmaev, V. M. Cherkashenko, *et al.*, J. Phys.: Condens. Matter **7**, 5529 (1995).

Translated by N. Korovin

Physics of the Solid State, Vol. 42, No. 7, 2000, pp. 1199–1203. Translated from Fizika Tverdogo Tela, Vol. 42, No. 7, 2000, pp. 1164–1168.

METALS AND SUPERCONDUCTORS

Peculiarities of the Electronic Structure of Yb, In, Ag, and Cu in the Heavy-Fermion System $YbIn_{1-x}Ag_xCu_4$

V. A. Shaburov*, A. E. Sovestnov*, Yu. P. Smirnov*, A. V. Tyunis*, and A. V. Golubkov**

**Konstantinov Institute of Nuclear Physics, Russian Academy of Sciences, Gatchina, St. Petersburg, 188350 Russia*
e-mail: asovest@hep486.pnpi.spb.ru

***Ioffe Physicotechnical Institute, Russian Academy of Sciences, Politekhnicheskaya ul. 26, St. Petersburg, 194021 Russia*

Received December 23, 1999

Abstract—The method of x-ray spectral line displacement is used for studying the electronic structure, i.e., the population of the 4*f* shell of Yb, 5*s* shells of In and Ag, and 4*s* shell of Cu, in the $YbIn_{1-x}Ag_xCu_4$ heavy-fermion system ($0 \le x \le 1$, $T = 300$ K; $T = 77$, 300, and 1000 K for $YbIn_{0.7}Ag_{0.3}Cu_4$). It is shown that Yb is in a state with fractional valence whose value is independent of x (or on the type of the partner, i.e., In and Ag) in the entire range of compositions and is equal to $\bar{m} = 2.91 \pm 0.01$ at $T = 300$ K. An increase in the population of the *s* states of In, Ag, and Cu (as compared to metals) is observed: $\overline{\Delta n_s}$(In) $= 0.65 \pm 0.05$ el/at, $\overline{\Delta n_s}$(Ag) $= 0.71 \pm 0.09$ el/at, and $\overline{\Delta n_s}$(Cu) $= 0.08 \pm 0.02$ el/at. A practically linear decrease in the valence of Yb to the value $m(T = 1000\text{ K}) = 2.81 \pm 0.02$ is observed in $YbIn_{0.7}Ag_{0.3}Cu_4$ upon an increase in temperature from $T = 77$ to 1000 K. © *2000 MAIK "Nauka/Interperiodica".*

An analysis of microscopic and macroscopic properties reveals that $YbIn_{1-x}Ag_xCu_4$ is a system with an intermediate (fluctuating) valence (IV); thus, the "increase in the mass" of electrons in it can be associated with the emergence of a 4*f* electron at the Fermi level (delocalization). The effect of an increase in the population of the *s* states of Yb partners is due to the 4*f* electron of Yb being hybridized upon a transition to an IV state (mainly) with 5*s* electrons of the neighboring atoms of In, Ag, and (to a smaller extent) Cu, but not with the Yb electrons. The total increase in the population of these states $\overline{\Delta n_\Sigma}$(In, Ag, Cu) $= 1.0 \pm 0.1$ virtually coincides with the observed decrease in the population of the 4*f* shell of Yb upon a transition to the IV state: $\Delta n_{4f} = 0.91 \pm 0.01$.

"Heavy"-fermion systems (HFSs) belong to a specific class of intermetallic compounds based on rare-earth and actinide elements [1]. The main indication of an affiliation to HFSs is an anomalously high value of the electronic specific heat coefficient γ, which suggests the presence of a very narrow energy band with a high density of states near the Fermi level in such systems. The fact that all known HFSs are formed on the basis of lanthanides and actinides whose *f* levels are quite close to the Fermi level, as in systems with an intermediate (fluctuating) valence (see, for example, [2]), indicates a significance of atomic properties of the *f* shells of these elements in the formation of a heavy-fermion (HF) state.

The mechanism of the emergence of a "heavy" electron band at the Fermi level has not been completely established. It is not clear whether it is connected with the emergence of the *f* level at the Fermi level (in this case, *f* electrons become delocalized, and the band width is determined directly by the *f-sd* hybridization [3]) or with collective processes, where the *f* level is still relatively deep, and the properties of electrons near the Fermi level can be determined by collective effects of the type of the Kondo effect, i.e., by the resonance scattering of conduction electrons at localized magnetic moments of *f* centers [4]. If the "increase" in the conduction electron mass occurs as a result of the "emergence" of the *f* level at the Fermi level, the states with the f^n and $f^{n-1} + e$ configurations (*e* is the conduction electron) become degenerate, and a state with a fractional valence is realized. In the case of the formation of a HFS due to the scattering of conduction electrons at localized magnetic moments of *f* centers, *f* electrons lie below the Fermi level, and a state with an integral valence is realized. Thus, the fractional or integral valence of *f* atoms can be regarded as a manifestation of one of the two mechanisms of the HFS formation.

In the recent 3–5 years, the intermetallic compound $YbIn(Ag)Cu_4$ possessing unique physical (crystallographic, electrical, magnetic, thermal, spectral, etc.) properties have been studied intensely (see, for example, [5–9]).

1063-7834/00/4207-1199$20.00 © 2000 MAIK "Nauka/Interperiodica"

In $YbIn_{1-x}Ag_xCu_4$ ($x \approx 0$–0.3) under the atmospheric pressure and $T \approx 40$–80 K,[1] a first-order isostructural phase transition is observed, i.e., the crystal lattice parameter changes jumpwise by ≈0.13%, the lattice symmetry being preserved (the $AuBe_5$ type before and after the transition) [5]. The isomorphous Ce_γ–Ce_α phase transition in metallic cerium is an analog of such a transition. The electronic specific heat coefficient of $YbInCu_4$ $\gamma \approx 50$ mJ/(mol K^2) [6] is typical of systems with an intermediate valence and heavy-fermion systems (so-called light-fermion systems [10]). Doping with silver does not change the crystal lattice symmetry, but the value of γ increases and attains a value of ≈200–250 mJ/(mol K^2) for pure $YbAgCu_4$ [8, 9] (moderately heavy fermion system). At room temperature, the valence of Yb in $YbIn_{1-x}Ag_xCu_4$ varies from ~3 to ~2.9, according to various authors [5, 7, 9].

In the present work, the method of x-ray line displacement (XLD) (see, for example, [11, 12]) is used for studying the population of the 4*f* shell of Yb, 5*s* shells of In and Ag, and the 4*s* shell of Cu in $YbIn_{1-x}Ag_xCu_4$ ($0 \le x \le 1$, $T = 300$ K; $T = 77$, 300, and 1000 K for $YbIn_{0.7}Ag_{0.3}Cu_4$). The role of *f* atoms in the HFS mechanisms is more or less clear, while the electronic structure of the *s*(*p*) and *d* partners, as well as their contribution to this mechanism, has not been studied on the microscopic level to our knowledge.

1. DISCUSSION OF EXPERIMENTAL RESULTS

Polycrystalline samples of $YbIn_{1-x}Ag_xCu_4$ under investigation were synthesized from $YbInCu_4$ and $YbAgCu_4$, which in turn were obtained from stoichiometric mixtures of pure metals. Melting was carried out in an induction furnace in tantalum crucibles in a vacuum, followed by annealing at $T \approx 700$°C. The obtained samples contained only one phase and had a cubic lattice of the $AuBe_5$ type (*C*15*b* structure). The lattice parameter and its concentration dependence $a(x)$ at room temperature coincided with the available data [5, 9]. The composition x was controlled by the fluorescence analysis.

The displacements of the $K_{\alpha 1}$ lines of Yb, In, Ag, and Cu were measured on a specially designed crystal-diffraction spectrometer according to the Koshua technique. Fluorescent radiation is excited in the samples by an x-ray tube ($I = 10$ mA, $U = 140$ kV). The experimental setup and the measuring procedure are described in detail in our previous publications (see, for example, [11, 13]).

Ytterbium. Valence transformations in rare-earth elements are associated with a change in the number of 4*f* electrons. It was proved earlier (see, for example, [11, 12]) that such changes lead to anomalously large (as compared to the effects from 6*s*(*p*) and 5*d* electrons) variations in the energy (displacements) of emission *K* lines of the rare-earth element under investigation ($\left|\Delta E^{4f}_{K_{\alpha 1,2}}\right| \approx 500$–600 meV, $\left|\Delta E^{4f}_{K_{\beta 1,3}}\right| \approx 1500$–1700 meV, and $\left|\Delta E^{6s(p),\,5d}_{K_{\alpha,\beta}}\right| \approx 20$–80 meV). This make the XLD method quite sensitive for studying the mechanisms associated with the rearrangement of the 4*f* shell (change in the valence).

The experimental displacements of the $K_{\alpha 1}$ line of ytterbium in $YbIn_{1-x}Ag_xCu_4$ relative to the bivalent reference material (metallic Yb) are presented in the table. The sign and the anomalously large intensity of the effect unambiguously indicate a decrease in the number of 4*f* electrons (increase in the valence) of Yb. The difference in the number of 4*f* electrons of Yb in the compound and in the reference material was determined as $\Delta n_{4f}(x) = \Delta E(x)/\Delta E(Yb^{3+} - Yb^{2+})$, where $\Delta E(x)$ is the experimental displacement and $\Delta E(Yb^{3+} - Yb^{2+})$ is the calibration displacement corresponding to the displacement of the $K_{\alpha 1}$ line of Yb upon a decrease in the population of the 4*f* shell by unity. The valence of Yb in the sample under investigation is obviously $m = m_{ref} + \Delta n_{4f} = 2 + \Delta n_{4f}$. The calibration displacement was measured for the Yb_2O_3–Yb_{met} pair and was found to be $\Delta E(Yb^{3+} - Yb^{2+}) = -583 \pm 5$ meV. The concentration dependence of the Yb valence $m(x)$ at room temperature[2] is presented in Fig. 1, which shows that the Yb valence is virtually constant over the entire concentration range and has a fractional value $\bar{m}(0 \le x \le 1) = 2.91 \pm 0.01$.

The fractional value of the valence of an *f* atom is typical of the specific class of rare-earth and actinide compounds with the so-called intermediate (fluctuating) valence (IV). Macroscopic features typical of intermediate-valence compounds, i.e., the isostructural nature of the transition and temperature dependences of the magnetic susceptibility, electrical resistivity, and specific heat, etc., are also observed in Yb(In, Ag)Cu_4 [5, 8, 9].

The fractional valence $m = 2.91$ of Yb in Yb(In, Ag)Cu_4 observed by us differs insignificantly from the "conventional" value of 3 for Yb. However, such a small difference in the value of m leads to essentially different conclusions concerning the mechanism of a transition to the HF state (*f*–*sd* hybridization or collective processes of the Kondo effect type). The expected valence of Yb upon a transition to the IV state can be estimated quantitatively from a simple phenomenological model of interconfigurational fluctuations [14, 15]. The IV state is regarded as a resonance (fluctuations) between the initial $4f^n$ and the final $4f^{n-1} + e$ states of a 4*f* electron with close energies and is realized when the condition $|E_{ex}| = |E_n - E_{n-1}| \le \Gamma$ is satisfied, where

[1] The transition temperature depends on the preparation technology [poly(single)crystals, the excess (deficiency) of components in the compound etc.].

[2] The Yb valence is virtually constant and equal to $\bar{m}(x = 0, 0.3, 1) = 2.93 \pm 0.02$ at $T = 77$ K.

Experimental displacements of $K_{\alpha 1}$ lines of Yb, In, Ag, and Cu in $YbIn_{1-x}Ag_xCu_4$ and ionic compounds at room temperature

Compound	Displacements of $K_{\alpha 1}$ lines, meV			
	Yb	In	Ag	Cu
$YbIn_{1-x}Ag_xCu_4$				
$x = 0$	–544 ± 5	–28 ± 5	–	–1 ± 4
$x = 0.2$	–531 ± 6	–28 ± 5	–34 ± 9	–8 ± 3
$x = 0.3$	–530 ± 5	–25 ± 6	–54 ± 12	–10 ± 3
$x = 0.4$	–516 ± 6	–32 ± 5	–39 ± 10	–4 ± 2
$x = 0.6$	–527 ± 6	–49 ± 4	–45 ± 9	–13 ± 3
$x = 0.8$	–527 ± 5	–31 ± 7	–32 ± 9	–1 ± 4
$x = 1$	–528 ± 6	–	–53 ± 12	–2 ± 3
Yb_2O_3	–583 ± 5	–	–	–
$InCl_3$	–	133 ± 8	–	–
AgCl	–	–	122 ± 5 [24]	–
CuCl	–	–	–	164 ± 5

Note: Reference materials are metallic Yb, In, Ag, and Cu.

E_n and E_{n-1} are the energies of these configurations and Γ is the energy due to the Anderson hybridization of a 4*f* electron with the electrons from the conduction band (the width of the 4*f* energy level). The probability of an RE atom occupying the $4f^{n-1}$ state is determined by a Boltzmann-type distribution, taking into account the mixing interaction,

$$P(E_{n-1}) = \left[1 + \frac{M_n}{M_{n-1}} \exp\left(\frac{E_{ex}}{T + \Gamma}\right)\right]^{-1}, \qquad (1)$$

where M_n and M_{n-1} are the statistical weights of the f^n and the f^{n-1} states. Assuming that jumps of a 4*f* electron of Yb in Yb(In,Ag)Cu_4 from one site to another occur only among coinciding (degenerate) energy levels ($E_{ex} \approx 0$), which can be identified as an Anderson-type transition [16], we can find the probability of the Yb^{3+} state, which is determined in the present case only by the statistical weights of Yb^{2+} ($J = 0$, $M_n = 1$) and Yb^{3+} ($J = 7/2$, $M_{n-1} = 8$) states and is given by $P(Yb^{3+}) = M_{n-1}/(M_{n-1} + M_n) = 8/9$ corresponding to the value of $m = 2.89$, which matches well (for such a simple model) with our experimental value 2.91 ± 0.01.

The identification of the IV state only according to the value of *m* (integral or fractional) is not reliable. Fractional values of valence are also observed for compounds with a mixed valence, in which *f* atoms with a different valence coexist in the crystal lattice, but occupy nonequivalent positions. The fluctuational nature of the IV state (E_{ex}, Γ, and fluctuation time) can be identified unambiguously from the isomeric shift in the Mössbauer effect. Unfortunately, this method has a low sensitivity in the case of Yb, since the isomeric shift is an order of magnitude smaller than the line width [10].

High-temperature experiments can be regarded as indirect evidence of the IV state of Yb in Yb(In, Ag)Cu_4. The inset to Fig. 1 shows the temperature dependence of the Yb valence in $YbIn_{0.7}Ag_{0.3}Cu_4$. The value of *m* decreases upon an increase in temperature. Such a behavior can be explained if one assumes that E_{ex} is a function of temperature *T* (the theory does not rule out such a possibility in principle [17]). The effect of a decrease in the valence of rare-earth atoms at high temperatures in "classical" systems with an intermediate valence was observed by us earlier for a wide range of intermetallic compounds with cerium [18, 19] and europium in $EuRh_2$ and $EuCu_2Si_2$ [20] by the XLD

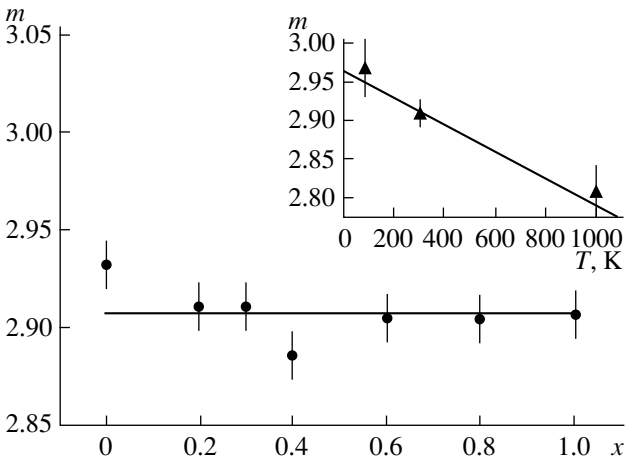

Fig. 1. Concentration dependence of the Yb valence *m* in $YbIn_{1-x}Ag_xCu_4$ at room temperature. The inset shows the temperature dependence of *m* for $YbIn_{0.7}Ag_{0.3}Cu_4$.

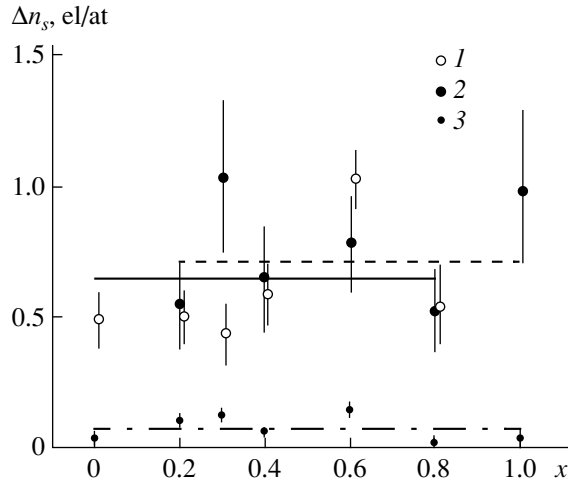

Fig. 2. Population of 5*s* states of In and Ag and 4*s* states of Cu as a function of composition (at room temperature): (*1*) solid line, (*2*) dashed line, and (*3*) dot-and-dash line are the data for In, Ag, and Cu, respectively.

method and in [21, 22] by the Mössbauer (NGR) technique in $EuCu_2Si_2$. The temperature dependences $m(T)$ demonstrate a fairly good agreement between the XLD and NGR spectroscopy data.

Thus, the combination of the microscopic and macroscopic properties of $YbIn_{1-x}Ag_xCu_4$ considered above, as well as the equivalence of positions of Yb atoms in the crystal lattice, allows us to consider this system as having an intermediate (fluctuating) valence and, accordingly, the "increase in the mass" of electrons in it as a result of the *f–sd* hybridization during a transition of a 4*f* electron of Yb to the IV state.

Indium, Silver, and Copper. A crucial point in the IV (and accordingly HFS) problem is the identification of the centers at which hybridization takes place. In the case of Yb(In, Ag)Cu_4, a 4*f* electron of Yb can be hybridized either with *s*(*p*)*d* electrons of the neighboring Yb atom,[3] or with *s*(*p*) electrons of In, Ag, and Cu. In the latter case, an increase in the population of the *s*(*p*) shells of Yb partners should be observed.

The table contains displacements of the $K_{\alpha 1}$ lines of In, Ag, and Cu. All the compositions $YbIn_{1-x}Ag_xCu_4$ under investigation display negative displacements relative to the corresponding metals. We proved earlier [24] that the removal of valence *s*(*p*) electrons[4] in heavy elements leads to positive displacements of the $K_{\alpha 1}$ lines (the scale of the effect for the ionic compounds of In, Ag and Cu are illustrated in the table). Nonzero displacements indicate that the populations of the outer shell *s*(*p*) states of In, Ag, and Cu differ from the population in metals, while negative values of the effects indicate an increase in the *s*(*p*) population upon the transition from the metallic state to the IV state.

The electronic structure (population of the 5*s* states of In and Ag and the 4*s* states of Cu) was determined from the experimental displacements of the $K_{\alpha 1}$ line by using atomic calculations of the Dirac–Fock type. The values of Δn for each $YbIn_{1-x}Ag_xCu_4$ sample was determined from the equation

$$\Delta E_{\text{calc}}(\Delta n) = \Delta E^M(x), \qquad (2)$$

where M stands for In, Ag, or Cu, $\Delta E^M(x)$ are the experimental displacements of the $K_{\alpha 1}$ lines, $\Delta E_{\text{calc}}(\Delta n)$ are the calculated displacements, and Δn is the difference in the number of 5(4)*s* electrons in the HF system and in the metallic reference sample (the electron configurations are $4d^{10}5p^25s^1$, $4d^{10}5s^1$, and $3d^{10}4s^1$ for In, Ag, and Cu, respectively). The $\Delta n(x)$ dependences obtained by the method described above are presented in Fig. 2. It can be seen that the values of $\Delta n(x)$ are virtually independent of both the composition x and the substituting partner (In and Ag). The weighted average values for $0 \le x \le 1$ are $\overline{\Delta n_s}(\text{In}) = 0.65 \pm 0.05$ el/at and $\overline{\Delta n_s}(\text{Ag}) = 0.71 \pm 0.09$ el/at; the value of Δn_s for copper is also independent of the composition, but the effect in this case is approximately an order of magnitude weaker ($\overline{\Delta n_s}(\text{Cu}) = 0.08 \pm 0.02$ el/at).

The observed considerable increase in the population of the outer 5*s* orbitals of In and Ag (and 4*s* orbitals of Cu to a smaller extent) can be attributed to one of the above-mentioned mechanisms of the *f–sd* hybridization, namely, the hybridization of a 4*f* electron of Yb with the conduction electrons of the neighbors (In, Ag, Cu). The version in which a 4*f* electron hops between the states of neighboring Yb atoms (Yb $\longleftrightarrow$ Yb) should not, in principle, change the electronic structure of the neighboring (other than Yb) atoms. On the other hand, the emergence of an extra electron *e* in the conduction band upon hybridization of a 4*f* electron with conduction electrons of the neighboring partner atoms as a result of the transition to the IV state ($4f^{14} - 4f^{13} + e$) should increase the population of the outer *s*(*p*) orbitals of Yb partners in the compound, which is actually observed in experiments with In, Ag (and Cu to a smaller extent). The total increase in the population of the *s* states of Yb partners is virtually independent of x [since $\overline{\Delta n_s}(\text{In}) \approx \overline{\Delta n_s}(\text{Ag})$]; its value is $\overline{\Delta n_\Sigma}(\text{In, Ag, Cu}) = 1.0 \pm 0.1$ and is close to the observed decrease in the population of the 4*f* shell of Yb upon a transition to the IV state: $\Delta n_{4f} = 0.91 \pm 0.01$.

The independence of the value of Δn_s on the type of the neighbor indicates that a 4*f* electron has the same probability of hybridization with 5*s* electrons of In and Ag. The difference in the effects (Δn_s) in $YbIn_{1-x}Ag_xCu_4$ for In and Ag on the one hand and for Cu on the other hand can be attributed to the features of

[3] We observed this hybridization channel (Sm $\longleftrightarrow$ Sm) in the IV system $Sm_{1-x}Gd_xS$ [23].

[4] Quantitatively, these effects from *s* and *p* electrons are practically equivalent.

the crystalline structure of this compound. A unit cell of $YbIn_{1-x}Ag_xCu_4$ consists of two sublattices: the Yb and In(Ag) sublattice and the Cu sublattice. We assume that the atoms of the first sublattice are coupled with one another strongly and with the atoms of the second sublattice weakly [25]; therefore, the exchange of electrons due to hybridization (and, accordingly, an increase in n_s) is mainly determined by the atoms of the first sublattice (In, Ag).

ACKNOWLEDGMENTS

The authors are grateful to O. I. Sumbaev for fruitful discussions and valuable remarks, E. G. Andreev for his assistance in carrying out the experiments, and P. L. Sokolova for preparing the manuscript.

This research was supported by the Russian Foundation for Basic Research (RFBR), project no. 99-02-16633. One of the authors (A. V. Golubkov) synthesized the samples, used in the experiments, with the financial support of the RFBR, grant no. 99-02-18078.

REFERENCES

1. G. R. Stewart, Rev. Mod. Phys. **56** (4), 755 (1984).
2. D. I. Khomskiĭ, Usp. Fiz. Nauk **129** (3), 443 (1979) [Sov. Phys. Usp. **22**, 879 (1979)].
3. A. W. Overhauser, Phys. Rev. B **31** (1), 193 (1985).
4. A. M. Tsvelick and P. B. Wiegmann, Adv. Phys. **32** (4), 453 (1983).
5. J. L. Sarrao, C. D. Immer, C. L. Benton, *et al.*, Phys. Rev. B **54**, 12207 (1996).
6. J. L. Sarrao, A. P. Ramírez, T. W. Darling, *et al.*, Phys. Rev. B **58** (1), 409 (1998).
7. A. L. Cornelius, J. M. Lawrence, J. L. Sarrao, *et al.*, Phys. Rev. B **56**, 7993 (1997).
8. S. Zherlitsyn, B. Lüthi, B. Wolf, *et al.*, Phys. Rev. B **60**, 3148 (1999).
9. J. L. Sarrao, C. D. Immer, Z. Fisk, *et al.*, Phys. Rev. B **59**, 6855 (1999).
10. I. Felner, I. Nowik, D. Vaknin, *et al.*, Phys. Rev. B **35**, 6956 (1987).
11. O. I. Sumbaev, in *Modern Physics in Chemistry* (Academic, New York, 1977), Vol. 1, p. 33.
12. O. I. Sumbaev, Usp. Fiz. Nauk **124** (2), 281 (1978) [Sov. Phys. Usp. **21**, 141 (1978)].
13. V. A. Shaburov, I. M. Band, A. I. Grushko, *et al.*, Zh. Éksp. Teor. Fiz. **65**, 1157 (1973) [Sov. Phys. JETP **38**, 573 (1973)].
14. L. L. Hirst, Phys. Rev. B **15** (1), 1 (1977).
15. B. C. Sales and D. K. Wohlleben, Phys. Rev. Lett. **35**, 1240 (1975).
16. P. W. Anderson, Phys. Rev. **109**, 1492 (1958).
17. D. K. Wohlleben, J. Phys. (Paris) **37**, 4 (1976).
18. V. A. Shaburov, Yu. P. Smirnov, A. E. Sovestnov, and A. V. Tyunis, Pis'ma Zh. Éksp. Teor. Fiz. **41** (5), 213 (1985) [JETP Lett. **41**, 259 (1985)].
19. Yu. P. Smirnov, A. E. Sovestnov, A. V. Tyunis, and V. A. Shaburov, Fiz. Tverd. Tela (St. Petersburg) **40**, 1397 (1998) [Phys. Solid State **40**, 1269 (1998)].
20. M. N. Groshev, V. I. Petrova, Yu. P. Smirnov, *et al.*, Fiz. Tverd. Tela (St. Petersburg) **29**, 1035 (1987) [Sov. Phys. Solid State **29**, 592 (1987)].
21. A. Scherzberg, Ch. Sauer, U. Köbler, and W. Zinn, Solid State Commun. **49**, 1027 (1984).
22. E. R. Bauminger, D. Froindlich, I. Nowik, and S. Ofer, Phys. Rev. Lett. **30**, 1053 (1973).
23. A. E. Sovestnov, Yu. P. Smirnov, A. V. Tyunis, *et al.*, Fiz. Tverd. Tela (St. Petersburg) **39**, 1017 (1997) [Phys. Solid State **39**, 913 (1997)].
24. E. V. Petrovich, Yu. P. Smirnov, A. I. Grushko, *et al.*, Zh. Éksp. Teor. Fiz. **61**, 1756 (1971) [Sov. Phys. JETP **34**, 935 (1971)].
25. H. R. Kirchmayr and C. A. Poldy, in *Handbook on the Physics and Chemistry of Rare Earths*, Ed. by K. A. Gschneidner and L. Eyring (North-Holland, Amsterdam, 1978; Metallurgiya, Moscow, 1982), p. 88.

Translated by N. Wadhwa

Physics of the Solid State, Vol. 42, No. 7, 2000, pp. 1204–1206. Translated from Fizika Tverdogo Tela, Vol. 42, No. 7, 2000, pp. 1169–1171.

METALS AND SUPERCONDUCTORS

Optical Investigation of Coherent and Thermal Phonons in High-T_c Superconductors

O. V. Misochko

Institute of Solid-State Physics, Russian Academy of Sciences, Chernogolovka, Moscow oblast, 142432 Russia
e-mail: misochko@issp.ac.ru

Received November 23, 1999

Abstract—Low-energy phonons in $NdBa_2Cu_3O_{7-x}$ and $Bi_2Sr_2CaCu_2O_{8+x}$ superconducting single crystals have been studied by Raman scattering and reflectivity measurements with femtosecond-scale resolution. Raman scattering provides information on equilibrium thermal phonons, whereas information about a coherent state of the phonon system is obtained by measuring in the time domain when the phonon system is pumped by an ultrashort pulse and subsequently probed by a properly gated second pulse. It is shown that both methods yield similar results for the phonon mode energies, while the energy relaxation and dephasing rates exhibit a tendency to disagreement. © *2000 MAIK "Nauka/Interperiodica".*

Most of the information regarding the dynamics of long-wavelength phonon modes in high-temperature superconductors (HTSC) has until recently been derived from Raman scattering (RS) and infrared (IR) spectroscopy studies [1, 2]. Because HTSC crystals are centrosymmetric, the rule of alternative forbiddenness limits the information extractable from RS spectra to even, and from IR spectra, to odd phonon modes. Being typical representatives of frequency-domain methods, both types of spectroscopy provide data on equilibrium, thermal phonons. Progress in laser technology has made it possible to reduce laser pulse lengths to a few femtoseconds, thus opening novel prospects of research. The availability and wide use of fs-scale pulses coincided in time with the discovery of HTSCs, thus allowing the investigation of lattice vibrations in real time. Besides, for pulse lengths smaller than the reciprocal lattice-vibration frequency, one can produce and study phonons in a coherent, rather than thermal, state. Real-time studies, whose typical representative is the method that involves pumping a given phonon state with its subsequent probing by two time-separated laser pulses [pump–probe (PP) method], are now being actively pursued on many condensed systems [3]. As a rule, in the time domain, one detects Raman-active phonons with energies less than the reciprocal length of the pump pulse, and for HTSCs such studies have been carried out to date only on the $YBa_2Cu_3O_{7-x}$ system deposited in the form of films on various substrates [4–6].

In order to follow the similarity and possible differences between the information derived from measurements in the frequency and time domains, we have performed a comparative investigation of the phonon characteristics of $NdBa_2Cu_3O_{7-x}$ (Nd123) and $Bi_2Sr_2CaCu_2O_{8+x}$ (Bi2212) single crystals by two mutually complementing RS and PP, optical methods. The Nd123 and Bi2212 crystals had the superconducting transition temperatures T_c = 94 and 91 K; however, all measurements in this work were made at room temperature. The optical response was studied from the *ab* crystal planes. The RS measurements were carried out in backscattering geometry with a triple-grating spectrometer equipped by a multichannel detector, with an Ar^+ laser (λ= 514 nm) used for pumping [7]. Measurements in the time domain made use of phase-sensitive detection and of a sapphire titanate laser (λ = 800 nm) that produced pulses less than 50 fs long [6].

Figure 1a shows a typical optical response obtained by excitation and subsequent probing of a Bi2212 crystal by fs pulses. The excited state of the crystal relaxes to equilibrium in times of the order of 300–400 fs. Superposed on this electronic relaxation are fast oscillations presented in the inset to Fig. 1a. This work studies only the oscillating part of the optical response generated by the excitation of coherent optical phonons. To check whether the oscillations observed by the PP method are related to Raman-active modes of the crystal, the data obtained in the time domain were numerically transformed to the frequency domain by the Fourier transformation. Figure 1b displays a typical spectrum thus obtained, and Fig. 1c shows an RS spectrum measured on the same crystal in the $x'x'$ polarization. The two distinct peaks at 60 and 125 cm^{-1} correspond to the fully symmetric phonon modes associated with displacements of the Bi and Cu ions. While lattice dynamics calculations suggest that both modes originate from ionic displacements perpendicular to the CuO_2 plane [8], an experimental analysis showed that the low-frequency mode can be polarized in the CuO_2 plane [9]. As follows from a comparison of the results obtained, the positions of the phonon peaks derived

1063-7834/00/4207-1204$20.00

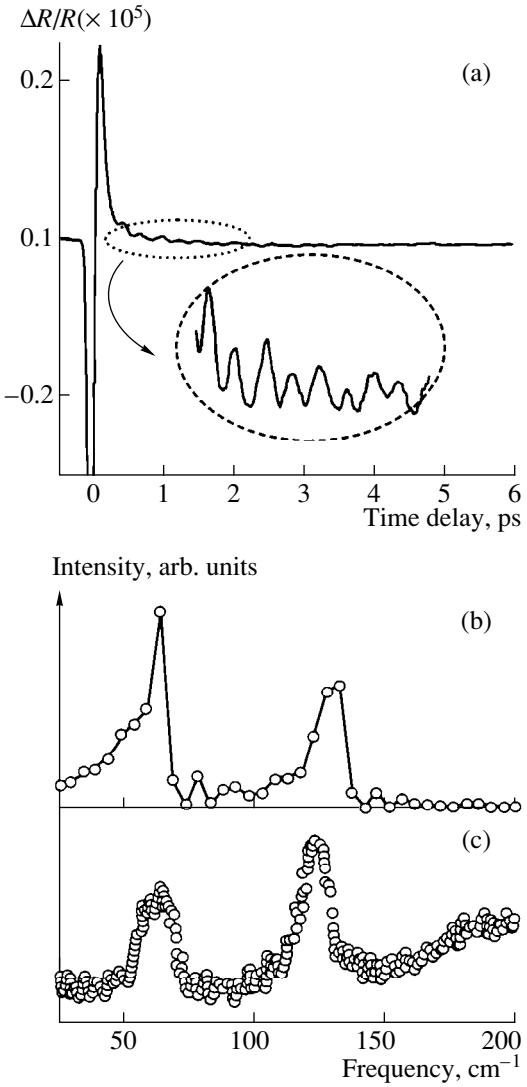

Fig. 1. (a) Time-resolved normalized reflectance for a $NdBa_2Cu_3O_{7-x}$ crystal. The inset shows oscillations. (b) Fourier-transformed time-domain response. (c) Raman spectrum.

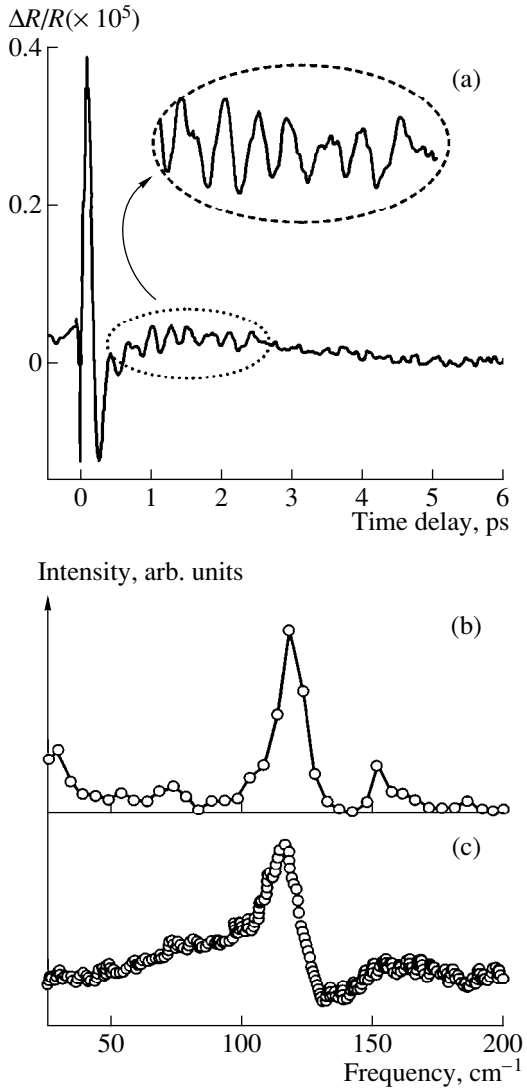

Fig. 2. (a) Time-resolved normalized reflectance for a $Bi_2Sr_2CaCu_2O_{8+x}$ crystal. The inset shows oscillations. (b) Fourier-transformed time-domain response. (c) Raman spectrum.

from measurements in the time and frequency domains coincide to within experimental accuracy. The relative peak intensities in the RS spectrum and the Fourier-transformed time-domain response also do not differ very strongly. However, the spectral-line half-width $\Delta\nu$ extracted from time measurements and, accordingly, the $Q = \nu/\Delta\nu$ parameter ($Q = 12$ and 22 for the low- and high-frequency modes, respectively) are always slightly larger than the corresponding values derived from RS data ($Q = 9$ and 17).

Figure 2 shows a similar set of data for the Nd123 crystal. While the oscillations in Nd123 have a larger amplitude than those in Bi2212, the oscillation amplitude is smaller than that observed in Y123 films [6]. The RS spectrum of Nd123 is dominated in the low-frequency part by the Ba ion mode at 120 cm^{-1} [10]. The intensity of the Cu ion mode at 152 cm^{-1} is considerably lower, which sets this compound apart from Y123, where the two low-frequency modes are comparable in intensity for the given polarization [6, 11]. As in Bi2212, both modes are fully symmetric and the displacements are polarized perpendicularly to the cuprate plane. The frequencies of the two low-frequency modes derived from the Fourier-transformed time-domain response of Nd123 are similar to those in the RS spectrum. Interestingly, the relative mode intensities observed in the Fourier-transformed time-domain response approximately coincide with those in the RS spectrum. Y123 was reported to exhibit considerable differences between the relative mode intensities in the frequency and time domains, and most room-temperature studies found the Cu ion mode to be substantially

weaker than the Ba mode in time-domain spectra [4–6]. As in Bi2212, the parameter Q observed in the Nd123 crystal in the time domain (21 and 30 for the low- and high-frequency modes, respectively) is larger than that in the RS spectrum, where $Q = 11$ for the low-frequency mode. The difference between the line shape parameters obtained in the time and frequency domains is not unexpected, because the two techniques measure wholly different states of the phonon system; indeed, femtosecond pump pulses transfer a system to a coherent state, where the phase is a well-defined quantity, whereas Raman spectroscopy probes a system in the thermal state with an indefinite phase. Therefore, the spectral width of the Fourier-transformed response in the temporal domain characterizes the dephasing rate (the loss of phase memory), while the phonon linewidth in a Raman spectrum relates to damping. Phonon damping is governed by interaction with the reservoir, which is represented in this case by all the other crystal modes, the dominant contribution being due to anharmonic decay into two modes, which are, as a rule, acoustic.

Note that a comparative study of superconducting Y123 films and semimetals revealed a similar trend for the Q parameter in both the temporal and frequency domains [5, 6, 12]. There was also an attempt [5] to assign the difference in linewidth between the time and frequency domains to different laser wavelengths used in experiments (Landau damping) [13]. These experiments also employed different pump wavelengths, and we therefore cannot exclude such an effect; however, our previous studies of such crystals made by RS did not reveal a threshold behavior in the dependence of linewidth on the pump laser wavelength [11]. It is possible that the absence of Landau damping in Raman spectra [14] is associated with structural disorder in the crystals under study, because there is disorder near the CuO_2 planes in Nd123 and near the Bi planes in Bi2212 [10, 11]. It should also be pointed out that, although information on the phonon subsystem is extracted in both techniques from measurements performed in a photon field, different correlation functions are measured in the time and frequency domains. The RS is associated with $\langle a_i^+ a_i \rangle$-type correlators, whereas the optical response in the time domain depends on correlators of the type $\langle a_i^+ a_i a_j^+ a_j \rangle$, where a_i^+ and a_i are the creation and annihilation operators, respectively. In the time domain, one measures intensity correlations, the dependence of which on the first-order correlations is determined by the statistics of the scattering particles (phonons) [15].

To conclude, we have compared the phonon thermal and coherent dynamics in $NdBa_2Cu_3O_{7-x}$ and $Bi_2Sr_2CaCu_2O_{8+x}$ single crystals by an optical study in the time and frequency domains. It has been shown that thermal and coherent phonons coincide in energy, but the dephasing in a coherent state is slower than the energy relaxation.

ACKNOWLEDGMENTS

The author expresses his gratitude to the Kansai Advanced Research Center and, in particular, to K. Sakani for supporting this project.

REFERENCES

1. R. Feile, Physica C (Amsterdam) **159**, 1 (1989); C. Thomsen, in *Light Scattering in Solids*, Ed. by M. Cardona and G. Guentherodt (Springer, Berlin, 1991), Vol. VI, p. 285.
2. D. N. Basov and T. Timusk, in *Handbook on the Physics and Chemistry of Rare Eaths*, Ed. by K. A. Dschneidner, L. Eyring, and M. B. Maple (North-Holland, Amsterdam, 1999).
3. R. Merlin, Solid State Commun. **102**, 207 (1997).
4. J. M. Chwalek, C. Uher, J. F. Whitaker, *et al.*, Appl. Phys. Lett. **58**, 980 (1991).
5. W. Albrecht, Th. Kruse, and H. Kurz, Phys. Rev. Lett. **69**, 1451 (1992).
6. O. V. Misochko, K. Kisoda, H. Harima, *et al.*, Physica C (Amsterdam) **320**, 213 (1999); O. V. Misochko, K. Kisoda, K. Sakai, and S. Nakashima, Phys. Rev. B **61**, 2000 (in press).
7. O. V. Misochko, Fiz. Tverd. Tela (Leningrad) **31** (11), 280 (1989) [Sov. Phys. Solid State **31**, 1998 (1989)].
8. J. Prade, A. D. Kulkarni, F. W. de Wette, *et al.*, Phys. Rev. B **39**, 2771 (1989).
9. R. Liu, M. V. Klein, P. D. Han, and D. A. Payne, Phys. Rev. B **45**, 7392 (1992).
10. O. V. Misochko, K. Kuroda, and N. Koshizuka, Phys. Rev. B **56**, 9116 (1997).
11. O. V. Misochko and E. Ya. Sherman, Int. J. Mod. Phys. B **24**, 2455 (1998).
12. T. K. Cheng, S. D. Brorson, A. S. Kazeroonian, *et al.*, Appl. Phys. Lett. **57**, 1004 (1990).
13. B. Friedl, C. Thomsen, H.-U. Habermeier, and M. Cardona, Solid State Commun. **81**, 989 (1992).
14. O. V. Misochko and E. Ya. Sherman, Phys. Rev. B **51**, 1326 (1995).
15. A. V. Belinskiĭ and M. V. Chekhova, Zh. Éksp. Teor. Fiz. **108**, 1956 (1995) [JETP **81**, 1067 (1995)]; S. Ruhman, A. G. Joly, and K. A. Nelson, IEEE J. Quantum Electron. **24**, 460 (1988).

Translated by G. Skrebtsov

Physics of the Solid State, Vol. 42, No. 7, 2000, pp. 1207–1210. Translated from Fizika Tverdogo Tela, Vol. 42, No. 7, 2000, pp. 1172–1175.

METALS AND SUPERCONDUCTORS

I–V Characteristics and the Electric-Field Effect in Melt-Grown $YBa_2Cu_3O_x/Y_2BaCuO_5$ HTSC Crystals

B. I. Smirnov*, T. S. Orlova*, S. Sengupta, and K. C. Goretta*****

**Ioffe Physicotechnical Institute, Russian Academy of Sciences, Politekhnicheskaya ul. 26, St. Petersburg, 194021 Russia*

@e-mail: smir.bi@pop.ioffe.rssi.ru

***Superconductive Components, Inc., Columbus, Ohio 43212, USA*

****Argonne National Laboratory, Argonne, Illinois 60439, USA*

Received December 9, 1999

Abstract—The effect of an electric field E = 120 MV/m in the electrode–insulator–superconductor system on *I–V* curves obtained at 77 K on two types of single-crystal samples cut from monolithic superconducting $YBa_2Cu_3O_x/Y_2BaCuO_5$ has been studied. The Y211 nonsuperconducting phase in the ingot was in the form of precipitates ≈1 μm in size. It has been found that an electric field applied to samples with a comparatively low Y211 content (volume fraction 8%) does not affect the critical current I_c while reducing the resistance R at currents slightly above I_c. In samples containing more than 35% Y211 phase, electric field results in an increase of I_c and a decrease of R for $I > I_c$. Data on the critical temperature T_c and the temperature dependence of I_c have also been obtained. © *2000 MAIK "Nauka/Interperiodica".*

INTRODUCTION

The problem of a possible effect of an electric field on the superconducting properties of materials in the electrode–insulator–superconductor system was considered as far back as the 1960s [1–3]. The first experimental study [1] on films of thickness d = 70 Å thick made in a field E = 30 MV/m revealed a change in conductivity and a shift of the critical temperature T_c by $\Delta T_c \approx 10^{-4}$ K, with the effects in indium and tin being of opposite signs. The effect of the electric field on T_c was later observed [4] also on $Ba(PbBi)O_3$ single-crystal solid solutions, where the maximum value of ΔT_c reached 0.6 K in a field E = 1 MV/m for d = 0.3–0.6 mm.

The interest in the field effect intensified after the discovery of high-temperature superconductors (HTSC) [5–14], where this effect could be expected to be considerably stronger because of the lower carrier concentration. It was finally established that an electric field applied to an electrode–insulator–superconducting $YBa_2Cu_3O_x$(Y123) film system can affect T_c and the *I–V* characteristics both above and below T_c, with the sign of the effect depending on that of the field. As for the magnitude of the effect, in most studies made on films [7–9], it was noticeable only in thin samples. For example [9], the field effect on conductivity above T_c practically vanished with d increasing from 1c to 8c, where c is the lattice constant.

At the same time, many publications reported observation of the field effect in less perfect samples at still larger d [4–6, 10–14]. For instance, a reversible change of the critical current I_c and of resistance R was observed to occur for $I > I_c$ in the Y123 HTSC ceramics in an external electric field [10, 12–14]. It was also found that the field effect and its magnitude depend on the actual composition and preparation technology of the ceramic. In particular, in Y123 ceramics, the field effect disappeared after hydrogen treatment [15] or silver doping [13, 16].

While the physical nature of the effect in HTSC ceramics remains unclear, the available experimental data permit the suggestion [12–14, 16] that it is related primarily to a possible influence of the field on weak links at grain boundaries. In thin films containing purposefully introduced weak links, the electric field effect also increases strongly [17, 18]. It thus appeared of interest to perform an experimental study on the possible field effect in HTSC crystals free of the above weak links.

The present paper reports a study on the *I–V* characteristics of $YBa_2Cu_3O_x/Y_2BaCuO_5$ crystals, which are of interest for the investigation and use of the levitation effect [19], and establishes the effect of an external electric field on the *I–V* characteristics at 77 K.

1. EXPERIMENTAL TECHNIQUE

The samples chosen for the study were cut from a large $YBa_2Cu_3O_x$(Y123)/Y_2BaCuO_5(Y211) single-domain crystal melt-grown by directional crystallization [19, 20], a technique which can be briefly described as follows. The starting powder mixture of Y123 (74 wt %), Y211 (24 wt %), and PtO_2 (1 wt %)

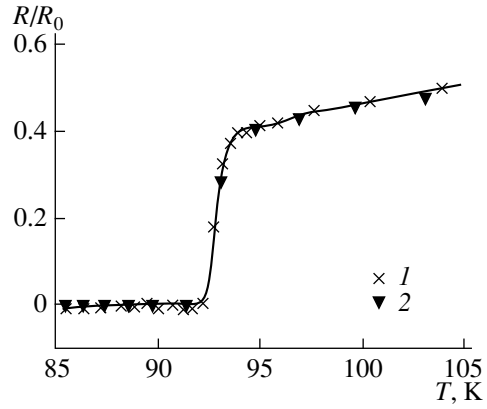

Fig. 1. Temperature dependences of reduced resistance R/R_0 for samples of the upper (*1*) and lower (*2*) layers of the monolithic crystal. R_0 is the value of R at 300 K.

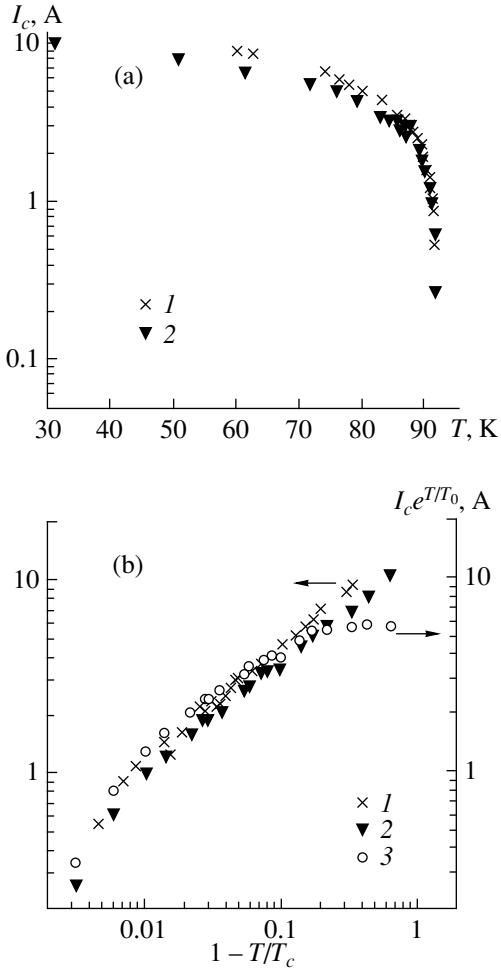

Fig. 2. Dependences of the critical current (a) on temperature and (b) on $(1 - T/T_c)$ for samples *U* (*1*) and *L* (*2*). Curve *3* is a plot of $I_c e^{T/T_0}$ *vs* $(1 - T/T_c)$ for the *L* sample.

was ball-milled and pressed into 29-mm-wide hexagonal pellets. Next a seed, which was a $Nd_{1+x}Ba_{2-x}Cu_3O_y$ single-crystal platelet with transverse dimensions of up to 1 mm, was deposited on the pellet at its center, after which the latter was placed in a furnace with a temperature gradient (up to 15°C/cm). After homogenization at a temperature at which the pellet already melts while the seed remains a crystal, the system was cooled slowly, a regime during which a Y123 crystal grew on the seed in the direction of the temperature gradient. The final product was a single-domain monolithic crystal of up to 15 mm in height, with the crystallographic orientation of the seed, namely, with the *ab* plane parallel, and the *c* axis, perpendicular, to the upper surface of the monolith.

As for the Y211 phase, it is present primarily in the form of particles about 1 μm in size, with their volume fraction being substantially larger in the lower part and in the periphery of the monolithic crystal [21]. For instance, the volume fraction of Y211 precipitates varies along the *c* growth direction from 8 at the top to 35% at a distance of 5 mm away [21]. By contrast, zones free of Y211 are observed around possible Pt-based inclusions.

The samples intended for measurement of the superconducting characteristics (the *I–V* curves and the temperature dependence of *R*) were approximately $2 \times 4 \times 1.5$ mm in size, respectively, along the *a*, *b*, and *c* directions, with four indium contacts deposited on their 2×4 mm side surface. X-ray diffraction ω scans showed the samples to be single crystals with block misorientation within 2–3°. Optical studies suggest that such monolithic crystals have a mosaic structure with small-angle misorientation not over 5°, the small-angle boundaries being clean and free of microcracks [20].

The experiments on the effect of an external electric field were performed in an electrode–insulator–superconductor system, similar to how this was done in [10], at 77 K, i.e., for $T < T_c$. A high negative voltage U ($U_{max} = 6$ kV) was applied to the metallic electrode, which was isolated from the sample with a teflon film of thickness $t = 50$ μm. Transport current I was passed through the current contacts, and voltage V was measured across the potential contacts. The critical current was determined by the 1 μV/mm criterion.

When studying the effect of the electric field, the latter could be turned on both before the experiment and during the *I–V* measurement at a certain current *I*. *I–V* characteristics were measured also in a magnetic field $B \leq 200$ G, which was generated by passing a current through a coil and along the *c* axis.

2. EXPERIMENTAL RESULTS AND DISCUSSION

Figure 1 presents temperature dependences of the resistance R of different samples (cut from the upper, *U*, and close to the lower, *L*, layers of the monolith). These layers were at a distance of ≈12 mm from one

another along the crystal height. One readily sees that the critical temperatures T_c are practically the same for the *U* and *L* samples and equal to ~92.5 K ($R = 0$), with a fairly narrow superconducting-transition width $\Delta T \leq 1.5$ K. Such values of T_c were also obtained by the authors earlier with a standard SQUID magnetometer.

The critical current densities J_c for the *U* and *L* samples were also similar and equal approximately to 200 A/cm^2 at 77 K. Note that J_c was magnetic-field independent (the measurements were carried out up to $B = 200$ G).

Figure 2 displays dependences of I_c on T (Fig. 2a) and on the quantity $(1 - T/T_c)$ (curves *1* and *2* in Fig. 2b) for samples of different types. The point is that the variation of I_c with temperature in HTSC single crystals is described primarily by relations of two types [22, 23]:

$$I_c \sim \exp(-T/T_0) \quad (1)$$

for the low-temperature range, and

$$I_c \sim (1 - T/T_c)^n \quad (2)$$

for the temperature interval close to T_c. Experimentally, one finds usually $T_0 = 20$–30 K, and $n = 0.5$–1.5.

As is seen from Fig. 2a, the $I_c(T)$ relation for the transport current can be fitted by relation (1) in our case only within the region of 30–70 K, with $T_0 = 67$ K. As for (2), this relation fits better to the experimental data obtained (points *1* and *2* in Fig. 2b) for $n = 0.6$ within the temperature region from 30 to 91 K, with *n* changing to 1.1 within a very narrow interval of 91.0–91.7 K.

Some authors use a combination of expressions (1) and (2) in the form [23]

$$I_c = I_{co}(1 - T/T_c)^n \exp(-T/T_0). \quad (3)$$

For this reason, we also present (points *3* in Fig. 2b) the experimental dependence of the quantity $I_c\exp(T/T_0)$ on $(1 - T/T_c)$ for *L* samples taken at $T_0 = 67$ K. One readily sees that relation (3) yields a variable value of *n*, which falls off smoothly with decreasing temperature from 1.1 to zero.

Thus, the experimental data obtained by us on the temperature dependence of I_c are fitted best of all by relation (2) in the region studied.

The effect of electric field on *I–V* characteristics is demonstrated by Fig. 3 for different samples. The magnitude of I_c in *U* samples is seen to be practically independent of the field, whereas for $I > I_c$, the field substantially reduces the resistance *R* (curves *1* and *1*'). At the same time, under a field, the *L* samples exhibit not only a decrease in *R* for $I > I_c$, but a noticeable increase of I_c as well (curves *2* and *2*').

Figure 4 shows the variation of voltage *V* in the *I–V* characteristics of an *L* sample occurring when the electric field is turned on and then turned off at $I = \text{const}$. We see that in both cases for $I \geq I_c$, the application of a

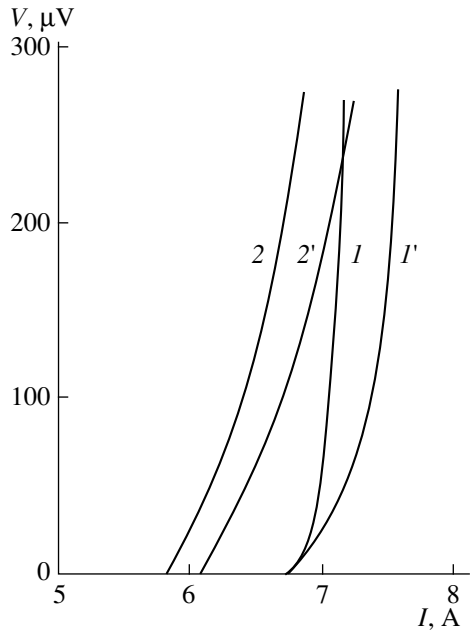

Fig. 3. *I–V* characteristics for samples *U* (*1*) and *L* (*2*) measured at *E* (MV/m): (*1*, *2*) 0 and (*1*', *2*') 120.

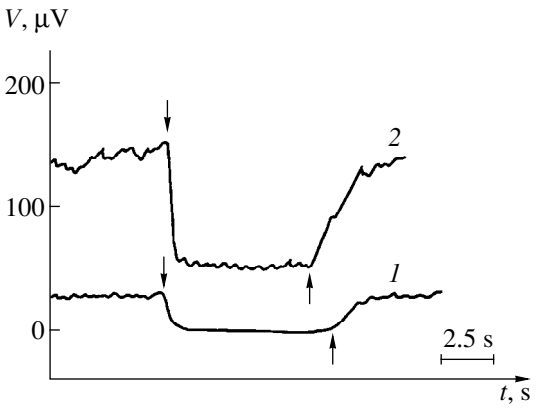

Fig. 4. Variation of voltage *V* at the turn on (↓) and off (↑) of a 120-MW/m electric field applied to the *L* sample for different values of *I* (A): (*1*) 6.1, (*2*) 6.5.

field $E = 120$ MV/m results in a substantial decrease of *V*, up to a transition of the sample from the resistive to superconducting state (curve *1*). Note that the field effect here is reversible. A similar result is observed in the *U* sample, except a region near I_c, where no field effect is observed.

In other words, application of an electric field $E = 120$ MV/m to Y123/211 single-crystal samples with a low content of Y211 precipitates (volume fraction 8%) does not affect the critical current I_c. At the same time, at currents slightly above I_c the sample resistance in a field decreases. If, however, a crystal contains a large

fraction of Y211 precipitates (in our case, above 35%), an electric field brings about an increase of I_c and a corresponding decrease of R for $I > I_c$. In our opinion, the key factor accounting for the electric field effect in Y123 crystals with Y211 precipitates is that the latter do not conduct an electric current.

Thus, our results indicate that the electric-field effect can also be observed in single crystals, provided the latter contain a large enough amount of nonconducting inclusions, the effect being more pronounced, the higher their concentration is.

ACKNOWLEDGMENTS

Support by the Russian Academy of Sciences of the work carried out at the Ioffe Physicotechnical Institute is gratefully acknowledged. In the USA, the work was supported by the US Department of Energy (Contract no. W-31-109-Eng-38).

REFERENCES

1. R. E. Glover and M. D. Sherill, Phys. Rev. Lett. **5**, 248 (1960).
2. V. B. Sandomirskiĭ, Pis'ma Zh. Éksp. Teor. Fiz. **2**, 396 (1965) [JETP Lett. **2**, 248 (1965)].
3. H. Meissner, Phys. Rev. **154**, 422 (1967).
4. V. V. Bogatko and Yu. N. Venevtsev, Fiz. Tverd. Tela (Leningrad) **29**, 2872 (1987) [Sov. Phys. Solid State **29**, 1654 (1987)].
5. Yu. V. Gomenyuk, V. Z. Lozovskiĭ, V. S. Lysenko, *et al.*, Dokl. Akad. Nauk Ukr. SSR, Ser. A **11**, 49 (1989).
6. Yu. V. Gomenyuk, N. I. Klyuĭ, V. Z. Lozovskiĭ, *et al.*, Sverkhprovodimost': Fiz., Khim., Tekh. **4**, 762 (1991).
7. J. Mannhart, J. G. Bednorz, K.A. Müller, and D. G. Schlom, Z. Phys. B **83**, 307 (1991).
8. J. Mannhart, D. G. Schlom, J. G. Bednorz, and K. A. Müller, Phys. Rev. Lett. **67**, 2099 (1991).
9. X. X. Xi, C. Doughty, A. Walkenhorst, *et al.*, Phys. Rev. Lett. **68**, 1240 (1992).
10. B. I. Smirnov, S. V. Krishtopov, and T. S. Orlova, Fiz. Tverd. Tela (St. Petersburg) **34**, 2482 (1992) [Sov. Phys. Solid State **34**, 1331 (1992)].
11. V. V. Lemanov, A. L. Kholkin, and A. B. Sherman, Pis'ma Zh. Éksp. Teor. Fiz. **56**, 580 (1992) [JETP Lett. **56**, 562 (1992)].
12. B. I. Smirnov, T. S. Orlova, and S. V. Krishtopov, Fiz. Tverd. Tela (St. Petersburg) **35**, 2250 (1993) [Phys. Solid State **35**, 1118 (1993)].
13. T. S. Orlova and B. I. Smirnov, Supercond. Sci. Technol. **6**, 899 (1994).
14. B. I. Smirnov, T. S. Orlova, and H.-J. Kaufmann, in *Proceedings of the Fourth International Conference and Exhibition: World Congress on Superconductivity, Lindon B. Johnson Space Center, Houston, Texas, 1994*, Ed. by K. Krishen and C. Burnham, Vol. 1, p. 232.
15. B. I. Smirnov, Yu. M. Baĭkov, A. N. Kudymov, *et al.*, Fiz. Tverd. Tela (St. Petersburg) **37**, 1794 (1995) [Phys. Solid State **37**, 977 (1995)].
16. T. S. Orlova, B. I. Smirnov, and J.-Y. Laval, Fiz. Tverd. Tela (St. Petersburg) **40**, 1195 (1998) [Phys. Solid State **40**, 1088 (1998)].
17. J. Mannhart, J. Strobel, J. G. Bednorz, and Ch. Gerber, Appl. Phys. Lett. **62**, 630 (1993).
18. Z. G. Ivanov, E. A. Stepansov, A. Y. Tzalenchuk, *et al.*, IEEE Trans. Appl. Supercond. **3**, 2925 (1993).
19. V. R. Todt, S. Sengupta, and D. J. Miller, Appl. Supercond. **3**, 175 (1995).
20. S. Sengupta, J. Corpus, M. Agarwal, and J. R. Gainer, Jr., Mater. Sci. Eng. B **53**, 62 (1998).
21. P. Diko, V. R. Todt, D. J. Miller, and K. C. Goretta, Physica C (Amsterdam) **278**, 192 (1997).
22. A. A. Zhukov and V. V. Moshchalkov, Sverkhprovodimost': Fiz., Khim., Tekh. **4**, 850 (1991).
23. S. Senoussi, J. Phys. III **2**, 1041 (1992).

Translated by G. Skrebtsov

Physics of the Solid State, Vol. 42, No. 7, 2000, pp. 1211–1214. Translated from Fizika Tverdogo Tela, Vol. 42, No. 7, 2000, pp. 1176–1179.

METALS AND SUPERCONDUCTORS

On the Origin of Orthorhombic Deformations in $YBa_2Cu_3O_{7-y}$

A. Yu. Gufan and Yu. V. Prus

North-Caucasian Science Center for Higher Education, Rostov-on-Don, 344006 Russia

e-mail: gufan@gufan.rnd.runnet.ru

Received September 14, 1999; in final form, December 17, 1999

Abstract—It is shown that orthorhombic deformations (ODs) in $YBa_2Cu_3O_{7-y}$ agree with the hypothesis of the proper ferroelastic transition in the praphase when the value of y decreases from 0.65 to 0.07. For $0.07 < y < 0.45$, ODs are probably of the improper ferroelastic type. © *2000 MAIK "Nauka/Interperiodica".*

1. The emergence of spontaneous orthorhombic deformations (ODs) in solid solutions based on $YBa_2Cu_3O_{7-y}$ upon a change in the oxygen concentration stimulated considerable interest as it was seen as a possible mechanism of the formation of one-dimensional structures responsible for anomalously high values of the superconducting transition temperature T_c [1]. The discovery of tetragonal high-temperature superconducting (HTSC) materials [2] and the absence of correlations between the electrodynamic characteristics of HTSC materials [3] and spontaneous deformations [4] (for example, the magnetic field penetration depth is independent of the oxygen concentration y which strongly affects the value of OD) has made this trend insignificant. However, a detailed experimental analysis of structural changes induced by ODs in $YBa_2Cu_3O_{7-y}$ has revealed many problems and made them an interesting object of investigation.

This work is devoted to an analysis of some structural characteristics of $YBa_2Cu_3O_{7-y}$ on the basis of the Landau phenomenological theory [5].

Several hypotheses concerning the origin of spontaneous ODs in $YBa_2Cu_3O_{7-y}$ have been put forth. For example, ODs are often associated with the ordering of oxygen and vacancies in positions 2(*f*) referred to the structure of the tetragonal phase [6] characteristic of oxygen-deficient compositions. However, the increase in the value of T_c as a result of ageing of the sample with $0.45 < y < 0.65$ in the orthorhombic phase [7], as well as direct measurements of the time dependence of spontaneous ODs and the degree of oxygen ordering [8], indicates unambiguously that ODs in $YBa_2Cu_3O_{7-y}$ are determined by an independent mechanism of the loss of stability. Consequently, ODs in $YBa_2Cu_3O_{7-y}$ should be characterized by a separate order parameter (OP).

2. A mechanism of the emergence of spontaneous deformations that is consistent with the results of [7, 8] is not quite clear. One of hypotheses suggests that these are proper ferroelectric deformations of a tetragonal crystal, which are determined by a one-component OP [7, 8] $\eta = 2(a - b)/(a + b)$. According to the Landau theory of second-order phase transitions [5], this hypothesis implies that the square of the amount of deformation (η^2) must be a linear function of the change in the external factors inducing the transition. In order to find the extent to which this hypothesis corresponds to the observed pattern, we calculate the equilibrium dependences of the quantity $2(a - b)/(a + b)$ on the oxygen concentration in $YBa_2Cu_3O_{7-y}$ from the values of the unit cell parameters given in tables and graphs in [7, 9–15]. Veal *et al.* [7] studied monocrystalline, as well as polycrystalline, samples. In [9, 10], the investigated quasi-monocrystalline films were in chemical equilibrium in oxygen with a bulk powder sample. The oxygen concentration was determined for the powder, while the unit cell parameters were measured both for the bulk sample and for the *c*- and *a*-oriented films of thicknesses 100–300 nm. In these three publications, the lattice parameters were determined by the x-ray diffraction method. Jorgensen *et al.* [11], as well as Cava *et al.* [12], used neutron diffraction from a powder sample. Mazaki *et al.* [13] and Fisher *et al.* [14] investigated a powder pressed into pellets and polycrystalline samples, respectively. A homogeneous polycrystal was studied by the x-ray diffraction technique in [15]. A comparison of the data obtained on different objects by using different methods of determining the oxygen concentration is required for eliminating possible systematic errors of the measuring technique. For example, the data on oxygen concentration obtained by the iodometric technique should always be compared with the limiting saturation of the Y–Ba–Cu–O compositions with oxygen while preserving the 123 structure [10–12].

3. The results of data processing [10–15] presented in Fig. 1 show that a transition from the tetragonal to the orthorhombic phase, which occurs for $y = 0.65$, is indeed close to a continuous phase transition; in other words, it can be considered in the theory of second-

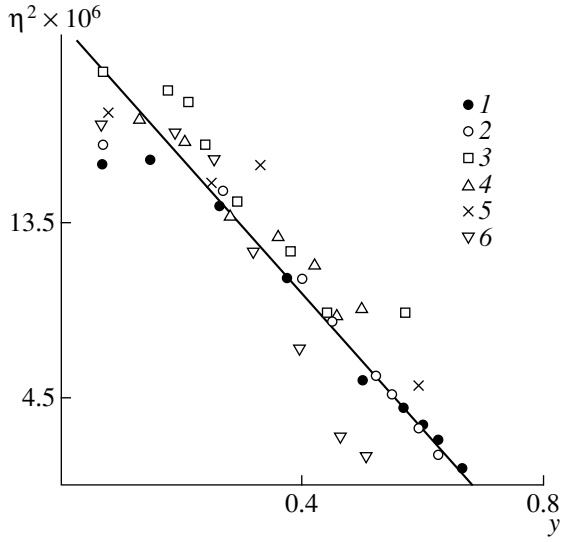

Fig. 1. Dependence of $2(a - b)/(a + b)$ on the oxygen concentration, calculated from the available data: (*1*) [10], (*2*) [11], (*3*) [12], (*4*) [13], (*5*) [14], and (*6*) [15].

order transitions. The solid straight line in Fig. 1 corresponds to the averaged dependence $\eta^2(y)$ for the experimental points obtained by different authors.

It can be seen from Fig. 1 that the straight line predicted by the Landau theory for the $\eta^2(y)$ dependence correctly describes the experimental data for $0.25 < y < 0.68$. However, for $0.07 < y < 0.25$, the experimental points do not fit to the straight line predicted by the theory of second-order phase transitions.

Another argument in favor of analyzing alternative hypotheses on the nature of ODs is associated with an essentially nonlinear dependence $T_c(y)$, including the 60 K plateau existing in the vicinity of $y \approx 0.45$. It should be noted that some ferroelectric structural rearrangements are observed for $y \approx 0.45$ in $YBa_2Cu_3O_{7-y}$ [16], which probably facilitate oxygen ordering in the positions (1/2 0 0) and (0 1/2 0).

4. An alternative hypothesis concerning the nature of ODs is based on the concept of a perovskite-like praphase of the 123 structure [2, 17–19]. In this hypothesis, the praphase is regarded as an oxygen-deficient perovskite-type cubic structure disordered in Y–Ba and having the chemical formula $Y_{1/3}Ba_{2/3}CuO_{3-x}$ [2, 17] (the second praphase, according to [18, 19]). The real structure of $YBa_2Cu_3O_{7-y}$ is interpreted as a structure determined by independent spontaneous breaking of the praphase cubic symmetry through the Y–Ba ordering and spontaneous "longitudinal" deformation specified by the differences $\eta_2 = u_{xx} - u_{zz}$ and $\eta_3 = u_{yy} - u_{zz}$. Ordering of the type …YBaBaYBa… along the fourfold axis of the cubic cell is responsible for the trebling of the primitive cell volume of the praphase; at the same time, it makes the primitive cell of the real structure tetragonal, singling out the *n* axis. In crystallography, the direction corresponding to the maximum period of the primitive tetragonal cell, i.e., the direction of trebling is referred to as the parameter *c*.

The spontaneously emerging deformations η_2 and η_3 can induce two types of tetragonal phases irrespective of the ordering [20]: the elongated phase $u_{xx} = u_{yy} \leq u_{zz}$ and the phase $u_{xx} = u_{yy} > u_{zz}$, compressed along the fourfold axis, which is assumed to be the **z** axis. If we disregard the trebling of the primitive cell along **n**, we obtain **a** ‖ **x**(**y**), **b** ‖ **y**(**x**) and **z** ‖ **c**/3 in accordance with conventional crystallographic rules for an elongated tetragonal phase. In the compressed phase, **a** ‖ **z**, **b** ‖ **x**(**y**), **c**/3 ‖ **y**(**x**).

The interrelation between the Y–Ba ordering and spontaneous deformations η_2 and η_3 is such that the **n** axis in oxygen-deficient compositions (with $y > 0.65$) is parallel to the largest parameter of the primitive cell and the praphase, i.e., **n** ‖ **c**/3 ‖ **z**. With such a mutual orientation of the **n** and **c**/3 axes, for which the **c**/3 direction is determined only by spontaneous deformations of the praphase, the crystal has tetragonal symmetry. The emergence of spontaneous ODs in $YBa_2Cu_3O_{7-y}$ for $y = 0.65$ under the hypothesis concerning the praphase (the T–O transition) is interpreted in [17] as a proper ferroelastic transition determined by η_2 and η_3. The components of the corresponding two-component OP, which are adapted to the cubic symmetry of the praphase, have the form of tetragonal ($e_1 = (2u_{zz} - u_{xx} - u_{yy})/6^{1/2}$) and orthorhombic ($e_2 = (u_{xx} - u_{yy})/2^{1/2}$) deformation components.

According to the crystallographic rules, the lattice parameters are referred to in accordance with their magnitudes as $c/3 \geq b \geq a$. Consequently, while calculating e_1 and e_2 from the experimental data for the orthorhombic phase, one must assume that

$$e_1(2c/3 - a - b)/(6^{1/2}d); \quad e_2 = (b - a)/(2^{1/2}d), \quad (1)$$

for $2b \leq a + c/3$ and

$$e_1 = (2a - b - c/3)/(6^{1/2}d); \qquad e_2 = (c/3 - b)/(2^{1/2}d), \quad (2)$$

for $2b > a + c/3$; here, $d = (a + b + c/3)/3$.

It should be noted that spontaneous deformations of the unit cell of the praphase, averaged over the unit cell of the real structure with an ordered Y–Ba cation distribution, are small (<1%). According to the Landau theory of proper ferroelastic transitions in cubic crystals, the orthorhombic phase for small OPs [20] must exist in a narrow range of variation of external factors. Then the tetragonal phase must appear again. As a result of this sequence of two phase transitions, the tetragonal phase elongated along the preferred axis ($c/3 > a = b$) must be transformed into another tetragonal phase compressed along the preferred axis ($c/3 = b > a$). The situation is complicated in the case of $YBa_2Cu_3O_{7-y}$ in

the presence of the second OP determining the extent of the Y–Ba ordering. It was mentioned above that the largest unit cell parameter of the praphase for oxygen-deficient crystals is directed along **n**. Consequently, $\mathbf{n} \perp \mathbf{a}$ in the phase compressed along **a**, and the crystal must remain orthorhombic even in the phase that would be tetragonal in the case of just one proper ferroelastic OP.

5. For determining the origin of ODs, it is significant that, according to the Landau theory [5, 20], orthorhombicity determined by e_2 and the coupling of the deformation e_2 with the Y–Ba ordering must have another dependence on external factors than the proper ferroelastic one. In the case in question (where the second OP describes the trebling of the crystal), the quantity e_2 must be a linear function of an external parameter determining the transition to the compressed tetragonal phase, i.e., oxygen concentration. Note that this is a necessary consequence of symmetry, and hence this mechanism of the emergence of improper ODs always takes place.

Figures 2a and 2b show the results obtained in [10–15] and processed by using formulas (1) and (2). The straight line in Fig. 2 is plotted according to the most reliable (in our opinion [16]) results [9, 10]. This line was obtained by the least squares method, taking into account all the experimental points with the same weight. It follows from these results that the dependence of ODs on y for $0.07 < y < 0.45$ is indeed linear, which corresponds to improper ferroelastic deformations. The OD variation with y for $0.45 < y < 0.65(0.68)$ is in complete accord with the Landau theory of spontaneous proper ferroelastic deformations of the praphase, i.e., $e_2^2 \sim (y - y_0)$.

Naturally, we can try to approximate by straight lines the left-hand side of Fig. 2b for such a small number of experimental points obtained by different authors. However, the standard deviation in such an approximation exceeds the standard deviation from the straight line on the left-hand side in Fig. 2a and on the right-hand side in Fig. 2b by a factor of five and is larger than the experimental error indicated in [9–15].

6. It should be noted, however, that in this work we cannot draw any final conclusions about the nature of interactions that induce orthorhombicity for $0.07 < y < 0.45$. As a matter of fact, improper deformations with the same dependence on y can be induced, for example, by oxygen ordering [3, 21]. It should be emphasized that the orthorhombicity induced by oxygen ordering, as well as that induced by the Y–Ba ordering, is an effect associated with symmetry, i.e., existing in all cases. Moreover, according to [22], the temperature of oxygen ordering can be elevated in this case due to coupling with spontaneous deformations of the praphase. In order to determine the actual origin of improper deformations, i.e., the quantitative contributions from various interactions, one must identify the lines of all

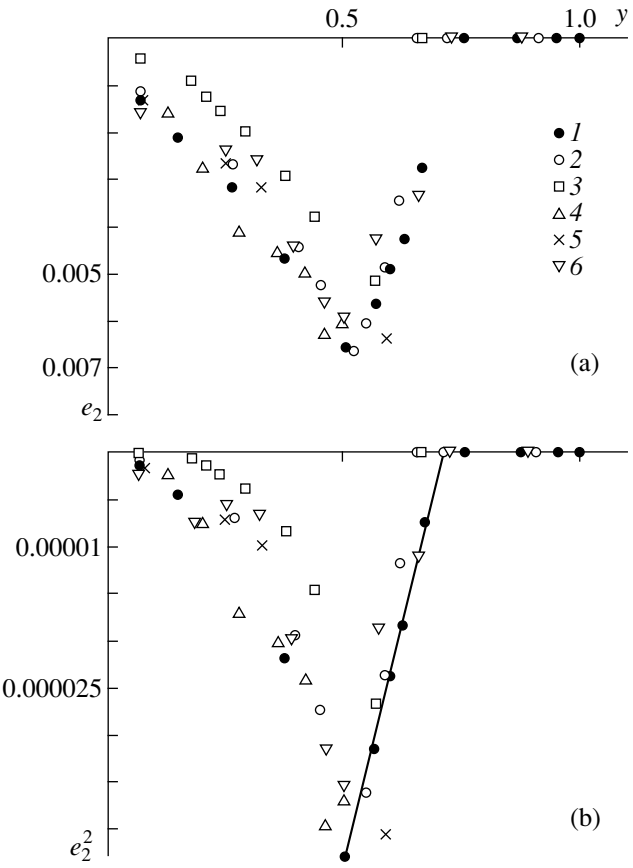

Fig. 2. Dependence of orthorhombic deformations of a unit cell of the praphase [2, 17–19] on the oxygen concentration; (a) and (b) illustrate the division of orthorhombic deformations into proper ferroelastic deformations and those induced by the coupling with other OPs. Notation *1–6* is the same as in Fig. 1.

structural transformations observed on the T–y diagrams of $YBa_2Cu_3O_{7-y}$. Such a task, however, is beyond the scope of the present brief communication.

ACKNOWLEDGMENTS

This work was supported by the Russian Foundation for Basic Research.

REFERENCES

1. V. V. Moshchalkov, *High-Temperature Superconductors* (Znanie, Moscow, 1987).
2. H. Shaked, P. M. Keane, J. C. Rodríguez, F. F. Owen, R. L. Hitterman, and J. D. Jorgensen, *Crystal Structures of the High-T_c Superconducting Copper-Oxides* (Elsevier, Amsterdam, 1994).
3. A. Fuchs, W. Prusseit, P. Berberich, and H. Kinder, Phys. Rev. B **53** (22), R14745 (1996).
4. K. Nakamura, A. Yu. Gufan, and Yu. M. Gufan, Kristallografiya **44** (3), 510 (1999) [Crystallogr. Rep. **44** (3), 469 (1999)]; Kristallografiya **44** (4), 650 (1999) [Crystallogr. Rep. **44**, 603 (1999)].

5. L. D. Landau and E. M. Lifshitz, *Statistical Physics* (Nauka, Moscow, 1964; Pergamon Press, Oxford, 1980).
6. G. P. Shveĭkin, V. A. Gubanov, A. A. Fotiev, G. V. Bazuev, and A. A. Evdokimov, *Electronic Structure and Physical–Chemical Properties of High-Temperature Superconductors* (Nauka, Moscow, 1990).
7. B. W. Veal, A. P. Paulikas, Hoydoo You, *et al.*, Phys. Rev. B **42** (10), 6305 (1990).
8. G. G. Gridneva, O. A. Bunina, O. F. Bazaev, and V. S. Filip'ev, Sverkhprovodimost': Fiz., Khim., Tekh. **4**, 1734 (1991).
9. K. Nakamura, J. Ye, and A. Ishii, Physica C (Amsterdam) **213** (1) (1993).
10. Jinhua Ye and K. Nakamura, Phys. Rev. B **48**, 7554 (1993).
11. J. D. Jorgensen, B. W. Veal, A. P. Paulikas, *et al.*, Phys. Rev. B **41**, 1863 (1990).
12. R. J. Cava, A. W. Hewat, E. A. Hewat, *et al.*, Physica C (Amsterdam) **165**, 419 (1990).
13. H. Mazaki, Yu. Ueda, Yu. Aihara, *et al.*, Jpn. J. Appl. Phys. **28**, 2368 (1998).
14. B. Fisher, J. Genossar, C. G. Kuper, *et al.*, Phys. Rev. B **47**, 6054 (1993).
15. J. M. Tarascon, in *Chemistry of High Temperature Superconductors*, Ed. by D. L. Nelson, M. S. Whitingham, and T. F. George (Amer. Chem. Soc., Washington, 1987), p. 198; *Novel Superconductivity*, Ed. by S. A. Wolf and V. Z. Kresin (Plenum, New York, 1987), p. 705.
16. K. Nakamura and A. Yu. Gufan, in *Proceedings of IMHTS-1R, 1998*, Ferroelectrics (1999).
17. Yu. M. Gufan, Pis'ma Zh. Éksp. Teor. Fiz. **61** (8), 646 (1995) [JETP Lett. **61**, 665 (1995)]; Kristallografiya **40** (2), 203 (1995) [Crystallogr. Rep. **40**, 181 (1995)].
18. V. P. Dmitriev and P. Toledano, Kristallografiya **40** (3), 548 (1995) [Crystallogr. Rep. **40**, 502 (1995)].
19. V. P. Dmitriev and P. Toledano, Phys. Lett. A **199**, 113 (1995).
20. V. P. Sakhnenko and V. M. Talanov, Fiz. Tverd. Tela (Leningrad) **21** (8), 2435 (1979) [Sov. Phys. Solid State **21**, 1401 (1979)]; Fiz. Tverd. Tela (Leningrad) **22**, 785 (1980) [Sov. Phys. Solid State **22**, 458 (1980)].
21. M. Iliev, C. Thomsen, V. Hadjiev, and M. Cardona, Phys. Rev. B **47**, 12341 (1993).
22. Yu. M. Gufan and V.I. Torgashev, Fiz. Tverd. Tela (Leningrad) **22** (6), 1629 (1980) [Sov. Phys. Solid State **22**, 951 (1980)]; Fiz. Tverd. Tela (Leningrad) **23** (4), 1129 (1981) [Sov. Phys. Solid State **23**, 656 (1981)].

Translated by N. Wadhwa

Physics of the Solid State, Vol. 42, No. 7, 2000, pp. 1215–1217. Translated from Fizika Tverdogo Tela, Vol. 42, No. 7, 2000, pp. 1180–1182.

METALS AND SUPERCONDUCTORS

Superconductivity of In-Doped $Sn_{0.62}Pb_{0.33}Ge_{0.05}Te$ Alloys

S. A. Nemov*, P. A. Osipov*, V. I. Proshin*, R. V. Parfen'ev, D. V. Shamshur**, and N. P. Shaĭnova*****

**St. Petersburg State Technical University, ul. Politekhnicheskaya 29, St. Petersburg, 195251 Russia*

***Ioffe Physicotechnical Institute, Russian Academy of Sciences, Politekhnicheskaya ul. 29, St. Petersburg, 194021 Russia*

****Herzen Russian State Pedagogical University, St. Petersburg, 191186 Russia*

Received January 12, 2000

Abstract—A study of the Hall and Seebeck coefficients and of resistivity has been carried out on an $Sn_{0.62}Pb_{0.33}Ge_{0.05}Te$ alloy doped by 5 and 10 at. % In. A superconducting transition with the maximum critical temperature $T_C \sim 4$ K has been discovered in samples with hole concentrations $p \geq 1 \times 10^{21}$ cm^{-3}. The dependence of T_C on hole concentration has been established to be of a threshold nature. The onset of superconductivity is accompanied practically simultaneously by a growth of the resistivity and a sharp drop of the Seebeck coefficient. These features in the experimental data indicate the existence of a band of In resonance states within the allowed valence-band spectrum and strong resonance hole scattering to impurity states. The threshold character of the $T_C(p)$ dependence is connected with the holes filling the resonance states. A positive correlation between the resonance scattering intensity and the critical temperature is observed. © *2000 MAIK "Nauka/Interperiodica".*

This work is a continuation of the studies on the electrophysical properties of In-doped $Sn_{0.62}Pb_{0.33}Ge_{0.05}Te$ alloys started in [1]. The studies were carried out on both bulk and film samples. The bulk samples were prepared by the metalloceramic method and subjected to homogenization anneal at 650°C for 120 h. They were subsequently used as a batch to prepare thin layers on mica by pulsed laser spraying [1]. The measurements of the electrical conductivity and of the Hall and Seebeck coefficients made on bulk and film samples showed their transport coefficients to be similar for comparable carrier concentrations. A study was made of the resistivity ρ in the low-temperature range, 0.4–4.2 K, both in a magnetic field $H \leq 13$ kOe and without it. The hole concentration p was derived from room-temperature Hall measurements by using the expression

$$p = (eR)^{-1}, \quad (1)$$

where R is the Hall coefficient. The samples and layers investigated had hole conduction with a carrier concentration varying from 3×10^{19} to 6×10^{21} cm^{-3}.

The measurements of the $\rho(T, H)$ dependences showed that only samples with hole concentrations $p \geq 1 \times 10^{21}$ cm^{-3}show a transition to the superconducting state (see Fig. 1). The critical temperature T_C of the superconducting transition was determined at the $0.5\rho_N$ level (where ρ_N is the residual resistivity before the superconducting jump). The dependence of T_C on hole concentration displayed in Fig. 2 follows a distinct threshold pattern.

Note that SnTe, GeTe, and the related solid solutions without an In impurity also undergo a superconducting transition. However, it occurs at critical temperatures and critical magnetic fields that are smaller by an order of magnitude, with the $T_C(p)$ relation passing through a broad smooth maximum [2].

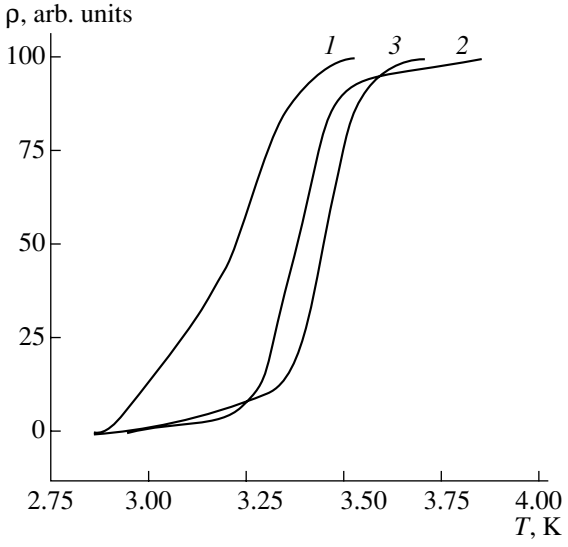

Fig. 1. Temperature dependence of the resistivity ρ of $Sn_{0.62}Pb_{0.33}Ge_{0.05}Te$: In samples with hole concentrations p (10^{21} cm^{-3}): (*1*) 1.5, (*2*) 2.25, and (*3*) 3.1, respectively.

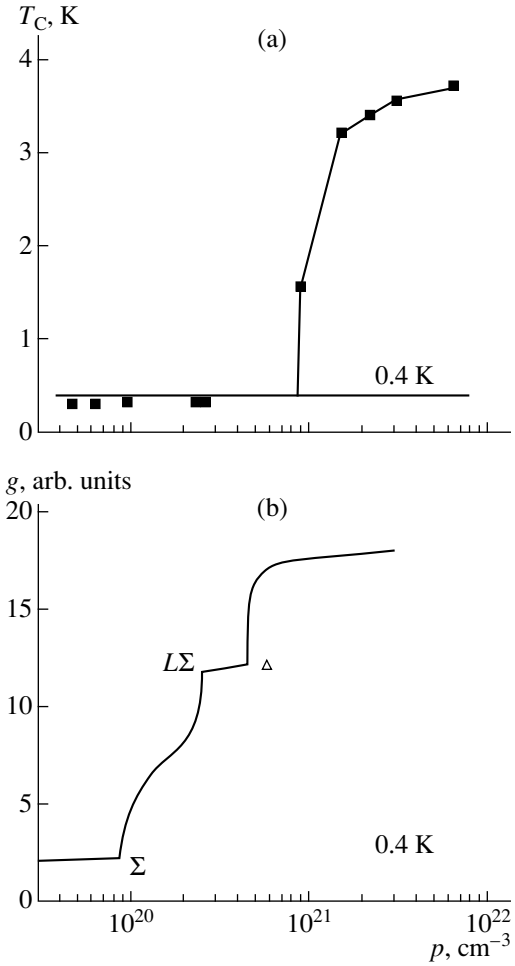

Fig. 2. Dependence of (a) critical temperature T_C and (b) density-of-states function g in $Sn_{0.62}Pb_{0.33}Ge_{0.05}Te$: In alloys on hole concentration p. The samples identified by points at $T < 0.4$ K did not become superconducting.

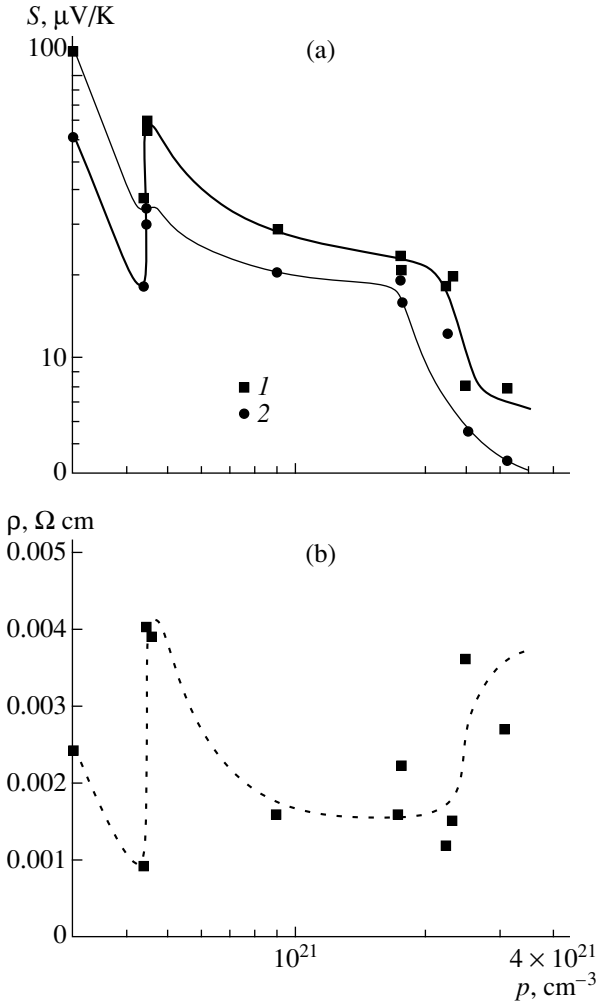

Fig. 3. Dependences of (a) the Seebeck coefficient and (b) resistivity in $Sn_{0.62}Pb_{0.33}Ge_{0.05}Te$: In alloys on hole concentration of temperatures T (*1*) 300 and (*2*) 120 K.

The onset of superconductivity in $Sn_{0.62}Pb_{0.33}Ge_{0.05}Te$: In alloys at $p \geq 1.5 \times 10^{21}$ cm^{-3} cannot be associated with the Fermi level ε_F falling into an additional valence-band extremum. The Δ extremum, closest in hole concentration in the valence band, could act as such an extremum. However, by [1], its filling by holes starts at $p \geq 4.5 \times 10^{20}$ cm^{-3} (Fig. 2), whereas the hole concentration at which superconductivity sets in the alloys studied is $p \approx 1 \times 10^{21}$ cm^{-3}. A threshold character of the $T_C(p)$ dependence, and just as high superconducting parameters T_C and H_{C2} were observed earlier in SnTe : In [3] and PbTe : Tl [4], and assigned to the Fermi level falling into the band of the impurity resonance states of In and Tl, respectively [5]. Therefore, it appears only natural, as this was done in [3, 5], to assign the onset of superconductivity in the $Sn_{0.62}Pb_{0.33}Ge_{0.05}Te$: In alloy to impurity resonance states.

The data on the resistivity and the Seebeck coefficient presented in Fig. 3 may serve as additional arguments for the existence in the $Sn_{0.62}Pb_{0.33}Ge_{0.05}Te$: In alloy of a band of indium resonance states with an edge at $p \approx 1 \times 10^{21}$ cm^{-3}. As seen from Fig. 3, for $p \geq 1 \times 10^{21}$ cm^{-3}, the onset of superconductivity in the alloys is accompanied practically simultaneously by a considerable decrease in the Seebeck coefficient and an increase in the resistivity at similar hole concentrations. These data agree with the concept of the existence of a band of impurity resonance states and of resonant hole scattering into these states [5]. Indeed, one of the characteristic signatures of impurity resonance states is efficient resonant-carrier scattering into an impurity band, which produces a characteristic minimum in the energy dependence of the relaxation time $\tau(\varepsilon)$ (Fig. 3). The minimum in $\tau(\varepsilon)$ results in the appearance of a maximum in the $\rho(\varepsilon_F)$ dependence, because $\rho \sim 1/\tau(\varepsilon_F)$, and of a deep minimum in $S(\varepsilon_F)$; in the case of a quadratic

dispersion law, the Seebeck coefficient in a degenerate sample is given by the expression

$$S = \frac{k_0}{e}\frac{\pi^2}{3}\frac{k_0 T}{\varepsilon_F}\left(\frac{d\ln\tau}{d\ln\varepsilon}\bigg|_{\varepsilon=\varepsilon_F} + \frac{3}{2}\right). \quad (2)$$

Therefore, as the Fermi level falls into the resonance-state band, one should observe a rise in the resistivity and a drop in the Seebeck coefficient. These model concepts agree with the experimental data obtained for the $Sn_{0.62}Pb_{0.33}Ge_{0.05}Te$: In alloy (Fig. 3). It should also be pointed out that one observes a clearly pronounced positive correlation between resonance scattering and the superconducting transition with a critical temperature record high for semiconductors, $T_C \sim 3$–4 K.

Thus, our study indicates the existence of a band of In resonance states within the allowed hole spectrum in the $Sn_{0.62}Pb_{0.33}Ge_{0.05}Te$: In solid solution. It has been established that the drop in the Fermi level into the In impurity band is accompanied by the observation of resonant hole scattering and the onset of superconductivity with critical temperatures $T_C \sim 3$–4 K.

REFERENCES

1. S. A. Nemov, S. F. Musikhin, P. A. Osipov, and V. I. Proshin, Fiz. Tverd. Tela (St. Petersburg) **42**, 623 (2000) [Phys. Solid State **42**, 638 (2000)].
2. M. L. Cohen *et al.*, in *Superconductivity*, Ed. by R. D. Parks (Dekker, New York, 1969), Chap. 12, p. 615.
3. G. S. Bushmarina, I. A. Drabkin, V. V. Kompaniets, *et al.*, Fiz. Tverd. Tela (Leningrad) **28**, 1094 (1986) [Sov. Phys. Solid State **28**, 612 (1986)].
4. I. A. Chernik, S. N. Lykov, and N. I. Grechko, Fiz. Tverd. Tela (Leningrad) **24**, 2931 (1982) [Sov. Phys. Solid State **24**, 1661 (1982)].
5. S. A. Nemov and Yu. I. Ravich, Usp. Fiz. Nauk **168**, 817 (1998) [Phys. Usp. **41**, 735 (1998)].

Translated by G. Skrebtsov

Physics of the Solid State, Vol. 42, No. 7, 2000, pp. 1218–1221. Translated from Fizika Tverdogo Tela, Vol. 42, No. 7, 2000, pp. 1183–1186.

METALS AND SUPERCONDUCTORS

Effect of Stress Fields of Small-Angle Tilt Grain Boundaries on Structural Inhomogeneities in High-Temperature Superconductors

A. Yu. Kraevskiĭ and I. A. Ovid'ko

Institute of Problems in Machine Science, Russian Academy of Sciences, Vasil'evskiĭ ostrov, Bol'shoĭ pr. 61, St. Petersburg, 199178 Russia

e-mail: ovidko@def.ipme.ru

Received November 16, 1999; in final form, January 19, 2000

Abstract—The effect of dilatational stresses of grain boundaries on the atomic structure rearrangement near these boundaries in high-temperature superconductors is discussed. The concentration profiles characterizing the spatially inhomogeneous distribution of oxygen near small-angle tilt boundaries in Bi–Sr–Ca–Cu–O superconductors are calculated. © *2000 MAIK "Nauka/Interperiodica".*

Polycrystalline superconductors with a high superconducting transition temperature T_c are characterized by values of the critical transport current density (J_c) that are much smaller (by several orders of magnitude) than its values in monocrystalline samples of the same chemical composition (see, for example, [1–5]). Such low values of J_c in polycrystalline HTSC are due to the presence of grain boundaries which "suppress" superconductivity (see reviews [3, 4]). Despite a considerable body of experimental data having been accumulated on the effect of grain boundaries on the critical density of transport current in HTSC, the physical mechanisms behind this effect have yet to be determined unambiguously [3, 4].

We believe that spatially inhomogeneous dilatational stress fields of grain boundaries cause local variations of the stoichiometry in grain boundaries and their surroundings, which may play a significant role in the deterioration of superconducting properties of polycrystalline HTSC. This assumption corresponds to the modern concepts on the influence of defects on the inhomogeneities of chemical composition in polyatomic solids (see, for example, [6]) and conforms (at least qualitatively) to the following experimental facts pertaining to HTSC: (1) The local departure from the stoichiometric composition in grain boundaries and their surroundings [3, 7, 8]. (2) The existence of regions with specific properties of the electron subsystem in the vicinity of grain boundaries [3, 9]. (3) The change in superconducting properties along grain boundaries [3, 4]. This paper aims mainly to provide a theoretical quantitative description of structural (stoichiometric) inhomogeneities induced by dilatational stress fields of small-angle tilt boundaries in the superconducting materials Bi–Sr–Ca–Cu–O.

1. EFFECT OF DILATATIONAL STRESSES ON SPATIAL DISTRIBUTION OF ATOMS IN POLYATOMIC SOLIDS

High-temperature superconductors are polyatomic crystalline solids. In a perfect (defect-free) polyatomic solid free from stress fields, the atoms of various chemical elements are arranged in order according to their chemical nature and concentration. The presence of defects that are responsible for the emergence of stress fields may cause local violations of the ideal distribution of atoms in polyatomic solids, since different atoms respond in different ways to applied stress fields. The dilatational stresses exert the strongest influence on the spatial distribution of atoms characterized by different atomic volumes in crystals subjected to elastic stresses [6]. Large (small) atoms tend to move towards regions with tensile (compressive) stresses.

Grain boundaries are planar defects capable of producing spatially nonuniform stresses (including dilatational ones) and, consequently, can cause a redistribution of atoms in the adjoining regions in the polyatomic material. However, the superconducting properties of HTSC materials are sensitive to their nonstoichiometry. Among other things, the value of J_c depends heavily on the concentration of oxygen in the Y–Ba–Cu–O superconductor [3, 10]. Hence, local departures from the stoichiometry induced by dilatational stresses of grain boundaries can significantly affect the value of J_c characterizing the superconducting current in polycrystalline HTSC.

Let us consider the structural inhomogeneities induced by dilatational stresses of small-angle tilt boundaries in the vicinity of these boundaries. Small-angle tilt boundaries are walls of edge dislocations periodically distributed over the crystal lattice [11]. The misorientation θ of the tilt boundary is connected with

1063-7834/00/4207-1218$20.00

the geometrical parameters of edge dislocations through the Frank relation [11]

$$\sin\theta = b/d, \tag{1}$$

where b is the magnitude of the Burgers vector of a dislocation and d is the separation between adjacent dislocations in the wall. In a reference frame with the z axis parallel to dislocation lines and the x axis parallel to the Burgers vectors, the fields of dilatational stresses σ_{xx}, σ_{yy}, and σ_{zz} generated by the edge dislocation wall can be defined as follows [11]:

$$\sigma_{xx}(x, y) = -\sigma_0 \sin\frac{2\pi y}{d} \times\left(\cosh\frac{2\pi x}{d} - \cos\frac{2\pi y}{d} + \frac{2\pi x}{d}\sinh\frac{2\pi x}{d}\right), \tag{2}$$

$$\sigma_{yy}(x, y) = -\sigma_0 \sin\frac{2\pi y}{d} \times\left(\cosh\frac{2\pi x}{d} - \cos\frac{2\pi y}{d} - \frac{2\pi x}{d}\sinh\frac{2\pi x}{d}\right), \tag{3}$$

$$\sigma_{zz}(x, y) = \nu(\sigma_{xx}(x, y) + \sigma_{yy}(x, y)), \tag{4}$$

$$\sigma_0 = \frac{Gb}{2d(1-\nu)\left(\cosh\frac{2\pi x}{d} - \cos\frac{2\pi y}{d}\right)^2}. \tag{5}$$

Here, G is the shear modulus and ν is the Poisson ratio.

The elastic interaction between dislocations in the wall and large/small atoms (whose atomic volume is larger/smaller than the average size of an atom) causes a redistribution of atoms in a polyatomic medium. This interaction between atoms of the ith type and the stress field is characterized by the energy [6]

$$E_i = -(\Delta V_i)\sigma_{ll}/3. \tag{6}$$

Here, $\sigma_{ll} = \sigma_{xx} + \sigma_{yy} + \sigma_{zz}$, and $\Delta V_i = V_i - \langle V\rangle$ is the difference between the volume V_i of an atom of the ith type and the average atomic volume $\langle V\rangle$ in a polyatomic solid.[1] In the model situation, when the polyatomic medium is an ideal solid solution, the elastic interaction (6) leads to the following equilibrium distribution of the atoms of the ith type [6]:

$$C_i(x, y, z) = C_i^0 \exp(E_i(x, y, z)/kT), \tag{7}$$

where k is the Boltzmann constant, T is the absolute temperature, and C_i^0 is the concentration of atoms of the ith type in the absence of stress fields. The distribution (7) corresponds to the minimum elastic energy of an ideal solid solution.

[1] In the general case, the unit cells in polyatomic solids (including high-temperature superconductors) are characterized by a variable stoichiometry. Hence, it is expedient to use in formula (7) the atomic volume $\langle V\rangle$ averaged over the entire crystal (and not just over a unit cell).

2. SPATIAL DISTRIBUTION OF OXYGEN ATOMS NEAR SMALL-ANGLE TILT BOUNDARIES IN HIGH-TEMPERATURE SUPERCONDUCTORS

In order to describe the real situation with polyatomic superconductors, we must impose certain physical constraints on using formula (7), which are based on the experimental data. For example, the results of experiments show [7, 8] that local variations of the chemical composition in the vicinity of the grain boundaries in the Y–Ba–Cu–O superconductors are correlated. To be more precise, the atomic structure rearrangement near grain boundaries occurs primarily on account of a redistribution of small Cu and O atoms. As a result of the redistribution, the characteristic numbers of Cu and O atoms in a unit cell of the Y–Ba–Cu–O superconductor change by not more than unity. In other words, the local rearrangement of atoms occurring in the vicinity of grain boundaries is predominantly of the type

$$Y_1Ba_2Cu_3O_7 \longrightarrow Y_1Ba_2Cu_2O_8, \tag{8a}$$

$$Y_1Ba_2Cu_3O_7 \longrightarrow Y_1Ba_2Cu_4O_6, Y_1Ba_2Cu_3O_6. \tag{8b}$$

Large Y and Ba atoms are also redistributed in the vicinity of the grain boundaries. However, this redistribution is rarer in occurrence than that of small atoms and leads only to insignificant variations of the local Y and Ba concentrations [7, 8].

Such peculiarities in the local transformations of the atomic structure of Y–Ba–Cu–O compounds can be explained naturally as follows. The displacements of small atoms (Cu, O) are characterized by low activation energies (since moving small atoms cause an only insignificant displacement of the surrounding atomic structure) and, hence, occur more frequently than for large atoms (Y, Ba), which have high activation energies. Since HTSC are usually characterized by high concentrations of vacancies [3, 10], the redistributions of Cu and O atoms take place effectively through the vacancy mechanism.

The Cu and O atoms are also small atoms in the Bi–Sr–Ca–Cu–O superconductors, while the Bi, Sr and Ca atoms are comparatively large. Hence, the redistribution of small atoms (Cu and O) occurs much more frequently than for large atoms. Moreover, significant variations (by more than unity) in the characteristic numbers of Cu and O atoms in unit cells of oxide ceramics are unlikely on account of factors of a chemical nature. Hence, in our subsequent estimates, we shall confine the analysis to such rearrangements for which the characteristic numbers of Cu and O atoms change by not more than unity in the unit cells of the Bi–Sr–Ca–Cu–O superconductors. In other words, we shall consider only the following rearrangements in the unit cells of these superconducting materials:

$$Cu_nO_m \longrightarrow Cu_{n+1}O_{m-1}, Cu_nO_{m-1}, \tag{9a}$$

$$Cu_nO_m \longrightarrow Cu_{n-1}O_{m+1}, \tag{9b}$$

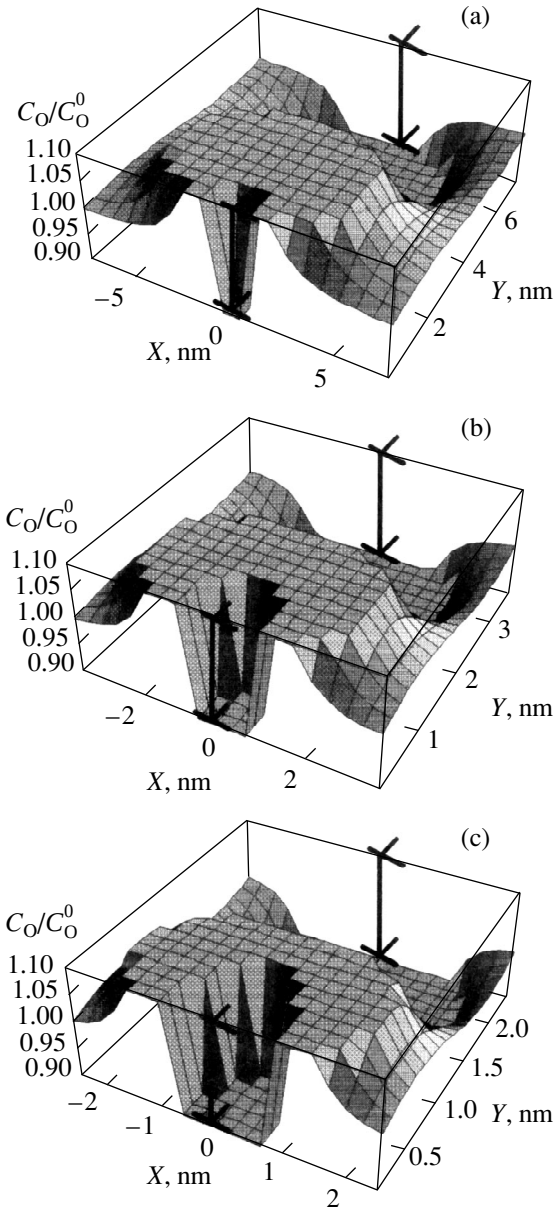

Fig. 1. Distribution of oxygen in units of C_O/C_O^0 near a periodic small-angle tilt boundary with different misorientation angles θ in the $Bi_2Sr_2Ca_2Cu_3O_{10}$ superconductor. θ (deg) : (a) 3, (b) 6, and (c) 9.

where n and m characterize an HTSC unit cell in the absence of stress fields.[2]

Taking into consideration the experimental data presented in [7, 8], we used formula (7) to calculate the distribution C_O of oxygen atoms in the $Bi_2Sr_2Ca_2Cu_3O_{10}$ superconductors in the vicinity of small-angle tilt boundaries (see Fig. 1). The following characteristic values of parameters were used: b = 0.39 nm, $G \approx 34.2$ GPa [13], $\nu \approx 0.2$ [13], $C_O^0 = 10/19$, $T = 77$ K, $\Delta V = V_O - (V_{Cu} + V_O)/2$, $V_O = 0.0017$ nm^3, and $V_{Cu} = 0.0089$ nm^3 (where the atomic volumes V_{Cu} and V_O of copper and oxygen, respectively, are calculated as volumes of spheres with radii specified in [14]). The cores of edge dislocations (described here as cylinders of radius $r_0 \approx 1.5b$ and characterized by a certain positive dilatation according to [15]) are treated as regions with a reduced concentration of oxygen (see Fig. 1).

The following peculiarities are observed in the distribution of atoms: Each period of the small-angle tilt boundary contains two regions with nonideal stoichiometry. The first of these regions consists of the cores of tilt lattice deformations (see Fig. 1). In the second region, which lies between the dislocation cores, the dilatational (tensile or compressive) stresses σ_{xx}, σ_{yy}, and σ_{zz} (defined by formulas (2)–(4)) are caused by departures from ideal stoichiometry.

Thus, the dilatational stresses at grain boundaries significantly affect the local stoichiometry in the vicinity of small-angle tilt boundaries in HTSC. The lattice edge dislocations constituting small-angle tilt boundaries play a decisive role as sources in dilatational stresses. The existence of local stoichiometric variations induced by dilatational stresses in the vicinity of grain boundaries may considerably affect the experimentally observed suppression of superconducting properties of polycrystalline HTSC.

It should be noted that the effect of local stoichiometric variations is just a part of the overall effect of grain boundaries on high-temperature superconductivity. Other factors responsible for a variation in the critical current in polycrystalline HTSC include the structure of cores of grain boundaries and adjoining regions [16–18], the d symmetry of the order parameter [19, 20], and the texture [21]. Further experimental and theoretical studies are required for a quantitative analysis of the role of all factors in HTSC containing small-angle and large-angle tilt and twist grain boundaries.

ACKNOWLEDGMENTS

One of the authors (I. A. O.) is grateful to R. A. Masumura, F. R. N. Nabarro, and C. S. Pande for fruitful discussions of the present work.

This work was supported by the Russian Foundation for Basic Research (grant no. 98-02-16075) and the Office of US Naval Research (grant no. 00014-99-1-0896).

REFERENCES

1. D. Dimos, P. Chaudhari, J. Mannhart, and F. K. LeGoues, Phys. Rev. Lett. **61**, 219 (1988).

[2] It should be noted that copper atoms exhibit variable valency in high-temperature superconductors with different stoichiometry [12]. Hence, the emergence of spatial inhomogeneities in the stoichiometry does not lead to spatial inhomogeneities in the distribution of the ionic charge in the crystal lattice, and is not accompanied by any significant variation in its electrostatic energy.

2. D. Dimos, P. Chaudhari, and J. Mannhart, Phys. Rev. B **41**, 4038 (1990).
3. S. E. Babcock and J. L. Vargas, Ann. Rev. Mater. Sci. **25**, 193 (1995).
4. M. Prester, Supercond. Sci. Technol. **11**, 333 (1998).
5. T. Amrein, M. Seitz, D. Uhl, *et al.*, Appl. Phys. Lett. **63**, 1978 (1993).
6. L. A. Girifalco and D. O. Welch, *Point Defects and Diffusion in Strained Metals* (Gordon and Breach, 1967), p. 312.
7. D. M. Kroeger, A. Choudhury, J. Brynestad, *et al.*, J. Appl. Phys. **64**, 331 (1988).
8. S. E. Babcock and D. C. Larbalestier, Appl. Phys. Lett. **55**, 393 (1989).
9. N. D. Browning, M. F. Chisholm, S. F. Pennycock, *et al.*, Physica C (Amsterdam) **212**, 185 (1993).
10. R. J. Cava, A. W. Hewat, E. A. Hewat, *et al.*, Physica C (Amsterdam) **165**, 419 (1990).
11. J. P. Hirth and J. Lothe, *Theory of Dislocations* (Wiley, New York, 1982).
12. N. M. Plakida, *High-Temperature Superconductors: International Education Program* (Moscow, 1966).
13. H. M. Ledbetter, S. A. Kim, R. B. Goldfarb, and K. Torgano, Phys. Rev. B **39**, 9689 (1989).
14. *Physical Quantities. Handbook*, Ed. by I. S. Grigor'ev and E. Z. Meĭlikov (Énergoizdat, Moscow, 1991).
15. A. Seeger and P. Haasen, Philos. Mag. **3**, 470 (1958).
16. M. F. Chisholm and S. J. Pennycook, Nature **351**, 47 (1991).
17. K. Jagannadham and J. Narayan, Philos. Mag. B **61**, 129 (1990).
18. D. Agassi, C. S. Pande, and R. A. Masumura, Phys. Rev. B **52**, 16237 (1995).
19. H. Hilgenkamp, J. Mannhart, and B. Mayer, Phys. Rev. B **53**, 14586 (1996).
20. J. Mannhart, Ch. Gerber, J. R. Kirtley, *et al.*, Phys. Rev. Lett. **77**, 2782 (1996).
21. L. N. Bulaevskii, L. L. Daemon, M. P. Maley, and J. Y. Coulter, Phys. Rev. B **48**, 13798 (1993).

Translated by N. Wadhwa

Physics of the Solid State, Vol. 42, No. 7, 2000, pp. 1222–1227. Translated from Fizika Tverdogo Tela, Vol. 42, No. 7, 2000, pp. 1187–1192.

SEMICONDUCTORS AND DIELECTRICS

Effect of Excitation Intensity and Electric Field on the Photoconductivity Relaxation in $Cd_xHg_{1-x}Te$/GaAs Polycrystalline Layers

A. I. Vlasenko, V. A. Gnatyuk, E. S. Gorodnichenko, and P. E. Mozol'

Institute of Semiconductor Physics, National Academy of Sciences of Ukraine, Kiev, 252650 Ukraine

e-mail: gnatyuk@class.semicond.kiev.ua

Received September 17, 1999

Abstract—The photoconductivity relaxation and the stationary photoconductivity in the *n*-$Cd_{0.8}Hg_{0.2}Te$ compensated polycrystalline layers at $T = 300$ K have been investigated as a function of the light intensity and the strength of applied electric field E. It is demonstrated that, at low excitation intensities, the saturation of stationary photoconductivity and a decrease in the relaxation time with an increase in E are caused by the minority carrier extraction. The effect of minority carrier extraction is analyzed with due regard for the internal electric field of potential barriers in intergranular layers. It is assumed that the features of nonequilibrium-carrier recombination, which proceeds through several channels and depends on the excitation intensity and extraction electric field strength, can stem from the polycrystalline structure of the $Cd_{0.8}Hg_{0.2}Te$ layers. © *2000 MAIK "Nauka/Interperiodica".*

1. INTRODUCTION

The lifetime of nonequilibrium charge carriers in crystals and layers of the $Cd_xHg_{1-x}Te$ semiconductor solid solutions depends on the structural perfection of samples and the quality of finishing their surface. The experimental conditions also can affect the character of light-induced processes. In particular, the extraction of minority charge carriers from the bulk of samples can be observed in strong electric fields. This leads to the change in stationary and kinetic characteristics of the photoconductivity with an increase in the strength of applied electric field [1–4]. In general, the kinetics of photoconductivity depends on the light intensity, because, at high excitation intensities, an increase in the concentration of nonequilibrium charge carriers brings about the modification of energy bands in a semiconductor and a change in the mechanism of nonequilibrium-carrier recombination [4, 5]. In most cases, the photoconductivity relaxation curves, from which the lifetime of nonequilibrium charge carriers can be directly determined, have a complex behavior and consist of several exponents corresponding to different recombination channels [6, 7]. The temperature dependences of the characteristic time for different components of the photoconductivity relaxation indicate that the fast component is caused by channels competing with the bulk recombination, rather than by the electron recombination [7]. These channels are associated with structural macrodefects such as the sample surface, grain and block boundaries, composition inhomogeneities, clusters, etc. In polycrystalline semiconductors, the grain boundaries can fulfill the function of efficient sinks for residual impurities and intrinsic point defects [8]. The intergranular layers produce potential barriers for nonequilibrium charge carriers due to an increased electric activity or can serve as regions of their enhanced recombination and, thus, can be responsible for electric and photoelectric properties of polycrystalline semiconductors [5, 9].

The aim of the present work was to investigate the relaxation characteristics of photoconductivity at different excitation intensities in the $Cd_{0.8}Hg_{0.2}Te$ polycrystalline layers, which were grown on GaAs substrates and exhibited high photosensitivity at room temperature [5], and also to elucidate how the strength of applied electric field affects the light-induced and recombination processes in the prepared layers upon excitation by nanosecond laser radiation pulses.

2. EXPERIMENTAL TECHNIQUE

The $Cd_{0.8}Hg_{0.2}Te$ polycrystalline layers ~20 μm thick were grown by the "evaporation–condensation–diffusion" technique on GaAs(100) semi-insulating substrates using a CdTe buffer layer under isothermal conditions. According to the electron probe microanalysis of the surface, the sample structure was identical to the polycrystalline structure of the substrate with a grain size of ~30 μm. The growth of the $Cd_xHg_{1-x}Te$ layers is accompanied by the formation of oxides due to doping intergranular layers by background impurities and substrate components. This leads to the formation of the grain boundary layer depleted in majority charge carriers and causes a high resistivity of intercrystalline regions. Indium contacts were applied to the as-etched surface of the $Cd_{0.8}Hg_{0.2}Te$ layer. The $1 \times 3 \times$

1063-7834/00/4207-1222$20.00 © 2000 MAIK "Nauka/Interperiodica"

3-mm samples were high-resistance ($\rho \approx 2 \times 10^3\ \Omega$ cm) and strongly compensated. They possessed the *n*-type conductivity with the effective electron concentration $n_{\text{eff}} = 3.2 \times 10^{13}$ cm^{-3} and the effective electron mobility $\mu_{\text{eff}} = 1.0 \times 10^2$ cm^2/(V s) at $T = 300$ K. The studied layers had a high photosensitivity in the spectral range 0.4–1.6 μm at $T = 77$ and 300 K [5].

The characteristic times for different photoconductivity relaxation components that corresponded to different channels of nonequilibrium-carrier recombination were calculated from the relaxation curves of photocurrent (nonstationary photoconductivity) excited by a neodymium laser radiation ($h\nu = 1.7$ eV; pulse length, 20 ns) with a linear variation in the intensity I. The intensity of photocarrier generation was changed using calibrated neutral gray filters. The stationary photoconductivity was measured according to the standard procedure at a constant modulation frequency of 400 Hz upon excitation by the monochromatic radiation with the photon energy $h\nu = 1.17$ eV by using an MDR-3 diffraction spectrometer and an incandescent lamp. The light intensity was of an order of 10^{12} photon/(cm^2 s). The dependences of the photoelectric characteristics on the excitation intensity I and the strength of applied electric field E were examined at $T = 300$ K in the ranges $I = 1 \times 10^{21}$–1.5×10^{25} photon/(cm^2 s) and E = 6–250 V/cm.

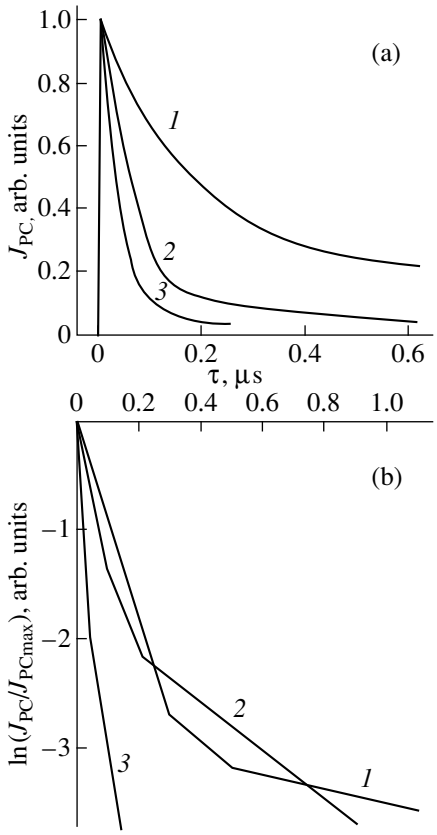

Fig. 1. (a) Oscillograms of the photoconductivity relaxation and (b) their representation on a semilogarithmic scale at (*1*, *2*) low [$I = 1 \times 10^{23}$ photon/(cm^2 s)] and (*3*) high [$I = 1 \times 10^{25}$ photon/(cm^2 s)] intensities of excitation by neodymium laser pulses with the photon energy $h\nu = 1.17$ eV. Extraction electric field strength E (V/cm): (*1*, *3*) 70 and (*2*) 250.

3. RESULTS AND DISCUSSION

3.1. Features of photoconductivity relaxation at different excitation intensities. The photoconductivity relaxation curves for the $Cd_xHg_{1-x}Te$ polycrystalline layers depend on the excitation level and extraction electric field strength. In our earlier work [5], it was found that, upon exposure of the studied samples to ruby or neodymium laser radiation at $T = 300$ K, the current–illuminance characteristics consist of two portions with slopes of ~0.5 and ~1 at radiation intensities below and above $I_0 \sim 4 \times 10^{23}$ photon/(cm^2 s), respectively. Figure 1a shows the photocurrent relaxation curves at a low excitation intensity (the slope of the current–illuminance characteristic is 0.5) for two electric field strengths $E = 70$ (curve *1*) and 250 V/cm (curve *2*) and at a high excitation intensity (the slope of the current–illuminance characteristic is equal to 1) for E = 70 V/cm (curve *3*). It should be noted that, at high excitation intensities $I > I_0$, the shape of the photoresponse did not depend on the extraction electric field strength over the entire range covered.

The kinetics of photoconductivity in the polycrystalline layers under consideration shows a complex behavior, because the nonequilibrium-carrier recombination proceeds through several channels. Figure 1b depicts the same relaxation curves (Fig. 1a) on a semilogarithmic scale. This enables us to reveal several exponents: three exponential portions of the photocurrent decay curve are observed at low excitation intensities (Fig. 1b, curves *1*, *2*), and two portions, at high excitation intensities (Fig 1b, curve *3*). In the latter case, the slow component of the photoconductivity relaxation is absent.

The presence of several exponential portions in the relaxation curves of photocurrent pulses can be explained by the nonequilibrium-carrier recombination in the bulk (inside the grains) and at different inhomogeneities, namely, at the surface inhomogeneities and internal macrodefects (grain boundaries, dislocations, etc.), which represent natural sinks of nonequilibrium charge carriers with a recombination rate exceeding the rate of bulk recombination [10]. As is known [5–9], the intergranular layer is the region in which the internal electric fields create potential barriers for charge carriers. Upon excitation of photocurrent in the $Cd_xHg_{1-x}Te$ layers by pulsed laser radiation with intensity $I \leq I_0$, the internal field of barriers induces the efficient spatial separation of photogenerated electron–hole pairs, prevents their recombination and electron transport toward the grain boundaries (sinks), and, thus, favors the development of recombination processes within the

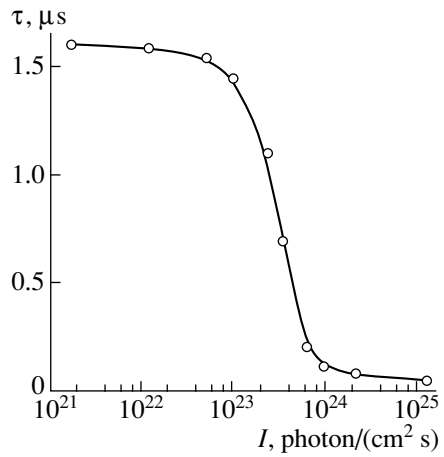

Fig. 2. Dependence of the nonequilibrium-carrier lifetime on the intensity of excitation by neodymium laser pulses with the photon energy $h\nu = 1.17$ eV.

grain whose structure is more perfect than that of the intergranular layer [5]. This increases the contribution of the bulk recombination channel to photocurrent relaxation and gives rise to the slow component (curves *1*, *2* in Fig. 1b).

Therefore, in the $Cd_xHg_{1-x}Te$ polycrystalline layers at low excitation intensities $I \le I_0$, the decay of photocurrent signal J_{PC} with time t is provided by three channels [6, 7], which are associated with the nonequilibrium-carrier recombination at the surface, internal macrodefects (primarily, at the grain boundaries), and in the bulk (inside the grain)

$$J_{PC}(t) = A\exp(-t/\tau_1) + B\exp(-t/\tau_2) + C\exp(-t/\tau_3). \quad (1)$$

These channels correspond to the exponential portions in the photoconductivity relaxation curves (Fig. 1b) with the characteristic times $\tau_1 = 0.14$ μs (fast component), $\tau_2 = 0.41$ μs (intermediate component), and $\tau_3 = 1.60$ μs (slow component) at the applied electric field $E = 70$ V/cm (curve *1*) and the characteristic times $\tau_1 = 0.07$ μs, $\tau_2 = 0.15$ μs, and $\tau_3 = 0.44$ μs at $E = 250$ V/cm (curve *2*).

At high excitation intensities $I \ge I_0$, when the concentration of nonequilibrium charge carriers becomes higher than the equilibrium concentration of electrons, the electric field of photoexcited carriers shields the potential barriers of intergranular layers, which impeded the escape of nonequilibrium charge carriers into the sinks [5], and the recombination processes predominantly proceed at the grain boundaries. The rate of nonequilibrium-carrier recombination at the macrodefects is higher than that in the bulk (inside the grain), and, hence, the contribution of the latter process to photoconductivity relaxation in this case becomes relatively small, which manifests itself in the disappearance of the slow component in the photocurrent relaxation curve (Fig. 1b, curve *3*). Consequently, the contributions of recombination channels are redistributed in such a way that the surface recombination and the recombination in intergranular layers become predominant in the photoconductivity relaxation. These two channels correspond to the two exponential portions in curve *3* (Fig. 1b) with the characteristic times $\tau' = 0.02$ and 0.05 μs and give rise to the photocurrent signal at high excitation intensities $I \ge I_0$

$$J'_{PC}(t) = A'\exp(-t/\tau'_1) + B'\exp(-t/\tau'_2). \quad (2)$$

Earlier [5], we demonstrated that, at the laser excitation intensity $I = I_0$, which provides the generation of nonequilibrium charge carriers in the concentration sufficient for the shielding of potential barriers at the grain boundaries, the slope of the current–illuminance curve abruptly changes from 0.5 (characteristic of the quadratic nonequilibrium-carrier recombination in the grain) to 1.0. This indicates a linear generation of carriers and their linear recombination, which is typical of homogeneous (without internal barriers) highly doped, compensated samples of the corresponding composition [11]. Additional evidence for the suppression of potential barriers, whose electric field efficiently separates the electron–hole pairs and ensures the long photocarrier lifetime τ at $I \le I_0$, is a sharp decrease in τ at the radiation intensity $I = I_0$ (Fig. 2). This dependence of the nonequilibrium-carrier lifetime, which was estimated from the slow component of the photocurrent relaxation, was measured at the electric field strength $E = 70$ V/cm.

This result essentially differs from the data obtained by Ivanov-Omskiĭ *et al.* [4] in similar experiments with the *n*-$Cd_{0.3}Hg_{0.7}Te$ homogeneous crystals at $T = 77$ K, in which the photoconductivity relaxation time did not depend on the light intensity. The threshold change in τ, i.e., its sharp decrease at $I = I_0$ (Fig. 2), coincides in excitation intensity with an abrupt change in the slope of the current–illuminance characteristic [5]. This confirms a decisive role of the potential barriers at the grain boundaries in recombination processes in the $Cd_{0.8}Hg_{0.2}Te$ polycrystalline layers at $T = 300$ K.

3.2. Effect of electric field strength on the photoconductivity relaxation. The electric field decreases potential barriers in the crystal matrix, changes the rate of nonequilibrium-carrier transfer to recombination macrodefects and the bending of energy bands, and, at high strengths, brings about the extraction of minority carriers from the bulk of samples [1–4]. These effects most strongly manifest themselves for inhomogeneous samples [7]. Apart from the general regularities observed for the $Cd_xHg_{1-x}Te$ structurally perfect crystals [1–4], the investigation of the stationary photoconductivity and the photoconductivity kinetics in the $Cd_{0.8}Hg_{0.2}Te$ polycrystalline layers as a function of the extraction electric field strength at different excitation intensities demonstrates that the materials under consideration are characterized by a number of specific

features. The dependence of the photocurrent amplitude J_{PC} on the pulsed radiation intensity of ruby or neodymium laser for the studied layers exhibits a typical linear behavior. The slope of this dependence decreases with an increase in the current passing through the sample. As was shown earlier for the n-$Cd_{0.3}Hg_{0.7}Te$ crystals at 77 K [4], such behavior is typical of highly sensitive materials and is not observed for crystals with a low photosensitivity. In our case, this suggests the evolution of recombination processes in the bulk of structurally perfect grains (polycrystallites) and an insignificant contribution of the recombination channels associated with the intergranular layers and the sample surface at low excitation intensities.

The stationary photocurrent Δi increases proportionally with the strength of applied electric field (Ohm law) and becomes saturated at $E > 70$ V/cm (Fig. 3, curve *4*). This field dependence of the photocurrent is characteristic of crystals with a high photosensitivity; however, the saturation of the photocurrent Δi in the polycrystalline layers under study is observed at higher electric field strengths compared to the $Cd_xHg_{1-x}Te$ crystals [3, 4]. The saturation of the stationary photocurrent with an increase in the electric field strength is explained by the extraction of minority carriers from the bulk, which should be accompanied by a decrease in the photoconductivity relaxation time [1–4]. This decrease in τ was experimentally observed and brought about the above decrease in the amplitude of nonstationary photocurrent J_{PC} with an increase in the current passing through the sample at a constant intensity of pulsed laser radiation.

Figure 3 displays the dependences of the photocurrent relaxation time on the electric field strength for the fast (curves *1*, *1*'), intermediate (curves *2*, *2*'), and slow (curve *3*) components at low (curves *1–3*) and high (curves *1*', *2*') excitation intensities corresponding to those presented in Fig. 1. At low excitation intensities, the field dependences for all three photocurrent relaxation components have a similar behavior: the relaxation times increase at weak fields (up to $E = 70$ V/cm), pass through a maximum, and decrease with an increase in the electric field strength E. At high electric field strengths ($E > 200$ V/cm), the $\tau(E)$ curves slightly descend and tend to saturation (curves *1–3*), which can be associated with variations in the rate of nonequilibrium-carrier transfer to the recombination macrodefects and a substantial change in the bending of energy bands [2]. As mentioned above, the relaxation times of photocurrent components at high excitation intensities (curves *1*', *2*') remain constant over the entire range of electric field strengths under study and are equal to the characteristic times corresponding to the minimum field strength applied in the experiment ($E = 6$ V/cm). The distinctive feature of the $\tau(E)$ dependences at low excitation intensities is the presence of ascending portions in the range of weak electric fields (curves *1–3*). This is likely caused by the internal electric field of potential barriers at the grain boundaries, which, in turn, is affected by the applied external field [5].

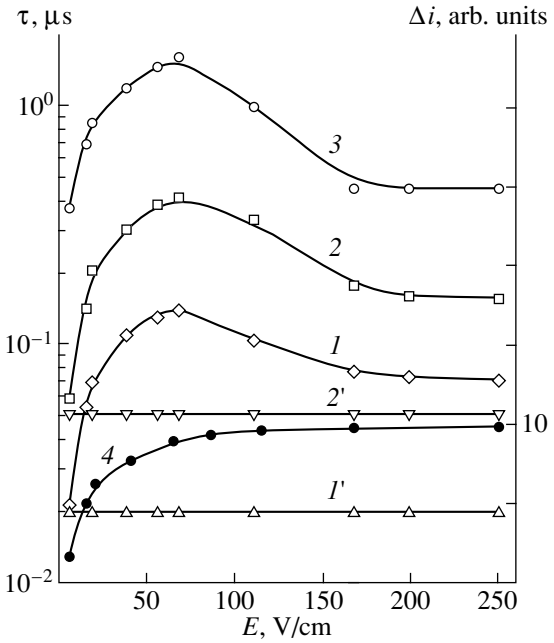

Fig. 3. Field dependences of the characteristic relaxation time for (*1*, *1*') fast, (*2*, *2*') intermediate, and (*3*) slow components of the photoconductivity at (*1–3*) low and (*1*', *2*') high excitation intensities (see Fig. 1). (*4*) The field dependence of the relative stationary photocurrent upon excitation by a continuous monochromatic radiation with the photon energy $h\nu = 1.17$ eV.

A decrease in the photocurrent relaxation time (curves *1–3*) and the saturation of the stationary photocurrent (curve *4*) with an increase in the extraction electric field strength ($E > 70$ V/cm) can be explained within the theory of extraction of minority carriers (in our case, holes) from the bulk of samples. According to the extraction theory [1], the photoconductivity relaxation time measured is the effective time τ_{eff}, which is related to the nonequilibrium-carrier lifetime τ and the flight time $l/\mu_a E$ by the expression

$$\frac{1}{\tau_{eff}} = \frac{1}{\tau} + \frac{\mu_a E}{l}, \qquad (3)$$

where μ_a is the ambipolar mobility, and l is the characteristic distance. The effective time coincides with the nonequilibrium-carrier lifetime when the latter time is considerably less than the flight time; i.e., $\tau \ll l/\mu_a E$. As was shown in [5], the nonequilibrium-carrier recombination in the $Cd_{0.8}Hg_{0.2}Te$ polycrystalline layers predominantly occurs through the Auger mechanism characterized by the same lifetimes of electrons and holes, which is typical of strongly compensated semiconductors and responsible for the bipolar photoconductivity. This is the reason why μ_a is used in relationship (3). Since the photoconductivity relaxation in the studied

layers at low excitation intensities (Fig. 1b, curves *1*, *2*) is governed by three recombination channels with the corresponding characteristic times, relationship (3) can be written for each component, namely, fast (μ_1), intermediate (μ_2), and slow (μ_3) components. Note that the time τ_{eff} is the effective time of photocurrent relaxation resulting from the recombination of nonequilibrium carriers at the surface for the fast component, at internal macrodefects (grain boundaries) for the intermediate component, and in the bulk (inside the grain) for the slow component. The characteristic distance in relationship (3) written for each of the components τ_1, τ_2, and τ_3 has the following meaning: (1) for the surface recombination, it is the distance from the point of the electron–hole pair generation to the surface, which can be taken as the absorption depth of exciting radiation (~1 μm), because this value is larger than the thermal diffusion length for $Cd_{0.8}Hg_{0.2}Te$ [11]; (2) the mean grain size (~30 μm) for the recombination at the grain boundaries; and (3) the distance between current contacts in the case of bulk recombination.

Let us analyze the last case, which is of the greatest practical importance. Since the photoconductivity is determined by the slow component of the photocurrent relaxation, τ in relationship (3) represents the nonequilibrium-carrier lifetime. Earlier [5], it was shown that the nonequilibrium-carrier lifetime in the $Cd_{0.8}Hg_{0.2}Te$ polycrystalline layers with potential barriers at the grain boundaries is given by

$$\tau = \tau_r \exp\left(\frac{E_\tau}{kT}\right), \tag{4}$$

where k is Boltzmann's constant, E_τ is the potential barrier height, and τ_r is the nonequilibrium-carrier recombination time in the absence of spatial separation of electrons and holes by the internal electric field of barriers. Then, taking into account formula (4), relationship (3) for the effective relaxation time takes the form

$$\frac{1}{\tau_{eff}} = \frac{1}{\tau_r \exp(E_\tau/kT)} + \frac{\mu_a E}{l}. \tag{5}$$

The external electric field enhances the separation of electron–hole pairs and, thus, prevents their recombination [9]. This can be treated as an increase in the potential barrier height E_τ in expression (5), which, as is evident from the first term, leads to an increase in the measured value of τ_{eff}. On the other hand, an increase in the strength of external extraction electric field E favors the transfer of nonequilibrium carriers to the macrodefects (including the grain boundaries) and brings about the extraction of minority carriers from the sample, which results in a decrease in the nonequilibrium-carrier lifetime. A decrease in τ_{eff} with an increase in E follows from the second term in relationship (5). The competitive contribution of these processes (an increase in the potential barrier height and the extraction effect) to the overall process of photoconductivity relaxation with an increase in the strength of applied electric field is responsible for the shape of the $\tau_{eff}(E)$ dependence (Fig. 3, curve *3*). Similar considerations can be applied to curves *1* and *2*. It is quite probable that, at weak electric fields $E < 70$ V /cm, an unusual increase in τ_{eff} is associated with a predominant increase in the potential barrier E_τ. As the electric field strength E increases above 70 V/cm, the predominant contribution to τ_{eff} [see formula (5)] is made by the second term accounting for the extraction effect. As a result, the time τ_{eff} decreases proportionally with $1/E$ (curves *1–3*), which is characteristic of the highly sensitive $Cd_xHg_{1-x}Te$ crystals [3, 4]. In order to determine the explicit form of the dependence of the potential barrier height E_τ on the electric field strength E, it is necessary to perform further investigations. However, it is obvious that, as the applied electric field E increases, E_τ also increases and reaches the saturation at $E = 70$ V/cm. This manifests itself in maxima in the $\tau_{eff}(E)$ curves for different components of the photocurrent relaxation (curves *1–3*). A further increase in the strength of applied electric field leads to a decrease in the flight time, which, according to relationship (5), results in a decrease in the effective nonequilibrium-carrier lifetime. This fact explains the saturation of the stationary photocurrent with an increase in E (curve *4*), which is easy to see by writing the photocurrent Δi in the form [7]

$$\Delta i = e\beta I\alpha\mu_a(b+1)E\tau_{eff}, \tag{6}$$

where e is the electron charge, β is the quantum yield, I is the intensity of incident radiation, α is the absorption coefficient, and b is the ratio between the mobilities of electrons and holes. In this case, expression (6) for the stationary photocurrent can include τ_{eff} only for the long-term component, because the time τ for the intermediate and fast components of the photocurrent relaxation is considerably shorter. The analytical dependences under consideration are in qualitative and quantitative agreement with the experimental data. According to relationship (6), the saturation of photocurrent Δi is observed at $\tau_{eff} \sim 1/E$. As follows from expression (5), this situation takes place when the flight time of nonequilibrium carriers becomes shorter than their lifetime τ. The estimates show that this situation occurs at the electric field strength $E = 70$ V/cm, at which the stationary photocurrent is saturated (curve *4*), and the field dependence of the characteristic time of photoconductivity relaxation begins to decay (curve *3*); the flight time is equal to ~0.2 μs, whereas the lifetime τ is 0.37 μs. Here, the lifetime was taken to be τ_{eff} at the minimum extraction electric field $E = 6$ V / cm, at which the carrier extraction is not observed.

The characteristic relaxation times of photoconductivity components τ_1' and τ_2' at high excitation intensities do not depend on the strength of applied electric field (Fig. 3, curves *1*', *2*'). In this case, the nonequilib-

rium-carrier recombination at the grain boundaries predominantly contributes to the photoconductivity relaxation, because the potential barriers at the grain boundaries appear to be shielded by the electric field induced by a large number of photogenerated carriers [5]. As already mentioned, the internal field of barriers associated with the intergranular layers efficiently separates the electron-hole pairs and impedes the escape of carriers toward the grain boundaries and their recombination. This is responsible for the slow component of the photoconductivity relaxation (Fig. 1b, curves *1*, *2*) and, hence, for the high sensitivity at low excitation intensities in contrast to the case of high excitation intensities (Fig. 1b, curve *3*).

At high excitation intensities, the nonequilibrium-carrier lifetime determined by the second component of the photocurrent relaxation (Fig. 3, curve *2*') is equal to 0.05 μs, which is less than the flight time at any electric field strength studied. According to relationship (5), the extraction of nonequilibrium charge carriers is not attained. This is observed in the experiment—the time τ'_{eff} is independent of E (curve *2*'), because this quantity is determined by the first term in expression (5) with due regard for the suppression of the potential barrier E_τ by the electric field created by a large number of photogenerated carriers. Taking into account the shielding of barriers at the grain boundaries, the distance l in calculations was taken as the distance between contacts, as for homogeneous samples [3, 4]. The independence of the photoconductivity relaxation time from the strength of applied electric field at high excitation intensities for the $Cd_{0.8}Hg_{0.2}Te$ polycrystalline layers is typical of the $Cd_xHg_{1-x}Te$ crystals with a low photosensitivity [4].

REFERENCES

1. R. L. Williams, B. H. Breazeale, and C. G. Roberts, in *Proceedings of the Third Photoconductivity Conference*, Ed. by E. M. Pell (Pergamon Press, New York, 1971), p. 237.
2. I. S. Virt, Fiz. Tekh. Poluprovodn. (S.-Peterburg) **31**, 936 (1997) [Semiconductors **31**, 797 (1997)].
3. A. I. Vlasenko and A. V. Lyubchenko, Fiz. Tekh. Poluprovodn. (S.-Peterburg) **28**, 1219 (1994) [Semiconductors **28**, 695 (1994)].
4. V. I. Ivanov-Omskiĭ, V. K. Ogorodnikov, and T. Ts. Totieva, Fiz. Tekh. Poluprovodn. (Leningrad) **14**, 699 (1980) [Sov. Phys. Semicond. **14**, 412 (1980)].
5. V. A. Gnatyuk, O. S. Gorodnychenko, P. E. Mozol', *et al.*, Semicond. Sci. Technol. **13**, 1304 (1998).
6. V. S. Lopes, A. J. Syllaios, and M. C. Chen, Semicond. Sci. Technol. **44**, 824 (1993).
7. S. M. Ryvkin, *Photoelectric Effects in Semiconductors* (Fizmatgiz, Moscow, 1963; Consultants Bureau, New York, 1964).
8. A. I. Vlasenko, V. A. Gnatyuk, E. P. Kopishinskaya, *et al.*, Poverkhnost', No. 2, 60 (1994).
9. A. Ya. Shik, Zh. Éksp. Teor. Fiz. **68**, 1859 (1975) [Sov. Phys. JETP **41**, 932 (1975)].
10. A. I. Elizarov, V. I. Ivanov-Omskiĭ, A. A. Korniyash, and V. A. Petryakov, Fiz. Tekh. Poluprovodn. (Leningrad) **18**, 201 (1984) [Sov. Phys. Semicond. **18**, 125 (1984)].
11. N. N. Berchenko, V. S. Krevs, and V. G. Shredin, *Semiconductor Solid Solutions and Their Applications* (Voenizdat, Moscow, 1982).

Translated by O. Borovik-Romanova

Physics of the Solid State, Vol. 42, No. 7, 2000, pp. 1228–1230. Translated from Fizika Tverdogo Tela, Vol. 42, No. 7, 2000, pp. 1193–1195.

SEMICONDUCTORS AND DIELECTRICS

Electrical Properties of $(PbS)_{0.59}TiS_2$ Crystals at High Pressure up to 20 GPa

V. V. Shchennikov, A. N. Titov, S. V. Popova, and S. V. Ovsyannikov

Institute of Metal Physics, Ural Division, Russian Academy of Sciences, ul. S. Kovalevskoĭ 18, Yekaterinburg, 620219 Russia

e-mail: phisica@ifm.e-burg.su

Received November 12, 1999; in final form, December 16, 1999

Abstract—The electrical resistance ρ and thermopower S of the $(PbS)_{0.59}TiS_2$ single-crystal compound with mismatched layers and the TiS_2 crystals have been investigated at room temperature in high-pressure chambers with synthetic diamond dies. The decrease in ρ and $|S|$ observed in $(PbS)_{0.59}TiS_2$ under the pressure $P \approx 2$ GPa is associated with the structural transformation of PbS from the cubic phase into the orthorhombic phase. The jumps of ρ and $|S|$ are presumably caused by the increase in the electron concentration in the TiS_2 layers. For $P \geq 4$ GPa, at which the gap is absent in the electronic spectrum of TiS_2, a decrease in $\rho(P)$ is observed for the $(PbS)_{0.59}TiS_2$ samples. © *2000 MAIK "Nauka/Interperiodica".*

Layered transition-metal dichalcogenides and their intercalates are promising materials for electronics. This explains considerable interest in studies of their properties [1–4]. The $(PbS)_{0.59}TiS_2$ crystals, which belong to these materials, consist of PbS and (TiS_2–TiS_2) alternating layers (Fig. 1) and can be considered as an intercalation of PbS into TiS_2 [1, 2]. The PbS lattice is distorted in the plane of layers as compared to the bulk crystal, which has the structure of a rock salt (a = 5.936 Å), and TiS_2 practically retains the structure of the bulk material (Fig. 1) [2]. The parameters of PbS and TiS_2 lattices coincide along the b axis (b = 5.783 Å), whereas in the perpendicular direction a, they are incommensurate: a = 5.761 Å for PbS and a = 3.390 Å for TiS_2 [1, 2]. Each layer of TiS_2 has a "sandwich" structure, in which Ti atoms are located between two interlayers of sulfur atoms (Fig. 1); as in the TiS_2 crystal, the layers are linked together by a weak van der Waals interaction [1–3].

A strong anisotropy of the electrical and mechanical properties is observed in the $(PbS)_{0.59}TiS_2$ crystals in the (ab) plane and in the perpendicular direction c [1, 2], as well as in the commensurate (b) and incommensurate (a) directions [4]. Since these crystals consist of mismatched layers, one can expect unusual behavior of the properties under the hydrostatic compression. The aim of this work was to study the influence of pressure P on the electrical resistance ρ and thermopower S of the $(PbS)_{0.59}TiS_2$ crystals. For comparison, similar studies were carried out on TiS_2 crystals, which exhibit similar temperature dependences of ρ and S along the plane (ab) of the layers at atmospheric pressure [1, 2].

The measurements were performed in high-pressure chambers with dies made of a BK6 hard alloy (up to 8 GPa) [5] and synthetic diamond (up to 30 GPa), in several cycles of the increase and decrease in P [6–8]. The values of P in a pressure-transferring medium (pyrophyllite, catlinite) were estimated from the calibrated dependences, which were drawn according to the phase transitions in the reference species (Bi, GaP, etc.) [6–8]. The $(PbS)_{0.59}TiS_2$ single crystals (~15 × 1.0 × 0.01 mm in size) were grown by the method of gas-transport reaction with a slight excess of sulfur as a carrier [4]. The lattice parameters of samples coincided with those given in [2]. The initial batch contained Pb (99.9%), S (99.99%), and TiS_2 powder in the ratio 0.59 : 0.59 : 1 [4]. The electron concentration determined from the Hall effect in the temperature range T = 77–350 K was $n = 3 \times 10^{21}$ cm^{-3}.

The samples in the form of plates ~0.5 × 0.2 × 0.01 mm in size were placed in an orifice with a diameter of 0.3 mm in a container made of catlinite (diamond chamber) or pyrophyllite (hard-alloy chamber [5]) at an angle to the plane of dies, which served as heaters and coolers in the thermopower measurements [6, 7]. The clamping electrical probes were the Pt–Ag ribbons 5 μm thick. The geometry of the experiments actually corresponded to the measurements of ρ and S along the (ab) plane. The relative errors in measurements of ρ and S (without regard for the change in the sample shape under compression) were ~5 and ~20%, respectively [4, 5].

The pressure dependences of ρ and S for each of the studied materials, which were measured in diamond and hard-alloy chambers, qualitatively coincide (Figs. 2a, 2b; the data on $\rho(P)$ are presented only for the hard-alloy chamber). The drop of ρ and $|S|$ is observed in the $(PbS)_{0.59}TiS_2$ sample at $P \approx 2$ GPa, and one more decay, at $P \geq 4$ GPa. The dependences $\rho(P)$ and $S(P)$ for TiS_2 samples have no anomalies (Fig. 2). In [9], TiS_2

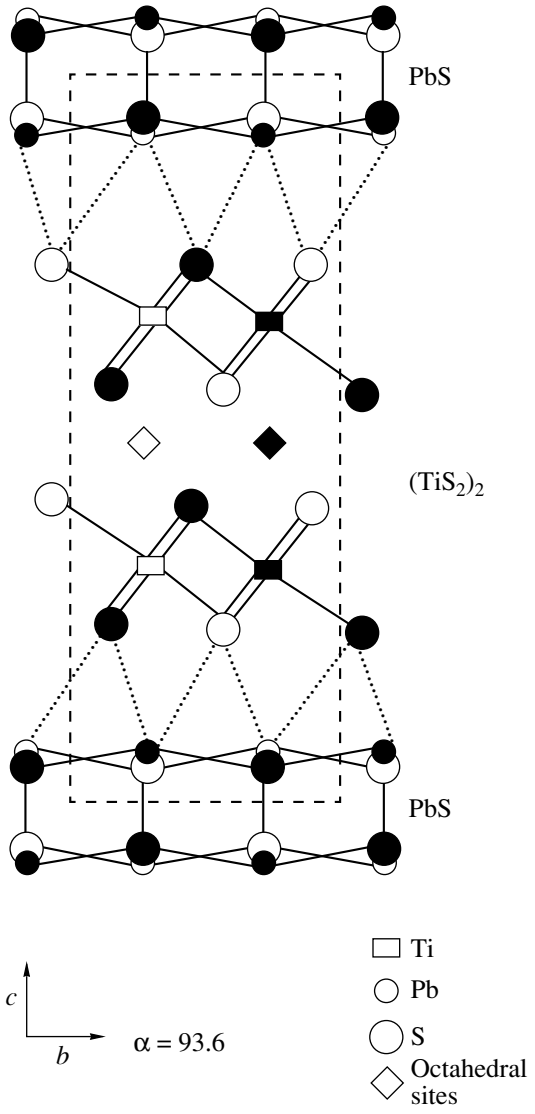

Fig. 1. Projection of the $(PbS)_{0.59}TiS_2$ crystal structure along the [100] axis [2]. The unit cell is shown by the dashed line. Solid lines represent the bonds in PbS and TiS_2 layers, and dotted lines are the bonds between these layers. Rhombs designate the positions of octahedral holes. Dark symbols correspond to the positions of atoms in the figure plane, and open symbols, to the positions of atoms in the lower-lying plane.

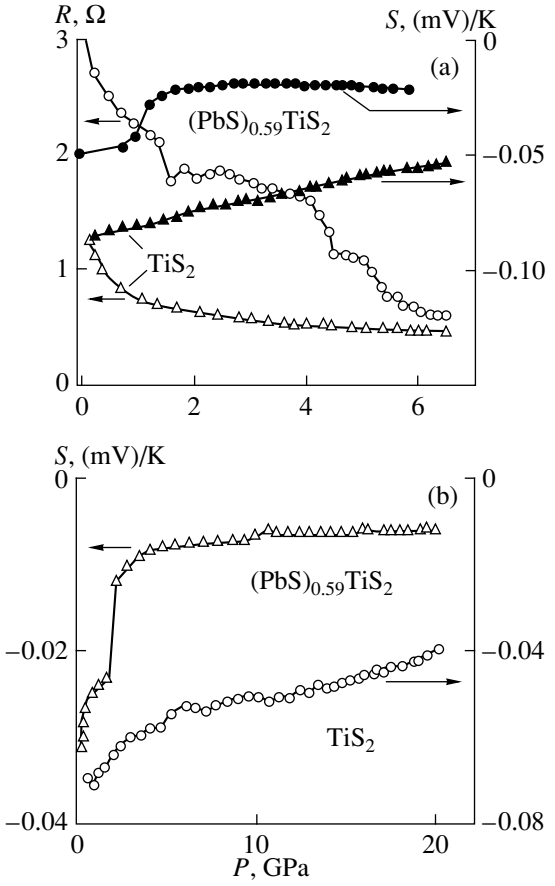

Fig. 2. Dependences of (a) the resistance and (a, b) the thermopower on pressure for $(PbS)_{0.59}TiS_2$ and TiS_2 crystals along the plane of layers at T = 293 K. Measurements are made in (a) a hard-alloy chamber and (b) a diamond chamber.

samples with the low electron concentration $n < 10^{21}$ cm^{-3} near P = 4–5 GPa showed the same decay of ρ as for the $(PbS)_{0.59}TiS_2$ crystal.

The sharp changes in ρ and S for $(PbS)_{0.59}TiS_2$ crystals can be induced by the phase transformations in PbS and TiS_2 layers. In bulk TiS_2 at P up to 9 GPa, the structural transformations were not established [9–11]; PbS under a pressure of 2.5 GPa transforms from the phase with a NaCl structure into the orthorhombic phase with the parameters a = 11.28 Å, b = 3.98 Å, and c = 4.21 Å [12–14], and at 21.5 GPa, PbS transforms into the phase with a bcc CsCl structure [15]. Thus, the jumps of ρ and S in $(PbS)_{0.59}TiS_2$ at ~2 GPa can be connected with the phase transition in the PbS layers. Simultaneous decays of ρ and S in the $(PbS)_{0.59}TiS_2$ crystals upon structural transformations in the PbS layers show that the conduction electron concentration increases. This can be due to an increase in the content of Ti atoms (which supply electrons in the conduction band [1, 2, 9]) in the van der Waals gap between TiS_2 layers. Indeed, at a high sulfur pressure, there is a tendency toward the transition $TiS_2 \longrightarrow TiS_3$ [16]. The electron concentration can also change by "readjusting" the TiS_2 lattice to PbS due to matching of the layers [1, 2, 15]. Note that the identation of similar $(PbS)_{0.59}TiS_2$ samples led to a strong residual deformation along the incommensurable direction [4], which could be a consequence of structural transitions in the PbS layers upon penetration of a diamond indenter [17, 18].

The drop of ρ in $(PbS)_{0.59}TiS_2$ at $P > 4$ GPa (Fig. 2) can be related to the semiconductor–semimetal transition in TiS_2 layers, which was predicted by the calculations of electronic structure [10] and experimentally observed in dependences of ρ(P) and S(P) [9]. Accord-

ing to the x-ray data [10], the pressure results in the compression of interlayers between TiS_2 layers and in the thickening of the layers themselves (Fig. 1). This corresponds to an increase in the charge density between the layers and the strengthening of the bonds between sulfur atoms [10]. According to the calculations made in [10] for P = 6–8 GPa, the conduction band of TiS_2 overlaps with the valence band. The electronic structures of TiS_2 and $(PbS)_{0.59}TiS_2$ in the model of weakly interacting layers likely are similar [19, 20].

ACKNOWLEDGMENTS

We are grateful to B.N. Goshchitskiĭ for his interest in our work.

This work was supported by the Russian Foundation for Basic Research (project no. 98-03-32656) and the State Program of Support for Leading Scientific Schools of the Russian Federation (project no. 96-15-96515).

REFERENCES

1. G. A. Wiegers and A. Meerschaut, Mater. Sci. Forum **100**–**101** (2), 1 (1992).
2. A. Meerschaut, C. Auriel, and J. Rouxel, J. Alloys Compd. **183**, 129 (1992).
3. H. Negishi, S. Ohara, and M. Inoue, Phys. Status Solidi B **151**, 441 (1989).
4. P. Panfilov, Yu. L. Gagarin, and A. N. Titov, J. Mater. Sci. Lett. **17**, 1049 (1998).
5. L. G. Khvostantsev, L. F. Vereshchagin, and N. M. Uliyanitskaya, High Temp.–High Pressures **5** (3), 261 (1973).
6. I. M. Tsidil'kovskiĭ, V. V. Shchennikov, and N. G. Gluzman, Fiz. Tekh. Poluprovodn. (Leningrad) **17**, 958 (1983) [Sov. Phys. Semicond. **17**, 604 (1983)].
7. V. V. Shchennikov and A. V. Bahzenov, Rev. High Pressure Sci. Technol. **6**, 657 (1997).
8. V. V. Shchennikov, A. Yu. Derevskov, and V. A. Smirnov, in *Proceedings of the 5th International Symposium on Diamond Materials, 1997*, Ed. by J. L. Davidson *et al.* (Electrochem. Soc., Pennington, 1998), Vol. 97–32, p. 597.
9. P. C. Klipstein and R. H. Friend, J. Phys. C **17**, 2713 (1984).
10. D. R. Allan, A. A. Kelsey, S. J. Clark, *et al.*, Phys. Rev. B **57**, 5106 (1998).
11. G. V. Lashkarev, A. V. Brodovoĭ, M. V. Radchenko, *et al.*, Fiz. Tverd. Tela (Leningrad) **32**, 980 (1990) [Sov. Phys. Solid State **32**, 577 (1990)].
12. G. A. Samara and H. G. Drickamer, J. Chem. Phys. **37**, 1159 (1962).
13. A. A. Semerchan, N. N. Kuzin, L. N. Drozdova, *et al.*, Dokl. Akad. Nauk SSSR **152**, 1079 (1963) [Sov. Phys. Dokl. **8**, 982 (1963)].
14. N. B. Brandt, D. V. Gitsu, N. S. Popovich, *et al.*, Fiz. Tekh. Poluprovodn. (Leningrad) **10** (1), 194 (1976) [Sov. Phys. Semicond. **10**, 117 (1976)].
15. T. Chattopadhyay, A. Werner, and H. G. Schnering, Mat. Res. Soc. Symp. Proc. **22** (3), 93 (1984).
16. K. Oshima, M. Yokoyama, H. Hinode, *et al.*, J. Solid State Chem. **65**, 392 (1986).
17. I. V. Gridneva, Yu. V. Milman, and V. I. Trefilov, Phys. Status Solidi A **14** (1), 177 (1972).
18. G. M. Pharr, W. C. Oliver, and D. S. Harding, J. Mater. Res. **6**, 1129 (1991).
19. Yu. M. Yarmoshenko, V. A. Trofimova, S. N. Shamin, *et al.*, J. Phys.: Condens. Matter **6**, 3993 (1994).
20. V. A. Kul'bachinskiĭ, *Two-Dimensional, One-Dimensional, and Zero-Dimensional Structures and Superlattices* (Mosk. Gos. Univ., Moscow, 1998).

Translated by T. Galkina

Physics of the Solid State, Vol. 42, No. 7, 2000, pp. 1231–1235. Translated from Fizika Tverdogo Tela, Vol. 42, No. 7, 2000, pp. 1196–1200.

SEMICONDUCTORS AND DIELECTRICS

Influence of the Relative Magnitude of the Jahn–Teller Effect and Level Splitting in a Cubic Crystal Field on the Properties of the Ground State of Vacancy Defects in Semiconductors

N. S. Averkiev, A. A. Gutkin, and S. Yu. Il'inskiĭ

Ioffe Physicotechnical Institute, Russian Academy of Sciences, Politekhnicheskaya ul. 26, St. Petersburg, 194021 Russia

Received December 23, 1999

Abstract—The spatial structure of a vacancy and the properties of its electronic energy levels in a semiconductor with a lattice possessing point symmetry T_d are considered for an arbitrary relationship between the Jahn–Teller stabilization energy (associated with the F_2 vibrational mode) and the t_2–a_1 splitting (Δ) caused by the cubic crystal field. The position of the minimum of the adiabatic potential and the distortion of the electronic density are calculated for the vacancy ground state for different relative values of Δ and coupling constants of the vacancy to the F_2 vibrational mode. It is shown that, if the ground state of a carrier bound to a vacancy is a t_2 state, the trigonal symmetry of the environment of the vacancy persists for any values of Δ, but the amount of displacements of atoms near the vacancy and the localization of the wave function of the bound carrier on the broken bond earmarked by the Jahn–Teller effect can depend heavily on Δ and are maximal at $\Delta \longrightarrow 0$. This is also the case when the ground state of the vacancy is the a_1 state, but the magnitude of Δ does not exceed a certain value, which is determined by the coupling constants and the elastic constant. The relation between Δ and the coupling constants is also shown to affect the properties of trigonal vacancy–shallow-donor complexes. For these complexes, calculations are performed of the dependence of the dipole direction determining the optical properties of the vacancy defect on the distortion of vacancy orbitals caused by the donor entering into the complex. © *2000 MAIK "Nauka/Interperiodica".*

INTRODUCTION

It is known that, for some defects in cubic semiconductors, the initial electronic state with its energy lying in the forbidden gap is the triply degenerate t_2 state. An example of such a defect is a vacancy in silicon [1, 2] or in III–V and II–VI semiconductors [3, 4]. The local electronic states of the vacancy are formed by hybridization between the four broken bonds from its four nearest neighbor atoms. As a result, two states arise in the cubic crystal field, one of which is a singlet of a_1 symmetry, while the other is a triplet of t_2 symmetry. The energy levels of these states are split by the crystal field, the splitting being of the order of 1 eV, according to theoretical estimations [1–6]. The t_2 state may also be split by virtue of the Jahn–Teller effect [7, 8], the amount of this splitting may be tens or hundreds of millielectron-volts and be comparable to splitting due to the crystal field. However, when analyzing the properties of such Jahn–Teller defects, the crystal field effect is usually assumed to be much stronger than the Jahn–Teller effect and the mixing of the a_1 and t_2 states is ignored.

The objective of this paper is to calculate the charge density distribution and the spatial structure of an isolated vacancy in a cubic crystal for arbitrary relative values of the Jahn–Teller stabilization energy E_{JT} and the crystal field splitting Δ. Besides, it is of interest to determine the direction of the optical dipole of the vacancy defect, in which one of the vacancy's four nearest neighbor atoms is replaced by a foreign atom, for example, by a donor, as in vacancy–shallow-donor complexes.

1. VACANCY

The simplest model that can be used to describe vacancies in Si and III–V semiconductors is a quasimolecule that consists of a vacancy and its four nearest neighbor atoms situated at lattice sites at the apexes of a tetrahedron. This molecule has six vibrational degrees of freedom.

The Jahn–Teller effect can be due to the coupling of electrons to nontotally symmetrical doubly degenerate E_2 vibrational modes or triply degenerate F_2 vibrational modes. Since the experiments show that, in a number of cases (e.g., Zn vacancy in ZnSe [9] and Ga vacancy in GaAs [10]), the coupling to F_2 modes plays a leading part, we consider only this case in what follows.

The simplest is the case where in vacancy orbitals there is only one charge carrier, electron or hole. The former corresponds to V_{Si}^{3+} in Si or V_{Ga}^{4+} in GaAs, while the latter means that seven electrons are localized in the

1063-7834/00/4207-1231$20.00

vacancy orbitals and corresponds to V_{Si}^{3-} in Si or V_{Ga}^{2-} in GaAs.

The wave functions of the electron states that arise as the result of hybridization of four broken bonds of the vacancy in the crystal field of the T_d symmetry have the form

$$\Psi_S = C_S(\varphi_1 + \varphi_2 + \varphi_3 + \varphi_4) \quad (1)$$

for the a_1 state and

$$\begin{aligned}\Psi_{1t} &= C_t(\varphi_1 + \varphi_2 - \varphi_3 - \varphi_4),\\ \Psi_{2t} &= C_t(\varphi_1 - \varphi_2 + \varphi_3 - \varphi_4),\\ \Psi_{3t} &= C_t(\varphi_1 - \varphi_2 - \varphi_3 + \varphi_4),\end{aligned} \quad (2)$$

for the t_2 state. Here, C_S and C_t are the normalization constants and φ_i are the functions describing the broken bonds from each of the vacancy's four neighbor atoms.

The coupling of charge carriers to the F_2 vibrational mode leads to the splitting of the t_2 state and mixing of the t_2 and a_1 states. Phenomenologically, the Hamiltonian describing this effect can be written in the form

$$H' = \begin{pmatrix} \Delta & 0 & 0 & 0 \\ 0 & 0 & 0 & 0 \\ 0 & 0 & 0 & 0 \\ 0 & 0 & 0 & 0 \end{pmatrix} + \begin{pmatrix} 0 & bQ_6 & bQ_5 & bQ_4 \\ bQ_6 & 0 & dQ_4 & dQ_5 \\ bQ_5 & dQ_4 & 0 & dQ_6 \\ bQ_4 & dQ_5 & dQ_6 & 0 \end{pmatrix}, \quad (3)$$

where Δ is the splitting of the t_2 and a_1 energy levels in the crystal field; Q_4, Q_5, and Q_6 are the generalized coordinates of the F_2 modes; and b and d are the coupling constants of a localized carrier to these modes. The ground state is the t_2 state at $\Delta > 0$ and the a_1 state at $\Delta < 0$.

The adiabatic potential (AP) W of the system under study is the sum of the eigenvalue $\varepsilon(Q_4, Q_5, Q_6)$ of the Hamiltonian (3) and the energy of elastic vibrations U_0, which can be written in the harmonic approximation as

$$U_0(Q_4, Q_5, Q_6) = \frac{k}{2}\{Q_4^2 + Q_5^2 + Q_6^2\}, \quad (4)$$

where k is the elastic constant for the F_2 mode.

In the adiabatic approximation, the equilibrium configuration of the quasi-molecule is determined by the position of the minimum of the adiabatic potential $W(Q_4, Q_5, Q_6)$.

Calculations by the method of Opik and Pryce [11] show that, in the space of the generalized coordinates Q_4, Q_5, and Q_6, the absolute minimum of the AP lies on the axes of the $\langle 111\rangle$ type, depending on the relative values of b, d, and Δ; that is, at the AP minimum, we have

$$|Q_{40}| = |Q_{50}| = |Q_{60}| \equiv Q_0(b, d, \Delta). \quad (5)$$

Since the generalized coordinates Q_4, Q_5, Q_6 correspond to the spatial coordinates X, Y, Z, this means that, in the general case, the symmetry of the quasi-molecule is lowered to the trigonal one, as in the case of $\Delta \longrightarrow +\infty$. Since the directions [111] and $[\bar{1}\,\bar{1}\,\bar{1}]$ are nonequivalent in the initial tetrahedral quasi-molecule, the AP minima correspond to the molecule distortions only along four directions of the [111] type. These equivalent directions are [111], $[\bar{1}\bar{1}1]$, $[\bar{1}1\bar{1}]$, and $[1\bar{1}\bar{1}]$ or the other four equivalent directions $[\bar{1}\bar{1}\bar{1}]$, $[11\bar{1}]$, $[1\bar{1}1]$, and $[\bar{1}11]$. In order to analyze the position of the AP minimum as a function of the parameters b, d, and Δ we find the variation of the AP along the $[\bar{1}\bar{1}\bar{1}]$direction in the space of the generalized coordinates. In this case, W depends only on the one variable $Q = Q_4 = Q_5 = Q_6$, and we obtain four branches of the AP described by the expressions

$$W_{1,2} = \frac{3k}{2}Q^2 + dQ, \quad (6)$$

$$\begin{aligned} W_{3,4} &= \frac{3k}{2}Q^2 + \frac{|\Delta|}{2} - dQ \\ &\mp \sqrt{(d^2 + 3b^2)Q^2 + \Delta dQ + \frac{\Delta^2}{4}}. \end{aligned} \quad (7)$$

The $W_i(Q)$ dependence is exemplified in Fig. 1 (in terms of the dimensionless quantities $\frac{kW_i}{d^2}$ and $X = \frac{k}{d}Q$) for positive and negative values of Δ. Analysis of (6) and (7) reveals that, for any values of the parameters, the AP reaches its absolute minimum in the W_3 branch. In the $W_{1,2}$ and W_4 branches shown in Fig. 1, the minima correspond to saddle points in the space of Q_4, Q_5, and Q_6 at $\Delta > 0$. When $\Delta < 0$, the point Q_0 at which the AP reaches its minimum in the W_3 branch shifts towards the point $Q = 0$ ($Q_4 = Q_5 = Q_6 = 0$) with an increasing Δ magnitude and comes to this point in a jump when the following inequality becomes true:[1]

$$\frac{k|\Delta|}{d^2} \geq 2\left[\frac{1}{3} + \left(\frac{b}{d}\right)^2\right]. \quad (8)$$

This is accompanied by the appearance of a minimum at $Q \neq 0$ in the W_4 branch of the AP; that minimum corresponds to an equilibrium distortion of the t_2 state due to the Jahn–Teller effect. Since the mixing of the t_2 state with the a_1 state corresponding to the W_3 branch and having a lower energy is already weak in this case, the equilibrium distortion of the quasi-molecule is zero in the a_1 state. The absolute minimum of W_3 is situated on

[1] This jump occurs because the second minimum in W_3 (Fig. 1) becomes the absolute minimum when condition (8) is fulfilled.

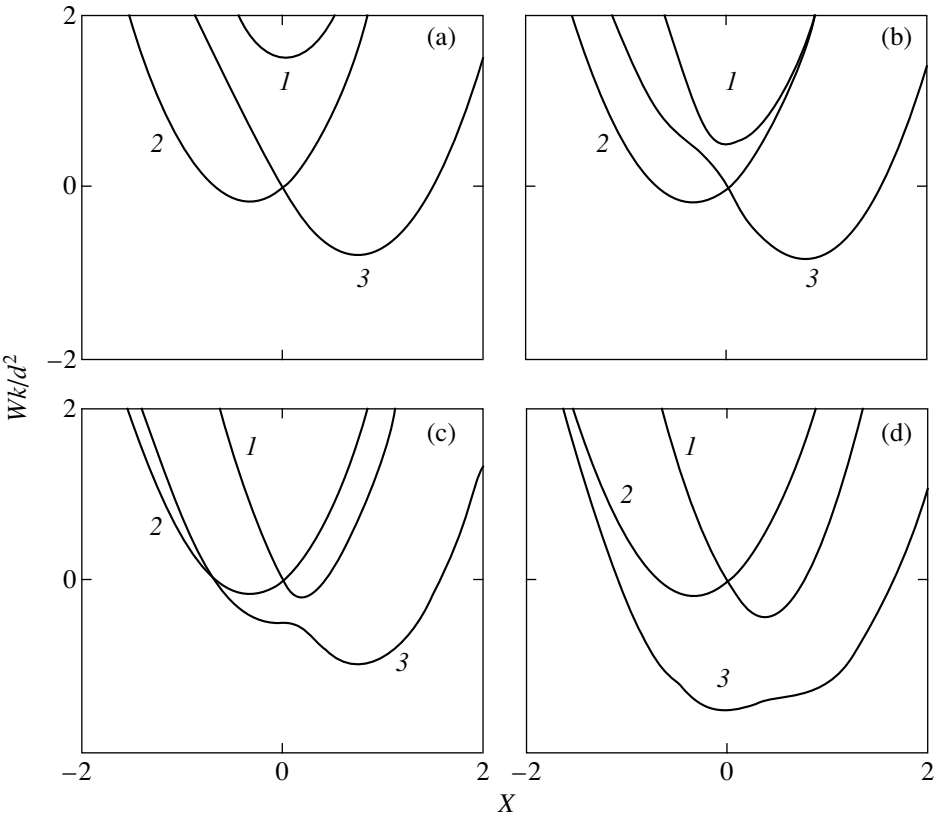

Fig. 1. Adiabatic potentials [(*1*) W_1 and W_2, (*2*) W_4, and (*3*) W_3] of the vacancy with one bound electron (or hole) as a function of Q for $d/b = 2$ and different values of the parameter $S = \Delta k/d^2$: (a) 1.5, (b) 0.5, (c) –0.5, and (d) –1.5.

the negative or positive Q semiaxis, depending on the sign of d; $Q_0 > 0$ if $d > 0$ and $Q_0 < 0$ if $d < 0$.

The Δ dependence of the point Q_0 of the AP absolute minimum is presented in Fig. 2, where $a = d/b$ and the quantities $X_0 = (k/d)Q_0$ and $S = (\Delta k/d^2)$ are dimensionless. At $d < 0$, the $Q_0(\Delta)$ dependence is the mirror reflection from the ordinate axis of the $Q_0(\Delta)$ curve for $d > 0$ shown in Fig. 2. From this figure, it is seen that the departure of the quasi-molecule from its initial tetrahedral form caused by the Jahn–Teller effect decreases with the increasing magnitude of the crystal field splitting Δ (all other parameters being fixed). When $\Delta \longrightarrow +\infty$ and, hence, the ground state of the quasi-molecule is the t_2 state not mixed with the a_1 state, we have $Q_0 \longrightarrow 2d/3k$. This agrees with the known result [12].

A distortion of the spatial structure of the quasi-molecule produces a change in the wave functions of the ground state compared to the wave functions of the T_d symmetry [expressions (1) and (2)]. In the adiabatic approximation, at the four points of the AP absolute minimum, the wave functions are determined by the Hamiltonian (3) and have the form

$$\begin{aligned}
\Phi_1 &= C_0\{\kappa\varphi_1 - \varphi_2 - \varphi_3 - \varphi_4\},\\
\Phi_2 &= C_0\{\kappa\varphi_2 - \varphi_1 - \varphi_3 - \varphi_4\},\\
\Phi_3 &= C_0\{\kappa\varphi_3 - \varphi_1 - \varphi_2 - \varphi_4\},\\
\Phi_4 &= C_0\{\kappa\varphi_4 - \varphi_1 - \varphi_2 - \varphi_3\},
\end{aligned} \tag{9}$$

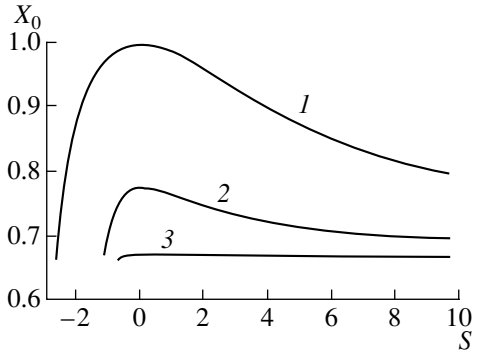

Fig. 2. Position of the minimum of the adiabatic potential for the ground state of the vacancy as a function of S for different values of the ratio between the coupling constants $a = d/b$: (*1*) 1, (*2*) 2, and (*3*) 10.

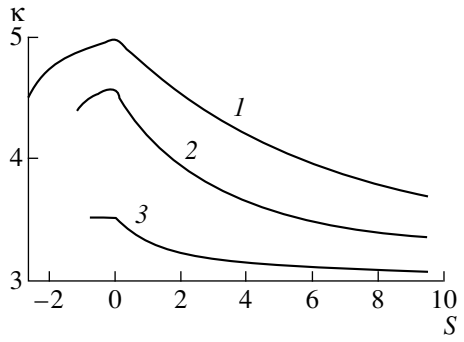

Fig. 3. Coefficient κ as a function of *S* for different values of *a*: (*1*) 1, (*2*) 2, and (*3*) 10.

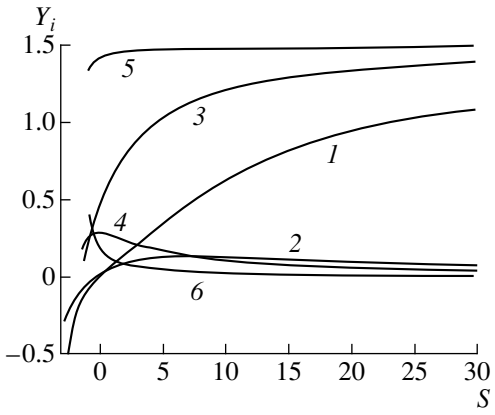

Fig. 4. Coefficients Y_1 (*1*, *3*, *5*) and Y_2 (*2*, *4*, *6*) as a function of *S* for different values of *a*: (*1*, *2*) 1, (*3*, *4*) 2, and (*5*, *6*) 10.

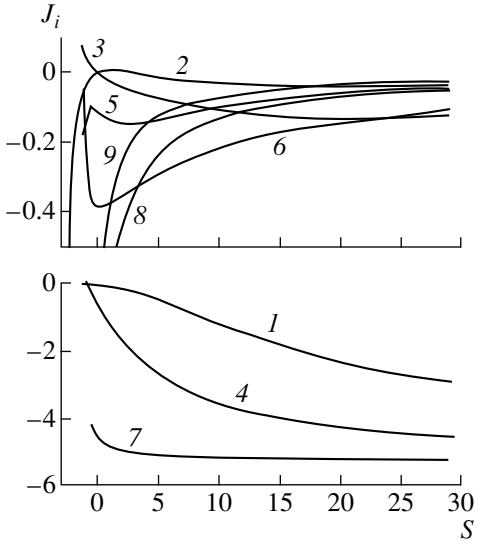

Fig. 5. Coefficients J_1 (*1*, *4*, *7*), J_2 (*2*, *5*, *8*), and J_3 (*3*, *6*, *9*) as a function of *S* for different values of *a*: (*1*, *2*, *3*) 1, (*4*, *5*, *6*) 2, and (*7*, *8*, *9*) 10.

where C_0 is a normalization constant and κ is a coefficient characterizing the localization of the carrier wave function in the broken bond earmarked by the Jahn–Teller effect and directed along the trigonal axis of the distorted quasi-molecule.

The dependence of κ on *S* is presented in Fig. 3. It is seen that κ is maximum at $\Delta = 0$, that is, when the quasi-molecule of the T_d symmetry is maximally distorted. In the limit $\Delta \longrightarrow +\infty$, we have $\kappa = 3$ and the functions Φ_1, Φ_2, Φ_3, and Φ_4 coincide with the wave functions of the four equivalent configurations in the case where $E_{JT} \ll \Delta$ [13]. At $\Delta < 0$, as the magnitude of Δ is increased, the coefficient κ decreases and, when inequality (8) becomes true, it drops discontinuously to the value $\kappa = -1$ (much as the coordinate Q_0 does).

2. VACANCY–DONOR COMPLEX

Vacancy–shallow-donor complexes were observed in Si [8, 14], gallium arsenide [15, 16], and a number of II–VI semiconductors [9, 17]. In many of these complexes, the donor atom substitutes for one of the four nearest neighbor atoms of the vacancy [8, 14–17]. An example of this type of defect is the $V_{Ga}Te_{As}$ complex in *n*-GaAs : Te [16]. In this paper, we restrict ourselves to a calculation of the influence of the donor in such a complex on the direction of the dipole characterizing the optical properties of the defect in the ground state; the defect is assumed to have one bound carrier (an electron or a hole) in the vacancy orbitals.

The angle defining the dipole direction is determined by the off-diagonal components of the Hamiltonian $\tilde{H}$ describing the effect of the donor. For this reason, we assume the diagonal components of $\tilde{H}$ to be zero. Hence, this Hamiltonian can be written in the form

$$\tilde{H} = \begin{pmatrix} 0 & \nu & \nu & \nu \\ \nu & 0 & \mu & \mu \\ \nu & \mu & 0 & \mu \\ \nu & \mu & \mu & 0 \end{pmatrix}, \qquad (10)$$

where μ and ν are phenomenological parameters.

The total Hamiltonian of the system H'' can be written as

$$H'' = H' + \tilde{H}, \qquad (11)$$

where the parameter Δ involved in H' [see (3)] may include the effect of the donor on the diagonal components.

We assume that the effect of the donor is less strong than the Jahn–Teller effect and the level splitting in the cubic crystal field and calculate the deflection angle θ of the optical dipole from its initial direction [111] in the isolated vacancy by the Opik–Pryce method to the

second order of perturbation theory in the small parameters μ and ν. The result is

$$\tan(35.2^\circ - \theta) = \frac{1}{\sqrt{2}}\{1 - Y_1\mu' - Y_2\nu' - J_1\mu'^2 - J_2\nu'^2 - J_3\mu'\nu'\}, \quad (12)$$

where $\mu' = k\mu/d^2$ and $\nu' = k\nu/d^2$. In (12), it has been taken into account that the angle between the [111] and [110] directions is equal to 35.2°.

The dependence of Y_1, Y_2, J_1, J_2, and J_3 on the relative values of the crystal-field splitting and Jahn–Teller effect are presented in Figs. 4 and 5 for different values of a.

At $\Delta \longrightarrow +\infty$, we have (Figs. 4, 5) $Y_1 \longrightarrow 3/2$, $J_1 \longrightarrow -21/4$, $Y_2 \longrightarrow 0$, $J_2 \longrightarrow 0$, and $J_3 \longrightarrow 0$. When $\Delta$is negative and increases in magnitude to the value at which inequality (8) becomes true and the coordinate Q_0 of the AP minimum point vanishes in a jump, all the coefficients Y_1, Y_2, J_1, J_2, and J_3 become equal to zero. However, formula (12) for the deflection angle of the optical dipole is invalid in this case, because the Jahn–Teller stabilization energy becomes zero and, hence, perturbation theory is inapplicable. From Figs. 4 and 5, it is seen that, at $S \geq 5$, the coefficients in the terms involving the parameter ν and describing the effect of the donor on the a_1 state are small when compared to the coefficients in the terms involving μ. Therefore, in this case, when calculating the direction of the optical dipole, the influence of the donor on the a_1 state can be neglected in comparison to its influence on the t_2 state. The value of S affects the coefficients Y_1 and J_1.

At $a < 1$, the coefficients Y_2, J_2, and J_3 are also close to zero in a wide range of positive values of S. However, the S range in which Y_1 is comparable to Y_2 and J_1 is comparable to J_2 and J_3 becomes wider. For example, at $a = 0.3$, this range extends from $S \approx 0$ to 40.

ACKNOWLEDGMENTS

This work was supported by the Russian Foundation for Basic Research, grant no. 98-02-18327.

REFERENCES

1. J. Bernholc, N. O. Lipari, and S. T. Pantelides, Phys. Rev. B **21**, 3545 (1980).
2. Osamu Sugino and Atsushi Oshiyama, Phys. Rev. Lett. **68**, 1858 (1992).
3. Hongqi Xu and U. Lindefelt, Phys. Rev. B **41**, 5979 (1990).
4. W. Pötz and D. K. Ferry, Phys. Rev. B **31**, 968 (1985).
5. J. van der Rest and P. Pecheur, J. Phys. C **17**, 85 (1984).
6. Hongqi Xu, J. Appl. Phys. **68**, 4077 (1990).
7. M. Jaros and S. Brand, Phys. Rev. B **14**, 4494 (1976).
8. G. D. Watkins, in *Radiation Damage in Semiconductors*, Ed. by P. Baruch (Dunod, Paris, 1965), p. 97.
9. F. C. Rong, W. A. Barry, J. F. Donegan, and G. D. Watkins, Phys. Rev. B **54**, 7779 (1996).
10. Y. Q. Jia, H. J. von Bardeleben, D. Stievenard, and C. Delerue, Phys. Rev. B **45**, 1645 (1992).
11. U. Opik and M. H. L. Pryce, Proc. R. Soc. London, Ser. A **238**, 425 (1957).
12. I. B. Bersuker, *The Electron State and Properties of Coordination Compounds* (Khimiya, Leningrad, 1986).
13. N. S. Averkiev, A. A. Gutkin, S. Yu. Il'inski, *et al.*, Z. Phys. Chem. (Munich) **200**, 209 (1997).
14. E. L. Elkin and G. D. Watkins, Phys. Rev. **174**, 881 (1968).
15. E. W. Williams, Phys. Rev. **168**, 922 (1968).
16. A. A. Gutkin, M. A. Reshchikov, and V. E. Sedov, Fiz. Tekh. Poluprovodn. (St. Petersburg) **31**, 1062 (1997) [Semiconductors **31**, 908 (1997)].
17. J. Schneider, A. Rauber, B. Dischler, *et al.*, J. Chem. Phys. **42**, 1839 (1965).

Translated by Yu. Epifanov

Physics of the Solid State, Vol. 42, No. 7, 2000, pp. 1236–1239. Translated from Fizika Tverdogo Tela, Vol. 42, No. 7, 2000, pp. 1201–1204.

SEMICONDUCTORS AND DIELECTRICS

Kinetic Coefficients of the Semiconducting Phase of $FeSi_2$ at Low Temperatures

M. I. Fedorov, V. V. Popov, I. S. Eremin, and V. K. Zaĭtsev

Ioffe Physicotechnical Institute, Russian Academy of Sciences, Politekhnicheskaya ul. 26, St. Petersburg, 194021 Russia

e-mail: M.Fedorov@shuvpop.ioffe.rssi.ru

Received December 28, 1999

Abstract—The results of studying the kinetic coefficients of β-$FeSi_2$ in the temperature range 4.2–300 K are considered. The resistivity decreases upon heating in the entire temperature range under investigation. The temperature dependences of the resistivity and thermal conductivity exhibit a break at ~20 K. In the range of 4.2–20 K, the resistivity is a linear function of temperature. The thermo-emf increases rapidly upon cooling and attains values exceeding 15 mV/K. The temperature dependence of the thermo-emf exhibits a break at ~40 K. The observed set of temperature dependences of the kinetic coefficients apparently cannot be explained by a superposition of the known effects only. A new effect probably exists that is associated with a strong electron–phonon interaction in $FeSi_2$ and which requires a further investigation. © *2000 MAIK "Nauka/Interperiodica".*

It is well known that the materials based on the low-temperature (semiconducting) phase of iron disilicide β-$FeSi_2$ are among the cheapest thermoelectric materials; this circumstance has essentially dictated the need to study their kinetic properties. Such investigations revealed the peculiar nature of the conductivity mechanism in β-$FeSi_2$. One such peculiarity is the exponential increase in thermo-emf with temperature in the interval 100–300 K [1]. Some samples exhibit a slight increase in thermo-emf upon cooling to 77 K. This, in turn, stimulated an investigation of the kinetic coefficients of β-$FeSi_2$ at low temperatures, right to the liquid helium temperature. The preliminary results were reported by us in [2].

The samples for investigations were prepared in three stages. At the first stage, the components were melted directly in aluminum oxide crucibles in argon atmosphere. At the second stage, cylindrical ingots of the metallic high-temperature α phase of iron disilicide were prepared by casting in a vacuum [3]. The third stage involved the transformation of the material into the semiconducting β phase as a result of prolonged (~100 h) annealing at a temperature ~700 K.

The resistivity of the samples was measured by the standard two-probe technique with a margin of error of approximately 5%. The thermo-emf and the thermal conductivity were measured in the steady-state heat flux with a margin of error of 5–10%. The temperature gradient varied in conformity with the average temperature of the sample and did not exceed 10% of its value.

The temperature dependences of the resistivity, thermo-emf, and thermal conductivity of an iron disilicide sample are shown in Fig. 1 (see curve *2* in Fig. 2). X-ray diffraction studies revealed that this sample is a well-formed single-phase β-$FeSi_2$ polycrystal. Two striking features are noteworthy in Fig. 1a: a sharp increase in the thermo-emf upon a decrease in temperature below 40 K, and a break on the temperature dependence of the resistivity at ~20 K. The thermo-emf thereby attains very high values typical of charge carrier drag by acoustic phonons. However, the considerable increase in the resistivity (by more than four orders of magnitude in the region of thermo-emf growth) during cooling from room temperature to the liquid helium temperature cannot be attributed to the phonon drag effect. It should be stated that the singularity in the temperature dependence of the thermal conductivity corresponds to the break on the temperature dependence of the resistivity at ~20 K.

The temperature dependence of the thermo-emf for the same sample is shown in Fig. 1b on the double logarithmic scale. In the temperature range of 40–100 K, this dependence has a well-defined linear segment which can be described by the relation

$$\alpha = -32 + 1.5 \times 10^5 T^{-1.57}, \quad (1)$$

where α is the thermo-emf and T is the temperature. The low-temperature segment of the dependence is also linear but has a larger slope relative to the abscissa axis. The temperature dependence of the thermo-emf on this segment can be described by the formula

$$\alpha = 6.24 \times 10^8 T^{-3.89}. \quad (2)$$

This dependence is quite close to the characteristic dependence for the drag of charge carriers by acoustic phonons: $\alpha \propto T^{-7/2}$ [4]. These relations apparently do not describe the freezing out of charge carriers, which

1063-7834/00/4207-1236$20.00

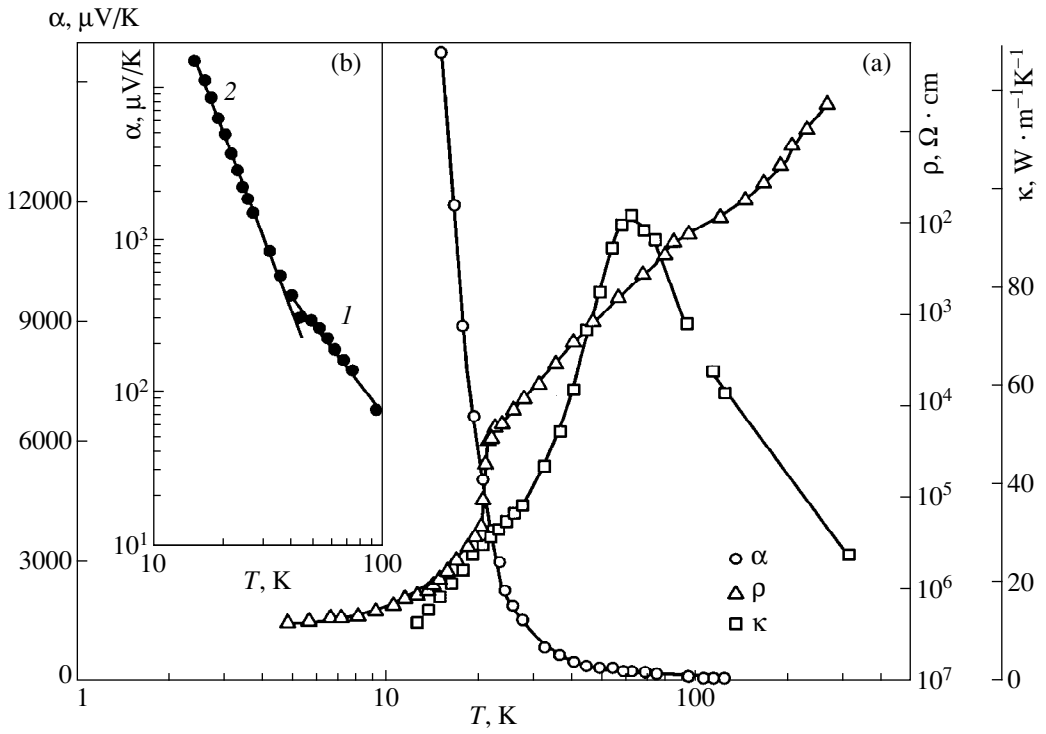

Fig. 1. (a) Thermo-emf α, resistivity ρ, and thermal conductivity κ of polycrystalline β-$FeSi_2$ in the temperature range of 4.2–300 K. (b) Temperature dependence of the thermo-emf α of polycrystalline β-$FeSi_2$ in the temperature range of 15–100 K. Segment *1* is described by formula (1), and segment *2*, by formula (2).

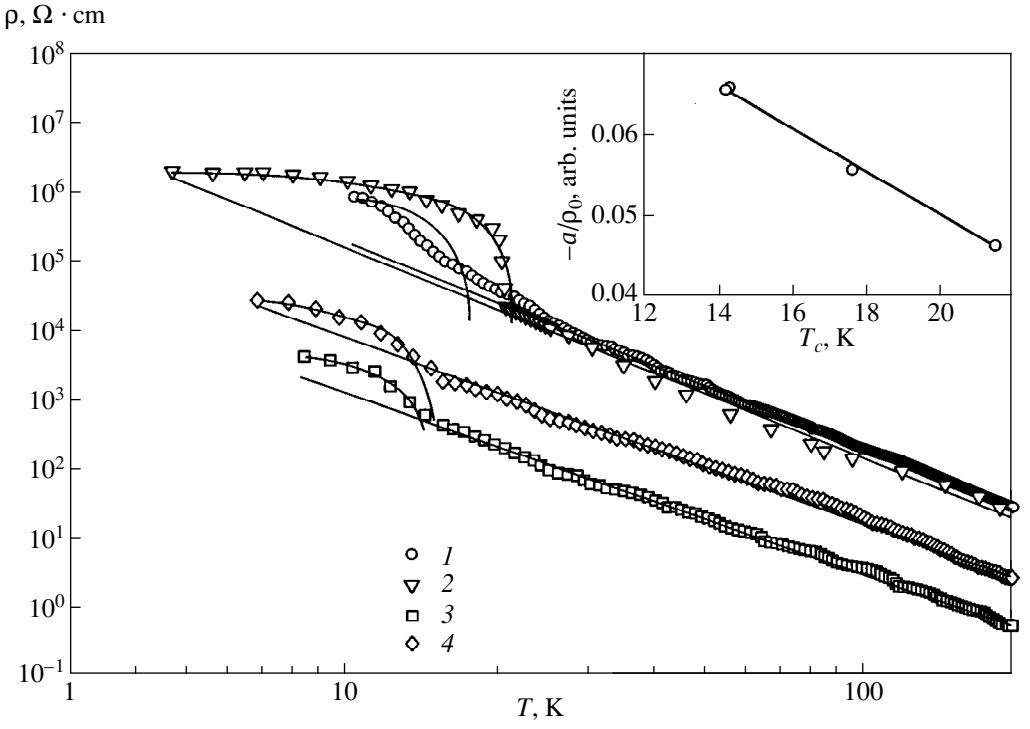

Fig. 2. Resistivity of some iron disilicide samples (labelled as in the table): curves *1–4* correspond to experimental data, while the solid curves are the calculated dependences. The inset shows the ratio between the parameters appearing in (4) as a function of T_c.

Values of parameters appearing in formulas (3) and (4) and of temperature T_c

No.	a, $\Omega \cdot$ cm K^{-1}	ρ_0, $\Omega \cdot$ cm	$\log(\rho_1, \Omega \cdot \text{cm} \cdot \text{K}^{-b})$	b	T_c, K	$-a/\rho_0$, K^{-1}
1	–128000	2300000	8.44	–3.05	17.7	0.0556
2	–138000	2980000	8.40	–3.13	21.5	0.0462
3	–696	10500	5.83	–2.66	14.3	0.0659
4	–3540	53900	6.62	–2.68	14.2	0.0658

corresponds to an exponential increase in the thermo-emf with decreasing temperature.

Figure 2 shows the temperature dependences of resistivity for a number of iron disilicide samples with different concentrations of an uncontrollable impurity. The temperature dependence of the resistivity ρ for all the samples in the region of 20–200 K is correctly described by the expression

$$\rho = \rho_1 T^b. \quad (3)$$

At temperatures from 15 to 20 K, the temperature dependences of resistivity for all the samples display a break corresponding to the transition from the exponential to a linear dependence $\rho(T)$ (Figs. 2 and 3). The temperature dependence of resistivity for all the samples at low temperatures is successfully described by a linear function of the form (see Fig. 3)

$$\rho = \rho_0 + aT. \quad (4)$$

The solid curves in Fig. 2a correspond to dependences (3) and (4). The temperature T_c corresponding to the point of intersection of curves of the type (3) and (4), as well as the values of the parameters ρ_0, ρ_1, a, and b ensuring the best agreement between the theory and the experiment, is given in the table.

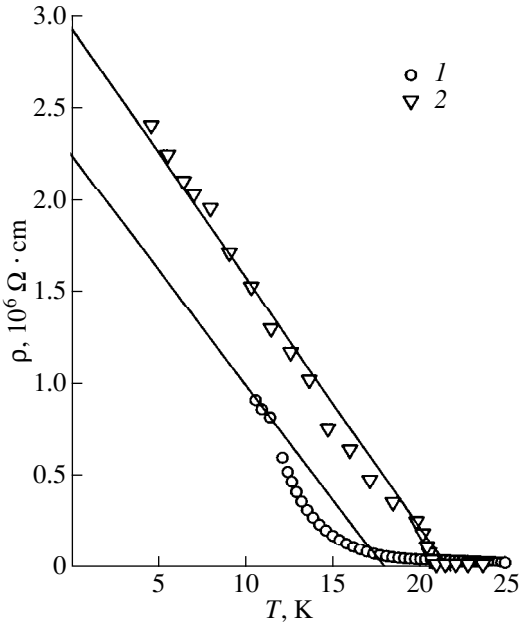

Fig. 3. Temperature dependence of the resistivity of samples *1* and *2* on a linear scale.

Figure 2 shows that the absolute values of resistivity for different samples differ significantly. However, the ratio of the parameter a to the parameter ρ_0 depends on the absolute value of resistivity only slightly (see table) and exhibits a linear dependence on T_c (see Fig. 2b). This dependence can be described by the relation

$$a/\rho_0 = -0.105 + 2.737 \times 10^{-3} T_c; \quad (5)$$

i.e., we can assume with a high probability that all the investigated samples display the same effect, which has slightly different manifestations for reasons unknown as of yet.

We are not in a position to compare our results on the kinetic coefficients of β-$FeSi_2$ at low temperatures with the available data, since we are not aware of the results of investigations of the thermo-emf and thermal conductivity of β-$FeSi_2$ at temperatures below the liquid nitrogen temperature. Lisunov *et al.* [5] reported the data on the resistivity of β-$FeSi_2$ single crystals at low temperatures down to 1.4 K, but they studied aluminum-doped samples whose resistivity at 20 K is approximately equal to one fourth of that for the sample with the lowest resistivity among all the samples investigated by us. The results of investigation of a β-$FeSi_2$ single crystal with a higher resistivity are reported in [6], but its resistivity was unfortunately measured only in the temperature range from 30 to 300 K. In the interval 30–60 K, the temperature dependence of the resistivity for this sample almost coincides with the temperature dependences of the resistivities for samples *1* and *2*.

At the present time, we cannot unambiguously interpret the effects observed in β-$FeSi_2$ at low temperatures. The observed set of temperature dependences of the kinetic coefficients apparently cannot be described by a superposition of known effects only. In all probability, there exists a new effect associated with a strong electron–phonon interaction in iron disilicide, which requires further investigations.

ACKNOWLEDGMENTS

The authors express their sincere gratitude to M.P. Shcheglov and N.F. Kartenko, who carried out X-ray diffraction measurements and to P.P. Konstantinov, E.P. Zayats, and G. T. Alekseeva for making measurements at low temperatures.

This research was supported by the Russian Foundation for Basic Research (grant no. 99-02-18035).

REFERENCES

1. M. I. Fedorov, Yu. V. Ivanov, M. V. Vedernikov, and V. K. Zaitsev, Mat. Res. Soc. Symp. Proc. **545**, 155 (1999).
2. M. I. Fedorov, V. K. Zaĭtsev, Yu. V. Ivanov, *et al.*, in *Proceedings of the V Intergovernmental Seminar, Physicotechnical Institute, St. Petersburg, 1997*, p. 92.
3. M. I. Fedorov, A. E. Engalychev, V. K. Zaĭtsev, *et al.*, in *Proceedings of XIII International Conference on Thermoelectrics*, AIP Conf. Proc. **316**, 324 (1994).
4. A. I. Ansel'm, *Introduction to the Theory of Semiconductors* (GIFML, Moscow–Leningrad, 1962).
5. K. G. Lisunov, E. K. Arushanov, C. Kloc, *et al.*, Phys. Status Solidi B **195** (1), 227 (1996).
6. E. Arushanov, C. Kloc, and E. Bucher, Phys. Rev. B **50**, 2653 (1994).

Translated by N. Wadhwa

Physics of the Solid State, Vol. 42, No. 7, 2000, pp. 1240–1241. Translated from Fizika Tverdogo Tela, Vol. 42, No. 7, 2000, pp. 1205–1206.

SEMICONDUCTORS AND DIELECTRICS

Birefringence of Porous Silicon

O. G. Sarbey, E. K. Frolova, R. D. Fedorovich, and D. B. Dan'ko

Institute of Physics, National Academy of Sciences of Ukraine, pr. Nauki 46, Kiev, 252650 Ukraine

e-mail: sarbey@iop.kiev.ua

Received September 20, 1999; in final form, December 30, 1999

Abstract—The paper reports the observation and studies of the birefringence in porous silicon samples obtained onto different crystallographic planes of silicon single crystals. © *2000 MAIK "Nauka/Interperiodica".*

Although the optical properties of porous silicon were studied in several works [1–5], we have no information regarding the observation of refractive index anisotropy. This can be explained by the fact that, on the one hand, silicon belongs to the cubic system and does not exhibit optical anisotropy, and, on the other hand, the coral-like structure of porous Si would seem by itself to possess the averaged isotropic properties.[1] Nonetheless, we revealed that, in the samples grown onto certain crystallographic planes, a well pronounced refractive index anisotropy is observed in the visible range of the spectrum. The results of measurements of this anisotropy and their interpretation will be given below.

The samples of porous silicon in the form of thin plates were obtained by the electrochemical etching (current density about 60 mA/cm^2) of *p*-Si single crystals with a resistivity of 0.02 Ω cm in a solution of concentrated hydrofluoric acid with ethanol in the ratio 1 : 1 at room temperature. The time of etching varied from 0.5 to 2 min. The thickness d of the samples for these etching periods of time varied from 1.5 to 7.5 μm. For more prolonged etching, the plates became defective and unsuitable for optical studies. The separation of samples from single crystals occurred as a result of an abrupt change in the current density. Then, they were thoroughly washed in distilled water and picked out onto a glass substrate. All further measurements referred to the samples, which were in the optical contact with a substrate.

The porous Si plates obtained by the electrochemical etching of the {211}, {110}, {100}, and {111} crystallographic planes of the same single-crystal Si ingot grown in the ⟨111⟩ direction were studied. The thicknesses of samples were measured on a Linnik interferometer or an electron microscope with an accuracy of about 15%. For studies of the refractive index anisotropy and its spectral dependence, the samples between the crossed polarizers were rotated at an angle of 45° with respect to the position of the complete darkening. All measurements were carried out at room temperature, at about 20°C.

A qualitative study of the porous silicon samples in a polarizing microscope revealed that the samples obtained on the {211} and {110} planes exhibit a pronounced birefringence, whereas in the samples obtained on the {100} and {111} planes, no indications of the refractive index anisotropy are observed. The spectral dependence of the birefringence was measured for the samples grown on the {211} crystallographic planes.

The figure shows the ratio between the transparency $T_\perp$ for three samples of different thickness, which were placed between crossed polarizers and rotated at an angle 45° with respect to the position of complete darkening, and the transparency $T_\parallel$ of the same samples between parallel polarizers. As is seen from the figure, the ratio $T_\perp/T_\parallel$ in the range 0.6–0.8 μm increases with an increase in the sample thickness. Such $T_\perp/T_\parallel$ behavior is caused by the birefringence in the samples.[2]

It is known that the intensity J of the light signal measured in this case is the result of the interference of two beams with the refractive indices n_1 and n_2 and can be described by the expression

$$J \approx \sin^2\left(\frac{\pi(n_1 - n_2)d}{\lambda}\right),$$

where λ is the wavelength of the incident light, and d is the sample thickness.

Actually, all the experimental points can be approximated by this formula, provided that the data in the figure are measured in the range of light absorption by the plates. In this range, the refractive index shows a considerable dispersion, and, consequently, the dispersion of its anisotropy is quite significant. To a first approxi-

[1] The birefringence observed sometimes in crystalline Si in the IR range is associated with the mechanical stresses induced by the nonuniform impurity distribution over the bulk of crystals.

[2] The absorption spectra measured for porous silicon samples at ordinary and extraordinary beams coincide within the accuracy of the experiment.

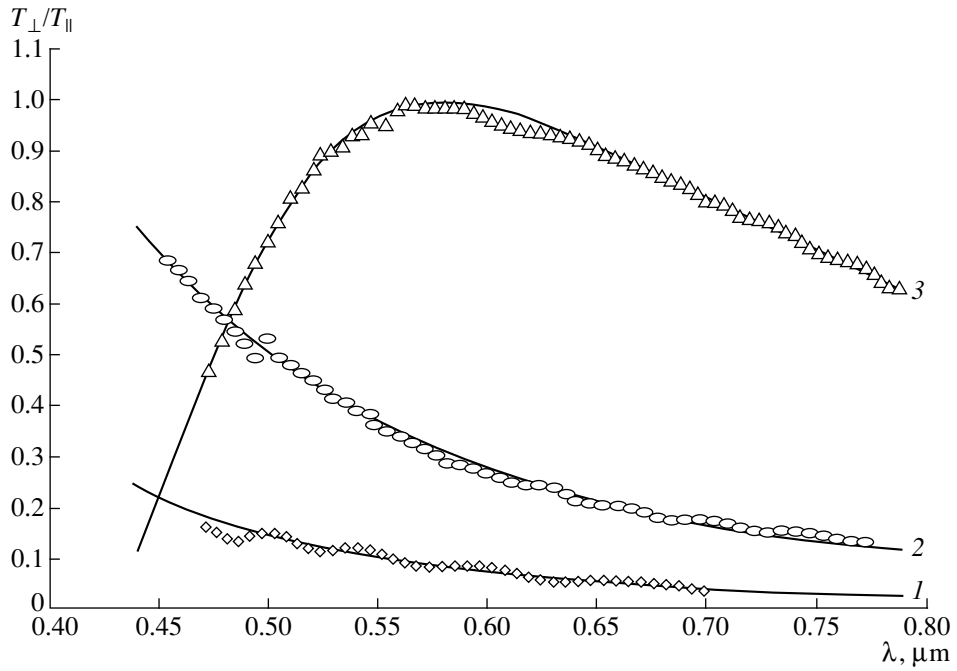

Transparency of porous silicon between the crossed polarizers ($T_\perp$), related to the transparency between the parallel polarizers ($T_\parallel$). *d*, μm: (*1*) 1.325, (*2*) 2.68, and (*3*) 7.2. (Points are the experimental data, and solid lines correspond to the calculations.)

mation, the dispersion can be taken into account by the formula

$$n_1 - n_2 = A\left(1 + \frac{B}{\lambda^2}\right),$$

where A and B are constants.

The results of the calculation at $A = 0.022$ and $B = 0.287$ (shown by solid lines in the figure) demonstrate a good fit to the experimental data. We note that the refractive index anisotropy is rather large and, at $\lambda = 0.5$ μm, is only four times less than that of Iceland spar ($n_1 - n_2 = 0.0472$ and 0.186, respectively).

It is our opinion that the anisotropy observed is due to the anisotropic etching of Si single crystals. The etching rate differs for different crystallographic directions. As a result, the pores in porous silicon are elongated in the direction of the larger etching rate and predominantly oriented in the direction perpendicular to the etching plane. This leads to the violation of the cubic symmetry, which is characteristic of silicon single crystals for sizes exceeding the size of the structural unit of porous silicon. Upon etching the {111} and {100} planes of the sample, the structure obtained should possess the threefold and fourfold symmetry axes, respectively. Consequently, the refractive index being the second-rank tensor should be isotropic in the plane of these samples. Upon etching the {112} and {110} planes, the structure obtained possesses only a twofold axis, and the refractive index should be anisotropic.

ACKNOWLEDGMENTS

This work was supported in part by the CRDF, project UP1-368.

REFERENCES

1. Y. H. Xie, M. S. Hybertsen, and W. L. Wilson, Phys. Rev. B **49**, 5386 (1994).
2. V. P. Bondarenko, V. E. Borisenko, and A. M. Dorofeev, J. Appl. Phys. **75**, 2727 (1994).
3. A. V. Andrianov, D. I. Kovalev, N. N. Zinkevich, and I. D. Yaroshetskiĭ, Pis'ma Zh. Éksp. Teor. Fiz. **58**, 417 (1993) [JETP Lett. **58**, 427 (1993)].
4. Y. Kanemitsu, H. Uto, and Y. Masumoto, Phys. Rev. B **48**, 2827 (1993).
5. S. V. Gaponenko, V. K. Kononenko, E. P. Petrov, and J. N. Germanenko, Appl. Phys. Lett. **67**, 3019 (1995).

Translated by T. Galkina

Physics of the Solid State, Vol. 42, No. 7, 2000, pp. 1242–1252. Translated from Fizika Tverdogo Tela, Vol. 42, No. 7, 2000, pp. 1207–1217.

SEMICONDUCTORS AND DIELECTRICS

Magnetic Absorption of Hexagonal Crystals CdSe in Strong and Weak Fields: Quasi-Cubic Approximation

A. B. Kapustina, B. V. Petrov, A. V. Rodina, and R. P. Seĭsyan

Ioffe Physicotechnical Institute, Russian Academy of Sciences, Politekhnicheskaya ul. 26, St. Petersburg, 194021 Russia

e-mail: rseis@ffm.ioffe.rssi.ru

Received October 21, 1999; in final form, January 10, 2000

Abstract—The spectra of ultrathin free samples of hexagonal CdSe in a magnetic field up to 8 T are studied at 1.7 K. The fan-shaped diagram contains information on weak (the Zeeman effect and diamagnetic shift), as well as strong fields (transitions between Landau levels). As a result of the application of two theoretical models for combined interpretation of strong- and weak-field experimental data, two sets of (band and polaron) parameters are calculated for hexagonal CdSe in the quasi-cubic approximation. The values of the obtained polaron/band parameters are: the electron effective mass $m_e = 0.125/0.116m_0$, the Luttinger parameters $\gamma_1 = 1.5/1.72$, $\gamma = 0.29/0.37$, $\kappa = -0.63$, and the effective electron g-factor $g_e = 0.7$. © *2000 MAIK "Nauka/Interperiodica".*

Interest in wide-band hexagonal semiconducting materials has grown substantially in recent years in conjunction with numerous effects to design a short-wave semiconducting laser emitting in the indigo–blue range. Recently synthesized structures with planar inclusions of the type of CdSe "quantum dots" in the ZnSe matrix [1] are being studied intensely and are seen as promising for short-wave lasers [2].

However, the band structure of hexagonal crystals (including CdSe) has been studied quantitatively much less comprehensively than the structure of cubic semiconductors. Magnetooptics, which is a recognized tool for obtaining the most reliable information on band structure, was used for studying hexagonal CdSe crystals as far back as in the early 1960s [3]. Optical absorption spectra for free excitons in weak magnetic fields (the Zeeman effect and diamagnetic shift) were analyzed and interpreted, and the values of the effective masses and g-factors of charge carriers were determined. However, Dimmock and Weeler [3] carried out their theoretical analysis on the basis of a semiphenomenological model that described the exciton states of various valence bands independently. The spectra of magnetic absorption of a strong magnetic field, which is due to exciton states associated with transitions between Landau levels, were studied much later [4]. The magnetoabsorption spectra were interpreted on the basis of the theory of Landau levels in hexagonal crystals with large spin–orbit splitting, and the applicability of the quasi-cubic approximation was demonstrated. However, effective parameters were not determined, due to the absence of methods for calculating the binding energy for excitons belonging to various transitions between Landau levels. This problem was solved later in a series of papers devoted to relatively wide-band semiconducting materials [5–7]. An analysis of magnetooptical spectra in strong fields and the calculation of a set of band parameters for CdSe were carried out recently in [8, 9]. The obtained results were distinguished by the values of the effective masses of charge carriers differing significantly from those obtained in [3]. A theory of the energy structure of excitons for hexagonal semiconductors in weak magnetic fields was developed recently in the quasi-cubic approximation [10].

The present work aims to study magnetoabsorption spectra for hexagonal CdSe in weak, as well as strong, magnetic fields and to jointly interpret the results in the quasi-cubic approximation.

1. SAMPLES AND EXPERIMENTAL TECHNIQUE

In experiments, we used monocrystalline plates of cadmium selenide with the optical axis in a plane parallel to the sample surface. We studied single crystals from the "ultrapure" series with a low concentration of impurity (below 10^{14} cm^{-3}). These crystals were grown by the Frerichs method (from the gaseous phase; the transport gas is hydrogen or hydrogen sulfide). The typical sample size was as follows: the thickness $d = 0.3$–3 μm and the area $S = 0.5$ mm^2. Since the samples had, as a rule, a smooth weakly corrugated surface, no additional treatment (e.g., annealing, polishing, or etching) was carried out. The samples for measurements were directly immersed in liquid helium during pumping in free form. The experiments were conducted mainly on a batch of 0.3–0.6 μm thick samples.

We obtained detailed experimental spectra of exciton absorption for these samples in a magnetic field up to 8 T at the temperature $T = 1.7$ K (Fig. 1).The oscillating structure of the spectra is clearly seen for the A exciton in relatively weak magnetic fields for the polarization $\mathbf{E} \perp \mathbf{C}$ ($\mathbf{C}$ is the hexagonal axis), but the A exci-

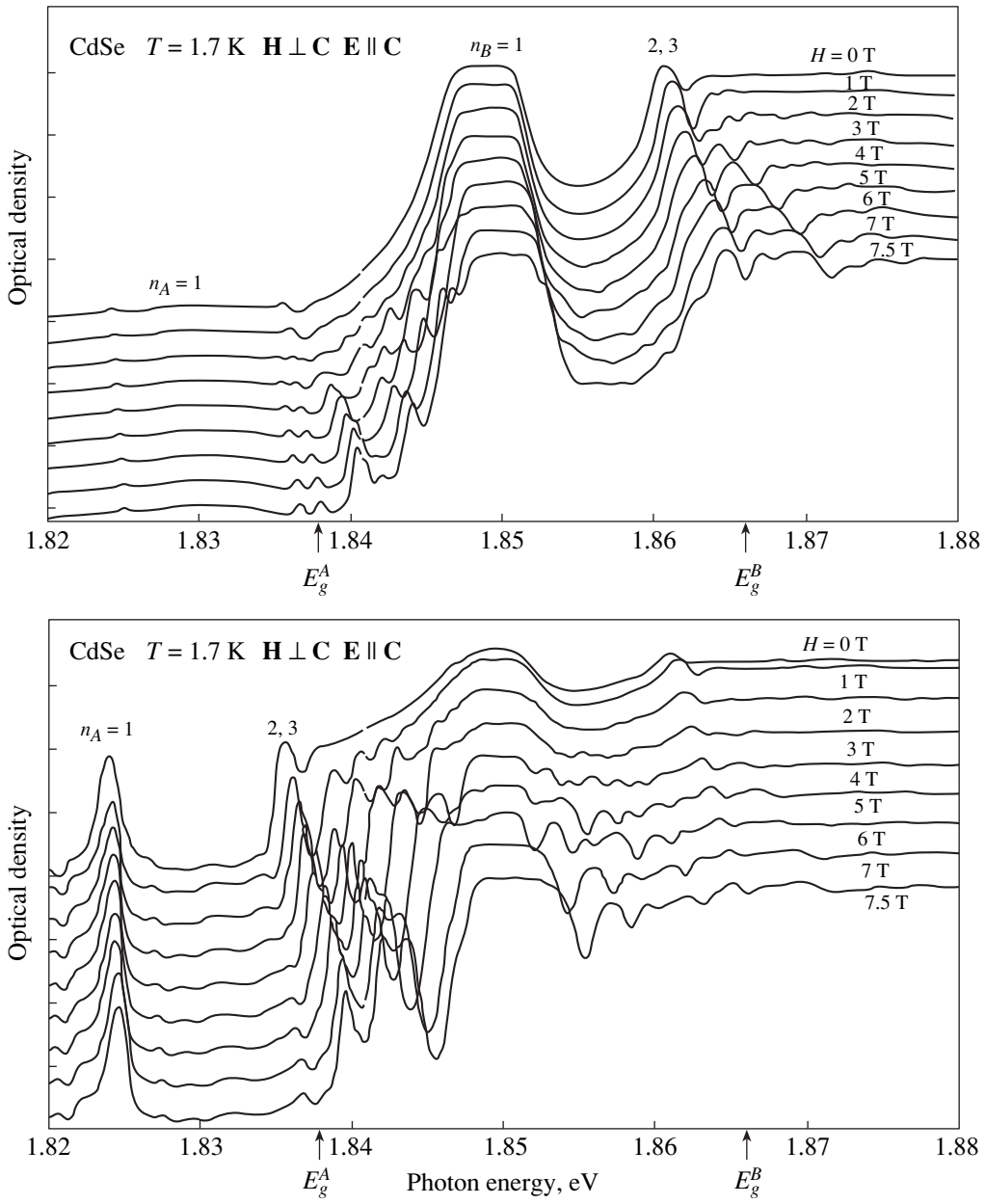

Fig. 1. General form of the absorption spectra of CdSe in various magnetic fields for the two polarizations, **E || C** and **E** ⊥ **C**; notation is given in the text.

ton spectrum ceases being informative as we go over to stronger fields due to the superposition onto the series of lines for a *B* exciton. In the **E || C** configuration, the ground state of the *A* exciton almost completely disappears, since in this configuration such a transition is forbidden in the first approximation.

2. SEPARATION OF STRONG- AND WEAK-FIELD DATA

The observed variety of lines and their behavior in a magnetic field cannot be solely identified with the well-studied Zeeman effect and the diamagnetic shift of three-dimensional exciton series *A* and *B*. For example, the form of their energy shift upon an increase in the magnetic field contradicts the simple model. The lines corresponding to ordinary exciton states must be shifted towards high energies in proportion to the square of the field, the shift being stronger, the larger the principal quantum number of the state is. The fan-shaped diagram plotted on the logarithmic scale (Fig. 2) clearly shows that the shift of a series of lines, which is quadratic in a weak magnetic field, is transformed into a linear shift in a strong field. On the other hand, the spectral line cannot be interpreted as transitions between the Landau levels of an electron and a

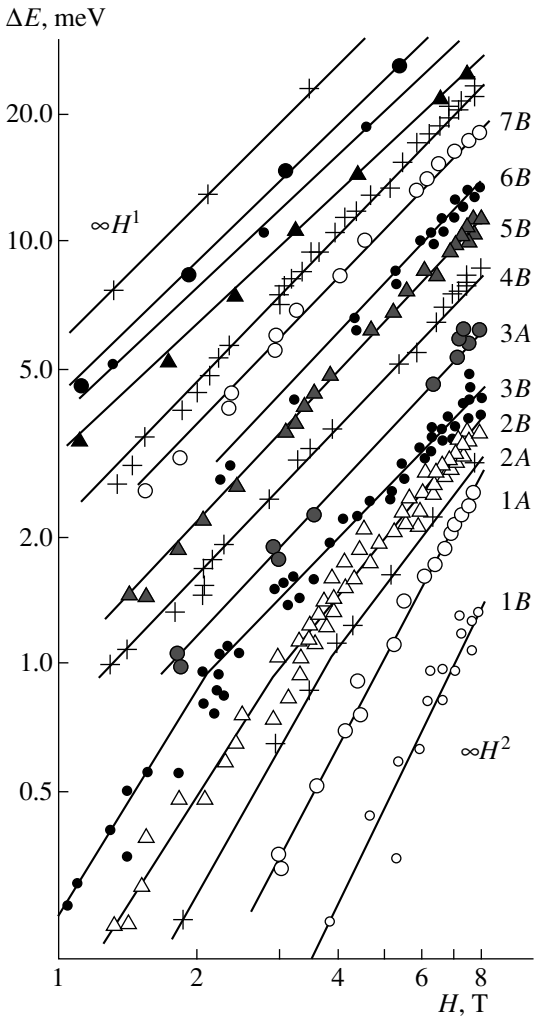

Fig. 2. Fan-shaped diagrams of magnetoabsorption in CdSe in the logarithmic coordinates. The most intense lines of the magnetooptical spectrum are shown. The notation reflects the serial number and affiliation to the *A* or *B* series; the initial energy (being subtracted) corresponds to the energy positions of the relevant discrete states of an exciton in a zero field.

hole, since the approximation of the dependences of the positions of the lines to zero magnetic field $H = 0$ gives an energy lower than that corresponding to the band edge. It is natural to assume that we observe here the exciton series under Landau levels, i.e., a manifestation of diamagnetic (quasi-one-dimensional) excitons.

The ratio of the squared exciton radius a_{exc} to the squared magnetic length L,

$$\beta = (a_{\text{exc}}/L)^2,$$

where $L = (c\hbar/eH)^{1/2}$, e is the electron charge, and c is the velocity of light, can be regarded as a criterion separating the weak- and strong-field modes. The condition $\beta < 1$ corresponds to a weak field, while for a strong field, the condition $\beta \gg 1$ must be satisfied [the Elliot–Loudon (EL) criterion]. However, the EL criterion in pure form is barely satisfied in wide-band semiconductors, and one has to use its modification for excited states of the exciton series, i.e., $\beta n^{*2} \gg 1$, where n^* is the highest excited exciton state observed experimentally or induced upon the application of a magnetic field. Thus, in real magnetooptical spectra and in magnetic field dependences, one can simultaneously observe the regions corresponding to the two modes: a weak field for the ground and lower excited states, and a strong field for higher states. This boundary will naturally be displaced depending on the field used in the experiment, since the value of β itself is proportional to H and can be regarded as a reduced magnetic field.

3. THEORY OF MAGNETOABSORPTION IN HEXAGONAL SEMICONDUCTORS IN WEAK AND STRONG FIELDS IN THE QUASI-CUBIC APPROXIMATION

At the present time, there exists no exact solution of the complete problem for an exciton in an arbitrary magnetic field, even for semiconductors with a simple parabolic conduction band and a nondegenerate valence band. The main difficulty lies in the requirement of simultaneous inclusion of the motion of an electron and a hole in the magnetic field, as well as the Coulomb interaction between the electron and the hole in an exciton. The problem is considerably simplified for weak or strong magnetic fields. In weak magnetic fields ($\beta < 1$), the problem of relative motion of the electron and hole in an exciton can be solved by considering the magnetic field as a perturbation. The effect of the magnetic field in this case is reduced to the linear Zeeman splitting of energy levels and to a quadratic diamagnetic shift [11]. In strong magnetic fields ($\beta \gg 1$), the problem is simplified in the case when the variables can be separated adiabatically [12]. At first, we consider the motion of electrons and holes in a plane perpendicular to the magnetic field (which leads to the formation of Landau levels). The subsequent inclusion of the Coulomb interaction between an electron and a hole leads to the formation of a quasi-one-dimensional diamagnetic exciton [12].

3.1. Direct-Exciton Model

Hexagonal semiconductors with a wurtzite structure are characterized by an axial symmetry with a sixfold axis *C*. The Hamiltonian describing the relative motion of an electron and a hole in a magnetic field in such semiconductors has the form

$$\hat{\mathbf{H}}_{\text{exc}}(\mathbf{k}) = \hat{\mathbf{H}}_e\left(\mathbf{k} + \frac{e}{\hbar c}\mathbf{A}\right) - \hat{\mathbf{H}}_h\left(-\mathbf{k} + \frac{e}{\hbar c}\mathbf{A}\right) - \frac{e^2}{\sqrt{\varepsilon_0^{\parallel}\varepsilon_0^{\perp}(x^2 + y^2) + \varepsilon_0^{\perp 2}z^2}}, \quad (1)$$

where the direction of the **z** axis is chosen parallel to the hexagonal **C** axis of the crystal, **k** is the wave vector of the relative motion, $\mathbf{r} = (x, y, z)$ is the relative coordinate of the electron and the hole, $\mathbf{A} = (1/2)[\mathbf{H} \times \hat{\mathbf{r}}]$ is the vector potential of the magnetic field, and $\varepsilon_0^{\parallel}$ and $\varepsilon_0^{\perp}$ are the values of the permittivity in the directions parallel and perpendicular to the **C** axis, respectively. If we disregard the relativistic terms linear in the momentum, the Hamiltonian $\hat{\mathbf{H}}_e$ for an electron in the conduction band (having the Γ_7 symmetry at the center of the Brillouin zone) has the form

$$\hat{\mathbf{H}}_e(\mathbf{k}) = \frac{\hbar^2}{2m_e^{\parallel}}k_z^2 + \frac{\hbar^2}{2m_e^{\perp}}(k_x^2 + k_y^2) + g_e^{\parallel}\mu_B(S_{ez}H_z) + g_e^{\perp}\mu_B(S_{ex}H_x + S_{ey}H_y), \quad (2)$$

where $m_e^{\parallel}$ and $m_e^{\perp}$ are the effective masses of an electron near the bottom of the conduction band in the directions parallel and perpendicular to the **C** axis, respectively, $\mu_B = e\hbar/2m_0c$ is the Bohr magneton, m_0 is the mass of a free electron, $g_e^{\parallel}$ and $g_e^{\perp}$ are the effective values of the electron *g*-factor in the conduction band for the magnetic field directions $\mathbf{H} \parallel \mathbf{C}$ and $\mathbf{H} \perp \mathbf{C}$, and $S_e = 1/2$ is the electron spin. We will describe the motion of a hole in the quasi-cubic approximation [13], disregarding the relativistic terms linear in the momentum. In this case, the hole in the valence band is regarded as a quasiparticle with the intrinsic orbital angular momentum $I = 1$ and the spin $S_h = 1/2$, and can be described by the effective Luttinger Hamiltonian for cubic semiconductors [14], in which the hexagonal crystal field is simulated by the effective field of deformation directed along the [111] axis of the cubic crystal (and coinciding with the *z* axis):

$$-\hat{\mathbf{H}}_h(\mathbf{k}) = \frac{\hbar^2}{2m_0}[(\gamma_1 + 4\gamma)\mathbf{k}^2 - 6\gamma(\mathbf{k}\hat{\mathbf{I}})] - \frac{2}{3}\Delta_{so}\left[(\hat{\mathbf{I}}\hat{\mathbf{S}}_h) - \frac{1}{2}\right] - \Delta_{cr}[\hat{\mathbf{I}}_z^2 - 1] - \mu_B(1 + 3\gamma + 3\kappa)(\hat{\mathbf{I}}\mathbf{H}) + \mu_B g_0(\hat{\mathbf{S}}_h\mathbf{H}). \quad (3)$$

Here, γ_1 and $\gamma = \gamma_2 = \gamma_3$ are the parameters introduced by Luttinger, κ is the Luttinger magnetic constant [14], $g_0 \approx 2$ is the *g*-factor for a free electron, Δ_{so} is the spin–orbit splitting of the valence band in the absence of crystal field splitting, and Δ_{cr} is the crystal-field splitting in the absence of the spin–orbit interaction. In zero magnetic field, the Hamiltonian $\hat{\mathbf{H}}_h$ describes three doubly degenerate valence subbands: *A* (with the symmetry Γ_9 at the center of the Brillouin zone), *B* (Γ_7 symmetry), and *C* (Γ_7 symmetry). For $\mathbf{k} = 0$, the separation between the bottom of the conduction band and the top of the upper valence subband *A* is equal to the forbidden band width E_g^A, while the distance between the upper subband *A* and the subbands *B* and *C* (Δ_{AB} and Δ_{AC}, respectively) are given by [13]

$$\Delta_{AB} = \frac{1}{2}\left[\Delta_{so} + \Delta_{cr} - \sqrt{(\Delta_{so} + \Delta_{cr})^2 - \frac{8}{3}\Delta_{so}\Delta_{cr}}\right],$$
$$\Delta_{AC} = \frac{1}{2}\left[\Delta_{so} + \Delta_{cr} + \sqrt{(\Delta_{so} + \Delta_{cr})^2 - \frac{8}{3}\Delta_{so}\Delta_{cr}}\right]. \quad (4)$$

The effective masses of holes in the valence subbands *A*, *B*, and *C* near the center of the Brillouin zone are connected with the Luttinger parameters and the values of the spin–orbit and crystal-field splitting through the following relations [13]:

$$\frac{m_0}{m_A^{\parallel}} = (\gamma_1 - 2\gamma), \quad \frac{m_0}{m_A^{\perp}} = (\gamma_1 + \gamma),$$
$$\frac{m_0}{m_B^{\parallel}} = \left(\gamma_1 + \gamma\left(1 - \frac{3\Delta_{cr} - \Delta_{so}}{\Delta_{AC} - \Delta_{AB}}\right)\right),$$
$$\frac{m_0}{m_B^{\perp}} = \left(\gamma_1 - \frac{1}{2}\gamma\left(1 - \frac{3\Delta_{cr} - \Delta_{so}}{\Delta_{AC} - \Delta_{AB}}\right)\right), \quad (5)$$
$$\frac{m_0}{m_C^{\parallel}} = \left(\gamma_1 + \gamma\left(1 + \frac{3\Delta_{cr} - \Delta_{so}}{\Delta_{AC} - \Delta_{AB}}\right)\right),$$
$$\frac{m_0}{m_C^{\perp}} = \left(\gamma_1 - \frac{1}{2}\gamma\left(1 + \frac{3\Delta_{cr} - \Delta_{so}}{\Delta_{AC} - \Delta_{AB}}\right)\right).$$

The value of the spin–orbit interaction in CdSe is much larger than the crystal-field energy ($\Delta_{so} \gg \Delta_{cr}$ and $\Delta_{AC} \gg \Delta_{AB}$), and the separation between the bottom of the conduction band and the top of the second valence subband *B* can be defined approximately as $E_g^B = E_g^A + \Delta_{AB} \approx E_g^A + 2/3\Delta_{cr}$. In this case, the expressions for the effective masses of holes in the subbands *B* and *C* can be considerably simplified, and the masses themselves are determined only by the Luttinger parameters:

$$\frac{m_0}{m_B^{\parallel}} = (\gamma_1 + 2\gamma), \quad \frac{m_0}{m_B^{\perp}} = (\gamma_1 - \gamma),$$
$$\frac{m_0}{m_C^{\parallel}} = \gamma_1, \quad \frac{m_0}{m_C^{\perp}} = \gamma_1. \quad (6)$$

3.2. Structure of Exciton Energy Levels in a Weak Magnetic Field: Perturbation Theory Method

The method of the perturbation theory enabling one to determine the energy level structure for an exciton in a weak magnetic field was first developed in [15, 16] for cubic semiconductors and recently extended to hexagonal semiconductors in a quasi-cubic approximation

[10]. Following [15, 16], we can write the Hamiltonian (1) in the form

$$\hat{\mathbf{H}}_{\text{exc}} = \hat{\mathbf{H}}_0 + \hat{\mathbf{H}}_{\text{int}} + \hat{\mathbf{H}}_l + \hat{\mathbf{H}}_q, \tag{7}$$

where the zeroth-approximation Hamiltonian $\mathbf{H}_0$ has the form

$$\hat{H}_0(\mathbf{k}) = \frac{\hbar^2}{2\mu_0}\mathbf{k}^2 - \frac{2}{3}\Delta_{\text{so}}\left[(\hat{\mathbf{I}}\hat{\mathbf{S}}_h) - \frac{1}{2}\right] - \Delta_{\text{cr}}[\hat{I}_z^2 - 1] - \frac{e^2}{\varepsilon_0 r},$$

$$\frac{1}{\mu_0} = \frac{1}{3}\left[\frac{2}{\mu_0^\perp} + \frac{\eta}{\mu_0^\parallel}\right], \quad \frac{1}{\mu_0^\perp} = \frac{1}{m_e^\perp} + \frac{\gamma_1}{m_0},$$
$$\frac{1}{\mu_0^\parallel} = \frac{1}{m_e^\parallel} + \frac{\gamma_1}{m_0}, \tag{8}$$
$$\varepsilon_0 = \sqrt{\varepsilon_0^\parallel \varepsilon_0^\perp}, \quad \eta = \frac{\varepsilon_0^\perp}{\varepsilon_0^\parallel}.$$

The eigenfunctions of the Hamiltonian $\mathbf{H}_0$ describe noninteracting hydrogen-like states of excitons of the series *A*, *B*, *C* in the zeroth approximation and have the form

$$\Phi_{\begin{bmatrix} n \\ t \end{bmatrix}, l, m, \alpha, i} = \Psi_{\begin{bmatrix} n \\ t \end{bmatrix}, l, m} u_{\alpha, i}, \tag{9}$$

where $\Psi_{\begin{bmatrix} n \\ t \end{bmatrix}, l, m}$ are the wave functions of the discrete (quantum number n =1, 2, …) and continuous (continuous variable t) spectra of the hydrogen atom, l is the orbital quantum number, m is the magnetic quantum number, and the functions $u_{\alpha, i}$ ($\alpha = A, B, C$; $i = 1, 2$) are the Bloch functions corresponding to the tops of the valence subbands *A*, *B*, and *C*. The corresponding energies of the discrete spectrum in the zeroth approximation are given by

$$E_{n, A} = -\frac{R_0}{n^2}, \quad E_{n, B} = \Delta_{AB} - \frac{R_0}{n^2},$$
$$E_{n, C} = \Delta_{AC} - \frac{R_0}{n^2}, \quad R_0 = \frac{\mu_0 e^4}{2\hbar^2 \varepsilon_0^2}. \tag{10}$$

The Hamiltonian $\mathbf{H}_{\text{int}}$ contains the terms describing the interaction of the valence subbands, the anisotropies of the effective masses of an electron and holes, and the anisotropy of the permittivities, which can be taken into account in the perturbation theory. The small parameters in this case are the quantities (μ_0/μ_1), (μ_0/μ_3), and $(1 - \eta)$, where

$$\frac{1}{\mu_1} = \frac{\gamma}{m_0}, \quad \frac{1}{\mu_3} = \frac{1}{3}\left[\frac{1}{\mu_0^\perp} - \frac{\eta}{\mu_0^\parallel}\right]. \tag{11}$$

The Hamiltonians $\mathbf{H}_l$ and $\mathbf{H}_q$ contain terms linear and quadratic in the magnetic field, respectively, which can also be taken into account in the perturbation theory for states with a characteristic binding energy R_0/n^2 much higher than the cyclotron energy $\hbar\omega_0 = 2\mu_B H$ for a free electron. The energy levels of excitons of the series *A*, *B*, and *C* in a weak magnetic field can be written in the final form

$$E_{n, \alpha}(\beta_e, \beta_h) = E_{n, \alpha} + \Delta E_{n, \alpha}$$
$$+ \mu_B H_{\parallel, \perp}(\beta_e g_e^{\parallel, \perp} + \beta_h g_{h, n, \alpha}^{\parallel, \perp}) + D_{n, \alpha}^{\parallel, \perp} H_{\parallel, \perp}^2, \tag{12}$$

where $\alpha = A, B, C$ and $\beta_e = \pm 1/2$, $\beta_h = \pm 1/2$. For the zero-field corrections $\Delta E_{n, \alpha}$, effective g-factors for holes $g_{h, n, \alpha}^{\parallel}$ and $g_{h, n, \alpha}^{\perp}$, and the diamagnetic shifts $D_{n, \alpha}^{\parallel}$ and $D_{n, \alpha}^{\perp}$ of the ground (n = 1) and excited (n = 2, 3) states of excitons of the *S*- and *P*-symmetry, we derived analytical expressions to the second order in the perturbation theory. These expressions contain numerical functions that depend on the separation Δ_{AC} and Δ_{AB} between the valence subbands. The expressions similar to (12) for the ground-state energy of excitons from the *A* and *B* series in zero magnetic field were obtained earlier in [17], taking into account the coupling of only two valence subbands.

3.3. Theory of Landau Levels in a Strong Magnetic Field in the Quasi-Cubic Approximation

It was noted above that in the case of a strong magnetic field, one should first solve the problem of the size quantization levels for electrons [the solutions for the Hamiltonian $\hat{\mathbf{H}}_e(\mathbf{k})$] and holes [the solutions for the Hamiltonian $\hat{\mathbf{H}}_h(\mathbf{k})$] moving in a plane perpendicular to the magnetic field and then take into account the Coulomb interaction between electrons and holes. For hexagonal semiconductors with $\Delta_{\text{so}} \gg \Delta_{\text{cr}}$, the problem of the Landau levels for electrons and holes was first solved in [4], where the relativistic terms in the electron and hole Hamiltonians, which are linear in momentum, were additionally taken into consideration, and it was assumed that the effective mass and the g-factor for the electron is anisotropic and that the magnetic field is directed along the z axis. In the quasi-cubic approximation disregarding the term linear in the momentum, the expressions for the Landau levels $E_n^{\pm}$ and $E_{l, \lambda}$ for electrons and holes derived in [4] for $k_z = 0$ are similar to the expressions for the Landau levels in diamondlike semiconductors (see [11, 12, 18]) and can be reduced to the following formulas:

$$E_n^{\pm} = \hbar\omega_0\left[\frac{m_0}{m_e}\left(n + \frac{1}{2}\right) \pm \frac{1}{4}g_e\right], \quad n = 0, 1, 2\ldots,$$

$$E_{l,\lambda} = \hbar\omega_0\left[\frac{\alpha_{l,\lambda}+\alpha_{l,\lambda_1}}{2} + \left(\frac{5}{4}-\lambda^2\right)\sqrt{\frac{(\alpha_{l,\lambda}-\alpha_{l,\lambda_1})^2}{2}+3l(l+\lambda+\lambda_1)\gamma^2}\right], \quad (13)$$

$$\alpha_{l,\lambda} = \gamma_1 l + (5/4-\lambda^2)(l+\lambda)\gamma + \lambda(\gamma_1-\kappa) + \delta(9/4-\lambda^2)/2,$$

where n and l are the indices of Landau levels for electrons and holes, respectively; $\delta = \Delta_{cr}/\hbar\omega_0$; and λ and the quantity $\lambda_1 = 4\lambda(\lambda^2 - 5/2)/3$ associated with it assume the values $\lambda = \pm 3/2, \pm 1/2$ and $\lambda_1 = \pm 3/2, \pm 1/2$. If we disregard the Coulomb interaction, the motion of electrons and holes along the magnetic field remains free, and the dependences of the energy levels on the wave number k_z allow us to determine the longitudinal effective masses of holes at Landau levels [11, 12]. The classification of the Landau levels for electrons and holes and the analysis of selection rules for optical transitions between them in hexagonal semiconductors with a strong spin–orbit splitting are presented in [4].

3.4. Binding Energies for Diamagnetic Excitons

The Coulomb interaction between an electron and a hole at Landau levels in a strong magnetic field leads to the formation of a diamagnetic exciton. The binding energy $R_{n,M,\lambda}$ of diamagnetic excitons formed by the electron Landau level with the index n and the Luttinger level for the hole with the index $l = n - M + 1/2$, which are determined by the component of the exciton magnetic moment along the magnetic field direction ($M = \pm 1/2$, $M = \pm 3/2$) can be determined in the adiabatic approximation from the one-dimensional Schrödinger equation [5, 11]

$$\left(-\frac{\hbar^2}{2\mu^{\parallel}_{l,\lambda}}\frac{d^2}{dz^2} + U_{n,M,\lambda}(z)\right)\psi(z) = -R_{n,M,\lambda}\psi(z), \quad (14)$$

where $\mu^{\parallel}_{l,\lambda}$ is the reduced longitudinal mass for the electron and the hole at the Landau level with the index l from the series λ ($\lambda = \pm 1/2; \pm 3/2$), and the quasi-one-dimensional potential of equation (14) can be obtained as a result of averaging the Coulomb potential for the wave functions $\Phi_{n,M,\lambda}$ describing the motion of excitons in a plane perpendicular to the magnetic field [12]:

$$U_{n,M,\lambda} = -\frac{e^2}{\varepsilon_0}\frac{1}{L}\int_0^{2\pi} d\varphi \int \frac{d\xi}{\sqrt{2\xi + z^2/L^2}}|\Phi_{n,M,\lambda}(\xi,\varphi)|^2. \quad (15)$$

Here, $\xi = \rho^2/2L^2$, ρ, and φ are the polar coordinates of the relative motion of the electron and the hole in the plane. The adiabatic potential $U_{n,M,\lambda}$ contains an infinite series of one-dimensional states of a diamagnetic exciton, adjoining the corresponding transition between Landau levels. The complete spectrum is given by

$$E^{\pm}_{n,M,\lambda} = E^{\pm}_n + E_{l,\lambda} - R_{n,M,\lambda}, \quad (16)$$

where $l = n - M + 1/2$ with the corresponding selection rules. The values of the binding energy for a diamagnetic exciton in CdSe calculated by the variational method are given in Table 1 with reference to the series and the Landau quantum number for an optical transition. It can be seen that the binding energy for a diamagnetic exciton in the fields under investigation is considerably smaller than the binding energy of the ground state of an exciton in zero magnetic field (R_0 = 15.6 meV), which is a consequence of the fulfillment of the EL criterion for excited states of the exciton only. It should also be noted that the calculated binding energy of the exciton states for the zeroth Landau level has an approximate value and differs from the actual binding energy by almost 50%, given the violation of the EL criterion for these states. The energy of excited states can be calculated almost exactly, since the EL criterion starts being observed for the first excited state (2*S*) of an exciton in fields of the order of H = 5 T and for the second excited state (3*S*), even at H = 2 T. The binding energy for a diamagnetic exciton increases slowly with the field and decreases slowly upon an increase in the Landau quantum number.

Table 1. Binding energy (meV) of the ground states of diamagnetic excitons in CdSe at H = 7.5 T

Landau level no.	b^-	a^-	b^+	a^+	b^-	a^-	b^+	a^+
0	5.8	6.1	12.0	11.9	11.2	9.6	6.1	7.6
1	5.3	5.6	8.1	8.2	7.9	6.6	5.4	6.5
2	4.8	5.1	6.5	6.2	6.5	5.5	4.9	5.8
3	4.5	4.7	5.7	5.4	5.7	4.9	4.5	5.2
4	4.2	4.4	5.1	4.8	5.1	4.5	4.2	4.8

Note: Calculations were based on polaron parameters presented in Table 2.

4. ANALYSIS OF EXPERIMENTAL RESULTS AND CALCULATION OF BAND PARAMETERS

4.1. Strong-Field Spectra Processing and Calculation of the Electron Effective Mass

The results considered in Section 3.3 show that Landau levels in hexagonal CdSe (in the quasi-cubic approximation neglecting the terms linear in the momentum) are described in analogy with Landau levels in diamondlike semiconductors. It is well known (see, for example, [11]) that, in the latter case, the system of Landau levels for holes consists of four sequences (ladders) of doubly degenerate hole levels (denoted by $a^{\pm}$ and $b^{\pm}$) and two ladders for electrons differing in the sign of the spin component $\pm 1/2$ (denoted by a^c and b^c). In the calculations based on (13), the system of Landau subbands for holes of a hexagonal semiconductor splits into two systems displaced by the interval $E_g^B - E_g^A$. In this case, the low-energy system of four subbands is formed by hole states with the angular momentum component $\pm 1/2$, while the high-energy system is formed by four ladders of states with $\pm 3/2$. A similar splitting of hole subbands also takes place in cubic diamondlike semiconductors as a result of the action of an elastic axial deformation, which induces a splitting of the top of the valence band. (Such a case is considered in detail in [6] for thin samples of CdTe cubic crystals glued to a "thick" glass substrate.)

Thus, strong-field magnetooptical spectra for hexagonal semiconductors CdSe in the given approximation can be interpreted and processed as the spectra of model deformed cubic semiconductors with the initial forbidden gap $E_g = (E_g^A + E_g^B)/2$ and with the deformation-induced splitting $\Delta_e = E_g^B - E_g^A$. In this case, we can use formulas (13), as well as other formulas describing the spectrum of Landau levels in diamondlike semiconductors, e.d., Pidgeon–Brown (PB) determinant equations [19] written by Aggarwal [20] in a modified form, taking into account the shear deformation. In this case, the effective mass of an electron is expressed in terms of the square of the interband matrix element of the angular momentum between the conduction and the valence band (P) and the correction F, taking into account the interaction between the conduction band and higher energy bands:

$$m/m_e = 1 + 2F + E_p(2/E_g + 1/(E_g + \Delta_{so}))/3, \quad (17)$$

where $E_p = (2m_0/\hbar^2)P^2$. Such a representation automatically takes into account the nonparabolicity effects and are widely used in magnetooptical investigations of diamondlike semiconductors.

The appropriate procedure of the data processing and the calculation of the electron effective mass can be described as follows. At first, a "bare" exciton spectrum for the maximum field (H = 7.5 T) used in the experiments is constructed by using the PB modified determinant equations [11] with the introduction of the experimental value $(E_g^B - E_g^A)$ as the deformation-induced splitting and with the application of the appropriate selection rules and calculated values of the binding energy for a diamagnetic exciton. The choice of the initial band parameters is based on the available band energies for $k = 0$, effective masses of an electron at the bottom of the conduction band, and longitudinal and transverse masses of holes determined using relations (6). Then the spectra are interpreted in terms of the cubic approximation (transitions $a^{\pm}a^c$ and $b^{\pm}b^c$ in the Faraday configuration, $\mathbf{H} \parallel \mathbf{q}$). The next step is reconstructing the actual position of transitions between Landau levels through the summation of the calculated values of the binding energy with the experimental values of energy corresponding to absorption peaks. After this, we can use one of the known methods for determining band parameters [11, 12]. In the present work, we applied the approach involving the direct calculation of cyclotron energies of electrons and holes with due account of the fact that the selection rules for two circular polarizations in the general form differ by 2: $\Delta n = +1$ for RCP (right circular polarization) and $\Delta n = -1$ for LCP (left circular polarization). Choosing two transitions from the same hole level to different electron levels with the Landau quantum numbers n_c and $n_c + 2$, we obtain the double cyclotron energy of an electron for the average energy $E_c(n_c + 1)$ equal to the difference between the chosen transition energies for coinciding fan-shaped diagrams for the A and B series. For example, for the total coincidence of the initial points of the "fan" for $H = 0$, the quantity $(E_g^B - E_g^A)/2$ is added to and subtracted from the series A and B respectively.

Figure 3 shows the general form of the fan-shaped diagrams obtained for the A and B series of CdSe, in which the reconstructed positions of transitions between Landau levels are indicated, and the identification of magnetoabsorption spectral lines is given in the quasi-cubic approximation. Subtracting the corresponding energies of the RCP spectrum from transition energies between Landau levels for the states of the LCP spectrum, we obtain the doubled cyclotron energy for the electron, $E_{e,H} = \hbar\omega_0(m_0/m_e)$:

$$(a, b)^{\pm}(n)(a, b)^c(n + 1) - (a, b)^{\pm}(n)(a, b)^c(n - 1) = 2E_{e,H}(n), \quad (18)$$

since the same hole level is involved in these transitions. The average value of the electron effective mass near the bottom of the conduction band calculated by using (18) amounted to $m_e = (0.116 \pm 0.005)m_0$. This value is considerably smaller than the most frequently used value $m_e = 0.13m_0$ [3]. It should be borne in mind that the value of the effective mass obtained by the above method corresponds to the band electron mass, while the value determined in [3] is essentially the

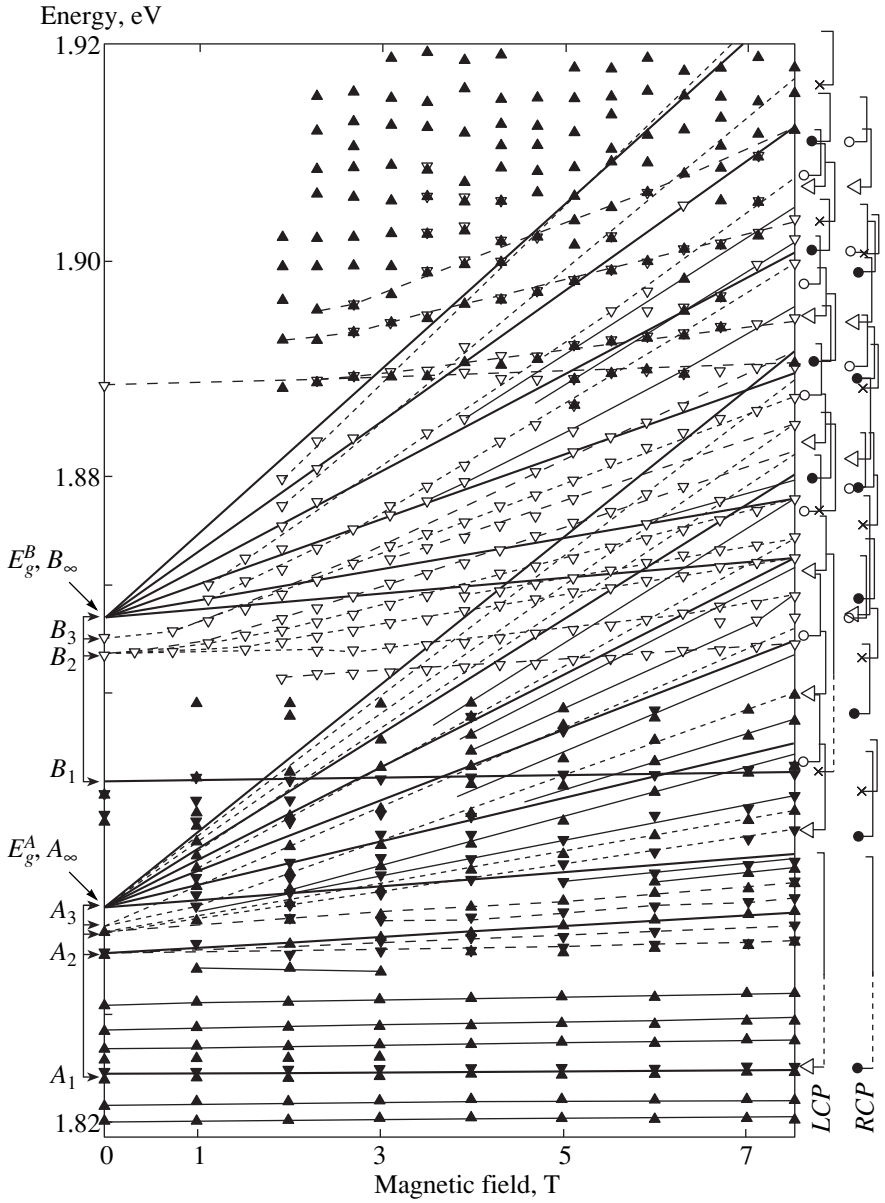

Fig. 3. General form of a fan-shaped diagram of the interband magnetoabsorption in CdSe. Solid lines present reconstructed energies of transitions between Landau subbands for holes and electrons. The experimental points are connected by dashed lines for better visualization. Combined data obtained in experiments with different polarizations and recording conditions are depicted. The corresponding points are denoted by different triangles. The difference can be neglected in this paper. The brackets and arrows on the left ordinate axis indicate series of exciton states from *A* and *B*. On the right ordinate axis, the spectra of transitions for a diamagnetic exciton are identified. The following notation typical of cubic semiconductors is used: (△) $a^+(l)a^c(l \pm 1)$, (○) $a^-(l)a^c(l \pm 1)$, (×) $b^+(l)b^c(l \pm 1)$, (●) $b^-(l)b^c(l \pm 1)$, l stands for the Landau quantum number, a^+, a^-, b^+, b^-, a^c, and b^c is the notation for ladders of light and heavy holes and electrons, respectively; $(l + 1)$ and $(l - 1)$ transitions correspond to the left- and right circular polarizations, respectively.

polaron mass (since the binding energy of an exciton is lower than the energy of optical phonons E_{LO} = 26.1 meV [21]). The value of the polaron mass corresponding to the obtained value of the band electron mass can be defined taking into account the electron–phonon interaction as $m_{ep} = m_e(1 + \alpha_{Fe}/6)$, where $\alpha_{Fe} = e^2(\varepsilon_\infty^{-1} - \varepsilon_0^{-1})(m_e/2E_{LO}\hbar^2)^{1/2}$. Using the average values of static (ε_0) and the high-frequency ($\varepsilon_\infty = \sqrt{\varepsilon_\infty^{\parallel}\varepsilon_\infty^{\perp}}$) permittivities ($\varepsilon_0^{\parallel} = 10.16$, $\varepsilon_0^{\perp} = 9.29$, $\varepsilon_\infty^{\parallel} = 6.2$, and $\varepsilon_\infty^{\perp} = 6.15$ [21]), we found that the polaron effective mass is $m_{ep} = (0.125 \pm 0.005)m_0$.

A similar procedure can be applied for determining the cyclotron energies and effective masses of heavy and light holes in a model cubic semiconductor [22].

Table 2. Preferable bond and polaron parameters of the energy spectra of electrons and holes obtained in the present work

Parameters	E_p, eV	F	$\frac{m_e}{m_0}$	g_e	γ_1	γ	κ	$\frac{m_A^{\parallel}}{m_0}$	$\frac{m_A^{\perp}}{m_0}$	$\frac{m_B^{\parallel}}{m_0}$	$\frac{m_B^{\perp}}{m_0}$
Polaron	18	0	0.125	0.7	1.5	0.29	−0.63	1.08	0.56	0.48	0.83
Band	19	−1.2	0.116	0.7	1.7	0.37	−0.63	1.01	0.48	0.41	0.75

However, this procedure has a low sensitivity to the mass of the heavy hole, since its contribution is smaller than that from the electron and is close to the experimental error. With regard to light holes, their exact parameters cannot be determined, due to the absence of the required number of points of the *A* spectrum that are not superimposed on the *B* spectrum. The average values of hole masses obtained by this method and consequently also being band masses are $m_{lh} = 0.24m_0$ and $m_{hh} = 0.63m_0$ for light and heavy holes, respectively. However, these values are not quite reliable due to the above factors. The effective Luttinger constants and the corresponding values of effective masses of holes will be determined below by processing the weak-field spectra.

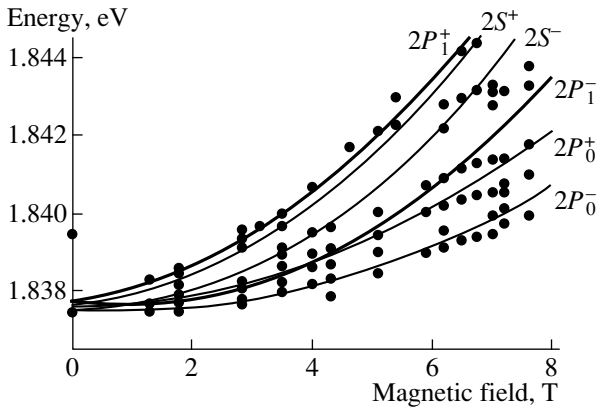

Fig. 4. Dependence of the optical transition energy of the excited state $n = 2$ for an *A* exciton on the magnetic field **H** ∥ **C**.

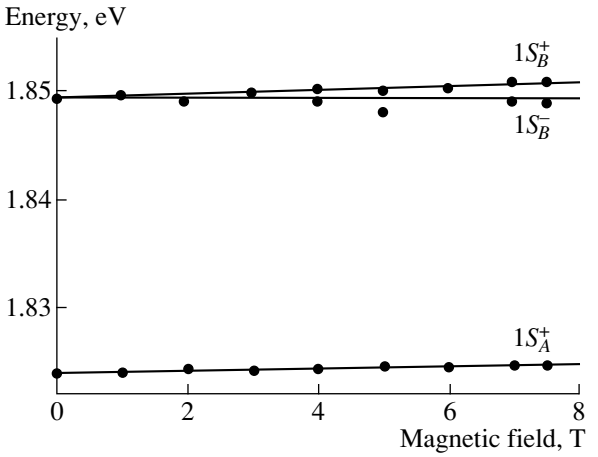

Fig. 5. Dependence of the optical transition energy of the ground state $n = 1$ for *A* and *B* excitons on the magnetic field **H** ⊥ **C**.

4.2. Processing of Weak-Field Spectra and Determination of Effective Luttinger Parameters

In order to describe the obtained magnetoabsorption spectra of CdSe in weak magnetic fields, we calculated the energies of the 1*S*, 2*S*, 2*P*, and 3*S* states of *A* and *B* excitons. The values of the effective *g*-factor for a hole and of the diamagnetic shifts for an exciton in all the states were calculated for magnetic fields directed parallel and perpendicular to the **C** axis. The calculations were based on the above anisotropic values of static permittivities and the isotropic value of the electron mass coinciding with the value of the polaron mass determined earlier: $m_e^{\parallel} = m_e^{\perp} = 0.125m_0$. All the remaining parameters for attaining the best coincidence with the experimental data varied.

The most informative magnetooptical spectra in weak magnetic fields **H** ∥ **C** were obtained for states of an A exciton with the principal quantum number $n = 2$ (Fig. 4). The linear and quadratic dependences of these states on the magnetic field formed the basis of the fitting procedure. An analysis of the Zeeman splitting of states of a *B* exciton in a magnetic field **H** ⊥ **C** (Fig. 5) enabled us to directly determine the Luttinger magnetic constant κ from the transverse effective *g*-factor for a hole, which differs from zero in the case of a *B* exciton. The parameters that are the most suitable for these two configurations were used for verification purposes in analyzing the remaining cases.

It should be noted that the Luttinger γ parameters required for calculating the exciton energies in weak magnetic fields and determining the masses of a hole are of the polaron type, like the electron mass. In the course of fitting, we took into account the relations between the Luttinger band and polaron parameters γ presented in [22], as well as the well-known relation between the Luttinger magnetic constant κ and the band parameters γ_1 and γ: $\kappa = (-2 + 5\gamma - \gamma_1)/3$.

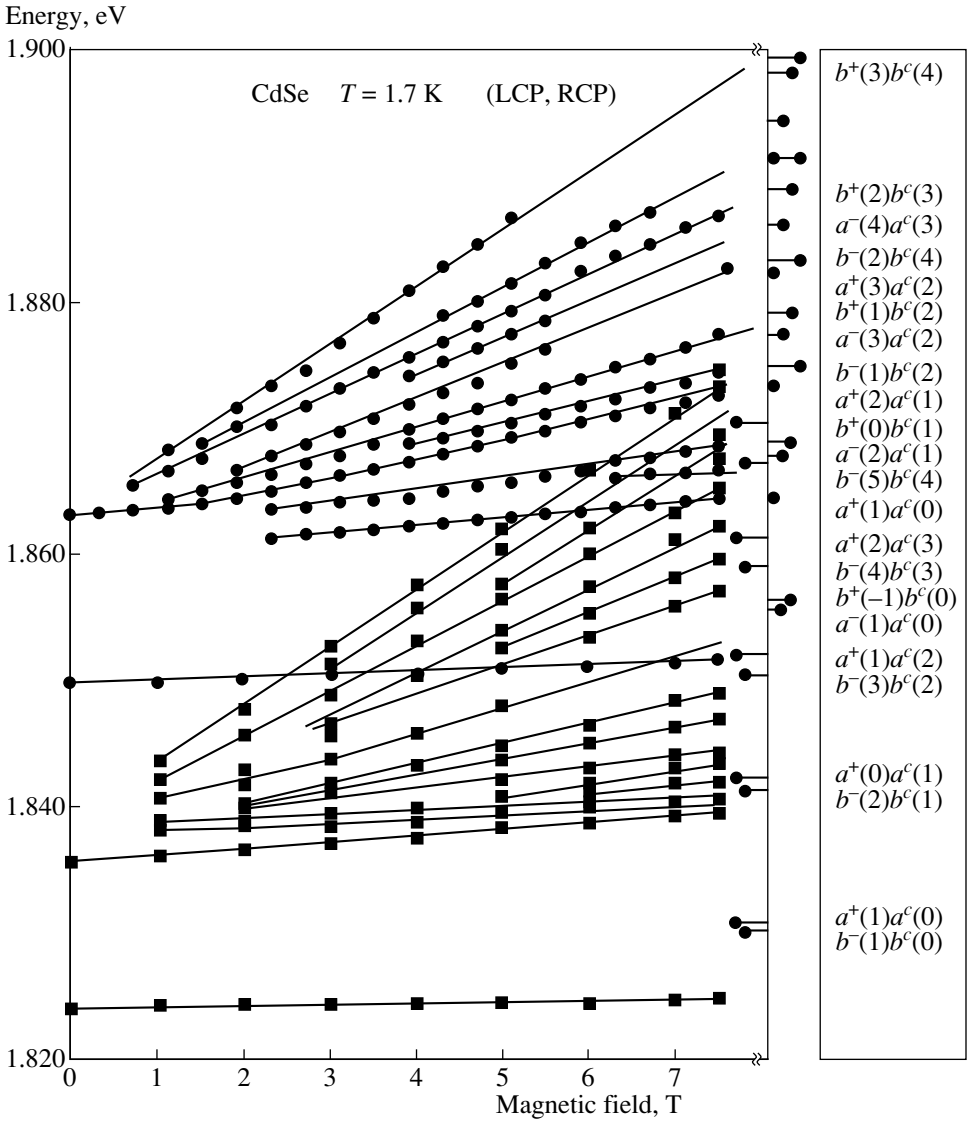

Fig. 6. Experimental fan-shaped diagram of a CdSe sample in the Faraday geometry of the LCP and RCP polarizations at $T = 1.7$ K. Solid lines are plotted for better visualization. The positions for transitions of a diamagnetic exciton calculated by using the obtained set of band and polaron parameters of CdSe for the *A* and *B* series are shown on the right. The frame on the right contains the quasi-cubic notation for transitions between Landau levels.

As a result of fitting, we determined the parameters leading to the best agreement in describing exciton spectra in a weak magnetic field: Luttinger polaron parameters $\gamma_1 = 1.5$ and $\gamma = 0.29$ (the corresponding Luttinger band parameters are $\gamma_1 = 1.7$ and $\gamma = 0.37$), the Luttinger magnetic constant $\kappa = -0.63$, the effective electron *g*-factors $g_e^{\parallel} = g_e^{\perp} = 0.7$. The complete set of parameters, together with the values of hole masses in valence subbands *A* and *B* [calculated by formulas (6)], is given in Table 2.

The obtained set of band and polaron parameters (Table 2) was subsequently used for checking the calculation of the spectrum of Landau levels and diamagnetic excitons in strong magnetic fields (Fig. 6). The binding energies of diamagnetic excitons were calculated by using polaron parameters, while the spectrum of the Landau levels was constructed in accordance with the band parameters. The observed agreement between the theoretical and experimental spectra can be seen as confirmation of the correctness of the chosen calculation method and as an estimate of the accuracy of the obtained parameters.

Thus, the results obtained in direct magnetooptical experiments on the optical transmission of ultrathin, free and highly perfect CdSe samples at $T = 1.7$ K in magnetic fields up to 8 T were assumed to contain weak- and strong-field information simultaneously. The corresponding regions of the spectra were interpreted in the quasi-cubic approximation with the help of the the-

oretical models developed for CdSe hexagonal crystals. Both models (for weak and strong fields) make it possible to calculate the sets of basic parameters of the band structure of the crystal, which were found to differ considerably. The Landau level spectroscopy makes it possible to calculate the band masses and the parameters. This method provides the most reliable value of the effective band mass for electrons, while the values of hole masses, as well as the corresponding band parameters, are not quite reliable for the reasons mentioned above. At the same time, weak-field data do not allow one to separate the electron and hole contributions and provide direct information on polaron parameters only. The combined interpretation of weak- and strong-field experimental data made it possible to determine the band and polaron parameters of CdSe hexagonal crystals self-consistently.

ACKNOWLEDGMENTS

The authors are grateful to A.L. Efros and D.L. Fedorov for their interest in this research.

This research was supported by the Russian Foundation of Basic Research (grant no. 99-02-16750), as well as the INTAS–1997 OPEN–1609.

REFERENCES

1. S. V. Ivanov, S. V. Sorokin, P. S. Kop'ev, *et al.*, J. Cryst. Growth **16**, 159 (1996).
2. N. N. Ledentsov, I. L. Krestnikov, M. V. Maximov, *et al.*, Appl. Phys. Lett. **69**, 1343 (1996).
3. J. O. Dimmock and R. G. Weeler, J. Appl. Phys. **32**, 2271 (1961).
4. B. L. Gel'mont, G. V. Mikhaĭlov, A. G. Panfilov, *et al.*, Fiz. Tverd. Tela (Leningrad) **29**, 1730 (1987) [Sov. Phys. Solid State **29**, 995 (1987)].
5. S. I. Kokhanovskiĭ, Yu. M. Makushenko, R. P. Seĭsyan, *et al.*, Fiz. Tverd. Tela (Leningrad) **33**, 1719 (1991) [Sov. Phys. Solid State **33**, 967 (1991)].
6. G. N. Aliev, O. S. Koshchug, A. I. Nesvizhskiĭ, *et al.*, Fiz. Tverd. Tela (St. Petersburg) **35**, 1514 (1993) [Phys. Solid State **35**, 764 (1993)].
7. G. N. Aliev, A. D. Andreev, O. Coschug-Toates, *et al.*, J. Cryst. Growth **184–185**, 857 (1998).
8. G. N. Aliev, A. D. Andreev, R. M. Datsiev, *et al.*, J. Cryst. Growth **184–185**, 315 (1998).
9. A. B. Kapustina, R. M. Datsiev, D. L. Fedorov, B. V. Petrov, and R. P. Seisyan, in *Excitonic Processes in Condensed Matter*, Ed. by R. T. Williams and W. M. Yen (Pennington, 1998), PV 98-25, p. 543.
10. A. V. Rodina, L. Eckey, M. Dietrich, *et al.*, Phys. Status Solidi B **216** (1), 21 (1999).
11. R. P. Seĭsyan, *Diamagnetic Exciton Spectroscopy* (Nauka, Moscow, 1984), p. 272.
12. R. P. Seisyan and B. P. Zakharchenya, in *Landau Level Spectroscopy*, Ed. by E. I. Rashba and G. Landwehr (North Holland, Amsterdam, 1991), Chap. 7, p. 345.
13. G. L. Bir and G. E. Pikus, *Symmetry and Strain-Induced Effects in Semiconductors* (Nauka, Moscow, 1972; Wiley, New York, 1975), p. 557.
14. J. M. Luttinger, Phys. Rev. **102**, 1030 (1956).
15. A. Baldereschi and N. C. Lipari, Phys. Rev. B **3**, 439 (1971); M. Altarelli and N. C. Lipari, Phys. Rev. B **7**, 3798 (1973).
16. L. Swierkowski, Phys. Rev. B **10**, 3311 (1974).
17. J. Flohrer, E. Jahne, and M. Porsch, Phys. Status Solidi B **91**, 467 (1979).
18. B. L. Gel'mont, R. P. Seĭsyan, A. L. Éfros, and A. V. Varfolomeev, Fiz. Tekh. Poluprovodn. (Leningrad) **11**, 238 (1977) [Sov. Phys. Semicond. **11**, 139 (1977)].
19. C. R. Pidgeon and R. A. Brown, Phys. Rev. **146**, 575 (1966).
20. R. L. Aggarwal, Semicond. Semimet. **9**, 151 (1973).
21. Landoldt-Börnstein, 17b (Springer, Berlin, 1982).
22. H.-R. Trebin, Phys. Status Solidi B **81**, 527 (1977); H.-R. Trebin and U. Roesler, Phys. Status Solidi B **70**, 717 (1975).

Translated by N. Wadhwa

Physics of the Solid State, Vol. 42, No. 7, 2000, pp. 1253–1258. Translated from Fizika Tverdogo Tela, Vol. 42, No. 7, 2000, pp. 1218–1222.

SEMICONDUCTORS AND DIELECTRICS

Moving Near-Gap Solitons in the Nonlinear Optical Medium

A. S. Kovalev*, O. V. Usatenko, and A. V. Gorbach****

** Kharkov Institute of Physics and Technology, Ukrainian Scientific Center, Akademicheskaya ul. 1, Kharkov, 310108 Ukraine*

*** Kharkov State University, pl. Svobody 4, Kharkov, 310077 Ukraine*

e-mail: Oleg.V.Usatenko@univer.kharkov.ua

Received November 4, 1999

Abstract—For a one-dimensional nonlinear optical medium with a periodic refraction index, new two-parameter soliton solutions of electrodynamics equations have been found. These solutions represent two interacting waves that propagate in two opposite directions. The oscillation frequency of each wave may fall either into the forbidden gap in the linear spectrum or outside it, and the group velocity may vary from zero to a maximal value that is determined by the parameters of the medium. Algebraic soliton solutions have been found as the limit of the nonlinear solutions, when the nonlinear wave frequency tends to the frequency of one of the linear-spectrum branches. © *2000 MAIK "Nauka/Interperiodica".*

INTRODUCTION

The existence of gap (Bragg) solitons was predicted theoretically by Mills, Trullinger, and Chen [1, 2] when studying the nonlinear Maxwell equations for nonlinear waves in the optical medium of spatially periodic refraction index. However, only motionless gap solitons of the frequency falling in the gap of a linear-wave spectrum (LWS) were found by them. Such nonlinear excitations may appear in other modulated systems as well, e.g., in crystals with complex unit cells [3–6] and in multi-sublattice magnets [7]. In [8–10], the possibility of more complex standing solitons of frequencies located near the gap in LWS was pointed out ("near-gap" solitons). Obtaining an explicit solution for solitons moving in modulated media is a more difficult problem. Such solutions for gap optical solitons were first discussed in [11, 12], and later, for moving elastic gap solitons, in [13].

In this work, the moving near-gap solitons are considered for the case of nonlinear optical medium with a modulated refraction index. Such solutions belong to the type of two-parameter solitons and represent localized excitations on the background of a nonlinear wave that does not decay at infinity. Envelope solitons move at a group velocity of linear waves. We have also considered the limiting case of immovable and so-called "algebraic" solitons, i.e., solitons whose parameters lie in one of the LWS branches separating the gap (in the linear limit) and near-gap solitons.

1. BASIC EQUATIONS

Let us consider a one-dimensional optical medium with a periodical refraction along the x axis, index $n(x) = n_0 + n_1\cos(2\beta_0 x)$. The refraction-index modulation results in a series of gaps in the dispersion law for linear waves $\omega = ck/n_0$, the gaps being associated with wave numbers $k_m = m\beta_0$ ($m = 1, 2, \ldots$). The width of the first gap is found to be proportional to the modulation amplitude n_1, and, in the general case, to n_1^m. We will study nonlinear waves with wave numbers and frequencies lying in the vicinity of the main gap, i.e., at $k \sim \beta_0$ and $\omega \sim \beta_0 c/n_0$. The dynamical equation for the electric field intensity of the nonlinear wave that propagates in the medium under consideration can be written in the form

$$c^2\frac{\partial^2 E}{\partial x^2} = \frac{\partial^2}{\partial t^2}\{n_0^2 E + 2n_0 n_1\cos(2\beta_0 x)E + \gamma|E|^2 E\}, \quad (1)$$

where γ is the Kerr nonlinear coefficient.

We seek the solutions of (1) in the form of superposition of two waves E_F and E_B propagating in opposite directions, which corresponds to a so-called two-wave approximation [12, 13]

$$E = [E_F(x, t)\exp(i\beta x) + E_B(x, t)\exp(-i\beta x)]\exp(-i\omega t) + \text{c.c.} \quad (2)$$

If the modulation amplitude of the refraction index n_1 and the field amplitude E are assumed to be small

$$n_1 \ll n_0, \quad \gamma E^2/n_0^2 \ll 1, \quad (3)$$

then the amplitudes E_F and E_B are smooth (slow) functions of the coordinate x and time t, i.e., $\partial E/\partial x \ll \beta E$ and $\partial E/\partial t \ll \omega E$. Therefore, substituting (2) in (1), we may restrict ourselves to the first derivatives with respect to the coordinate and time only. As a result, we

1063-7834/00/4207-1253$20.00 © 2000 MAIK "Nauka/Interperiodica"

arrive at a set of first-order partial differential equations for E_F and E_B

$$\frac{\partial E_F}{\partial x} + \frac{\omega n_0^2}{c^2\beta}\frac{\partial E_F}{\partial t} = -\frac{i}{2c^2\beta}E_F(c^2\beta^2 - \omega^2 n_0^2) + i\frac{n_0 n_1 \omega^2}{2c^2\beta}E_B\exp(-2i(\beta-\beta_0)x) + i\frac{\gamma\omega^2}{2c^2\beta}(|E_F|^2 + 2|E_B|^2)E_F, \quad (4)$$

$$-\frac{\partial E_B}{\partial x} + \frac{\omega n_0^2}{c^2\beta}\frac{\partial E_B}{\partial t} = -\frac{i}{2c^2\beta}E_B(c^2\beta^2 - \omega^2 n_0^2) + i\frac{n_0 n_1 \omega^2}{2c^2\beta}E_F\exp(2i(\beta-\beta_0)x) + i\frac{\gamma\omega^2}{2c^2\beta}(|E_B|^2 + 2|E_F|^2)E_B. \quad (5)$$

In zeroth approximation with respect to the small parameters (3), equations (4) and (5) define the spectrum of the linearized problem in absence of modulation $\omega_0 = c\beta/n_0$. From (4) and (5), it follows also that solution (2) is true, when $|\beta - \beta_0| \ll 1/a$, where a is the characteristic length of localization of the soliton solution. Introducing the notation $\kappa = \beta_0 n_1/2n_0$, $\alpha = \beta_0\gamma/2n_0^2$, $v = c/n_0$ and putting $\beta = \beta_0$, we obtain

$$\frac{\partial E_F}{\partial x} + \frac{1}{v}\frac{\partial E_F}{\partial t} = i\kappa E_B - i\alpha\{|E_F|^2 + 2|E_B|^2\}E_F,$$
$$-\frac{\partial E_B}{\partial x} + \frac{1}{v}\frac{\partial E_B}{\partial t} = i\kappa E_F - i\alpha\{|E_B|^2 + 2|E_F|^2\}E_B. \quad (6)$$

In a linear approximation, the spectrum of this set of equations is as follows:

$$\omega = \omega_0 \pm v\sqrt{\kappa^2 + k^2}, \quad (7)$$

where $k = \beta - \beta_0$.

Renormalizing the amplitudes, coordinates, and time: $e_1 = \sqrt{2\alpha/\kappa}E_F$, $e_2 = \sqrt{2\alpha/\kappa}E_B$, $\kappa x \longrightarrow x$, $v\kappa t \longrightarrow t$, we come to the equation in dimensionless variables

$$\frac{\partial e_1}{\partial t} + \frac{\partial e_1}{dx} = ie_2 - \frac{i}{2}\{|e_1|^2 + 2|e_2|^2\}e_1,$$
$$\frac{\partial e_2}{\partial t} - \frac{\partial e_2}{dx} = ie_1 - \frac{i}{2}\{|e_2|^2 + 2|e_1|^2\}e_2. \quad (8)$$

We look for a solution of (8) in the form

$$e_i = F_i\exp(i\Omega t), \quad (9)$$

where the frequency departure Ω from the gap center is one of the parameters of the two-parameter family of solutions. Moreover, we propose the F_i amplitude dependence on the coordinate and time to be of the form $F_i = F_i(x - Vt)$, i.e., we seek the soliton envelopes in the form of traveling waves with the group velocity V. In this case, equations (8) can be rewritten as

$$(1-V)\frac{\partial F_1}{\partial x} = iF_2 - i\Omega F_1 - \frac{i}{2}\{|F_1|^2 + 2|F_2|^2\}F_1,$$
$$-(1+V)\frac{\partial F_2}{\partial x} = iF_1 - i\Omega F_2 - \frac{i}{2}\{|F_2|^2 + 2|F_1|^2\}F_2. \quad (10)$$

For this set of equations, the spectrum of linear waves $F \sim \exp(i\Omega t - ik(x - Vt))$ is presented in the form

$$\Omega = -kV \pm \sqrt{1 + k^2} = \pm\sqrt{1 - V^2},$$

where $V = \partial\omega/\partial k$ is the group velocity.

Below, we will present the soliton solutions of these equations for both $V = 0$ (immovable solitons) and $V \neq 0$ (moving solitons).

2. IMMOVABLE SOLITONS

Immovable solitons in modulated media were analyzed time and again [1–10]. So, we will not dwell on this question, but consider only the particular case of near-gap solitons [8–10], which comprise the main subject of our work.

Putting $V = 0$ in (10), we obtain the equations

$$\frac{\partial F_1}{\partial x} = iF_2 - i\Omega F_1 - \frac{i}{2}\{|F_1|^2 + 2|F_2|^2\}F_1,$$
$$-\frac{\partial F_2}{\partial x} = iF_1 - i\Omega F_2 - \frac{i}{2}\{|F_2|^2 + 2|F_1|^2\}F_2. \quad (11)$$

Further, it is convenient to introduce real variables

$$g = F_1 + F_2, \quad f = i(F_1 - F_2). \quad (12)$$

With respect to these variables, we have the following equations:

$$\frac{\partial g}{\partial x} = -f(1+\Omega) - \frac{3}{8}f(g^2 + f^2),$$
$$-\frac{\partial f}{\partial x} = g(1-\Omega) - \frac{3}{8}g(g^2 + f^2). \quad (13)$$

An analysis of these equations was performed in detail in [3, 7]. They have an "integral of motion"

$$E = -(1+\Omega)f^2 + (1-\Omega)g^2 - \frac{3}{16}(g^2 + f^2)^2. \quad (14)$$

We will be interested in near-gap solitons at $\Omega < -1$. In this case, the soliton solutions are

$$g = \sqrt{\frac{8}{3}}(1+\Omega)\frac{1 \pm \sqrt{-\Omega}\cosh(2\sqrt{-1-\Omega}x)}{\Omega\cosh^2(2\sqrt{-1-\Omega}x)+1},$$
$$f = \sqrt{\frac{8}{3}}\sqrt{\Omega(1+\Omega)}\sinh(2\sqrt{-1-\Omega}x) \qquad (15)$$
$$\times\frac{1 \pm \sqrt{-\Omega}\cosh(2\sqrt{-1-\Omega}x)}{\Omega\cosh^2(2\sqrt{-1-\Omega}x)+1}.$$

At $\Omega \longrightarrow -1$, the solutions transform into the so-called "algebraic" soliton featured by a power-law decrease of the amplitudes at infinity

$$g_* = \frac{4\sqrt{2}}{\sqrt{3}}\frac{1}{1+4x^2}, \quad f_* = \frac{4\sqrt{2}}{\sqrt{3}}\frac{2x}{1+4x^2}. \qquad (16)$$

This solution separates the gap and near-gap solitons.

At the initial variables F_1 and F_2, the near-gap soliton takes the form

$$F_1 = F_2^*$$
$$= -\sqrt{\frac{2}{3}}\sqrt{-1-\Omega}\sqrt{\frac{\sqrt{-\Omega}\cosh(2\sqrt{-1-\Omega}x)-1}{\sqrt{-\Omega}\cosh(2\sqrt{-1-\Omega}x)+1}} \qquad (17)$$
$$\times\exp\left[-i\arctan\left(\sqrt{\frac{\Omega}{1+\Omega}}\sinh(2\sqrt{-1-\Omega}x)\right)\right].$$

3. MOVING NEAR-GAP SOLITONS

To analyze the moving near-gap solitons, we return to equation (10). Replacing the variables

$$F_1 = u_1\exp(iq+is), \quad F_2 = u_2\exp(iq-is), \qquad (18)$$

we arrive at the following effective "dynamical system" in terms of u_1, u_2, s, q:

$$\frac{\partial u_1}{\partial x} = \frac{u_2\sin(2s)}{(1-V)},$$
$$\frac{\partial u_2}{\partial x} = \frac{u_1\sin(2s)}{(1+V)},$$
$$\frac{\partial s}{\partial x} = \frac{\cos(2s)}{1-V^2}\frac{(1+V)u_2^2+(1-V)u_1^2}{2u_1u_2}$$
$$-\frac{\Omega}{1-V^2}+\frac{3(u_1^2+u_2^2)-V(u_2^2-u_1^2)}{4(1-V^2)} = 0, \qquad (19)$$
$$\frac{\partial q}{\partial x} = \frac{\cos(2s)}{1-V^2}\frac{(1+V)u_2^2-(1-V)u_1^2}{2u_1u_2}$$
$$-\frac{V\Omega}{1-V^2}+\frac{(u_1^2-u_2^2)-3V(u_2^1+u_2^2)}{4(1-V^2)} = 0.$$

From the first two equations, we obtain the integral of motion

$$(1-V)u_1^2-(1+V)u_2^2 = C, \qquad (20)$$

where the constant C is defined by the relation between the amplitudes u_1 and u_2 at infinity ($x \longrightarrow \pm\infty$). For gap solitons, this constant is equal to zero, because both fields fall to zero at infinity in these solitons. In near-gap solitons, one or both fields may have nonzero asymptotics at infinity, which corresponds to so-called "solitons-on-platform." Thus, for these solitons, the constant C, in general, may be nonzero. In this case, it is the third independent parameter of the soliton (the first two ones are the frequency Ω and the velocity V). In this work, we restrict ourselves to a discussion of two-parameter solitons. Three-parameter solitons will be studied at a later time.

To study the properties of two-parameter solitons, we put the constant C equal zero in (20) and obtain the relation between the amplitudes u_1 and u_2:

$$u_2 = \sqrt{\frac{1-V}{1+V}}u_1. \qquad (21)$$

Introducing the renormalized coordinate $z = (x - Vt)/\sqrt{1-V^2}$ and excluding, we obtain the following equations for u_1, s, and q:

$$\frac{du_1}{dz} = u_1\sin(2s),$$
$$\frac{ds}{dz} = \cos(2s)-\nu-\alpha(V)u_1^2, \qquad (22)$$
$$\frac{dq}{dz} = -\nu V-\delta(V)u_1^2,$$

where

$$\nu = \Omega/\sqrt{1-V^2}, \ \alpha(V) = (3-V^2)/2(1+V)\sqrt{1-V^2},$$

and

$$\delta(V) = V/(1+V)\sqrt{1-V^2}.$$

The first two equations may be isolated. They represent the effective Hamiltonian system characterized by the Hamiltonian

$$H = [\cos(2s)-\nu]u_1^2-\frac{\alpha}{2}u_1^4 \qquad (23)$$

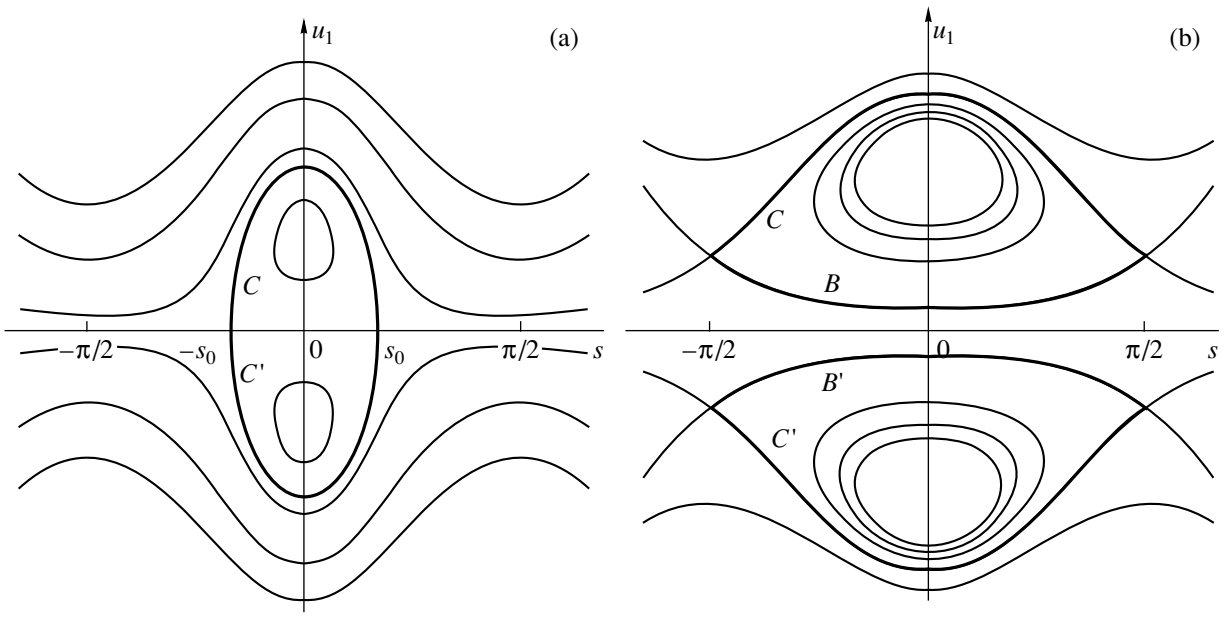

Fig. 1. Phase portrait of system (22). (a) $-\sqrt{1-V^2} < \Omega < \sqrt{1-V^2}$ (the frequency and the wave vector lie inside the region bounded by two branches of the LWS). The coordinates of the saddle points are $u_1 = 0$ and $\cos(2s_0) = \nu$. (b) $\Omega < -\sqrt{1-V^2}$ (the frequency and the wave vector lie under the lower branch of the LWS). The coordinates of the saddle points are $u_1 = \pm\sqrt{(-1-\nu)/\alpha}$ and $s = \pm\pi/2$.

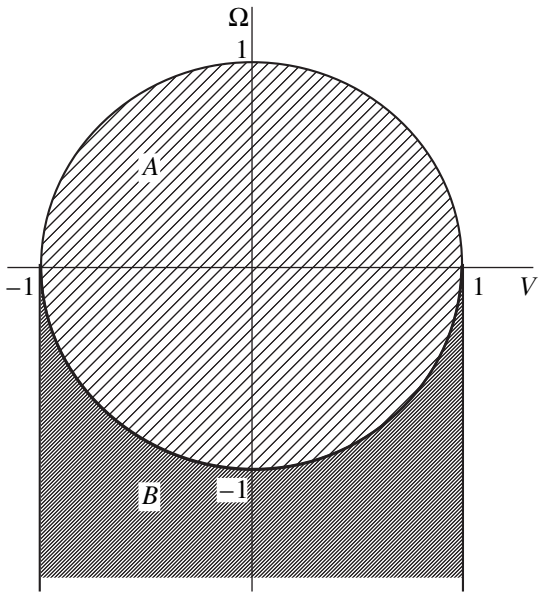

Fig. 2. Region of existence of soliton solutions in the parameter plane (Ω, V). The circle corresponds to the dispersion law of the linear waves $\Omega = \pm\sqrt{1-V^2}$. The shaded region A inside the circle corresponds to the gap solitons, the lower arc of the circle, to the "algebraic" solitons, and the band under the circle (region B), to the near-gap solitons.

for the canonically conjugated generalized coordinate $2s$ and the momentum u_1^2. The existence of the integral of motion H allows one to integrate system (22).

The phase portraits of this system for different values of the frequency Ω are shown in Figs. 1a and 1b. At $\Omega > \sqrt{1-V^2}$ (which corresponds to the value $\nu > 1$), there are no singular points in the (u_1, s) phase plane and, hence, there are no soliton solutions in this region.

At $\Omega = \sqrt{1-V^2}$, i.e., when $\nu = 1$ (which corresponds to the upper branch of the LWS), a single singular point is the point $s = u_1 = 0$, which is split into four singular points lying in the interval $-1 < \nu < 1$ (these are centers $s = 0$, $u_1 = \pm\sqrt{(1-\nu)/\alpha}$, and saddles $s = \pm 0.5 \arccos\nu$, $u_1 = 0$). In this interval (region A in Fig. 2), there are moving gap solitons, which correspond to separatrices C and C' in Fig. 1a. In the case $\Omega < -\sqrt{1-V^2}$, i.e., when $\nu < -1$ (region B in Fig. 2), each saddle point is split into two points given by the coordinates $s = \pm\pi/2$, $u_1 = \pm\sqrt{(-1-\nu)/\alpha}$, which corresponds to a nonzero field of the system at infinity. The separatrices C, C', B, B', which connect these points, describe two types of moving near-gap solitons of the frequencies lying under the lower branch of the LWS. The solutions for

such near-gap solitons have the form

$$s = \arctan\left(\sqrt{\frac{\nu}{1+\nu}}\sinh(2\sqrt{-1-\nu}z)\right),$$
$$u_1 = \left\{\frac{1}{\alpha}(-1-\nu)\left[\frac{2}{\sqrt{-\nu}\cosh(2\sqrt{-1-\nu}z)\pm 1}\right]\right\}^{\frac{1}{2}}. \quad (24)$$

After substituting (24) into the equation for the variable q, we obtain an explicit expression for this function

$$q = Vz\left(-\nu + 2\frac{1+\nu}{3-V^2}\right) + \frac{4V}{3-V^2}\arctan\left(\frac{\sqrt{-\nu}\exp(2\sqrt{-1-\nu}z)\pm 1}{\sqrt{-1-\nu}}\right). \quad (25)$$

Using (9), (18), and (24) and returning to the initial variables, we obtain

$$e_1 = \sqrt{\frac{2(1+V)}{3-V^2}}\sqrt{-\sqrt{1-V^2}-\Omega}\sqrt{1-\frac{2}{\sqrt{-\nu}\cosh\zeta\pm 1}} \times \exp\left[i\arctan\left(\sqrt{\frac{\nu}{1+\nu}}\sinh\zeta\right)\right] \times \exp\left[i\Omega t + i\frac{V(x-Vt)}{\sqrt{1-V^2}}\left(-\nu + 2\frac{1+\nu}{3-V^2}\right) + i\frac{4V}{3-V^2}\arctan\left(\frac{\sqrt{-\nu}\exp\zeta\pm 1}{\sqrt{-1-\nu}}\right)\right], \quad (26)$$

$$e_2 = \sqrt{\frac{2(1-V)}{3-V^2}}\sqrt{-\sqrt{1-V^2}-\Omega}\sqrt{1-\frac{2}{\sqrt{-\nu}\cosh\zeta\pm 1}} \times \exp\left[-i\arctan\left(\sqrt{\frac{\nu}{1+\nu}}\sinh\zeta\right)\right] \times \exp\left[\left(i\Omega t + t\frac{V(x-Vt)}{\sqrt{1-V^2}}\left(-\nu + 2\frac{1+\nu}{3-V^2}\right) + i\frac{4V}{3-V^2}\arctan\left(\frac{\sqrt{-\nu}\exp\zeta\pm 1}{\sqrt{-1-\nu}}\right)\right],$$

where $\zeta = 2\sqrt{-1-\nu}\,(x-Vt)/\sqrt{1-V^2}$.

The near-gap solitons found represent the so-called "solitons-on-platform," which move with the same velocity as the nonlinear waves of the constant amplitude do. It can be easily verified by considering the solution asymptotics at infinity

$$e_{1,2}^{\infty} = \pm i\sqrt{\frac{2(1\pm V)}{3-V^2}}\sqrt{-\sqrt{1-V^2}-\Omega} \times \exp\left(i\Omega t + i\frac{V(x-Vt)}{\sqrt{1-V^2}} + i\frac{2V\pi}{3-V^2}\right), \quad (27)$$

which coincide with the solution of (8) for spatially uniform nonlinear waves.

When the coordinate ζ varies from $-\infty$ to $+\infty$, the phase of the soliton high-frequency "contents" acquires the shift $\Delta = \pi(3 + 2V - V^2)/(3 - V^2)$.

Of special interest is the limit passage from moving near-gap solitons to moving gap solitons. In the limit $\nu \longrightarrow -1$, i.e., when $\Omega \longrightarrow -\sqrt{1-V^2}$, (26) transforms to the expression for an "algebraic" soliton

$$e_{1,2}^{*} = \sqrt{\frac{2(1\pm V)(1-V^2)}{3-V^2}}\frac{2}{\sqrt{1-V^2+4(x-Vt)^2}} \times \exp\left[\pm i\arctan\left(2\frac{x-Vt}{\sqrt{1-V^2}}\right)\right] \times \exp\left[i\Omega t + i\frac{V(x-Vt)}{\sqrt{1-V^2}} + i\frac{4V}{3-V^2}\arctan\left(2\frac{x-Vt}{\sqrt{1-V^2}}\right)\right]. \quad (28)$$

It is natural that this solution can also be obtained from the expression for the gap solitons in the limit $\nu \longrightarrow -1$.

Putting $V = 0$ in (26) and going over to the variables f, g (see (12)), we obtain the above expressions for immovable "algebraic" soliton (16).

CONCLUSIONS

In this work, the soliton solutions for nonlinear optical medium with a modulated refraction index were derived and analyzed. The soliton parameters fall either into the LWS gap (so-called gap solitons) or outside it (near-gap solitons). We have pioneered an analytical expression for moving near-gap solitons, which represent the localized excitations on the background of the nonlinear waves of an amplitude which does not decrease at infinity (so-called "solitons-on-platform"). The velocity of the near-gap soliton is equal to the group velocity of the background nonlinear wave.

We had considered the case of so-called focusing nonlinear optical medium, which is characterized by the positive coefficient γ in (1). In this case, the near-gap soliton solutions exist in the region under the lower branch of the LWS. In the case of the negative γ (defocusing medium), the character of the soliton solutions

does not change qualitatively, but near-gap solitons exist in the region above the upper branch of the LWS.

REFERENCES

1. W. Chen and D. L. Mills, Phys. Rev. Lett. **58**, 160 (1987).
2. D. Mills and J. Trullinger, Phys. Rev. B **36**, 947 (1987).
3. O. Chubykalo, A. Kovalev, and O. Usatenko, Phys. Rev. B **47**, 3153 (1993).
4. A. S. Kovalev, K. V. Kladko, and O. V. Usatenko, J. Phys. Soc. Jpn. **64**, 2464 (1995).
5. O. V. Usatenko, A. S. Kovalev, and A. A. Vialov, in *Fluctuation Phenomena: Disorder and Nonlinearity*, Ed. by A. R. Bishop, S. Jiménez, and L. Vázquez (World Scientific, Singapore, 1994), p. 286; O. V. Usatenko, A. S. Kovalev, and A. A. Vyalov, Fiz. Tverd. Tela (St. Petersburg) **37**, 2487 (1995) [Phys. Solid State **37**, 1362 (1995)].
6. O. Chubykalo and Yu. Kivshar, Phys. Rev. E **48**, 4128 (1993).
7. A. S. Kovalev, O. V. Usatenko, and A. V. Gorbatch, Phys. Rev. E **60**, 2309 (1999).
8. J. Coste and J. Peyraud, Phys. Rev. B **39**, 13086 (1989).
9. J. Coste and J. Peyraud, Phys. Rev. B **39**, 13096 (1989).
10. J. Peyraud and J. Coste, Phys. Rev. B **40**, 12201 (1989).
11. S. Wabnitz, Opt. Lett. **14**, 1071 (1989).
12. A. B. Aceves and S. Wabnitz, Phys. Lett. A **141**, 37 (1989).
13. A. S. Gorshkov, O. N. Ermakova, and V. F. Marchenko, Nonlinearity **10**, 1007 (1997).

Translated by N. Ostrovskaya

Physics of the Solid State, Vol. 42, No. 7, 2000, pp. 1259–1265. Translated from Fizika Tverdogo Tela, Vol. 42, No. 7, 2000, pp. 1223–1229.

SEMICONDUCTORS AND DIELECTRICS

Temperature Behavior of the 6.05-eV Band in Optical Absorption Spectra of Oxygen-Deficient Corundum

I. A. Vaĭnshteĭn and V. S. Kortov

Ural State Technical University, ul. Mira 19, Yekaterinburg, 620002 Russia

e-mail: wia@dpt.ustu.ru

Received December 6, 1999

Abstract—The effect of temperature on the 6.05-eV absorption band in α-Al_2O_3 has been studied in the 80–515 K region. The data obtained are analyzed in terms of a one-coordinate model with strong electron–phonon coupling. This band is shown to be formed by two peaks at 5.91 and 6.22 eV (T = 293 K) originating from absorption at the F^+ and F centers, respectively. An analysis of the experimental temperature dependences has allowed us to calculate the energies of effective phonons responsible for the broadening and shift of the peaks. The energies calculated agree with the data obtained in other studies and lie in the region of corundum acoustic-vibration frequencies. The Huang–Rhys factors have been evaluated for both centers and found to be close to the estimates made by other authors. The results are discussed in detail and compared with independent data on optical absorption and luminescence of anion centers in colored and irradiated α-Al_2O_3 single crystals. © *2000 MAIK "Nauka/Interperiodica".*

INTRODUCTION

Anion-defective α-Al_2O_3 crystals belong to a class of materials used in development of high-sensitivity detectors of ionizing radiation [1, 2]. Defects on the oxygen sublattice play the key role in the behavior of the optical, spectral, and temperature characteristics of these materials, as well as in their response to irradiation [3–6].

Anion off-stoichiometry in corundum can be obtained by thermochemical coloring or by irradiating it by particles [1, 7–9]. Optical absorption spectra of such crystals in the UV range are well studied, and they exhibit a strong 6.05 (6.1) eV band associated with the F center (oxygen vacancy with two trapped electrons) [2–4], as well as a band at 4.8 eV and a strongly polarized one at 5.4 eV, which are assigned to absorption by the F^+ center (oxygen vacancy with one trapped electron) [3, 4]. Besides the optical absorption by anion centers, comprehensive spectral luminescence studies have recently been made on α-Al_2O_3, with peaks found at 3.0 eV (luminescence of the F center) and at 3.8 eV (radiative transitions involving the F^+ center) [3–6, 10–12]. Models were proposed for these processes, in which the oxygen-vacancy centers were considered as isolated [3, 4] or involved in charge transfer [13].

At the same time, it should be pointed out that, despite the enormous amount of papers dealing with this problem, very few of them systematically study the effect of temperature on absorption spectra of α-Al_2O_3. While data obtained at room and cryogenic temperatures [2–5] and information on the annealing of F and F^+ centers and on the corresponding optical bands [2, 7, 9] are certainly available, an overall analysis of temperature effects in the dynamics, like the one done, for instance, for the F^+ center luminescence [4, 5], is lacking. Such an approach permits one, however, to directly isolate and take into account the electron–phonon interaction, which plays a substantial part in α-Al_2O_3. Besides, absorption spectra are, as a rule, a starting point in a discussion of many properties, including irradiation-induced ones, of the oxygen-deficient corundum. Therefore, one should know and bear in mind the transformation of these spectra under heating.

This work was aimed at investigating the effect of temperature on the behavior of the 6.05-eV absorption band in spectra of α-Al_2O_3 single crystals with oxygen vacancies and at establishing the main parameters of the center(s) responsible for this band.

1. SUBJECTS OF THE INVESTIGATION

We studied nominally pure α-Al_2O_3 single crystals grown by the Stepanov method in an atmosphere which was strongly reducing due to the presence of graphite (thermochemical coloring). A detailed description of the growth conditions can be found in [14]. The concentrations of iron and of other impurities having absorption bands in the spectral region under study were so low as not to affect the results of the experiment [15]. The final samples were 0.8-mm-thick polished disks 5-mm in diameter, with surfaces of optical quality. Note that the α-Al_2O_3 single crystals used in this work are employed in fabrication of thermoluminescent radiation detectors (TLD-500K, TU 2655-006-02069208-95). The samples to be used in the measurements were chosen at random from the lot having dif-

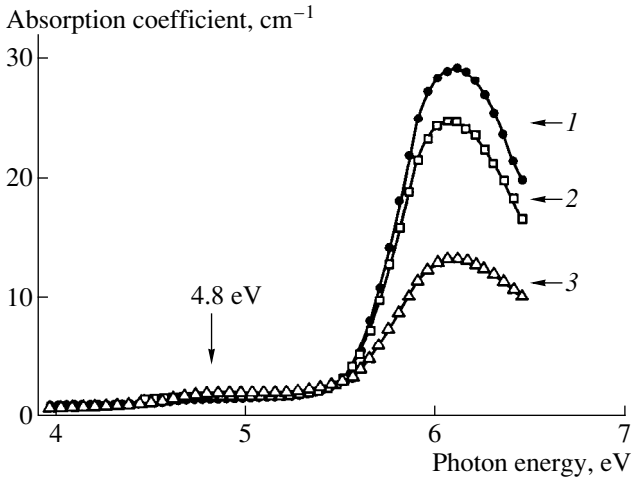

Fig. 1. Optical absorption spectra measured at $T = 293$ K on samples differing in sensitivity: (*1*) moderate sensitivity $\approx 4.5 \times 10^8$ quanta/Gy, (*2*) high sensitivity $\approx 8.5 \times 10^8$ quanta/Gy, and (*3*) low sensitivity $\approx 1.9 \times 10^8$ quanta/Gy.

ferent sensitivities to radiation. The instrumental and methodological aspects of estimation of the sensitivity, which was determined preliminarily from thermoluminescence yield, were discussed in [16].

All measurements were carried out on a Specord-M40 spectrophotometer in a vacuum cryostat within the temperature range of 80 to 515 K. The experiment covered the 4–6.45-eV UV range.

2. EXPERIMENTAL RESULTS

In the first stage of the work, room-temperature optical absorption spectra were measured on samples with different sensitivities (Fig. 1). All the samples are seen to have a clearly pronounced band at 6.05 eV. The sample with moderate sensitivity exhibits the strongest peak (curve *1*). Besides, all samples show a weak band in the 4.8-eV region. This peak is assigned to the $1A \longrightarrow 1B$ transition of the F^+ center [4]. The variation in peak intensity from one sample to another is associated with the nonuniformity of the defect concentration distribution along the starting corundum rod from which the samples were cut [14]. It is also worth noting that we are not aware of any data on a correlation between this sensitivity of α-Al_2O_3 single crystals and the band intensity in the absorption spectrum. Such studies are of independent interest and are beyond the scope of the present work.

Subsequent temperature measurements were performed only on sample *1*. Figure 2 shows absorption spectra taken in the 80–515 K range. The positions of the band maximum E_m are given in Table 1 for all temperatures. As seen from Fig. 2 and Table 1, the band half-width increases, and the value of E_m remains practically constant, with increasing temperature. Let us analyze the observed variation of the shape and the temperature behavior of the 6.05-eV peak under study.

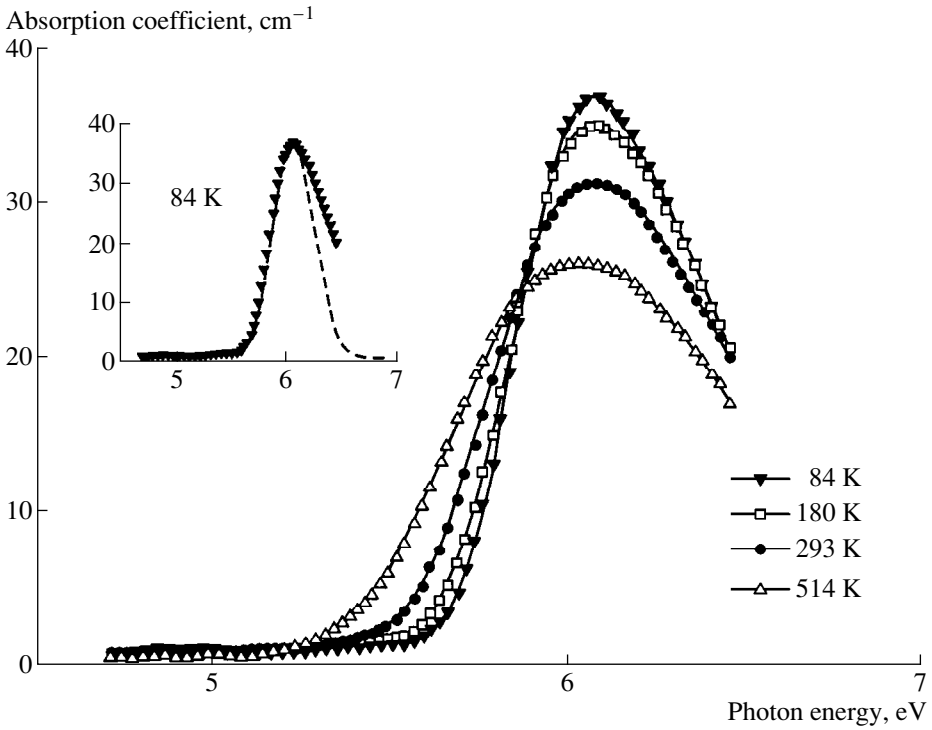

Fig. 2. Optical absorption spectra measured at different temperatures.

3. DISCUSSION

3.1. The Band Shape

Note, first of all, that the absorption bands in Fig. 2 are asymmetrical, with the high-energy wings being smoother and extended. This is particularly clearly seen in the inset showing an 84-K spectrum. The dashed line in the inset is a Gaussian centered at 6.05 eV, which fits accurately to the low-energy side of the band while deviating from its high-energy wing. The spectral region beyond 6.2 eV is certainly outside the limits of the spectrophotometer used. However, the observed asymmetry is not the result of measurement errors and is present in numerous independent works done on various α-Al_2O_3 samples [2–5, 8, 9, 11].

Figure 3 compares the results obtained in the present study with the data of other authors relating to room temperature measurements on additively colored single crystals, where *F* centers are of growth origin (Fig. 3a), and on samples irradiated by particles (Fig. 3b), where the concentration of these centers is also high. To simplify the comparison, the spectra are normalized to their maxima. With the exclusion of [11], where the band half-width is noticeably larger, all the bands agree very well not only in the peak position, but in shape as well, a point which appears significant.

The spectral shape suggests that, in this region, more than one center can absorb radiation, as already pointed out in some papers [4, 5, 10]. Another feature of the 6.05-eV band (see Fig. 2, Table 1) is that the maximum does not shift to lower energies with increasing *T*, as is the case with most crystals [17]. The absence of any band maximum shift in α-Al_2O_3 under heating was reported in [5]. The temperature-independent behavior of E_m can also be due to the existence of several absorbing transitions.

Accordingly, the experimental spectra obtained at different temperatures were decomposed into independent Gaussians (linear electron–phonon coupling model). This operation yielded two sets of peaks, *G*1 and *G*2 (Fig. 4), which most closely reproduce the observed profile of the 6.05-eV band. The value of E_m, the half-width *H*, and the approximation error (the sum of squared differences) are given in Table 1 for all temperatures. As seen from Fig. 4, at low temperatures (84 K) the peaks resolve clearly, whereas at room temperature and higher, the *G*1 peak is overlapped by the *G*2 peak. Hence, at high *T*, the behavior of the 6.05-eV band is determined by the dominant *G*2 maximum.

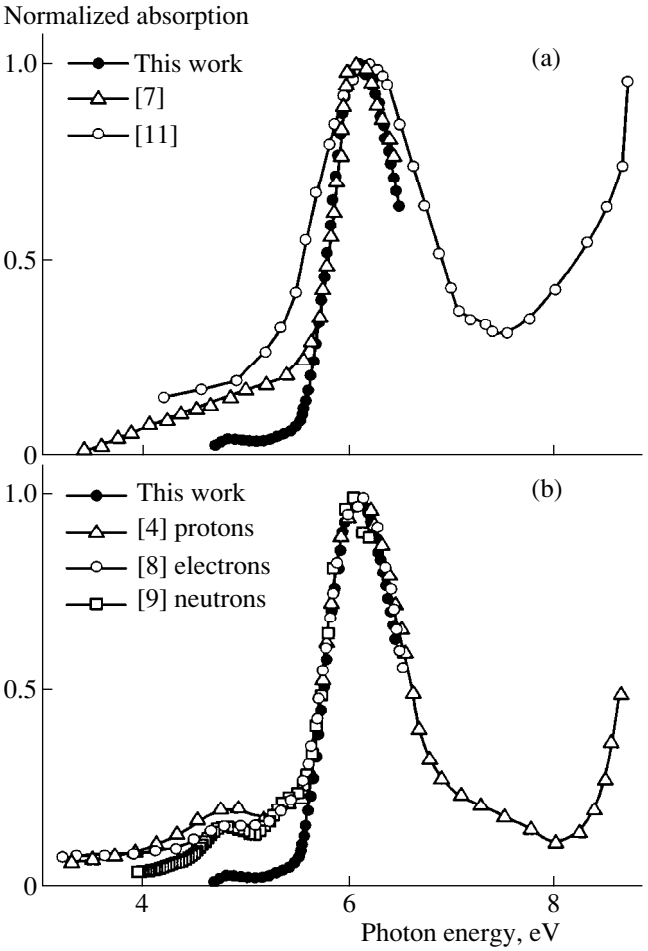

Fig. 3. Comparison of the results of this work with data from independent experiments: (a) additively colored α-Al_2O_3 single crystals and (b) irradiated crystals. The particles used to irradiate the starting α-Al_2O_3 single crystals are specified after the reference numbers.

Table 1. Spectral characteristics of decomposition into Gaussians

T, K	6.05-eV band	Peak *G*1		Peak *G*2		Error, $(cm^{-1})^2$
	E_m, ±0.03 eV	E_m, ±0.005 eV	*H*, ±0.010 eV	E_m, ±0.012 eV	*H*, ±0.012 eV	
84	6.08	5.975	0.355	6.263	0.540	0.085
180	6.05	5.952	0.366	6.242	0.589	0.051
240	6.05	5.935	0.389	6.237	0.635	0.056
293	6.05	5.908	0.410	6.221	0.683	0.030
364	6.05	5.889	0.434	6.212	0.723	0.021
435	6.08	5.852	0.449	6.183	0.771	0.020
514	6.05	5.820	0.490	6.174	0.825	0.020

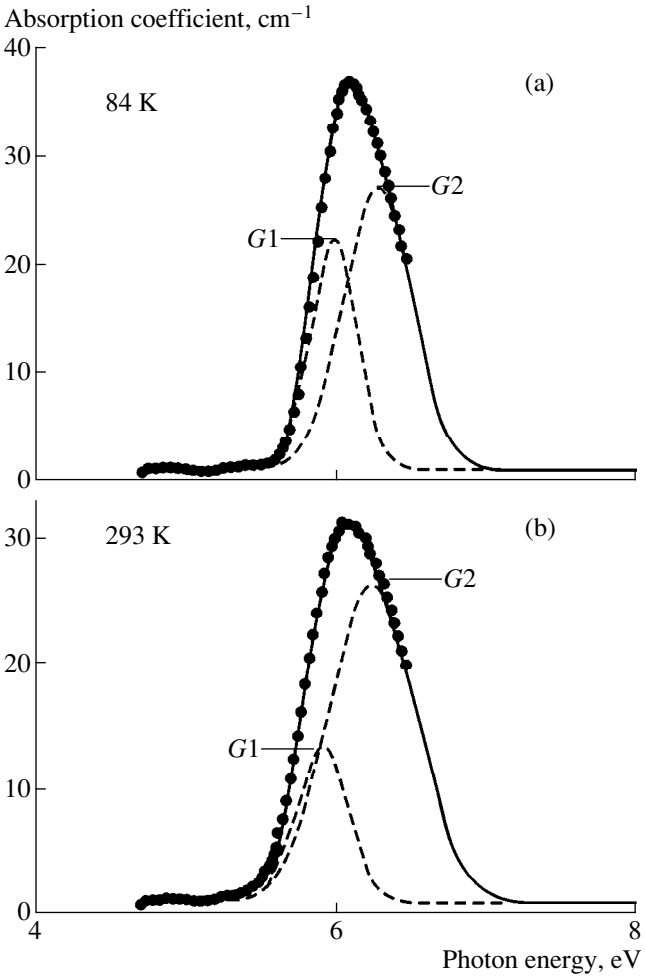

Fig. 4. Decomposition of the 6.05-eV absorption band into independent Gaussians: circles are the experiment, dashed lines are independent Gaussians, and the solid line is a calculated resultant curve.

It is essential that the decomposition of the optical bands at room temperature made for other samples shown in Fig. 1 also yield pairs of Gaussians with the same E_m and H within experimental errors (see Table 2).

Thus, by analyzing the 6.05-eV band in the absorption spectrum of the anion-defective α-Al_2O_3, one can obtain a set of two Gaussians, whose superposition reproduces with a high accuracy the measurements made at different temperatures and on different samples. The dominant peak is $G2$ (E_m = 6.22 eV, H = 0.68 eV for 293 K), while peak $G1$ (E_m = 5.91 eV, H = 0.41 eV for 293 K) is substantially weaker and becomes totally absorbed by $G2$ at high temperatures.

Table 2. Parameters of decomposition into Gaussians for different samples and T = 293 K

Sample no.	Peak $G1$		Peak $G2$		Error, $(\text{cm}^{-1})^2$
	E_m, ±0.005 eV	H, ±0.010 eV	E_m, ±0.005 eV	H, ±0.010 eV	
1	5.908	0.410	6.221	0.683	0.030
2	5.917	0.405	6.233	0.682	0.018
3	5.918	0.391	6.235	0.726	0.020

Prior to identifying the peaks obtained with specific centers, let us analyze the spectral parameters given in Table 1 as functions of temperature.

3.2. Analysis of Temperature Dependences

The shift of the peak position with increasing T can be approximated by the relation of Fan for the variation of the gap width under phonon-induced energy-level displacement [18]

$$E_m(T) = E_m(0) - A\langle n_s\rangle, \quad (1)$$

where $E_m(0)$ is the position of the maximum at zero temperature, A is the Fan parameter, which depends on microscopic characteristics of the material [19] and is related to the second-order deformation-potential constant [20], and $\langle n_s\rangle = [\exp(\hbar\omega_s/kT) - 1]^{-1}$ is the Bose–Einstein factor for phonons of energy $\hbar\omega_s$ responsible for the energy-level shift. The universality and applicability of relation (1) to a variety of materials, both crystalline and not, has been discussed earlier [20–22]. Note that expression (1) for the energy level shift takes into account only the contribution due to electron–phonon coupling. The contribution of thermal lattice expansion is not explicitly included. It was shown however, that, for α-Al_2O_3, this contribution is negligible within the temperature range under study [4]. Besides, for high temperatures, where $kT \gg \hbar\omega_s$, expression (1) is linear, and the linear contribution due to thermal expansion turns out to be implicitly included [23].

The temperature dependence of the peak half-width is described, in its turn, by the well-known relation (see, e.g., [4, 5, 17])

$$H^2(T) = H^2(0)(2\langle n_b\rangle + 1), \quad (2)$$

where $H(0)$ is the peak half-width at zero temperature, and $\langle n_b\rangle$ is the Bose–Einstein factor for phonons of energy $\hbar\omega_b$ responsible for level broadening. Expression (2), which is cast here intentionally not in the traditional form through the hyperbolic cotangent but, identically, through the average number of occupied phonon states, is obviously equivalent to (1). The fact that the temperature dependences of the shift and broadening of energy levels are formally the same and proportional to the Bose–Einstein factor is discussed in considerable detail in [19]. We also note that both these expressions can be directly derived using the dynamic disorder parameter, i.e., the rms deviation of atoms from their equilibrium positions [20]. The band-maxi-

mum shift and homogeneous broadening are connected with the thermal disorder.

Figure 5 presents fits to the experimental characteristics $E_m(T)$and $H(T)$ made for both peaks with expressions (1) and (2). The calculated curves are seen to approximate the observed relations well. Table 3 lists the values of the parameters for both relations, which were obtained by the fitting. Note that the effective phonons responsible for the shift and broadening for both peaks differ in energy, with $\hbar\omega_s < \hbar\omega_b$ in both cases. This implies that the processes under study involve interaction with different vibration modes, and should be characterized by different one-coordinate models of the center. Note that the values $\hbar\omega_b$ = 424 and 328 cm^{-1} obtained here are close to the acoustic vibration energies of corundum, 432 and 378 cm^{-1} [24]. This is a logical and physical result indicating that oxygen vacancies interact with long-wavelength modes of their closest neighbors, the heavy aluminum atoms. Besides, the one-phonon model used and the Gaussian peak shape permit estimation of the Huang-Rhys factor $S = H^2(0)/(\hbar\omega_b)^2 8\ln 2$. The values thus obtained are listed in Table 3.

Thus, the temperature dependences of the spectral characteristics of peaks *G*1 and *G*2 have been fitted by relations (1) and (2). The energies of the effective phonons responsible for the broadening and shift of both peaks lying in the region of the acoustic vibrations of α-Al_2O_3 have been obtained. The Huang-Rhys factors have been calculated.

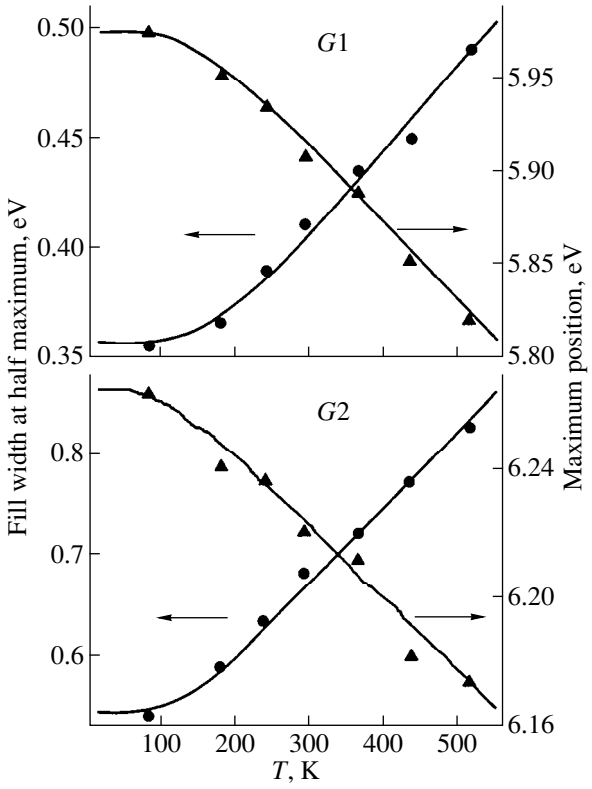

Fig. 5. Temperature dependences of the spectral characteristics of peaks *G*1 and *G*2. The symbols refer to the corresponding experimental values. Solid lines are fits done using formulas (1) and (2).

3.3. The F and F$^+$ Centers

A comparative analysis of our results and of the numerous data taken from independent studies permits the following conclusion. The *G*1 peak is due to absorption by the F^+ center, while the *G*2 peak is connected with the *F* center. Consider the main arguments underlying this conclusion.

Peak *G*1 (5.91 eV) $\longrightarrow$ F^+ center:

1. It is not the main peak. At high temperatures, it is fully dominated by the main peak. An earlier analysis of the F^+-center optical properties already suggested that this center absorbs in the 5.9–6.3 eV region, but that its band is obscured by the stronger band of the *F* center [4, 5, 10].

2. Under excitation by light with 6.05 eV (at T = 293 K) [6] and 6.4 eV (at T = 77 K) [5], one observed strong 3.0-eV luminescence associated with the *F* center and a weak luminescence at 3.8 eV assigned to the F^+ center. This agrees with Fig. 4, if one recalls that the oscillator strength f for the F^+center is twice as small (see Table 3).

3. The excitation spectrum of the 3.8-eV luminescence obtained at 77 K has a shoulder at 5.9 eV [5]. This indicates F^+-center absorption in this region. Steady-state and time-resolved excitation spectra of the same luminescence produced by synchrotron radiation at T = 10 and 297 K exhibit a band at 5.95 ± 0.03 eV, which was assigned to the F^+ center [25]. These data are in a good agreement with our results.

Table 3. Parameters derived from temperature behavior of the peaks

Parameters	Peak *G*1 (F^+ center)	Peak *G*2 (*F* center)
$E_m(0)$, eV	5.976 ± 0.005	6.265 ± 0.010
$\hbar\omega_s$, cm^{-1}	268 ± 20	171 ± 20
A, eV	0.18 ± 0.03	0.06 ± 0.005
$\hbar\omega_b$, cm^{-1}	424 ± 20	328 ± 20
	400 [4]	
	340 ± 20 [5]	
$H(0)$, eV	0.356 ± 0.004	0.546 ± 0.008
S	8.26	35.8
	8.65 [4]	
	12 [5]	
N, $\times 10^{16}$ cm^{-3}	5.73	9.24
	10.7 [4]	18.5 [4]
f	0.66 [4]	1.33 [4]

4. The values $\hbar\omega_b = 424$ cm^{-1} and $S = 8.26$ obtained in this work agree well with the results derived from the temperature behavior of the F^+-center luminescence peak at 3.8 eV, namely, 400 cm^{-1} and 8.65, respectively (Table 3) [4].

5. The $G1$ peak observed by us can be associated with the $1A \longrightarrow 2B$ electronic transition of the F^+ center, whose energy was reported as 6 eV in [10] and 6.3 eV in [4], while theory [26] predicted 5.15 eV.

Peak $G2$ (6.22 eV) $\longrightarrow$ F^+ center:

1. It is a dominant peak. Above room temperature, it forms the 6.05-eV band, whose behavior is connected unambiguously with the F centers present in α-Al_2O_3 [3–7].

2. See argument 2 above for peak $G1$.

3. The value $H = 0.54$ eV, which we obtained for $G2$ at $T = 84$ K, is close to the half-width of the 6.05-eV band in polarized light (0.67 eV at $T = 77$ K) [4]. For the polarization used ($\mathbf{E} \perp \mathbf{c}$, the $1A \longrightarrow 2B$ electronic transition of the F^+ center has a low oscillator strength $f_{F^+} = 0.020$ [4]. For the other polarization ($\mathbf{E} \parallel \mathbf{c}$), $f_{F^+} = 0.935$, and the half-width of the 6.05-eV band increases to 0.78 eV [4].

4. The calculated Huang-Rhys parameter $S = 35.8$ is close to the values obtained for the F center in MgO ($S = 39$) and in LiF ($S = 41$) [27].

5. Note that all excitation spectra of the 3.0-eV luminescence known to us always exhibit a peak at 6.1 eV, rather than at 6.22 eV, as is the case in our work. This may be due to an error in the determination of E_m for $G2$, because the spectrum was measured only up to 6.45 eV, and higher-energy peaks present [8, 11, 25] may affect the final estimate of the peak position.

In our opinion, the arguments presented here are in favor of the above peak assignment.

Knowing the oscillator strengths (see Table 3), we can use Smakula's formula to estimate the concentration N of the corresponding defects in the sample under study. The values of N thus obtained are compared in Table 3 with the results quoted in other works. Note that, in other studies, N_{F^+} was estimated from the 4.8- and 5.4-eV bands, while N_F was calculated from the total 6.05-eV band, which, according to the present study, could bring about overestimated figures. We also calculated the concentrations of the F-type centers in samples *2* and *3* (Fig. 1) and obtained $N_{F^+} = 4.89 \times 10^{16}$, $N_F = 7.37 \times 10^{16}$ for sample *2* and 2.61×10^{16} and 4.38×10^{16} cm^{-3}, respectively, for sample *3*. These values of N provide one more argument for the F and F^+ centers being distributed nonuniformly over the starting ingot, and for their concentration varying from one sample to another.

Our results permit a suggestion that for $N_{F^+} \gg N_F$ the 6.05-eV band has two maxima. Indeed, it was observed in [28] that, in the absorption spectrum of single-crystal corundum with $N_{F^+}/N_F = 2$, the 6.05-eV band transformed to a band peaking at 6.33 eV and a shoulder at 5.95–6.10 eV. We see that this agrees well with our data. Interestingly, in [28], the 6.33-eV peak was assigned to absorption by F^+ centers, and the shoulder, to traces of a band due to F centers present at lower concentrations. Our results suggest, however, that one has here a reverse situation.

CONCLUSION

Thus, we have studied absorption spectra of oxygen-deficient corundum within the 4–6.45-eV region at temperatures from 80 to 515 K. Using the linear electron–phonon coupling model, we succeeded in showing that the band at 6.05 eV can originate from absorption by F and F^+ centers with maxima at 6.22 and 5.91 eV, respectively, at room temperature. The resultant curve of these peaks very accurately reproduces the shape of the 6.05-eV band obtained at different temperatures and in samples with a different anion-defect concentration ratio. The results obtained can be used to interpret the transformation of absorption spectra in samples dominated by F^+ centers.

We have calculated the energies of phonons responsible for the broadening and shift of the peaks. The calculated values $\hbar\omega_b = 424$ and 328 cm^{-1} for the F^+ and F centers, respectively, lie in the region of corundum acoustic vibration frequencies. The Huang-Rhys factors obtained for the F and F^+ centers ($S = 35.8$ and 8.26, respectively) agree with independent estimates of other works.

ACKNOWLEDGMENTS

The authors are grateful to A. A. Maslakov for assistance in the optical measurements.

REFERENCES

1. V. S. Kortov, I. I. Milman, V. I. Kirpa, and Ja. Lesz, Radiat. Prot. Dosim. **65**, 255 (1996).
2. M. S. Akselrod, V. S. Kortov, D. J. Kravetsky, and V. I. Gotlib, Radiat. Prot. Dosim. **32**, 15 (1990).
3. K. H. Lee and J. H. Crawford, Jr., Phys. Rev. B **15**, 4065 (1977).
4. B. D. Evans and M. Stapelbroek, Phys. Rev. B **18**, 7089 (1978).
5. B. G. Draeger and G. P. Summers, Phys. Rev. B **19**, 1172 (1979).
6. S. W. S. McKeever, M. S. Akselrod, L. E. Colyott, *et al.*, Radiat. Prot. Dosim. **84**, 163 (1999).
7. K. H. Lee and J. H. Crawford, Jr., Appl. Phys. Lett. **33**, 273 (1978).

8. E. W. J. Mitchell, J. D. Rigden, and P. D. Townsend, Philos. Mag. **5**, 1013 (1960).
9. P. W. Levy, Phys. Rev. B **123**, 1226 (1961).
10. K. H. Lee and J. H. Crawford, Jr., Phys. Rev. B **19**, 3217 (1979).
11. Ya. A. Valbis, P. A. Kulis, and M. E. Springis, Izv. Akad. Nauk Latv. SSR, Ser. Fiz. Tekh. Nauk **6**, 23 (1979).
12. M. S. Aksel'rod, V. S. Kortov, and I. I. Mil'man, Ukr. Fiz. Zh. (Russ. Ed.) **28**, 1053 (1983).
13. Sang-il Choi and T. Takeuchy, Phys. Rev. Lett. **50**, 1474 (1983).
14. M. S. Aksel'rod, V. S. Kortov, I. I. Mil'man, *et al.*, Izv. Akad. Nauk SSSR, Ser. Fiz. **52**, 1981 (1988).
15. M. S. Akselrod, V. S. Kortov, and E. A. Gorelova, Radiat. Prot. Dosim. **47**, 159 (1993).
16. I. I. Mil'man, S. V. Nikiforov, V. S. Kortov, and A. K. Kil'metov, Defektoskopiya **11**, 64 (1996).
17. A. M. Stoneham, *Theory of Defects in Solids: The Electronic Structure of Defects in Insulators and Semiconductors* (Clarendon, Oxford, 1975; Mir, Moscow, 1979).
18. H. Y. Fan, Phys. Rev. **82**, 900 (1951).
19. H. Y. Fan, *Photon–Electron Interaction: Crystals Without Fields* (Springer, Berlin, 1967; Mir, Moscow, 1969).
20. I. A. Vaĭnshteĭn, A. F. Zatsepin, and V. S. Kortov, Fiz. Tverd. Tela (St. Petersburg) **41**, 994 (1999) [Phys. Solid State **41**, 905 (1999)].
21. I. E. Weinstein, A. F. Zatsepin, and Yu. V. Schapova, Physica B (Amsterdam) **263**–**264**, 167 (1999).
22. I. A. Vaĭnshteĭn, A. F. Zatsepin, V. S. Kortov, and Yu. V. Shchapova, Fiz. Tverd. Tela (St. Petersburg) **42**, 224 (2000) [Phys. Solid State **42**, 230 (2000)].
23. T. Skettrup, Phys. Rev. B **18**, 2622 (1978).
24. W. Kappus, Phys. B **21**, 325 (1975).
25. A. I. Syurdo, V. S. Kortov, V. A. Pustovarov, and F. F. Sharafutdinov, in *Proceedings of the 10th International Conference on Physics and Chemistry of Inorganic Matter, Tomsk, Russia, 1999*, p. 369.
26. S. Y. La, R. H. Bartram, and R. T. Cox, J. Phys. Chem. Solids **34**, 1079 (1973).
27. B. Henderson, R. D. King, and A. M. Stoneham, J. Phys. C, Ser. 2 **1**, 586 (1968).
28. T. S. Bessonova, L. A. Avvakumova, T. I. Gimadova, and I. A. Tale, Zh. Prikl. Spektrosk. **54**, 258 (1991).

Translated by G. Skrebtsov

Physics of the Solid State, Vol. 42, No. 7, 2000, pp. 1266–1269. Translated from Fizika Tverdogo Tela, Vol. 42, No. 7, 2000, pp. 1230–1233.

SEMICONDUCTORS AND DIELECTRICS

Ligand Hyperfine Interactions and the Model of the Paramagnetic Center Gd^{3+} in α-$LiIO_3$ Single Crystals

A. A. Davituliani, D. M. Daraselia, D. L. Japaridze, R. I. Mirianashvili, O. V. Romelashvili, and T. I. Sanadze

Tbilisi State University, Tbilisi, 380028 Georgia

e-mail: root@boklomy.ge

Received December 14, 1999

Abstract—The ligand hyperfine interaction (HFI) of Gd^{3+} ions in α-$LiIO_3$ single crystals is studied by the method of rf discrete saturation, and the tensor components of ligand HFI are determined. The model of a paramagnetic center is proposed on the basis of the analysis of the obtained results, and the mechanism of lattice distortion is discussed. *© 2000 MAIK "Nauka/Interperiodica".*

Single crystals of lithium iodate α-$LiIO_3$, which possess unique nonlinear optical properties, are among the quantum electronics materials that have been studied intensively in recent years by various methods, including radiospectroscopy. By the end of the 1980s, the EPR spectra of almost all the ions of the iron group in this crystal had been studied by various authors. The investigations of ligand hyperfine interactions using the rf discrete saturation (RFDS) technique [1–3] enabled us to unambiguously establish the models of implantation of these ions in the lattice.

Quests to enhance the stability to laser radiation of materials for optical transformations led to the synthesis of lithium iodate single crystals doped with certain elements of the rare-earths group in the late 1980s. We studied EPR spectra and determined the spin–Hamiltonian parameters of Er^{3+} and Gd^{3+} ions in α-$LiIO_3$ [4,5]. In this work, we present the results of investigating ligand HFI of Gd^{3+} ions and discuss the model of a paramagnetic center.

1. EXPERIMENTAL TECHNIQUE

The RFDS technique, which is a pulse analog of the electron–nuclear double resonance, is described in detail in [6]. Experiments were carried out on a 3-cm superheterodyne spectrometer at liquid helium temperature. Single crystals of lithium iodate were grown by vaporizing the solution at a temperature of 40–50°C at the Kirovokan Chemical Plant. The investigations of EPR spectra revealed that annealing of crystals increases the intensity of EPR lines of Gd^{3+} almost by an order of magnitude. Since lithium iodate is thermally unstable at temperatures above 75°C, a technique was developed to increase the annealing temperature to 200°C. Single crystals of α-$LiIO_3$ were placed in a high-pressure bomb made of a thick-walled hollow bronze cylinder with a screw cap having a sealing gasket made of annealed copper. Along with the samples, the bomb also contained iodine crystals whose sublimation created an excess pressure of iodine vapor. The bomb was immersed in a container with glycerine and heated to the required temperature. The experiments were carried out on samples subjected to annealing for two hours at a temperature of 200°C, followed by natural cooling with the bomb. The concentration of Gd in the charge varied from 10^{-3} to 10^{-2} mol % (limiting concentration for rare-earth elements).

2. CRYSTAL STRUCTURE

The hexagonal modification (α phase) of lithium iodate belongs to the space group $P6_3$. The crystal structure consists of covalent IO_3 complexes in the form of right trigonal pyramids whose principal axes coincide with the sixfold axis **c**. A strong interaction between adjacent IO_3 groups leads to the formation of a strong three-dimensional net with lithium ions in the octahedral voids. Figure 1 shows the projections of the crystal lattice on two planes parallel and perpendicular to the **c** axis of the crystal.

3. DISCUSSION OF EXPERIMENTAL RESULTS

We studied the RFDS spectra only for lithium nuclei because their ligand HFI are known to be of a purely dipole type, while a significant covalent contribution is observed in the case of iodine nuclei. The spectra were measured in a magnetic field **B** ∥ **c** for various electron transitions, and the angular dependences for the spectra were obtained by rotating the magnetic field in a plane perpendicular to **c**. The dots in Fig. 2 describe such an angular dependence for the electron transition $M = -5/2 \longleftrightarrow M = -3/2$. It can be seen clearly that this plot is qualitatively similar to the analogous angular dependences obtained for ions of the iron group (see, for

example, [1, 2]). In the case of Gd^{3+}, however, the lines *A* and *B* corresponding to lithium nuclei on the **c** axis [Li(*3*) and Li(*4*)] are not isotropic. Calculations show that this anisotropy is connected to the angular dependence of the resonant magnetic field of the EPR spectral line associated with the presence of fine-structure terms in the electron Hamiltonian of Gd^{3+} and does not contain a contribution from the off-diagonal elements of the ligand HFI tensor.

We choose a reference frame with the origin at the nucleus Li(*0*), the *Z* axis coinciding with the hexagonal axis **c** of the crystal, and the *X* axis being along the Li(*0*)–Li(*8*) direction (see Fig. 1). According to [1], the angular dependence of the RFDS lines of equivalent pairs of lithium nuclei Li(*5*) and Li(*8*) in the plane $Z = 0$ and pairs Li(*11*) and Li(*14*), as well as Li(*17*) and Li(*20*), lying in the planes $Z = \pm c_0/2$, respectively, for each electron state $|\bar{M}\rangle$ of the transition $|\bar{M}\rangle \longleftrightarrow |\bar{M}'\rangle$ is described by the formula

$$\nu = \sqrt{\{(\gamma B - S_{\perp}^{\bar{M}} A_{xx})^2 + (S_{\perp}^{\bar{M}} A_{xz})^2\}\cos^2\varphi + \{\gamma B - S_{\perp}^{\bar{M}} A_{yy}\}^2 \sin^2\varphi}, \quad (1)$$

where $A_{xz} = 0$ for Li(*5*) and Li(*8*) nuclei. Here, A_{ik} are the components of the ligand HFI tensor, $S_{\perp}^{\bar{M}} = \langle \bar{M}|\hat{S}_x|\bar{M}\rangle$ is the effective magnetic quantum number, $|\bar{M}\rangle$ is a linear combination of the state with the projection of the electron spin *M* ($S = 7/2$ for Gd^{3+}) that diagonalizes the total electron Hamiltonian of Gd^{3+} [4]. The angular dependences of the remaining pairs of ions are obtained by replacing φ with $\varphi \pm 60°$ in (1).

The spectrum of the nuclei Li(*3*) and Li(*4*) (*A* and *B*), lying on the same axis **c** with Gd^{3+}, is described by the formula

$$\nu = \gamma B - S_{\perp}^{\bar{M}} A_{xx}. \quad (2)$$

Quadrupole splitting $Q = 51$ kHz is observed for the nucleus *A* ($I = 3/2$ for Li^7), while quadrupole splitting is not resolved for the remaining Li nuclei.

It was mentioned that the slight angular dependence of the spectral lines *A* and *B* is associated only with the angular dependence of the EPR line in a plane perpendicular to the **c** axis, and Gd^{3+} is the only ion among all those investigated in α-$LiIO_3$ by the RFDS technique for which such a dependence is observed. This circumstance makes it possible to draw conclusions about the direction of the crystal electric field and the distortion of the coordination oxygen octahedron of the magnetic ion. For this purpose, we analyzed the RFDS spectra by defining the magnetic field in (1) in an analytical form through the approximating formula

$$B = B_1 + B_2\cos^2(3\varphi + \Delta\varphi), \quad (3)$$

where B_1 and B_2 were determined by the least squares method from the angular dependences of the EPR spectra of Gd^{3+} presented in [4]. The parameters $B_1 = 296.96$ and $B_2 = 1.49$ mT approximate this dependence with a high degree of precision for the transition $-5/2 \longleftrightarrow -3/2$. Since the HFI tensors A_{ik} are defined in the above reference frame and the *X*' axis of the crystal field is not known *a priori* (the *Z*' axis coincides with the **c** axis), we introduce the parameter $\Delta\varphi$ in formula (3), viz., the angle between *X* and *X*', which is determined from an analysis of the RFDS spectra, along with the components A_{ik} of the HFI tensors.

Processing the spectra involves using a computer to minimize the dispersion $\sum(\nu_i^{\text{calc}} - \nu_i^{\text{exp}})^2$ taken over all the experimentally measured points in the orientations $\mathbf{B} \parallel \mathbf{c}$ and $\mathbf{B} \perp \mathbf{c}$. Minimization was carried out over all the parameters, including primarily the param-

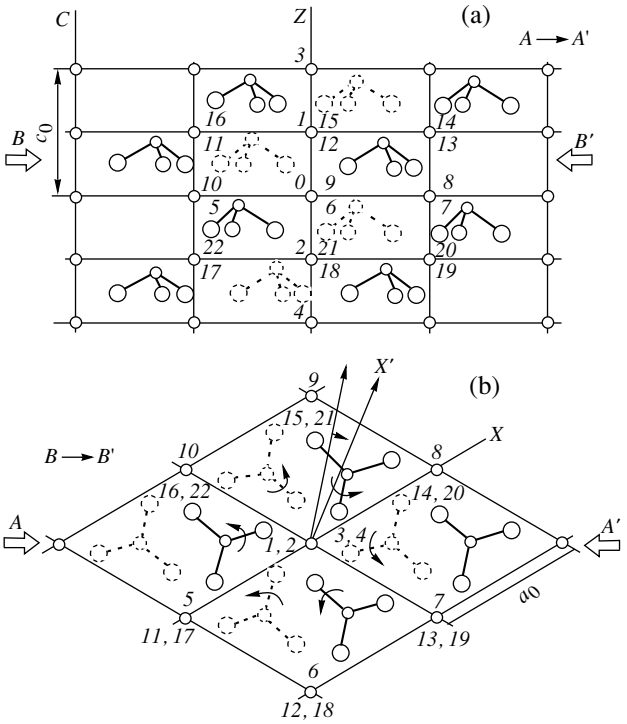

Fig. 1. Crystal structure of α-$LiIO_3$ in two projections, parallel ($A \longrightarrow A'$) and perpendicular ($B \longrightarrow B'$) to the **c** axis. (a) ($A \longrightarrow A'$) the solid lines indicate the IO_3 groups in which iodine atoms lie in the plane of the cross section; (b) ($B \longrightarrow B'$) the solid lines indicate the IO_3 groups in which oxygen atoms lie in the plane of the cross section. The remaining groups are shown by dashed lines. The numbers correspond to lithium atoms for which ligand HFI was measured; $a_0 = 5.4815$, $c_0 = 5.1709$ Å.

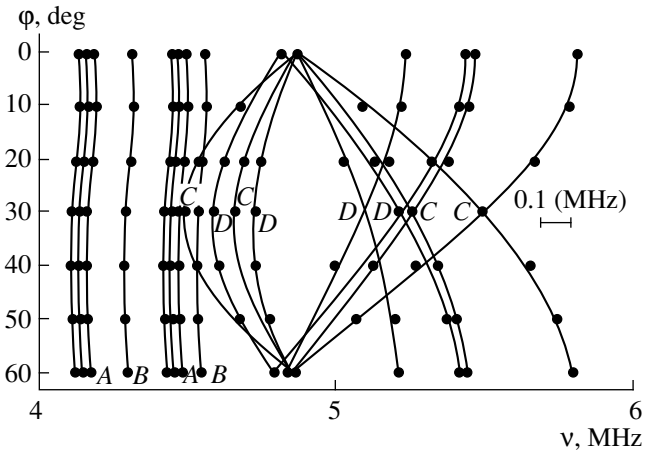

Fig. 2. Angular dependence of the RFDS spectrum of lithium nuclei for α-$LiIO_3$ in the plane perpendicular to the **c** axis. Curves *A*, *B*, *C* and *D* correspond to Li(*3*), Li(*4*), Li(*5*)–Li(*10*), and Li(*11*)–Li(*22*), respectively. Curves *A* have a quadrupole splitting $Q = 51$ kHz, $S_\perp^{\bar{M}} = -1.4811$, and $S_\perp^{\bar{M}'} = -2.4885$.

eter Δφ. The effective magnetic quantum numbers $S_\perp^{\bar{M}}$ and $S_Z^{\bar{M}}$ were calculated from the wave functions obtained by diagonalizing the total electron Hamiltonian of Gd^{3+} with parameters described in [4]. The variation of $S_\perp^{\bar{M}}$ associated with the angular dependence of the EPR spectrum is less than 0.01% and was disregarded in computations.

The values of the components of the ligand HFI tensors for all the nearest lithium nuclei are presented in the table. These tensors have a dipole form and zero traces within the limits of the experimental error. Since lithium ions are in the *S* state, we assumed the interaction to be of a purely dipole type and calculated the absolute displacements from the equilibrium position of the nearest lithium ions, which are presented in the table. It should be mentioned that spectra from the lithium nuclei closest to the Gd^{3+} nuclei along the **c** axis were not observed, which indicates the presence of vacancies compensating the excess charge of the paramagnetic ion. Thus, the paramagnetic center model of the rare-earth ion Gd^{3+} is completely identical to the ions of the iron group investigated earlier.

The value of Δφ was found to be $+38.8 \pm 1.6°$. Let us consider the local lattice distortions using the simplest billiard ball model based on the crystal structure data [7]. We choose the oxygen ion radius to be 1.38 Å [8], the value following from the crystal structure of α-$LiIO_3$ under the assumption that the oxygen ions are in contact in the IO_3^- complex. The ionic radii for Gd^{3+} and Li^+ are 0.938 and 0.68 Å, respectively. The octahedral voids in the oxygen lattice of α-$LiIO_3$ are capable of accommodating ions with a radius smaller than 0.74 Å; hence, a Gd^{3+} ion substituted for lithium [say, Li(*0*)] must push apart the oxygen ions. It was assumed by Karthe [9] that IO_3^- complexes rotate as a whole around iodine in the vertical plane passing through the **c** axis, making room for the substituting paramagnetic ion. We would like to substantiate another mechanism according to which the IO_3 complexes rotate around iodine through an angle δ in the plane perpendicular to the **c** axis. Calculations show that replacing Li(*0*) by a Gd^{3+} ion causes the six nearest IO_3 groups associated with the coordination oxygen octahedron of gadolinium to rotate around the **c** axis through an angle $\delta = 13.3°$ (clockwise, as shown in Fig. 1). In this case, the oxygen octahedron rotates as a whole through an angle –8.9°. The *X*' axis of the crystal electric field in the undistorted crystal forms an angle 45.6° with the *X* axis. This gives the value 36.7° of the angle for Gd^{3+} : α-$LiIO_3$, which is quite close to the value 38.8° obtained by us. The displacements of Li(*3*) and Li(*4*) ion must also be accompanied by a distortion of the oxygen surroundings. According to the model we proposed, a displacement of Li(*3*) by 0.57 Å towards the vacancy Li(*1*) corresponds to a rotation of six IO_3 complexes through an angle –11.9°, while a displacement

Components of ligand HFI tensors A_{ik} (MHz) and absolute displacements Δ (Å) of lithium ions

Nucleus	A_{zz}	A_{xx}	A_{yy}	A_{xz}	Δ
Li(*3*)	0.633 ± 0.004	–0.313 ± 0.002	–0.313 ± 0.002	0	$\Delta_z = -0.57$
	(0.626)	(–0.313)	(–0.313)		
Li(*4*)	0.512 ± 0.003	–0.252 ± 0.002	–0.252 ± 0.002	0	$\Delta_z = 0.22$
	(0.504)	(–0.252)	(–0.252)		
Li(*5*)–Li(*10*)	–0.179 ± 0.002	0.352 ± 0.002	–0.172 ± 0.002	0	$\Delta_x = 0.1$
	(–0.176)	(0.352)	(–0.176)		
Li(*11*)–Li(*22*)	–	0.195 ± 0.002	–0.313 ± 0.002	0.154 ± 0.006	$\Delta_x = 0.06$
	(–0.053)	(0.182)	(–0.129)	(0.153)	

Note: Theoretical dipole values taking lattice distortions into account are shown in parentheses.

of Li(*4*) by 0.22 Å towards the vacancy Li(*2*) corresponds to a rotation through the angle –7.4°.

The approximate nature of the model we used does not allow us to draw unambiguous conclusions about the mechanism of distortions. However, the closeness of the computed direction of the crystal field to the experimentally obtained value serves as a weighty argument in favor of the lattice distortion mechanism that we proposed.

REFERENCES

1. A. Brauer and D. M. Daraselia, Fiz. Tverd. Tela (Leningrad) **19** (8), 1250 (1977) [Sov. Phys. Solid State **19**, 1318 (1977)].
2. D. M. Daraselia and A. Brauer, Phys. Status Solidi B **109**, 223 (1982).
3. D. M. Daraselia and D. L. Japaridze, Phys. Status Solidi B **119**, K57 (1983).
4. D. L. Japaridze, S. V. Alchangyan, D. M. Daraselia, and T. I. Sanadze, Phys. Status Solidi B **58**, K195 (1990).
5. D. L. Dzhaparidze, S. V. Alchyangyan, D. M. Daraseliya, and T. I. Sanadze, Fiz. Tverd. Tela (Leningrad) **31** (3), 268 (1989) [Sov. Phys. Solid State **31**, 502 (1989)].
6. T. I. Sanadze and G. R. Khutsishvili, in *Magnetic-Resonance Problems* (Nauka, Moscow, 1978), p. 206.
7. A. Émiramiev, A. G. Kocharov, I. I. Yamzin, and V. A. Lyubimtsev, Kristallografiya **21** (2), 391 (1976) [Sov. Phys. Crystallogr. **21**, 214 (1976)].
8. R. D. Shanon and C. T. Previtt, Acta Crystallogr. B **25**, 925 (1969).
9. W. Karthe, Phys. Status Solidi B **81**, 323 (1977).

Translated by N. Wadhwa

Physics of the Solid State, Vol. 42, No. 7, 2000, pp. 1270–1276. Translated from Fizika Tverdogo Tela, Vol. 42, No. 7, 2000, pp. 1234–1239.

DEFECTS, DISLOCATIONS, AND PHYSICS OF STRENGTH

Diffusion Kinetics and Spinodal Decomposition in Quasi-Equilibrium Solid Solutions

M. A. Zakharov

Novgorod State University, ul. Sankt-Peterburgskaya 41, Novgorod, 173003 Russia

e-mail: theorphy@info.novsu.ac.ru

Received November 16, 1999

Abstract—A phenomenological theory of the transformation of multicomponent solid solutions with the hierarchy of atomic mobilities of the components has been developed within the local-equilibrium approximation. At the hydrodynamic stage, the evolution of these solutions is treated as a sequence of quasi-equilibrium states, for which only a part of conditions for the complete equilibrium are fulfilled. The equations describing the evolution of the distributions of "fast" components in the quasi-equilibrium solid solutions at arbitrary stages of the transformation are derived within the generalized lattice model accounting for the specific volumes of components by using the separation of "fast" and "slow" components of diffusion and the method of contracted descriptions. The conditions of the stability of quasi-equilibrium solutions against the spinodal decomposition are determined, and the equations for the metastability boundaries in these systems are obtained. *© 2000 MAIK "Nauka/Interperiodica".*

INTRODUCTION

The actual solid solutions are nonequilibrium systems virtually on any time scale, because the processes of their transformation are rather slow. Of possible forms of nonequilibrium such as mechanical, thermal, and chemical, the chemical nonequilibrium in condensed systems is the slowest and, hence, as a rule, is most essential. Another property inherent in the majority of multicomponent solid solutions is the hierarchy of atomic mobilities of components [1, 2] and, as a consequence, the hierarchy of relaxation times of different components.

Among the experimental evidences on the atomic mobilities of components in the solid solutions, a prominent example illustrating the hierarchy of mobilities is provided by the diffusion of noble metals (Au, Ag, and Cu) in the matrix of low-melting metals (Sn, Pb, In, and Tl), in which the diffusion rate of the former metals is 8–12 orders of magnitude greater than the self-diffusion rate [3]. Such a well-known phenomenon as the inhibition of the martensite decomposition by carbide-forming elements is the consequence of considerable differences in the atomic mobilities of components [4].

The hierarchy of the atomic mobilities of components allows one to treat the transition of a nonequilibrium solution to the complete equilibrium as a sequence of quasi-equilibrium states [5, 6], for which only a part of conditions for the complete equilibrium are met on the appropriate time scale. An arbitrary quasi-equilibrium state is described by equilibrium distributions of high-mobility components and fixed distributions of low-mobility (on a given time scale) components, which play the role of a nonequilibrium "medium." To put it differently, the quasi-equilibrium (intermediate) states of multicomponent systems with the hierarchy of atomic mobilities can be described by way of separating "fast" and "slow" components of the transformation [separating fast and slow variables in kinetic equations (see, for example, [7–11])]. Particularly, the quasi-equilibrium states of solid solutions were treated within the local-equilibrium approximation [5, 6], and the problems associated with the stability of solutions in these states were studied in the framework of the generalized lattice model [12, 13] (see also [14]). Note that the description of quasi-equilibrium solutions was thermostatic in character, which did not allow one to study the evolution of a solution from one quasi-equilibrium state to another quasi-equilibrium state.

In the present work, I continued to develop the theory of quasi-equilibrium states in multicomponent solid solutions. The aim of this work was to derive the evolution equations describing the diffusion kinetics of quasi-equilibrium solutions on different time scales and to examine the stability of these systems against the spinodal decomposition.

The first section of the paper presents the thermodynamic formalism of the proposed approach and the general phenomenological scheme for the derivation of closed systems of equations describing the evolution of solid solution from one quasi-equilibrium state to the next quasi-equilibrium state. The approach is based on the contracted descriptions of nonequilibrium systems with the hierarchy of relaxation times (see, for example, [15, 16]), which goes back to the Bogolyubov works [17].

1063-7834/00/4207-1270$20.00

In Section 2, the approach is illustrated with the generalized lattice model, which enables one to take into account the volume effects by introducing specific atomic volumes of components and the long-range part of interatomic interactions within the effective-field approximation.

The inclusion of interatomic interactions in the evolution equations makes it possible to describe not only the homogenization processes in the system, but also the kinetics of the precipitation of new phases in the quasi-equilibrium solutions. In Section 3, within the framework of the generalized lattice model, the stability of the quasi-equilibrium solid solution against the spinodal decomposition is investigated using the concentration wave method proposed by Krivoglaz [18] and Khachaturyan [19] and extended by Olemskoĭ [20–22]. Moreover, the equation for the boundaries of quasi-equilibrium metastability in this system is deduced.

1. METHOD

At the hydrodynamic stage, the evolution of *m*-component solid solution can be described by the following set of equations:

$$\frac{\partial n_i(\mathbf{r}, t)}{\partial t} + \operatorname{div}\mathbf{J}_i(\mathbf{r}, t) = 0, \quad (i = 1 - m), \tag{1}$$

where $n_i(\mathbf{r}, t)$ is the local particle number density of the *i*th component of the solution, $\mathbf{J}_i(\mathbf{r}, t)$ is the local flux of the *i*th component, and the spatial variable $\mathbf{r}$ is taken in the "hydrodynamic" sense. When the relation between the distributions of densities and fluxes of components is known, the set of continuity equations (1) with due regard for initial and certain boundary conditions determining the specificity of a particular problem uniquely describes the solution transformation within the diffusion approximation. The appearance of fluxes of matter in the chemically nonequilibrium solution is caused by nonzero gradients of local chemical potentials. Within the linear theory of irreversible processes, the above relation has the form

$$\mathbf{J}_i(\mathbf{r}, t) = -\sum_{j=1}^{m} L_{ij}\nabla\left(\frac{\mu_j(\mathbf{r}, t)}{T}\right), \tag{2}$$

where L_{ij} are the Onsager coefficients, $\mu_j(\mathbf{r}, t)$ is the local chemical potential of the *j*th component (dependent on the local densities of all the components), and T is the temperature in energy units. Therefore, the distributions of components of chemically nonequilibrium solution can be obtained as solutions of the following system of equations:

$$\frac{\partial n_i(\mathbf{r}, t)}{\partial t} = \operatorname{div}\left\{\sum_{j=1}^{m} L_{ij}\nabla\left(\frac{\mu_j(n_1(\mathbf{r}, t), \ldots, n_m(\mathbf{r}, t))}{T}\right)\right\}, \quad (i = 1 - m). \tag{3}$$

For the uniqueness of the solutions of system (3), we complement it with the initial conditions

$$n_i(\mathbf{r}, t) = f_i(\mathbf{r}) \tag{4}$$

and, thus, formulate the Cauchy problem.

Allowance made for the hierarchy of atomic mobilities of solution components by separating fast and slow diffusion components leads to the fact that the evolution of the solution on different time scales will be represented in a form essentially differing from system (3).

Let us number *m* components of the solution in the decreasing order of their atomic mobility. Introduce the set of the characteristic times $\tau_1, \tau_2, \ldots, \tau_{m-1}$, which play the role of relaxation times and satisfy the system of the inequalities $\tau_1 \ll \tau_2 \ll \ldots \ll \tau_{m-1}$. The evolution of the solution to the first quasi-equilibrium state is accompanied by the appearance of diffusive fluxes of the two fastest (on the τ_1 time scale) components in the nonequilibrium medium of the remaining slow components. In this case, the distributions of slow solution components have no time to change considerably as compared to the initial distributions. For this reason, the variables $n_3(\mathbf{r}, t), \ldots, n_m(\mathbf{r}, t)$ slow on the τ_1 time scale are the pseudointegrals of motion with respect to the fast variables $n_1(\mathbf{r}, t)$ and $n_2(\mathbf{r}, t)$. Consequently, the slow variables entering into the evolution equation (3) for the fast variables can be treated as fixed parameters defined by the initial conditions (4); i.e.,

$$n_i(\mathbf{r}, t) \approx n_i(\mathbf{r}, 0) \equiv f_i(\mathbf{r}), \quad (i = 3 - m). \tag{5}$$

Then, at the first transformation stage, the evolution of the local densities of the fast components in the given solution is described by the following closed system of equations:

$$\frac{\partial n_i(\mathbf{r}, t)}{\partial t} = \operatorname{div}\left\{\sum_{j=1}^{m} L_{ij}\nabla \times \left(\frac{M_j(n_1(\mathbf{r}, t), n_2(\mathbf{r}, t), f_3(\mathbf{r}), \ldots, f_m(\mathbf{r}))}{T}\right)\right\}, \quad (i = 1, 2) \tag{6}$$

at $0 \le t \le \tau_1$. The solutions of system (6) with the initial conditions (4) are unique and completely determine not only the evolution of the fast components, but also permit us to represent the evolution of the slow components in an implicit form. Actually, by using system (3) and the initial conditions (5), we obtain the closed (relative to the slow variables) system of $(m - 2)$ equations describing the evolution of the local densities of the

slow components at the first stage of the solution transformation

$$\sum_{j=1}^{m} L_{ij}\nabla\left(\frac{\mu_j(n_1(\mathbf{r}, t), \ldots, n_m(\mathbf{r}, t))}{T}\right) = C_i, \quad (i = 3 - m), \tag{7}$$

where C_i are the constants determined from the initial conditions (4), and $n_1(\mathbf{r}, t)$ and $n_2(\mathbf{r}, t)$ are the known solutions of system (6). By analogy with the Haken terminology [15], the reduced equations of system (7) will be referred to as the "subordinate" equations. It should be emphasized that the time dependence of the solutions of the system of subordinate equations (7) is determined by the solutions of system (6) describing the diffusion kinetics of the fast variables in the solution.

Therefore, on the first characteristic time scale at the hydrodynamic stage of transformation, the evolution of the fast solution components is described by the solutions of system (6), and the time dependence of the densities of the slow components is represented by the solutions of subordinate equations (7).

The first stage of the solution transformation is completed with the disappearance of fluxes of the fast components, which, according to (6), gives

$$\sum_{j=1}^{m} L_{ij}\nabla\left(\frac{\mu_j(n_1(\mathbf{r}, \tau_1), n_2(\mathbf{r}, \tau_1), f_3(\mathbf{r}), \ldots, f_m(\mathbf{r}))}{T}\right) = 0, \quad (i = 1, 2). \tag{8}$$

Note that, within the diagonal approximation, relationships (8) go over into the usual conditions of chemical equilibrium with respect to the fast variables (the constancy of the corresponding chemical potentials). This agrees with the definition of the quasi-equilibrium (intermediate) states of the solid solution, which was introduced earlier in the thermostatic description of locally equilibrium systems [5, 6]. In the general nondiagonal case resulting in the inclusion of "cross effects," the attainment of a quasi-equilibrium state, according to (8), is not reduced to the constancy of the corresponding chemical potentials, but is determined by a linear dependence of the gradients of local chemical potentials (the equality of the "resultant" of generalized thermodynamic forces to zero). However, owing to the known smallness of nondiagonal elements of the matrix of kinetic coefficients, the diagonal elements make the decisive contribution to relationships (8).

The second stage of the transformation of the quasi-equilibrium solution is connected with the change to a new rougher time scale and exhibits a number of features as compared to the first stage. Indeed, on the τ_2 time scale, in addition to two fast components, it is necessary to take into account the third fastest component and its flux $\mathbf{J}_3(\mathbf{r}, t)$. The less mobile components continue to fulfill the role of the nonequilibrium medium. Therefore, at the second transformation stage, the evolution of the densities of the fast solution components is described by the system involving three equations of type (6). In this case, the number of slow variables and control equations (7) decreases by unity, which agrees with the Bogolyubov hypothesis of contracted descriptions of nonequilibrium systems with the hierarchy of relaxation times. It should be remembered that the initial conditions at the second transformation stage are changed in comparison with the initial conditions (4) at the first stage. Actually, the initial distributions of the first two components on the new τ_2 time scale are determined as the limiting values $\lim_{t \to \tau_1} n_i(\mathbf{r}, t)$ of the solutions of system (6) describing the first stage of the solution transformation, and the initial conditions for the densities of the remaining components are derived from the asymptotics of the solution of the system of control equations (7). As a result, the transformation of the solution from one quasi-equilibrium state to the next quasi-equilibrium state is a typical "non-Markovian" process, because the behavior of the nonequilibrium system under consideration, in general, appears to be dependent on the prehistory, which is characteristic of the hydrodynamic regime as a whole.

In the framework of the advanced thermodynamic approach, the subsequent transformation stages are described in a similar way: a further change to a rougher time scale leads, on the one hand, to an increase in the number of fast variables and evolution equations of type (6) and, on the other hand, to a decrease (reduction) in the number of control equations (7). The initial conditions for each stage are determined by the asymptotic distributions of the solution composition at the preceding stage.

The given approach is general in character for locally equilibrium systems, because an explicit dependence of the chemical potentials on the local densities of components is not specified. We now invoke the generalized lattice model to illustrate the developed approach.

2. EVOLUTION EQUATIONS FOR QUASI-EQUILIBRIUM SOLUTIONS WITHIN THE GENERALIZED LATTICE MODEL

In the framework of the generalized lattice model, the relation between the constant chemical potentials and the spatial distributions of components of the chemically equilibrium solution is given by [6]

$$\mu_i = \sum_{j=1}^{m} \int \nu_{ij}(\mathbf{r} - \mathbf{r}')n_j(\mathbf{r}')dV'T\ln\left(\frac{n_i(\mathbf{r})}{n(\mathbf{r})}\right) - \omega_i\Psi(\mathbf{r}), \tag{9}$$

where the first term is the variational derivative of the configurational part of the Helmholtz energy functional (written within the self-consistent field approximation with allowance made only for pair interactions) with

respect to the local density of the ith component, $\nu_{ij}(\mathbf{r} - \mathbf{r}')$ is the long-range part of pair interatomic potentials, the second term is the variational derivative of the entropy part of the Helmholtz energy functional within the regular solution approximation, $n(\mathbf{r})$ is the total local particle number density, the integration is performed over the entire volume of the solution V, ω_i is the specific volume of the ith component, and $\Psi(\mathbf{r})$ is the Lagrange undetermined multiplier. The appearance of the undetermined multiplier in system (9) is connected with the minimization of the Helmholtz energy functional with inclusion of the additional relationship between the local densities

$$\sum_{i=1}^{m} \omega_i n_i(\mathbf{r}) = 1, \tag{10}$$

which, hereafter, will be termed the close packing condition.

Generally speaking, at the hydrodynamic stage of the solution transformation, the gradients of chemical potentials still differ from zero, but the quantities $\{\mu_i\}$ and $\{n_i\}$ already obey relationships of type (9). Note that μ_i and n_i are functions of coordinates and time. By using relationships (9) for the locally equilibrium system, within the given lattice model, it is possible to obtain a set of evolution equations describing the transformation of the solid solution from the $(s-1)$th quasi-equilibrium state to the next quasi-equilibrium state on an τ_s arbitrary characteristic time scale.

On the characteristic time scale τ_s, the evolution of the m-component solution is described by the $(s+1)$ fast variables and the $(m-s-1)$ slow variables. From relationships (6) and (9), we have the set of equations representing the evolution of the fast solution components within the generalized lattice model approximation

$$\frac{\partial n_i(\mathbf{r}, t)}{\partial t} = \operatorname{div}\left\{\sum_{j=1}^{m} L_{ij}\nabla\left(\frac{1}{T}\varphi_j(\mathbf{r}, t) + \ln\left(\frac{n_j(\mathbf{r}, t)}{n(\mathbf{r}, t)}\right) - \frac{1}{T}\omega_j\Psi(\mathbf{r}, t)\right)\right\}, \quad (i = 1-(s+1)), \tag{11}$$

where

$$\varphi_j(\mathbf{r}, t) = \sum_{k=1}^{m}\int \nu_{jk}(\mathbf{r} - \mathbf{r}')n_k(\mathbf{r}', t)dV'. \tag{12}$$

Note that only s equations in system (11) are linearly independent. Actually, from the close packing condition (10) and continuity equations (1), we obtain the equation relating the fluxes

$$\sum_{i=1}^{s+1}\omega_i\frac{\partial n_i(\mathbf{r}, t)}{\partial t} = -\nabla\left(\sum_{i=1}^{s+1}\omega_i\mathbf{J}_i(\mathbf{r}, t)\right) = 0. \tag{13}$$

The absence of fluxes at infinity allows us to simplify equation (13)

$$\sum_{i=1}^{s+1}\omega_i\mathbf{J}_i(\mathbf{r}, t) = 0. \tag{14}$$

From relationships (1), (11), and (14), one obtains the system of $(s+1)$ evolution equations for the fast variables at the given stage of the solution transformation

$$\frac{\partial n_i(\mathbf{r}, t)}{\partial t} = \operatorname{div}\left\{\sum_{j=1}^{m} L_{ij}\nabla\left[\frac{\varphi_j(\mathbf{r}, t)}{T} + \ln\left(\frac{n_j(\mathbf{r}, t)}{n(\mathbf{r}, t)}\right)\right] - \frac{\sum_{j=1}^{m} L_{ij}\omega_j}{\sum_{k=1}^{s+1}\sum_{k'=1}^{m}\omega_k L_{kk'}\omega_{k'}}\sum_{k=1}^{s+1}\sum_{k'=1}^{m}\omega_k L_{kk'} \times \nabla\left[\frac{\varphi_{k'}(\mathbf{r}, t)}{T} + \ln\left(\frac{n_{k'}(\mathbf{r}, t)}{n(\mathbf{r}, t)}\right)\right]\right\}. \tag{15}$$

It should be remarked that the local densities of the slow components in system (15) [as in equations (11), (12), and (14)] are the time-independent parameters, which, according to (5), are determined from the initial conditions.

The system of nonlinear integro-differential equations (15) is closed and, at the specified initial conditions (4), uniquely describes the evolution of the fast components of the solid solution on the given time interval.

Unlike ordinary diffusion equations, the equations deduced are nonlocal [see, equation (12)]. Note also that the Onsager kinetic coefficients entering into the equations of system (15) are the functions of the temperature and the local densities of all the components

$$L_{ij} = L_{ij}(T, n_1(\mathbf{r}, t), \ldots, n_{s+1}(\mathbf{r}, t), f_{s+2}(\mathbf{r}), \ldots, f_m(\mathbf{r})), \tag{16}$$

and the character of the dependence on these arguments cannot be established within the given semimicroscopic approach.

The presence of interatomic potentials [see, relationships (12)] in the system of evolution equations (15) provides a way to study the homogenization of the quasi-equilibrium solution and its separation on arbitrary time scales.

3. CONDITIONS OF STABILITY AND BOUNDARIES OF METASTABILITY OF QUASI-EQUILIBRIUM SOLUTION

Let us use system (15) to investigate the stability of the solid solution in an arbitrary quasi-equilibrium state against spinodal decomposition. It is expected that the nonequilibrium medium consisting of slow components should considerably affect the solution stability and the phenomena under consideration should exhibit a nonequilibrium behavior.

With the aim of examining the solution stability against small fluctuations of mobile components, we consider the transition from the homogeneous to inhomogeneous distribution of components. The local densities of $(s + 1)$ fast components at the initial instant of the given transformation stage can be written as

$$n_i(\mathbf{r}, 0) = n_i^0 + \delta n_i(\mathbf{r}, 0), \quad |\delta n_i(\mathbf{r}, t)| \ll n_i^0, \qquad (17)$$

where $\delta n_i(\mathbf{r}, 0)$ is the infinitesimal deviation of the local density of the ith component from the equilibrium value n_i^0. Furthermore, assume that all the nonequilibrium slow components are also quasi-homogeneously distributed over the system and fluctuate about the n_i^0 values. This assumption enables us to represent the local densities of all the components (both fast and slow) by using relationships (17). The linearization of system (15) with respect to the fluctuations of the fast components $\delta n_i(\mathbf{r}, t) = n_i(\mathbf{r}, t) - n_i^0$ $(i = 1 - (s + 1))$ and the fluctuations of the slow components $\delta f_i(\mathbf{r}) = f_i(\mathbf{r}) - n_i^0$ at $i = (s + 2) - m$ [according to conditions (5), $\delta f_i(\mathbf{r})$ do not depend on the time] gives the linear [with respect to $\delta n_i(\mathbf{r}, t)$] inhomogeneous system of integro-differential equations

$$\frac{\partial \delta n_i(\mathbf{r}, t)}{\partial t} = \Delta\left(A_i(\mathbf{r}, t) + B_i(\mathbf{r}) - \frac{\sum_{j=s+1}^{m} L_{ij}^0 \omega_j}{\sum_{k=1}^{s+1}\sum_{k'=s+1}^{m} \omega_k L_{kk'}^0 \omega_{k'}} \sum_{k=1}^{s+1} \omega_k (A_k(\mathbf{r}, t) + B_k(\mathbf{r}))\right), \qquad (18)$$

where

$$L_{ij}^0 = L_{ij}(T, n_1^0, \ldots, n_m^0),$$

$$A_i(\mathbf{r}, t) = \sum_{j=s+1}^{m}\sum_{k=1}^{s+1} L_{ij}^0\left[\frac{1}{T}\int \nu_{jk}(\mathbf{r} - \mathbf{r}')\delta n_k(\mathbf{r}', t)dV' - \frac{\delta n_k(\mathbf{r}, t)}{n^0}\right] + \sum_{j=1}^{s+1} L_{ij}^0 \frac{\delta n_j(\mathbf{r}, t)}{n^0}, \qquad (19)$$

$$B_i(\mathbf{r}) = \sum_{j=s+1}^{m}\sum_{k=s+2}^{m} L_{ij}^0\left[\frac{1}{T}\int \nu_{jk}(\mathbf{r} - \mathbf{r}')\delta f_k(\mathbf{r}')dV' - \frac{\delta f_k(\mathbf{r})}{n^0}\right] + \sum_{j=s+2}^{m} L_{ij}^0 \frac{\delta f_i(\mathbf{r})}{n^0}.$$

Note that, when the fluctuations of the slow components are absent, system (18) becomes homogeneous.

Applying the spatial Fourier transform to system (18), we obtain the linear [with respect to $\delta\tilde{n}_i(\mathbf{p}, t)$] inhomogeneous system of ordinary differential equations

$$\frac{\partial \delta\tilde{n}_i(\mathbf{p}, t)}{\partial t} = -p^2\left(\tilde{A}_i(\mathbf{p}, t) + \tilde{B}_i(\mathbf{p}) - \frac{\sum_{j=s+1}^{m} L_{ij}^0 \omega_j}{\sum_{k=1}^{s+1}\sum_{k'=s+1}^{m} \omega_k L_{kk'}^0 \omega_{k'}} \sum_{k=1}^{s+1} \omega_k (\tilde{A}_k(\mathbf{p}, t) + \tilde{B}_k(\mathbf{p}))\right), \qquad (20)$$

where, according to (19),

$$\tilde{A}_i(\mathbf{p}, t) = \sum_{j=s+1}^{m}\sum_{k=1}^{s+1} L_{ij}^0\left[\frac{1}{T}\tilde{\nu}_{jk}(\mathbf{p}) - \frac{1}{n^0}\right] \times \delta\tilde{n}_k(\mathbf{p}, t) + \sum_{j=1}^{s+1} L_{ij}^0 \frac{\delta\tilde{n}_j(\mathbf{p}, t)}{n^0},$$

$$\tilde{B}_i(\mathbf{p}) = \sum_{j=s+1}^{m}\sum_{k=s+2}^{m} L_{ij}^0\left[\frac{1}{T}\tilde{\nu}_{jk}(\mathbf{p}) - \frac{1}{n^0}\right] \times \delta\tilde{f}_k(\mathbf{p}) + \sum_{j=s+2}^{m} L_{ij}^0 \frac{\delta\tilde{f}_j(\mathbf{p})}{n^0} \qquad (21)$$

[here, $\tilde{\nu}_{ij}(\mathbf{p})$ are the Fourier transformers of the long-range parts of pair interatomic potentials].

It is worth noting that the quantities $\tilde{B}_i(\mathbf{p})$ resulting in the inhomogeneity of system (20) do not depend on the time; hence, there exists a particular solution of inhomogeneous system (20), which is time independent (but dependent on the $\mathbf{p}$ parameter). This particular solution of the inhomogeneous system shifts the general solution of system (20) by the time-independent

function **p** and does not affect the conditions for the stability of the quasi-equilibrium solution. However, this does not mean that the solution stability is unaffected by the slow components, because, according to (19), the kinetic coefficients L_{ij}^0 in system (20) depend on the distribution of all the components, including the slow components.

The solutions of the homogeneous system corresponding to system (20) take the form

$$\delta\tilde{n}_i(\mathbf{p}, t) = \delta\tilde{n}_i(\mathbf{p}, 0)\exp(\alpha p^2 t). \quad (22)$$

Substitution of solutions (22) into system (20) at $\tilde{B}_i(\mathbf{p}) \equiv 0$ leads to the linear [with respect to $\delta\tilde{n}_i(\mathbf{p}, 0)$] homogeneous system of $(s+1)$ algebraic equations

$$\alpha\delta\tilde{n}_i(\mathbf{p}, 0) = -\tilde{A}_i(\mathbf{p}, 0) + \frac{\sum_{j=s+1}^{m} L_{ij}^0\omega_j}{\sum_{k=1}^{s+1}\sum_{k'=s+1}^{m}\omega_k L_{kk'}^0\omega_{k'}}\sum_{k=1}^{s+1}\omega_k\tilde{A}_k(\mathbf{p}, 0), \quad (23)$$

where

$$\tilde{A}_i(\mathbf{p}, 0) = \sum_{j=s+1}^{m}\sum_{k=1}^{s+1} L_{ij}^0\left[\frac{1}{T}\tilde{\nu}_{jk}(\mathbf{p}) - \frac{1}{n^0}\right]\delta\tilde{n}_k(\mathbf{p}, 0) + \sum_{j=1}^{s+1} L_{ij}^0\frac{\delta\tilde{n}_j(\mathbf{p}, 0)}{n^0}. \quad (24)$$

The characteristic equation in α is found from the condition that the determinant of linear system (23) is equal to zero:

$$\det A(\alpha) = 0. \quad (25)$$

The set of $(s+1)$ roots $\{\alpha_j(\mathbf{p}, t)\}$ is the solution of this characteristic equation.

The homogeneous distribution of components of the quasi-equilibrium solution becomes unstable in the small when the real part of even if one root of characteristic equation (25) becomes positive at any **p**. In other words, as long as

$$\max_{\{j\},\{\mathbf{p}\}}\Re\alpha_j(\mathbf{p}, T) < 0, \quad (26)$$

the local density fluctuations (22) tend to disappear; otherwise, the quasi-equilibrium solution turns out to be unstable toward the spinodal decomposition.

All the components of the system are indiscriminately involved in the evolution processes at the last stage of the solution transformation, and the condition determining the equation of the metastability boundary is changed qualitatively. Hence, we first treat the last stage as the special case, and then turn to general considerations.

At the last stage of the solution transformation, $\alpha = 0$ is always one of the m roots of the characteristic equation, because the close packing condition (10) leads to the linear dependence of the density fluctuations $\{\delta\tilde{n}_i(\mathbf{p}, t)\}$

$$\sum_{i=1}^{m}\omega_i\delta\tilde{n}_i(\mathbf{p}, t) = 0. \quad (27)$$

In this case, the Wronskian of system (23) with continuous coefficients is zero, and, at the stability boundary, $\max_{\{j\},\{\mathbf{p}\}}\alpha_j(\mathbf{p}, T) = 0$ is the double root. At the last transformation stage, the equation for the boundary of solution metastability has the form [13]

$$\min_{\{j\},\{\mathbf{p}\}}\left(\frac{\partial}{\partial\alpha_j}[\det A(\mathbf{p}, T, \alpha_j, n_1^0, \ldots, n_m^0)]\right)_{\alpha_j = 0} = 0. \quad (28)$$

At an arbitrary stage of the transformation of the s fast components, a linear dependence of the density fluctuations of fast components is absent, because

$$\sum_{i=1}^{s+1}\omega_i\delta\tilde{n}_i(\mathbf{p}, t) = -\sum_{i=s+2}^{m}\omega_i\delta\tilde{f}_i(\mathbf{p}) \neq 0 \quad (29)$$

and the Wronskian of system (23) is nonzero. Therefore, $\alpha = 0$ is not the root of characteristic equation (25), and, at the stability boundary, $\max_{\{j\},\{\mathbf{p}\}}\alpha_j(\mathbf{p}, T) = 0$ is the simple root. Then, taking into account condition (26), the equation for the boundary of quasi-equilibrium metastability is written as

$$\max_{\{j\},\{\mathbf{p}\}}\Re\alpha_j(\mathbf{p}, T) = 0. \quad (30)$$

Thus, the equation for the boundary of the solid solution metastability essentially depends on the transformation stage, is determined by condition (30) up to the last evolution stage, and degenerates into condition (28) at the last evolution stage.

The metastability boundary can be described by the equation of type (30) only at intermediate transformation stages in multicomponent condensed systems with the hierarchy of atomic mobilities of components until the complete chemical equilibrium of the quasi-equilibrium system is attained. The true (equilibrium) metastability boundary is described by equation (28).

In conclusion, let us summarize the main results obtained in this work.

(1) The evolution equations describing the transformation of quasi-equilibrium solid solutions are derived within the diffusion approximation without regard for the mobility of nonequilibrium slow components.

(2) An arbitrary step of the hydrodynamic stage of transforming the quasi-equilibrium solid solution with inclusion of volume effects is described in the framework of the generalized lattice model.

(3) The stability of quasi-equilibrium solutions against the spinodal decomposition is studied, and the equations for the metastability boundary in these systems are deduced for different stages of the diffusion kinetics.

REFERENCES

1. B. S. Bokshteĭn, S. Z. Bokshteĭn, and A. A. Zhukhovitskiĭ, *Thermodynamics and Kinetics of Diffusion in Solids* (Metallurgiya, Moscow, 1974).
2. B. Ya. Lyubov, *Diffusion Processes in Inhomogeneous Solids* (Nauka, Moscow, 1981).
3. V. V. Brik, *Diffusion Phase Transformations in Metals and Alloys* (Naukova Dumka, Kiev, 1985).
4. Yu. I. Ustinovshchikov, *Precipitation of the Second Phase in Solid Solutions* (Nauka, Moscow, 1988).
5. M. A. Zakharov, Fiz. Tverd. Tela (S.-Peterburg) **41**, 60 (1999) [Phys. Solid State **41**, 51 (1999)].
6. M. A. Zakharov, Fiz. Tverd. Tela (S.-Peterburg) **41**, 1609 (1999) [Phys. Solid State **41**, 1476 (1999)].
7. N. G. van Kampen, Phys. Rep. **124** (2), 69 (1985).
8. J. A. M. Janssen, Physica A (Amsterdam) **137**, 477 (1986).
9. V. V. Slezov and V. V. Sagalovich, Usp. Fiz. Nauk **151**, 67 (1987) [Sov. Phys. Usp. **30**, 23 (1987)].
10. E. P. Feldman and L. I. Stefanovich, Phys. Status Solidi B **195**, 137 (1996).
11. W.-M. Ni, Notices of the AMS **45** (1), 9 (1998).
12. A. Yu. Zakharov and S. V. Terekhov, in *Mathematical Problems of Chemical Thermodynamics* (Nauka, Novosibirsk, 1985), p. 173.
13. A. Yu. Zakharov and S. V. Terekhov, Fiz. Met. Metalloved. **59**, 261 (1985).
14. M. A. Zakharov, Zh. Fiz. Khim. **74**, 54 (2000).
15. H. Haken, *Advanced Synergetics: Instability Hierarchies of Self-Organizing Systems and Devices* (Springer-Verlag, New York, 1983; Mir, Moscow, 1985).
16. J. Kaiser, *Statistical Thermodynamics of Nonequilibrium Processes* (Springer-Verlag, Heidelberg, 1987; Mir, Moscow, 1990).
17. N. N. Bogolyubov, in *Studies in Statistical Mechanics*, Ed. by J. de Boer and G. E. Uhlenbeck (Gostekhizdat, Moscow, 1946; Wiley, New York, 1961), Vol. 1.
18. M. A. Krivoglaz, *Theory of X-ray and Thermal Neutron Scattering by Real Crystals* (Nauka, Moscow, 1967; Plenum Press, New York, 1969).
19. A. G. Khachaturyan, *The Theory of Phase Transformations and the Structure of Solids Solutions* (Nauka, Moscow, 1974).
20. A. I. Olemskoĭ, Izv. Vyssh. Uchebn. Zaved., Fiz. **24** (9), 48 (1980).
21. A. I. Olemskoĭ, Fiz. Met. Metalloved. **51**, 917 (1981).
22. A. A. Katsnel'son and A. I. Olemskoĭ, *The Microscopic Theory of Inhomogeneous Structures* (Mosk. Gos. Univ., Moscow, 1987).

Translated by O. Borovik-Romanova

Physics of the Solid State, Vol. 42, No. 7, 2000, pp. 1277–1279. Translated from Fizika Tverdogo Tela, Vol. 42, No. 7, 2000, pp. 1240–1242.

DEFECTS, DISLOCATIONS, AND PHYSICS OF STRENGTH

Mixed Crystals of *p*-Dichlorobenzene with *p*-Bromchlorobenzene in the Presence of Vacancies in the Structure

V. F. Shabanov and M. A. Korshunov

Kirenskiĭ Institute of Physics, Siberian Division, Russian Academy of Sciences, Akademgorodok, Krasnoyarsk, 660036 Russia
e-mail: mspec@iph.krasnoyarsk.su

Received July 16, 1999; in final form, December 9, 1999

Abstract—Polarization studies of low-frequency Raman spectra of solid solutions of *p*-dichlorobenzene with *p*-bromchlorobenzene (50% *p*-dichlorobenzene) were carried out. Analysis of the lattice vibration spectra of these mixed crystals shows that vacancies can be present in their structure. The presence of vacancies is responsible for the emergence of additional lines, including those in the 70 cm^{-1} region. The calculation of the diffusion activation energy in a mixed crystal proves that its magnitude is determined by the spatial arrangement of *p*-bromchlorobenzene molecules in the lattice, their orientation relative to parahalides, and (to a lesser extent) temperature variations. *© 2000 MAIK "Nauka/Interperiodica".*

The application of low-symmetry organic crystals in molecular electronics has increased significantly. These materials are promising in information recording and data processing [1]. The crystals for practical applications may contain defects such as vacancies. The presence of vacancies in a crystal leads to diffusion impeding a decrease in the area of information recording [2]. The diffusion rate depends on the temperature variation as well as on the impurity distribution in the crystal (for mixed crystals).

The presence of vacancies in a crystal can be determined with the help of low-frequency Raman scattering, since their presence affects lattice vibrations and is manifested in the spectra. An analysis of spectra for mixed crystals consisting of centrosymmetric molecules (*p*-dichlorobenzene with *p*-dibromobenzene) reveals additional low-intensity lines whose emergence is associated with a disorder in the distribution of impurity molecules and the presence of vacancies [3]. Besides, the activation energy in these mixed crystals depends on the temperature variation and on the crystallographic direction to a lesser extent than in the component crystals.

It would be interesting to find out whether this dependence is preserved for solid solutions in which noncentrosymmetric molecules constitute one of the components.

For our experiments, we chose isomorphic crystals of *p*-dichlorobenzene (α modification) and *p*-bromchlorobenzene forming solid solutions for any concentration.

According to the x-ray diffraction data [4] and NQR data [5], noncentrosymmetric molecules of *p*-bromchlorobenzene, as well as *p*-dichlorobenzene (α modification), are crystallized in the centrosymmetric space group $P2_1/a$ with two molecules in a unit cell owing to statistically disordered distribution of molecules relative to parahalides. The spectra of lattice vibrations for such crystals must contain six high-intensity lines associated with orientational vibrations and three lines associated with translational vibrations.

Figure 1a shows the lattice vibration spectrum (the *xz* component of the scattering tensor) for a mixed crystal of *p*-dichlorobenzene with *p*-bromchlorobenzene with 50% of *p*-dichlorobenzene.

The experimental spectrum contains six high-intensity lines three of which are of the B_g type (25.1, 44.4, and 100.7 cm^{-1}) and the remaining three, of the A_g type (45.4, 50.1, and 92.5 cm^{-1}) as well as a series of low-intensity lines (19.5, 29.5, 38.4, 62.2, 72.3, and 83.0 cm^{-1}).

In order to interpret the experimental spectra, we calculated the lattice vibration spectrum for a mixed crystal of *p*-dichlorobenzene with *p*-bromchlorobenzene (50% *p*-dichlorobenzene). It was assumed that the *p*-bromchlorobenzene molecules in the structure of the mixed crystal are distributed at random relative to parahalides as in pure *p*-bromchlorobenzene.

The molecular structure was assumed to be perfectly rigid. The interaction between the molecules was described by the atom–atom potentials method [6]. The coefficients in the interaction potential were the same as in analysis of the frequency spectra of *p*-dichlorobenzene and *p*-dibromobenzene [3]. The spectra of disordered crystals were calculated by Dean's method [7], which allows one to determine the eigenvalues for high-order matrices. The results of calculations were used to plot histograms that indicate the probability of the emergence of spectral lines in the chosen frequency range.

1063-7834/00/4207-1277$20.00 © 2000 MAIK "Nauka/Interperiodica"

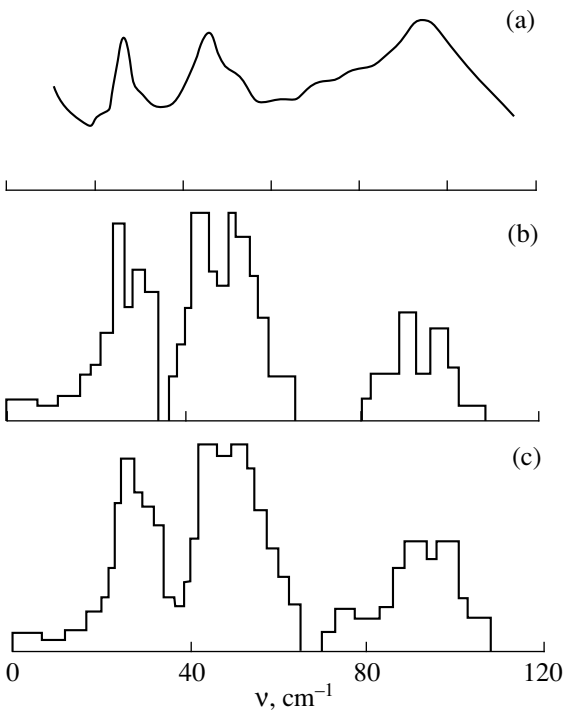

Fig. 1. Experimental low-frequency spectrum for a mixed crystal of *p*-dichlorobenzene with *p*-bromchlorobenzene containing 50% *p*-dichlorobenzene [(a) the *xz* component of the scattering tensor] and histograms obtained from calculations (b) in the presence of vacancies in the structure and (c) in the absence of vacancies.

Figures 1b and 1c show the histogram of the frequency spectrum of lattice vibrations for a mixed crystal without vacancies and in the presence of vacancies, respectively. In the latter case, additional lines emerge in the region of 70 cm^{-1}, which agrees with the experimental data.

Values of the energies E_L, E_r, E_f, E_m, and E_d (kcal/mol) at 100 and 300 K

	5% *p*-dichlorobenzene and 95% *p*-bromchlorobenzene		95% *p*-dichlorobenzene and 5% *p*-bromchlorobenzene	
T	300	100	300	100
E_L	15.55	17.0	16.4	17.43
E_r	0.55	0.56	0.58	0.68
E_f	15.0	16.44	15.82	16.75
$E_m^{[001]}$	4.0	4.2	4.8	4.9
$E_d^{[001]}$	19.0	20.64	20.62	21.65
$E_m^{[010]}$	3.3	3.4	3.1	3.3
$E_d^{[010]}$	18.3	19.84	18.92	20.05

An analysis of eigenvectors revealed that all vibrations are mixed with dominating translational or orientational vibrations. It was found that the lines in the vicinity of 29.5, 38.4, and 62.2 cm^{-1} are associated predominantly with translational vibrations. This agrees with the IR absorption data for *p*-bromchlorobenzene (26.0, 32.0, and 54.0 cm^{-1}) [8]. Therefore, the emergence of extra lines in the region of 70 cm^{-1} is due to the presence of vacancies.

We calculated the energies of the lattice, of vacancy formation, and of migration of molecules of mixed crystals of *p*-dichlorobenzene with *p*-bromchlorobenzene at 300 and 100 K. The analysis was carried out for two cases of low impurity concentrations. In the first case, 5% of *p*-bromchlorobenzene were added to the lattice of *p*-dichlorobenzene, and second, 5% of *p*-dichlorobenzene were added to the lattice of *p*-bromchlorobenzene.

The table contains the calculated values of lattice energy (E_L) for a mixed crystal without vacancies at 300 and 100 K for the two cases of component concentrations.

In order to determine the arrangement of molecules in the lattice of a mixed crystal with vacancies, the free energy was minimized in the orientations and displacements of the centers of mass of the molecules under investigation. In view of relaxation, the energy of the mixed crystal changed by E_r. The table also contains the calculated value of the energy of vacancy formation E_f.

In an analysis of the energy of migration, a molecule was displaced step by step from the position (0, 0, 0) along a chosen direction towards a vacancy. The length of a step was 0.2 Å. After each step, the crystal energy was minimized in accordance with the above-described procedure. The results of calculations are presented in Fig. 2 and in the table, where $E_m^{[001]}$ is the energy for migration of an impurity molecule along the crystallographic direction [001] and $E_m^{[010]}$ is the same along the direction [010]. The calculated values of the activation energy E_d are also presented in the table. The activation energy increases upon cooling, which is manifested in a change in the diffusion rate. The energy for migration changes insignificantly in this case. This is also observed for mixed crystals consisting of centrosymmetric molecules (*p*-dibromobenzene with *p*-dichlorobenzene) [3].

The curves in Fig. 2 show the variation of the potential energy upon a displacement of an impurity molecule in the lattice of a mixed crystal of *p*-dichlorobenzene with *p*-bromchlorobenzene along the crystallographic directions [001] (Fig. 2a) and [010] (Fig. 2b).

Curves *1* in Fig. 2 correspond to the concentration of a mixed crystal (5% of *p*-dichlorobenzene and 95% of *p*-bromchlorobenzene), while curves *2* correspond to

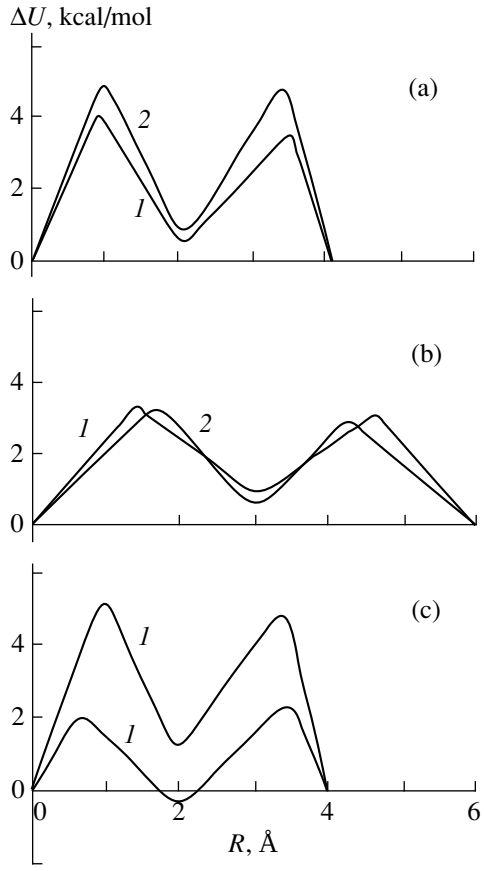

Fig. 2. Variation of potential energy upon the displacement of a migrating molecule towards a vacancy in crystallographic directions (a) [001] and (b) [010]. (c) Energy variation for various distributions of *p*-bromchlorobenzene molecules over *p*-positions.

the 5% *p*-bromchlorobenzene and 95% *p*-dichlorobenzene concentrations of the components.

In view of the disordered arrangement of *p*-bromchlorobenzene molecules in the lattice of the mixed crystal, the environment of a migrating molecule is different at different points of the crystal, which is manifested in the energy for migration. By way of an example, Fig. 2c graphically shows the potential energy variation upon a displacement of a *p*-dichlorobenzene molecule in the mixed crystal (with 95% of *p*-bromchlorobenzene) for a uniform distribution of molecules over the crystal volume, but for different orientations of *p*-bromchlorobenzene molecules relative to parahalides.

It can be seen from the figures that the energy for migration can vary over a wide range. This distinguishes mixed crystals formed by noncentrosymmetric molecules from those composed of centrosymmetric molecules, in which the variation of the energy for migration from cell to cell depends only on the distribution of impurity molecules over the crystal volume.

While comparing the experimental results on the activation energy of mixed crystal with the calculated values, one must apparently consider the averaged energy values along the chosen direction. However, we are not aware of any experimental results on the diffusion activation energy in mixed crystals of *p*-dichlorobenzene with *p*-bromchlorobenzene.

Thus, we have proved that the structure of mixed crystals of *p*-dichlorobenzene with *p*-bromchlorobenzene contains vacancies. Their presence is manifested in the emergence of extra spectral lines in the vicinity of 70 cm^{-1}. The analysis of migration energy in these mixed crystals reveals that its magnitude depends not only on the spatial distribution of an impurity over the crystal volume, but also on the arrangement of *p*-bromchlorobenzene molecules relative to parahalides. For a certain distribution of molecules in the structure of the crystal consisting of a mixture of noncentrosymmetric and centrosymmetric molecules, the variation of the migration energy with temperature is insignificant; this is also observed for mixed crystals consisting of centrosymmetric molecules.

REFERENCES

1. *Novel Physical Principles of Optical Information Processing*, Ed. by S. A. Akhmanov and M. A. Vorontsov (Nauka, Moscow, 1990), p. 399.
2. H. Gibbs, *Optical Bistability: Controlling Light with Light* (Academic, New York, 1985; Mir, Moscow, 1988).
3. V. F. Shabanov and M. A. Korshunov, Fiz. Tverd. Tela (St. Petersburg) **39** (9), 1564 (1997) [Phys. Solid State **39**, 1393 (1997)].
4. A. I. Kitaĭgorodskiĭ, *X-ray Diffraction Analysis* (GITTL, Moscow, 1950).
5. V. S. Grechishkin, *Nuclear Quadrupole Interactions in Solids* (Nauka, Moscow, 1973).
6. A. I. Kitaĭgorodskiĭ, *Molecular Crystals* (Nauka, Moscow, 1971).
7. P. Dean, in *Computational Methods in Solid State Theory* (Mir, Moscow, 1975), p. 207.
8. M. B. Wincke, A. Hadni, and X. Gerbaux, J. Phys. (Paris) **31**, 893 (1970).

Translated by N. Wadhwa

Physics of the Solid State, Vol. 42, No. 7, 2000, pp. 1280–1286. Translated from Fizika Tverdogo Tela, Vol. 42, No. 7, 2000, pp. 1243–1249.

DEFECTS, DISLOCATIONS, AND PHYSICS OF STRENGTH

Preparation of Disordered and Ordered Highly Nonstoichiometric Carbides and Evaluation of Their Homogeneity

A. A. Rempel and A. I. Gusev

Institute of Solid-State Chemistry, Ural Division, Russian Academy of Sciences, Pervomaĭskaya ul. 91, Yekaterinburg, 620219 Russia

e-mail: rempel@chem.ural.ru, rempel@ihim.uran.ru

e-mail: gusev@chem.ural.ru, gusev@ihim.uran.ru

Received September 14, 1999; in final form, December 15, 1999

Abstract—The features of solid-phase synthesis of highly nonstoichiometric carbides with controlled concentration of structural vacancies in the carbon sublattice have been considered. Four main stages are distinguished in the synthesis of nonstoichiometric carbides by the solid-phase sintering technique. It is shown that the inhomogeneity of highly nonstoichiometric compounds leads to the broadening of diffraction reflections. The analytical relation between the broadening and the inhomogeneity is obtained for the first time, and the method based on diffraction measurements is proposed for the quantitative evaluation of the degree of homogeneity of nonstoichiometric compounds. As an illustration of the advanced approach, the degree of homogeneity of nonstoichiometric niobium carbide is evaluated from the experimental data on the width of x-ray diffraction peaks. The heat treatment conditions providing the preparation of nonstoichiometric Group IV and V transition metal carbides in the disordered and ordered states are determined. © *2000 MAIK "Nauka/Interperiodica".*

The precise stoichiometric composition is the exception rather than the rule for crystalline compounds, because real crystals always contain defects. However, the defect concentration in many compounds over a wide range of temperatures and pressures is so low that falls outside the current possibilities of composition determination. Since absolutely defect-free crystals cannot exist at $T > 0$ K, the presence of defects by itself is an indication of the nonstoichiometry. The evidence of the nonstoichiometry is the inconsistency between the chemical composition and the concentration of lattice sites occupied by components of a compound. The nonstoichiometry brings about the appearance of vacant lattice sites, i.e., structural vacancies □.

In many binary and more complex compounds, the concentration of defects (vacancies or interstitials) is sufficiently low and, at 300 K, does not exceed 0.01 at. %, the distance between the nearest defects is very large and can be as great as tens of nanometers and more, and, therefore, the defects do not interact with each other. However, the absence of interaction between defects directly results from their low concentration, and, at concentrations higher than 0.1 at. %, defects interact. The compounds with structures involving defects of the structural vacancy type and with homogeneity regions characterized by such vacancy concentrations that ensure the interaction between defects are referred to as the highly nonstoichiometric compounds. The homogeneity region is the region of existence of the nonstoichiometric compound, in which the type of its crystal structure remains unaltered with a change in its composition. The similar notion "highly nonstoichiometric phases" was first used by Anderson [1] in consideration of the nonstoichiometry in chalcogenides and sulfides. The group of highly nonstoichiometric intercalation compounds involves carbides, nitrides, and lower oxides of transition metals MX_y with the *B*1-type structure; hexagonal carbides and nitrides M_2X_y with the *L*'3 (W_2C) structure; and some related ternary compounds [carbosilicides $M_5Si_3C_x$, siliconitrides $M_5Si_3N_x$, and silicoborides $M_5Si_3B_x$ with the $D8_8$ (Mn_5Si_3) structure and aluminidonitrides M_2AlN_x and $M_3Al_2N_x$ with the Cr_2AlC and *A*l3 (β-Mn) structures]. Substantial deviations from the stoichiometry with the formation of vacancies in the metal sublattice are observed in wüstite $Fe_{0.88}O$, iron sulfide $Fe_{0.85}S$, and copper sulfide $Cu_{1.73}S$.

In the highly nonstoichiometric intercalation compounds, the structural vacancies are analogues of interstitials, i.e., are quasiparticles and, in its sublattice, play the role identical to that of atoms occupying the sites of the same sublattice. Hence, the homogeneity region associated with the deviation from the stoichiometry is treated as a substitutional solid solution whose components are atoms and vacancies. The concept considering the vacant site as a crystal structure element similar to the occupied site was introduced in analysis of the nonstoichiometry and the ordering in oxides, sulfides, and chalcogenides [1, 2]. The distribution of atoms and

1063-7834/00/4207-1280$20.00 © 2000 MAIK "Nauka/Interperiodica"

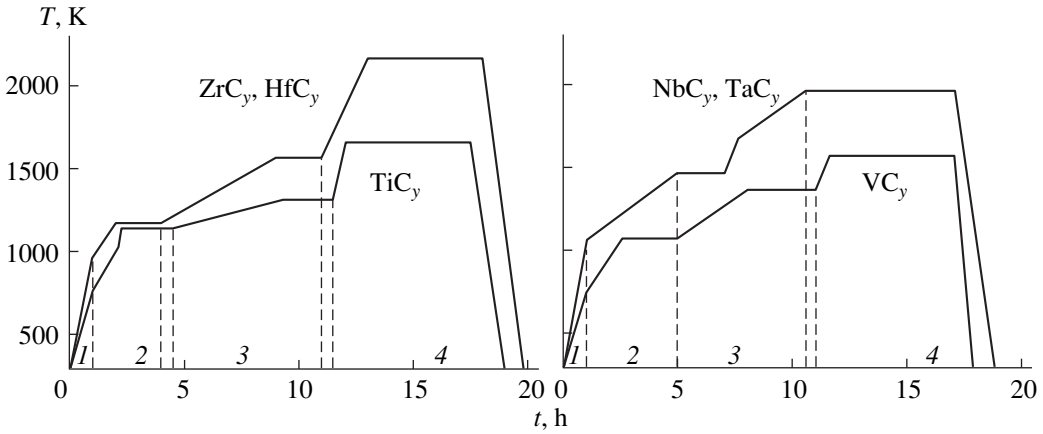

Fig. 1. Temperature conditions for the solid-phase vacuum synthesis of TiC_y, ZrC_y, HfC_y, VC_y, NbC_y, and TaC_y carbides: (*1*) degassing and evacuation, (*2*) preliminary sintering, (*3*) metal–carbon interaction and carbide formation, and (*4*) carbide homogenization.

vacancies over the sublattice sites can be disordered (random) or ordered. In the nonstoichiometric compound MX_y with a disordered distribution, the probability that the atom X occupies a particular site in the nonmetallic sublattice is equal to its atomic fraction *y*.

The highest concentration of vacancies is observed in Group IV and V transition metal carbides MC_y ($MC_y\square_{1-y}$). The concentration of the structural vacancies □ in the compounds corresponding to the lower boundary of the homogeneity region can be as high as 30–50 at. %; i.e., the compounds can exist when up to half the number of nonmetallic sublattice sites are vacant.

The disordered carbides MC_y exhibit extremely wide homogeneity regions, namely, from $MC_{0.48–0.70}$ to $MC_{1.00}$ [3], within which the carbon atoms C and the structural vacancies □ form the substitutional solution in the nonmetallic sublattice. Structural analysis of the highly nonstoichiometric carbides MC_y allows one to distinguish two opposite tendencies—the ordering and the disordering [4–7]. The ordered distribution of the vacancies is more probable at low temperatures, whereas the disordered distribution is observed at high temperatures when the entropy contribution to the free energy of the nonstoichiometric compound is sufficiently large [8]. The completely ordered and completely disordered distributions are the limiting states of the nonstoichiometric carbide. The ordering leads to the appearance of one or several ordered phases in the homogeneity region of the nonstoichiometric compound. These ordered phases also can have the homogeneity regions [7, 9, 10].

Therefore, it is this nonstoichiometry that is a prerequisite for the disordered or ordered distribution of atoms and vacancies in the structure of highly nonstoichiometric carbides. The atomic and vacancy ordering considerably affects the structure and properties of the highly nonstoichiometric carbides MC_y [3, 4]. At the same time, the investigation into such a fine physical process as the ordering and accompanying effects requires the preparation of homogeneous carbide samples with precisely known and different (within the homogeneity region) carbon contents. Only in this case, it is possible to obtain reliable and reproducible results.

Traditionally, the transition metal carbides are prepared by the thermal carbon reduction of oxides. This method is rather simple and most frequently used for the synthesis of the $MC_{1.0}$ carbides of stoichiometric composition. However, the thermal carbon reduction gives no way of producing high-purity carbides MC_y that have the controlled carbon content, contain no oxygen and free (chemically unbound) carbon impurities, and are suitable for the physical investigation of the atomic and vacancy ordering and related effects. Carbides obtained by the self-propagating high-temperature synthesis are characterized by an inhomogeneous microstructure and call for further heat treatment for reaching a homogeneous state. According to Lundström *et al.* [11], single crystals of high-melting carbides with various carbon content cannot be prepared at all because of the presence of thermodynamic restrictions. In the best case, within a very wide homogeneity region, it is possible, in principle, to obtain only single crystals of the $MC_{1.0}$ stoichiometric carbide and the MC_y carbide that corresponds to the maximum melting temperature in the phase diagram of the M–C system. Moreover, the preparation of single crystals does not solve the problem of impurities and homogeneity of carbides. In addition, the single crystals of nonstoichiometric carbides are cracked after the homogenizing annealing used for obtaining the ordered state [12].

The direct interaction between the metal and carbon in mixtures of their powders at high temperatures under vacuum is the optimum solid-phase technique for synthesizing the homogeneous nonstoichiometric carbides with the controlled content of structural vacancies in

the carbon sublattice and the minimum impurity content [13].

Figure 1 shows the temperature regimes for the vacuum synthesis of nonstoichiometric carbides. The first stage of heating for 1 h provides evacuation of the batch. The second stage involves the preliminary solid-phase sintering of the batch, which is attended by the removal of adsorbed impurity oxygen in the form of gaseous oxide CO. At the third stage, the metal and carbon chemically interact to give the MC_y carbide. The homogenization of carbide with the formation of disordered state and its annealing occur at the last stage. The duration and the temperature of the homogenization stage depend on the character (congruent or incongruent) and the rate of evaporation of the nonstoichiometric carbide [14] and are chosen in such a way as to prevent changes in the carbide composition in the course of homogenization.

So far, the homogeneity has been considered a qualitative characteristic. However, by using the diffraction data and interpreting the inhomogeneity as a lattice imperfection, i.e., as a structural defect, it is possible to treat the homogeneity as a quantitative characteristic. Actually, the inhomogeneity is the fluctuation of the concentration c in a certain volume V of solid solution or nonstoichiometric compound. In the crystal, the concentration fluctuations at the points $\mathbf{r}$ are described by the continuous fluctuation distribution $\delta c(\mathbf{r})$, which can be expanded into the Fourier series

$$\delta c(\mathbf{r}) = \sum_{\mathbf{k}} c_{\mathbf{k}} \exp(-i\mathbf{kr}),$$

where $c_{\mathbf{k}} = \frac{1}{V}\int \delta c(\mathbf{r})\exp(i\mathbf{kr})dV$, and $\mathbf{k}$ is the fluctuation wave. Since the fluctuations reduce only to the redistribution of the concentration among different crystal regions without its change, $\int \delta c(\mathbf{r})dV = 0$. The concentration fluctuations in the crystal give rise to the inhomogeneities, which lead to various static displacements.

In diffraction experiments, structural defects in polycrystals are identified from the broadening of diffraction reflections. The defects of any type lead to the displacements of atoms from the lattice sites and (or) the change in the scattering power of atoms. Krivoglaz [15] obtained the known relationship for the intensity of Bragg reflections for defect crystals, which makes it possible to conventionally separate all defects into two groups. The defects of the first group only decreases the intensity of diffraction reflections without their broadening. The defects of the second group are responsible for the broadening of reflections. The broadening can be brought about by the small size D of crystallites ($D < 150$ nm) and the packing defects. In these cases, the broadening is proportional to $\sec\theta$. The broadening caused by the microstrains and randomly distributed dislocations is proportional to $\tan\theta$. The general method usually used for examining the size of crystallites and the distribution of distortions in them from the data of x-ray scattering in polycrystals is the Fourier analysis of the diffraction reflection shape, which was developed by Warren and Averbach [16] and extended in [17, 18].

In the nonstoichiometric compounds MX_y, which have been extensively studied only in the last decades, there is one more reason for the broadening—the inhomogeneity of compound composition over the bulk of a sample. The influence of small inhomogeneity in solid solutions due to impurity atoms with the concentrations $c \le 0.01$ on the x-ray scattering was considered by Krivoglaz [19]. However, the x-ray effects associated with the inhomogeneity of phases containing from 1 to 30–50 at. % of defects were not discussed.

Let the polycrystal be a set of crystallites with different compositions y and sizes exceeding several hundreds of nanometers. Moreover, assume that the crystallites are spatially distributed in a randomly disordered manner. In this case, the broadening of reflections is determined by the fluctuations of the number of defects in different crystallites. As a result of these fluctuations, the mean deformations and shifts in maxima of ideal reflections upon introduction of defects into the crystal turn out to be different for different crystallites. Since the reflections for different crystallites merge, the resultant distribution of the intensity appears to be broadened in the neighborhood of reciprocal lattice sites.

As an example, let us consider the nonstoichiometric carbide MC_{y_0} with the $B1$ structure. In the case when the distribution of the carbon concentration y in carbide is described by the normal distribution law

$$g(y) = [1/(\Delta y\sqrt{2\pi})]\exp[-(y-y_0)/(2\Delta y^2)] \quad (1)$$

[where y_0 is the relative carbon content in carbide, and Δy is the half-width of the distribution function $g(y)$], the composition of the MC_{y_0} carbide is given with the accuracy $y = y_0 \pm \Delta y$, and the quantity Δy is the degree of inhomogeneity of carbide. Note that the usual normalizing conditions are met: $\int_{-\infty}^{\infty} g(y)\,dy = 1$ and $\int_{-\infty}^{\infty} y\,g(y)dy = y_0$. Let us now turn from the distribution in y to the distribution in the diffraction angle θ by using the Bragg reflection formula written for the first-order diffraction reflections in the form $\theta_0 = \arcsin\left[\frac{\lambda}{2d_{hkl}(y)}\right] = \arcsin\left(\frac{\lambda\sqrt{h^2+k^2+l^2}}{2a_{B1}(y)}\right)$ [here, d_{hkl} is the interplanar spacing for the (hkl) reflection with the diffraction angle θ_0, $a_{B1}(y)$ is the composition dependence of the lattice spacing for the MC_y carbide,

and λ is the wavelength of the diffracted radiation]. Then, distribution (1) takes the form

$$g(\theta) = (1/\Delta y\sqrt{2\pi})\exp[-(\theta-\theta_0)^2/(2\theta_y^2)], \quad (2)$$

where $\theta_y = \dfrac{a'_{B1}(y)|_{y=y_0}}{K(\theta_0)}\Delta y$, and $K(\theta_0) = \dfrac{\pi\lambda\sqrt{h^2+k^2+l^2}}{360}\dfrac{\cos\theta_0}{\sin^2\theta_0}$. The experimental intensity of the diffraction reflection $I(\theta) = \int_{-\infty}^{\infty} R(\theta'-\theta)g(\theta')d\theta'$ is the convolution of the distribution function $g(\theta)$ with the instrumental resolution function $R(\theta) = (1/\theta_R\sqrt{2\pi})\exp[-(\theta-\theta_0)^2/(2\theta_R^2)]$ and has the form

$$I(\theta) = [1/\sqrt{2\pi(\theta_R^2+\theta_y^2)}] \times \exp\{-(\theta-\theta_0)^2/[2(\theta_R^2+\theta_y^2)]\}. \quad (3)$$

From relationship (3), it is clear that the half-width θ_{exp} of the experimental function can be found from the equation

$$\theta_{exp}^2 = \theta_R^2+\theta_y^2 = \theta_R^2+\left[\frac{a'_{B1}(y)|_{y=y_0}}{K(\theta_0)}\Delta y\right]^2, \quad (4)$$

and the broadening $\beta = \sqrt{\theta_{exp}^2-\theta_0^2}$ is represented as

$$\beta = \frac{a'_{B1}(y)|_{y=y_0}}{K(\theta_0)}\Delta y. \quad (5)$$

Taking into account the angular dependence of the coefficient $K(\theta_0)$, from formula (5), it follows that the broadening brought about by the inhomogeneity Δy is proportional to $(\sin^2\theta)/\cos\theta$. The size and deformation broadenings are proportional to $\sec\theta$ and $\tan\theta$. Therefore, different angular dependences permit one to separate three different contributions to the broadening.

In the absence of the size and deformation broadenings, the inhomogeneity Δy can be determined from the broadening of the diffraction reflections from the relationship

$$\Delta y = \frac{K(\theta_0)}{a'_{B1}(y)|_{y=y_0}}\sqrt{\theta_{exp}^2-\theta_R^2}. \quad (6)$$

Hereafter, the quantity $(1-\Delta y)$ will be termed the degree of homogeneity. It is evident that the closer the quantity $(1-\Delta y)$ to unity, the higher the homogeneity of the crystal of the nonstoichiometric compound. In formulas (4) and (6), the half-width θ_{exp} of the experimental function and the half-width θ_R of the resolution function are expressed in terms of angles θ. For a Gaussian distribution, the half-width θ_R expressed in terms of θ and the full width at half maximum $\mathrm{FWHM}_R \equiv \Delta(2\theta_R)$ measured in terms of 2θ are related by the known expression $\theta_R(\theta) = \Delta(2\theta_R)/(2\times 2.35)$. This formula can be easily obtained by integrating a function described by the Gaussian distribution.

In order to collaborate the drawn conclusions on the possibility of evaluating the degree of homogeneity of nonstoichiometric compounds from the broadening of diffraction reflections, we carried out the experimental investigations of the TiC_y, ZrC_y, HfC_y, VC_y, NbC_y and TaC_y nonstoichiometric carbides belonging to the group of highly nonstoichiometric compounds.

Now, we evaluate the degree of homogeneity of disordered nonstoichiometric niobium carbide $NbC_{0.83}$ prepared by the solid-phase sintering under a vacuum no worse than 0.0013 Pa according to the procedure represented in Fig. 1. The carbide was synthesized from high-purity powders of metallic niobium and MT-900 carbon black with an ash content of less than 0.04 wt %. The total impurity content in niobium was less than 0.1 wt %. The contents of particular impurities were as follows (wt %): 0.01 Ta, 0.005 Fe, 0.003 W, 0.003 Mo, 0.002 Si, 0.001 Ti, 0.002 Al, 0.0003 Ni, 0.055 O, 0.016 C, and 0.010 N. According to the chemical analysis, the synthesized niobium carbide had the composition $NbC_{0.83}$ and contained 90.20 wt % Nb, 9.72 wt % C, 0.05 wt % O, and 0.01 wt % N. No free carbon was found. The microscopic examination showed that the grain size in bulk samples of the NbC_y disordered carbide ranges from 1–2 μm at $y \approx 1.0$ to 10–15 μm at $y \le 0.70$. Therefore, the size broadening of diffraction reflections is absent. In order to relieve stresses, the samples were additionally annealed at a temperature of 800 K. The structural characterization performed on Siemens D-500 and STADI-P (STOE) x-ray automated diffractometers by using the powder method indicates a high degree of homogeneity of the carbides synthesized: the splitting of the $\mathrm{Cu}K_{\alpha_{1,2}}$ doublets is observed even for reflections at small 2θ angles and with small Miller indices. Figure 2 displays the x-ray diffraction pattern of the disordered nonstoichiometric niobium carbide $NbC_{0.83}$, for which the doublets are split already beginning with the (311) reflection, suggesting a high degree of homogeneity of the carbide. The diffraction pattern was taken on a Siemens D-500 automated diffractometer ($\mathrm{Cu}K_\alpha$ radiation, Bragg–Brentano geometry). The half-width θ_R of the instrumental resolution function was determined in special experiments with a single crystal of hexagonal silicon carbide 6*H*-SiC and stoichiometric tungsten carbide WC. For the $\mathrm{Cu}K_{\alpha_1}$ radiation, $\theta_R = 0.0301°$ at $\theta = 35°$. By using the composition dependence of the lattice spacing $a_{B1}(y)$ for the NbC_y disordered carbide taken from [4], we obtain $a'_{B1}(y)|_{y=0.83} = 0.01655$ nm. For the first component of the (311) doublet in the case of the $\mathrm{Cu}K_{\alpha_1}$ radiation, the experimental full width at half maximum $\Delta(2\theta_{exp})$ is equal to 0.15°. Therefore, the experimental half-width

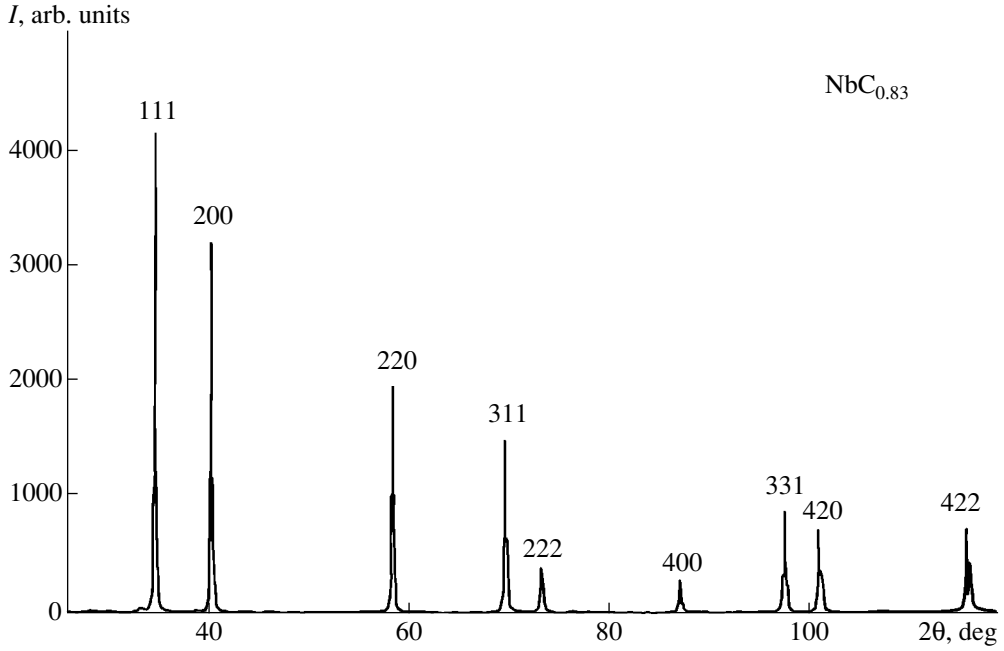

Fig. 2. X-ray diffraction pattern of disordered nonstoichiometric niobium carbide $NbC_{0.83}$.

$\theta_{exp}(\theta) = \Delta(2\theta_{exp})/(2 \times 2.35)$ measured in terms of θ for the $(311)_{\alpha_1}$ reflection is equal to 0.0319° [note that the half-width measured in terms of 2θ is $\theta_{exp}(2\theta) = \Delta(2\theta_{exp})/2.35$]. For the $(311)_{\alpha_1}$ reflection at the diffraction angle $\theta_0 = 35°$, the coefficient $K(\theta_0)$ is equal to 0.636 nm/rad (0.0111 nm/deg). The above values of $K(\theta_0)$, $a'_{B1}(y)|_{y=0.83}$, θ_{exp}, and θ_R allow us to determine the inhomogeneity Δy from the broadening of the $(311)_{\alpha_1}$ reflection, which appears to be equal to 0.007; i.e., the degree of homogeneity of the $NbC_{0.83}$ nonstoichiometric carbide synthesized is equal to 0.993 and close to unity. The estimates made with other reflections result in the same degree of homogeneity $(1 - \Delta y) = 0.993$ for the $NbC_{0.83}$ niobium carbide. The MC_y nonstoichiometric carbides with such small inhomogeneity cannot be produced by other techniques. As follows from the estimates for carbides obtained using the thermal carbon reduction or the self-propagating high-temperature synthesis, the inhomogeneity Δy varies from 0.015 to 0.02 and even more.

Thus, the described regimes of solid-state vacuum synthesis (Fig. 1) make preparing the TiC_y, ZrC_y, HfC_y, VC_y, NbC_y, and TaC_y high-purity homogeneous carbides in the form of bulk samples and powders with the specified carbon content y possible with an accuracy no worse than ±0.005–0.007. The powders of nonstoichiometric carbides are characterized by a narrow size distribution of particles: the grain-size analysis demonstrates that the size of 80% of particles is equal to 2–3 μm. The size of grains in the bulk samples of the MC_y disordered nonstoichiometric carbides varies from 1–2 μm at $y \approx 1.0$ to 10–20 μm at $y \leq 0.70$.

In the x-ray experiment with the use of the Cu $K_{\alpha_{1,2}}$ radiation, the splitting of diffraction reflections indicates the homogeneity of nonstoichiometric compounds. The splitting of reflections into the α_1 and α_2 components is observed when the distance $\Delta(2\theta(\alpha_1, \alpha_2))$ between the α_1 and α_2 peaks is larger than twice the half-width of the experimental function (Fig. 3); i.e., $\Delta(2\theta(\alpha_1, \alpha_2)) \geq 2\theta_{exp}(2\theta) = \Delta(2\theta_{exp})/1.175$. Hence,

$$\Delta(2\theta_{exp}) \leq 1.175\Delta(2\theta(\alpha_1, \alpha_2)). \quad (7)$$

Taking into consideration equation (4) and the fact that $\theta_{exp} = \Delta(2\theta_{exp})/4.7$ and $\theta_R = \Delta(2\theta_R)/4.7$, inequality (7) representing the condition for the splitting of doublets in the x-ray diffraction pattern can be rewritten in the form

$$[\Delta(2\theta_R)]^2 + \left[4.7\frac{a'_{B1}(y)|_{y=y_0}}{K(\theta_0)}\Delta y\right]^2 \leq [1.175\Delta(2\theta(\alpha_1, \alpha_2))]^2. \quad (8)$$

Inequality (8) enables one to evaluate the inhomogeneity Δy of the MX_y compound from the distance $\Delta(2\theta(\alpha_1\alpha_2))$ between the α_1 and α_2 components of the first split reflection.

Special heat treatment conditions are used for the preparation of nonstoichiometric carbides in the ordered and disordered states (Fig. 4). The quenching from 1850–2300 to 300 K at a rate of 2000 K/min (regime *a*) is applied to obtain carbides in a disordered

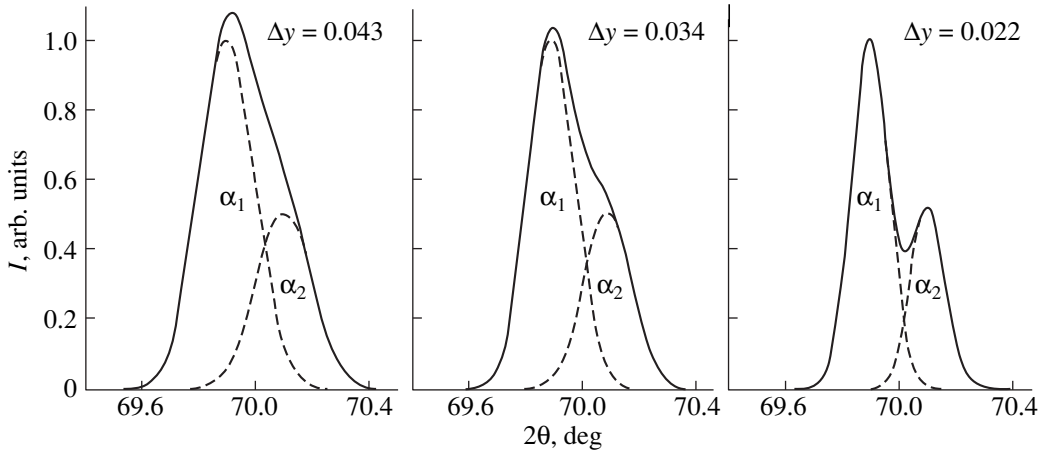

Fig. 3. Splitting of the (311) diffraction reflection into α_1 and α_2 components as a function of the degree of homogeneity Δy for $NbC_{0.83}$ nonstoichiometric carbide (the smaller value of Δy corresponds to more homogeneous carbide).

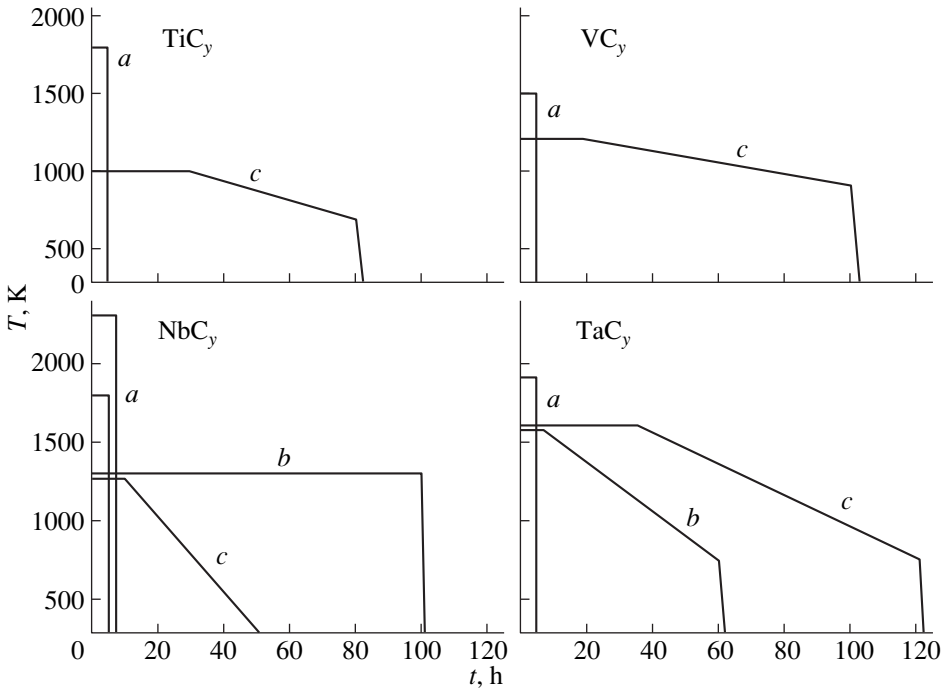

Fig. 4. Heat treatment conditions used for obtaining TiC_y, VC_y, NbC_y, and TaC_y carbides in the disordered and ordered states: (*a*) quenching for preparation of disordered carbides and (*b*, *c*) annealing for preparation of nonstoichiometric carbides with different degree of long-range order.

state metastable at room temperature. Regimes *b* and *c* are employed for preparing carbides in equilibrium ordered states with a long-range order in the arrangement of carbon atoms and structural vacancies. These regimes are prolonged (up to 100 h) annealings with a slow decrease in the temperature from 1000–1600 K (depending on the kind of metal atoms in carbide) down to 600–800 K. The cooling rate is equal to 0.05–0.20 K/min. Compared to regime *b*, regime *c* (with a lower cooling rate) furnishes a way of producing the nonstoichiometric carbides with larger long-range order parameters.

As follows from experimental investigations, the use of the annealing regimes makes it possible to obtain the $TiC_{0.50}$–$TiC_{0.58}$ carbides with the Ti_2C-type order and the long-range order parameter $\eta = 0.74$ [20], the $VC_{0.79}$ and $VC_{0.83}$ carbides with the V_6C_5-type order and $\eta \sim 0.80$ [21], the $VC_{0.87}$ carbide with the V_8C_7-type order and $\eta \sim 0.96$ [12, 21], the $NbC_{0.83}$ carbide with the

M_6C_5-type order and $\eta \sim 0.85$ [4], and the $TaC_{0.83}$ carbide with the M_6C_5-type order and $\eta \sim 0.65$ [22]. Analysis of structure and superstructure x-ray diffraction reflections for ordered carbides made it possible to determine the degree of homogeneity of ordered phases and to confirm the absence of disordered phases in the samples.

Therefore, it was demonstrated that the inhomogeneity of the nonstoichiometric compounds leads to the broadening of diffraction reflections. Analysis of the broadening allows one to evaluate the degree of homogeneity and, by using this quantitative parameter, to control and optimize the conditions of preparing the highly nonstoichiometric carbides with the high degree of homogeneity. The degree of homogeneity is the useful parameter for the characterization of carbides in the ordered state, because it provides a way of differentiating the inhomogeneous and two-phase samples. The quantitative characteristic of the degree of homogeneity is applicable to all the compounds characterized by the nonstoichiometry and the substitutional solid solutions (alloys).

ACKNOWLEDGMENTS

This work was supported by the Russian Foundation for Basic Research, project nos. 95-02-03549a, 98-03-32856a, 98-03-32890a, and 99-03-32208a.

REFERENCES

1. J. S. Anderson, in *Problems of Nonstoichiometry*, Ed. by A. Rabenau (North Holland, Amsterdam, 1970), p. 15.
2. *Problems of Nonstoichiometry*, Ed. by A. Rabenau (North Holland, Amsterdam, 1970; Metallurgiya, Moscow, 1975).
3. A. I. Gusev and A. A. Rempel, *Structural Phase Transitions in Nonstoichiometric Compounds* (Nauka, Moscow, 1988).
4. A. A. Rempel, Usp. Fiz. Nauk **166**, 33 (1996) [Phys. Usp. **39**, 31 (1996)].
5. A. I. Gusev, Phys. Status Solidi B **163**, 17 (1991).
6. A. I. Gusev and A. A. Rempel, Phys. Status Solidi A **135**, 15 (1993).
7. C. H. de Novion, B. Beuneu, T. Priem, *et al.*, in *The Physics and Chemistry of Carbides: Nitrides and Borides***,** Ed. by R. Freer (Kluwer Academic, Dordrecht, 1990), p. 329.
8. N. N. Sirota, *The Physicochemical Nature of Phases of Variable Composition* (Nauka i Tekhnika, Minsk, 1970).
9. R. Collongues, *La non-stoechiometrie* (Masson, Paris, 1971; Mir, Moscow, 1974).
10. A. I. Gusev and A. A. Rempel, Phys. Status Solidi A **163**, 273 (1997).
11. T. Lundström, M. M. Korsukova, and V. N. Gurin, Prog. Cryst. Growth Charact. **16**, 143 (1988).
12. A. A. Rempel and A. I. Gusev, Pis'ma Zh. Éksp. Teor. Fiz. **69**, 472 (1999) [JETP Lett. **69**, 472 (1999)].
13. L.-M. Berger, M. Hermann, A. I. Gusev, and A. A. Rempel, *Offenlegungsshrift DE 198 07 589 A1. Int. Cl.6*: C 01 B 31/30 (C04 B 35/36), Bundesrepublik Deutschland: Deutsches Patentamt (1998).
14. A. I. Gusev, Teplofiz. Vys. Temp. **29**, 595 (1991).
15. M. A. Krivoglaz, *Theory of X-ray and Thermal Neutron Scattering by Real Crystals* (Nauka, Moscow, 1967; Plenum Press, New York, 1969), p. 120.
16. B. Warren and B. Averbach, J. Appl. Phys. **21**, 595 (1950); **23**, 497 (1952); **23**, 1059 (1952).
17. B. Warren, Prog. Met. Phys. **8**, 147 (1959).
18. D. M. Vasil'ev and B. I. Smirnov, Usp. Fiz. Nauk **73**, 503 (1961) [Sov. Phys. Usp. **4**, 226 (1961)].
19. M. A. Krivoglaz, Fiz. Met. Metalloved. **12**, 465 (1961).
20. L. V. Zueva and A. I. Gusev, Fiz. Tverd. Tela (S.-Peterburg) **41**, 1134 (1999) [Phys. Solid State **41**, 1032 (1999)].
21. V. N. Lipatnikov, A. I. Gusev, P. Ettmayer, and W. Lengauer, J. Phys.: Condens. Matter **11**, 163 (1999).
22. A. I. Gusev, A. A. Rempel, and V. N. Lipatnikov, J. Phys.: Condens. Matter **8**, 8277 (1996).

Translated by O. Borovik-Romanova

Physics of the Solid State, Vol. 42, No. 7, 2000, pp. 1287–1289. Translated from Fizika Tverdogo Tela, Vol. 42, No. 7, 2000, pp. 1250–1252.

DEFECTS, DISLOCATIONS, AND PHYSICS OF STRENGTH

Effect of Complete Restoration of the Ice Surface after Indentation in the Temperature Range 243–268 K

Yu. I. Golovin, A. A. Shibkov, and O. V. Shishkina

Derzhavin State University, 392622 Tambov, Russia

e-mail: golovin@tsu.mtts-tambov.ru

Received December 16, 1999

Abstract—The effect of complete restoration of the ice surface after indentation in the temperature range 243–268 K has been detected and studied. The observed effect lies in the growth of new ice grains on the faces of the indent during several hours after the removal of the indenter. The rate of restoration is found to increase considerably after the microindentation of the boundary of an initial grain of polycrystalline ice. Possible mechanisms of this phenomenon are considered. © *2000 MAIK "Nauka/Interperiodica".*

The mechanisms of dent formation during indentation, the role of defects of various dimensions, and the structure of the deformed region remain subjects of discussion [1–9]. The nature of secondary phenomena accompanying indentation and structural relaxation, e.g., polymorphic phase transformations in the pricking region [6, 7] and partial restoration of the indent [2, 9], is also not completely clear. The restoration of the indent normally involves the bending of its faces; the relative change in the indent volume $\xi = |V - V_0|V_0^{-1}$ (where V_0 and V are the volumes of the initial and relaxed indents, respectively) does not exceed 10% as a rule when the indent depth ≥ 1 μm [2]. In this work, we report the discovery of the effect of complete restoration of the indent region ($\xi \approx 1$) after the microindentation of the surface of polycrystalline ice in the premelting temperature range $T/T_m = 0.90$–0.98 (where T is the temperature at which the tests were carried out and $T_m = 273$ K is the melting point of ice).

The sample of polycrystalline ice grown from distilled water (with an average grain size $\bar{d} = 800$ μm) were subjected to microindentation by the Vickers pyramid according to the standard technique on the PMT-3M equipment in a refrigerating chamber whose temperature varied from –5 to –30°C. The microhardness of ice under these thermal conditions amounted to $(5–8) \times 10^7$ Pa. After removing the indenter, we observed the kinetics of restoration of the indent region. It was found that the indents disappear completely with the average linear rate of restoration $\bar{v}_h = h_0/\bar{\tau} \approx 0.1$ μm/min, and the average bulk restoration rate $\bar{v}_V = V_0/\bar{\tau} \approx 10$ μm^3/s, where h_0 is the depth of the initial indent and $\bar{\tau}$ is the average restoration time [for example, an indent with a diagonal of 180 μm disappears completely $\bar{\tau} = 5$ hours after pricking at a temperature of –20°C (Fig. 1)]. Microscopic observations of the restoration process for more than 100 indents show that the restoration occurs due to the "filling" of the indent by "new" ice grains. A new "grain" having a size of 20–30 μm appears at the lower part of one of the faces just two or three minutes after pricking (Fig. 2). The number of such grains first increases, after which some of them start growing due to absorption of smaller grains (in analogy to the coalescence stage during first-order phase transitions [10]), and ultimately two or three "new" grains with a size commensurate with the diagonal of the initial indent remain in the region of the almost completely healed indent. Besides, the effect of initial grain boundaries of polycrystalline ice on the kinetics of restoration of the

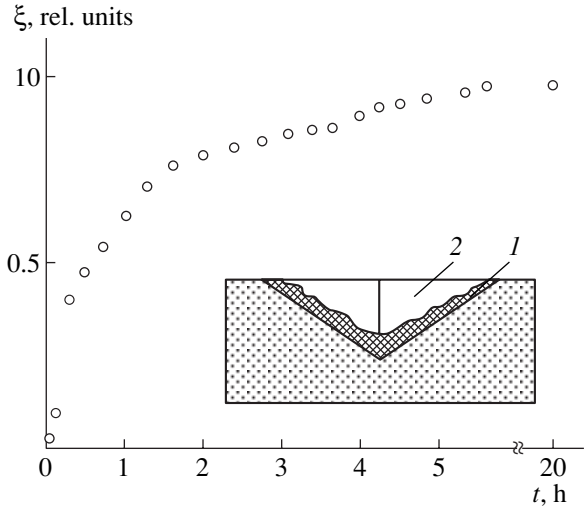

Fig. 1. Kinetics of the restoration of an indented ice surface at the center of a grain at $T = -25$°C in the $\xi = \dfrac{|V_0 - V|}{V_0}$ vs. t coordinates (where $V_0 - V$ is the restored volume, V_0 is the initial volume of the indent, and t is the time in hours after unloading). The inset shows the cross section of the initial (*1*) and partially restored (*2*) indent region.

1063-7834/00/4207-1287$20.00 © 2000 MAIK "Nauka/Interperiodica"

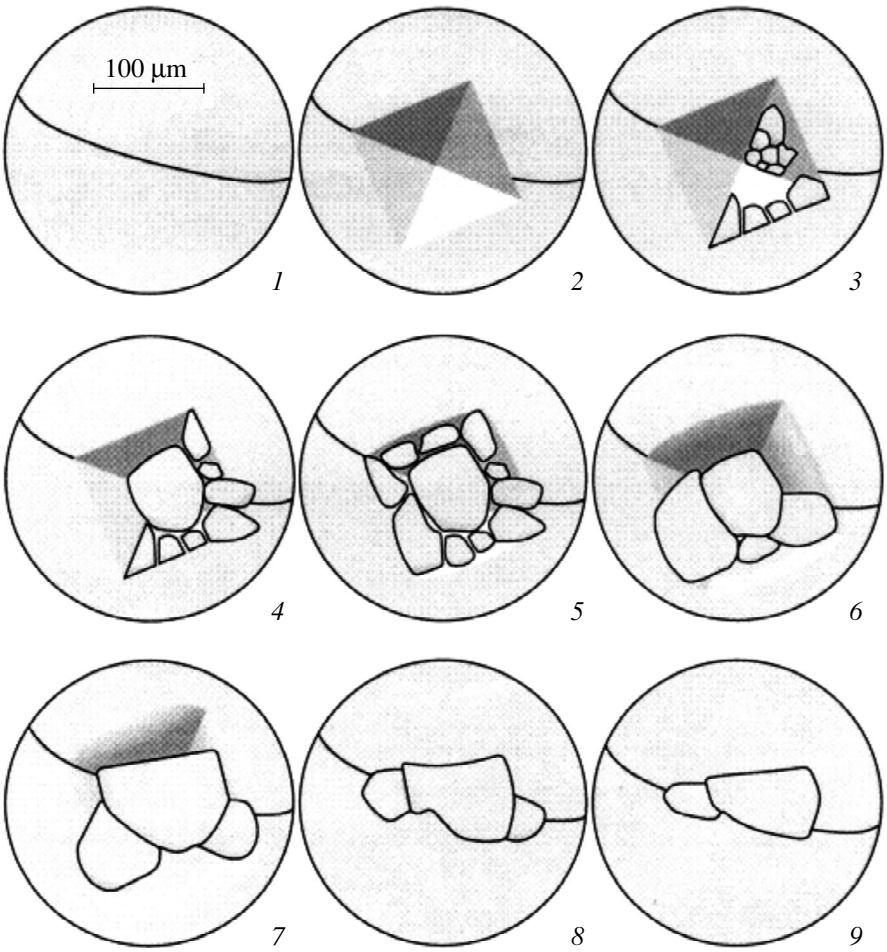

Fig. 2. Filling of the indent after microindentation at $T = -7°C$: (*1*) initial surface of polycrystalline ice containing a grain boundary; an indent after a time (*2*) $t = 10$ s following pricking and t (min): (*3*) 5, (*4*) 10, (*5*) 20, (*6*) 40, (*7*) 55, (*8*) 140, and (*9*) 150.

indent region is revealed: after pricking a grain boundary, the bulk restoration rate increased by ten percent as compared to the indent restoration rate in the central region of the grain, while the restoration rate after pricking the triple joint showed a manifold increase (by a factor of 2 or 3 at $T = -(5–20)°C$).

In order to estimate the effect of crystallization of supercooled vapor on the filling of the indent, the sample surface was covered in some experiments with a thin glass plate whose perimeter was sealed meticulously a few seconds after the withdrawal of the indenter. In the entire range of variation of the experimental conditions (the range of indent diagonals and experimental temperatures), the presence of the glass plate did not affect the kinetics of restoration of the indent region significantly.

Let us consider possible mechanisms of the observed effect.

(1) In view of the high mobility of lattice defects at premelting temperatures, the relaxation of the pit left after pricking can lead to a radical rearrangement of the dislocation structure of the lattice, for example, as a result of the annihilation of dislocations of opposite polarities and the alignment of dislocations of the same polarity into polygonal walls. Under the effect of residual elastic stresses, dislocation pileups of the same polarity can emerge at the surface of the indent, thus forming a protrusion, viz., the outer part of a "new grain". Thus, residual elastic stresses can be the driving force of such a relaxation process, while the dominating mechanism may be the premelting-temperature recrystallization annealing of the dislocation pit left after pricking.

(2) It is well known that polycrystals start melting along grain boundaries [11]. Therefore, it is likely that not only the walls of grain-boundary dislocations, but also dislocation pileups in the pit left after pricking are high-entropy perturbations of the crystal lattice with an anomalously high local value of chemical potential, and hence, a lower melting temperature. The liquid phase formed in the rays of a dislocation pit is squeezed out by capillary forces and/or residual elastic stresses to the outer surface of the indent face, accompanied by the formation of ice granules ("new grains"). The fact that the rate of filling of the indent with "new" ice grains is

significantly higher in the case where a grain boundary and especially a triple joint are pricked speaks in favor of the mechanism involving dislocation pileups (and/or dislocation walls) being in the premelting state.

(3) Ice is known to have a complex P–T_m phase diagram (where P is the hydrostatic pressure). A distinguishing feature of hexagonal ice Ih is that its melting temperature decreases with increasing pressure, which is known as rejection, i.e., melting under pressure [12]. According to estimates, a liquid-phase domain may be formed under the indenter in the indentation pit in the range of temperatures and stresses under investigation. Another important feature of ice Ih is the presence of a quasi-liquid layer of thickness ~0.1 μm on its surface [13]. Consequently, new ice "grains" can appear as a result of crystallization of water due to ice rejection or as a result of quasi-liquid layer flowing into the indent under the action of capillary forces. Additional experiments are required to make a proper choice between these mechanisms.

It should be noted, in conclusion, that in the region of premelting temperatures, the crystal is a nonlinear object due to a strong anharmonism of lattice vibrations, which is responsible for the emergence of a number of anomalous preliminary effects [14, 15]. The introduction of a strongly nonequilibrium dislocation structure of the indentation pit into the crystal creates conditions favoring the emergence (self-organization) of new structures. Filling the indent by the grains of "new" ice is essentially a morphogenesis of such a structure. However, the question arises of whether the observed effect is associated with peculiar features of ice, such as the presence of a quasi-liquid layer on its (outer and inner) surface and rejection, or it is typical of various materials in the premelting region and, hence, is of a universal thermodynamic origin due to a combination of strong deviation from equilibrium and the nonlinearity of the initial structure of the damaged region with a high mobility of its structural and kinetic elements. The answer to this question requires further systematic investigations into the mechanisms of indentation, the structure of the deformed region and its relaxation in the case of high-temperature indentation of a wide class of materials.

ACKNOWLEDGMENTS

This research was supported by the Russian Foundation for Basic Research (project no. 98-0217054).

REFERENCES

1. S. I. Bulychev and V. P. Alekhin, *Testing of Materials by Continuous Indentation* (Mashinostroenie, Moscow, 1990).
2. Yu. S. Boyarskaya, D. Z. Grabko, and M. S. Kats, *Physics of the Processes of Microindentation* (Shtiintsa, Chisinau, 1986).
3. Yu. I. Golovin and A. I. Tyurin, Fiz. Tverd. Tela (St. Petersburg) **38**, 1812 (1996) [Phys. Solid State **38**, 1000 (1996)].
4. Yu. I. Golovin and A. I. Tyurin, Pis'ma Zh. Éksp. Teor. Fiz. **60** (10), 722 (1994) [JETP Lett. **60**, 742 (1994)].
5. B. Ya. Farber, V. I. Orlov, and A. H. Heuer, Phys. Status Solidi A **166**, 115 (1998).
6. A. Kailer, Y. G. Gogotsi, and K. G. Nickel, J. Appl. Phys. **81** (7), 3057 (1997).
7. M. Sh. Akchurin and V. R. Regel, Chem. Rev. **23**, 59 (1998).
8. T. E. Page, W. C. Oliver, and C. J. McHargue, J. Mater. Res. **7**, 450 (1992).
9. V. K. Grigorovich, *Hardness and Microhardness of Metals* (Nauka, Moscow, 1976).
10. P. W. Voorhees, J. Stat. Phys. **38** (1–3), 231 (1985).
11. A. P. Poshekhonov, Fiz. Met. Metalloved. **69** (3), 39 (1990).
12. P. V. Hobbs, *Ice Physics* (Clarendon, Oxford, 1974).
13. N. H. Fletcher, Philos. Mag. **18** (156), 1287 (1968).
14. L. L. Boyer, Phase Transit. **5**, 1 (1985).
15. L. A. Bityutskaya and E. S. Mashkina, Pis'ma Zh. Tekh. Fiz. **21** (24), 90 (1995) [Tech. Phys. Lett. **21**, 1032 (1995)].

Translated by N. Wadhwa

Physics of the Solid State, Vol. 42, No. 7, 2000, pp. 1290–1293. Translated from Fizika Tverdogo Tela, Vol. 42, No. 7, 2000, pp. 1253–1255.

DEFECTS, DISLOCATIONS, AND PHYSICS OF STRENGTH

Analytical Estimation of Dislocation Distribution at the Tip of Arrested Cracks

Yu. I. Tyalin, V. A. Fedorov, T. N. Pluzhnikova, and V. A. Kuranova

Derzhavin State University, 392622 Tambov, Russia

e-mail: feodorov@feodorov.tstu.ru

Received November 15, 1999; in final form, January 21, 2000

Abstract—Computer simulation technique is used for studying the plastic flow at the tip of an arrested crack in lithium fluoride crystals. Two stages of the dislocation structure formation at the tip of a crack are analyzed: the formation of slip lines at the instant of crack arresting, and their evolution after sample unloading and partial healing of the crack. The size and the number of dislocations in a slip line are determined as functions of the loading force at the instant of crack arresting and on frictional stresses. It is shown that, during sample unloading and healing, some dislocations emerge at the plane of the crack under the action of mutual repulsion and image forces, so that the dislocation density attains its maximum value at a distance from the crack tip. A finite region free of dislocations exists in the immediate vicinity of the crack tip. *© 2000 MAIK "Nauka/Interperiodica".*

The fracture of most crystalline solids is accompanied by a plastic deformation whose intensity and extent of localization are determined by the rate of crack evolution [1, 2]. Partial or complete arrest of a crack in alkali-halide crystals is accompanied by the formation of plastic regions in the form of a typical "dislocation cross" [3]. The emitted dislocations create a plastic opening [4] and bend the banks of a crack, which hampers its healing after unloading [5]. In this work, we attempt to estimate the emissive capacity of a crack in lithium fluoride crystals. Experiments with such crystals reveal various etching figures at the tip of a crack depending on the conditions of its deceleration and arrest. In the case of an asymmetric cleavage, both completely symmetric slip lines and those having a forward direction are detected. For cracks propagating jumpwise under the action of a pulsed load, slip lines and bands normally have the direction opposite to the direction of movement of the crack. As a rule, the total number of dislocations does not depend significantly on the way the crack is arrested. For this reason, we will consider the simplest version of a plastic region typical of a jumpwise propagating crack, namely, the slip in half-planes adjoining the crack surface.

We present the plastic region by solitary slip lines symmetric about the crack plane (Fig. 1) and distinguish between the two stages of the formation of the dislocation structure at the crack tip; the formation of slip lines at the instant of crack arrest when the sample remains loaded, and their evolution after unloading.

We assume that the crack lies in the (010) plane and that it moved in the [100] direction before it was arrested. While writing the equilibrium equations for dislocations emitted by the crack in the slip plane, one must take into account the image forces (exerted on a dislocation by the crack) as well as the interaction of dislocations and the resistance offered by the crystal to shear. For the case of a plastic flow (Fig. 1), the equilibrium equations have the form

$$\tau^T(x_n) + \sum \tau^D(x_n, x_j) - \tau_S - \tau_i = 0, \quad n = 1, 2, \ldots, m,$$

where $\tau^T(x_n)$ are the stresses created by the crack in the slip plane, $\tau^D(x_n, x_j)$ are the stresses exerted on the nth dislocation by the jth dislocation and the one conjugate to it, τ_S are frictional stresses of the lattice, and τ_i are the stresses created by the image force [6].

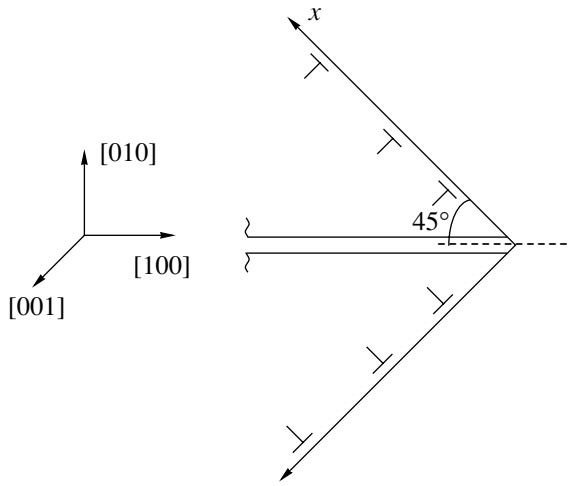

Fig. 1. Schematic of a plastic flow at the crack tip.

1063-7834/00/4207-1290$20.00 © 2000 MAIK "Nauka/Interperiodica"

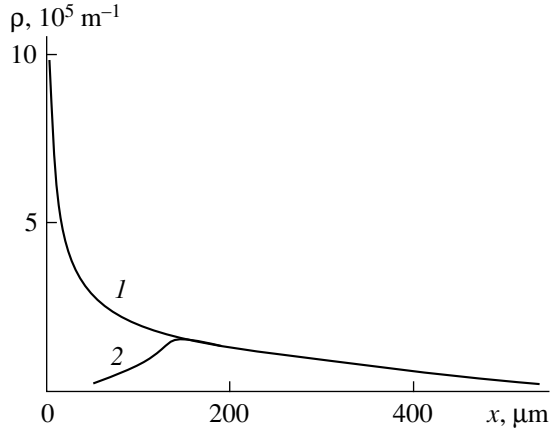

Fig. 2. Dislocation density in a slip line: (*1*) loaded sample and (*2*) after unloading.

The emission of dislocations ceases when the maximum magnitude of frictional stresses becomes smaller than the stresses initiating the plastic flow.

The system of equilibrium equations was solved numerically by a successive overrelaxation method [7]. It was proven that the dislocation density $\rho(x) = \Delta N/\Delta x$ (curve *1* in Fig. 2) in the tailing part of a slip line adjoining the crack amounts to $\approx 10^6$ m^{-1}. In the region of leading dislocations, its value decreases by more than an order of magnitude.

The total number of dislocations in a slip line depends on the load at the instant of crack arresting, as well as on the frictional stresses, and may vary over wide limits (Fig. 3). In the general case, a decrease in the resistance offered by the crystal to the motion of dislocations leads to the removal of leading dislocations to large distances from the crack, thus reducing the value of stresses blocking the dislocation source. The total number N of dislocations increases in this case. For a constant value of τ_S, the number of dislocations in the slip line increases with the wedging force p; i.e., a more intense plastic flow should also be expected in crystals with a large surface energy γ in view of an increase in the value of stresses at the crack tip.

The length l of slip lines (curves *1–3* in Fig. 4) exhibits approximately the same dependence on p (or γ) and τ_S. The path length of a leading dislocation varies from tens of micrometers to $\approx 2 \times 10^{-3}$ m for the values of load and frictional stresses used in our calculations.

It is interesting to note that $\tau^T(x) < \tau_S$ at the head of a dislocation pileup; i.e., the contribution to the path length of leading dislocations from mutual repulsion of dislocations in a slip line is larger than that from the shear stress due to the crack. Indeed, if we confine the size of the plastic region by the condition $\tau^T(x) = \tau_S$, we obtain the expression $l^* = (K/\tau_S)^2$ for the pileup length, where K is the stress intensity factor. The values of l^* calculated according to this expression are presented in Fig. 4 (curves *4–6*). It can be seen that l^* is always

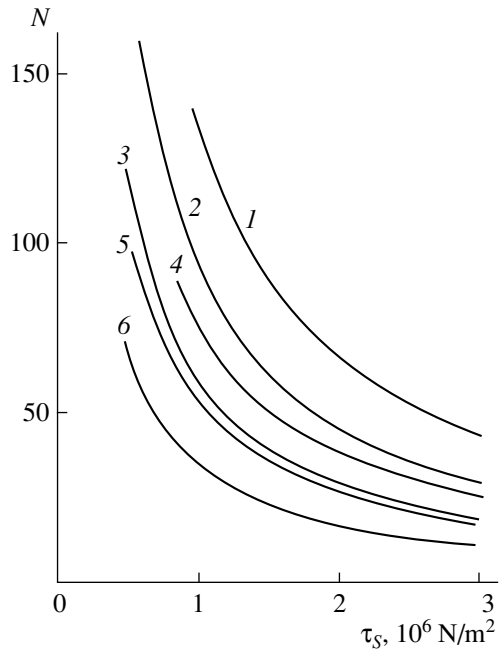

Fig. 3. Number of dislocations in a slip line as a function of wedging forces P, N: (*1*) 6, (*2*) 5, and (*3*) 4 (curves *4–6* correspond to unloading).

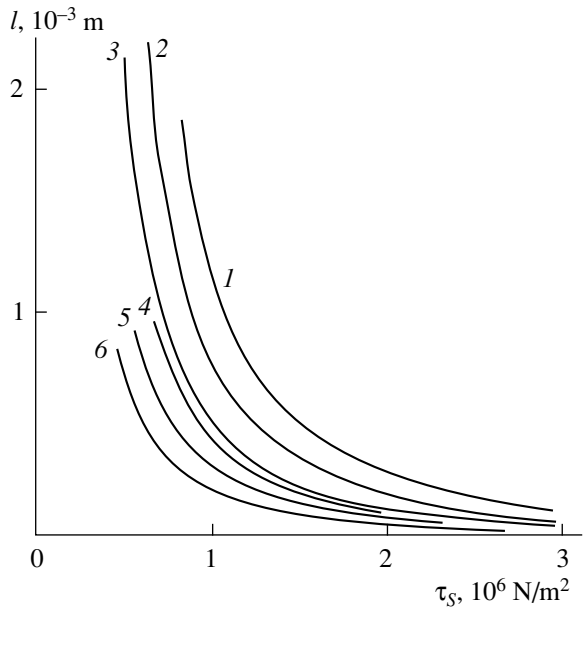

Fig. 4. Dependence of the slip line length on frictional stresses P, N: (*1*) 6, (*2*) 5, and (*3*) 4 (curves *4–6* correspond to unloading).

smaller than l, the difference between them increasing with the pileup length (or the number of dislocations in the pileup).

The above-mentioned fact is obviously of general nature and is manifested when dislocations are generated at any structural inhomogeneity creating a local stress concentration. The plastic region size in this case is controlled by the amplitude value of shear stresses rather than by the spatial distribution of the stressed state.

Next, we analyzed the second stage of the formation of the dislocation structure at the crack tip, i.e., the transformation of the pileup calculated above after the removal of the external load and partial healing of the crack. Dislocations can move from their initial positions under the action of their mutual repulsion and image forces (the calculation procedure at this stage is similar to that used in [8]). The dislocations for which the magnitude of the acting forces does not exceed the frictional forces are regarded as stationary. Some dislocations may leave the crystal and emerge at the crack surface if they approach the crack to a distance $r = A/\tau_S$ during their motion (here, $A = Gb/4\pi(1 - \nu)$, G is the shear modulus, b is the Burgers vector for a dislocation, and ν is the Poisson ratio), at which image forces exceed frictional forces. Thus, the relaxation of the pileup changes not only the spatial arrangement of individual dislocations, but also their number.

Calculations showed that the arrangement of dislocations at the pileup head (dislocations with numbers $j \le 37$) remained unchanged. However, the number of dislocations in the region adjoining the crack decreased and their mutual separation changed. The distribution of dislocation density over the pileup length also changed significantly (see curve *2* in Fig. 4). The dependence of ρ on x is no longer monotonic, but has a complex form with an extremum at a considerable distance from the crack tip. The maximum value of the dislocation density is 2×10^5 m^{-1}.

Figure 3 (curves *4–6*) gives information on the number of dislocations remaining in the crystal after unloading. The general situation corresponds to the emergence of ~40% of dislocations at the crack surface; in other words, a noticeable reversible plastic deformation is observed along with a one-way flow. The amount of plastic opening is determined by the number of dislocations emitted by the crack in the $\langle 110 \rangle \{110\}$ slip system. As the sample is unloaded, the crack opening decreases by $\delta = \sqrt{2}\, n_1 b$, where n_1 is the number of dislocations emerging at the cleavage surface. The final opening is determined by the number of dislocations remaining in the crystal at the tip of the crack.

If the plasticity at the tip of a crack being arrested is insignificant and $\delta < 20$ nm, its banks can converge (as a result of the emergence of dislocations at the crack surface) to distances short enough for restoration of ionic bonds. In this case, self-healing takes place.

We also studied the variation of plastic flow parameters at the crack tip for the cases when the deformed region could be presented by a set of several slip lines. We assumed that the slip lines are spaced at small distances such that the interaction of a dislocation with those on adjacent planes can be taken into account by increasing the Burgers vector in proportion to the number of slip lines. The total Burgers vector for dislocations in a slip line is approximately conserved: $b_1N_1 \cong b_2N_2 \cong b_3N_3$; i.e., plastic opening of the crack does not depend on whether the plastic region is modeled by discrete lattice dislocations or by superdislocations with the Burgers vector $B = nb$. The slip line length decreases with increasing Burgers vector of dislocations; hence, $l_1 > l_2 > l_3$. The relative decrease in the plastic region size is also small; for example, a threefold increase in the Burgers vector of a dislocation reduces the slip line length approximately by 10%.

It should be noted that the separation between the Nth dislocation and the crack tip is much larger than the distance between this dislocation and the $(N - l)$th dislocation; i.e., a finite dislocation-free region exists in the immediate vicinity of the crack tip. The existence of these regions was confirmed in [8] for shear cracks. In order to explain the experimentally observed features of the dislocation distribution at the crack tip, Shu-Ho and Li [9] considered a model of plastic flow in the form of a slip line on the continuation of the crack. In contrast to the flow model developed in [10], which predicts no dislocation-free region, the authors of [8] proposed that the emission of dislocations by a crack ceases when the stress intensity factor at the crack tip decreases to a preset value (zero in [10]). Thus, they actually considered a slip line at the crack tip in which the number of dislocations is insufficient for blocking the crack tip as a source of dislocations. In this approach, the existence of a region free of dislocations is a natural consequence of sample unloading, when a fraction of dislocations emerges at the cleavage surface under the action of their mutual repulsion and image forces.

ACKNOWLEDGMENTS

This work was supported by the Russian Foundation for Basic Research, grant no. 98-01-00617.

REFERENCES

1. A. Tetelmen, in *Fracture of Solids* (Interscience, New York, 1963; Metallurgiya, Moscow, 1967), p. 261.
2. A. N. Orlov and V. L. Indenbom, in *Physics of Brittle Fracture* (Kiev, 1976), Part 2, p. 18.

3. M. P. Shaskol'skaya, Wang Yan-Wen, and Gu Shu-Zhao, Kristallografiya **6** (4), 605 (1961) [Sov. Phys. Crystallogr. **6**, 483 (1961)].
4. V. A. Fedorov, T. N. Pluzhnikova, and Yu. I. Tyalin, Fiz. Tverd. Tela (St. Petersburg) **42** (4), 685 (2000) [Phys. Solid State **42**, 703 (2000)].
5. V. M. Finkel', O. G. Sergeeva, and V. V. Shegaĭ, Kristallografiya **36** (1), 170 (1991) [Sov. Phys. Crystallogr. **36**, 97 (1991)].
6. Yu. I. Tyalin, V. A. Fedorov, T. N. Pluzhnikova, and V. A. Kuranova, Vestn. Tamb. Gos. Univ. **4** (1), 23 (1999).
7. J. Ortega and W. Rheinboldt, *Iterative Solution of Nonlinear Equations in Several Variables* (McGraw-Hill, New York, 1970; Mir, Moscow, 1975).
8. V. I. Vladimirov and Sh. Kh. Khannanov, Fiz. Met. Metalloved. **30** (2), 281 (1970).
9. Dai Shu-Ho and Y. C. M. Li, Scr. Metall. **16** (2), 183 (1982).
10. S. Kobayashi and S. H. Ohr, Philos. Mag. **42** (6), 763 (1980).

Translated by N. Wadhwa

Physics of the Solid State, Vol. 42, No. 7, 2000, pp. 1294–1298. Translated from Fizika Tverdogo Tela, Vol. 42, No. 7, 2000, pp. 1256–1260.

DEFECTS, DISLOCATIONS, AND PHYSICS OF STRENGTH

Mechanochemical Penetration of Helium Atoms into $Pd_{84.5}$–$Si_{15.5}$ and Ni_{78}–Si_8–B_{14} Eutectic Amorphous Films Extended in Liquid ^{3}He and ^{4}He

O. V. Klyavin*, B. A. Mamyrin*, L. V. Khabarin*, Yu. M. Chernov*, V. Z. Bengus, E. D. Tabachnikova**, and S. É. Shumilin****

** Ioffe Physicotechnical Institute, Russian Academy of Sciences, Politekhnicheskaya ul. 26, St. Petersburg, 194021 Russia*
*** Physicotechnical Institute of Low Temperatures, National Academy of Sciences of Ukraine, Kharkov, 310086 Ukraine*
Received November 24, 1999

Abstract—The penetration of helium atoms into amorphous films extended to fracture in liquid helium has been investigated. It is found that helium atoms penetrate into the eutectic alloy films $Pd_{84.5}$–$Si_{15.5}$ in ^{3}He (T = 0.5 K) and Ni_{78}–Si_8–B_{14} in ^{4}He (T = 4.2 K). The spectra of helium liberation from these materials after deformation are obtained upon dynamic (4–5 K/min) annealing at T = 293–1323 K. The maximum amount of helium is observed in the regions of local plastic microshears running across the whole width of films and also in the sample regions containing fracture macrocracks and isolated groups of slip bands. The spectra of helium liberation from different regions of destroyed samples show several peaks that correlate with the temperatures of crystallization and melting of the studied films. The data obtained are interpreted within the model of mechanochemical penetration of helium atoms through the dynamically excited dislocation-like defects, which are typical of the amorphous films under consideration. © *2000 MAIK "Nauka/Interperiodica"*.

1. INTRODUCTION

Investigations into the dynamic dislocation pipe diffusion [1–4]—the penetration of atoms (molecules or their fragments) into crystalline materials in the course of their plastic deformation through nucleating and moving dislocations—bring up the question about the generality of this phenomenon for different-type solids. Earlier [5], it was shown by the example of a helium medium that, under plastic deformation, helium atoms penetrate not only into crystalline materials with different-type lattices, but also into polymer materials such as fluoroplastic. As is known [6], the plastic deformation of polymer materials can be described by the Somigliana dislocations with the variable Burgers vector. Therefore, the same approach can be applied to the penetration of impurity atoms of a medium into these materials.

The question as to whether the particles of the surrounding medium penetrate into amorphous metallic materials, namely, metallic glasses (for example, films without crystal structure), in the course of their plastic deformation is of crucial importance. In order to answer this question, we studied films of the Ni_{78}–Si_8–B_{14} and $Pd_{84.5}$–$Si_{15.5}$ eutectic amorphous alloys (Vacuum Schmelze, Germany) prepared by the liquid-phase technique—the quenching from the melt.

2. RESULTS

The film samples Ni_{78}–Si_8–B_{14} ($10 \times 60 \times 0.125$ mm) and $Pd_{84.5}$–$Si_{15.5}$ ($2 \times 60 \times 0.06$ mm) were extended to fracture at a rate of 0.02 mm/min in liquid ^{4}He at T = 4.2 K (the former film) and in liquid ^{3}He at T = 0.5 K (the latter film) by using a special mechanical testing machine [7]. The strain diagrams of these objects represent the straight lines. However, prior to fracture (at $\sigma \approx 0.8\sigma_f$, where σ_f is the fracture stress), the diagrams exhibit a number of small jumps associated with the appearance of single slip bands or groups of several slip bands 0.1–3 mm long. The fracture of films is accompanied by their separation into two or more parts and the macroplastic deformation in the form of 1–2 corrugations (wrinkles), which run across the whole width of the samples and have sizes of an order of ~1 mm. The corrugations arise from the joint action of elastic waves generated during the propagation of a destroying main crack, i.e., longitudinal unloading waves reflected from sample grips in the form of compression and flexural waves [8].

It should be noted that one side of the film surface has many technological macrodefects (stress concentrators)—craters or cavities (extended along the film length) with rough edges and also other smaller-sized surface defects (Fig. 1a). A large number of very thin plastic shears (slip bands) are found on this surface in the $Pd_{84.5}$–$Si_{15.5}$ films after their fracture. The slip bands are partially located in cavities or enclose them (Fig. 1b) and also emerge in the form of fans or bundles from different defect surface regions on both sides of the film (Fig. 2a). The branched slip bands are also observed along the front of macrocrack propagation and fringe them throughout the length (Fig. 2b). Com-

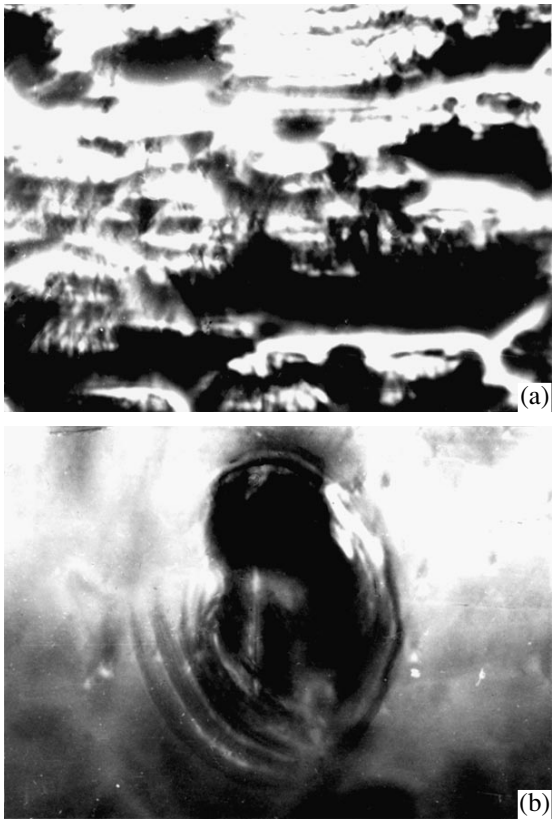

Fig. 1. (a) Surface relief and (b) ring slip bands enclosing the crater-type defect in the $Pd_{84.5}$–$Si_{15.5}$ film extended to fracture at $T = 0.5$ K (magnification, × 750).

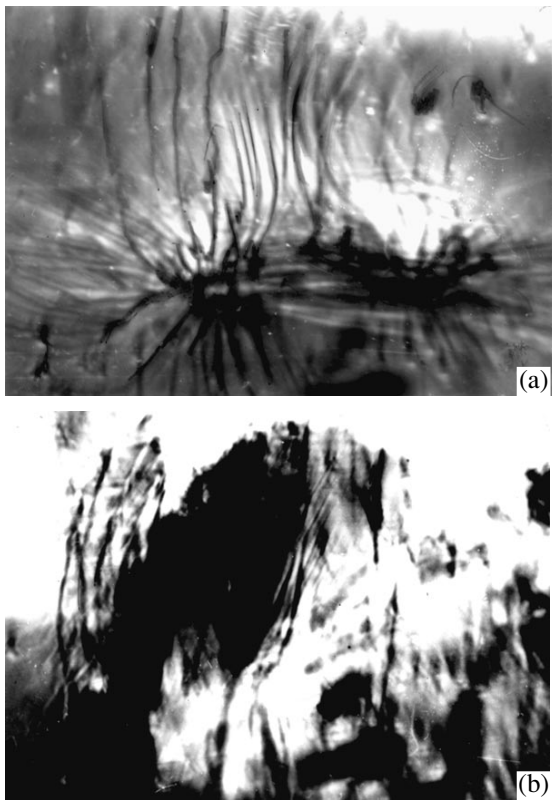

Fig. 2. (a) Fan-shaped bundles of slip bands emerging from surface defects and (b) slip bands fringing the fracture region in the $Pd_{84.5}$–$Si_{15.5}$ film extended to fracture at $T = 0.5$ K (magnification, × 750).

pared to the $Pd_{84.5}$–$Si_{15.5}$ films, the Ni_{78}–Si_8–B_{14} films have a lower plasticity and a higher strength. The fracture stresses for the Ni_{78}–Si_8–B_{14} films ($\sigma_f \approx 2600$ MPa) are approximately twice as large as those for the $Pd_{84.5}$–$Si_{15.5}$ films ($\sigma_f \approx 1200$ MPa). In the Ni_{78}–Si_8–B_{14} films, the slip bands (apart from corrugations) are predominantly observed in the vicinity of the fracture macrocracks, and their number on the rest of the film surface is small. The shear in the slip bands was measured with an interference microscope. Its magnitude was found to be large and equal to 1.5. In the film regions with a macroshear (corrugation) running across the whole width of films, the shear magnitude was measured from the sample bending in these regions and reached 5.

It can be seen that, according to [8, 9], the studied films remain plastic even at liquid-helium temperatures, and their fracture is viscous in character. Consequently, the helium atoms can penetrate into the regions of the local shears—the slip bands arisen upon loading and the subsequent fracture of the films.

Different regions of the fractured films were analyzed using a magnetic resonance mass spectrometer with a high resolution and a high sensitivity (the threshold of sensitivity is equal to $\sim 5 \times 10^9$ atoms for ^{4}He and $\sim 10^5$ atoms for ^{3}He [10]). Moreover, the film parts were cut with the aim of separating the regions with slip bands and cracks or only those with large shears (corrugations) running across the whole width of the samples. The results obtained are listed in the table. As follows from the table, helium is found in all the studied parts of samples nos. 1 and 2 of the Ni_{78}–Si_8–B_{14} films and sample no. 3 of the $Pd_{84.5}$–$Si_{15.5}$ films. The smallest amount of helium is observed in parts nos. 1 and 2 (marked by asterisk), which are shared in the grips. The presence of helium in these parts can be explained by a very small local plastic deformation, which does occur because of the slip of films in the grips upon their loading. Examination under an optical microscope reveals the presence of a small number of local slip bands that are randomly arranged in the films over the entire surface of grips.

Next, we investigated the film parts involving groups of local shears (0.1–3.0 mm in length), one macroshear (corrugation) running across the whole width of the film, single macrocracks with fringing slip bands, and fan-shaped groups (bundles) of slip bands. The helium contents (averaged over all the samples) in different film parts are as follows: 4×10^9 atoms/cm^2 in parts nos. 1 and 2 shared in the grips, 40×10^9 atoms/cm^2 in parts nos. 3–7 containing macrocracks and slip bands, and 160×10^9 atoms/cm^2 in parts nos. 8, which contain corrugations. As can be seen, among different film regions,

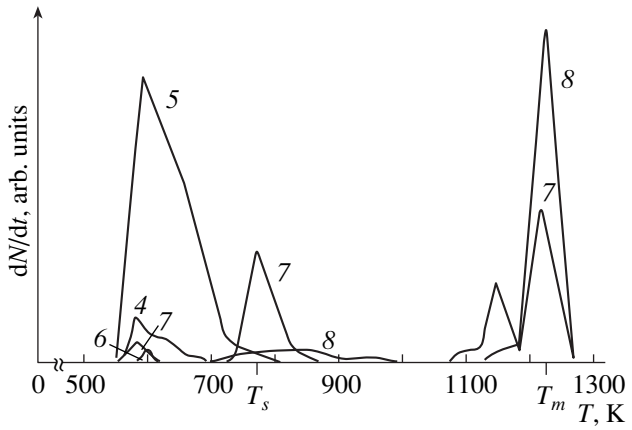

Fig. 3. Spectra of helium liberation from sample no. 1 (Ni_{78}–Si_8–B_{14}) upon dynamic annealing of its different parts containing (*4*, *5*) macrocracks with fringing slip bands, (*6*, *7*) group of slip bands of different lengths (0.2–3.0 mm), and (*8*) corrugations (macroshear) running across the whole width of the film (see table).

the maximum helium amount is observed in the corrugation regions (see table) containing a large number of slip bands, which occupy almost their entire surface area.

Let us now turn to the spectra of helium liberation from amorphous films, which were obtained upon dynamic annealing (at a rate of 4–5 K/min) in the temperature range 293–1323 K. For samples nos. 1 and 2 of the Ni_{78}–Si_8–B_{14} films, a number of peaks of helium liberation from different sample parts are observed at the same temperatures T = 573–623, 723, 1123–1143, and 1223 K (Figs. 3, 4). The location of a peak at T = 773 K virtually coincides with the crystallization temperature of the film (T_s = 713–753 K), and the location of a peak at T = 1223 K agrees with the melting temperature of the film. The latter peak, like some other peaks, exhibits a three-point structure, which suggests an explosive character of the helium liberation (the booster effect). The height of peaks at T = 573–623 K depends on the helium content in the initial parts of the film. The spectrum of helium liberation from the $Pd_{84.5}$–$Si_{15.5}$ film (Fig. 4, curve *8*) differs only slightly from that for the Ni_{78}–Si_8–B_{14} film. The temperatures of two peaks at 573–593 and 880 K coincide for both films (Figs. 3, 4). For the $Pd_{84.5}$–$Si_{15.5}$ film, the location of the third main peak at T = 820°C correlates with the melting temperature (T_m ~ 1100 K), and the location of a peak at T = 630 K corresponds to the crystallization temperature (T_s = 630–650 K). However, the total number of peaks for the $Pd_{84.5}$–$Si_{15.5}$ film is less than that for the Ni_{78}–Si_8–B_{14} film.

It can be assumed that, upon heating up to 290 K, holding, and subsequent dynamic annealing of samples up to ~1270 K, helium penetrated into the films due to the plastic deformation is redistributed among energy traps (including bubbles) different in depth and configuration. The appearance of peaks at T = 570–590 and 860–880 K for both types of films is likely caused by the presence of helium traps with identical energy characteristics even with the differences in their initial structure and composition. At the same time, these differences are responsible for the difference in the character of helium liberation from films of both types (the shape of the spectra and the location, width, and height of peaks) and also for the presence of additional peak at T = 860°C for the Ni_{78}–Si_8–B_{14} film. In order to obtain an unambiguous answer to this problem, it is necessary to determine the energy parameters of some traps and the depth of their occurrence in the bulk of films upon dynamic and isothermal annealing at different rates and temperatures. Solving this problem calls for further investigations.

3. DISCUSSION

The above experiments showed that helium is retained in the $Pd_{84.5}$–$Si_{15.5}$ and Ni_{78}–Si_8–B_{14} amorphous films upon heating up to their melting temperatures and can be liberated even from the melt (Figs. 3, 4). As follows from the mass-spectrometer measurements, the helium content in the samples strained in liquid helium remains constant even after their heat treatment at 290 K for five years. This suggests that helium penetrates into the studied materials through a nonadsorption mechanism and the energy traps for helium are sufficiently deep. These facts can be explained under the assumption that helium atoms are trapped and chemically bound to the atomic amorphous structure of films during their dynamic interaction in the regions in which the slip bands and attendant micro- and macrocracks

Helium content $N \times 10^{-9}$ atoms/cm^2 in Ni_{78}–Si_8–B_{14} and $Pd_{84.5}$–$Si_{15.5}$ amorphous films

Sample no.	Film	Sample part no.							
		1	2	3	4	5	6	7	8
1	Ni_{78}–Si_8–B_{14}	5.2*	4.4*	28	25	67	53	10	237**
2	Ni_{78}–Si_8–B_{14}	6.2*	1.2*	75	17		55		114**
3	$Pd_{84.5}$–$Si_{15.5}$	6.5*							120**

*Sample parts with grips.

**Sample parts with corrugations (empty squares correspond to the absence of measurements).

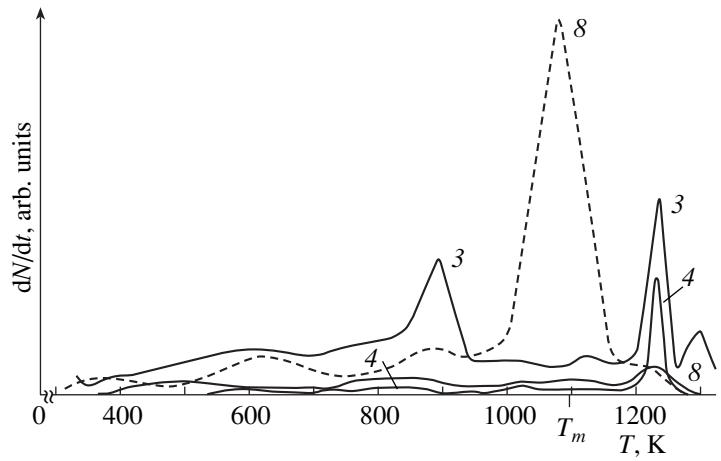

Fig. 4. Spectra of helium liberation from (*3*, *4*) sample no. 2 (Ni_{78}–Si_8–B_{14}) and (*8*) sample no. 3 ($Pd_{84.5}$–$Si_{15.5}$) (dashed line) upon dynamic annealing of the sample parts containing (*3*, *4*) macrocracks with fringing slip bands and (*8*) corrugation.

originate and propagate. The presence of chemical bonds between helium atoms and atoms of crystal lattice was experimentally demonstrated with ionic crystals by helium flaw detection [11].

According to [1–4], the penetration of particles (atoms, molecules, or their fragments) of the surrounding medium into crystalline materials in the course of their plastic deformation occurs through nucleating and moving dislocations. In the unstrained amorphous film, defects of the dislocation type in the explicit form are absent. However, as was shown in [12, 13], the amorphous structure of eutectic alloys strained at T = 20–300°C transforms to the crystal structure in the regions of local slip bands, and the slip bands exhibit compression and tension regions arisen from the short-range stresses, which gives rise to an x-ray diffraction contrast and spots in the electron diffraction patterns. Consequently, we cannot rule out the presence of dislocations and disclinations in slip bands, even though the shape, sizes, and density of these defects should considerably differ from those in the crystal structures subjected to tensile strain. Moreover, the preparation of amorphous films is accompanied by the formation of a large number of point defects (vacancies and interstitials) and their complexes. Therefore, the loose and disordered atomic structure of amorphous films substantially facilitates the penetration of helium atoms.

Now, we consider two contributory factors for this process: the presence of high internal stresses in amorphous films [14–17] and a strong local heating of the slip bands during the plastic deformation of films in liquid helium [9].

The atomic structure of metallic films is formed by the metal–metalloid clusters, which, in the case of nonisomorphous clusters, are characterized by the internal stress tensor components σ_{ik} of the disclination type with shearing and bending stresses [15]. This provides the plasticity and, as a consequence, the ductile fracture of the amorphous films studied. The internal stresses in the films increase with a decrease in the temperature, which leads to the anomalous dependence $\sigma_f = f(T)$ with a maximum at T = 2 K [8, 9]. Within the disclination approach, the values of σ_{ik} for the Ni_{78}–Si_8–B_{14} films at T = 1 K were estimated at about $0.01G$ (where G is the shear modulus) [8].

As was shown earlier in [9], the plastic deformation and fracture of the $Pd_{84.5}$–$Si_{15.5}$ and Ni_{78}–Si_8–B_{14} films at T = 4.2–0.5 K are accompanied by a strong local heating (up to the melting temperature) of the regions in which the slip bands, microcracks, and macrocracks are formed. This conclusion is confirmed by the theoretical estimates of the local heating of films in the regions of slip bands under adiabatic conditions at liquid-helium temperatures (the adiabatic heating of slip bands was evaluated in [18]) and the fractographic investigation into the fracture surface of amorphous eutectic alloy films extended in liquid helium [9]. A large number of "veins" (necks) formed upon fracture of the samples were found at the fracture surface. Moreover, balls of the materials itself were also observed at the fracture surface, which indicates the melting of the material.

Thus, the initial structure of amorphous films that is strongly disordered on the atomic level undergoes radical changes in the regions of slip bands. This is explained by considerable displacements of atoms and their groups at the expense of both external mechanical stresses in the field of high local internal stresses and the local heating of slip bands up to the melting temperature of the film. These factors are responsible for the efficient penetration of helium atoms into the amorphous films through the dislocation–vacancy defects inherent in the metal–metalloid clusters whose number in the slip bands sharply changes in the course of plastic deformation.

The helium atoms penetrated into the above defects can fix and stabilize these high-energy atomic structures. Hence, it is not surprising that a considerable

amount of helium was found in the studied films after their testing in liquid helium and prolonged holding at room temperature.[1]

The data obtained demonstrate that the atoms of the surrounding medium penetrate not only into crystalline materials, but also into metallic glasses (eutectic amorphous alloys) during their plastic deformation in liquid ^{3}He and ^{4}He. Therefore, in metallic glasses, the phenomenon of dynamic dislocation pipe diffusion, which is characteristic of crystalline materials, transforms to the phenomenon of mechanochemical penetration of particles from the surrounding medium through defects of other types considered above. Consequently, the carriers that provide the penetration of helium atoms into solids under plastic deformation can be both the nucleating or moving dislocations and different chemically active defect centers—localized states of atomic (or molecular) groups. The electronic structure of these states experiences dynamic transformations. This brings about a decrease in potential barriers of their initial atomic structure due to the plastic deformation or other dynamic processes, which result in a change in the energy parameters of the correlated interactions between atoms and molecules of solid subjected to external forces of different physical nature.

ACKNOWLEDGMENTS

We are grateful to V. V. Pustovalov for the performance of experiments in liquid helium.

This work was supported in part by the Russian Foundation for Basic Research, project no. 99-03-32526.

REFERENCES

1. O. V. Klyavin, B. A. Mamyrin, L. V. Khabarin, and Yu. M. Chernov, Fiz. Tverd. Tela (Leningrad) **18**, 1281 (1976) [Sov. Phys. Solid State **18**, 736 (1976)].
2. O. V. Klyavin, *Physics of Crystal Plasticity at Helium Temperatures* (Nauka, Moscow, 1987).
3. O. V. Klyavin, N. P. Likhodedov, and A. N. Orlov, Prog. Surf. Sci. **33** (4), 259 (1990).
4. O. V. Klyavin, Fiz. Tverd. Tela (S.-Peterburg) **35** (3), 513 (1993) [Phys. Solid State **35** (3), 261 (1993)].
5. O. V. Klyavin, B. A. Mamyrin, L. V. Khabarin, and Yu. M. Chernov, Fiz. Tverd. Tela (Leningrad) **24**, 2001 (1982) [Sov. Phys. Solid State **24**, 1143 (1982)].
6. V. V. Vladimirov and N. A. Pertsev, Fiz. Tverd. Tela (Leningrad) **28**, 1976 (1986) [Sov. Phys. Solid State **28**, 1104 (1986)].
7. I. N. Kuz'menko, V. V. Pustovalov, and S. É. Shumilin, Prib. Tekh. Éksp. **1**, 196 (1988).
8. E. D. Tabachnikova, V. Z. Bengus, and V. I. Startsev, Fiz. Nizk. Temp. (Kiev) **10**, 420 (1984) [Sov. J. Low Temp. Phys. **10**, 222 (1984)].
9. E. D. Tabachnikova, V. Z. Bengus, S. É. Shumilin, *et al.*, Metallofizika **13** (4), 47 (1991).
10. B. A. Mamyrin, B. N. Shustrov, G. S. Anufriev, *et al.*, Zh. Tekh. Fiz. **42**, 2577 (1972) [Sov. Phys. Tech. Phys. **17**, 2001 (1972)].
11. A. I. Kupryazhkin and A. Yu. Kurkin, Fiz. Tverd. Tela (S.-Peterburg) **35**, 3003 (1993) [Phys. Solid State **35**, 1475 (1993)].
12. N. I. Noskova, N. F. Vildanova, Yu. I. Filippov, and A. P. Potapov, Phys. Status Solidi A **87**, 549 (1985).
13. T. Musamoto and R. Maddin, Acta Metall. **19**, 725 (1971).
14. V. P. Alekhin and V. A. Khonik, *Structure and Physical Regularities of the Deformation of Amorphous Alloys* (Metallurgiya, Moscow, 1992).
15. N. Rivier and D. M. Duffy, J. Phys. (Paris) **43** (2), 293 (1982).
16. H. S. Chen, Rep. Prog. Phys. **43**, 353 (1980).
17. T. Egami, H. Maeda, and V. Vitek, Philos. Mag. A **40**, 883 (1980).
18. G. A. Malygin, in *Problems of Strength and Plasticity of Solids* (Nauka, Leningrad, 1979), p. 200.

Translated by O. Borovik-Romanova

[1] The pinning of cores and kinks of moving screw dislocations by impurity atoms was found in the α-Fe body-centered lattice upon their interaction with helium and carbon atoms in the course of computer experiments [3, 4].

Physics of the Solid State, Vol. 42, No. 7, 2000, pp. 1299–1305. Translated from Fizika Tverdogo Tela, Vol. 42, No. 7, 2000, pp. 1261–1267.

DEFECTS, DISLOCATIONS, AND PHYSICS OF STRENGTH

Effect of Post-Deformation Ageing on the Recrystallization of KCl–$SrCl_2$ Crystals

E. B. Borisenko and B. A. Gnesin

Institute of Solid-State Physics, Russian Academy of Sciences, Chernogolovka, Moscow oblast, 142432 Russia
e-mail: borisenk@issp.ac.ru

Received January 12, 2000

Abstract—Room-temperature recrystallization of KCl single crystals, both pure and doped with 0.02 and 0.06 wt % Sr, deformed preliminarily at 250°C is studied. It is found that annealing of the original single crystals at 650°C results in the precipitation of the $SrCl_2$ phase from the solid solution. X-ray diffraction studies reveal that the deformed crystals undergo ageing at room temperature, which is accompanied by a change in the phase composition. In the first place, particles of the KSr_2Cl_5 phase are formed instead of the phase $SrCl_2$ observed in the original and deformed crystals. These particles, which are located at the boundaries of growing recrystallized grains (twins of the original single crystal) occupying not more than 8% of the volume, impede the motion of grain boundaries and hamper further recrystallization. Second, it is shown that post-deformation ageing occurring in the remaining 92% of the deformed crystal region that has not undergone recrystallization lends stability to the strain-hardened state of alkali halide crystals over a period of at least two years at room temperature. © *2000 MAIK "Nauka/Interperiodica".*

Investigations of the recrystallization of alkali halide crystals (AHC) have revealed not only the existence of several mechanisms of recrystallization [1–6], such as the nucleation and growth of recrystallized grains having large-angle boundaries of the general type [2, 5] or special twin boundaries [5, 6], migration of grain boundaries growing from the deformed matrix, and their coalescence [2], but also the difference in the kinetics of AHC recrystallization under different conditions of deformation [1–6]. It was shown in a number of works [1, 2] that at temperatures above $0.45T_m$ (T_m is the melting point of the crystal), the growth of grains under dynamic or static recrystallization in ionic crystals of KCl is in many respects similar to the analogous process in metals. However, it was established that in many cases recrystallization of AHC also occurs at much lower homologous temperatures ($0.3T_m$) [3–6]. Experiments show that a characteristic feature of recrystallization of AHC at lower temperatures (close to room temperature, RT) is the growth of recrystallized grains with twin orientation relative to the original single crystal [5, 6]. The emergence of recrystallized grains with twin orientations at RT was detected in AHC doped with chlorides of divalent metals after deformation up to 70% [3, 6] and in undoped KCl after reversible polymorphic transformation $B1 \longleftrightarrow B2$ [5].

This work is mainly devoted to investigating phase composition transformations in deformed KCl crystals doped with small quantities of strontium, and the effect of post- deformation ageing on the recrystallization of these crystals.

1. MATERIALS AND EXPERIMENTAL TECHNIQUE

We studied single crystals of KCl, both pure and doped with strontium chloride, grown by the Czochralski method. The chemical composition of the samples for a number of elements is presented in the table.

The samples were deformed by upsetting on the Instron test machine in air in a closed chamber at a deformation temperature $T_d = 250 \pm 5$°C at the rate of $\varepsilon' = 0.1$ mm/min. Samples of size $3 \times 3 \times 7$ mm intended for testing by compression were chipped out along the cleavage planes {100}. In order to detect grain boundaries on a metallographic section, a mixture of saturated aqueous solution of KCl and ethyl alcohol was used for etching. The volume fraction of the structural components in the deformed crystals was determined by using Glagolev's dot technique [7] during the ageing process at RT. The microhardness of structurally inhomogeneous samples was measured on the PMT-3 device under a load of 20 g.

Qualitative phase analysis was carried out on a DRON-3.0 diffractometer, using the monochromatized MoK_α radiation for recording. The error in the measurement of diffraction angle was ≤0.02°. The x-ray diffraction analysis was carried out for single crystals and hence, not all the lines of the phase being determined were observed. The reliability of the determination of relatively weak diffraction lines was evaluated by using the Student's criterion for comparing the intensity distribution in the vicinity of the peak with the surrounding background. The texture of the samples was studied with the help of pole figures (PF) obtained

Concentration of some impurity elements in a KCl sample according to the results of atomic emission analysis with the specimen ionization in the inductively coupled ICP–AES plasma on the ICAP-61 device (Thermo Jarral Ash., USA)

Element	Sensitivity of measurement, μg/g	KCl, μg/g	KCl : 0.02 wt % Sr, μg/g	KCl : 0.06 wt % Sr, μg/g
Sr	0.10	2	200	590
Ca	1	<1	5	3
Na	2	<2	8	3
Rb	0.09	0.64	–	–
Br	6	79.4	–	–
Cs	0.01	0.22	–	–

Note: The results of analysis show that the concentration of other impurities characteristic of alkali halides, viz., Mg, Cd, Ti, Mn, Cu, I and Pb, is lower than the measurement sensitivity which does not exceed 1 μg/g. The accuracy of the method is ±5% (1 μg/g corresponds to 10^{-4} wt %).

on the automated texture-diffractometer by the Shultz (slope) method [8], the maximum slope was 65°, while the step in polar (ϑ) and azimuthal (φ) angles was $\Delta\vartheta = \Delta\varphi = 5°$. The characteristic size of the spot being illuminated on the sample surface was (3–5) × (8–16) mm. The size and position of the spot on the sample depends on the angles ϑ and φ, respectively. Soller slits were used for collimation of the incident and diffracted beams. The level of the intensity of reflexes at each PF is a fraction of the maximum value recorded over the entire PF, taking into account the correction for the background and defocusing. In order to estimate the anisotropy of diffuse scattering, the recording was made under conditions analogous to the PF recording, but with the counter installed at an angular separation 1–3° from the exact position of the diffraction peak. In the following, the patterns of intensity distribution will be termed as "diffuse scattering patterns (DSP)". The samples were observed in transmitted polarized light by using the optical Docuval microscope. The experimental results presented here are based on an analysis of the behavior of more than 20 samples, 30 diffraction patterns, 80 PF and DSP.

2. DISCUSSION OF RESULTS

The crystals of pure and strontium-doped KCl, which were grown from the melt, were subjected (before deformation) to annealing in a furnace at a temperature T_{an} = 600°C for eight hours, followed by slow cooling with the furnace. Figures 1a and 1b show the diffraction patterns of Sr-doped single crystals of KCl after such a thermal treatment. The surface of the sample on which diffraction patterns were recorded was perpendicular to the diffraction vector. It can be seen from the figures that, apart from the diffraction peaks corresponding to the single crystal of KCl, the diffraction pattern also contains some additional lines. The angles of diffraction at which these intensity peaks appear do not correspond to any of the possible conditions of reflection from the lattice planes of KCl. It is quite possible that the positions of additional lines in the case of the doped and annealed single crystals correspond to the planes {111} and {311} for β-$SrCl_2$ as indicated in Figs. 1a and 1b. Apart from these two lines, an additional line {331} for β-$SrCl_2$ (06–0537 according to the JCPDS catalog) was also observed for a number of samples.

After deformation of single crystals up to 70% at a temperature T_d = 250°C, the {200} KCl lines and their multiples continue to be the lines with the highest intensity on the diffraction patterns obtained from untilted surfaces of the samples containing 0.02 and 0.06 wt % Sr. However, samples held at room temperature undergo a change in the orientation of the crystallites of the KCl host matrix, as well as in the phase composition of the samples. Apart from the KCl diffraction lines {200} and {400} corresponding to the orientation of the initial single crystal and the texture of deformation [2, 6], the diffraction pattern also displays peaks {111}, {222}, {220}, and {420} for the KCl lattice (Figs. 2a and 2b), thus pointing clearly towards a transformation of the single crystal into a polycrystal. It also follows from the diffraction patterns shown in these figures that with the passage of the time of holding at RT, the lines corresponding to the β-$SrCl_2$ become weaker and finally vanish altogether. Instead, additional lines appear after 1–2 months holding time, their position corresponding in all probability to the reflexes (022) and (044) of the KSr_2Cl_5 phase (39–1136 according to JCPDS). The diffraction patterns of Sr-doped KCl crystals acquire up to five different lines corresponding to the KSr_2Cl_5 phase after deformation and holding at RT. Attempts at phase identification with the help of diffraction patterns recorded for specially prepared powders proved futile, both for doped and annealed single crystals, as well as for deformed and aged crystals, since diffraction lines not corresponding to KCl could not be observed in the powders. Apparently, there exist orientational relations between the KCl lattice and the lattices of Sr-containing phases. Unfortunately, we were not able to establish these relations.

While observing the recrystallization process in samples by transmission optical electron microscopy in polarized light, we discovered particles of the precipitated phase, which could be observed owing to their optical anisotropy against the background of optically isotropic KCl (Fig. 3a). The volume fraction of these particles in a deformed and aged crystal of KCl : 0.06 wt % Sr^{2+}, measured from the fraction occupied by them on the metallographic section is $\alpha = 0.06 \pm 0.01\%$. The average diameter of particles in this phase is about 5 μm. It can be seen from Figs. 3a and 3b that the particles of the second phase precipitated during the ageing of crystals

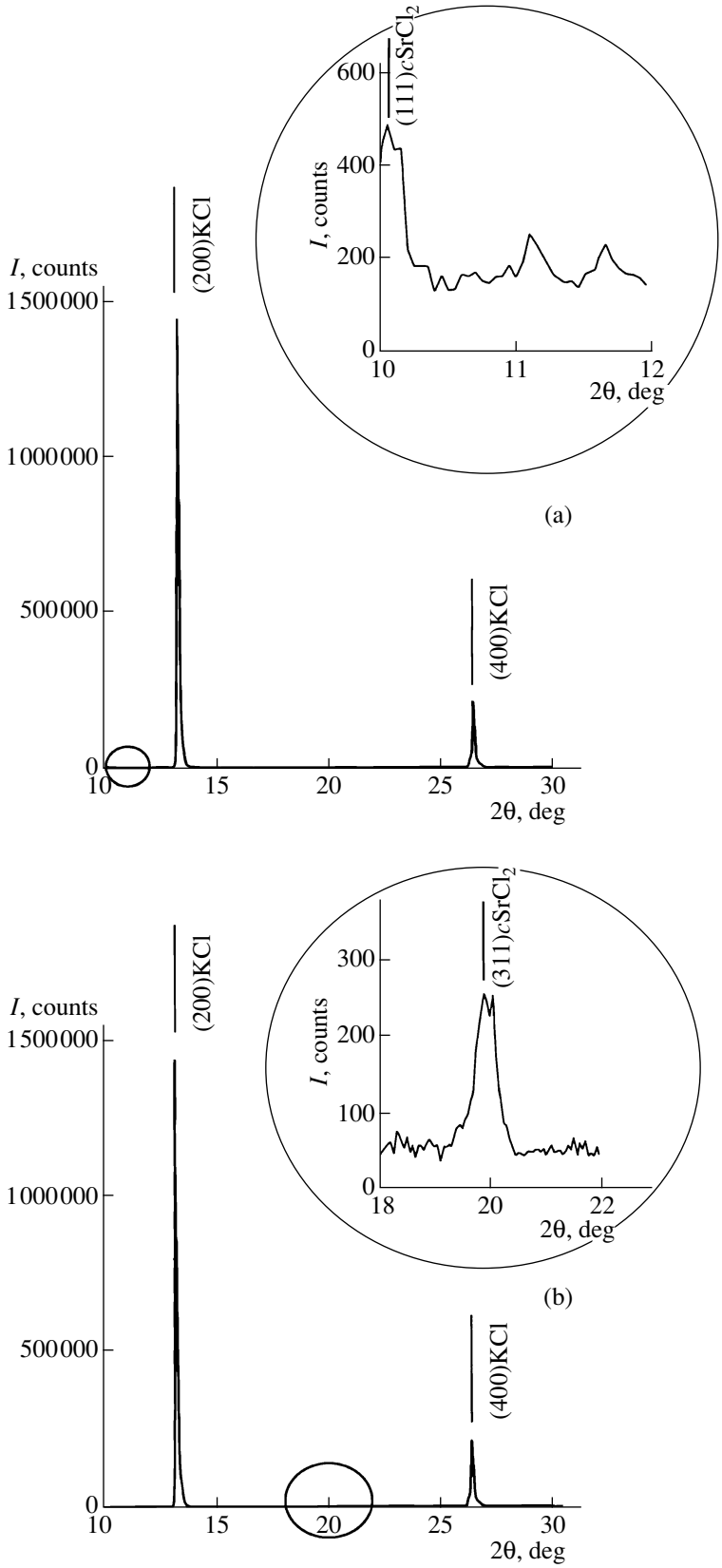

Fig. 1. Diffraction pattern for a KCl : 0.06 wt % Sr^{2+} single crystal after annealing at T_{an} = 650°C, face {100}; (a) segment of the diffraction pattern 2ϑ = 10–12 deg and (b) segment of the diffraction pattern 2ϑ = 18–22 deg.

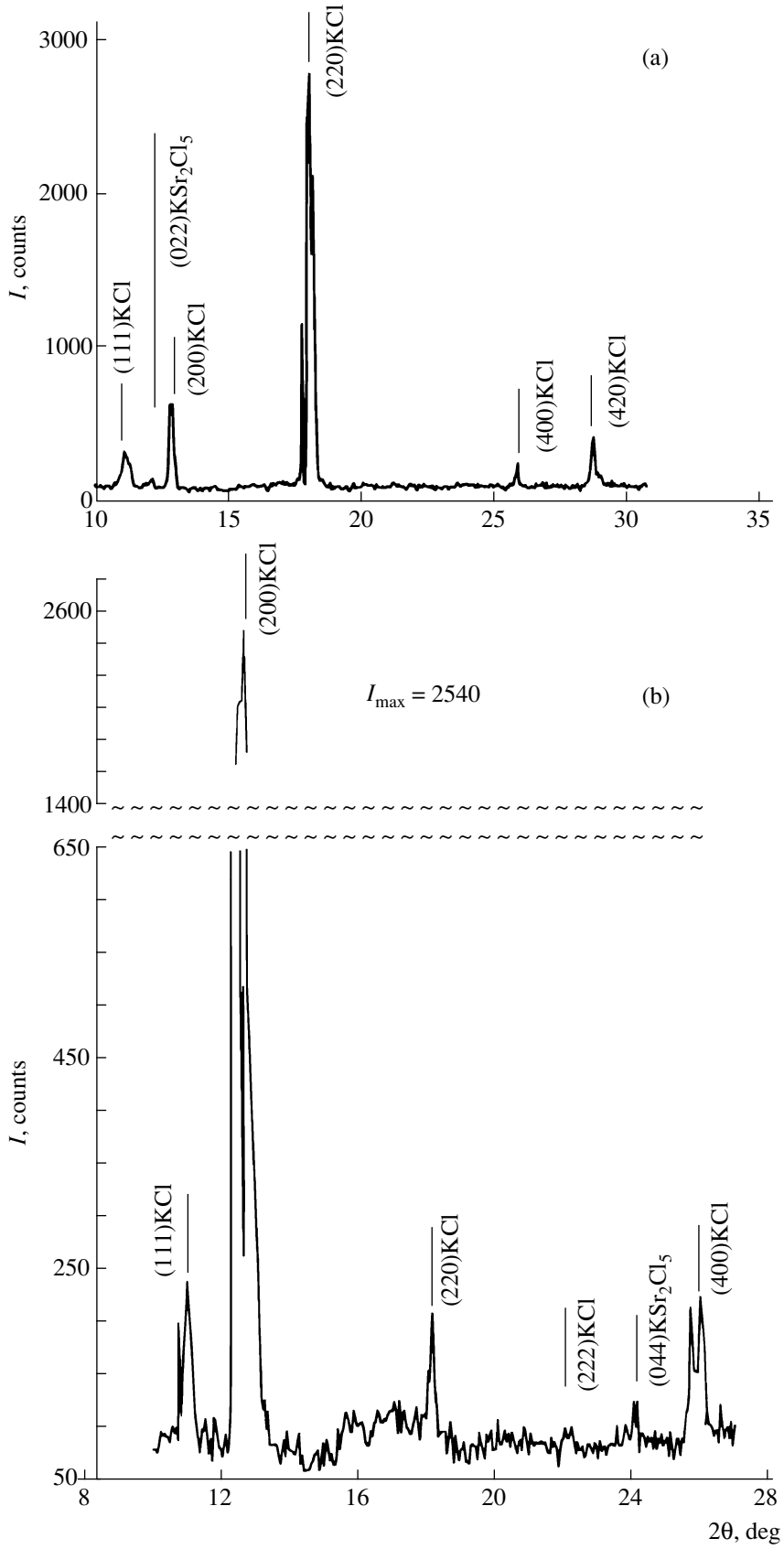

Fig. 2. Diffraction pattern for a metallographic section of the KCl : 0.06 wt % Sr^{2+} crystals parallel to {100} after deformation ε = 70%, T_d = 250°C and subsequent ageing for eight months at room temperature.

are located at the boundaries of the growing recrystallized grains, which are in twin orientations relative to the initial orientation of KCl {100}⟨001⟩ [6].

According to the estimates made on the basis of the model [9] assuming the presence of particles of KSr_2Cl_5 crossed by dislocations (the phase density determined by the x-ray studies is 2.176 g/cm^3), the volume fraction of such particles in a deformed and subsequently aged crystal of KCl : 0.06 wt %Sr may be as high as 0.05% for the observed diameter of about 5μm of the deformed grain, which agreed with our experimental data.

According to our estimates, the diffusion coefficient for strontium in such crystals is about 10^{-11} cm^2/s, which is an order of magnitude higher than the diffusion coefficient for divalent cations in KCl in the investigated temperature range [10]. The diffusion coefficient $D \sim \lambda^2\tau$ was estimated by using the experimentally obtained values of the diffusion length $\lambda \cong 0.015$ cm (the average radius of the recrystallized grain) and the diffusion time $\tau \cong 5 \times 10^6$ s (two months, during which the phase composition changed after deformation). Such high values of D are apparently due to faster-diffusion channels provided by the KCl lattice defects including grain boundaries.

Measurements of microhardness in crystals of KCl : 0.06 wt % Sr^{2+} after deformation under the above-mentioned conditions and subsequent "bivalent" holding at RT recorded that the microhardness in the recrystallized grains falls to values characteristic of pure undeformed KCl and amounts to 135 MPa, while the microhardness of non-recrystallized matrix is equal to 185 ± 5 MPa, which means that the increase in microhardness due to both doping and subsequent deformation is preserved almost entirely. Judging by the softening effect, the composition of the material in the recrystallized grains becomes close to pure KCl. The volume fraction of the recrystallized material in such crystals held at room temperature for two years does not exceed 8%.

The entire body of data obtained from the x-ray diffraction analysis, the measured microhardness of recrystallized grains and the deformed matrix, as well as measured and estimated volume fraction of the observed particles, suggests that the particles precipitated near the boundaries of the recrystallized grains and visible in polarized light are just the particles of the KSr_2Cl_5 phase.

According to [9], the effective deceleration of the growth of grains by the particles of the second phase precipitated along the boundaries can be ensured if the Zener criterion

$$d/D \le 3\alpha/2 \qquad (1)$$

is satisfied. This is indeed true for the case of KSr_2Cl_5 particles of diameter $d = 5\mu$m (having a volume fraction $\alpha = 0.06\%$) precipitated along the boundaries of recrystallized grains of diameter $D = 300$ μm (Figs. 3a and 3b).

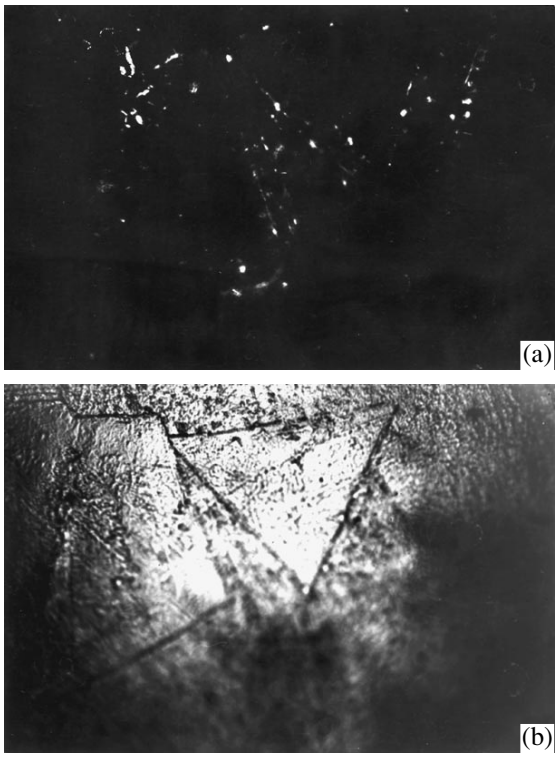

Fig. 3. Metallographic section of a KCl : 0.06 wt % Sr^{2+} crystal parallel to {100} after deformation $\varepsilon = 70\%$, T_d = 250°C and subsequent ageing for ten months at room temperature: (a) as seen in polarized light; (b) etching pattern.

This means that one of the reasons for the durability of these materials is a restriction on the increase in the volume fraction of the recrystallized material due to an impediment to the growth of new recrystallized grains by the second phase particles in accordance with the Granato–Lücke theory [11].

A noticeable factor in the analysis of diffraction patterns of deformed and aged Sr-doped KCl crystals (see Figs. 2a and 2b) is that prolonged holding at room temperature not only changes the orientations of the KCl matrix and the phase composition as mentioned above, but also causes the emergence and gradual intensification of the line {111} of KCl, which is usually quite weak (with a relative intensity 1%) or is not observed at all for the KCl phase (41–1476 according to the JCPDS catalog).

Apart from carrying out the phase analysis, we also analyzed a number of DSP of crystals in the initial, deformed, and aged state, recorded in the vicinity (1°–3°) of a reciprocal lattice site. The distribution of the intensity of diffuse background in the DSP of the initial single crystal, recorded in the vicinity of the Bragg peak {220}, displays a fourth-order symmetry (Fig. 4). Apparently, such a symmetry is associated with the nature of intensity distribution in the vicinity of diffraction peaks of single crystals. The symmetry pattern changes as a result of deformation. The DSP recorded

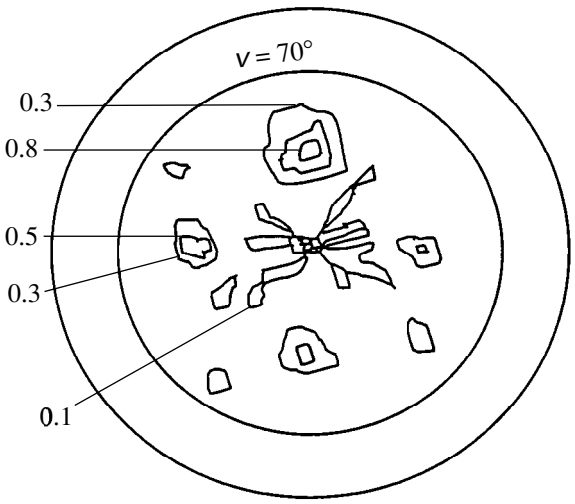

Fig. 4. Distribution of the diffuse scattering intensity in a KCl : 0.06 wt % Sr^{2+} single crystal, ϑ = 19.4 deg. The numbers in Figs. 4–6 show the intensity levels in fractions of the maximum value recorded on the given DSP.

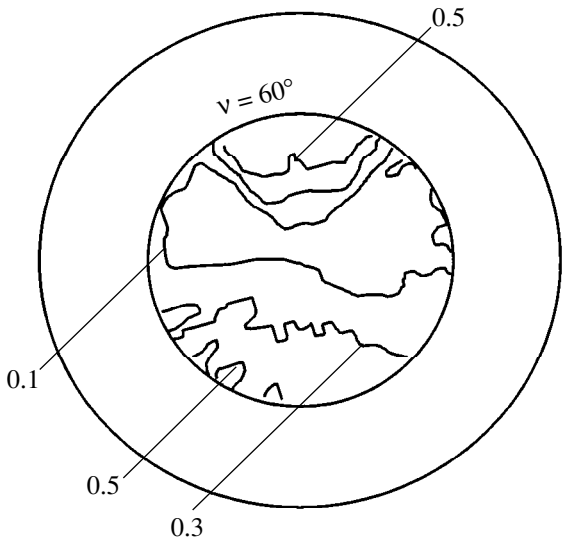

Fig. 5. DSP for a KCl : 0.06 wt % Sr^{2+} crystal after deformation ε = 70%, T_d = 250°C and ϑ = 19.4 deg.

under the same conditions now shows a twofold symmetry of the intensity of diffuse background (Fig. 5). The intensity of diffuse peaks is 4–5 times as high in the DSP of the initial doped single crystals, thus pointing towards a difference in the origin of the diffuse background symmetry in such cases and the absence of a connection between the symmetry of diffuse peaks of a deformed crystal and its orientational symmetry. As the holding time of the sample at RT is increased to two months, the diffuse scattering pattern changes, and a threefold symmetry is observed in the distribution of the intensity peaks (Fig. 6). The threefold symmetry of DSP is preserved upon subsequent holding at room temperature. A noticeable increase in the intensity and the emergence of threefold symmetry in the distribution of the diffuse scattering intensity peaks are observed in the vicinity of the Bragg reflexes. According to Huang [12, 13], this is the region in which the diffuse scattering of x-rays is observed at substitutional and interstitial point defects as well as their clusters. The emergence of the {111} KCl line on the diffraction patterns and of the threefold symmetry on DSP in the vicinity of the {220} KCl site were always observed simultaneously in our experiments. The simultaneous emergence of the threefold symmetry on diffraction patterns and on DSP leads to the assumption of the existence of yet another ageing mechanism for deformed Sr-doped KCl crystals, involving the interaction of the KCl lattice defects and the impurity. In particular, the contribution to the observed diffuse scattering pattern may come from impurity atmospheres, which interact with small- and medium-angle boundaries of deformed subgrains, dislocations and their pileups, as well as stacking faults, and thus ensure the stability of the deformed reinforced matrix.

The change in the symmetry of the light scattering indicatrix (λ = 550 nm) was observed earlier in ageing crystals of KCl : 0.01 mol % Sr [14], where the emergence of threefold symmetry in the scattering pattern was attributed by the authors of [14] to phase precipitation in a plane parallel to {111} KCl.

Thus, the measurements of mechanical properties reveal that under the combined action of strontium doping in amounts slightly exceeding the solubility limit (~0.01% [12]) and deformation under conditions which rule out dynamic recrystallization, it is possible to obtain a metastable structure, which is stable for 24 months, with a yield stress and hardness that are,

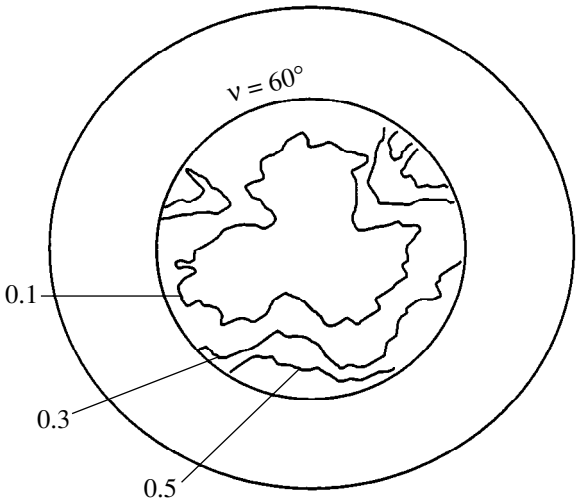

Fig. 6. DSP for a KCl : 0.06 wt % Sr^{2+} crystal after deformation ε = 70%, T_d = 250°C and subsequent ageing for one month at room temperature, ϑ = 19.4 deg.

respectively, 2.5 and 1.5 times the corresponding strength characteristics for pure KCl single crystals.

The main results of our investigations can be summarized as follows.

At least two ageing mechanisms are realized simultaneously in KCl : 0.02 wt % Sr^{2+} and KCl : 0.06 wt % Sr^{2+} crystals over a period of two months from the moment of their deformation ($\varepsilon = 70\%$ for $T_d = 250°C$), which ensure the preservation of high strength properties, acquired as a result of deformation, at least two years during which the crystals were held at room temperature.

The first mechanism of ageing is associated with the precipitation of particles of the KSr_2Cl_5 phase (39–1136 in JCPDS) along the boundaries of growing grains during recrystallization. These particles impede the growth of recrystallized twin grains, thus preventing the increase of the volume fraction of the recrystallized material beyond 8%.

The second type of ageing, reflected in the simultaneous emergence of the {111} KCl line on the diffraction patterns and an increase in the intensity of diffuse scattering according to Huang's mechanism, involves the interaction of KCl lattice defects with the impurity, ensuring stability of the matrix reinforced by deformation.

ACKNOWLEDGMENTS

The authors are indebted to V. K. Karandashev for analyzing the concentration of impurity elements in KCl samples.

REFERENCES

1. M. Guillope, *Contribution a l'Etude de la Recrystallisation Dynamique. These* (A l'Universite Pierre et Marie Curie, Paris, 1982).
2. E. B. Borisenko, B. A. Gnesin, O. O. Likhanova, and I. B. Savchenko, Fiz. Tverd. Tela (St. Petersburg) **37**, 2029 (1995) [Phys. Solid State **37**, 1105 (1995)].
3. S. N. Val'kovskiĭ and M. F. Imaev, Fiz. Tverd. Tela (Leningrad) **24**, 3229 (1982) [Sov. Phys. Solid State **24**, 1832 (1982)].
4. B. G. Koepke, R. H. Anderson, E. Bernal, and R. S. Stokes, J. Appl. Phys. **45**, 969 (1974).
5. E. B. Borisenko and B. A. Gnesin, Textures Microstruct. **26–27**, 369 (1996).
6. E. B. Borisenko and B. A. Gnesin, Fiz. Tverd. Tela (St. Petersburg) **41** (2), 259 (1999) [Phys. Solid State **41**, 230 (1999)].
7. S. A. Saltykov, *Stereometric Metallography* (Metallurgiya, Moscow, 1970).
8. M. M. Borodkina and É. N. Spektor, *X-ray Diffraction Analysis of the Texture of Metals and Alloys* (Metallurgiya, Moscow, 1981).
9. M. A. Shtremel', *Strength of Alloys* (Mosk. Inst. Stali i Splavov, Moscow, 1997), Chap. II, p. 390; *Strength of Alloys* (Mosk. Inst. Stali i Splavov, Moscow, 1999), Chap. I, p. 339.
10. P. Suptitz and J. Teltow, Phys. Status Solidi **23**, 9 (1967).
11. K. Lücke and H. P. Stüwe, Acta Metall. **19**, 1087 (1971).
12. U. Schubert, H. Metzger, and J. Peisl, J. Phys. F: Met. Phys. **14**, 2457 (1984).
13. H. Dosch, U. Schubert, H. Metzger, and J. Peisl, J. Phys. F: Met. Phys. **14**, 2467 (1984).
14. V. G. Kononenko and V. D. London, Fiz. Tverd. Tela (Leningrad) **14**, 2560 (1972) [Sov. Phys. Solid State **14**, 2217 (1972)].

Translated by N. Wadhwa

Physics of the Solid State, Vol. 42, No. 7, 2000, pp. 1306–1309. Translated from Fizika Tverdogo Tela, Vol. 42, No. 7, 2000, pp. 1268–1271.

MAGNETISM AND FERROELECTRICITY

Nonlinear Effects of Magnetization Precession near Ferromagnetic Resonance

A. M. Shutyĭ and D. I. Sementsov

Moscow State University (Ul'yanovsk Branch), ul. L. Tolstogo 42, Ul'yanovsk, 432700 Russia

e-mail: sements@quant.univ.simbirsk.su

Received December 7, 1999

Abstract—The features of precession of the magnetic moment of a film near ferromagnetic resonance are investigated which are due to the magnetic-moment nutation in the effective field and to the frequency-doubling effect. The contribution to this precession from harmonics with frequencies which are multiples of the basic resonance frequency is analyzed for a garnet ferrite film of the (111) type in a perpendicular bias magnetic field.

INTRODUCTION

Nonlinear dynamics of the magnetization in magnetically ordered crystals is of interest because of the variety of nonlinear effects that occur when the dissipative spin system is subjected to a microwave (MW) pumping field [1–3]. One of the manifestations of the nonlinear behavior of the magnetization at large precession angles is the frequency-doubling effect, which takes place only when the MW field is linearly polarized. Only this nonlinear effect, as a rule, is considered in the case of the uniform magnetization precession in a transverse MW field. In this paper, however, it is shown that, for certain symmetry of the anisotropy field of the material, which is correlated with the crystallographic symmetry, higher harmonics of the basic precession frequency are dominant in the dynamics of the magnetic moment in its nutation under ferromagnetic-resonance (FMR) conditions. The behavior of the magnetization in the case of large angles of its precession is also of interest, because this phenomenon can be used for modulation of laser radiation, the effectiveness of which depends on the precession angle [4–6]. In this paper, we consider the features of the dynamics of the magnetization vector under nonlinear FMR conditions in a film of a cubic crystal in the case where the [111] crystallographic axis is perpendicular to the plane of the film.

There are two mechanisms of the energy transfer to spin waves from the uniform magnetization precession in a perpendicular bias magnetic field [2, 3]. One of these mechanisms is associated with a three-magnon process, in which one magnon (with wave vector $\mathbf{k} = 0$) is destroyed and two magnons are created with wave vectors $\mathbf{k}$ and $-\mathbf{k}$, respectively, and the frequency $\omega_k = \omega/2$, where ω is the frequency of uniform precession. The other mechanism is associated with a four-magnon process, in which two magnons with $\mathbf{k} = 0$ are destroyed and other two magnons are created with wave vectors $\mathbf{k}$ and $-\mathbf{k}$ and the frequency $\omega_k = \omega$. Therefore, for the angles of uniform precession to be large, its frequency must coincide with the lowest frequency of the spin wave spectrum, that is, with the frequency of spin waves the wave vector of which is parallel to the bias field and $\mathbf{k} = 0$ (the FMR frequency). In this case, neither of the two mechanisms of energy transfer from uniform precession to spin waves operates. In [7, 8], it was shown that, at the FMR frequency, the precession angles are as large as $\phi \simeq 20°$–$25°$ in a $Y_{2.9}La_{0.1}Fe_{3.9}Ga_{1.1}O_{12}$ garnet ferrite film grown on a gadolinium gallium garnet substrate.

1. BASIC EQUATIONS AND RELATIONSHIPS

Epitaxial garnet ferrite films are monocrystalline and have a cubic crystal lattice. In this paper, the direction [111] is assumed to be normal to the film surface and is taken as the *x* axis, while the *y* and *z* axes are parallel to the directions $[11\bar{2}]$ and $[\bar{1}10]$, respectively. The polar and azimuthal angles θ and ψ of the magnetization vector **M** are measured from the *x* and *y* axes, respectively. The dynamics of the magnetization in an external static (**H**) and a time-dependent (**h**) magnetic field (which are assumed to be mutually perpendicular, $\mathbf{H} \perp \mathbf{h}$, in what follows) is described by the following equations of motion, written in the spherical coordinate system [2]:

$$\begin{aligned} \dot{\psi} M \sin\theta &= \gamma \frac{\partial F}{\partial \theta} + \frac{\lambda}{M} \frac{1}{\sin\theta} \frac{\partial F}{\partial \psi}, \\ \dot{\theta} M &= \frac{\lambda}{M} \frac{\partial F}{\partial \theta} - \gamma \frac{1}{\sin\theta} \frac{\partial F}{\partial \psi}, \end{aligned} \tag{1}$$

where γ is the gyromagnetic ratio, λ is the damping parameter, and F is the free energy density. Solving these equations allows one to find the precession frequency of the magnetic moment about its equilibrium

direction and the time dependence of the angles ψ and θ for given geometry of applied fields and a given time-dependent external field. The resonance frequency ω_r is given by

$$\omega_r = \gamma H_{\text{eff}} = \frac{\gamma}{M\sin\theta}(F_{\theta\theta}F_{\varphi\varphi} - F_{\theta\varphi}^2)^{1/2}, \qquad (2)$$

where the second derivatives of the free energy density are taken for equilibrium angles θ_0 and ψ_0, which are found from the conditions $\partial F/\partial\theta = 0$ and $\partial F/\partial\psi = 0$. For the orientation of the crystallographic axes indicated above, the free energy density has the form

$$F = -\mathbf{M}(\mathbf{H} + \mathbf{h}) + (K_u - 2\pi M^2)\sin^2\theta + K_1 \times\left(\frac{1}{4}\sin^4\theta + \frac{1}{3}\cos^4\theta + \frac{\sqrt{2}}{3}\sin^3\theta\cos\theta\cos 3\psi\right), \qquad (3)$$

where K_u and K_1 are the growth-induced and crystalline anisotropy constants, respectively. Substituting (3) into (2), the resonance frequency can be found for an arbitrary orientation of the equilibrium magnetization.

The character of precession of the magnetization depends heavily on its amplitude (which is a function of the amplitude and polarization of the MW field), as well as on the strength and type of magnetic anisotropy. When the precession angle ϕ is small, the linear FMR occurs at frequencies $\omega \approx \omega_r$, for which the time dependences $\theta(t)$ and $\psi(t)$ can be found from the equations of motion linearized with respect to small deflections of the magnetization vector from its equilibrium position. As the precession angle increases, the contribution to these dependences from higher harmonics of the basic precession frequency grows and nutation of the vector **M** becomes significant. In this case, the linear approximation to equations (1) is inadequate. In order to qualitatively evaluate the nonlinear effects, we expand the time-dependent precession angle $\phi(t)$ into the series

$$\phi(t) = \sum \phi_{n\omega}\exp(i\omega n t). \qquad (4)$$

At small precession angles, $\phi(t)$ is approximated with a high degree of accuracy by the constant angle ϕ_0, and higher harmonics can be neglected when describing the magnetization motion. Solving the equations of motion shows that, when the MW field is linearly polarized and the precession angle of the magnetic moment is large, the nonlinear frequency-doubling effect [2] becomes significant and leads to the growth of the second harmonic $\phi_{2\omega}$ in (4). Approximate analytical expressions for this effect can be obtained by writing the projection of the magnetization onto its equilibrium direction in the form $M_{\phi=0} \simeq M - m^2/2M$ (valid for $m \ll M$) and substituting the instantaneous MW magnetization m calculated from the linearized equations of motion. As a result, we obtain the following expression for the precession angle oscillating with the double frequency when the precession amplitude is large:

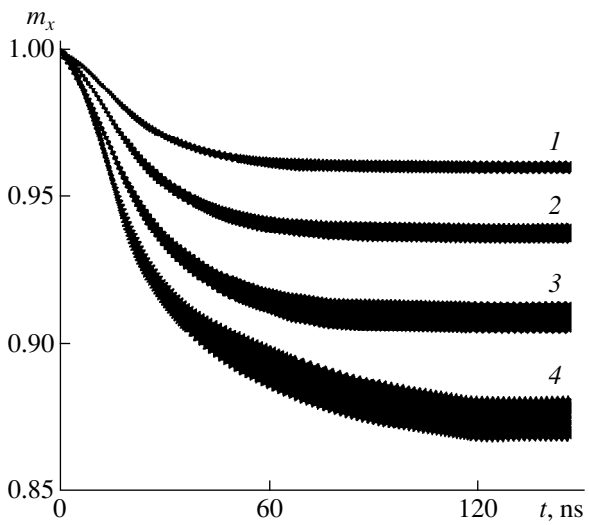

Fig. 1. Time dependence of the longitudinal component of the magnetization precessing under FMR conditions in an MW field of h = 2, 2.5, 3, and 3.5 Oe and a bias field of H = 616, 613, 611, and 607 Oe (curves *1* to *4*, respectively).

$$\cos\phi = \cos\phi_0 - \frac{m}{M}\cos(2\omega t + \theta), \qquad (5)$$

where θ is the initial phase of nutation, which depends on the orientation of the linearly polarized MW field in the plane perpendicular to the direction of the equilibrium magnetization vector. In this case, the average precession angle ϕ_0 and the amplitude of oscillations are given by

$$\cos\phi_0 = 1 - \frac{h^2}{4M^2}(|\chi|^2 + |\chi_a|^2),$$
$$m = \frac{h^2}{4M}(\chi^2 - \chi_a^2), \qquad (6)$$

where $\chi = \chi' - i\chi''$ and $\chi_a = \chi_a' - i\chi_a''$ are the diagonal and off-diagonal complex components, respectively, of the high-frequency susceptibility tensor, which determines the linear relationship between the MW field and magnetization. In the resonance, we have $\chi' = M/2H_{\text{eff}}$, $\chi_a' = 0$, $\chi'' = M\omega_r/2\gamma H_{\text{eff}}$, and $\chi_a'' = M^2\gamma/2\lambda H_{\text{eff}}$.

2. NUMERICAL ANALYSIS

In order to further analyze the features of the magnetization precession and to treat the effects of the crystal structure, the type of magnetic anisotropy of the film, and the amplitude and polarization of the MW field, one has to solve equation (1) numerically. In what follows, we consider a structure with parameters that are approximately equal to those of a concrete garnet fer-

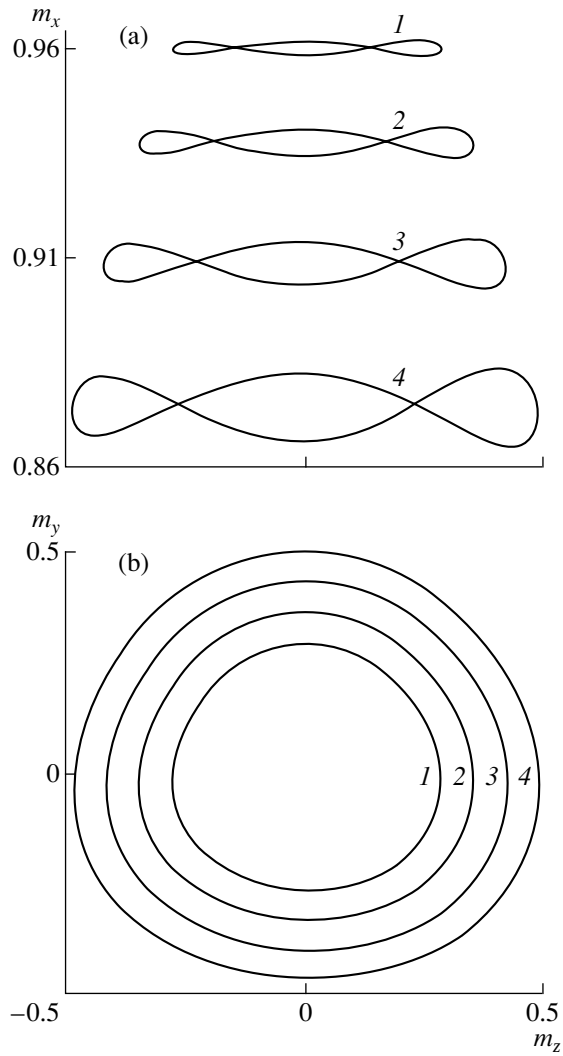

Fig. 2. Projections $m_\alpha = M_\alpha/M$ onto (a) the *xz* plane and (b) the *yz* plane of the magnetization which precesses along a stationary orbit in a field *H* parallel to the [111] axis normal to the film surface. The curves are labeled as in Fig. 1.

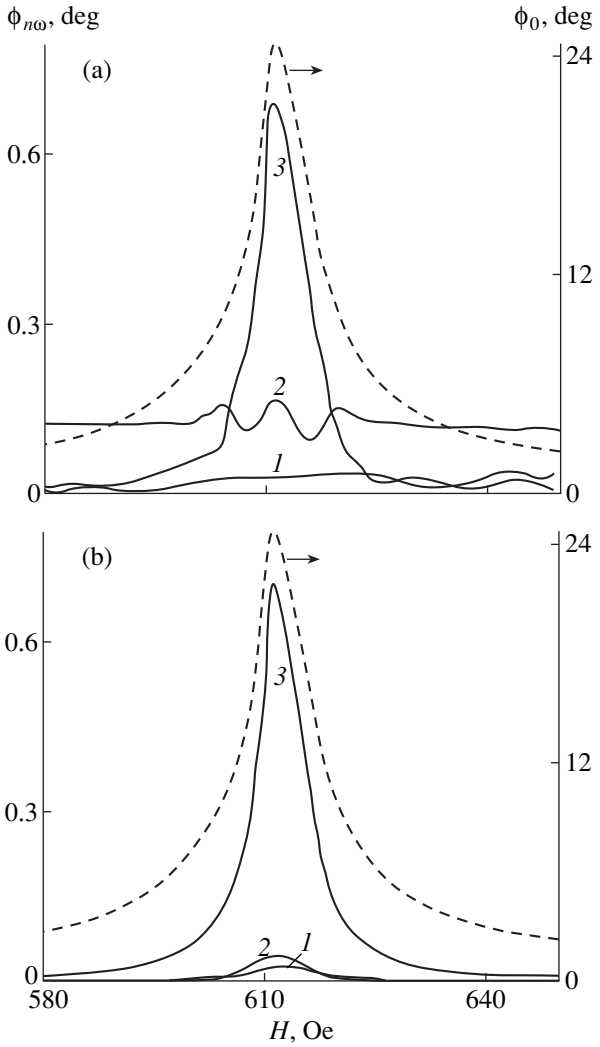

Fig. 3. Contributions to the precession angle from the different harmonics $\phi_{n\omega}$ ($n = 0$ for dashed lines; and $n = 1, 2, 3$ for solid lines) as a function of bias magnetic field **H** for (a) the linear polarization and $h = 3$ Oe and (b) the circular polarization and $h = 1.5$ Oe of the MW field.

rite film [9]: $4\pi M = 214.6$ G; $\gamma = 1.755 \times 10^7$ (Oe · s)$^{-1}$; $\lambda = 3 \times 10^6$ s^{-1}; $K_u = -10^3$ erg/cm^3; and $K_1 \simeq -10^3$ erg/cm^3. For the sake of simplicity, we assume that the static magnetic field **H** is normal to the film surface and its magnitude is such that the equilibrium magnetization vector is also normal to the film ($\theta_0 = 0$). In this case, the resonant precession frequency turns out to be $\omega_r = \gamma H_{\text{eff}}$, where, according to (2), the effective field is given by

$$H_{\text{eff}}(0) = H - 4\pi M + \frac{2}{M}\left(K_u - \frac{2}{3}K_1\right). \qquad (7)$$

Figure 1 shows the time dependence of the reduced longitudinal component $m_x = M_x/M$ of the magnetization vector precessing with the FMR frequency $\omega_r = 6.3 \times 10^9$ s^{-1}. The MW field is assumed to be linearly polarized and applied along the *y* axis. In order to fulfill the resonance conditions, the crystalline anisotropy constant is adjusted using (7) for each of the magnetic-field values of Fig. 1 and lies in the range $K_1 \approx -1000 \pm 60$ erg/cm^3. The results presented in Fig. 1 show that, for the material parameters chosen, the precession orbit of the magnetic moment becomes stationary within 60–120 ns, depending on the precession angle; nutation of the magnetic moment becomes more pronounced with an increase in the precession amplitude. Figure 2 presents the projections of the magnetic moment onto the coordinate planes *xz* (Fig. 2a) and *yz* (Fig. 2b) as calculated for the stationary precession orbits in magnetic fields of Fig. 1. From the shape of the trajectories, it follows that, for the given FMR geometry, the third harmonic of the resonance frequency ω_r is dominant in the nutation of **M**. The numerical analysis also reveals that the change in the direction of MW field oscillations in the *yz* plane has no effect on the orientational contribution

from the third harmonic $\phi_{3\omega}$ to the magnetization precession, but affects the orientational contribution from the second harmonic [6], as is seen from (5). Thus, under the FMR conditions, both the shape and the orientation of the trajectory of the magnetic moment depend only slightly on the direction of the MW field for the orientation of the bias magnetic field and of the crystallographic axes in question.

Figure 3 shows the average precession angle ϕ_0 (dashed lines) and the contributions to the magnetic-moment nutation from the first three harmonics $\phi_{n\omega}$ (n = 1, 2, 3, solid lines *1–3*, respectively) as a function of the bias magnetic field H; the MW field is linearly polarized along the y axis and has an amplitude of h = 3 Oe (Fig. 3a) or is circularly polarized in the yz plane and has an amplitude of h = 1.5 Oe (Fig. 3b). In both cases, the crystalline anisotropy constant is the same and equal to $K_1 = -10^3$ erg/cm^3. It is seen that, although the MW field amplitudes are significantly different, the amplitudes of the fundamental harmonics of the precession angle for the linear and circular field polarizations are virtually equal ($\phi_0 \cong 24°$). At the resonance frequency, where ϕ_0 is maximum, the magnitude of the third harmonic $\phi_{3\omega}$ far exceeds those of the first (ϕ_ω) and second ($\phi_{2\omega}$) harmonics. This is the case for both the linear and circular polarizations of the MW field. Away from the FMR, for the linear MW field polarization, only the frequency doubling effect is noticeable and the second harmonic dominates. However, the magnitude of the latter is virtually independent of the bias magnetic field and is small ($\phi_{2\omega} \simeq 0.1°$) for the given MW field amplitude. In the case of the circular polarization of the MW field, the contribution from the second harmonic to the magnetization vector nutation is roughly equal to that from the first harmonic and can be neglected in all range of the field H covered.

The nutation amplitude increases with the precession angle, but the contribution from the third harmonic only becomes significant near the resonance. Figure 4 shows the dependence of the zeroth harmonic $\phi_0^{(r)}$ of the resonant magnetization precession on the static field H. As before, for each value of H, the crystalline anisotropy constant K_1 is adjusted to fulfill the resonance conditions at frequencies $\omega_r/2\pi$ = 1, 0.975, and 0.95 GHz (curves *1* to *3*, respectively). The amplitude of the linearly polarized MW field is h = 3 Oe (solid lines) and h = 2.5 Oe (dashed lines). We also note that the dashed lines coincide with the curves calculated for the circularly polarized MW field with h = 1.5 Oe. Similar curves are also obtained when K_1 is kept fixed, while K_u is adjusted to fulfill the resonance conditions. For the MW field with a given frequency, polarization, and amplitude, the angle of resonant precession is maximum only at certain values of the static and induced and crystalline anisotropy fields. As the amplitude of the MW field is increased, the peak of the $\phi_0^{(r)}(H)$ dependence shifts to lower H values and becomes more pronounced.

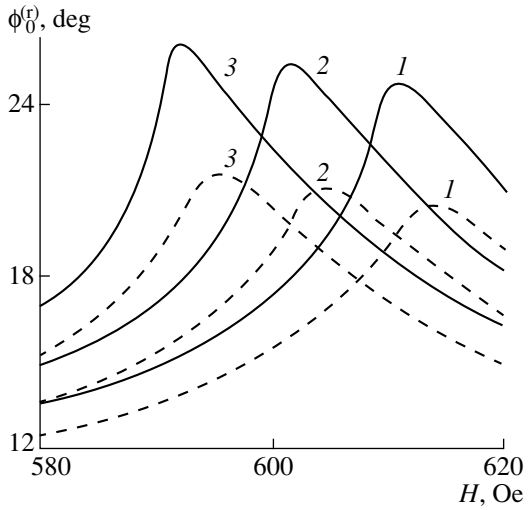

Fig. 4. Zeroth harmonic $\phi_0^{(r)}$ in the resonant magnetization precession at frequencies $\omega_r/2\pi$ = 1, 0.975, and 0.95 GHz (curves *1* to *3*, respectively) as a function of the bias field H for h = 3 Oe (solid lines) and h = 2.5 Oe (dashed lines).

Thus, the analysis has shown that, in a film of a cubic crystal, when the magnetic moment precesses with a large angle about the crystallographic axis [111] at the FMR frequency, the dominant contribution to the magnetization nutation is from the third harmonic of the basic precession frequency. This is the case for both the linear and circular polarizations of the MW field. Since the [111] axis is a threefold symmetry axis, one can expect that, when the magnetic moment precesses about a fourfold symmetry axis of the [100] type, the third harmonic will make only a negligible contribution to the magnetization nutation, whereas the fourth harmonic will be dominant.

REFERENCES

1. Ya. A. Monosov, *Nonlinear Ferromagnetic Resonance* (Nauka, Moscow, 1971).
2. A. G. Gurevich and G. A. Melkov, *Magnetic Oscillations and Waves* (Nauka, Moscow, 1994).
3. S. M. Rezende and F. M. de Agiar, Proc. IEEE **78** (6), 5 (1990).
4. A. M. Prokhorov, G. A. Smolenskiĭ, and A. N. Ageev, Usp. Fiz. Nauk **143** (1), 33 (1984) [Sov. Phys. Usp. **27**, 339 (1984)].
5. A. A. Stashkevich, Izv. Vyssh. Uchebn. Zaved. Fiz. **3** (4), 5 (1989).
6. D. I. Sementsov and A.M. Shutyĭ, Opt. Spektrosk. **84** (2), 280 (1998) [Opt. Spectrosc. **84**, 238 (1998)].
7. B. Neite and H. Dötsch, J. Appl. Phys. **62** (2), 648 (1987).
8. B. Neite and H. Dötsch, Proc. SPIE **1018**, 115 (1989).
9. V. V. Randoshkin and A. Ya. Chervonenkis, *Applied Magnetooptics* (Énergoatomizdat, Moscow, 1990).

Translated by Yu. Epifanov

Physics of the Solid State, Vol. 42, No. 7, 2000, pp. 1310–1312. Translated from Fizika Tverdogo Tela, Vol. 42, No. 7, 2000, pp. 1272–1274.

MAGNETISM AND FERROELECTRICITY

Electrical and Magnetic Properties of Lead-Substituted Lanthanum Ferrimanganites

V. V. Parfenov, Sh. Sh. Bashkirov, A. A. Valiullin, and A. V. Aver'yanov

Kazan State University, ul. Lenina 18, Kazan, 420008 Tatarstan, Russia

e-mail: Viktor.Parfenov@ksu.ru

Received December 15, 1999

Abstract—The temperature dependences of the electrical conductivity, thermopower, and magnetoresistance for single crystals of lead-substituted lanthanum ferrimanganites are investigated. The data on the magnetic microstructure obtained by Mössbauer spectroscopy are analyzed. An inversion of the magnetoresistance sign with an increase in temperature and the giant positive magnetoresistance are found for one of the samples. The magnetoresistance quadratically depends on the field, and its temperature dependence exhibits a maximum.

In the present work, we measured the temperature dependences of the electrical parameters and magnetic susceptibility for two samples of lead-substituted lanthanum ferrimanganites (see table) and obtained the Mössbauer spectra of these samples. The principal difference between these samples and the diamagnetically substituted rare-earth manganites, which have been studied in many works (see, for example, [1]), lies in the partial substitution of the Fe^{3+} ions for Mn^{3+} ions in the 3*d* sublattice. The second important difference is that both samples were single crystals, whereas the majority of the aforementioned works dealt with the ceramic samples or thin films. This circumstance is essential, because the assumption on the structural imperfection of polycrystalline samples is of fundamental importance in the models describing unusual kinetic phenomena in manganites [2].

The measurements of the magnetic susceptibility at room temperature demonstrated that the susceptibility χ is less than 10^{-4} for both crystals. This result is unexpected, because, according to [1], the $La_{0.6}Pb_{0.4}MnO_3$ compound, which is close to our samples in the degree of diamagnetic substitution, represents the ferromagnet with T_c = 370 K. In order to refine the character of magnetic ordering at T = 295 K, we measured the Mössbauer spectra for these crystals. The Mössbauer spectrum of the first sample shows a hyperfine magnetic structure (Fig. 1a). The spectrum treatment gave two sextets with the effective fields $H_{\text{eff}}(1)$ = 515 kOe and $H_{\text{eff}}(2)$ = 505 kOe. The low magnetic susceptibility and the data of Mössbauer spectroscopy indicate an antiferromagnetic ordering in sample 1. The Mössbauer spectrum of the second crystal at T = 295 K exhibits a paramagnetic doublet (Fig. 1b).

The electrical properties of the ferrimanganites studied in this work also substantially differ from those of the $La_{1-x}D_xMnO_3$ manganites (D = Ca^{2+}, Sr^{2+}, Pb^{2+}, …). The resistivity of ferrimanganites is several orders of magnitude greater than that of manganites with the same degree of diamagnetic substitution (the table). The semiconductor-type conductivity is observed for both the magnetically ordered sample 1 and paramagnetic sample 2 over the entire temperature range under investigation (290–700 K). The thermopower sign for both samples corresponds to the hole-type conductivity. However, the thermopower of the first sample is almost independent of temperature, whereas this quantity for the second sample has a maximum at 370 K. A variation in the activation energy of conduction for this sample is observed at approximately the same temperature (table).

The electrical properties of our samples drastically differ from those of the rare-earth manganites, which are close to our samples in the degree of diamagnetic substitution. In our opinion, this difference can be explained within the model of the magnetic two-phase state of these objects [1]. In the case of rare-earth manganites, when the concentration of doubly charged ions (Ca, Pb, etc.) is equal to 0.3 per formula unit, the ferromagnetic phase with a high conductivity is the main magnetic

Electrical parameters of studied samples

No.	Composition	E_a, eV	Θ, μV/K	R, kΩ cm
1	$La_{0.67}Pb_{0.33}Mn_{0.63}Fe_{0.37}O_3$	0.24	26	8.02
2	$La_{0.67}Pb_{0.33}Mn_{0.78}Fe_{0.22}O_3$	0.14	250*	5.95
		0.25		
3	$LaMnO_3$**	–	–	0.2
4	$La_{0.6}Sr_{0.4}MnO_3$**	–	–	10^{-6}

*Thermoelectric coefficient Θ at a maximum.

**According to the data from [1].

1063-7834/00/4207-1310$20.00 © 2000 MAIK "Nauka/Interperiodica"

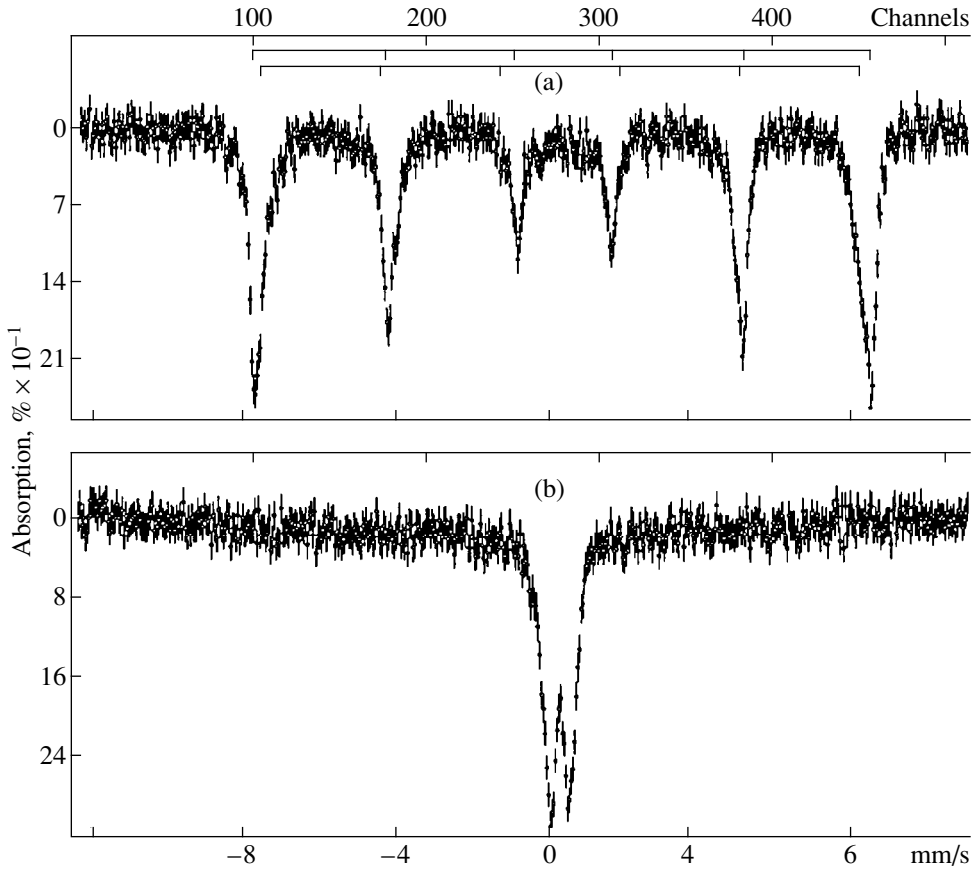

Fig. 1. Mössbauer spectra for (a) sample 1 and (b) sample 2.

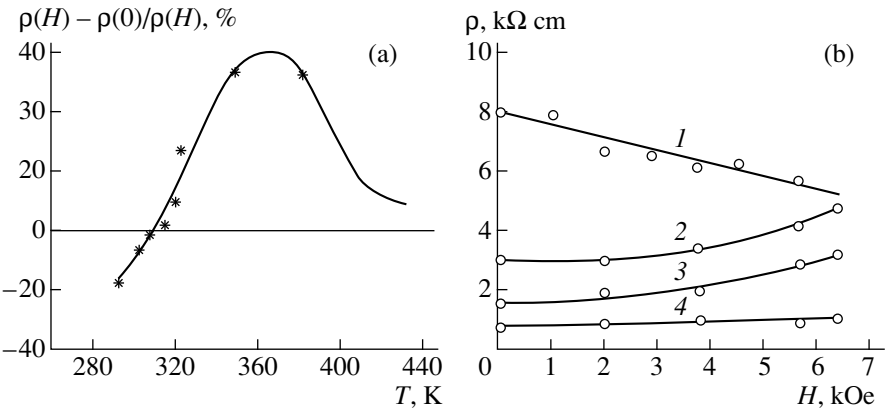

Fig. 2. Magnetoresistance of sample 1: (a) temperature dependence and (b) dependence of the resistivity on the magnetic field. Temperature, K: (*1*) 290, (*2*) 345, (*3*) 382, and (*4*) 427.

phase. However, upon a partial substitution of the Fe^{3+} ions for Mn^{3+} ions in the 3*d* sublattice, the antiferromagnetic "dielectric" phase with inclusions of the ferromagnetic phase in the form of small clusters ("ferrons") is stabilized in the samples. A possible reason for this phenomenon is a high degree of indirect exchange interaction in the Fe–O–Fe and Fe–O–Mn chains compared to the Mn–O–Mn exchange interaction [3].

The behavior of magnetoresistance is also unusual. This parameter was measured in magnetic fields of 0–7 kOe in the range from room temperature to 500 K. In order to quantitatively describe the effect of magne-

toresistance, we chose the ratio of the difference in resistivities in the presence of the external field and without field to the resistivity in the presence of the external field. This ratio is conventionally used for describing the giant magnetoresistance effect.

The measurements for the $La_{0.67}Pb_{0.33}Mn_{0.78}Fe_{0.22}O_3$ sample demonstrated an increase in the resistivity in the magnetic field, i.e., the positive magnetoresistance, over the entire range of magnetic fields and temperatures. The magnetoresistance did not exceed 4% for all temperatures (290–500 K) and magnetic fields; i.e., no giant magnetoresistance was observed.

A radically different situation is observed for the $La_{0.67}Pb_{0.33}Mn_{0.63}Fe_{0.37}O_3$ sample (Fig. 2). The magnetoresistance is negative at temperatures equal or close to room temperature. Although the magnetoresistance is not giant, its value is one order of magnitude greater than the magnetoresistance of nonmagnetic semiconductors. The magnetoresistance decreases in absolute value with an increase in temperature and changes the sign at $T = 310$ K. The magnetoresistance is positive at a temperature above 310 K, reaches a maximum at $T = 365$ K, and decreases at higher temperatures. The maximum positive magnetoresistance reaches ~100%. As far as we know, our findings are the first experimental observations of the positive magnetoresistance in oxide magnets whose magnetoresistance is two orders of magnitude greater than the typical effect observed for "classical" semiconductors.

In many works (see, for example, [1]) concerned with the theoretical justification of the giant magnetoresistance effect in manganites and the related compounds, the electrical parameters of samples are considered in the temperature range below the Curie (Néel) temperature when the magnetoresistance is negative. An attempt to describe the behavior of the electrical parameters for a magnetic semiconductor in both the spin-wave and paramagnetic regions by using an unified approach was made in [4]. In order to describe the interrelation between the electrical properties of samples and the magnetic ordering, the magnetoelectric parameter Γ was introduced in [4]. This parameter modifies the permittivity ε

$$\zeta = \varepsilon(1 - \Gamma), \tag{1}$$

where ζ is the "effective" permittivity. It is precisely this quantity which appears in the expression for the density of states in the band tails and in the formula for the charge carrier concentration

$$n \sim g(\zeta), \tag{2}$$

as well as in the expression for the relaxation time of carrier momentum τ, that is,

$$\tau \sim \zeta^2. \tag{3}$$

Since the resistivity is a function of the charge carrier concentration and time τ, it depends on Γ. For the magnetically ordered sample,

$$\Gamma \sim T \sim H^{-2}, \tag{4}$$

i.e., the Γ parameter and, consequently, the sample resistivity ρ monotonically decreases with an increase in the external field. As a result, the magnetoresistance of the sample is negative and linearly depends on the field, as is the case in sample 1.

On the other hand, the magnetoelectric parameter in the paramagnetic region is quadratic in the field (or increases as the square of the magnetic moment M), which leads to the positive magnetoresistance of the sample,

$$\Gamma \sim \chi M^2. \tag{5}$$

The Γ parameter in the paramagnetic region should decrease with an increase in temperature due to a decrease in the magnetic susceptibility χ of the sample. In this case, the magnetoresistance passing through a maximum remains positive and decreases in magnitude decreases. Such behavior is observed experimentally in sample 2 over the entire temperature range under investigation and in sample 1 at temperatures above the inversion point of the magnetoresistance sign.

ACKNOWLEDGMENTS

This work was supported by the Ministry of Science and Technology of the Russian Federation, project no. 01.960.010018.

REFERENCES

1. É. L. Nagaev, Usp. Fiz. Nauk **166** (8), 833 (1996) [Phys. Usp. **39**, 781 (1996)].
2. N. I. Solin, A. A. Samokhvalov, and S. V. Naumov, Fiz. Tverd. Tela (S.-Peterburg) **40**, 1881 (1998) [Phys. Solid State **40**, 1706 (1998)].
3. Sh. Sh. Bashkirov, A. B. Liberman, and V. I. Sinyavskiĭ, *Magnetic Microstructure of Ferrites* (Kazan Univ., Kazan, 1978).
4. É. L. Nagaev, Fiz. Tverd. Tela (S.-Peterburg) **39**, 1589 (1997) [Phys. Solid State **39**, 1415 (1997)].

Translated by N. Korovin

Physics of the Solid State, Vol. 42, No. 7, 2000, pp. 1313–1316. Translated from Fizika Tverdogo Tela, Vol. 42, No. 7, 2000, pp. 1275–1278.

MAGNETISM AND FERROELECTRICITY

Magnetic Anisotropy of Antiferromagnet $(CH_3)_4NMnCl_3$

A. M. Vorotynov, S. G. Ovchinnikov, V. V. Rudenko, and A. N. Sudakov

Kirenskiĭ Institute of Physics, Siberian Division, Russian Academy of Sciences, Akademgorodok, Krasnoyarsk, 660036 Russia

e-mail: rlm@cc.krascience.rssi.ru

Received September 22, 1999; in final form, December 16, 1999

Abstract—The parameters of the electron paramagnetic resonance (EPR) spectra of *S* ion pairs in diamagnetic crystals are analyzed. A relation between the spin Hamiltonian constants is established for solitary ions and pairs for $(CH_3)_4NCdCl_3 : Mn^{2+}$ crystals. In contrast to solitary ions, an additional contribution (which is a linear function of the exchange field) to the "single-ion" spin Hamiltonian constants appears in the case of pairs. It is shown that anisotropic exchange mechanisms do not play a significant part in the formation of the axial constant of the spin Hamiltonian for this crystal. Some aspects of the method of studying "single-ion" anisotropy predicted by the two-ion model are developed with the help of an isostructural diamagnetic analog with impurity concentration of the paramagnetic ions of a magnetically concentrated substance sufficiently high for observing the EPR spectrum of the pairs. It is found that the microscopic quantities determined partially from the EPR spectra for pairs and solitary Mn^{2+} ions in $(CH_3)_4NCdCl_3$ are in accord with the experimental value of the effective field for the $(CH_3)_4NMnCl_3$ crystal anisotropy which can be described primarily by the dipole and "single-ion" mechanisms of the exchange origin. © *2000 MAIK "Nauka/Interperiodica".*

1. The discrepancy between magnetic anisotropy microscopic theories and experiments with compounds containing *S* ions prompted the computations based on the two-ion models [1]. These computations differ from those carried out using the existing theories of magnetic anisotropy in that they have different values of ionic spins in the excited and the ground states. In this model, anisotropy appears in the third order of the perturbation theory and is a linear function of the exchange interaction energy and a quadratic function of the spin–orbit interaction energy. It was noted in [1] that the "single-ion" anisotropy of the exchange origin, which emerges from the two-ion mechanism, may play a significant role in the description of experimental data. The existence of the "single-ion" exchange anisotropy was studied experimentally in [2, 3].

A detailed theoretical analysis of the two-ion anisotropy was carried out by Moskvin *et al.* [4]. Among other things, they explained the behavior of the of anisotropy energy hematite in a wide temperature range by using the two-ion model. Moskvin *et al.* [4] succeeded in the removal of approximately 23%-discrepancy between the theoretical and experimental curves (describing the antiferromagnetic resonance frequency) in the high-temperature range, which existed according to the results obtained in [5]. The temperature dependence of anisotropy was described in [4] with the help of four fitting parameters (three of which were employed for normalizing the anisotropic exchange contributions).

The available publications on the two-ion mechanism facilitated an advance in understanding the origin of anisotropy in magnetically-ordered crystals with *S* ions; however, more detailed studies are required to determine anisotropy sources conclusively. A more comprehensive investigation of anisotropy requires a quantitative comparison of the results of calculations with experiment. At the present stage, an attempt of such a comparison can be made using the EPR data for the *S*-ion pair spectra in diamagnetic analogs isostructural to magnetically-concentrated substances. It is assumed that the equality of lattice parameters is a sufficient condition for identical values and the same symmetry of paired interactions in these crystals. According to Rudenko [6], the necessary condition for the coincidence of the axial constants of the spin Hamiltonian for solitary ions in rhombohedral crystals is the equality of the ratio c_H/a_H of the hexagonal lattice parameters.

However, several conditions must be satisfied for carrying out such investigations.

(1) The relation between the constants in the spin Hamiltonian of pairs and solitary ions should be established, which is not observed in the literature.

(2) The main mechanisms governing the formation of the constants in the spin Hamiltonian for pairs in a given diamagnetic compound should be determined.

(3) A magnetically-concentrated crystal, having an isostructural diamagnetic analog (with close values of the ratio c_H/a_H) and a preferably simple magnetic structure, should be chosen.

(4) The constants of the spin Hamiltonian for pairs in a diamagnetic and a magnetically-concentrated crystal should be put in correspondence.

(5) Reliable and detailed information on the effective anisotropy fields in the magnetically-concentrated crystal and for the constants of the spin Hamiltonian for

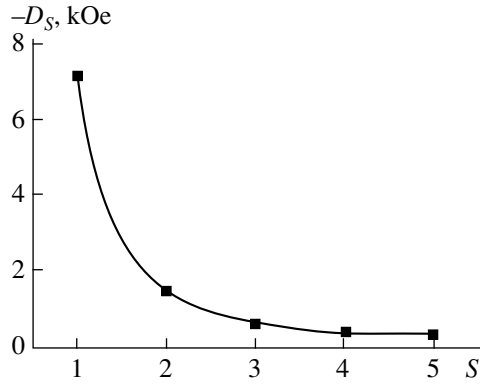

Fig. 1. Dependence of the axial constant D_s of the spin Hamiltonian, which is determined for pairs in $(CH_3)_4NCdCl_3 : Mn^{2+}$ on the total spin S (according to [7]).

pairs and solitary ions of the diamagnetic crystals must be available.

Conditions (3) and (5) are satisfied for $(CH_3)_4NMnCl_3$ and $(CH_3)_4NCdCl_3 : Mn^{2+}$, and the most comprehensive analysis of the EPR spectra for pairs of S ions has been carried out for $(CH_3)_4NCdCl_3 : Mn^{2+}$ crystals [7]. These crystals belong to the hexagonal system with the space group C_{6h}^2. A structural fragment important for EPR studies comprises chains of octahedra formed by Cl^- ions arranged along the sixfold axis of the crystal. The local symmetry of the positions of the Cd^{2+} ions in the octahedra is C_{3i}. The separation between Cd^{2+} ions in a chain is 3.36 Å, while the separation between the chains is 9.13 Å [7]. The lattice parameters are $a_H = 9.138$ Å and $c_H = 6.723$ Å [8]. The compound $(CH_3)_4NMnCl_3$ crystallizes into the $(CH_3)_4NCdCl_3$ structure [8, 9]. The ratio of hexagonal unit cell parameters is $[c_H/a_H] = 0.710$ [9]), which is quite close to the value $[c_H/a_H] = 0.736$ [8]) for $(CH_3)_4NCdCl_3$. The magnetic structure of $(CH_3)_4NMnCl_3$ is that of a quasi-one-dimensional antiferromagnet, the spins lie in the basal plane, the Néel temperature T_N is 0.835 K, and the exchange interaction parameter $[J/k]$ is 13 K.

2. The Hamiltonian for Mn^{2+} paired ions in a $(CH_3)_4NCdCl_3$ crystal in the strong-exchange approximation disregarding the hyperfine interaction can be written in the form [7, 10]

$$\mathcal{H} = g\beta\mathbf{HS} + (J/2)[S(S+1) - S_i(S_i+1) - S_j(S_j+1)] + D_s[S_z^2 - (1/3)S(S+1)], \quad (1)$$

where $\mathbf{H}$ is the external magnetic field; $\mathbf{S} = \mathbf{S}_i + \mathbf{S}_j$ is the spin operator; S is the total spin which can assume the values $S = S_i + S_j, S_i + S_j - 1, \ldots, S_i - S_j$; $S_i = S_j = 5/2$; $D_s = 3\alpha_s D_e + \beta_s D_c$; $\alpha_s = (1/2)\{[S(S+1) - 4S_i(S_i+1)]/[(2S-1)(2S+3)]\}$; $\beta_s = \{[3S(S+1) - 3 - 4S_i(S_i+1)]/[(2S-1)(2S+3)]\}$; $D_e = D_E + D_{dip}$; D_E being the anisotropic exchange constant; $D_{dip} = -g^2\beta^2/r_{ij}^3$; and D_c the "single-ion" constant. The Hamiltonian (1) can describe the experimental results for crystals with a dipole and single-ion anisotropy (including that of the exchange origin) and with an anisotropic exchange described by a second-order invariant in the spin operators. However, the fourth-order anisotropic exchange terms calculated in [1, 4] are not taken into account in (1).

Expression (1) shows that each multiplet of a pair with spin S is in an exchange field which can be directed along the z axis of the reference frame ($z \parallel C_6$) if $H = H_z$. This means that the quantization axis for the total spin moment is directed along z. With this orientation of the exchange field, each ionic spin (for multiplets) will be regarded as lying in the xz plane and deflected from the x axis towards the z axis. In this case, the expression for the exchange field can be written as $H_z^{ex} = -[(1/g\beta)\partial E_s/\partial S_z] = -(J/g\beta)(S_z + 1/2) = -(J/g\beta)(S + 1/2)$, where the E_s are exchange energy levels of the Hamiltonian (1).

The experimental results [7] for this crystal are plotted in the form of a graph in Fig. 1.

We present D_s in the form $D_s = 3\alpha_s D'_{dip} + \beta_s(P_1 + P_2 S)$, where P_k are fitting parameters ($k = 1, 2$). The parameters P_1 and P_2 are used for describing the linear dependence of the "single-ion" constant D_c of the spin Hamiltonian on the exchange field. A dependence of this type was obtained in [2, 3] for the system of magnetically concentrated crystals $MnCO_3$, $FeBO_3$, and α-Fe_2O_3. The expression for D'_{dip} is written taking into account additional dipole contributions emerging as a result of deviation from the point model and delocalization of the electrons of paramagnetic ions due to covalent effects [11]. It is also assumed that exchange–striction interactions [11] do not play any significant role in this crystal. Note that the exchange–striction model was used in [7, 12] for describing the experimental data obtained for a $(CH_3)_4NCdCl_3 : Mn^{2+}$ crystal. However, the fitting parameters used by the authors of [7, 12] led to a lattice distortion upon a change in the spin number S that was too strong.

Let us estimate D'_{dip} from the experimental data for D_s. Since β_3 has a small value, we can write $D'_{dip} \approx [D_3/3\alpha_s] = -398.1$ Oe. Fitting the value of D_s with the help of the parameters P_1 and P_2 by the least square technique, we obtain $D'_{dip} = \{[D_3 - \beta_3(P_1 + P_2 S)]/3\alpha_s\} = -391.4$ Oe. Expressing the "single-ion" constant from D_s and plotting $D_c = P'_1 + P'_2 S'$ as a function of $H_z^{ex}(S')$ ($S' = S + 1/2$) with a subsequent fitting, we find that the experimental points indeed fall well on the theoretical dependence that is a linear function (Fig. 2) with the parameters $P'_1 = 619.8 \pm 25$ Oe and $P'_2 = -110.2 \pm 7$ Oe.

The parameter P_1' can be obtained by extrapolating the curve in Fig. 2 to zero exchange field for the multiplets of a pair and should be equal to the sum of the constant $D_{cf} = 43.9$ Oe of the spin Hamiltonian for a solitary ion [7] and the contribution D_{c0} due to the distortion of the $(CH_3)_4NCdCl_3$ lattice by "foreign" pair. In order to compare the effect of lattice distortions produced by a pair on D_{c0}, we consider the slopes of the linear dependence of the spin Hamiltonian constant for a solitary Fe^{3+} ion in $GaBO_3$, $InBO_3$, $LuBO_3$, and $ScBO_3$ crystals [6] and D_{c0} relative to c_H/a_H. We shall assume that local lattice distortions can also be described by the parameter c_H/a_H. For the most precisely determined value of $\Delta(c_H/a_H)$, for D_{c0}, we obtain $\Delta(c_H/a_H)[(D_{cf} - P_1')/\Delta(c_H/a_H)] = -2.2 \times 10^4$ Oe. For the set of diamagnetic crystals investigated by us, we have $[\Delta D_{cf}/\Delta(c_H/a_H)] = -2.6 \times 10^3$ Oe. These quantities have the same sign and can be comparable even for the actual lattice distortions in $(CH_3)_4NCdCl_3$.

The obtained results can be used for calculating the magnetic anisotropy of a $(CH_3)_4NMnCl_3$ crystal. The "single-ion" constant of the spin Hamiltonian for a magnetically concentrated crystal can be written in the form

$$D_{mc} = D_{cf} + D_{ex} = D_c(H_{zn}^{ex}) - D_{c0}.$$

Here, D_{ex} is the contribution of the two-ion mechanism to the "single-ion" constant of the spin Hamiltonian for the magnetically-concentrated crystal and H_{zn}^{ex} is the exchange field at the multiplets of a pair, which corresponds to definite parameters of the magnetically-concentrated crystal.

In order to find the relation between the exchange energy parameters of a magnetically-concentrated crystal in the molecular field approximation and of a pair, we carry out the following calculations. We write the exchange interaction energy of the ith ion for a magnetically-concentrated crystal at $T = 0$ K in the form $E_{mc}(T = 0\text{ K}) = -nJS_iS_j$, where n is the number of the magnetically-active nearest neighbors of the ith ion. Putting $n = n_0 = 1$ and equating

$$E_{mc}(T = 0, n_0) = E_S, \qquad (2)$$

we establish the value of the effective spin number S_{n0} for a pair, which corresponds to the energy $E_{mc}(T = 0)$ of the lower level for the ith ion in the magnetically-concentrated crystal. The solution of the quadratic equation (2) gives the value of the spin number $S_{n0} = 1.8$. Further, carrying out the summation over the pair bonds of the ith ion, we find the exchange energy $E_{mc}(T = 0) = nE_s(S_{n0})$ of interaction of the ith ion with its nearest neighbors for the magnetically-concentrated crystal at $T = 0$ K in terms of S_i, S_j, S_{n0}, and n. The energy $E_{mc}(T = 0)$ corresponds to the exchange field $H_{zn}^{ex} = -2.3n(J/g\beta)$. For the corresponding exchange field of the $(CH_3)_4NMnCl_3$ crystal, the value of the "single-ion" constant of the spin Hamiltonian can be defined as $D_{mc} = [D_{cf} + P_2'|H_{zn}^{ex}|/(J/g\beta)] = D_{cf} - 0.00115|H_{zn}^{ex}|$. The slope calculated for the dependences for $MnCO_3$, $FeBO_3$, and α-Fe_2O_3 crystals [2, 3] is given by $\tan\alpha = [D_{ex}/H_E'] = -0.00048$. The obtained values of the slopes of the straight lines describing the constants of the spin Hamiltonian as functions of the exchange field are quite close, indicating that the obtained results reflect the actual pattern of the interaction.

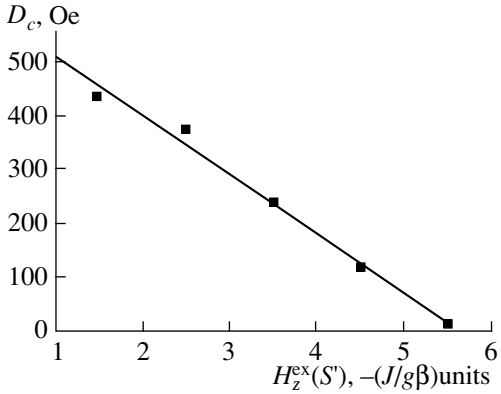

Fig. 2. Dependence of the "single-ion" constant D_c of the spin Hamiltonian on the exchange field for spin multiplets of a pair.

Thus, the results presented above lead to the following conclusions.

(1) The "single-ion" constant of the spin Hamiltonian in zero exchange field at the multiplets of a pair is equal to the constant of a solitary ion plus the contribution D_{c0} due to distortions emerging when a "foreign" pair appears in a diamagnetic crystal.

(2) In contrast to solitary ions, pairs acquire an additional contribution to the "single-ion" constant of the spin Hamiltonian, which is a linear function of the exchange field. This contribution is determined by the two-ion mechanism.

(3) The anisotropic exchange mechanisms calculated and estimated in [4] as very strong for hematite do not play any significant role in the formation of the spin Hamiltonian constant in $(CH_3)_4NCdCl_3 : Mn^{2+}$ and $(CH_3)_4NMnCl_3$ crystals.

Taking into account the uniaxial anisotropy, we can write the thermodynamic potential in the form

$$\Phi = (1/2)Bm^2 + (1/2)al_z^2, \qquad (3)$$

where $\mathbf{m} = (\mathbf{M}_1 + \mathbf{M}_2)/M$, $\mathbf{l} = (\mathbf{M}_1 - \mathbf{M}_2)/M$, and $M = 2|\mathbf{M}_1| = 2|\mathbf{M}_2|$.

The contribution of the dipole interaction at $T = 0$ K is estimated as $H_{A,dip} = 5.39$ kOe [13]. In accordance with (3) and [6], the "single-ion" contribution to the

uniaxial anisotropy constant at $T = 0$ K can be written in the form

$$a_{sf}(0) = 2NS_i(S_i - 1/2)[D_{cf} + P_2'|H_{zn}^{ex}|/(J/g\beta)],$$

where the spin Hamiltonian constants are expressed in energy units. Substituting the available data, we find the contributions of the single-ion and two-ion exchange mechanisms to $H_{A,cf} = [a_{cf}(0)/M(0)] = 0.18–2.02 = –1.84$ kOe, which gives $H_A(0) = H_{A,cf}(0) + H_{A,\mathrm{dip}}(0) = 3.55$ kOe. The experimental results obtained for $(CH_3)_4NMnCl_3$ by using various methods and compiled in [14] give the following values of $H_A(0)$: 3.31, 3.89, and 4.73 kOe, which are, on the average, in good agreement with the estimate presented above.

3. It should be noted, in conclusion, that the expression for the magnetic anisotropy constant can be used for any magnetically-concentrated crystal of an appropriate symmetry, which contains paramagnetic Mn^{2+} ions; the pairwise anisotropic interactions between these ions in the diamagnetic analog are described by the dipole and the "single-ion" constants of the spin Hamiltonian. It is also assumed that the exchange–striction contribution to these constants is insignificant.

ACKNOWLEDGMENTS

The authors express their gratitude to É. A. Petrakovskaya for fruitful discussions and valuable remarks.

REFERENCES

1. A. E. Nikiforov, V. Ya. Mitrofanov, and A. N. Men, Phys. Status Solidi B **45** (1), 65 (1971).
2. O. A. Bayukov and V. V. Rudenko, Preprint No. 669F (Institute of Physics, Siberian Division, Russian Academy of Sciences, Krasnoyarsk, 1990).
3. O. A. Bayukov and V. V. Rudenko, Fiz. Tverd. Tela (St. Petersburg) **34**, 2665 (1992) [Sov. Phys. Solid State **34**, 1428 (1992)].
4. A. S. Moskvin, I. G. Bostrem, and M. A. Sidorov, Zh. Éksp. Teor. Fiz. **104**, 2499 (1993) [JETP **77**, 127 (1993)].
5. K. S. Aleksandrov, L. N. Bezmaternykh, G. V. Kozlov, *et al.*, Zh. Éksp. Teor. Fiz. **92**, 1042 (1987) [Sov. Phys. JETP **65**, 591 (1987)].
6. V. V. Rudenko, Author's Abstract of Candidate's Dissertation (Simferopol', 1983).
7. M. Heming, G. Lehmann, H. Mosebach, and E. Siegel, Solid State Commun. **44** (4), 543 (1982).
8. B. Morosin, Acta Crystallogr. B **28**, 2303 (1972).
9. B. Morosin and E. J. Graeber, Acta Crystallogr. **23** (5), 766 (1967).
10. J. Owen, J. Appl. Phys., Suppl. **32** (3), 213S (1961).
11. E. A. Harris, J. Phys. C **5**, 338 (1972).
12. S. N. Martynov and S. B. Petrov, Phys. Status Solidi B **149**, K41 (1988).
13. A. I. U. Heilmann, J. K. Kjems, Y. Endoh, *et al.*, Phys. Rev. B **24**, 3939 (1981).
14. M. E. Gouvea and A. S. T. Pires, Phys. Rev. B **34**, 306 (1986).

Translated by N. Wadhwa

Physics of the Solid State, Vol. 42, No. 7, 2000, pp. 1317–1321. Translated from Fizika Tverdogo Tela, Vol. 42, No. 7, 2000, pp. 1279–1283.

MAGNETISM AND FERROELECTRICITY

Dissipation of the Spin Wave Energy in Magnetic Multilayer Films

A. M. Zyuzin, A. G. Bazhanov, S. N. Sabaev, and S. S. Kidyaev

Mordovian State University, Bol'shevistskaya ul. 68, Saransk, 430000 Russia

Received December 23, 1999

Abstract—It is shown that the penetration of standing spin waves into a layer with high damping is one of the channels of energy dissipation of these waves. The line broadening of spin wave modes due to this layer increases with the mode index and may be much larger than the natural linewidth associated with a layer having low damping. The linewidths of spin wave modes are found to be anisotropic, which is due to the dependence of the penetration depth of spin waves into the high-damping layer on the orientation of the external magnetic field with respect to the film. A theoretical model is proposed, which is consistent with the experimental data. *© 2000 MAIK "Nauka/Interperiodica".*

INTRODUCTION

Investigations of relaxation processes in magnetic spin systems are of current interest because, in particular, considerable attention is now focused on magnetic multilayer films, having the potential for device applications (see, e.g., [1–4]).

According to ferromagnetic-resonance and spin-wave (SW) theory [5–7], the linewidth $2\Delta H$ of SW modes excited in a film by a microwave field of a constant frequency is independent of the mode index n. The relaxation process in the layer where SWs are excited does not render their spectral linewidths dependent on the mode index. However, experimentally, the SW linewidths are often observed [8–12] to be dependent on n; namely, $2\Delta H$ increases with n in all such cases.

In [8], spin-wave resonance (SWR) was investigated in amorphous and polycrystalline films and it was found that the dependence of $2\Delta H$ on n showed a kink, the position of which was related in [8] to the fluctuation correlation radius of magnetic parameters. Unfortunately, in [8], as well as in other papers, no account was taken of the influence on $2\Delta H$ of SW energy dissipation in the high-damping layers of multilayer structures.

The objective of this paper is to investigate the influence of this channel of SW energy dissipation on the effective damping parameter and the linewidths of SW modes.

1. EXPERIMENT

The SWR spectra were measured on bilayer and trilayer single-crystal films of garnet ferrites, the layers of which had various values of the thickness h, Gilbert damping parameter α, and magnetization $4\pi M$. The films were produced by the liquid-phase epitaxy method on the (111) surface of gadolinium gallium garnet substrates by successively immersing them in different solutions in melt. The films had the following structure. The lower layer (closest to the substrate) had a high damping parameter $\alpha \geq 0.12$ ($\alpha = \Delta H\gamma/\omega$, where ΔH is the half-width of the absorption line, γ is the gyromagnetic ratio, and ω is the circular frequency of the microwave field). In this layer, the spins were pinned. The next layer had a low damping parameter ($\alpha \leq 0.003$). Spin waves were excited in this layer. In contrast to bilayers, the trilayers had one more (uppermost) layer with a high value of α.

For the measurements and control of the parameters, single-layer analogs were grown on clean sub-

Parameters of multilayer films

Sample	Layer	Composition	h, μm	γ, 10^7 Oe^{-1} s^{-1}	α	$4\pi M$, G	H_k^{eff}, Oe
1	1*	$Y_{2.98}Sm_{0.02}Fe_5O_{12}$	1.08	1.76	0.003	1740	–1715
	2*	$(LaEr)_3(FeGa)_5O_{12}$	1.2	1.66	0.84	450	–78
2	1*	$Y_3Fe_{4.97}Ge_{0.03}O_{12}$	0.36	1.76	0.0009	1680	–1620
	2*	$(YSmCa)_3(FeGe)_5O_{12}$	2.0	1.74	0.12	560	980

Note: 1* is the excitation layer of harmonic spin wave modes and 2* is the pinning layer.

1063-7834/00/4207-1317$20.00 © 2000 MAIK "Nauka/Interperiodica"

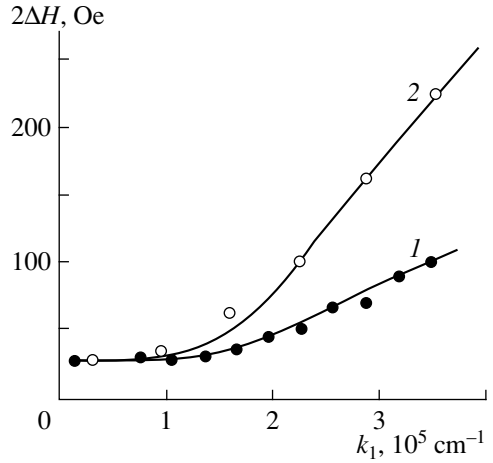

Fig. 1. Spin wave mode linewidth $2\Delta H$ as a function of the wavenumber k_1 for sample 1 for the different excitation layer thickness h_1, μm: (*1*) 1.08 and (*2*) 0.4. The dots are experiment and the lines are calculations for $\beta = 5.5 \times 10^{10}$ cm^{-2}.

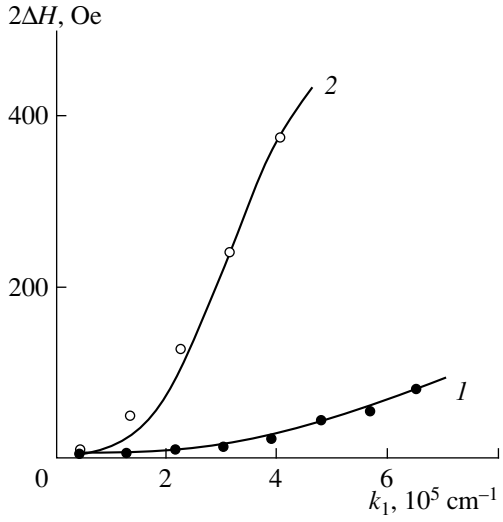

Fig. 2. Dependences of $2\Delta H$ on k_1 for sample 2 for (*1*) perpendicular and (*2*) parallel orientations of the magnetic field. The dots are experiment and the lines are calculations for different values of β, cm^{-2}: (*1*) 4×10^{11} and (*2*) 1.8×10^{11}.

strates for every single layer of bilayers and trilayers. The thickness of a layer was considered equal to the thickness of its single-layer analog, which was measured by the interference method and also determined from the time required for its complete etching. The film parameters are listed in the table. In all samples, the thickness of the "pinning layer" was 1 to 2 μm, which is much larger than the penetration depth of spin waves into the layer, as calculations and experimental data show [13]. The SWR spectra were recorded at room temperature for the microwave field frequency equal to 9.34×10^9 Hz. The magnetic field was measured by an NMR magnetometer. In the figures, for the sake of convenience, the linewidths of SW modes are plotted not against the mode index n, but against the wave number k_1, the values of which are close to $(n + 1/2)\pi/h_1$ for a bilayer film or to $(2n + 1)\pi/h_1$ for a trilayer film [14]; here, $n = 0, 1, 2, \ldots$, and h_1 is the thickness of the "excitation layer."

We note that, in sample 1, the dissipative mechanism of spin pinning [15] was dominant. This mechanism operates in multilayer films the layers of which differ dramatically in the damping parameter. Even under uniform-resonance conditions, the precession angle of the magnetization vector **M** in a layer with a high damping parameter α_2 is smaller than in a layer with a low damping parameter α_1 by a factor of α_2/α_1. Because of this and owing to the exchange coupling between layers, when the oscillatory magnetization is excited, one of the nodes of the standing spin wave is situated at the interface between the layers or near this interface. The dissipative mechanism of spin pinning differs qualitatively from the dynamic mechanism in that its operation is independent of the orientation of the external magnetic field **H** with respect to the film, which is due to the isotropic damping parameter α. According to the data available in the literature and to our experimental results, the possible anisotropy of α of garnet ferrite films does not exceed 6%, the measurement error of this parameter. Since the region where standing harmonic spin waves are excited is localized in the low-damping layer for any orientation of **H**, the SWR spectrum will be virtually isotropic if the dissipative mechanism of spin pinning is dominant. We note that the dispersion and reactive (elastic) properties of the high-damping layer also affect the spin pinning.

The experimental results we obtained are as follows. In bilayers in which the layers differ drastically in the α value (sample 1), the linewidth of SW modes noticeably increases with the wavenumber k_1 (curve *1* in Fig. 1).

With a decrease of the thickness of the layer where standing harmonic spin waves are excited, the dependence of $2\Delta H$ on k_1 becomes sharper (curve *2* in Fig. 1). In the case of a trilayer film, where there are pinning layers both above and below the excitation layer, the dependence of $2\Delta H$ on k_1 is stronger. At the same value of k_1, the broadening of the SW mode line (difference between the linewidth of the nth SW mode and $2\alpha_1\omega/\gamma_1$) in a trilayer is nearly twice as large as that in a bilayer.

The linewidths of SW modes are found to be anisotropic. If the dissipative mechanism of spin pinning dominates (as in samples like sample 1), the $2\Delta H(k_1)$ dependences are identical (within the margin of measurement error of $2\Delta H$, 6%) for the perpendicular and parallel orientations of **H** with respect to the film; however, these dependences become essentially different from each other when the dissipative mechanism ceases to be dominant. This is illustrated in Fig. 2, where the $2\Delta H(k_1)$ dependences are shown for sample 2.

2. THE LINEWIDTHS OF SPIN WAVE MODES

In order to explain the measured $2\Delta H(k_1)$ dependences, we analyzed the influence of the region of the pinning layer, where standing SWs decay, on the SW mode linewidth. It can be shown that, for both dissipative and dynamic mechanisms of spin pinning, the penetration depth l of an SW into the pinning layer depends on the wavenumber k_1 of the part of the SW that is harmonic in space and localized in the excitation layer. This is seen from Fig. 3, where the real (k_2') and imaginary ($k_2'' = 1/l$) parts of the wavenumber in the pinning layer, as well as the wavenumber k_1 in the excitation layer, are shown as a function of **H**. The values of k_2' and k_2'' are found from an equation following from the dispersion relation [16]. For the perpendicular orientation of **H** with respect to the film plane, this equation has the form

$$\frac{\omega}{\gamma_2} = H + H_2^{\text{eff}} + \frac{2A_2}{M_2}(k_2'^2 - k_2''^2), \quad (1)$$

where H_2^{eff} is the effective uniaxial anisotropy field and A_2 is the exchange constant in the second layer.

In (1), k_2' and k_2'' are related by the equation [16]

$$k_2'' = \frac{\alpha_2 \omega M_2}{4A_2\gamma_2}\frac{1}{k_2'} = \frac{\beta'}{k_2'}, \quad (2)$$

where $\beta' = \alpha_2\omega M_2/4A_2\gamma_2$. From Fig. 3, it is seen that k_1 and k_2' increase, while $k_2'' = 1/l$ decreases with decreasing H. Therefore, l increases with k_1. It should be noted that variation of the SW configuration with n may also occur in a thin surface layer if one assumes spin pinning to be due to surface anisotropy and ignores the thickness of the surface layer. Whatever the mechanism of spin pinning, the standing SW can considered as consisting of two exchange-coupled parts, one of which is harmonic and localized in the excitation layer, while the other, damped part, is in the pinning layer.

Of interest to us is the relaxation characteristic, the SW mode linewidth $2\Delta H_n$, which can be written as

$$2\Delta H_n = 2\alpha_n^{\text{eff}}\omega/\gamma_n^{\text{eff}}, \quad (3)$$

where α_n^{eff} is an effective damping parameter depending on α, $4\pi M$, and γ of each of the layers and on the configuration of the SW mode, and γ_n^{eff} is the effective gyromagnetic ratio for the nth mode.

The calculation of α_n^{eff} was performed as follows. As is known, damping in an oscillatory system can be characterized by the quality factor $Q = W/P$, where W is the energy of the system and P is the dissipated energy per cycle. The Q factor of a magnetic spin system is related to the Gilbert damping parameter α by the equation $Q = 1/2\alpha$ [16]. Therefore, P can be expressed in terms of α and W.

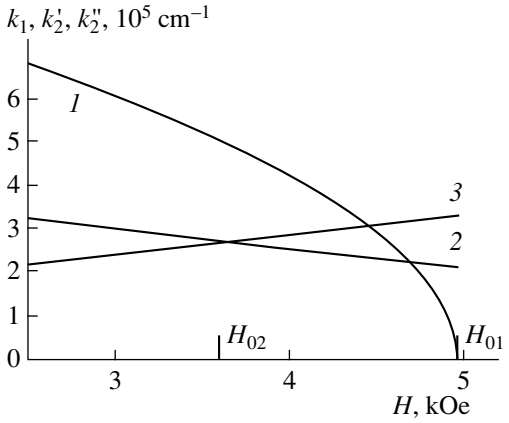

Fig. 3. Dependences of the wave numbers in the layers (*1*) k_1, (*2*) k_2', and (*3*) k_2'' on H for sample 1 for the perpendicular orientation of **H** with respect to the film. H_{01} and H_{02} are the uniform-resonance fields for the corresponding layers.

Let us consider a magnetic film consisting of two layers with different values of α. SW modes are excited in the low-damping layer (with parameter $\alpha(\alpha_1)$), while spin pinning occurs in the high-damping layer (with parameter $\alpha(\alpha_2)$). From the above discussion, it follows that the energy of a standing SW excited in this film can be written as the sum of the energy of the harmonic part of the wave localized in the excitation layer and the energy of the damped part in the pinning layer, $W = W_1 + W_2$. Accordingly, the dissipated energy per cycle is written as $P = P_1 + P_2$, or

$$P = 2(\alpha_1 W_1 + \alpha_2 W_2). \quad (4)$$

On the other hand, we can write

$$P = 2\alpha^{\text{eff}} W, \quad (5)$$

where $W = W_1 + W_2$. Combining (4) and (5) yields

$$\alpha^{\text{eff}} = \frac{\alpha_1 W_1 + \alpha_2 W_2}{W_1 + W_2}. \quad (6)$$

For the sake of convenience, the W_i are considered as the energies per unit area of the film in what follows. We can write these energies as

$$W_i = \int_{z_{i_1}}^{z_{i_2}} U_i(z)dz, \quad (7)$$

where U_i is the (volume) energy density of spin oscillations, which includes the energy of nonhomogeneous exchange interaction U', as well as the sum of the Zeeman energy, anisotropy energy, and demagnetizing-field energy U'' [16]. In the case of a film with uniaxial

anisotropy and of the perpendicular orientation of **H**, where spin waves have a circular polarization, we have

$$U' = \frac{A}{M^2}k^2m^2, \quad U'' = \frac{1}{2M}(H + H^{\text{eff}})m^2$$

or

$$U = \frac{1}{2M}\left(H + H^{\text{eff}} + \frac{2A}{M}k^2\right)m^2 = \frac{1}{2M}\frac{\omega_0}{\gamma}m^2, \quad (8)$$

where

$$\omega_0 = \gamma\left(H_0 + H^{\text{eff}} + \frac{2A}{M}k^2\right).$$

In resonance with the nth SW mode, the frequency ω_0 is equal to the microwave field frequency ω and we have

$$U_i = \frac{1}{2M}\frac{\omega}{\gamma_i}m_i^2. \quad (9)$$

It is also an easy matter to obtain an expression for U in the case where spin precession is elliptical, which takes place, for instance, for the parallel orientation of **H** with respect to the uniaxial film.

With (7) and (9), expression (6) for α_n^{eff} takes the form

$$\alpha_n^{\text{eff}} = \frac{\dfrac{\alpha_1}{\gamma_1 M_1}\displaystyle\int_0^{h_1} m_{1n}^2 dz + \frac{\alpha_2}{\gamma_2 M_2}\int_{h_1}^{h_1+h_2} m_{2n}^2 dz}{\dfrac{1}{\gamma_1 M_1}\displaystyle\int_0^{h_1} m_{1n}^2 dz + \frac{1}{\gamma_2 M_2}\int_{h_1}^{h_1+h_2} m_{2n}^2 dz}, \quad (10)$$

where h_1 and h_2 are the thicknesses of the corresponding layers.

For a standing SW, excited in the bilayer, the distribution of the magnetization m in the excitation and pinning layers can be written as

$$m_{1n}(z) = B_n\cos k_1 z,$$
$$m_{2n}(z) = C_n\exp[-i(k_2' - ik_2'')(z - h_1)], \quad (11)$$

respectively, where B_n and C_n are constants and the $z = 0$ plane is the free boundary of the excitation layer.

It should be noted that, if $2\Delta H(k_1)$ is calculated using k_2'' obtained from (1) and (2) (Fig. 3), the results do not agree with the experimental data. One of the reasons for this discordance may be the fact that, when a spin wave decaying in space in the high-damping layer is excited by spin oscillations localized in the low-damping layer, the configuration of this wave is determined not only by the layer parameters (α_2, A_2, M_2, H_2^{eff}) and the value of H, but also, to a large extent, by the wavenumber k_1 of the harmonic part of the spin wave excited in the low-damping layer by a microwave field. The calculated $2\Delta H(k_1)$ dependences can be fitted to the experimental data if one assumes that the penetration depth of the spin wave into the pinning layer varies in proportion to k_1 and, hence, k_2'' has the form

$$k_2'' = \beta/k_1, \quad (12)$$

where β is a constant. The value of β at which the agreement between the experimental and calculated $2\Delta H(k_1)$ dependences is the best is close to the value of $\beta' = \alpha_2\omega M_2/4A_2\gamma_2$ involved in expression (2), which relates k_2'' to k_2' ($k_2'' = \beta'/k_2'$). For instance, for sample 1, we have $\beta = 5.5 \times 10^{10}$ and $\beta' = 7.2 \times 10^{10}$ cm^{-2}.

We ignored k_2' in calculating $2\Delta H_n$ in the case where the dissipative mechanism of spin pinning is dominant. The possible values of the wavenumber and the relation between B_n and C_n can be found from the boundary conditions [14]

$$\frac{m_1}{M_1} = \frac{m_2}{M_2}, \quad \frac{A_1}{M_1}\frac{dm_1}{dz} = \frac{A_2}{M_2}\frac{dm_2}{dz} \quad (13)$$

and expressions (11). The result is

$$\tan(k_1h_1) = p/k_1, \quad (14)$$

$$C_n = \frac{M_2}{M_1}B_n\cos k_1h_1. \quad (15)$$

Here, $p = A_2k_2''/A_1 = A_2\beta/A_1k_1$ is a parameter, which determines the degree of spin pinning and is inversely proportional to the penetration depth of a spin wave into the pinning layer. In the case of the dissipative mechanism of spin pinning, the value of p is determined fundamentally by α_2, A_2, $4\pi M_2$, and k_1. It is worth noting that, if the values of γ in the layers are different, a standing SW will be characterized by an effective quantity γ^{eff}, which, as well as α^{eff}, is dependent on the mode index. It can be shown that, for spin waves under study, we have

$$\gamma_n^{\text{eff}} = \frac{\dfrac{1}{M_1}\displaystyle\int_0^{h_1} m_{1n}^2 dz + \frac{1}{M_2}\int_{h_1}^{h_1+h_2} m_{2n}^2 dz}{\dfrac{1}{\gamma_1 M_1}\displaystyle\int_0^{h_1} m_{1n}^2 dz + \frac{1}{\gamma_2 M_2}\int_{h_1}^{h_1+h_2} m_{2n}^2 dz}. \quad (16)$$

3. DISCUSSION OF RESULTS

The $2\Delta H(k_1)$ dependences calculated from (3) and (10) are presented in Figs. 1 and 2. The figures show good agreement between the calculations and the experimental data. From Fig. 1, it is seen that the linewidth increases with the wavenumber (or with the mode index, for $k_1 \sim n$). This is due to an increase in the relative contribution from the damping region to $2\Delta H_n$.

In the numerator in (10), the first integral (normalized to B_n) varies with n only slightly, whereas the second integral increases. When $\alpha_2 \gg \alpha_1$, the contribution from the second term to α^{eff} becomes quite large. It is also seen from Fig. 1 (curve *2*) that the relative contribution from the damping region to the SW mode linewidth increases as the thickness of the excitation layer decreases. For the calculated linewidth $2\Delta H(k_1)$ of a trilayer, where there are two damping regions and the boundary conditions are symmetrical, the line broadening is twice as large. This was experimentally observed for all trilayers investigated.

Figure 2 shows the calculated and experimental $2\Delta H(k_1)$ dependences for sample 2, in which the dynamic and dissipative mechanisms of spin pinning make comparable contributions. The clearly defined anisotropy of the SW mode linewidths in sample 2 is due to the strong dependence of the SW penetration depth l into the pinning layer on the orientation of **H** with respect to the film. For the perpendicular orientation, the pinning layer is a reactive (elastic) medium for spin waves in the field range where the SWR spectrum was observed ($H > H_{02}$). In this case, k_2'' far exceeds k_2' and its value is large. This is due to the fact that the uniform-resonance fields in the layers differ dramatically in value ($H_{01} - H_{02} = 2330$ Oe); hence, the dynamic mechanism of spin pinning is highly effective and causes a considerable decrease in the penetration depth l. In the pinning layer, the oscillatory magnetization component steeply falls off with distance from the layer interface. The varying magnetic moment of the damping region decreases, and so does the dissipated energy in this region. The decrease in l in the case of the perpendicular field orientation causes the degree of spin pinning to increase, as indicated by numerous modes observed in this case.

At the parallel field orientation, the SWR spectrum is observed in a field range below H_{02} and, therefore, $k_2'' < k_2'$. In this case, the pinning layer is a dispersive (transparent) medium for spin waves. These are harmonic waves and decay by an exponential law. The penetration depth l is determined only by dissipation and is much larger than in the case of the perpendicular field orientation. Therefore, the damping region has a larger oscillatory magnetic moment, which leads to broader SW mode lines. In calculating $2\Delta H(k_1)$ for sample 2, the factors indicated above were taken into account by choosing appropriate values of β.

CONCLUSIONS

Thus, in this paper, it was found that spin wave damping in the pinning layer is one of the channels of energy dissipation of spin waves. The broadening of the SW mode lines due to this damping increases with the mode index and can be many times larger than the natural SW linewidth of the excitation layer.

The SW mode linewidths were observed to be anisotropic, which is due to the dependence of the SW penetration depth into the pinning layer on the orientation of the external magnetic field with respect to the film.

ACKNOWLEDGMENTS

This work was supported by the Russian Foundation for Basic Research, grant no. 98-02-03320.

REFERENCES

1. B. Hillebrands, Phys. Rev. B **41**, 530 (1990).
2. Kh. Pashaev and D. L. Mills, Phys. Rev. B **43**, 1187 (1991).
3. S. L. Vysotskiĭ, G. T. Kazakov, M. L. Kats, and Yu. A. Filimonov, Fiz. Tverd. Tela (St. Petersburg) **35**, 1190 (1993) [Phys. Solid State **35**, 606 (1993)].
4. Yu. I. Gorobets, A. N. Kuchko, and S. A. Reshetnyak, Fiz. Tverd. Tela (St. Petersburg) **38**, 575 (1996) [Phys. Solid State **38**, 315 (1996)].
5. N. M. Salanskiĭ and M. Sh. Erukhimov, *Physical Properties and Applications of Magnetic Films* (Nauka, Novosibirsk, 1975).
6. P. Lubitz, S. M. Bhagat, G. C. Bailey, and C. Vittoria, Phys. Rev. B **11**, 3585 (1975).
7. A. G. Gurevich and G. A. Melkov, *Magnetic Oscillations and Waves* (Nauka, Moscow, 1994).
8. R. S. Iskhakov, A. S. Chekanov, and L. A. Chekanova, Fiz. Tverd. Tela (Leningrad) **30**, 970 (1988) [Sov. Phys. Solid State **30**, 563 (1988)].
9. P. E. Wigen, Phys. Rev. A **133**, 1557 (1964).
10. T. G. Phillips and H. M. Rosenberg, Phys. Lett. **8** (5), 298 (1964).
11. G. Suran and R. J. Gambino, J. Appl. Phys. **50**, 7671 (1979).
12. A. M. Zyuzin, V. V. Randoshkin, R. V. Telesnin, *et al.*, Pis'ma Zh. Tekh. Fiz. **8**, 844 (1982) [Sov. Tech. Phys. Lett. **8**, 365 (1982)].
13. A. M. Zyuzin and A. G. Bazhanov, Zh. Éksp. Teor. Fiz. **111**, 1667 (1997) [JETP **84**, 912 (1997)].
14. B. Hoekstra, R. P. van Stapele, and J. M. Robertson, J. Appl. Phys. **48**, 382 (1977).
15. A. M. Zyuzin, N. N. Kudel'kin, V. V. Randoshkin, and R. V. Telesnin, Pis'ma Zh. Tekh. Fiz. **9**, 177 (1983) [Sov. Tech. Phys. Lett. **9**, 78 (1983)].
16. A. G. Gurevich, *Magnetic Resonance in Ferrites and Antiferromagnets* (Nauka, Moscow, 1973).

Translated by Yu. Epifanov

Physics of the Solid State, Vol. 42, No. 7, 2000, pp. 1322–1324. Translated from Fizika Tverdogo Tela, Vol. 42, No. 7, 2000, pp. 1284–1286.

MAGNETISM AND FERROELECTRICITY

Transition from the Kondo Regime to Long-Range Magnetic Order in the $Fe_xV_{1-x}S$ System

G. V. Loseva, S. G. Ovchinnikov, A. D. Balaev, N. B. Ivanova, and N. I. Kiselev

Kirenskiĭ Institute of Physics, Siberian Division, Russian Academy of Sciences, Akademgorodok, Krasnoyarsk, 660036 Russia

e-mail: sgo@post.krascience.rssi.ru

Received November 10, 1999; in final form, December 24, 1999

Abstract—A study is reported on the electrical and magnetic characteristics of the $Fe_xV_{1-x}S$ solid-solution system with $x \le 0.5$. A maximum in the temperature dependence of resistivity $\rho(T)$ characteristic of the Kondo effect has been observed for small x ($x < 0.01$). For $x > 0.1$, long-range magnetic order sets in in the system with $T_K \sim 100$ K. Near $x = 0.05$, the Fe^{2+} impurity behavior crosses over to a magnetically ordered phase. The electronic properties of $Fe_xV_{1-x}S$ are typical of those of strongly correlated electronic systems. Both the electrical and magnetic data imply that carrier delocalization is the strongest at $x = 0.4$. *© 2000 MAIK "Nauka/Interperiodica".*

Many vanadium compounds differing in crystalline structure, such as oxide spinels $Li_xMe_{1-x}V_2O_4$ (Me stands for Zn and Mg) [1], perovskites $Sr_xLa_{1-x}TiO_3$ [2], and NiAs-type sulfides with a superstructure, such as $Me_xV_{1-x}S$ (with Me standing for a 3*d* metal) [3, 4], undergo a metal–insulator transition and are studied intensely to understand specific features of the electronic and magnetic states in strongly correlated electronic systems. Spin fluctuations play a prominent part in such electronic systems.

This paper reports a temperature study of the electrical resistivity ρ and magnetization σ of the $Fe_xV_{1-x}S$ system with compositions $0 < x \le 0.5$ in the 4.2–300 K temperature range. The concentration dependences of ρ and σ for compositions with $0.1 \le x \le 0.5$ are presented in [3].

1. EXPERIMENTAL TECHNIQUES

The preparation technology of polycrystalline $Fe_xV_{1-x}S$ samples, which is the same for all compositions studied, is described in [3].

The resistivity was measured by the four-probe dc potentiometric method. The samples intended for resistivity measurements were pressed to $10 \times 5 \times 2$-mm parallelepipeds and fired in evacuated quartz ampoules at 1200 K for an hour.

The magnetization was measured in an automated vibrating-sample magnetometer with a superconducting coil in magnetic fields of up to 0.1 T.

Temperature measurements of the real part of the initial magnetic susceptibility χ' were carried out on a setup including an inductance bridge and a phase-sensitive detector.

The magnetic and resistivity measurements were done on the same samples.

2. EXPERIMENTAL RESULTS

2.1. X-ray Diffraction Characterization and DTA

X-ray diffraction studies of $Fe_xV_{1-x}S$ compounds with isomorphous substitution of Fe for V were performed at $T = 300$ K and showed them to be isostructural with V_5S_8 (monoclinic superstructure $F2/m$–C^3) for $0.1 \le x \le 0.5$ [3]. The compositions with low iron concentrations $x = 0.005$, 0.01, 0.02, and 0.05 had a distorted superstructure close to that of V_5S_8. All the compositions studied revealed in DTA curves two reversible endothermic effects at 800–900 K falling into the metal–insulator transition region of the starting monosulfide VS [3]. In the present work, the DTA range was extended to 1300 K, which allowed the determination a peak at 1020–1100 K in DTA curves obtained on $0.1 \le x \le 0.5$ compositions. The peak corresponded to the Curie temperature θ_C, and its observation provided an indirect method for measuring this temperature.

2.2. Electrical Resistivity

The concentration dependence of the electrical resistivity obtained at 80 and 300 K exhibits a strong increase of ρ to 0.6 Ω cm for $x = 0.1$ at room temperature, with its subsequent drop by an order of magnitude with increasing iron concentration, which evidences the electron localization to be the strongest at $x = 0.1$. Figure 1 presents $\rho(T)$ curves for compositions with low iron concentrations. As is seen from Fig. 1a, the $\rho(T)$ dependence obtained for the $x = 0.005$ composition (0.25 at. % Fe) passes through a maximum at $T \sim 90$ K. Such $\rho(T)$ behavior was observed for dilute metal

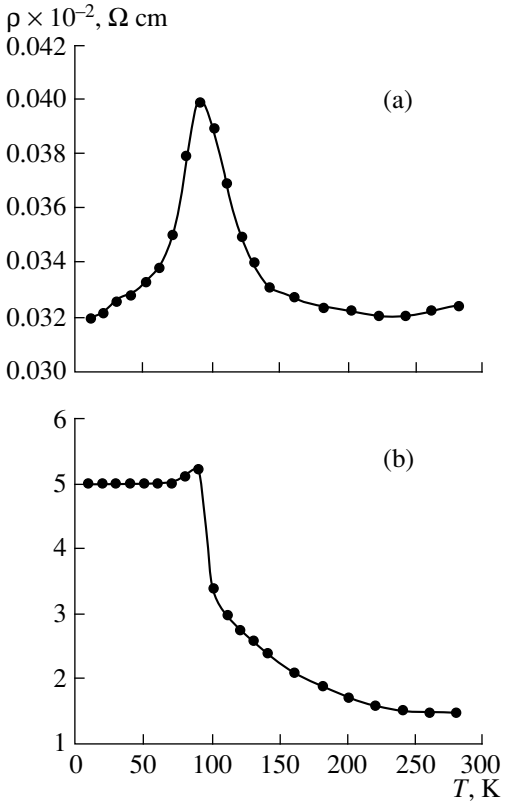

Fig. 1. Temperature dependences of the electrical resistivity of $Fe_xV_{1-x}S$ samples for compositions with (a) $x = 0.005$ and (b) $x = 0.05$.

alloys with low concentrations of paramagnetic impurities in the lattice in the absence of magnetic order, i.e., the Kondo effect [5]. The amplitude of the peak in $\rho(T)$ was found to depend on the paramagnetic impurity concentration and external magnetic field and to become suppressed as the latter increase.

As the iron concentration increases to $x = 0.05$, the general resistivity increase by more than two orders of magnitude is accompanied by the disappearance of the $\rho(T)$ peak, although traces of the temperature anomaly can still be detected around 90 K (Fig. 1b). For $T > 90$ K, the $\rho(T)$ curves follow a close-to-activated behavior for both compositions.

The influence of a further increase of the iron concentration can be seen from Fig. 2, which shows that the $\rho(T)$ dependence levels off with increasing x, to approach a semimetallic conduction pattern at $x = 0.4$ throughout the temperature range studied.

2.3. Magnetic Properties

Measurements of the low-frequency magnetic susceptibility $\chi'(T)$ did not reveal long-range magnetic order in samples with iron concentration $x < 0.1$.

As for compositions with higher iron contents, the saturation field, as seen from the magnetization curves displayed in Fig. 3, is approximately the same for all samples with $x \geq 0.1$, with the magnetization varying noticeably in magnitude. It is apparently the high values of θ_C that account for the fact that the values of $\sigma(H)$ measured at 68 and 300 K differ by not more than 5%. The fact that the magnetization curves reach saturation at magnetic fields of about 0.1 T, as well as the high values of the magnetization, suggests that the exchange interaction has a ferromagnetic component, which is buttressed by the observation of hysteresis loops with a coercive force $H_C \sim (3–5) \times 10^{-4}$T.

The magnetic moments M per iron atom derived from the magnetization curves are displayed in Fig. 4, and Fig. 5 presents the values of θ_C obtained for various compositions. We note with interest a correlation between these two dependences within the concentration range studied.

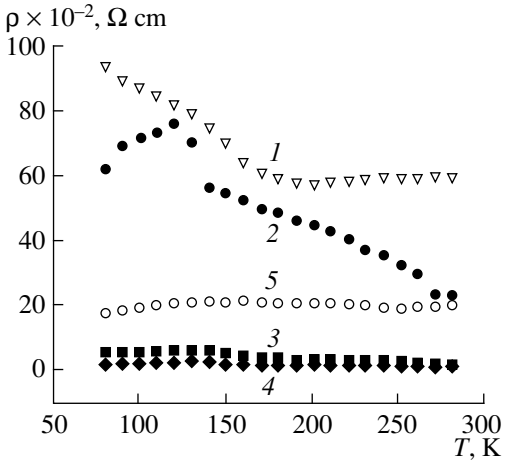

Fig. 2. Temperature dependences of the electrical resistivity of $Fe_xV_{1-x}S$ samples for compositions with x: (*1*) 0.1, (*2*) 0.2, (*3*) 0.3, (*4*) 0.4, and (*5*) 0.5.

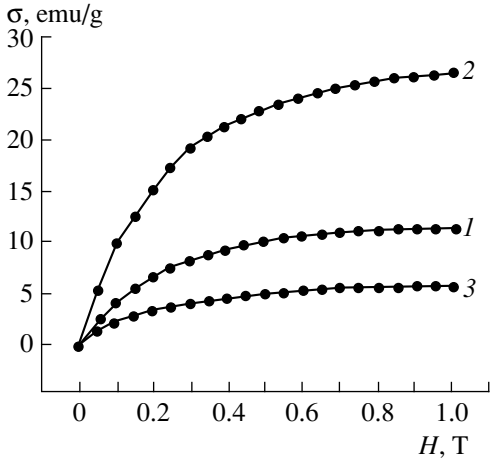

Fig. 3. Magnetization curves of $Fe_xV_{1-x}S$ samples for x: (*1*) 0.1, (*2*) 0.2, and (*3*) 0.4.

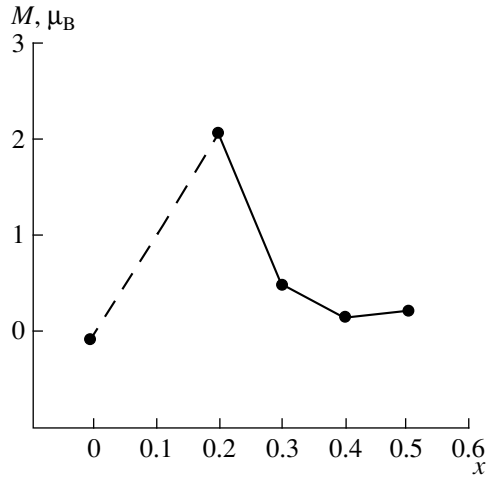

Fig. 4. Concentration dependences of the magnetic moment M per Fe atom.

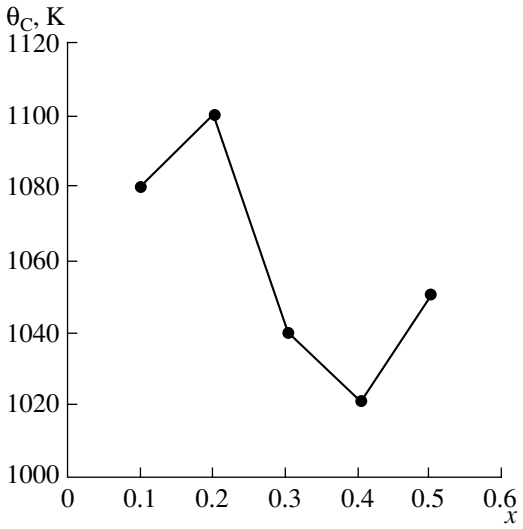

Fig. 5. Concentration dependences of the Curie temperature θ_C.

3. DISCUSSION OF RESULTS

As follows from the x-ray diffraction data, $Fe_xV_{1-x}S$ and V_5S_8 with ordered vacancy layers have similar structures and the substitutional Fe atoms are ordered in hexagonal layers. An analysis of the electronic structure [3] showed that, at low concentrations, each iron atom forms a localized magnetic impurity with $S = 1$. It is carrier scattering from such impurities that produces, as is well known, the Kondo effect, and therefore, its manifestation in $\rho(T)$ curves with $x = 0.005$ does not appear strange. For $x \geq 0.1$ there is long-range magnetic order, where the Kondo effect is suppressed. The crossover between the Kondo regime and long-range magnetic order occurs at an impurity concentration x_C such that $T_K \sim x_C\theta_C$ [5], where T_K is the Kondo temperature and θ_C is the Curie temperature of a concentrated magnetic system. In our case, $T_K \sim 100$ K and $\theta_C \sim 1000$ K, so that $x_C \sim 0.1$. Indeed, for $x = 0.05$, as seen from Fig. 1b, $\rho(T)$ follows an intermediate behavior with a pronounced spin fluctuation contribution for $T > 100$ K, i.e., this composition apparently lies near the crossover from one regime to the other.

At $x \sim 0.1$–0.2, the magnetically ordered phase is characterized by magnetic moments localized on Fe atoms which evidences strong *d*-electron correlations in Fe. As x increases still further, the wave-function overlap of the *d* electrons becomes enhanced to give rise to their partial delocalization, which is seen from the sharp drop of the magnetic moment of Fe atoms and the leveling off of the temperature dependence $\rho(T)$. Judging from both electrical and magnetic measurements, the delocalization is strongest near $x = 0.4$.

ACKNOWLEDGMENTS

Support of the Russian Foundation for Basic Research (grant 99-02-17405) is gratefully acknowledged.

REFERENCES

1. M. Onoda, H. Imai, Y. Amako, and H. Nagasawa, Phys. Rev. B **57**, 3760 (1997).
2. Y. Fusukawa, Physica C (Amsterdam) **285**, 68 (1997).
3. G. V. Loseva, S. G. Ovchinnikov, G. A. Gaĭdalova, *et al.*, Fiz. Tverd. Tela (St. Petersburg) **40**, 1890 (1998) [Phys. Solid State **40**, 1715 (1998)].
4. G. V. Loseva, L. I. Ryabinkina, S. S. Aplesnin, *et al.*, Fiz. Tverd. Tela (St. Petersburg) **39**, 1428 (1997) [Phys. Solid State **39**, 1267 (1997)].
5. S. V. Vonsovskiĭ, *Magnetism* (Nauka, Moscow, 1971; Wiley, New York, 1974).

Translated by G. Skrebtsov

Physics of the Solid State, Vol. 42, No. 7, 2000, pp. 1325–1328. Translated from Fizika Tverdogo Tela, Vol. 42, No. 7, 2000, pp. 1287–1290.

MAGNETISM AND FERROELECTRICITY

Axially Symmetrical Domain Structures in Garnet Ferrite Films

M. V. Chetkin, T. B. Shapaeva, and L. L. Savchenko

Moscow State University, Vorob'evy gory, Moscow, 119899 Russia

e-mail: shapaeva@magn145.phys.msu.su

Received October 25, 1999; in final form, January 13, 2000

Abstract—The process of domain structure formation and evolution after magnetization of a small area of a garnet ferrite film to saturation was examined with the use of modified two-step high-speed photography. It was found that the radial deformation caused by magnetizing coil breaks the uniaxial anisotropy of the specimen and results in formation of the axially oriented stripe domain structure inside the magnetization reversal area. The period of this domain structure decreases with the increasing amplitude of the pulsed field. The formation of the axially oriented stripe domain structure occurs under the axially symmetrical magnetostatic field. © *2000 MAIK "Nauka/Interperiodica"*.

In recent years, together with ordered domain structures, such as hexagonal lattices of bubble domains [1], lattices of dumbbell-like domains [2], and stripe domain structures [3], the magnetic states that exhibit a partly or fully disordered domain structure (DS) attract great interest. These magnetic states may be exemplified by spiral domains [4] and closely-packed structures of spiral domains [5]. In uniaxial garnet ferrite films (GFFs) with the easy magnetic axis normal to the film surface, the specific character of anisotropy allows no preferable direction and is favorable for disordering domain wall (DW) arrangement [6].

In this work, we investigate the formation and evolution of a domain structure in GFFs after a small area of the specimen is magnetized by a coil, pasted directly on the specimen. We examined the $(BiLaTm)_3(FeGa)_5O_{12}$ garnet ferrite films with the following characteristics: $4\pi M_s$ = 100 G and the mobility μ = 120 cm/(s Oe). The plane of the film substrate was perpendicular to the [111] axis. In our experiments, we used the modified method of two-step high-speed photography [7]. This method allows one to fix two successive positions of a DW at two time instants. The time interval between two light pulses (Δt) was created by electronic delay line. It might be varied from 1 to 1000 μs. In our work, in contrast to the classic method of two-step high-speed photography [8], we registered the DS image with a TV camera. The further image processing and its visualization were performed using a personal computer, which allowed the image to be registered at any given point in time. An additional advantage of the modified method is that the results are seen directly in the process of work, which provides the possibility of an adaptable control in the course of experiment.

We investigated GFFs in pulsed magnetic fields of a frequency of several hertz and an amplitude H_i exceeding the saturation field. In our experiments, we used field pulses the duration of which can be varied in the interval from 1 to 10 μs. The field was produced by a round coil of the radius, which was substantially smaller than the specimen size. The coil was pasted directly on the specimen.

When the pulse duration was 10 μs, the specimen magnetization reached saturation in the first 8 μs. The system held this magnetization during several microseconds after the pulse was turned off. To describe further evolution of the system, the time t was measured from the instant the pulse was cut off. After several tens of microseconds from the pulse cutting-off, on the periphery of the region covered by the coil, an axially symmetrical stripe DS starts to develop with domains oriented along the coil radius. In Fig. 1, a two-step view of the axially oriented DS is shown in the first several microseconds of its development. In this figure, bright domains correspond to the DS after 60 μs following the field pulse cut-off (t = 60 μs). Dark areas near rounded ends of the bright domains are the sections that were passed by the DW during the time between two light pulses (Δt = 5 μs). The domain walls move predominantly along the coil radius. The rate with which the DS growths into the coil (V = 8 m/s) remains constant up to the instant the stripe domains come together at the center of the coil. In the figure, the swellings are seen at the ends of the stripe domains at both the time t and $t + \Delta t$. In addition, it is evident that the DW moves not only to the coil center. The small narrow white regions near the bright domain illustrate the compression of the stripe domain ends.

We recall that the classic method of two-step high-speed photography allows one to observe DW displacement during a certain time, but it is impossible to obtain information about the initial state of the DS in that case. In the classic method, the light pulses of the equal intensity are used. In Fig. 1, besides DW displacing during the time Δt, the formation of a domain structure

1063-7834/00/4207-1325$20.00

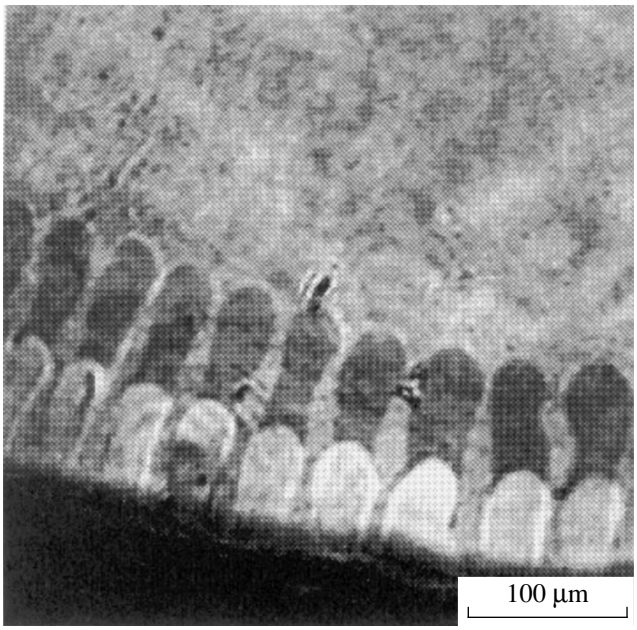

Fig. 1. Evolution of the axially symmetrical DS in the GFF during the time between two light pulses (Δt = 5 μs). The displayed initial DW position corresponds to time instant 60 μs after the field pulse was cut off. The pulse was of amplitude H_i = 520 Oe (H_s = 160 Oe) and of a length t_i = 10 μs.

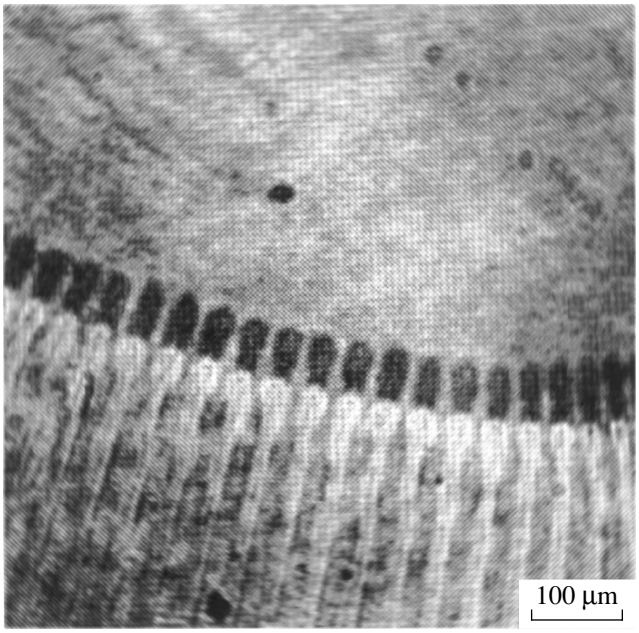

Fig. 2. Evolution of the axially symmetrical DS in the GFF during the time between two light pulses (Δt = 2 μs). The displayed initial DW position corresponds to time instant 85 μs after the field pulse was cut off. The pulse was of amplitude H_i = 520 Oe (H_s = 238 Oe) and of a length t_i = 10 μs.

is seen well. To achieve this, we used the light pulses of different intensity.

In Fig. 2, the view of the DS is presented at time t = 85 μs. The period of the stripe DS is approximately 1.5 times smaller than the period of a labyrinth DS in the case of zero external field. At t = 140 μs, the stripe domains come together at the coil center and form quasi-static axially symmetrical stripe DS (Fig. 3). This structure remains unchanged up to the instant of the next field pulse coming. It is seen in the figure that some neighboring domains merge with each other in the process of evolution. As the amplitude of field pulses increases, the period of the axially oriented stripe DS decreases.

It is known that, with an increase of the in-plane field amplitude in a GFF, the period of DS decreases [9]. But when the normal component of the pulse field increases, the in-plane component of this field increases as well. This fact explains the above-mentioned dependence of the period of the axially oriented DS on the pulse field amplitude.

The qualitative explanation of the above-described results is as follows. Due to the radial tensile deformation, which is caused by the magnetizing coil pasted on the specimen, a correction F_σ to the free energy arises [10]. This addition equals $F_\sigma \approx \lambda_{110}\sigma$, where λ_{110} is the magnetostriction constant along the [110] axis ($\lambda_{110} = 1.4 \times 10^{-6}$) and σ is the mechanical stress arising in the coil when the current is nonzero. For the used specimens, F_σ is several percent of the anisotropy energy. Thus, under the radial deformation, the easy magnetic axis deflects from the normal to the film plane through a small angle along each radius. The set of these axes forms the easy magnetization cone.

After the area of the specimen that is covered by the coil is magnetized to saturation, the axially symmetrical magnetostatic field is generated in the specimen. This field determines the way of evolution of the radially oriented stripe DS. The existence of this field explains nucleation and development of axially symmetrical stripe domains in the specimen.

The crucial role of the radial deformation in the formation of the axially oriented stripe DS was verified experimentally in the following way. The magnetic field was applied by using not a coil pasted on the specimen, but Helmholtz coils with the air gaps between the coils and the specimen being equal to ≈0.5 mm. In this case, the DS reconstruction occurs basically because of randomly arising regions with a labyrinth DS. For this reason, the uniform orientation of domains did not occur.

Thus, when the specimen was magnetized to saturation with the pulse field generated by the pasted coil, the radial tensile stress in the specimen caused by this coil determined the orientation of the stripe DS. With this conclusion in mind, to create the stripe DS, we used the magnetic field generated by a rectangular coil of the internal size 1.5×7 mm, which was pasted on the specimen as before. The stripe domains of the period, which is approximately 1.4 times smaller than the period of a

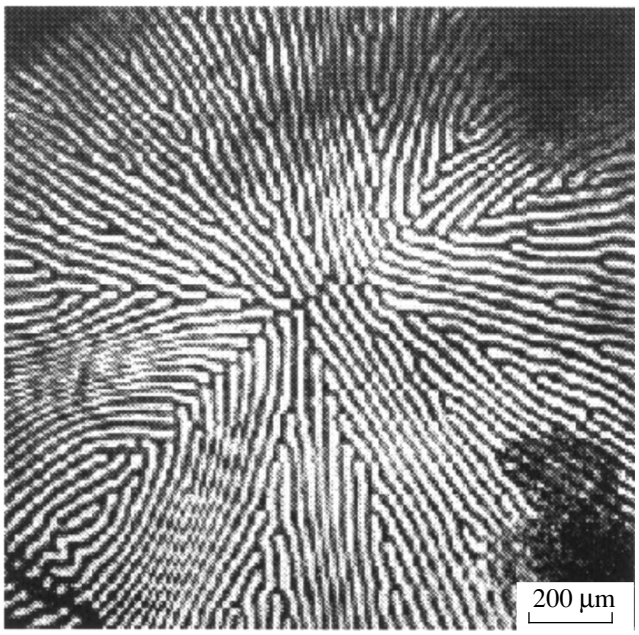

Fig. 3. Axially oriented stripe DS of the specimen 140 μs after the field pulse was cut off. The pulse was of amplitude H_i = 255 Oe (H_s = 238 Oe) and of a length t_i = 10 μs.

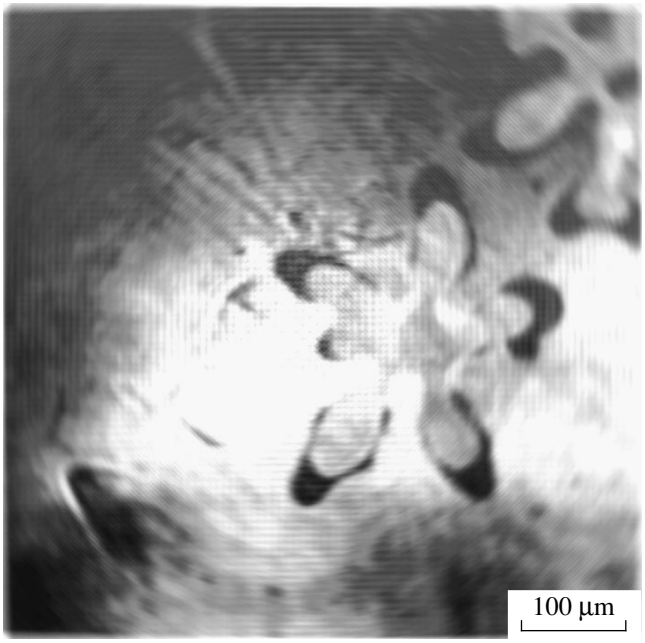

Fig. 4. Evolution of a nucleus of reversed magnetization in the GFF during the time between two light pulses (Δt = 3 μs). The displayed initial DW position corresponds to time instant 25 μs after the field pulse was cut off. The pulse was of amplitude H_i = 193 Oe (H_s = 110 Oe) and of a length t_i = 10 μs.

labyrinth DS in absence of any external field, were aligned along the normal to the region covered by the coil. In the center of the coil, the domains intergrowing from the opposite sides of the coil do not merge when they come together; in this case, the domains that are magnetized in a specific direction and intergrow from one side, stand opposite to the domains that intergrow from the other side and are magnetized reversely. When the pulse field is turned off, the stripe DS remains unchanged. Some negligible distortions of the DS may arise only in the area, where domains that intergrew from the opposite sides are within short distances of each other. The results of our experiment are in good agreement with the qualitative explanation of the formation of a radially oriented stripe DS generation.

When the pulse field amplitude exceeds the saturation field only slightly, nuclei of reversed magnetization may arise chaotically in the magnetically saturated specimen. These nuclei are bubble domains the radius of which increases with time t under the action of the axially symmetrical demagnetizing field. After the radius reaches its maximum value, the bubble domain is distorted and takes the elliptical form. With the passage of time, it acquires branching appendices with the central part of the domain being compressed. In this process, a labyrinth domain structure arises. In Fig. 4, the two-step view of the DS illustrates the development of nuclei of reversed magnetization. The bright area is a reversed domain within 25 μs after the pulse field was turned off (t = 25 μs). The black region around this domain displays the pathway traversed by the DW during the time Δt between the first and the second light pulses (Δt = 3 μs). In the process of above-described evolution of nuclei of reversed magnetization, the DW velocity did not exceed 8 m/s. The domains similar to the reversed domain presented in Fig. 4 were described in [11].

Our investigations revealed that the domain growth takes place in the main on the boundaries of a nucleus of reversed magnetization. At a certain instant, together with chaotically arising regions of labyrinth DS, axially oriented stripe domains occur in the specimen. In the process, the regions of labyrinth DS are enlarged with concurrent development of stripe domains in the way described above. Such coexistence of DSs of different types lasts up to the axially oriented stripe DS formation being completed. It is the axially symmetrical magnetic field that causes the development both of the regions of a labyrinth DS and of axially-oriented domains.

It is likely that the generation of nuclei of reversed magnetization in the specimen after the turning-off of the field pulse of an amplitude that is close to the saturation field is due to nondemagnetized regions remained inside the specimen after the pulse action. These regions are nuclei of reversed magnetization, and their random array is responsible for the random distribution of reversed domains. If the amplitude of the

pulse field is high enough, the specimen is fully demagnetized, and the described effect is not observed.

With use of modified method of two-step high-speed photography, we were fortunate to trace and fix the development of axially oriented stripe DS. In the result of our experiments, it was revealed that the orientation of such DS is uniquely determined by radial tensile deformation, which was caused by the coil directly pasted on the specimen, when it experienced a pulse current flow, and by axially symmetrical magnetostatic field.

REFERENCES

1. V. G. Pokazan'ev, V. Yu. Politov, and Yu. I. Yalyshev, Fiz. Met. Metalloved. **58**, 637 (1984).
2. F. V. Lisovskiĭ, E. G. Mansvetova, E. G. Nikolaeva, and A. V. Nikolaev, Zh. Éksp. Teor. Fiz. **103**, 213 (1993) [JETP **76**, 116 (1993)].
3. A. H. Eschenfelder, *Magnetic Bubble Technology* (Springer, Berlin, 1980; Mir, Moscow, 1983).
4. G. S. Kandaurova and A. É. Sviderskiĭ, Zh. Éksp. Teor. Fiz. **97**, 1218 (1990) [Sov. Phys. JETP **70**, 684 (1990)].
5. M. V. Chetkin, A. I. Akhutkina, and T. B. Shapaeva, Mikroélektronika **27**, 370 (1998).
6. I. E. Dikshteĭn, F. V. Lisovskiĭ, E. G. Mansvetova, and E. S. Chizhik, Zh. Éksp. Teor. Fiz. **100**, 1606 (1991) [Sov. Phys. JETP **73**, 888 (1991)].
7. M. V. Chetkin, I. V. Parygina, and L. L. Savchenko, Zh. Éksp. Teor. Fiz. **110**, 1873 (1996) [JETP **83**, 1031 (1996)].
8. M. V. Chetkin, S. N. Gadetskiĭ, A. P. Kuz'menko, and V. N. Filatov, Fiz. Tverd. Tela (Leningrad) **26**, 2655 (1984) [Sov. Phys. Solid State **26**, 1609 (1984)].
9. V. G. Bar'jakhtar, M. V. Chetkin, B. A. Ivanov, and S. N. Gadetskiy, *Dynamics of Topological Magnetic Solitons. Experiment and Theory*, Springer Tracts in Modern Physics (Springer, Berlin, 1994), Vol. 129.
10. S. V. Vonsovskiĭ, *Magnetism* (Nauka, Moscow, 1971; Wiley, New York, 1974).
11. V. V. Randoshkin, L. R. Ivanov, and R. V. Telesnin, Zh. Éksp. Teor. Fiz. **75**, 960 (1978) [Sov. Phys. JETP **48**, 486 (1978)].

Translated by N. Ostrovskaya

Physics of the Solid State, Vol. 42, No. 7, 2000, pp. 1329–1333. Translated from Fizika Tverdogo Tela, Vol. 42, No. 7, 2000, pp. 1291–1295.

MAGNETISM AND FERROELECTRICITY

Specific Features of Structural, Dielectric, and Optical Properties of $CdTiO_3$

Yu. V. Kabirov*, M. F. Kupriyanov*, Ya. Dets, and P. Wawzala****

** Rostov State University, pr. Stachki 194, Rostov-on-Don, 344090 Russia*

*** Silesian University, PL-40-007, Katowice, Poland*

Received October 4, 1999

Abstract—The optical and dielectric properties and the structure of crystalline and ceramic perovskite $CdTiO_3$ modifications have been investigated. The multiplication of the unit cell along three perovskite axes is found. The new possible space groups of symmetry D_{2h}^{18} and D_{2h}^{21} are determined. It is elucidated how small radiation doses affect the structure and properties of crystalline and ceramic perovskite modifications. Analysis of the intensities of diffraction reflections demonstrate that the defect formation leads to an increase in the antiparallel displacements of Cd atoms in the unit cell. *© 2000 MAIK "Nauka/Interperiodica".*

1. INTRODUCTION

Among the double oxides $ATiO_3$ (where A is Ba, Pb, Sr, Ca, and Cd), cadmium titanate $CdTiO_3$ is distinctive in that it exhibits either a perovskite structure or ilmenite-type structure depending on the crystallization conditions [1, 2]. In a series of oxide niobates $ANbO_3$ (where A is Ag, K, Na, and Li), the $AgNbO_3$, $KNbO_3$, and $NaNbO_3$ compounds always have a perovskite structure, and $LiNbO_3$ exhibits an ilmenite-type structure [3]. Up to now, all attempts to change $LiNbO_3$ (and $LiTaO_3$) to the perovskite modification by using any possible methods of additional treatment have been unsuccessful, whereas $CdTiO_3$ can be readily transformed from the ilmenite-type structure to the perovskite structure by high-temperature annealing [2]. So far, it remains unclear whether this reconstructive phase transition is monotropic or enantiotropic (reversible). The low-temperature ferroelectric phase transition in the perovskite $CdTiO_3$ modification at 50–60 K was first observed by Smolenskiĭ [4] and, more recently, by Sugai and Wada [5]. Since that time, the investigations into the structure and physical properties of this phase have received considerable attention of many researchers [6–12]. The ilmenite-like modification of $CdTiO_3$ is still not clearly understood [13, 14], even though it, like $LiNbO_3$ and $LiTaO_3$, can possess the ferroelectric properties with a high Curie temperature. By now, the features in optical, dielectric, and other physical properties of $CdTiO_3$ over wide ranges of temperatures and frequencies of measuring electric fields have not been adequately explored. The structural features of two $CdTiO_3$ modifications, their temperature transformations, and the influence of different defects on their physical properties and structure are also poorly known; furthermore, the low-temperature transition has never been structurally investigated.

In the present work, we studied the features of crystal structure and a number of optical and dielectric properties of the $CdTiO_3$ single crystals of perovskite modification.

2. EXPERIMENTAL TECHNIQUE

Single crystals of $CdTiO_3$ were grown from solutions in the melt of mixtures $NaBO_2 + KBO_2 + CdTiO_3$ by Proskuryakov and Spinko. Polycrystalline samples of $CdTiO_3$ were prepared from the stoichiometric mixtures of CdO and TiO_2 according to the standard solid-phase synthesis procedure. The x-ray powder diffraction analysis of the $CdTiO_3$ samples revealed that the ilmenite-like $CdTiO_3$ modification is formed at synthesis temperatures of 800–900°C. Upon annealing of the samples at 1100°C in air, this phase transforms to the perovskite modification.

The crystals and powders of the perovskite and ilmenite $CdTiO_3$ modifications were checked for stoichiometry by the x-ray fluorescence analysis on an EDAX-DX-95 instrument with the use of reference mixtures of CdO and TiO_2.

The x-ray structure investigations of the $CdTiO_3$ single crystals were carried out on a WBG-2 goniometer and a DRON-3M diffractometer (CuK_α radiation). The optical properties of the $CdTiO_3$ crystals were examined with a MIN-8 polarizing microscope and a special setup (at the Silesian University), which made it possible to measure the birefringence and its temperature dependence in small regions of the crystal.

The dielectric properties of the $CdTiO_3$ crystals (the temperature–frequency dependences of the permittivity) were measured in the temperature range 20–310°C at measuring field frequencies from 100 Hz to 20 kHz. Note that no pyroelectric and piezoelectric effects were observed in polycrystalline samples of both $CdTiO_3$ modifications.

1063-7834/00/4207-1329$20.00

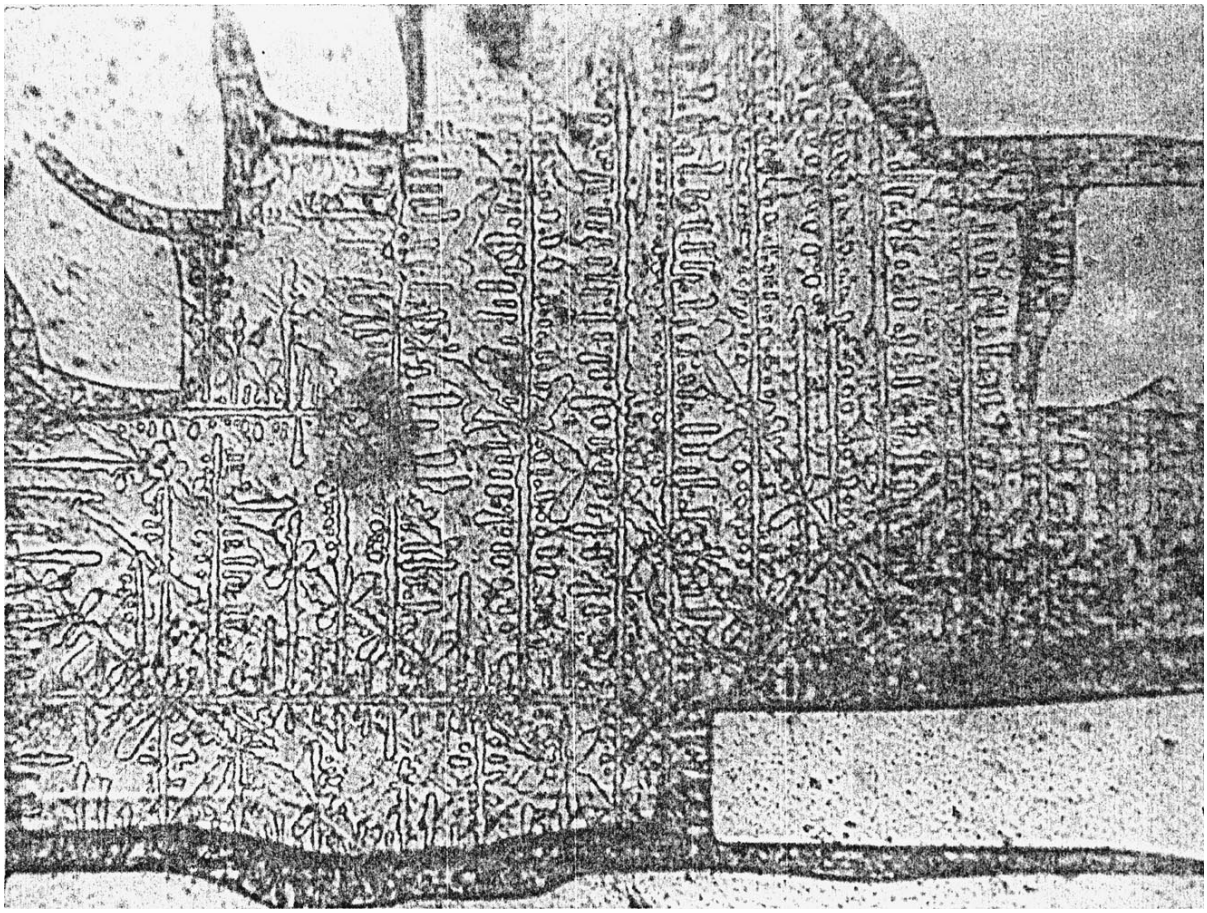

Fig. 1. Etch profile of the $CdTiO_3$ crystals.

3. RESULTS

3.1. Optical Investigations

The etch profile of the studied crystals is closely similar to the structure of 180-degree domains revealed by the etching in the $BaTiO_3$ and $PbTiO_3$ crystals and other perovskite ferroelectrics. These small-sized [(1–2) × 10^{-4} cm] configurations are oriented in two mutually perpendicular directions in parallel to the crystal faces (Fig. 1). Crystals of the perovskite $CdTiO_3$ modification are orthorhombic and, hence, can be characterized by the refractive indices n_A, n_B, and n_C for the corresponding orientations of the optical indicatrix. In our case, the [010] direction, as a rule, is normal to the surface of the scaly $CdTiO_3$ crystals, which allowed us to determine the birefringence $\Delta n = n_A - n_C$. Figure 2 displays the temperature dependence of the birefringence for the $CdTiO_3$ crystal. It should be noted that the $\Delta n(T)$ dependence exhibits a small kink at temperatures of 200–250°C.

3.2. Structural Investigations

At the first stage of structural studies, the $CdTiO_3$ crystal was examined by the rolling-crystal and rotating-crystal methods. It was revealed that the [010] crystallographic direction of the perovskite structure is aligned along the axis of suspension (rotation). Analysis of the reflection shape demonstrated that the crystal is not twinned but, at the same time, has a developed microblock structure. Then, the crystal was examined on the diffractometer by using separate scanning of the crystal (ω) and a detector (2Θ). This enabled us to determine the angles between the blocks, which are equal to several angular minutes. The rotating-crystal x-ray photographs clearly demonstrate superstructure (with respect to perovskite) layer lines that correspond to the doubling of the parameter b_p = 3.803(4) Å of the perovskite unit cell. The following results were obtained from the indexing of the zeroth, first, and second layer lines by the Weissenberg method. First, the parameters a_p and c_p of the monoclinic perovskite cell are doubled: $a_p = c_p$ = 3.790(3) Å and β_p = 91.0(3)°. Taking into account the superstructure, the true symmetry of the $CdTiO_3$ crystal can be considered orthorhombic with the unit cell parameters $\mathbf{A}_0 = 2\mathbf{b}_p$, $\mathbf{B}_0 = 2(\mathbf{a}_p + \mathbf{c}_p)$, $\mathbf{C}_0 = 2(\mathbf{a}_p - \mathbf{c}_p)$, A_0 = 7.606(4) Å, B_0 = 10.607(5) Å, and C_0= 10.831(5) Å, which, within the limits of experimental error, is in agreement with the results obtained

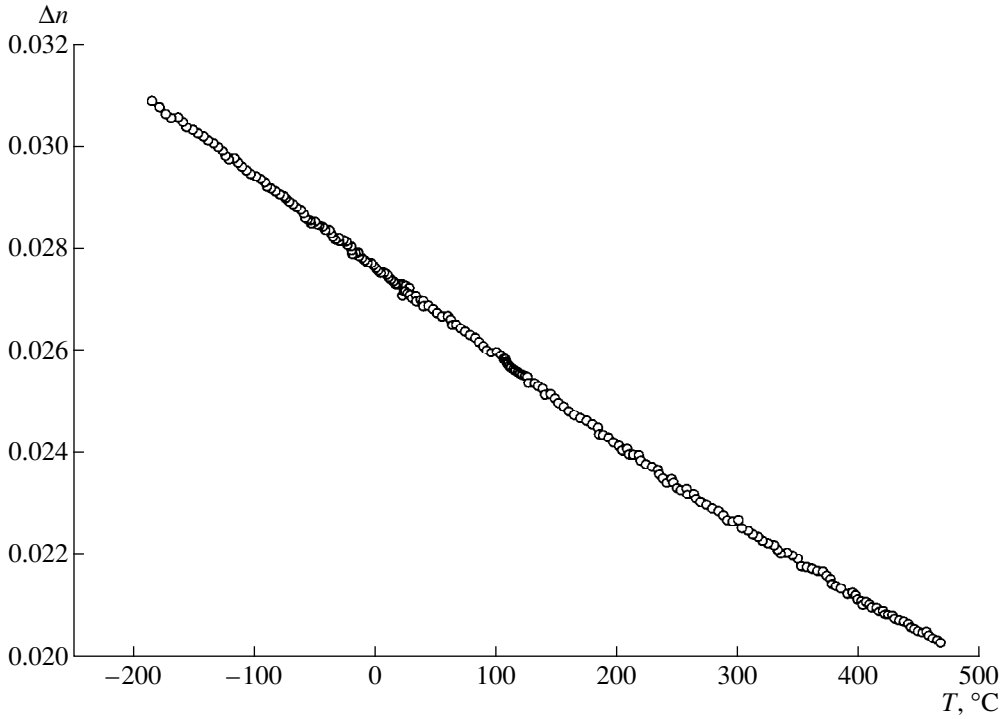

Fig. 2. Temperature dependence of the birefringence for the $CdTiO_3$ crystal.

by Megaw [1] but contradicts the conclusion that the multiplication of the orthorhombic superstructure cell along the Y_0 and Z_0 axes is absent [9, 10]. Second, the diffraction reflections observed obey the following regularities: among the H_0, K_0, and L_0 reflections, there occur only the reflections with $K_0 + L_0 = 2n$; among the $0K_0L_0$ reflections, only the reflections with $K_0 = 2n$ and $L_0 = 2n$; among the H_0K_00 reflections, only the reflections with $K_0 = 2n$; and for two observed reflections of the $0K_00$ type, only the reflections with $K_0 = 4n$. These regularities correspond to the space symmetry groups with the base-centered orthorhombic cells C_{2v}^{15} = *Abm*2, C_{2v}^{17} = *Aba*2, C_{2h}^{18} = *Abam*, and D_{2h}^{21} = *Abmm*, which are indistinguishable in absences. The preliminary analysis of the intensities of x-ray diffraction reflections and the absence of clearly pronounced indications of the piezoelectric and pyroelectric effects at room temperature indicates that the D_{2h}^{18} and D_{2h}^{21} centrosymmetric groups are more probable.

The diffractometric investigations of the $CdTiO_3$ crystal revealed that the intensities of superstructure reflections of the H_0^{22} type increase with an increase in H_0 (from 1 to 7) and, at the large vectors **H** of the reciprocal lattice, are of the same order of magnitude as the intensities of the main (perovskite) reflections. This suggests considerable antiparallel displacements of atoms along the *y* axis of the perovskite cell (i.e., along the X_0 axis of the superstructure cell).

In order to verify the hypothesis concerning the influence of radiation-induced defects on the structural

Variations in the intensities of x-ray diffraction reflections for the $CdTiO_3$ crystal under α- and γ-irradiation

Perovskite reflections			Superstructure reflections		
$H_0K_0L_0$	I_0^*	I_r^*	$H_0K_0L_0$	I_0	I_r
2 2 2	420	350	1 2 2	30	170
4 2 2	40	40	3 2 2	16	20
6 2 2	1060	1040	5 2 2	40	40
8 2 2	230	160	7 2 2	88	88
2 4 4	50	40	1 4 4	280	280
4 4 4	50	40	3 4 4	18	15
2 6 6	400	380	5 4 4	45	44
4 6 6	90	90	7 4 4	43	97
2 8 8	10	10	1 6 6	345	320
0 2 2	390	380	3 6 6	217	240
0 4 4	1950	1150	5 6 6	185	185
0 6 6	240	80	1 8 8	540	520
0 8 8	750	90			
2 0 0	770	500			
4 0 0	2530	2160			
6 0 0	620	500			
8 0 0	1490	1320			

Note: I_0^* and I_r are the counting rates (s^{-1}) prior to and after the irradiation, respectively.

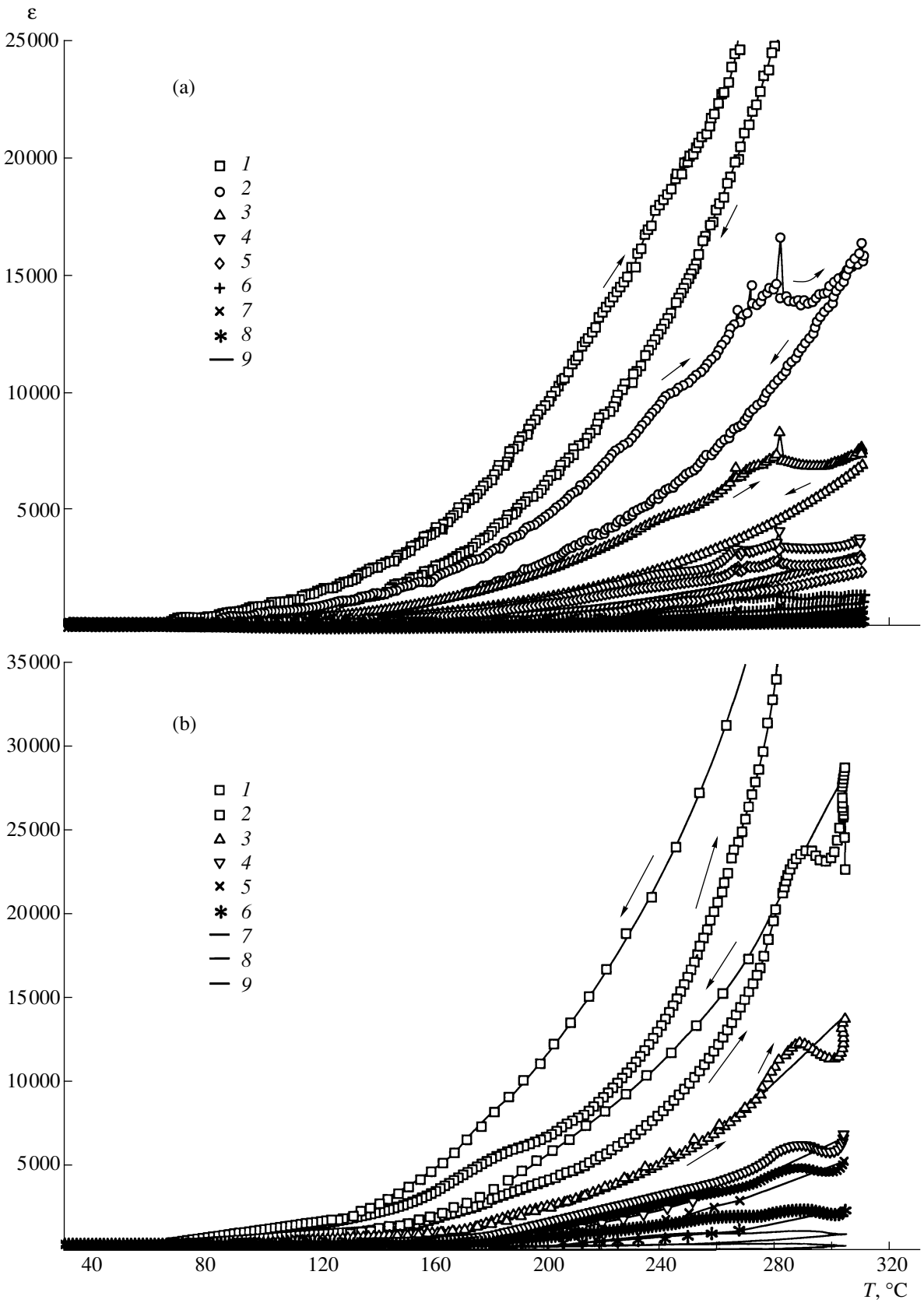

Fig. 3. Temperature dependences of the permittivity for the $CdTiO_3$ crystal (a) prior to and (b) after γ-irradiation. Frequencies f (kHz): (*1*) 0.1, (*2*) 0.2, (*3*) 0.4, (*4*) 0.8, (*5*) 1, (*6*) 2, (*7*) 4, (*8*) 10, and (*9*) 20.

state of $CdTiO_3$ crystals, we investigated how the crystal structure is affected by small dozes of α- and γ-radiation (~10^{13} cm^{-2}) from a ^{239}Pu source. The results obtained are listed in the table.

It is worth noting that a decrease in the intensity of the perovskite diffraction reflections due to irradiation is accompanied by both an increase and a decrease in the intensity of a number of superstructure reflections. This allows us to assume that even a small amount of radiation-induced defects in the $CdTiO_3$ crystal brings about an increase in the antiparallel displacements of atoms (primarily, the Cd atoms [1]). The irradiation results in an increase in the perovskite unit cell parameters: a_p = 3.7774(3) Å and b_p = 3.8011(3) Å prior to the irradiation and a_p = 3.7809(3) Å and b_p = 3.8035(3) Å after the irradiation. Details of structural investigations will be described in a separate paper.

4. DIELECTRIC INVESTIGATIONS

Figure 3 demonstrates the results of dielectric measurements performed with the $CdTiO_3$ single crystal of perovskite modification. Noteworthy are the following features in the temperature–frequency dependences of the permittivity ε for the $CdTiO_3$ crystal prior to and after γ-irradiation on a B-25/30 betatron (E_γ = 23 MeV; dose, ~10^3R).

First, these two states of the crystal are characterized by a strong dependence of the permittivity ε on the frequency of measuring electric fields, specifically in the frequency range from 100 Hz to 1 kHz. The permittivities ε appear to be sufficiently large and can reach 20000 in the temperature range 200–300°C.

At the same time, no sharp maxima of the permittivity ε are observed in the given temperature range. The permittivity exhibits weak maxima at a temperature of approximately 280°C only upon heating of the crystal. It is quite probable that these anomalies are explained by the presence of defects (charged particle traps) with appreciable relaxation times in the structure.

Second, at relatively low frequencies, the temperature dependences of the permittivity ε upon cooling after the heating are shifted toward the high-temperature range for the unirradiated $CdTiO_3$ crystal and toward the low-temperature range for the irradiated $CdTiO_3$ crystal. It can be assumed that, in the former case, the growth defects of the crystal are annealed at high temperatures. In the latter case, in addition to the structural changes, the γ-irradiation generates defects of another type, which are responsible for the features observed in the ε(T) dependences. The elucidation of the origin of strong low-frequency dispersion is a separate problem that calls for further investigations.

ACKNOWLEDGMENTS

We are grateful to E. I. Éknadiosyants and Yu. N. Zakharov for their assistance in performance of a part of the experiment.

REFERENCES

1. H. D. Megaw, Proc. Phys. Soc. London **58**, 133 (1946).
2. M. L. Sholokhovich, O. P. Kramarov, B. F. Proskuryakov, and E. I. Éknadiosyants, Kristallografiya **13**, 1102 (1968) [Sov. Phys. Crystallogr. **13**, 967 (1968)].
3. H. D. Megaw, Acta Crystallogr. **7**, 187 (1954).
4. G. A. Smolenskiĭ, Dokl. Akad. Nauk SSSR **70**, 405 (1950).
5. T. Sugai and M. Wada, Jpn. J. Appl. Phys. **18**, 1709 (1979).
6. G. A. Smolenskiĭ, Dokl. Akad. Nauk SSSR **85**, 985 (1952).
7. M. A. Yakubovskiĭ, V. I. Zametin, and L. M. Rabkin, Izv. Vyssh. Uchebn. Zaved., Fiz. **1**, 150 (1978).
8. I. N. Geĭfman, M. L. Sholokhovich, V. I. Molochaeva, and V. É. Dugin, Fiz. Tverd. Tela (Leningrad) **25**, 2506 (1983) [Sov. Phys. Solid State **25**, 1440 (1983)].
9. H. F. Kay and J. L. Miles, Acta Crystallogr. **10**, 213 (1957).
10. S. Sasaki, Ch. T. Prewitt, J. D. Bass, and W. A. Schulze, Acta Crystallogr. C **43**, 1668 (1987).
11. E. J. Baran and J. L. Botto, Z. Anorg. Allg. Chem. **448**, 188 (1979).
12. X. Lin and R. C. Liebermann, Phys. Chem. Miner. **20**, 171 (1993).
13. M. L. Sholokhovich, O. P. Kramarov, B. F. Proskuryakov, and E. K. Zvorykina, Kristallografiya **14**, 1021 (1969) [Sov. Phys. Crystallogr. **14**, 884 (1969)].
14. G. L. Catchen, S. J. Wukitch, and D. M. Spaar, Phys. Rev. B **42**, 1885 (1990).

Translated by O. Borovik-Romanova

Physics of the Solid State, Vol. 42, No. 7, 2000, pp. 1334–1340. Translated from Fizika Tverdogo Tela, Vol. 42, No. 7, 2000, pp. 1296–1302.

MAGNETISM AND FERROELECTRICITY

Polarization and Depolarization of Relaxor Ferroelectric Strontium Barium Niobate

V. V. Gladkiĭ*, V. A. Kirikov*, S. V. Nekhlyudov*, T. R. Volk*, and L. I. Ivleva**

** Shubnikov Institute of Crystallography, Russian Academy of Sciences, Leninskiĭ pr. 59, Moscow, 117333 Russia*

*** Institute of General Physics, Russian Academy of Sciences, ul. Vavilova 38, Moscow, 117942 Russia*

Received December 15, 1999

Abstract—The anomalies of polarization (mismatch of hysteresis loops for several first repolarization cycles, the absence of specific coercive field, etc.) in quasi-static and dc electric fields have been found in the strontium barium niobate relaxor ferroelectric. The anomalies are associated with a highly inhomogeneous structure of the crystal, which is considered a clearly defined nonergodic system with a random distribution of strong local internal fields. The energy distributions of potential barriers for the polarization and the depolarization are obtained at different electric field strengths and temperatures. *© 2000 MAIK "Nauka/Interperiodica".*

1. INTRODUCTION

Crystals with a perovskite structure and inhomogeneous composition were the first materials termed the relaxor ferroelectrics [1]. More recently, other compounds with a tungsten bronze structure, in particular, the $Sr_xBa_{1-x}Nb_2O_6$(SBN) solid solutions ($0.75 \geq x \geq 0.25$), were assigned to this class of materials [2]. The relaxor ferroelectrics are promising materials for the use in piezoelectric technology, nonlinear optics, and holography [3, 4]. The physical properties of these compounds are characterized by a number of features. The anomalies of properties due to the transition of strontium barium niobate from the nonpolar phase (point group D_{4d} [5]) to the polar phase (point group C_{4v} [2]) are substantially smeared in temperature. For example, the permittivity ε in a weak electric field exhibits a broad maximum at a specific temperature T_m. In the range of T_m, the characteristic dispersions of ε and dielectric loss are observed in the low-frequency range. Narrow, "extended" dielectric hysteresis loops occur over a wide range of temperatures below and above the T_m point and slowly degrade on heating [6, 7]. An increase in the Sr concentration [2] and doping of strontium barium niobate by rare-earth elements [3, 8] bring about a drastic decrease in T_m, and the characteristic properties of relaxors become more pronounced.

The smearing of the phase transition and the features of physical properties stem from the structural disordering and composition fluctuations [1, 2, 7], which induce local symmetry distortions and internal electric fields over a wide temperature range, including the T_m point. For strontium barium niobate, this disorder is associated with the disordering of strontium ions over two cation sites. As a result, the crystal can be considered a nonpolar matrix with randomly embedded inclusions of small spontaneously polarized regions (nanodomains) [7].

As a rule, the dielectric properties of relaxors have been investigated in ac electric fields [1, 2, 7]. In the present work, we studied the polarization of strontium barium niobate in slowly varying (quasi-static) and dc electric fields, which made it possible to take into account the contribution of the longest-lived relaxation centers whose low-frequency boundary of polarizability dispersion is as low as 10^{-5} Hz.

2. EXPERIMENTAL TECHNIQUE

The $Sr_xBa_{1-x}Nb_2O_6$crystals (x = 0.61) containing rare-earth elements were grown by the Czochralski method at the Research Center for Laser Materials and Technology, Institute of General Physics, Russian Academy of Sciences. The $Sr_xBa_{1-x}Nb_2O_6$ composition with x = 0.61 is congruent and possesses the best optical quality [9]. The polarization was investigated using the $Sr_xBa_{1-x}Nb_2O_6$single crystal (x = 0.61) doped with 1 wt % La and 0.01 wt % Ce in the melt (0.44 mol % La and 0.023 mol % Ce in the crystal [10]). Cerium was introduced in small amounts in order to perform the investigations of photorefractive effects in this crystal as the most promising material for dynamic holography [4]. The crystal has the lowest temperature T_m. Therefore, the anomalous behavior expected for polarization near T_m is more conveniently examined by the precision electrometry whose application requires the relatively large electrical resistance R of the sample, which decreases with an increase in the temperature. According to our estimates, $R \sim 9.8 \times 10^{12}$ Ω at 0°C and $\sim 22 \times 10^{12}$ Ω at 20°C. Figure 1 depicts the temperature dependences of the permittivity ε_{33} for the studied and undoped strontium barium niobate crystals (x = 0.61) at a measuring field of ~ 0.5 V/cm. It can be seen that the doping leads to an considerable shift in T_m, smearing of the maximum of ε_{33}, and dispersion of ε_{33}.

1063-7834/00/4207-1334$20.00

The polarization P was measured under the following conditions of changing the external electric field E and temperature T: (i) a slow stepwise change in T at $E = 0$ or $E \neq 0$ in measurements of the pyroelectric effect, (ii) a slow stepwise cyclic change in E with a period of ~1 h at different temperatures T = const in measurements of the hysteresis loops, and (iii) instantaneous application or removal of dc electric field E at T = const in measurements of the polarization relaxation. Prior to each measurement, the sample was heated above the T_m temperature and then was cooled to a specific temperature.

The main element of a setup involved an equal-arm bridge with a V7-29 electrometer as a null indicator. The minimum measured voltage was equal to 20 μV, and the minimum charge was 4×10^{-6} μC. The voltage in a diagonally opposite pair of junctions of the bridge was compensated with a step of 0.15 mV by a program-simulated method on a personal computer and peripheral controlled blocks. The relaxation measurements were carried out in the real time mode. The setup and its operation were described in detail in [11]. In order to measure the hysteresis loops, the setup was additionally equipped with a B5-50 controlled voltage source (0–300 V) with the variable output polarity and a program-driven unit. This made it possible to sequentially measure several repolarization cycles with a voltage step multiple of 1 V and a time step multiple of 1 s. The maximum number of steps was equal to 1200. The voltage step, its duration, and the maximum voltage could be changed in the course of measurements. The electric field polarity for the initial part of the hysteresis loop was specified prior to measurements.

For measurements of the pyroelectric effect, the setup was equipped with an Shch-300 voltmeter for measuring the voltage across a differential thermocouple (melting ice—sample holder) and also with a program-driven unit providing the processing of temperature data. The temperature was calculated in the program-driven unit with the use of the polynomial of degree 4.

The ground sample of the polar section had the shape of a rectangular plate $4 \times 4 \times 0.7$ mm in size. The large faces of the plate were coated with a conducting silver paste. The error in the regulation of thermostat temperature was equal to ~0.03 K.

3. RESULTS AND DISCUSSION

In any crystal, a change in the polarization with a variation in the temperature in the absence of the external electric field E (pyroelectric effect) first of all indicates the spontaneous polarization P_s and, in the case of inhomogeneous structure, the nonequality of the volumes of regions with mutually opposite directions of P_s (unipolarity). The variation in the polarization ΔP upon cooling and heating of the strontium barium niobate sample in the temperature range below T_m at $E = 0$ and

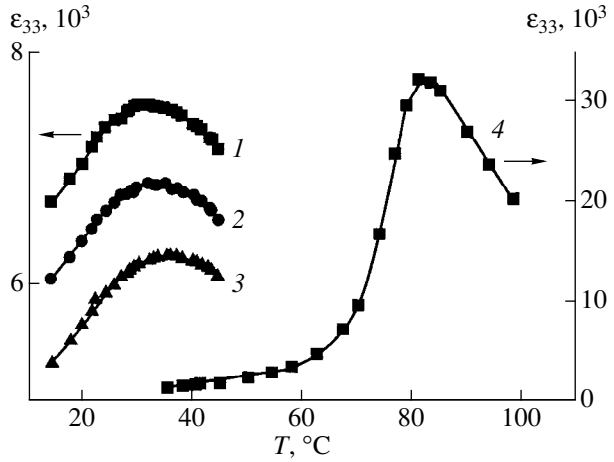

Fig. 1. Temperature dependences of the permittivity ε_{33} for the (*1–3*) doped and (*4*) undoped strontium barium niobate crystals. Frequency, kHz: (*1*) 0.1, (*2*) 1, and (*3*) 20.

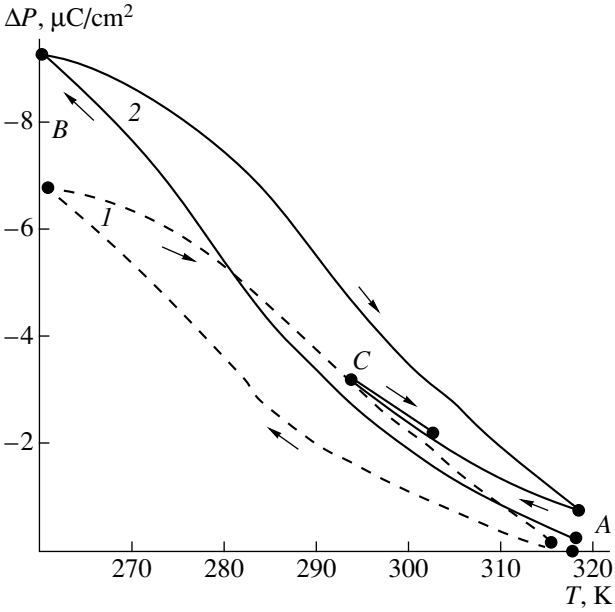

Fig. 2. Variation in the polarization ΔP upon cooling and heating of the strontium barium niobate crystal. Field strength E, V/cm: (*1*) 0 and (*2*) 300.

$E \neq 0$ is displayed in Fig. 2. The directions of the field E and the initial polarization P_0 coincide. The time of cooling from point A to point B or heating from point B to point A is equal to ~160 min. The temperature hysteresis suggests the presence of long-lived metastable states in the crystal. As a result, after the cycle of cooling and subsequent heating, the polarization exceeds its initial value. Upon cooling to a higher intermediate temperature (point C), the temperature hysteresis decreases, and, upon heating, the curve $\Delta P(T)$ runs below.

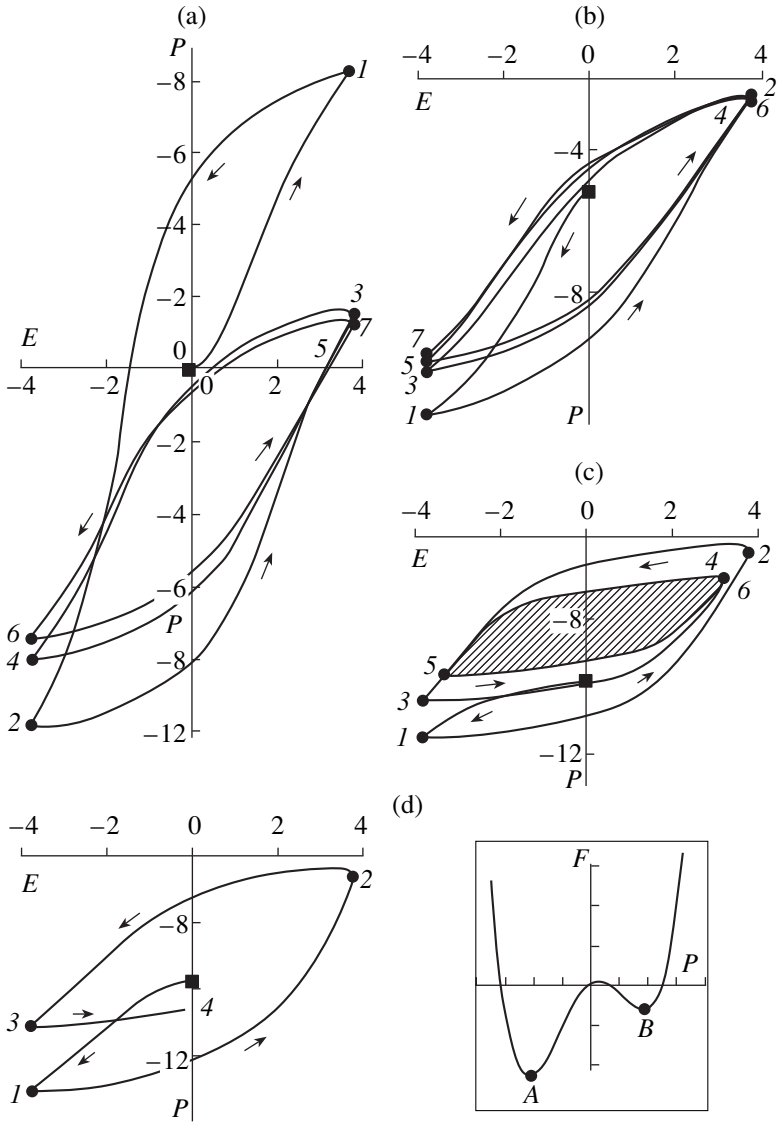

Fig. 3. Dielectric hysteresis loops P ($\mu C/cm^2$) versus E (kV/cm) at different temperatures and directions of the initial field E for the strontium barium niobate crystal. Directions of the initial E and P_0: (a) opposite and (b–d) identical. Temperature, K: (a, b) 274, (c) 250, and (d) 236. The inset shows the local free energy F as a function of the polarization P.

The dielectric hysteresis loops P versus E exhibit a specific shape. Figure 3 demonstrates the loops in the cases when, in the first quarter of the period, the directions of the polarization P induced by the field E and the initial nonzero spontaneous polarization P_0 are opposite (Fig. 3a) and identical (Figs. 3b–3d) at three temperatures: 274 (Figs. 3a, 3b), 250 (Fig. 3c), and 236 K (Fig. 3d). The onset of the repolarization process is marked by filled squares, and the limiting values of P that correspond to the maximum fields E are designated by filled circles and numerals in the temporal order.

Unlike the hysteresis loops of standard homogeneous ferroelectrics, all the loops under consideration are characterized by the common feature—the mismatch of the P trajectories for the preceding and succeeding cycles of variation in E. This effect is especially pronounced for the first cycle of variation in E when the polarizations P at the beginning and at the end of the period differ considerably. After many times repeated cycles, the P trajectories virtually follow each other (merge together), the loops take the usual form, and the loop amplitude of variation in P becomes considerably lesser as compared to that for the first cycle. The loops are shifted along the P axis; i.e., the sample has the initial polarization $P_0 \neq 0$ (unipolarity), whose direction (sign) coincides with the direction of P_0 observed in measurements of the pyroelectric effect (Fig. 2). As the amplitude of E decreases, the loop does not change its shape and remains alike but with a smaller amplitude of variation in P (hatched region in Fig. 3). A decrease in the temperature leads to an

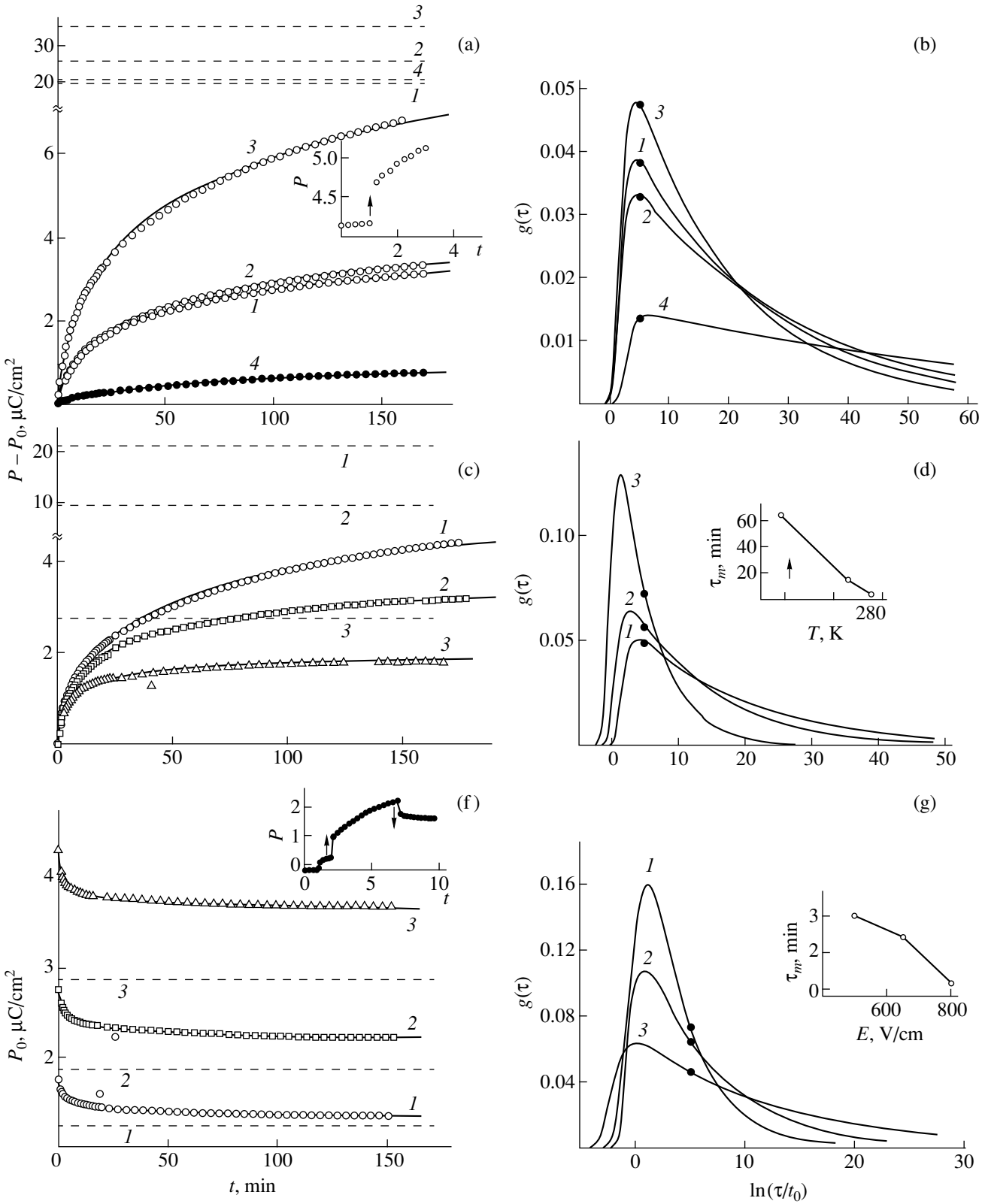

Fig. 4. (a, c, f) Relaxation curves of the polarization P and (b, d, g) distribution functions of relaxation times $g(\tau)$ at different electric fields E and temperatures T for the strontium barium niobate crystal. (a, b) T = 274 K; E = (*1*) 300, (*2*, *4*) 400, and (*3*) 600 V/cm; the inset shows the initial stage of polarization in the applied field E. (c, d) E = 500 V/cm; T = (*1*) 274, (*2*) 288, and (*3*) 294 K; the inset shows the dependence of τ_m on T. (f, g) T = 274 K; E = (*1*) 500, (*2*) 650, and (*3*) 800 V/cm; insets show the initial stage of depolarization upon removal of the applied field E and the dependence of τ_m on T. Horizontal dashed lines represent the equilibrium polarizations P_e, t_0 = 1 min. Arrows in insets indicate the jumps of P upon application and removal of the field E.

Parameters of the relaxation and distribution functions $g(\tau)$ for strontium barium niobate crystal

Process	T, K	E, V/cm	P_0, μC/cm^2	P_e, μC/cm^2	a, min	n	τ_m, min	S
Polarization	274	300	4.69	4.5 ± 0.016	3.724 ± 0.012	0.045 ± 0.001	82.2 ± 0.3	0.14
		400	0.98	6.97 ± 0.019	4.35 ± 0.013	0.038 ± 0.001	114.5 ± 0.4	0.11
		600	2.69	8.41 ± 0.013	4.799 ± 0.007	0.058 ± 0.001	82.74 ± 0.2	0.16
	274*	400	6.809	7.09 ± 0.065	11.75 ± 0.11	0.0149 ± 0.0001	788 ± 10	0.03
	274	500	1.0767	2.18 ± 0.01	3.942 ± 0.011	0.061 ± 0.001	64.7 ± 0.2	0.18
	288		2.3486	1.97 ± 0.008	1.207 ± 0.006	0.081 ± 0.001	14.8 ± 0.09	0.29
	293		1.7522	.522 ± 0.005	0.679 ± 0.01	0.201 ± 0.001	3.38 ± 0.06	0.56
Depolarization	274	500	1.75	.217 ± 0.003	0.82 ± 0.06	0.273 ± 0.004	2.98 ± 0.26	0.65
		650	2.77	.874 ± 0.004	0.38 ± 0.02	0.157 ± 0.001	2.40 ± 0.14	0.47
		800	4.328	.866 ± 0.006	0.094 ± 0.004	0.081 ± 0.001	1.16 ± 0.06	0.29

Note: The temperature was stabilized after cooling or heating (*) of the crystal.

increase in the unipolarity (polarization P_0) and a decrease in the amplitude of variation in P (Figs. 3c, 3d).

The features of the dielectric properties confirm the proposed concepts of relaxor structure [1, 2, 7]. The disordered distribution of Sr ions in the lattice results in the gradient of their concentration, a local lowering of symmetry, the internal electric field, and, as a consequence, the asymmetric dependence of the local free energy F on the polarization P with two minima (see inset in Fig. 3) [7]. The depths of minima F_A and F_B (at points A and B in the inset) are randomly distributed over the bulk of the crystal. Since the mutually opposite directions of equilibrium P are equiprobable, there should occur the regions in which either the inequality $F_A < F_B$ or the inequality $F_A > F_B$ is met. In general, the volumes of these regions are not equal, and, hence, in the absence of the electric field E, the nonzero, summarized (over the sample) polarization and the pyroelectric effect (Fig. 2) can be observed even under equilibrium conditions.

The probability of the slow thermally activated, local repolarization from a metastable state to a stable state is determined by the barrier height (the value of F_A or F_B). The external field E of a certain orientation and magnitude decreases the barrier heights and accelerates the repolarization. If the barrier in the field E disappears (for example, $F_A = 0$), the avalanche-like (over-the-barrier) transition to the state with $F_B < 0$ takes place. The hysteresis loops in Fig. 3 indicate that, in the strontium barium niobate relaxor, there are the regions with a considerable asymmetry of $F(P)$ ($F_A \gg F_B$ or $F_A \ll F_B$), which is retained in the electric fields applied. As a result, the first cycle of the field variation changes many crystal regions to the equilibrium states that correspond to deep minima of $F(P)$ and, in actual fact, prevents their further participation in the repolarization. Therefore, upon subsequent cycles, the volume of repolarized regions and the amplitude of variation in P decrease substantially. The difference in the polarizations P at the beginning and at the end of the first cycle gives an estimate of the unipolarity observed in the crystal even prior to the application of the field. As the temperature decreases, all the barrier heights increase, and the features of hysteresis loops become less pronounced.

More detailed data on the structure of potential barriers in the relaxor were obtained in the investigation into the kinetics of polarization and depolarization upon instantaneous application and removal of the dc electric field E. The main results of this study are given below. With an abrupt change in the field of any magnitude (smaller and larger than the half-width of the hysteresis loop), the polarization P always changes, first, jumpwise (over-the-barrier process) and, then, slowly through the mechanism of thermal activation. The slow change in the polarization P with time t in the course of both polarization and the depolarization follows the empirical power law

$$p(t) = (P_e - P(t))/(P_e - P_0) = 1/(1 + t/a)^n, \quad (1)$$

where P_0 is the initial polarization at $t = 0$ (P_0 is the sum of polarizations arisen from the unipolarity and the jump observed upon abrupt change in the field E); P_e is the equilibrium polarization; and a, n, and P_e are the parameters dependent on T and E.

Under the assumption that relaxation centers (microdomains) are independent, their contribution to the polarization can be treated as additive. In this case, the dimensionless polarization can be written as

$$p(t) = \int_0^\infty f(\tau)\exp(-t/\tau)d\tau.$$

Here, $f(\tau)$ is the normalized distribution function of relaxation times τ, $\int_0^\infty f(\tau)\,d\tau = 1$, related to $p(t)$ by the Laplace transform. The distribution has the form $f(\tau) =$

$\{a^n/\Gamma(n)\}(1/\tau)^{n+1}\exp(-a/\tau)$, where $\Gamma(n)$ is the gamma function. Generally, it is more convenient to use the dimensionless function

$$g(\tau) = \tau f(\tau) = (1/\Gamma(n))(a/\tau)^n \exp(-a/\tau), \quad (2)$$

which characterizes the density of distribution $\ln\tau$ for the sample or the distribution of the barrier energies U related to $\ln\tau$ by the Arrhenius law $\ln(\tau/\tau_0) = U/kT$ (where τ_0 is the kinetic coefficient). The function $g(\tau)$ has a maximum at $\tau_m = a/n$ [12].

The experimental data on $P(t)$ were approximated with the power function (1) by the least-squares method according to the standard program with three free parameters P_e, a, and n. In Fig. 4, the experimental data are depicted by different symbols, and the results of calculations are displayed by the solids lines. The horizontal dashed lines represent the equilibrium values P_e or $P_e - P_0$, to which the measured quantities asymptotically approach. The insets in Figs. 4a and 4f show the initial portions of the time dependences of P upon abrupt switching of the field E, which precedes the slow thermally activated relaxation. The jumps of P that correspond to over-the-barrier processes are seen in the figures. The curves of the distribution function $g(\tau)$ defined by formula (2) contain the points at which τ is equal to the maximum time t_{max} of measurements. It is evident that the fraction of processes directly observed in the experiment is insignificant; it is equal to the area S under the curve $g(\tau)$ in the range between the short time $\tau = \tau_0$ and t_{max}. Hence, the other portions of the curves of distribution functions $g(\tau)$ were obtained by the extrapolation of the experimental data to the large relaxation times τ. The relaxation parameters P_e, a, n, and τ_m and the areas S for all the studied cases are listed in the table. The errors (dependent on the duration of measurements) in determination of the parameters were evaluated in the same fashion as in [12].

Let us now consider the main features of the distribution spectra of potential barriers for the relaxation centers in the strontium barium niobate crystal. For the fields of no more than the half-width of the hysteresis loop, the spectra remain virtually unchanged. However, an increase in E leads to an increase in the equilibrium polarization P_e (Fig. 4b). At the same time, in the case of stabilizing a given temperature after the heating (rather than cooling) of the sample, the changes in the distribution spectra are noticeable: the relaxation rate dP/dt decreases, because the processes of switching over higher barriers are involved in the relaxation (Figs. 4a, 4b, curves *4*). An increase in the sample temperature brings about a decrease in the relaxation rate dP/dt and the equilibrium polarization P_e (Fig. 4c). Nonetheless, the processes characterized by lower barriers begin to predominantly contribute to the distribution (Fig. 4d). At the early stage, the depolarization occurs at a relatively high rate (see table and Fig. 4f). However, the stronger the field E of the preliminary polarization of the crystal, the larger the equilibrium polarization P_e and the more the broadening of the distribution, which is predominantly contributed by the giant relaxation times τ and high barriers (see table and Figs. 4f, 4g). This means that the crystal virtually never approaches its equilibrium state at the large value of P_e.

The above findings on the polarization relaxation and the features of hysteresis loops for strontium barium niobate are in agreement with the concepts of local lowering of symmetry, internal electric field, and asymmetric dependence of the free energy F with two minima (Fig. 3, inset) [7]. The ratio between the depths of minima varies over the bulk of the crystal in a wide range. Upon cooling to the given temperature, one part of the crystal appears to be in the stable state with a deep minimum, whereas the other part occurs in the metastable state with a shallow minimum of F. Upon application of the external field E, some regions undergo over-the-barrier (or thermally activated) transition to stable states (the probability of the transition from these states is virtually equal to zero), and the other regions, to metastable states, which, in turn, transform to the stable states upon removal of the field (upon depolarization). An increase in the field E and its subsequent removal lead to an increase in the number of these long-lived states (crystal memory) and the mean (over the sample) equilibrium polarization (Figs. 4a, 4f). The form of the energy distribution of barriers and their quantitative estimates upon polarization in fields E with different strengths and upon depolarization can be obtained within the above phenomenological approach to the kinetics of these processes (see table and Fig. 4). Certainly, the metastable state of the crystal, as a whole, changes and virtually regains its initial form upon repeat heating (annealing) and subsequent cooling of the crystal, as evidenced by the decrease in the barrier height with an increase in the temperature (Fig. 4d) and also a satisfactory reproducibility of the data on the pyroelectric effect.

First and foremost, the results obtained in the investigation into the polarization of strontium barium niobate crystal indicate that this crystal and, most likely, other relaxors over a wide range of temperatures are not ferroelectrics in the strict sense, because they exhibit neither particular coercive field E_c nor typical macroscopic domain structure. The features of polarization and inhomogeneous macroscopic structure of relaxors provide an example of anomalous properties of a clearly defined nonergodic system whose space of all possible states consists of nonoverlapping subspaces with the volume ratio dependent on the electric field. In this respect, it is of particular interest to investigate the polarization of relaxors in strong electric fields.

ACKNOWLEDGMENTS

This work was supported by the Russian Foundation for Basic Research, project no. 99-02-17303.

REFERENCES

1. G. A. Smolenskiĭ, V. A. Isupov, and A. I. Agranovskaya, Fiz. Tverd. Tela (Leningrad) **1**, 167 (1959) [Sov. Phys. Solid State **1**, 147 (1959)].
2. M. E. Lines and A. M. Glass, *Principles and Applications of Ferroelectrics and Related Materials* (Oxford Univ. Press, Oxford, 1977; Mir, Moscow, 1981), p. 736.
3. R. R. Neurgaonkar, J. R. Oliver, W. K. Cory, *et al.*, Ferroelectrics **160**, 265 (1994).
4. R. R. Neurgaonkar, W. K. Cory, M. D. Ewbank, and W. F. Hall, Opt. Eng. (Bellingham, Wash.) **26** (5), 392 (1987).
5. A. S. Bhalla, R. Guo, L. E. Cross, *et al.*, Phys. Rev. B **36**, 2030 (1987).
6. W. H. Huang, D. Viehland, and R. R. Neurgaonkar, J. Appl. Phys. **76**, 490 (1994).
7. L. E. Cross, Ferroelectrics **76**, 241 (1987).
8. T. Volk, Th. Woike, U. Doerfler, *et al.*, Ferroelectrics **203**, 457 (1997).
9. Yu. S. Kuz'minov, *Ferroelectric Crystals for Control over Laser Radiation* (Nauka, Moscow, 1982).
10. L. I. Ivleva, N. V. Bogodaev, N. M. Polozko, and V. V. Osiko, Opt. Mater. **4**, 168 (1995).
11. V. V. Gladkiĭ, V. A. Kirikov, S. V. Nekhlyudov, and E. S. Ivanova, Fiz. Tverd. Tela (S.-Peterburg) **39**, 2046 (1997) [Phys. Solid State **39**, 1829 (1997)].
12. V. V. Gladkiĭ, V. A. Kirikov, E. S. Ivanova, and S. V. Nekhlyudov, Fiz. Tverd. Tela (S.-Peterburg) **41**, 499 (1999) [Phys. Solid State **41**, 447 (1999)].

Translated by O. Borovik-Romanova

Physics of the Solid State, Vol. 42, No. 7, 2000, pp. 1341–1347. Translated from Fizika Tverdogo Tela, Vol. 42, No. 7, 2000, pp. 1303–1309.

MAGNETISM AND FERROELECTRICITY

EPR and Dielectric Properties of $Pb_5Ge_3O_{11}$ Crystals with Off-center Cu^{2+} Ions

M. P. Trubitsyn*, S. Waplak, and A. S. Ermakov***

**Dnepropetrovsk State University, pr. Gagarina 72, Dnepropetrovsk 10, 320625 Ukraine*

e-mail: elf@ff.dsu.dp.ua

*** Institute of Molecular Physics, Poznan, Poland*

Received December 28, 1999

Abstract—The electron paramagnetic resonance (EPR) and dielectric properties of $Pb_5Ge_3O_{11}$ crystals activated by copper ion are investigated. It is shown that Cu^{2+} ions replace Pb^{2+} in trigonal symmetry positions and occupy three off-center positions displaced from a crystal lattice site in a plane perpendicular to the polar axis **C**. The temperature variation of EPR spectra and dielectric properties indicates the presence of thermally activated jumps of Cu^{2+} ions between off-center positions. The EPR and dielectric data are used to determine the activation energy $W = 0.24$ eV and the eigenfrequency $\tau_0^{-1} \sim 10^{12}$ Hz of local dynamics of Cu^{2+} ions. © *2000 MAIK "Nauka/Interperiodica".*

It is well known that the influence of defects is most strongly manifested for crystalline systems undergoing structural phase transitions [1]. Among the various types of defects, off-center impurity ions whose position is displaced from crystal lattice sites have garnered considerable attention [2, 3]. Impurity ions can jump between structurally equivalent off-center positions. The frequencies of such jumps are considerably lower than the eigenfrequencies of lattice vibrations and often lie in the working range of radiospectroscopy. Therefore, radiospectroscopic methods are most effective for studying such system, since they make it possible to study static and dynamic phenomena associated with off-center positions of impurity ions to a high degree of accuracy owing to the local nature of magnetic resonance [3].

The off-center position of copper impurity ions in the structure of lead germanate was reported earlier by Vazhenin *et al.* [4]. The crystal of $Pb_5Ge_3O_{11}$ is well known as a model uniaxial ferroelectric undergoing a transition from the paraelectric (space symmetry group C_{3h}^1) to the polar phase (C_3^1 group) at $T_C = 451$ K [5, 6]. The present work is devoted to the study of EPR and dielectric properties of $Pb_5Ge_3O_{11}$: Cu (0.2, 0.5 wt %) crystals. The experimental single crystals grown by the Czochralski method have the shape of hexagonal prisms having a diameter of ~1 and a length of up to 10 cm. The crystals are transparent and are characterized by a high optical quality and green tint, the intensity of which increases with the impurity concentration. The EPR spectra were recorded in the *X* range with the help of a commercial radiospectrometer. We used samples in the form of $3 \times 3 \times 3$ mm parallelepipeds with the faces perpendicular to the crystal axes. The dielectric properties were measured by the bridge technique. In this case, the samples were cut in the form of plane-parallel plates of a thickness ~0.3 mm, on which platinum electrodes were subsequently deposited by the vacuum sputtering method.

1. ANGULAR AND TEMPERATURE DEPENDENCES OF EPR SPECTRA FOR Cu^{2+}

The recorded spectrum was typical of Cu^{2+} ions in the ground state $^2D_{5/2}$ ($S = 1/2$, $I = 3/2$). The orientational dependences of the positions of resonance lines measured at $T = 287$ K are shown in Fig. 1. The rotation of the magnetic field **B** in the crystallographic planes of orthogonal orientation leads to the emergence of three hyperfine quartets having identical angular dependences and turned through an angle $\pi/3$ about the trigonal axis $C_3 \parallel \mathbf{c}$ relative to one another. The spectra were described by using the spin Hamiltonian (SH), taking into account the electron Zeeman and hyperfine interactions:

$$\mathcal{H} = \beta \mathbf{BgS} + \mathbf{SAI}. \quad (1)$$

While choosing magnetic axes corresponding to ultimate orientations of the field **B**, the principal axis **Z** was taken along the direction in which the *g*-factor and the hyperfine splitting have the largest values. For the three hyperfine quartets observed by us, the axes $\mathbf{Z}_i$ (i = 1, 2, 3 enumerate the magnetically nonequivalent centers) lie in the crystallographic plane (**ab**) and are turned through an angle $2\pi/3$ relative to one another in view of the central symmetry of the magnetic spectra. In the chosen orientation, the axes $\mathbf{X}_i$ line in the (**ab**) plane perpendicular to the corresponding $\mathbf{Z}_i$, while $\mathbf{Y}_i$

1063-7834/00/4207-1341$20.00

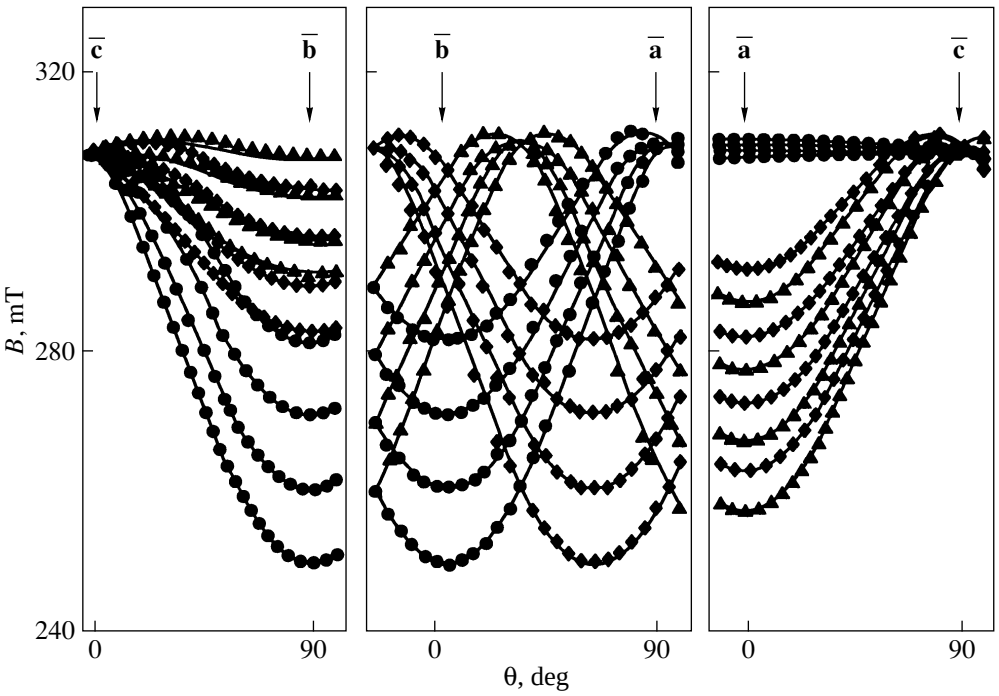

Fig. 1. Angular dependences of the spectra of Cu^{2+} in $Pb_5Ge_3O_{11}$ for the magnetic field **B** rotating in crystallographic planes (T = 287 K). Circles, rhombi, and triangles correspond to positions of the components of three hyperfine quartets; solid curves are calculated on the basis of relations (1) and (2).

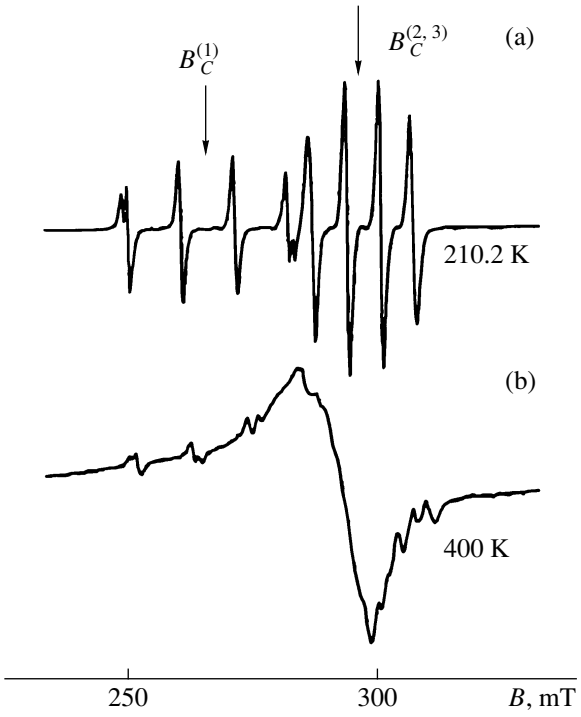

Fig. 2. Temperature variation of the EPR spectra of Cu^{2+}: (a) below ~320 K, the LT spectrum is observed in the form of three hyperfine quartets with centers at $B_C^{(i)}$; (b) above ~350 K, the spectrum consists of a broad HT line [its intensity is magnified 51 times as compared to the LT spectrum in (a)]. **B** ∥ **Z** (∠**Bb** = 4°, **B** ⊥ **c**).

are identical and parallel to **c**. The principal values of the tensors **g** and **A** (in the magnetic field units $A/g\beta$) are defined as

$$g_Z = 2.410, \quad g_X = 2.066, \quad g_Y = 2.069;$$
$$A_Z = 10.85 \text{ mT}; \qquad (2)$$
$$|A_X| \approx |A_Y| \le 0.5 \text{ mT}; \quad \angle\mathbf{Zb} = 4°, \quad \mathbf{Y} \parallel \mathbf{c}.$$

For **B** ∥ **X**, **Y**, the hyperfine splitting becomes indistinguishable from the intrinsic width of the individual components. Hence, formula (2) contains the upper limits of the values of A_X, A_Y obtained by taking into account the intrinsic width of the individual lines $\delta B \sim$ 2 mT and the number of components in the hyperfine structure. The theoretical angular dependences obtained by using formulas (1) and (2) are shown by solid curves in Fig. 1.

The exact measurement of the positions of hyperfine lines shows that the components of quartets are not equidistant. The difference in the intervals can be described in the second order of the perturbation theory taking into account the off-diagonal matrix elements of hyperfine interaction and including the nuclear electric quadrupole interaction **IPI** [7] in the SH (1). According to the estimate we obtained, the contributions of the second-order effects are ~0.5% of the diagonal terms of the hyperfine interaction, and the orientation dependence of spectra (Fig. 1) can be described quite accurately by calculations to the first order of the perturba-

tion theory. The anisotropy and multiplicity ($k_M = 3$) of hyperfine quartets indicate a structural equivalence and a common position (C_1) of the paramagnetic centers in the unit cell of the ferroelectric phase of lead germanate [6, 8].

The Cu^{2+} spectra were measured in the temperature range 200–400 K. Below ~260 K, doubling of hyperfine components (Fig. 2a) is observed, which is due to the presence of ^{63}Cu and ^{65}Cu isotopes. For this reason, the SH parameters (2) should be regarded as the quantities averaged for the two isotopes. As the temperature increases, the low-temperature (LT) triclinic spectral lines are broadened (Fig. 3), and the hyperfine quartets of three magnetically nonequivalent centers become indistinguishable for $T > 320$ K. Above ~350 K, the high-temperature (HT) spectrum consisting of a single broad line (Fig. 2b) with an unresolved hyperfine structure is formed. The position and width of the HT line are characterized by an axial anisotropy. The values of the g-factor are given by

$$g_{\parallel}^{TA} \approx 2.07, \quad g_{\perp}^{TA} \approx 2.19; \quad \mathbf{Z}^{TA} \parallel \mathbf{c}, \tag{3}$$

the magnetic axis being directed along **c**. The unit multiplicity ($k_M = 1$) and the preferred direction of the $\mathbf{Z}^{TA}$ are features of the trigonal (C_3) position symmetry of active centers [6, 8]. The transformation of LT spectra into the HT line is observed most clearly for the magnetic field **B** oriented in the (**ab**) plane. For **B** ∥ **c**, hyperfine LT quartets merge into a single narrow line (see Fig. 1) which does not change significantly in the entire temperature range under investigation. The parameters obtained for the LT and HT spectra agree with the results obtained by Vazhenin *et al.* [4].

The averaging of three low-symmetry spectra into a single trigonal spectrum demonstrates the presence of dynamic transitions of copper centers between three equivalent states with a temperature dependent frequency [9, 10]. The triclinic hyperfine quartets can be measured up to ~320 K. As the temperature increases above ~350 K, the HT spectrum acquires a quite definite shape, and the parameters of a solitary line can now be measured approximately. The temperature dependences of the width and position of LT and HT spectral lines are presented in Figs. 4a and 4b for the magnetic field orientation **B** ∥ **Z** ($\angle$**Bb** = 4°, **B** ⊥ **c**). In the temperature range 320–350 K, the determination of spectral parameters is hampered by the superposition of broadened hyperfine components of LT spectra and the HT resonant signal.

We can derive analytic expressions for the width and position of resonance lines depending on the relation between the transition rate and the magnitude of frequency splitting between low-symmetry spectra [9, 10]. At low temperatures, the slow-motion approximation is valid, in which the broadening of the LT spectral components is uniform and inversely proportional to the mean lifetime τ' in one of the low-symmetry states. The simulation of the spectral contour by a convolution

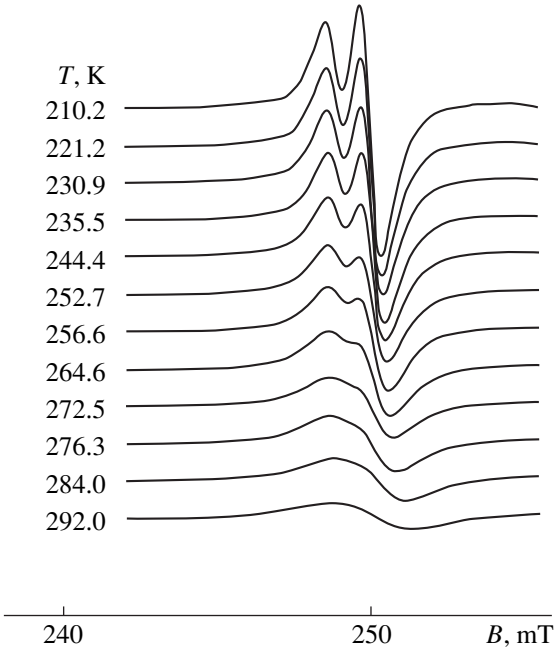

Fig. 3. Broadening of the low-field hyperfine line $m_1 = 3/2$ with increasing temperature.

of the Lorentzian with the Gaussian has allowed us to exactly reproduce the experimental spectrum by the theoretical spectrum and to obtain the temperature dependence of the homogeneous contribution to the hyperfine line width of the LT spectrum (Fig. 5a). Under the assumption of an exponential temperature dependence $\tau = \tau'/3 = \tau_0 \exp(W/k_B T)$ of the mean lifetime in the three low-symmetry positions, the temperature dependence of the line broadening of the LT spectrum was described as

$$\delta B = \delta B_0 + A \exp\left(-\frac{W}{k_B T}\right). \tag{4}$$

The fitting of this expression to the experimental data was carried out in the temperature range 210–300 K. The values of the parameters appearing in (4) were $\delta B_0 = 0.68$, $A = 6.9 \times 10^3$ mT, and the values of the activation energy W are given in the table. The theoretical curve is presented by the solid curve in Fig. 5a. Since the temperature interval under investigation is quite broad (~100 K), we must obviously justify the choice of the background frequency δB_0 as a constant quantity. In our opinion, this is important since, presuming a considerable broadening due to the spin–lattice interaction, we can interpret the observed deviation of $\delta B(T)$ from the exponential dependence as a result of the temperature dependence of the activation energy $W(T)$. Figure 2b shows the residual spectrum consisting of low-intensity lines against the background of a broad HT line. The positions of these lines correspond to the positions of the LT hyperfine quartets averaged upon heating. We can assume that the copper centers respon-

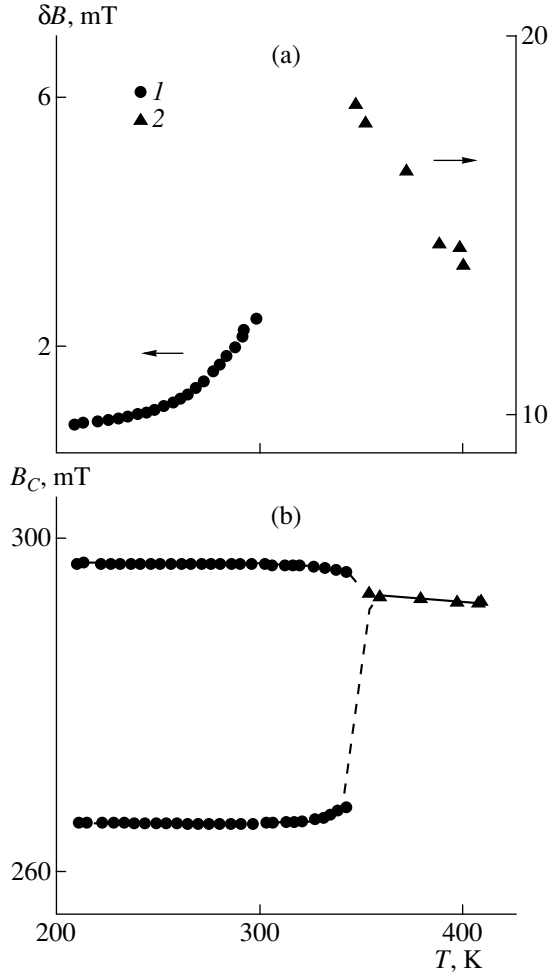

Fig. 4. Temperature dependences of (a) the width of the hyperfine component of the LT spectrum (*1*) and the HT line (*2*); and (b) positions of hyperfine quartets of the LT spectrum (*1*) and HT line (*2*).

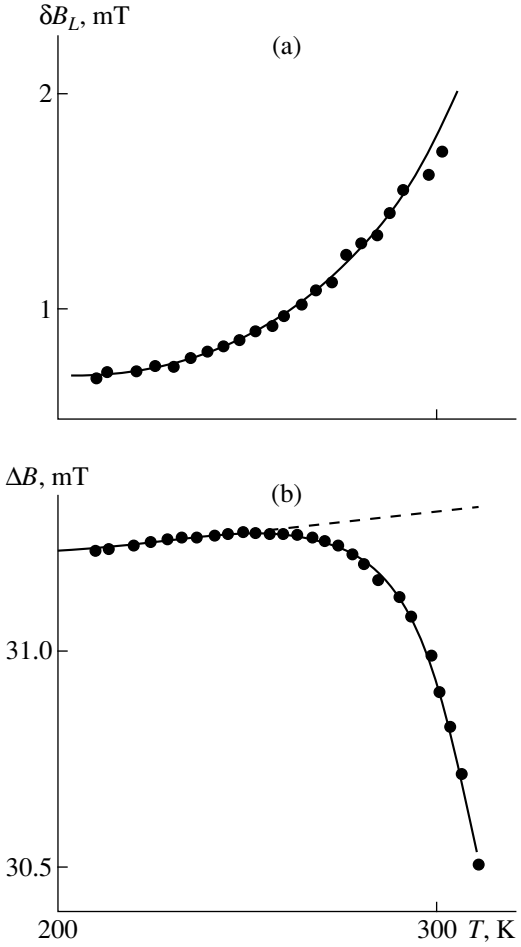

Fig. 5. Temperature dependences (a) of the homogeneous contribution δB_L to the hyperfine line width of the LT spectrum and (b) of the separation ΔB between the centers of hyperfine quartets of the LT spectrum. The circles correspond to experimental results and the solid curves are calculated by formulas (3) and (4).

sible for the low-intensity spectrum are in the same positions, but they do not participate in transitions between low-symmetry positions in view of a certain perturbation. In this case, the line width of the residual spectrum is determined by the same mechanisms of the spin–lattice interaction, but does not contain the dynamic contribution associated with transitions, i.e., can serve as a measure of δB_0. It can be seen from Fig. 2b that the lines of the residual spectrum do not show visible broadening: the isotopic splitting is well resolved even at 400 K. Consequently, disregarding the temperature dependence of the background width δB_0 is justified.

With increasing temperature, the rate τ^{-1} of transitions between low-symmetry positions increases and becomes comparable to the frequency analog of the separation between the centers of hyperfine quartets $\Delta B = (B_C^{(2,3)} - B_C^{(1)}) \sim \Delta\nu$ (Fig. 2a) The spectra corresponding to individual positions are displaced towards one another, their convergence being determined by the mean lifetime of low-symmetry configurations $(\Delta B_0^2 - \Delta B^2(T))^{1/2} \sim \tau^{-1}$, where ΔB_0 stands for the separation between hyperfine quartets in the absence of transitions [9, 10]. The temperature dependence $\Delta B(T)$ is shown in Fig. 5b. As the temperature increases up to ~240 K, the splitting ΔB increases almost linearly due to the thermal expansion of the crystal lattice. Starting from about 250 K, the separation ΔB rapidly decreases. The experimental dependence of the splitting was described by the formula

$$\Delta B = \sqrt{\Delta B_0^2 - C\exp\left(-\frac{2W}{k_B T}\right)}. \qquad (5)$$

The temperature drift of the separation between hyperfine quartets in the absence of transitions was approximated by the straight line ΔB_0 [mT] = 31.05 + 8.9 × 10^{-4} T

(dashed line in Fig. 5b). The theoretical curve obtained by fitting (5) to the experimental data corresponding to the temperature interval 260–320 K is presented by the solid curve in Fig. 5b. The proportionality factor in (5) is $C = 7 \times 10^9$ mT^2, and the value of the activation energy W is given in the table.

Upon further heating under the condition $\tau \sim 1/(2\pi\Delta\nu)$, low-symmetry spectra merge into a single HT signal (see Figs. 2 and 4) [9, 10]. The HT line width decreases (Fig. 4a) in inverse proportion to the transition rate $(\delta B^{TA} - \delta B_0^{TA}) \sim \tau$. In the temperature range 350–400 K, the HT line has an asymmetric shape (see Fig. 2b), and its width can be estimated only qualitatively. Although the estimate of the activation energy from the narrowing of the HT line is quite rough, it agrees with the values obtained from the temperature variation of the width and position of the lines of LT triclinic spectra to within the experimental error.

2. DIELECTRIC FEATURES INDUCED BY Cu^{2+} IMPURITY IONS

If the low-symmetry positions are associated with the emergence of dipole moments, we can expect that the dielectric properties of $Pb_5Ge_3O_{11} : Cu^{2+}$ are characterized by the presence of additional features of the temperature and frequency dependence $\varepsilon(T, \omega)$ [11]. The results of measurements made for **E** || **a** in the temperature range 80–300 K are presented in Fig. 6. The obtained dependences are characterized by a stepwise increase in the permittivity $\varepsilon(T)$ and a peak of the dielectric loss tangent $\tan\delta(T)$, which are displaced towards higher temperatures upon an increase in the measuring field frequency. These features are anisotropic, since they are observed for directions of the measuring field **E** lying in the (**ab**) plane and are not manifested along the polar axis for **E** || **c**. In order to find the parameters of the observed relaxation dynamics, we describe the experimental dependences by the Debye dispersion relation

$$\varepsilon^* = \varepsilon_\infty + \frac{\varepsilon_0 - \varepsilon_\infty}{1 + i\omega\tau}, \qquad (6)$$

where the static permittivity varies with temperature according to the Curie law $\varepsilon_0 = \varepsilon_\infty + C/T$, and the relaxation time is described by the Arrhenius law. The activation energy W and the eigenfrequency τ_0^{-1}, which are independent in the Debye model, were determined by the dependences $\tan\delta(T)$ measured at various frequencies. A comparison of experimental dependences with the theoretical curves (see Fig. 6) indicates the Debye nature of peculiarities in $\varepsilon^*(T)$. The activation energy for the relaxation process under investigation is presented in the table, the eigenfrequency is $\tau_0^{-1} = 2 \times 10^{12}$ Hz, and the Curie constant $C = 170$ K.

It should be noted that in order to describe the experimental curves correctly, we must take into account two more relaxation features. These features are manifested in the dependences in Fig. 6 as a distortion of the high-temperature wing of the high-intensity peak of $\tan\delta(T)$ and a weak peak in the region of ~240 K. The experiments with various directions of the measuring field proved that the additional peaks of $\tan\delta(T)$ correspond to residual contributions of relaxation processes that are observed mainly along the polar axis **c** and are characterized by the activation energies of 0.4 and 0.8 eV. The experiments with pure and doped crystals indicate that these features can hypothetically be attributed to

Values of activation energy obtained from the temperature behavior of EPR spectra and from dielectric measurements

Measured characteristics	Activation energy W (eV)
LT spectral line broadening	0.23 ± 0.01
Displacement of the LT spectral line position	0.26 ± 0.02
Narrowing of HT line	0.16 ± 0.1
Dependence $\tan\delta(T, \omega)$	0.24 ± 0.02

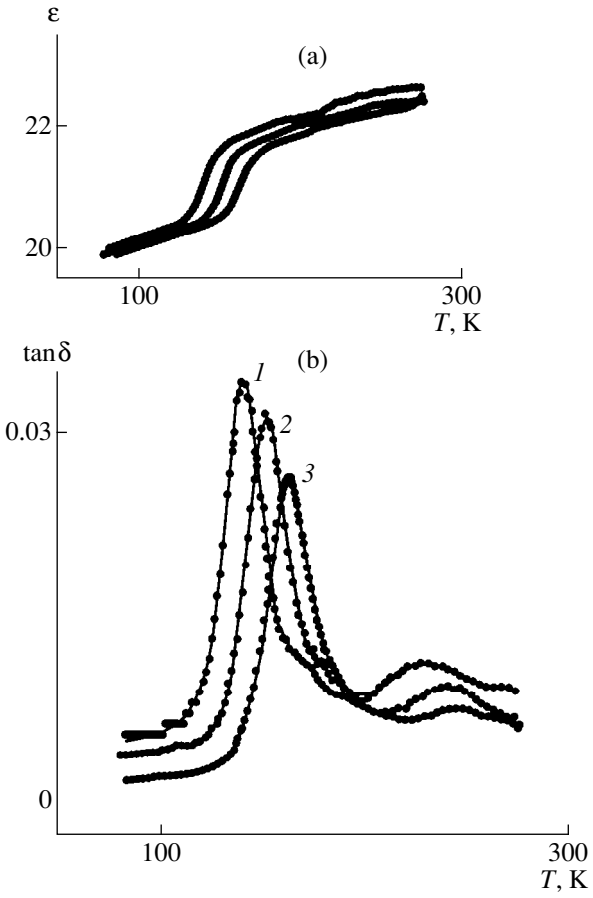

Fig. 6. Dependences $\varepsilon(T)$ (a) and $\tan\delta(T)$ (b) for the measuring field direction **E** || **a** and frequencies f = 1 (*1*), 4 (*2*), and 15 kHz (*3*). The circles correspond to experimental results and solid curves are the results of calculations.

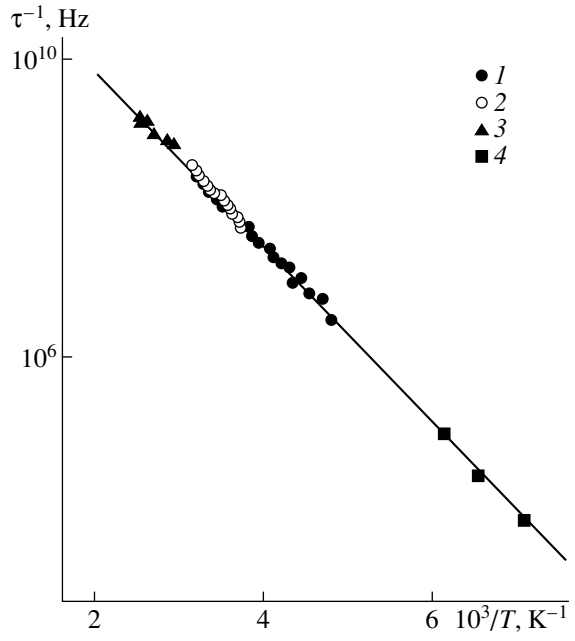

Fig. 7. Rate τ^{-1} of the jumps of Cu^{2+} ions between off-center positions as a function of 1/T, obtained from the temperature dependence of uniform broadening of hyperfine lines of the LT spectrum (*1*), separation between the centers of hyperfine LT quartets (*2*), narrowing of the HT line (*3*), and the dielectric loss tangent (*4*). The solid line is obtained with the help of the parameters described in the text.

associated dipole complexes on the basis of OH^- groups [12, 13].

The anisotropy of EPR spectra and dielectric properties, as well as a comparison of activation energies (see the table), confirm that the relaxation features of ε and $\tan\delta$ in the (**ab**) plane (see Fig. 6) are determined by the local dynamics of Cu^{2+} centers. The existence of a dielectric response indicates that low-symmetry distortions of copper complexes are associated with the emergence of local dipole moments.

3. DISCUSSION OF RESULTS AND MAIN CONCLUSIONS

The temperature averaging of triclinic LT EPR spectra demonstrates the existence of dynamic transitions of active centers between three positions. The probability of jumps of active centers between structurally equivalent low-symmetry (C_1) lattice sites is apparently very low. Consequently, the trigonal HT spectrum carries information on the symmetry of positions of the ions being replaced. Six structurally inequivalent lead ions (Pb2A, Pb2B, Pb3A, Pb3B, Pb4, and Pb5) are arranged at the trigonal symmetry sites in the cation subsystem of the unit cell of the ferroelectric phase of $Pb_5Ge_3O_{11}$. According to the notation adopted in [6], indices A and B define the positions associated with the pseudoplane of specular reflection and become equivalent in the paraelectric phase. Consequently, the substitution of copper for Pb2 and Pb3 ions must be equiprobable for A and B positions. In this case, two structurally equivalent spectra (corresponding to A and B) should be observed, which contradicts the experimental results. Therefore, we can speak of the substitution of Cu^{2+} centers for lead ions in positions Pb4 or Pb5 located in trihedral prisms formed by oxygen ions [6]. A comparison of the directions of magnetic axes of the triclinic spectra with lead–oxygen bonds suggests the substitution of copper centers for ions in Pb5 positions.

The anisotropy of LT spectra indicates the presence of triclinic distortions of the coordination complex of active centers. The nearest neighbors of Pb^{2+} at trigonal sites are determined by O^{-2} ions constituting quite rigid germanium–oxygen tetrahedrons [6], which form the structural skeleton of a whole range of germanium oxide compounds. For this reason, the deformation of oxygen surroundings of Cu^{2+} centers is hardly probable. On account of the isovalence of the substitution of Cu^{2+} ions for Pb^{2+}, the possible presence of a mobile defect in the neighborhood of all active centers is not associated with its charge state and is also doubtful. We can assume that copper ions occupy three off-center positions displaced from a trigonal site in a plane perpendicular to the **c** axis with equal probability. This assumption agrees with the dielectric response of local dipoles induced by impurity centers, which was detected in the (**ab**) plane. A noticeable difference in the ionic radii of the ion being substituted and the substituting ions ($r_{Pb^{2+}}$ = 1.32 Å and $r_{Cu^{2+}}$ = 0.70 Å) also confirms the off-center arrangement of Cu^{2+} ions in Pb^{2+} positions. The reason behind the off-center position in the structure is apparently associated with the crystal field symmetry and quasi-degeneracy of the orbital states of Cu^{2+} and is a consequence of the Jahn–Teller pseudoeffect.

The results of EPR and dielectric measurements make it possible to obtain the temperature dependence of the rates of jumps between off-center positions. In Fig. 7, the rate τ^{-1} is plotted in semilogarithmic coordinates as a function of the reciprocal temperature. While processing the EPR data, we used the parameter τ_0^{-1} determined from the dielectric measurements. Taking into account the spread in the obtained parameters, we find that the equality of the jump rate and the frequency splitting $\tau^{-1} \sim \Delta\nu \approx 979$ MHz between hyperfine quartets of the LT spectra is observed in the temperature range 330–360 K. Consequently, the eigenfrequency $\tau_0^{-1} \sim 10^{12}$ Hz determined from the dielectric data agrees in the order of magnitude with radiospectroscopic results and makes it possible to explain the temperature behavior and the qualitative transformation of EPR spectra.

In the temperature range under investigation, the experimental data indicate an exponential temperature dependence of the jump rate (see Fig. 7). As a rule, such

behavior presumes that the jumps occur above the barriers. At the same time, the exponential temperature dependence is also possible in the case of tunneling between potential wells from excited vibrational states [3]. In the latter case, the exponent indicates the splitting between the ground and excited vibrational levels, and the preexponential factor is determined by the frequency of tunneling. The values of the activation energy $W/k_B \approx 3000$ K and the eigenfrequency $\tau_0^{-1} \sim 10^{12}$ Hz indicate that the jumps of Cu^{2+} ions between off-center positions can be regarded as a classical above-the-barrier process. This conclusion is confirmed by the results of calculating the Debye temperature from the thermal and elastic properties of lead germanate ($\Theta_D = 210$–220 K), which corresponds to lattice frequencies $\sim 4 \times 10^{12}$ Hz [14].

Summarizing what has been said above, we conclude that an analysis of the EPR and dielectric properties of $Pb_5Ge_3O_{11}$: Cu^{2+} crystals demonstrates the off-center position of copper ions. The temperature dependence of the probability of jumps between off-center positions leads to the transformation of the EPR spectra and to the emergence of typical features in dielectric properties. The results of measurements of local spectral and macroscopic dielectric characteristics agree to a high level of accuracy, thus confirming the reliability of the obtained parameters of the local dynamics of copper centers.

ACKNOWLEDGMENTS

The authors are grateful to A. Yu. Kudzin for useful discussions and to V. G. Linnik for providing lead germanate single crystals.

REFERENCES

1. A. P. Levanyuk and A.S. Sigov, *Defects and Structural Phase Transitions* (Gordon and Breach, New York, 1988).
2. M. F. Deĭgen and M. D. Glinchuk, Usp. Fiz. Nauk **114** (2), 185 (1974) [Sov. Phys. Usp. **17**, 691 (1974)].
3. L. S. Sochava, in *Spectroscopy of Crystals* (Nauka, Leningrad, 1978), p. 166.
4. V. A. Vazhenin, A. D. Gorlov, and A. I. Krotkiĭ, in *EPR Spectroscopic Studies of Impurity Centers in Crystals Showing Phase Transitions*, Preprint No. 10, IPM (Kiev, 1989).
5. S. Nanamatsu, H. Sugiyama, K. Doi, and Y. Kondo, J. Phys. Soc. Jpn. **31** (2), 616 (1971).
6. M. I. Kay, R. E. Newnham, and R. W. Wolfe, Ferroelectrics **9** (1), (1975).
7. A. Abragam and B. Bleaney, *Electron Paramagnetic Resonance of Transition Ions* (Clarendon, Oxford, 1970; Mir, Moscow, 1972), Vol. 1.
8. M. L. Meĭl'man and M. I. Samoĭlovich, *Introduction to EPR Spectroscopy of Activated Single Crystals* (Atomizdat, Moscow, 1977).
9. J. A. Pople, W. G. Schneider, and H. J. Bernstein, *High-Resolution Nuclear Magnetic Resonance* (McGraw-Hill, New York, 1959; Inostrannaya Literatura, Moscow, 1962).
10. J. E. Wertz and J. R. Bolton, *Electronic Spin Resonance: Elementary Theory and Practical Applications* (McGraw-Hill, New York, 1972; Mir, Moscow, 1975).
11. Yu. M. Poplavko, *Physics of Dielectrics* (Vishcha Shkola, Kiev, 1980).
12. A. Yu. Kudzin, M. D. Volnianskii, V. M. Duda, *et al.*, Condens. Matter Phys., 2000 (in press).
13. A. A. Bush and Yu. N. Venevtsev, *Single Crystals of Pb–O–GeO_2 Compounds with Ferroelectric and Related Properties and Their Potential for Applications* (NIITÉKhIM, Moscow, 1981).
14. A. M. Antonenko, *Nonlinear Elastic Properties of Single Crystals of Some Complex Oxides*, Author's Abstract of Candidate's Dissertation (Dnepropetrovsk, 1980).

Translated by N. Wadhwa

Physics of the Solid State, Vol. 42, No. 7, 2000, pp. 1348–1353. Translated from Fizika Tverdogo Tela, Vol. 42, No. 7, 2000, pp. 1310–1315.

LATTICE DYNAMICS AND PHASE TRANSITIONS

Lattice Dynamics of $M\mathrm{F}_3$ Crystals (M = Al, Ga, and In)

V. I. Zinenko and N. G. Zamkova

Kirenskiĭ Institute of Physics, Siberian Division, Russian Academy of Sciences, Akademgorodok, Krasnoyarsk, 660036 Russia
e-mail: zinenko@iph.krasnoyarsk.su

Received December 7, 1999

Abstract—The phonon spectra, Born effective charges, and dielectric constants ε_∞ for the $\square\mathrm{AlF}_3$, $\square\mathrm{GaF}_3$, and $\square\mathrm{InF}_3$ crystals (where $\square$ is a vacancy) have been calculated in terms of the generalized Gordon–Kim method. The calculated spectra of lattice vibrations contain no imaginary vibrational frequencies. This suggests the stability of the cubic phase of these compounds but contradicts the observable structural transition from cubic to rhombohedral phase. It is assumed that such a transition in the $\square\mathrm{AlF}_3$, $\square\mathrm{GaF}_3$, and $\square\mathrm{InF}_3$ crystals is brought about by structural defects. The calculated spectrum of lattice vibrations of the "completely defective" crystal $M\square\mathrm{F}_3$ (M = Al, Ga, and In) indicates a strong instability of the cubic phase. Within the mean crystal approximation, the cubic phase of $M_xM_{1-x}\mathrm{F}_3$ crystals appears to be unstable at small $x \le 0.05$. © *2000 MAIK "Nauka/Interperiodica".*

1. INTRODUCTION

Structural phase transitions and the nature of instability in compounds with a perovskite-type structure have been studied experimentally and theoretically over many years. The majority of the theoretical investigations were dedicated to oxide compounds with a perovskite-type structure. Calculations of the band structure, crystal lattice dynamics, and static mechanics of ferroelectric and antiferroelectric phase transitions in terms of the density functional method yielded the satisfactory results (see, for example, [1–6]). These calculations provided a deeper insight into the origin of crystal lattice instability and the nature of ferro- and antiferroelectricity in oxide compounds with a perovskite-type structure. At the same time, halide compounds with a perovskite structure, in which the structural phase transitions, as a rule, are associated with the crystal lattice instability toward antiferroelectric distortions, have received little attention in the *ab initio* calculations.

The crystals $\square M\mathrm{F}_3$ (M = Al, Ga, and In; $\square$ is a vacancy) are structurally isomorphic with the ReO_3 compound. The ReO_3 compound has the simplest perovskite-like structure. The metal ion is located at the center of an octahedron whose vertices are occupied by the anions (Fig. 1a). The centers of anionic cubooctahedra are empty. The $M\mathrm{F}_3$ crystals undergo a phase transition from cubic to rhombohedral phase due to a "rotation" of the octahedron around the threefold symmetry axis of the cubic cell [7–9]. The phase transition and lattice dynamics of the AlF_3, GaF_3, and InF_3 crystals were the subjects for a few experimental and theoretical works, including the structural investigations by x-ray diffraction, calorimetric studies, measurements of the cutoff Raman-active frequencies of lattice vibrations in the distorted rhombohedral phase, and calculations of the phonon spectrum of the cubic phase within the rigid ion model with adjustable parameters describing the short-range interactions [8, 9]. Information on the overall phonon spectrum of the crystal is of crucial importance for investigations into displacive phase transitions and the understanding of the nature of crystal lattice instability.

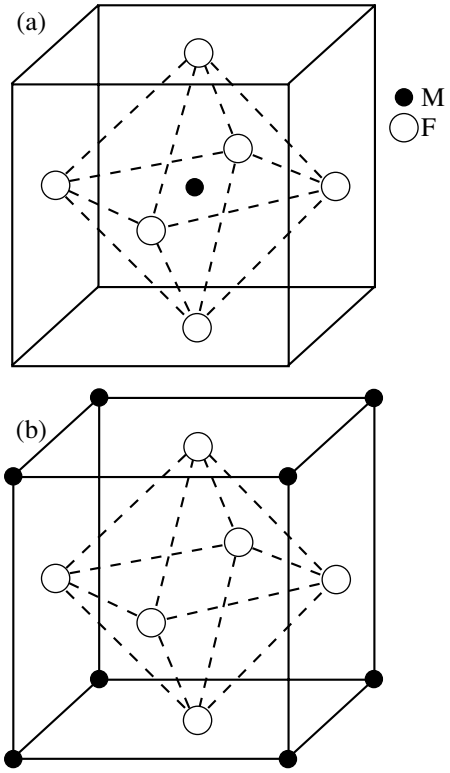

Fig. 1. Unit cells of (a) $\square M\mathrm{F}_3$ crystals and (b) $M\square\mathrm{F}_3$ hypothetical crystals.

1063-7834/00/4207-1348$20.00

The purpose of this work was to calculate the phonon spectra, Born dynamic charges, and rf permittivities of the AlF_3, GaF_3, and InF_3 crystals in terms of the microscopic ionic-crystal model, which takes into account the ion deformability and polarizability [10]. The calculation procedure is briefly described in Section 2. Section 3 presents the results of calculations. It is shown that, within the model employed, the calculated spectrum of lattice vibrations in the cubic phase of the crystals under consideration exhibits no vibrations with imaginary frequencies and, thus, indicates the stability of the cubic phase at zero temperature. However, the vibrational spectrum contains a branch (between the *R* and *M* points in the Brillouin zone) with anomalously low vibrational frequencies. We calculated the vibrational spectrum of an $M\square F_3$ hypothetical crystal with the same cubic lattice in which the cations are located at the centers of cubooctahedra (Fig. 1b). The vibrational spectra of the hypothetical crystals show a large number of vibrations with imaginary frequencies. Within the mean crystal approximation, we also calculated the vibrational spectrum of the $M_xM_{1-x}F_3$ crystals. It is found that the cubic phase of these crystals is unstable at small $x \le 0.05$.

2. CALCULATION PROCEDURE

In the present work, the vibrational spectrum of the crystal lattice was calculated within the ionic crystal model proposed by Ivanov and Maksimov [10]. This model generalizes the Gordon–Kim approximation with due regard for the influence of crystalline environment on the ion deformability and polarizability. The total electron density of the crystal in this model is written as

$$\rho(\mathbf{r}) = \sum_i \rho_i(\mathbf{r} - \mathbf{R}_i).$$

Here, the summation is performed over all ions in the crystal. The total lattice energy within the pair interaction approximation has the form

$$E_{cr} = \frac{1}{2}\sum_{i \neq j} \frac{Z_i Z_j}{|\mathbf{R}_i - \mathbf{R}_j|} + \sum_i E_i^{self}(R_w^i) + \frac{1}{2}\sum_{i \neq j} \Phi_{ij}(R_w^i, R_w^j, |\mathbf{R}_i - \mathbf{R}_j|), \quad (1)$$

where *Z* is the charge of the *i*th ion,

$$\Phi_{ij}(R_w^i, R_w^j, |\mathbf{R}_i - \mathbf{R}_j|) = E\{\rho_i(\mathbf{r} - \mathbf{R}_i) + \rho_j(\mathbf{r} - \mathbf{R}_j)\} - E\{\rho(\mathbf{r} - \mathbf{R}_i)\} - E\{\rho(\mathbf{r} - \mathbf{R}_j)\}, \quad (2)$$

the $E\{\rho\}$ energy is calculated within the Thomas–Fermi approximation and in the local approximation for the kinetic and exchange-correlation energies [10],

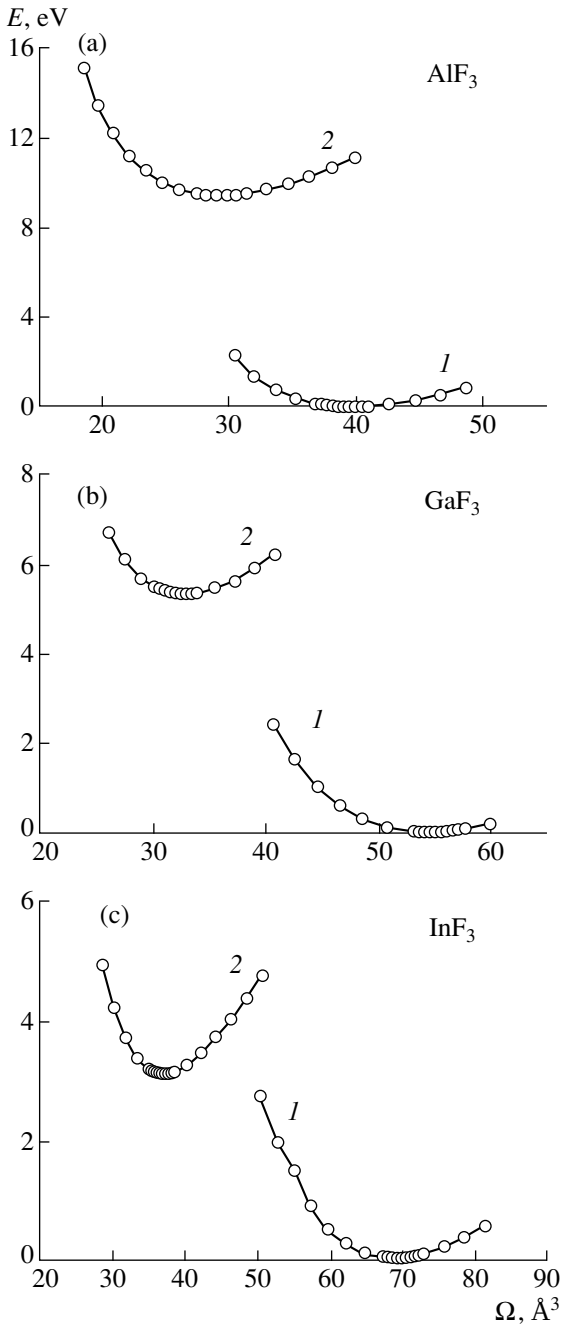

Fig. 2. Dependences of the total lattice energy on the volume. Curves *1* and *2* correspond to the $\square MF_3$ and $M\square F_3$ structures, respectively. The energies are reckoned from (a) –14965.6141, (b) –61438.7235, and (c) –168862.7272 eV.

and $E_i^{self}(R_w^i)$ is the self-energy of the ion. The electron density of an individual ion and its self-energy are calculated with allowance made for the crystal potential, which was approximated by the charged sphere (Watson's sphere)

$$v(r) = \begin{cases} Z_i^{ion}/R_w & r < R_w \\ Z_i^{ion}/r & r > R_w, \end{cases}$$

Table 1. Equilibrium values of the lattice parameters, Born effective charges (Z^*), rf permittivity ε_∞, and ion polarizabilities α_M and α_F

Crystal	a_0, Å (calculation)	a_0, Å (experiment)	$Z^*(M)$	$Z_\perp^*$ (F)	$Z_\parallel^*$ (F)	ε_∞	α_M, Å^3	α_F, Å^3
□AlF_3	3.42	3.56[a]	3.08	–0.66	–1.76	1.86	0.03	0.65
□GaF_3	3.80	3.69[b]	2.87	–0.78	–1.32	1.64	0.12	0.69
□InF_3	4.11	4.07[b]	2.99	–0.79	–1.41	1.59	0.37	0.72

Note: [a] [8]. [b] [7].

Table 2. Calculated frequencies of modes at the $\Gamma(0, 0, 0)$ and $R(\pi/a, \pi/a, \pi/a)$ points of the Brillouin zone (PIB is the breathing ion model, and PPIB takes into account the ion deformability and polarizability)

Mode	□AlF_3			□GaF_3			□InF_3		M□F_3		
	PPIB	PIB	RI	PPIB	PIB	RI	PPIB	PIB	Al	Ga	In
$2\Gamma_{10}(3)$											
LO	651	735	765	521	564	553	449	495	465	407	357
TO	521	558	641	466	504	513	399	456	401	375	337
LO	307	503	481	245	374	392	200	304	350	306	294
TO	222	401	378	185	259	278	154	201	362*i*	27	44*i*
$\Gamma_9(3)$	194	240	219	152	172	194	126	137	225*i*	148*i*	143
$R_1(1)$	645	644	669	486	558	585	433	499	340	328	300
$R_{10}(3)$	445	446	487	265	267	265	193	195			
$R_4(3)$									449	376	311
$R_3(2)$	372	407	481	424	424	418	400	403	289	269	247
$R_4(3)$	246	415	383	210	305	338	189	195	272*i*	97	119
$R_5(3)$	58	79	50	68	73	50	63	65	490*i*	359*i*	253*i*

Note: The results of calculations within the rigid ion (RI) model [9] are presented for comparison. The parenthetic numerals indicate the mode degeneracy. Frequencies are given in cm^{-1}.

where R_w is the radius of the Watson sphere. The radius of the sphere R_w^i for each ion is determined from the condition of the minimum total energy of the crystal.

In order to calculate the crystal lattice dynamics, equation (2) should contain additional terms that describe the change in the energy upon displacements of the ions from their equilibrium positions. Moreover, the calculations of the vibrational spectrum allowed for the ion polarizability and deformability caused by the change in the crystal environment. The expression for the dynamic matrix was given in [11].

3. RESULTS AND DISCUSSION

The equilibrium unit cell parameters of the crystals under consideration were determined from the condition of the minimum total energy of the crystal as a function of the volume (Fig. 2). Table 1 presents the equilibrium lattice parameters, experimental data, and the calculated values of ion polarizability, rf permittivity ε_∞, and the Born effective charges. For the metal ions, the effective charge tensor is isotropic and close in magnitude to the nominal charge of the ion (+3). The fluorine ion is characterized by two tensor components, namely, $Z_\parallel^*$ (F) and $Z_\perp^*$(F), which correspond to the displacements of the F^- fluorine ion in the directions parallel and perpendicular to the M–F bond, respectively. As is seen from Table 1, there is a substantial difference between $Z_\parallel^*$ (F) and $Z_\perp^*$(F) components, as for oxide compounds with a perovskite structure, but the $Z_\parallel^*$ (F) values are considerably less than $Z_\parallel^*$ (O).

The calculated phonon spectra of the AlF_3, GaF_3, and InF_3 crystals are shown in Figs. 3–5. For comparison with the calculations within the rigid ion model [9], Table 2 lists the frequencies of vibrations at the $\Gamma(0, 0, 0)$ and $R(\pi/a, \pi/a, \pi/a)$ points of the Brillouin zone. Table 2 also presents the vibrational frequencies calculated in the present work in terms of the "breathing" ion model, i.e., without regard for the ion polarizability. It follows

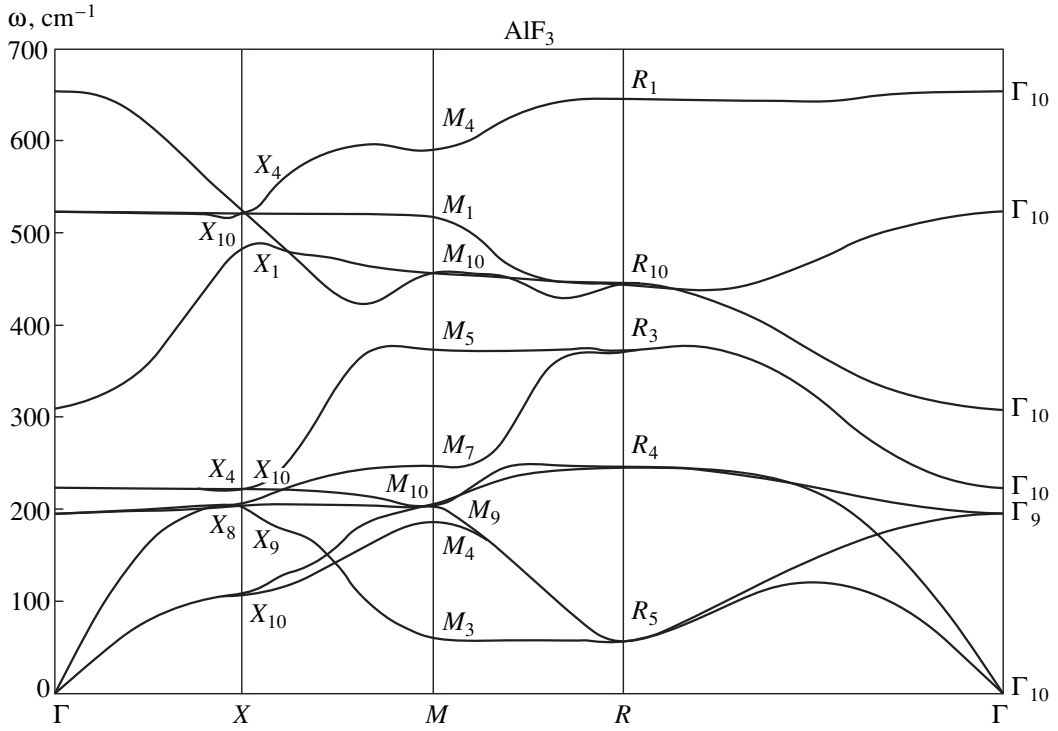

Fig. 3. Calculated phonon spectrum of the □AlF_3 crystals.

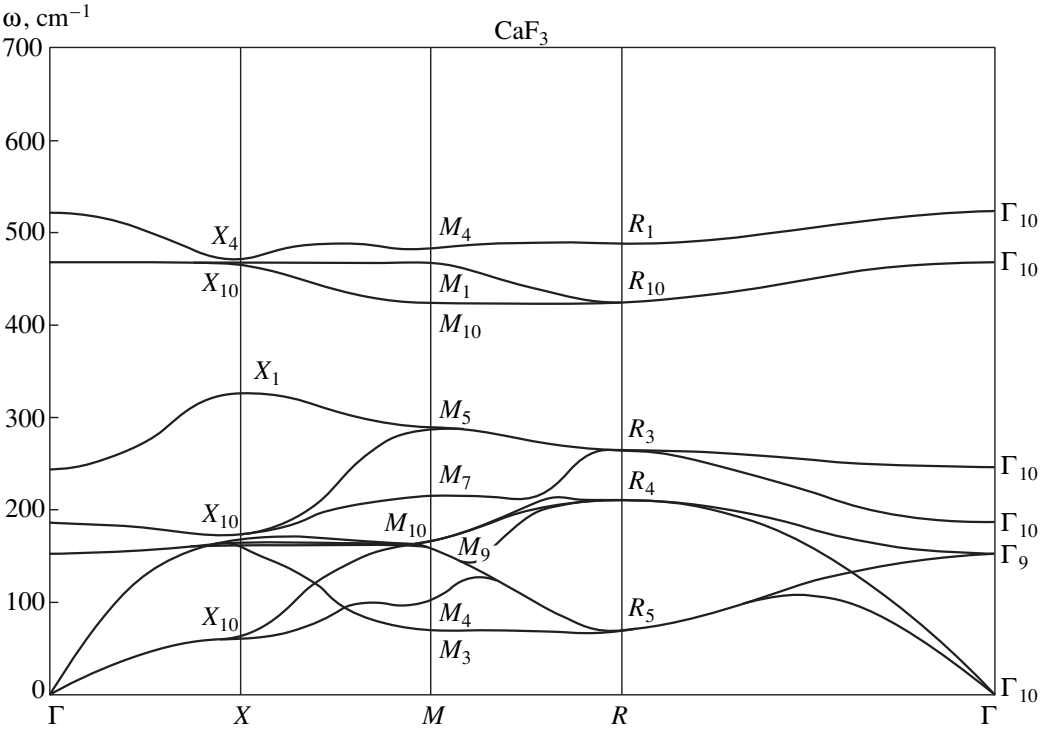

Fig. 4. Calculated phonon spectrum of the □GaF_3 crystals.

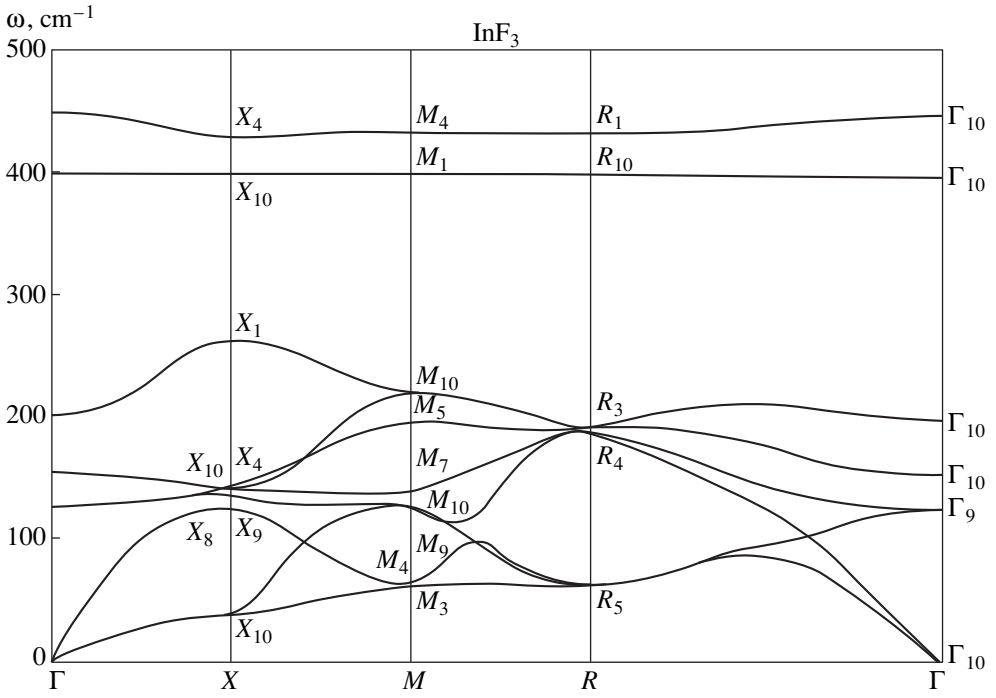

Fig. 5. Calculated phonon spectrum of the $\square InF_3$ crystals.

from Table 2 that the results of calculations within the rigid ion model with adjustable parameters describing the short-range interactions are in good agreement with those obtained in the breathing ion model, i.e., without adjustable parameters. At the same time, the inclusion of ion polarizability substantially affects the frequencies of lattice vibrations, in particular, significantly reduces the LO–TO splitting for frequencies of the IR-active modes.

As can be seen from Figs. 3–5 and Table 2, the vibrational spectra of all the studied crystals exhibit no imaginary frequencies but contain a weakly dispersive branch (between the *M* and *R* points in the Brillouin zone) with anomalously low frequencies (≈60 cm^{-1}). The same result was obtained within the rigid ion model [8, 9]. Therefore, our calculations of the lattice dynamics within the method employed indicate that the cubic phase in the AlF_3, GaF_3, and InF_3 crystals remains stable to $T = 0$. However, this result is contradictory to the experiment, which revealed the structural phase transition in these compound at a finite temperature. The instability of the cubic phase in the crystals under study can be explained by the disturbance of the $\square MF_3$ perfect structure when a small number of metal ions occupy vacant sites at the center of a cubooctahedron. In order to verify this assumption, we calculated the phonon spectra of the "completely defective" hypothetical structure $M\square F_3$ (*M* = Al, Ga, and In). The total lattice energy in this structure considerably exceeds the energy in the $\square MF_3$ structure (Fig. 2). The calculated phonon spectra of the $Al\square F_3$, $Ga\square F_3$, and $In\square F_3$ hypothetical crystals essentially differ from the spectra of the $\square AlF_3$, $\square GaF_3$, and $\square InF_3$ crystals. For the defective structure, the phonon spectrum exhibits many imaginary frequencies of vibrations, and the unstable modes occupy the whole phase space in the first Brillouin zone. The calculated frequencies of lattice vibrations in the $M\square F_3$ crystals at the $\Gamma(0, 0, 0)$ and $R(\pi/a, \pi/a, \pi/a)$ points of the Brillouin zone are given in Table 2. As follows from this table, the "softest" mode is the threefold degenerate mode R_5, which belongs to the boundary point of the Brillouin zone. The eigenvector of the R_5 mode corresponds to the "rotation" of the octahedron whose center, in this case, is free from metal ion. The phase transition experimentally observed in the AlF_3, GaF_3, and InF_3 compounds is associated with the condensation of just this R_5 mode, and, hence, this mode alone will be discussed below. The frequency of the R_5 mode in two structures ($\square MF_3$ and $M\square F_3$) is described by the same analytical expression

$$\omega^2(R_5) = \frac{4\pi e^2}{\Omega M_F}(S + C),$$

Table 3. Coulomb contribution of points charges *C* and contribution of short- and long-range dipole–dipole interactions *S* in $\omega^2(R_5)$ for MF_3 in two structures

Constant		$\square MF_3$	$M\square F_3$
C		0.68346	−0.82566
S	Al	−0.65178	−0.83688
	Ga	−0.62259	−0.17220
	In	−0.61643	0.25450

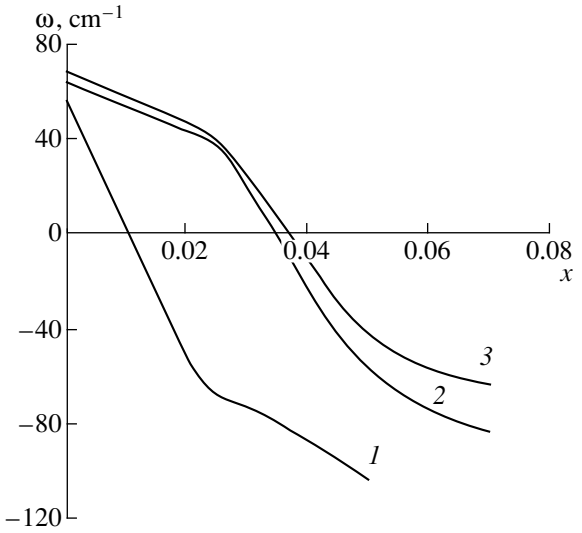

Fig. 6. Dependences of the frequency $\omega(R_5)$ on the concentration x for the $M_xM_{1-x}F_3$ crystals: (*1*) M = Al, (*2*) M = Ga, and (*3*) M = In. Negative value of ω signifies the imaginary quantity.

where Ω is the unit cell volume, and M_F is the mass of fluorine. The constant C describes the contribution of point charges to $\omega^2(R_5)$, and the constant S accounts for all short- and long-range dipole–dipole interactions. The constants C and S for the three crystals under consideration are listed in Table 3. It is seen from this table that, for the $\square MF_3$ structure, the sum of the C and S constants is positive but small in magnitude for all the crystals. On the other hand, the sum of the contributions for the $M\square F_3$ structure is negative but large in magnitude for all the crystals. It can be assumed that, in real crystals, a small number of metal ions occupy vacant sites at the center of the cubooctahedron formed by fluorine ions, and this imperfection results in the instability of the cubic phase. In order to make a rough estimate of the defect concentration at which the cubic phase becomes unstable, we calculated the vibrational spectrum of the "mean crystal" $M_xM_{1-x}F_3$ (M = Al, Ga, and In). The dependence of $\omega(R_5)$ on the concentration x for the mean crystals is displayed in Fig. 6. It is seen that the cubic phase at zero temperature appears to be unstable at a rather low concentration of defects.

Thus, we calculated the lattice dynamics of the $\square AlF_3$, $\square GaF_3$, and $\square InF_3$ crystals with a perovskite-type structure. The calculations were performed within the generalized Gordon–Kim model, which takes into account the ion polarizability and deformability. It was found that, for all the crystals at $T = 0$, the spectra of lattice vibrations contain no vibrations with imaginary frequencies, which suggests the stability of the cubic phase in these crystals. In our opinion, the structural phase transition from cubic to rhombohedral phase, which is experimentally observed in these crystals, can be associated with structural defects when a number of metal ions are located at the centers of cubooctahedra that are vacant in the perfect structure. The origin of these defects remains unclear. Since the total lattice energy in the completely defective structure considerably exceeds the energy of the perfect structure, the formation of defects of this type at the expense of temperature is unlikely. However, these defects apparently can arise upon crystal growth. The above assumption on the origin of instability of the cubic phase in the MF_3 crystals requires the experimental verification.

ACKNOWLEDGMENTS

We would like to thank O.V. Ivanov and E.G. Maksimov for allowing us to use the special programs in calculations of the energy and ion polarizability.

This work was supported by the Krasnoyarsk Regional Scientific Foundation (project no. 8E0039) and the International Association of Assistance for the promotion of co-operation with scientists from the New Independent States of the former Soviet Union (project INTAS no. 97-10177).

REFERENCES

1. R. E. Cohen and H. Krakauer, Ferroelectrics **136**, 65 (1992).
2. R. E. Cohen and H. Krakauer, Phys. Rev. B **42**, 6416 (1990).
3. D. J. Singh and L. L. Boyer, Ferroelectrics **136**, 95 (1992).
4. R. D. King-Smith and D. Vanderbilt, Phys. Rev. B **49**, 5828 (1994).
5. K. M. Rabe and U. V. Waghmare, Ferroelectrics **164**, 15 (1995).
6. U. V. Waghmare and K. M. Rabe, Phys. Rev. B **55**, 6161 (1997).
7. F. M. Bremer, G. Garton, and D. M. L. Goodminde, J. Inorg. Nucl. Chem. **9**, 56 (1989).
8. P. Daniel, A. Bulou, M. Rousseau, *et al.*, J. Phys.: Condens. Matter **2**, 5663 (1990).
9. P. Daniel, A. Bulou, M. Rousseau, *et al.*, Phys. Rev. B **42**, 10545 (1990).
10. O. V. Ivanov and E. G. Maksimov, Zh. Éksp. Teor. Fiz. **108**, 1841 (1995) [JETP **81**, 1008 (1995)].
11. V. I. Zinenko, N. G. Zamkova, and S. N. Sofronova, Zh. Éksp. Teor. Fiz. **114**, 1742 (1998) [JETP **87**, 944 (1998)].

Translated by O. Borovik-Romanova

Physics of the Solid State, Vol. 42, No. 7, 2000, pp. 1354–1360. Translated from Fizika Tverdogo Tela, Vol. 42, No. 7, 2000, pp. 1316–1321.

LATTICE DYNAMICS AND PHASE TRANSITIONS

On Calculation of Volume Fractions of Competing Phases

N. V. Alekseechkin

Kharkov Institute of Physics and Technology, Ukrainian Scientific Center, ul. Akademicheskaya 1, Kharkov, 310108 Ukraine
e-mail: n.alex@kipt.kharkov.ua

Received November 30, 1999

Abstract—A method for calculating the volume fractions of phases in a system with several simultaneously growing phases is proposed. A solution of the problem is obtained for two- and three-dimensional spaces. The approximation of independent phases is considered, in which expressions for volume fractions have the simplest form. The high accuracy of this approximation is demonstrated. © *2000 MAIK "Nauka/Interperiodica".*

The kinetics of phase transformation in the case when only one new phase is formed can be successfully described by well-known expressions derived by Kolmogorov [1] and by Johnson, Mehl, and Avrami [2–4]:

$$X(t) = 1 - \exp\left[-\int_0^t I(t')V(t', t)dt'\right], \qquad (1)$$

where $X(t)$ is the volume fraction of the growing phase, $I(t)$ is the rate of nucleation of the new phase, $V(t', t)$ is the volume at the instant t of a freely growing nucleus generated at the time t',

$$V(t't) = gR^D(t', t), \quad R(t', t) = \int_{t'}^{t} u(\tau)d\tau, \qquad (2)$$

$u(t)$ is the nucleus growth rate, $R(t', t)$ is the nucleus radius, D is the dimensionality of space, and g is a geometrical factor, $g = 2$, π, and $4\pi/3$ for $D = 1$, 2, and 3, respectively.

In addition to this type of phase transformations, the phase transformations occurring through simultaneous growth of two or more different phases are also possible. An example of such processes is the solidification of a supercooled liquid with the competing formation of crystalline and amorphous phases in it. The idea concerning the formation of "anticrystalline" clusters in a liquid along with crystalline clusters and the role of the former clusters in the glass-formation process was apparently put forth by Ubbelohde [5]. The kinetics of the solidification of a liquid with the competing formation of two or more phases in it was calculated in [6, 7].

In this connection, the problem of calculating the volume fractions of phases in such systems, i.e., the generalization of expression (1) to this case, is of considerable interest. In contrast to the single-phase case, one encounters here specific difficulties associated with different growth rates of the phases. In the present work, a geometrical–probabilistic approach is developed for solving this problem. Exact solutions are obtained for volume fractions in spaces with $D = 2$ and 3 (under constraints existing in the Kolmogorov model [1, 4]) and simpler expressions are also derived in the independent phase approximation (IPA). An analysis of the solution obtained proves the high accuracy of IPA expressions.

1. SINGLE PHASE

We will carry out a description of the proposed method, which can be referred to as the "method of critical regions", using the example of a single-phase transformation; in other words, we will derive expression (1) in a way differing from that in [1, 2].

We shall determine the probability $dX(t)$ of the absorption of a randomly chosen point O in the system by the growing phase during the time interval $[t, t + dt]$. The following two conditions are necessary and sufficient for this event to occur: (a) point O has not been absorbed before the instant t and (b) a nucleus of a new phase capable of absorbing point O during the time interval $[t, t + dt]$, appears at a certain instant t' $(0 \le t' \le t)$. Such a nucleation center will be referred to as critical. We will denote by $Q(t)$ and $dP(t)$ the probabilities of the former and the latter events, respectively. Let us consider the space–time diagram of realizing such a process, in which both conditions are satisfied.

We select a region with the center at point O and the radius $R(t', t)$ (critical region). At the instant t', the boundary of this region moves at a velocity $u(t')$ so that the radius decreases from the maximum value $R(0, t)$ to $R(t, t) \equiv 0$. The fulfillment of condition (a) implies that the emergence of the new phase that centers in the region is ruled out through the entire time interval $0 \le t' \le t$. On the basis of this condition, the value of $Q(t)$ is calculated directly [1]. On the other hand, $Q(t)$ can be determined from condition (b).

The critical nucleation center emerging at the instant of time t' must be separated from point O by a distance $R(t', t)$ and situated in a ring of width

1063-7834/00/4207-1354$20.00

$dR(t', t) = (\partial R(t', t)/\partial t)dt$. Consequently, the probability of the emergence of such a center is

$$dP(t', t) = I(t')dt'\dot{V}(t', t)dt, \quad (3)$$

where $\dot{V}(t', t) \equiv \partial V(t', t)/\partial t$. The probability of the emergence of the critical center in the time interval $0 \le t' \le t$ is defined by the integral

$$dP(t) = \left(\int_0^t I(t')\dot{V}(t', t)dt'\right)dt. \quad (4)$$

Thus, the simultaneous fulfillment of conditions (a) and (b) leads to the following condition for $dX(t)$:

$$dX(t) = Q(t)\left(\int_0^t I(t')\dot{V}(t', t)dt'\right)dt. \quad (5)$$

It can be easily seen that $X(t) = 1 - Q(t)$. Consequently, (5) is a differential equation for $X(t)$, whose solution under the initial condition $X(0) = 0$ is given by (1). According to the geometrical definition of the probability [8], $X(t)$ gives the fraction of transformed substance and $Q(t)$ is the fraction of the initial phase.

2. SEVERAL PHASES

In the case when the number of phases in a system is greater than one, the premises of the Kolmogorov model [1, 4] are assumed to hold for each phase. We also assume that the shape of phase nuclei is spherical and remains unchanged during the growth of a nucleus. The latter assumption appears to be natural, since the growth occurs due to processes at the interface, namely, through the addition of matter from the initial phase. Consequently, the boundary of a nucleus of the ith phase is displaced parallel to itself over a time dt through a distance $\delta r_i = u_i(t)dt$.

Let us first consider the two-phase case. We suppose that two phases are growing in the initial medium, which will be denoted by indices 1 and 2. The rates of nucleation of the phases are $I_i(t)$ and the growth rates are $u_i(t)$, $i = 1, 2$, where $u_2(t) > u_1(t)$ for all t. We determine the probability $dX_1(t)$ [$dX_2(t)$] of the event that an arbitrary point O is absorbed by phase 1 (2) in the time interval $[t, t + dt]$.

Generalizing the one-phase case, we define two regions, *1* and *2*, with their centers at point O and with radii $R_1(t', t)$ and $R_2(t', t)$, respectively (Fig. 1):

$$R_i(t', t) = \int_{t'}^{t} u_i(\tau)d\tau. \quad (6)$$

We shall refer to the ring of width $\Delta R(t', t) = R_2(t', t) - R_1(t', t)$ confined between the boundaries of the regions *1* and *2* as the *1–2* region.

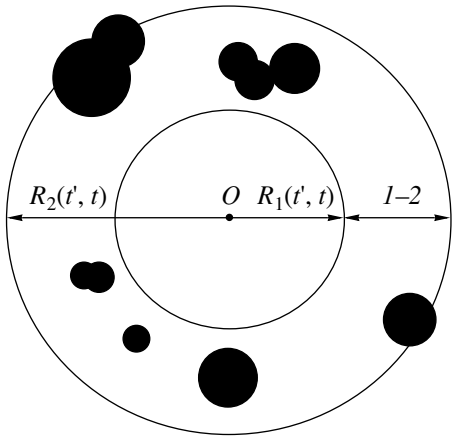

Fig. 1. Critical regions in the two-phase problem. Dark circles depict nuclei of phase 1 in the *1–2* region.

Let us consider conditions (a) and (b) as applied to phase 1. The necessary and sufficient conditions for point O to be absorbed during the time interval $[t, t + dt]$ by phase 1 are: (a) it is not absorbed by any of the phases before the instant t [the probability of such an event is $Q(t)$] and (b) a critical nucleation center of phase 1 appears at a certain instant t', $0 \le t' \le t$.

The fulfillment of condition (a) implies that the emergence of nuclei of phase 1 in the entire time interval $0 \le t' \le t$ is ruled out for the entire region *1*. Outside region *1*, such nuclei can appear without any limitations, since they cannot reach the point O by the instant t (Fig. 1). Besides, nucleation centers of phase 2 cannot appear in region *2*. The fulfillment of condition (b) implies that a nucleation center of phase 1 must appear at a certain instant t' at the boundary of region *1*. The probability of this event is defined by (4). Consequently, for $dX_1(t)$, we have

$$dX_1(t)/(dt) = Q(t)\int_0^t I_1(t')\dot{V}_1(t', t)dt'. \quad (7)$$

For the phase 2, condition (a) remains unchanged. Consequently, we consider only condition (b). If the *1–2* region contained no grains of phase 1, this condition would have led to an equation for the volume fraction of phase 2 that is identical to equation (7) with index 1 replaced by 2. However, the presence of grains of phase 1 in this region means that a critical nucleation center of phase 2 can appear only in a part $dV_2(t', t)$ of the volume. Therefore, we obtain the following expression for the probability of this event:

$$dP_2(t) = \left(\int_0^t I_2(t')\dot{V}_2(t', t)q^{(1)}(t', t)dt'\right)dt, \quad (8)$$

where $q^{(1)}(t', t)$ is the probability that the point on the boundary of region *2*, at which a critical nucleation cen-

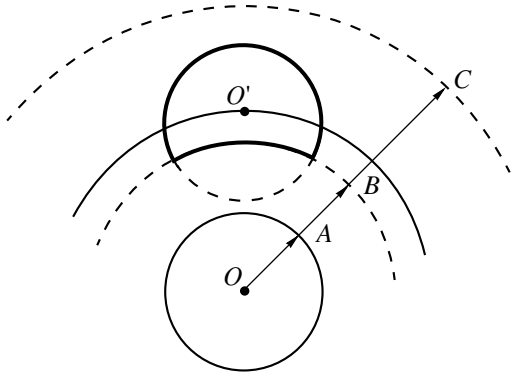

Fig. 2. Evaluation of the function $q^{(1)}(t', t)$. Solid curves are the boundaries of regions *1* and *2* at the instant t', and dashed curves, at the instant $t'' < t'$: $|OA| = R_1(t', t)$, $|OB| = R_1(t'', t)$, $|OO'| = R_2(t', t)$, and $|OC| = R_2(t'', t)$. The region of volume $v(t'', t', t)$ (16) is marked by bold lines.

ter of phase 2 appears at the instant t', lies in the untransformed region.

Accordingly, the expression for the volume fraction of the second phase has the form

$$dX_2(t)/dt = Q(t)\int_0^t I_2(t')\dot{V}_2(t', t)q^{(1)}(t', t)dt'. \quad (9)$$

Since $Q = 1 - (X_1 + X_2)$, the integration of the system of equations (7) and (9) leads to the following expressions for the required volume fractions:

$$Q(t) = \exp\left[-\int_0^t I_1(t')V_1(t', t)dt' - \int_0^\tau d\tau\int_0^\tau dt' I_2(t')\dot{V}_2(t', \tau)q^{(1)}(t', \tau)\right], \quad (10)$$

$$X_1(t) = \int_0^t d\tau Q(\tau)\int_0^\tau dt' I_1(t')\dot{V}_1(t', \tau), \quad (11)$$

$$X_2(t) = \int_0^t d\tau Q(\tau)\int_0^\tau dt' I_2(t')\dot{V}_2(t', \tau)q^{(1)}(t', \tau). \quad (12)$$

Going over to the case of $n > 2$ phases, where $u_n(t) > u_{n-1}(t) > \ldots > u_1(t)$, we supplement Fig. 1 with the regions 3, 4, …, n having the radii $R_i(t', t)$ (6). Condition (a) implies that nucleation centers of phase i can appear only outside the region i. Consequently, the $(i-1)$–i ring between the boundaries of the regions $i-1$ and i contains nuclei of the phases 1, 2, …, $i-1$, and only the fraction $q^{(i-1)}(t', t)$ of volume $dV_i(t', t)$ is accessible for the emergence of a critical center of phase i. Thus, for the volume fraction of phase i, we have

$$dX_i(t)/dt = Q(t)\int_0^t I_i(t')\dot{V}_i(t', t)q^{(i-1)}(t', t)dt', \quad (13)$$

$i = 1, 2, \ldots, n$, $q^{(0)} \equiv 1$.

This leads to the following expression for the volume fraction of the untransformed substance:

$$Q(t) = \exp\left[-\int_0^t I_1(t')V_1(t', t)dt' - \sum_{i-2}^{n}\int_0^t d\tau\int_0^\tau dt' I_i(t')\dot{V}_i(t', \tau)q^{(i-1)}(t', \tau)\right]. \quad (14)$$

3. EVALUATION OF FUNCTIONS $q^{(i)}(t', t)$

In order to determine the function $q^{(1)}(t', t)$, we shall use the geometrical diagrams shown in Fig. 2. The problem can be formulated as follows: find the probability that an arbitrary point O' lying on a circle of radius $R_2(t', t)$ is in the initial phase. This event must take place when the condition imposed earlier is satisfied: point O also lies in the initial phase before the time t. Thus, for point O', we modify the single-phase problem by an additional condition. We denote by *1'* a region of radius $R_1(t'', t')$, $0 < t'' < t'$, around the point O'. For the above-mentioned event to take place, the emergence of phase-1 nucleation centers in this region is ruled out in the entire interval $0 \le t'' \le t'$. The additional condition also rules out the emergence of such centers in region *1*, i.e., in the region of radius $R_1(t'', t)$ with the center at point O. Consequently, we must take a part of region *1'*, which lies outside region *1*. We denote the volume of this region by $v(t'', t', t)$ (Fig. 2). Analyzing the intersection of two spheres of radii r_1 and r_2 with a separation h between their centers in the 3*D* space, we can easily obtain the following expression for the part of volume of the second sphere outside the first sphere:

$$\Omega(r_1, r_2; h) = \pi\left[\frac{2}{3}(r_2^3 - r_1^3) - \frac{1}{12}h^3 + \frac{1}{2}h(r_1^2 + r_2^2) + \frac{1}{4}\frac{(r_1^2 - r_2^2)^2}{h}\right], \quad (15)$$

where $r_1 > r_2$; $r_1 - r_2 \le h \le r_1 + r_2$. Using this formula, we can find $v(t'', t', t)$:

$$v(t'', t', t) = \Omega[R_1(t'', t), R_1(t'', t'); R_2(t', t)]. \quad (16)$$

Using the result of the single-phase problem (1), we

now obtain $q^{(1)}(t', t)$:

$$q^{(1)}(t', t) = \exp\left[-\int_0^{t'} I_1(t'')\nu(t'', t', t)dt''\right]. \quad (17)$$

The overlapping of regions *1* and *1'* takes place if the condition $r_1 + r_2 > h$ is satisfied, i.e.,

$$R_1(t'', t) + R_1(t'', t') > R_2(t', t), \quad (18)$$

and is observed starting from an instant of time t_c' defined by the equation

$$R_1(0, t) + R_1(0, t_c') = R_2(t_c', t). \quad (19)$$

In the time interval $0 < t' < t_c'$, these regions do not overlap as long as the radius $R_1(0, t')$ is quite small. For $t' > t_c'$, the regions overlap in the time interval $0 < t'' < t_c''$, after which the overlapping disappears since the boundaries move with a velocity $u_1(t'')$, i.e., the radii $R_1(t'', t')$ and $R_1(t'', t)$ decrease at a given rate. The time instant t_c'' can be found from the equation

$$R_1(t_c'', t) + R_1(t_c'', t') = R_2(t', t). \quad (20)$$

For constant rates of growth u_k, condition (19) has the form

$$u_1 t + u_1 t_c' = u_2(t - t_c'), \quad (21)$$

whence

$$t_c' = t\frac{u_2 - u_1}{u_2 + u_1} \equiv t\frac{1 - \alpha}{1 + \alpha}, \quad \alpha \equiv \frac{u_1}{u_2}. \quad (22)$$

In the limiting case $u_1 \ll u_2$ or $\alpha \ll 1$, we have $t_c' \approx t$. Therefore, overlapping is absent in almost the entire interval $0 < t' < t$, and $\nu(t'', t', t) = V_1(t'', t')$.

In this case, $q^{(1)}$ becomes a function of t' only, and expression (10) is simplified as follows:

$$Q(t) = \exp\left[-\int_0^t I_1(t')V_1(t', t)dt' - \int_0^t I_2(t')V_2(t', t)q^{(1)}(t')dt'\right]. \quad (23)$$

The functions $q^{(i)}(t', t)$ for $i > 1$ can be calculated in a similar way. For example, $q^{(2)}(t', t)$ is the fraction of the untransformed substance in the region extending to the distance $R_3(t', t)$ from point *O*. Since the *2–3* region contains nuclei of the first and second phases, we can calculate this function by using the result (10) of the two-phase problem, taking into account the above-described correlation with point *O*:

$$q^{(2)}(t', t) = \exp\left[\int_0^{t'} I_1(t'')\nu_1(t'', t', t)dt'' - \int_0^{t'} d\tau \int_0^{\tau} dt'' I_2(t'')\frac{\partial \nu_2(t'', \tau, t)}{\partial \tau} q^{(1)}(t'', \tau)\right], \quad (24)$$

where

$$\nu_1(t'', t', t) = \Omega[R_1(t'', t), R_1(t'', t'); R_3(t', t)],$$
$$\nu_2(t'', t', t) = \Omega[R_2(t'', t), R_2(t'', t'); R_3(t', t)]. \quad (25)$$

4. INDEPENDENT-PHASE APPROXIMATION

It can be seen that the calculation of the functions $q^{(i)}(t', t)$ is a cumbersome procedure. Consequently, it would be expedient to obtain approximate but simpler expressions for volume fractions. Let us consider the simplest of all possible approximations. We disregard the existence of phases between the boundaries of regions $(i - 1)$ and i, i.e., we put $q^{(i-1)} = 1$, $i = 2, \ldots, n$. In this case, the expressions for the volume fractions become identical:

$$dX_i^0(t)/dt = Q^0(t)\int_0^t I_i(t')\dot{V}_i(t', t)dt', \quad i = 1, \ldots, n, \quad (26)$$

which gives

$$Q^0(t) = \exp\left[-\sum_{i=1}^n \int_0^t I_i(t')V_i(t', t)dt'\right], \quad (27)$$

$$X_i^0(t) = \int_0^t d\tau Q^0(\tau)\int_0^\tau dt' I_i(t')\dot{V}_i(t', \tau). \quad (28)$$

For constant rates of nucleation and growth, the integrals can be evaluated easily:

$$Q^0(t) = \exp\left[-\left(\sum_{i=1}^n k_i\right)t^{D+1}\right], \quad (29)$$

$$X_i^0(t) = \frac{k_i}{\sum_{i=1}^n k_i}\left\{1 - \exp\left[-\left(\sum_{i=1}^n k_i\right)t^{D+1}\right]\right\}, \quad (30)$$

where $k_i \equiv (g/(D + 1))I_i u_i^D$.

In this approximation, all the phases are equivalent in spite of the difference in the rates of growth. Equation (26) for the volume fraction of the *i*th phase has the same

form as in the single-phase case, and expression (27) for the fraction of the untransformed substance splits into the product of similar quantities $Q_i^0 = \exp(-Y_i(t))$ for each phase in the corresponding single-phase problem [$Y_i(t)$ is the integral in (27)]. For these reasons, the given approximation can be referred to as the "independent-phase approximation."

We now have to find the magnitude of the error introduced by this approximation. Let us first derive some preliminary inequalities. If we calculate the functions $q^{(i)}(t', t)$ in the IPA and replace $V_j(t'', t', t)$ by $V_j(t'', t')$ in them, these functions acquire the form

$$q^{(i)}(t') = \exp\left[-\sum_{j=1}^{i}\int_0^{t'} I_j(t'')V_j(t'', t')dt''\right]. \quad (31)$$

Let us use $Q^{\text{ex}}(t)$ and $X_i^{\text{ex}}(t)$ to denote the values of volume fractions calculated by formulas (14) and (13), respectively, and $Q^{\text{ap}}(t)$ and $X_i^{\text{ap}}(t)$ to denote the volume fractions calculated by the same formulas, but with functions (31) instead of exact functions, where

$$Q^{\text{ap}}(t) = Q^0(t) \times \exp\left[\sum_{i=2}^{n}\int_0^{t} I_i(t')V_i(t', t)(1 - q^{(i-1)}(t'))\right]. \quad (32)$$

This leads to the following inequalities:

$$Q^0(t) < Q^{\text{ex}}(t) < Q^{\text{ap}}(t), \quad (33)$$

$$X_1^0(t) < X_1^{\text{ex}}(t) < X_1^{\text{ap}}(t). \quad (34)$$

In order to obtain estimates, we will assume that the nucleation and growth rates are constant. Let us first consider the two-phase case. Expression (32) in this case assumes the form

$$Q^{\text{ap}}(t) = \exp[-(k_1 + k_2)t^{D+1} + \varphi^{(1)}(t)], \quad (35)$$

where

$$\varphi^{(1)}(t) = (D+1)k_2\int_0^t (t-t')^D[1 - \exp(-k_1 t'^{D+1})]dt'.$$

The function $\varphi^{(1)}(t)$ specifies the difference between $Q^{\text{ap}}(t)$ and $Q^0(t)$. Its expansion into a power series in t has the form

$$\varphi^{(1)}(t) = \frac{k_1k_2}{A}t^{2(D+1)} - \frac{k_1^2k_2}{B}t^{3(D+1)} + O(t^{4(D+1)}), \quad (36)$$

where $A = 20$ and 70, $B = 168$ and 990 for $D = 2$ and 3, respectively.

For the difference $\Delta Q(t) = Q^{\text{ap}}(t) - Q^0(t)$, we have

$$\Delta Q(t) = \exp(-(k_1 + k_2)t^{D+1})[\exp(\varphi^{(1)}(t)) - 1]. \quad (37)$$

It should be noted that $\Delta Q(t) < \exp(-k_1 t^{D+1})$ in view of the fact that $\varphi^{(1)}(t) < k_2 t^{D+1}$. It follows, hence, that $\Delta Q(t)$ tends to zero for large t. Besides, $\Delta Q(0) = 0$. Consequently, the function $\Delta Q(t)$ is not monotonic but has a peak. In order to estimate the peak value $\Delta Q_{\max}$ of the function, we replace it by a simpler function $\Delta Q(\xi)$ and confine expansion (36) to the first two terms only:

$$\Delta Q(\xi) = (a\xi^2 - b\xi^3)\exp(-\xi), \quad \xi = (k_1 + k_2)t^{D+1}, \quad (38)$$

where $a = X_1^0X_2^0/A$, $b = (X_1^0)^2X_2^0/B$, and $X_i^0 = k_i/(k_1 + k_2)$ are the volume fractions of the phases in the IPA in the final state ($t = \infty$). The maximum values of the coefficients a and b are as follows: $\max(a) = 1/4A$ and $\max(b) = 4/27B$. These are small quantities even in a two-dimensional space. The substitution of $\Delta Q(\xi)$ for $\Delta Q(t)$ is justified by the smallness of the coefficients a and b. Thus, $\max(\Delta Q(\xi)) < 4ae^{-2} < e^{-2}/A$, and we have the following estimate for $\Delta Q_{\max}$:

$$\Delta Q_{\max} < \varepsilon = e^{-2}/A, \quad (39)$$

$\varepsilon \approx 7 \times 10^{-3}$ and 2×10^{-3} for $D = 2$ and 3, respectively.

Let us also calculate the correction to the volume fraction of the first phase, obtained in the IPA, in the final state:

$$X_1^{\text{ap}} = (D+1)k_1\int_0^\infty t^D\exp\left[-(k_1 + k_2)t^{D+1} + \frac{k_1k_2}{A}t^{2(D+1)} - \frac{k_1^2k_2}{B}t^{3(D+1)}\right]dt. \quad (40)$$

After the substitution $\xi = (k_1 + k_2)t^{D+1}$, we have

$$X_1^{\text{ap}} = X_1^0\int_0^\infty e^{-\xi + a\xi^2 - b\xi^3}d\xi. \quad (41)$$

In view of the smallness of the coefficients a and b, this integral can be replaced by

$$X_1^{\text{ab}} = X_1^0\int_0^\infty e^{-\xi}(1 + a\xi^2 - b\xi^3)d\xi = X_1^0(1 + \delta), \quad (42)$$

where $\delta = 2a - 6b$. This leads to the following estimate for δ: $\delta < 2a \le 1/2A$.

The estimates $\xi, \delta \ll 1$ together with inequalities (33) and (34) show that the exact values of volume fractions in the two-phase system are virtually the same as those calculated in the IPA.

Going over to the case of n phases, we can easily

write by induction the following expression for $Q^{ap}(t)$:

$$Q^{ap}(t) = \exp\left[-\left(\sum_{i=1}^{n} k_i\right)t^{(D+1)} + \varphi^{(n-1)}(t)\right], \quad (43)$$

$$\varphi^{(n-1)}(t) = (D+1)\int_0^t (t-t')^D \times \left\{k_2[1-e^{-k_1 t'^{D+1}}] + k_3[1-e^{-(k_1+k_2)t'^{D+1}}] + \ldots + k_n\left[1-e^{-\left(\sum_{i=1}^{n-1} k_i\right)t'^{D+1}}\right]\right\}dt'. \quad (44)$$

The expansion of $\varphi^{(n-1)}(t)$ has the form

$$\varphi^{(n-1)}(t) = \frac{k_1k_2 + (k_1+k_2)k_3 + \ldots + (k_1+\ldots+k_{n-1})k_n}{A}t^{2(D+1)} - \frac{k_1^2k_2 + (k_1+k_2)^2k_3 + \ldots + (k_1+\ldots+k_{n-1})^2k_n}{B}t^{3(D+1)} + O(t^{4(D+1)}). \quad (45)$$

Repeating the above procedure of obtaining estimates for the given phase, we substitute the variables $\xi = (k_1 + k_2 + \ldots + k_n)t^{D+1}$. Accordingly, the coefficients a and b now have the form

$$a = f_A(X_1^0, \ldots, X_n^0)/A, \quad b = f_B(X_1^0, \ldots, X_n^0)/B,$$
$$f_A = X_1^0X_2^0 + (X_1^0 + X_2^0)X_3^0 + \ldots + (X_1^0 + \ldots + X_{n-1}^0)X_n^0, \quad (46)$$
$$f_B = (X_1^0)^2X_2^0 + (X_1^0 + X_2^0)^2X_3^0 + \ldots + (X_1^0 + \ldots + X_{n-1}^0)^2X_n^0.$$

We can easily find that $\max(f_A(X_1^0, \ldots, X_n^0)) = (n-1)/2n < 1/2$; consequently, $a < 1/2A$, and the above estimates with ε and δ twice as large as in the two-phase case hold.

Thus, the difference of the expressions obtained in the IPA from the exact expressions for a system with an indefinitely large number of phases can be regarded as negligibly small.

Returning to the case of an arbitrary time dependence of the nucleation and growth rates, it is worthwhile to note the following fact. The expansion of the function $Y_i(t) = \int_0^t I_i(t')\,V_i(t', t)dt'$ into a power series in t starts from t^{D+1}, while the expansion of the function $\tilde{Y}_i(t) = \int_0^t I_i(t')\,V_i(t', t)[1 - q^{i-1}(t')]$ starts from $t^{2(D+1)}$. Consequently, the given case does not differ in principle from that considered above.

5. DISCUSSION OF RESULTS

The main results obtained in this work are the expressions for the volume fractions of competing phases, as well as the substantiation of the application of the IPA. Besides, the proposed geometrical–probabilistic method itself can be useful for solving other problems associated with the calculation of volume fractions.

It should be noted that this problem can also be solved by any of the two well-known approaches, viz., the Kolmogorov [1] and the Johnson–Mehl methods [2]. The latter approach is most visual, as it deals directly with nuclei of phases. For this reason, it would be interesting to analyze the solution (10)–(14) from the viewpoint of this method.

The following two assumptions are crucial in the Johnson–Mehl approach: (1) nuclei can grow into one another without changing their shape, and (2) new nucleation centers can emerge in the entire volume of the system, including the transformed region (fictitious centers). It is important that, in the single-phase case, these assumptions simplify the solution of the problem considerably without distorting the pattern of the actual process, and expression (1) is exact. In the case of two competing phases ($u_2 > u_1$), assumption (2) distorts the actual pattern: fictitious nuclei of the rapidly growing phase within the slowly growing phase emerge with time in the untransformed region and contribute to the increase in the actual volume. The IPA expressions disregard this effect and, hence, overestimate the volume fraction of the rapidly growing phase. At the same time, expressions (10)–(14) take this effect into consideration: the factor $q^{(i-1)}(t', t)$ compensates the contribution to the volume fraction of the ith phase from the fictitious nucleation centers. These expressions can also be obtained in the Johnson–Mehl approach reformulated in terms of the probability theory. This, however, is beyond the scope of the present publication.

The analysis of the solution proves that the effect of fictitious nucleation centers is negligibly small. The reason is that this effect "cannot" manifest itself. This is obvious for short periods of time. For longer periods, the effect of fictitious nuclei is restricted on account of the exhaustion of the untransformed volume. For this reason, the IPA expressions are virtually exact within the limitations of the model.

ACKNOWLEDGMENTS

This research was supported by the Ukrainian Center of Science and Technology (project no. 442).

REFERENCES

1. A. N. Kolmogorov, Izv. Akad. Nauk SSSR, Ser. Mat. **3**, 355 (1937).
2. W. A. Johnson and R. F. Mehl, Trans. AIME **135**, 416 (1939).
3. M. Avrami, J. Chem. Phys. **7**, 1103 (1936); **8**, 212 (1939); **9**, 177 (1941).
4. V. Z. Belen'kiĭ, *Geometrical–Probabilistic Models of Crystallization* (Nauka, Moscow, 1980).
5. A. R. Ubbelohde, *Melting and Crystal Structure* (Clarendon, Oxford, 1965; Mir, Moscow, 1969).
6. N. V. Alekseechkin, A. S. Bakaĭ, and N.P. Lazarev, Fiz. Nizk. Temp. **21**, 565 (1995) [Low Temp. Phys. **21**, 440 (1995)].
7. N. V. Alekseechkin, A. S. Bakaĭ, and C. Abromeit, Metallofiz. Noveĭshie Tekhnol. **20** (6), 15 (1998).
8. B. V. Gnedenko, *Theory of Probability* (Fizmatgiz, Moscow, 1961; Central Books, London, 1970).

Translated by N. Wadhwa

Physics of the Solid State, Vol. 42, No. 7, 2000, pp. 1361–1369. Translated from Fizika Tverdogo Tela, Vol. 42, No. 7, 2000, pp. 1322–1330.

LOW-DIMENSIONAL SYSTEMS AND SURFACE PHYSICS

Negative Magnetoresistance and Hall Coefficient of a Two-Dimensional Disordered System

A. G. Groshev and S. G. Novokshonov

Physicotechnical Institute, Ural Division, Russian Academy of Sciences, ul. Kirova 132, Izhevsk, 426000 Russia

e-mail: nov.@otf.fti.udmurtia.su

Received August 9, 1999

Abstract—Localization corrections to the longitudinal ($\delta\rho$) and Hall ($\delta\rho_H$) resistivities of a two-dimensional disordered system are calculated in all ranges of classical magnetic fields, up to the values at which the mean free path of charge carriers l is less than or of the order of the cyclotron radius R_c. It is shown that the physical reason for the departure of the l dependence of these resistivities from the logarithmic law $\propto \ln(l_B/l)$ (l_B is the magnetic length) at $l_B \ll l \ll R_c$ is the nonlocal process of diffusion in the Cooper channel, rather than the transition to a quasi-ballistic regime. Analytical expressions are obtained that allow one to analyze the interference effect in $\delta\rho$ and $\delta\rho_H$ in quantizing magnetic fields ($R_c \ll l$), including the quantum limit. Contrary to popular opinion, the localization corrections to ρ_H are shown to be nonzero. They have a sign opposite to that of the charge carriers and lead to a decrease in the magnitude of the Hall resistivity. Their field dependence has the same features and their relative magnitude is of the same order as in the case of the longitudinal resistivity. The quantum corrections to the Hall resistivity are due to the Larmor precession of the closed paths that electrons follow in the process of their multiple scattering by randomly distributed impurities. © *2000 MAIK "Nauka/Interperiodica".*

INTRODUCTION

Quantum corrections to the electrical conductivity (due to weak electron localization) are the result of the quantum interference of electronic waves subjected to multiple scattering by randomly distributed impurities. The theory of these corrections [1] is the most completely developed and experimentally verified part of the theory of disordered systems. One of the most important results of this theory is the explanation of the negative magnetoresistance (NMR) [2, 3], which is observed in low-dimensional semiconducting structures [4]. For the past twenty years, significant progress has been made in this area. The quantitative theory of the NMR was developed, which is valid in a wide range of classical magnetic fields ($l \ll R_c$) [5–9] and consistently includes the major contributions to this effect to the first order in the small parameter $1/k_F l$ [6, 9]. The quantum corrections to the electrical conductivity of disordered systems were adequately interpreted in terms of the quasi-classical theory [9, 10].

However, some important problems remain unsolved. There is no theory of quantum corrections in the range of quantizing magnetic fields ($R_c \ll l$), although some steps have been made in its development [10, 11]. In our opinion, no physical explanation was provided for the departure of the quantum corrections to the electrical conductivity from the diffusion approximation [1], which takes place at short phase diffusion times τ_φ and strong magnetic fields, $l_B \ll l$.

The interference contributions to the Hall resistivity ρ_H were shown [12] to be zero to the first order in $1/k_F l$. For this reason, it is believed that the dominant quantum corrections to ρ_H are due to the electron–electron interaction [3, 13–15].

In this paper, we calculate the interference quantum corrections to the longitudinal (ρ) and Hall (ρ_H) resistivities by the method developed in [5, 7, 9]. The expressions obtained are valid in a wide range of magnetic fields, including quantizing ones. It is shown that, contrary to the wide-spread opinion, the localization corrections to the Hall resistivity $\delta\rho_H$ are nonzero to the first order in $1/k_F l$. The physical nature of $\delta\rho_H$ is elucidated, analytical asymptotic expressions are obtained, and a numerical analysis is conducted of the field dependence of these corrections.

The cooperon, which determines the localization corrections to the transport coefficients, is shown to hold its diffusion propagator form in the particle–particle channel in virtually the entire range of classical magnetic fields, $l < R_c$. However, at higher magnetic fields, one should take into account the spatial and time nonlocality (dispersion) of the generalized diffusion coefficient. A departure from the diffusion propagator form occurs at relatively high fields and is associated with the violation of the time reversal invariance, rather than with the crossover to the ballistic regime [8, 9].

1. BASIC EQUATIONS

Let us consider a two-dimensional degenerate gas of electrons that are elastically scattered by static impurities having a concentration n_I and distributed by a Pois-

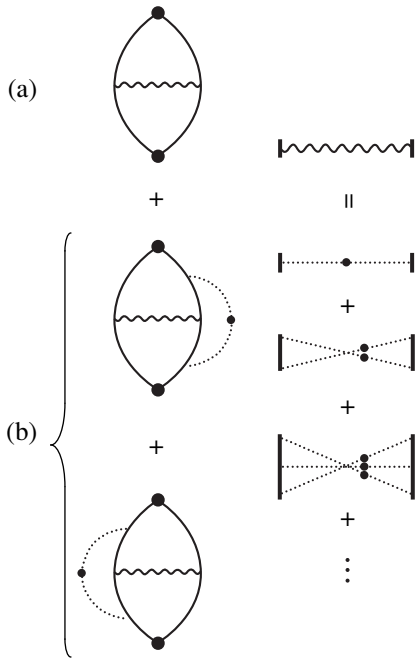

Fig. 1. Contributions to quantum corrections to σ from (a) coherent backward scattering and (b) scattering through arbitrary angles. The wavy line represents the sum of maximally crossed diagrams.

son distribution in the sample. The one-electron Hamiltonian of the problem under study has the form

$$\mathcal{H} = \mathcal{H}_0 + \mathcal{U} = \frac{1}{2m}\left(\mathbf{p} - \frac{e}{c}\mathbf{A}\right)^2 + \sum_{\mathbf{R}} U(\mathbf{r} - \mathbf{R}), \quad (1)$$

where $\mathbf{A} = (0, Bx)$ is the vector potential of the magnetic field in the Landau gauge. We assume that an impurity localized at a point $\mathbf{R}$ is characterized by a short-range potential, which can be approximated by a δ function, $U(\mathbf{r} - \mathbf{R}) = U_0\delta(\mathbf{r} - \mathbf{R})$. This approximation is valid if the radius of action of the impurity potential r_0 is small compared to the de Broglie wavelength of an electron at the Fermi energy level $\mathscr{E}_F$. We also assume that the scattering of an electron by an isolated impurity is weak and treat it in the first Born approximation.

The electrical conductivity tensor of the system under study has a single independent circularly polarized component σ, for which we have $\mathrm{Re}\sigma = \sigma_{xx}$ and $\mathrm{Im}\sigma = \sigma_{yx}$. We write this component in the form ($\hbar = 1$)

$$\sigma = \sigma_B^0 + \delta\sigma = \frac{\sigma_0}{1 - i\omega_c\tau} + \frac{e^2}{2\pi}\langle Sp V_+ \delta R^+ V_- \delta R^- \rangle. \quad (2)$$

Here, $\sigma_0 = ne^2\tau/m$, $\omega_c = |e|B/mc$ is the cyclotron frequency; $V_\pm = V_x \pm iV_y$ are the circularly polarized components of the electron velocity operator in the magnetic field; $R^\pm(\mathscr{E}) = (\mathscr{E} - \mathcal{H} \pm i0)^{-1}$ is the resolvent of the Hamiltonian (1); $\delta R^\pm = R^\pm - \langle R^\pm \rangle$, where the angular brackets $\langle \ldots \rangle$ denote configuration averaging (the volume of the system is taken equal to unity):

$$\langle R^\pm \rangle = G^\pm = (\mathscr{E} - \mathcal{H}_0 - \Sigma^\pm(\mathscr{E}))^{-1},$$
$$\Sigma^\pm(\mathscr{E}) = \Delta(\mathscr{E}) \mp i\Gamma(\mathscr{E})/2, \quad (3)$$

where $\Sigma^\pm(\mathscr{E})$ is the electron self-energy operator, determining the shift Δ and width $\Gamma = 1/\tau$ of one-electron energy levels in the random field of impurities.

The first term in (2) is the electrical conductivity calculated in terms of classical electron transport theory, which is valid in a wide range of magnetic fields up to classically strong ones (but not quantizing ones, $\omega_c\tau \lesssim 1$). The quantum corrections to σ, which represent the weak-localization effects or the NMR, are included in the second term in (2). They are due to the interference of the wave functions of electrons that move along closed paths in opposite directions in the process of multiple scattering by impurities. It was shown [6] that, in strong magnetic fields, the dominant contribution to these corrections is from processes of the two types corresponding to skeleton diagrams in Figs. 1a and 1b, respectively. A detailed analysis revealed [9] that, as the phase diffusion time τ_φ decreases or the magnetic field increases, the relative contribution from the processes represented by the diagrams in Fig. 1b grows, and these processes should be included when the weak-localization effects are calculated.

Using the identity

$$G^\pm V_\mp G^\mp = \mp i\tau \frac{V_\mp G^\mp - G^\pm V_\mp}{1 - i\omega_c\tau} \quad (4)$$

and passing over to the coordinate representation, we write the quantum corrections to σ as

$$\delta\sigma = -\frac{\sigma_0^2}{(1 - i\omega_c\tau)^2}\frac{2\pi^2}{e^2}\Delta, \quad (5)$$

where $\Delta = \Delta_a + \Delta_b$,

$$\Delta_a = \frac{1}{\pi k_F^3 l}\int d\mathbf{r}\int d\mathbf{r}' \left\langle \mathbf{r}\middle| G^- V_+ - V_+ G^+ \middle|\mathbf{r}'\right\rangle$$
$$\times \left\langle \mathbf{r}\middle| V_- G^- - G^+ V_- \middle|\mathbf{r}'\right\rangle C(\mathbf{r}', \mathbf{r}),$$
$$\Delta_b = \frac{W}{\pi k_F^3 l}\int d\mathbf{r}\int d\mathbf{r}'\int d\mathbf{r}_1 \left\langle \mathbf{r}\middle| G^- \middle|\mathbf{r}_1\right\rangle \quad (6)$$
$$\times \left\langle \mathbf{r}\middle| V_- G^- - G^+ V_- \middle|\mathbf{r}_1\right\rangle \left\langle \mathbf{r}_1\middle| G^- \middle|\mathbf{r}'\right\rangle$$
$$\times \left\langle \mathbf{r}_1\middle| G^- V_+ - V_+ G^+ \middle|\mathbf{r}'\right\rangle C(\mathbf{r}', \mathbf{r}).$$

Here, $C(\mathbf{r}', \mathbf{r})$ is the cooperon, equal to the series of maximally crossed (fan-shaped) diagrams and represented by a wavy line in Fig. 1. In (6), we have explicitly written out the corrections that correspond to the

diagrams in Fig. 1a and to the first of the two fan-shaped diagrams in Fig. 1b; the correction corresponding to the second fan diagram is written in much the same way. Using the quasi-classical interpretation [9] of quantum corrections to the electrical conductivity, it can be shown that, in contrast to the correction Δ_a, which is associated with an anomalous increase in the backward-scattering amplitude ($\theta \approx \pi$), the correction Δ_b also contains a comparable contribution from scattering through all other angles $0 < \theta < \pi$.

Experimentally measured quantities are the longitudinal (ρ) and Hall (ρ_H) resistivities related to σ by the equations $\rho = \mathrm{Re}\sigma^{-1}$and $\rho_H = \mathrm{Im}\sigma^{-1}$. Assuming the localization corrections to the conductivity to be small enough ($|\delta\sigma| \ll |\sigma_B^0|$), we calculate the reciprocal of (2) to the first order in Δ and obtain the following quantum corrections to ρ and ρ_H (in units of $2\pi^2/e^2$)

$$\delta\rho = \rho - \rho_0 = \mathrm{Re}\Delta, \quad \delta\rho_H = \rho_H - \rho_{H_0} = \mathrm{Im}\Delta, \quad (7)$$

where $\rho_0 = 1/\sigma_0$ and $\rho_{H_0} = \rho_0\omega_c\tau = B/enc$. As expected, expressions (7) do not contain factors like $1/(1 + \omega_c^2\tau^2)$. Indeed, in terms of the classical theory, such factors appear in the components of the conductivity tensor (2) and (5), because the paths of electrons are bent under the action of a magnetic field; that is, the factors are of kinematic origin. However, in degenerate semiconductors with one group of carriers, as is well known (see, e.g., [16]), this does not affect the resistivity tensor. Hence, in the one-electron model we consider here, the field dependence of $\delta\rho$ and $\delta\rho_H$ is determined solely by the localization corrections to the electrical conductivity in the entire range of classical magnetic fields ($\omega_c\tau \lesssim 1$). This circumstance is of critical importance in interpreting the experimental data.

2. THE ONE-ELECTRON GREEN'S FUNCTION

Our further calculations are based on the averaged one-electron Green's function in the coordinate representation $G^{\pm}(\mathbf{r}, \mathbf{r}', \mathscr{E}) = \langle\mathbf{r}|G^{\pm}(\mathscr{E})|\mathbf{r}'\rangle$, which is proportional to the probability amplitude for finding an electron at point $\mathbf{r}'$ if its last collision was at point $\mathbf{r}$. In a zero magnetic field, this function has a simple asymptotic form, valid for $\rho = |\mathbf{r} - \mathbf{r}'| > \lambda_F$,

$$G^{\pm}(\mathbf{r}, \mathbf{r}'; \mathscr{E}) = \frac{\mp im}{\sqrt{2\pi k_F\rho}}\exp\left[\pm ik_F\rho - \frac{\rho}{2l} \mp i\frac{\pi}{4}\right], \quad (8)$$

where $l = v_F\tau$ is the mean free path of the electron.[1] In a weak magnetic field ($\omega_c\tau \ll 1$), expression (8) should be multiplied by the phase factor $\exp(-i\Phi) = \exp[-i(x + x')(y - y')/2l_B^2]$, where $l_B = \sqrt{c/|e|B}$ is the magnetic length.

In [5–7, 9], approximation (8) was used to analyze the NMR in strong magnetic fields $B \gg B_{tr} = c/2|e|l^2$. This can be done if $\omega_c\tau \ll 1$ (or $l \ll R_c$, where $R_c = l_B^2 k_F$ is the cyclotron radius) and one can neglect the bending of quasi-classical electron paths in a magnetic field. However, in stronger fields ($l \gtrsim R_c$), account should be taken of both the phase change and the fact that the free electron motion is confined to a $\rho < 2R_c$ region. Appropriate approximations can be obtained from the exact expression for the retarded Green's function $G^+(\mathbf{r}, \mathbf{r}'; \mathscr{E})$, which is the product of the phase factor $\exp(-i\Phi)$ (as in the case of a weak magnetic field) and the gauge- and translation-invariant function

$$G^+(\rho; \mathscr{E}) = -\frac{m\omega_c}{4\pi}\int_0^{+\infty}\frac{dt}{\sin(\omega_c t/2)} \times \exp\left[ia^+\omega_c t + i\frac{m\omega_c}{4}\rho^2\cot\frac{\omega_c t}{2}\right], \quad (9)$$

where $a^+ = (\mathscr{E} + i/2\tau)/\omega_c = k_F R_c(1 + i/k_F l)/2$; $G^-(\rho; \mathscr{E}) = [G^+(\rho; \mathscr{E})]^*$.

The integral in (9) can be expressed in terms of the Tricomi degenerate hypergeometric function $\Psi(a, c; x)$ [17]

$$G^+(\rho; \mathscr{E}) = -\frac{m}{2\pi}\exp\left(-\frac{x}{2}\right)\Gamma\left(\frac{1}{2} - a^+\right)\Psi\left(\frac{1}{2} - a^+, 1; x\right) \quad (10)$$

($x = \rho^2/2l_B^2$), which, in turn, can be approximated by its asymptotic expressions for large values of the parameter and argument ($|a^+| \gg 1$, $x \gg 1$). However, it is more convenient here to apply a simple and physically clear method proposed by Gornyĭ [10], according to which the integral in (9) is estimated by the stationary phase method. Applying this method in the region accessible to classical motion ($\rho < 2R_c$) at $k_F l = \infty$ and analytically continuing the result into the upper complex half plane $k_F \longrightarrow k_F(1 + i/k_F l)^{1/2}$, one easily obtains[2]

$$G^+(\rho; \mathscr{E}) = -i\exp(-i\pi/4)\frac{m}{\sqrt{2\pi k_F\rho}}\left(1 - \frac{\rho^2}{4R_c^2} + \frac{i}{k_F l}\right)^{-1/4} \times\left[\frac{\exp(i\xi^+)}{1 + \exp(2\pi i a^+)} - i\frac{\exp(-i\xi^+)}{1 + \exp(-2\pi i a^+)}\right], \quad \rho < 2R_c, \quad (11)$$

[1] If phase diffusion takes place, the quantity $1/\tau$ should be replaced by $1/\tau + 1/\tau_\varphi$ in all expressions for the one-electron Green's functions.

[2] The same result is obtained using the corresponding asymptotic expressions for the Tricomi function in (10) [17].

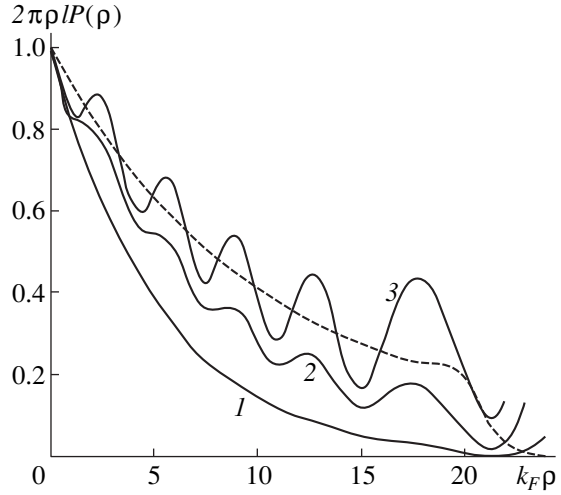

Fig. 2. Probability density for finding an electron at a distance ρ from the point of its last collision as calculated using approximation (11) for $k_F R_c$= 10.0 and different values of l/R_c: (*1*) 0.5, (*2*) 0.75, and (*3*) 1.0. The dashed line is calculated for l/R_c = 1.0 ignoring the contribution from reflected waves and describes the $2\pi\rho lP(\rho)$ dependence in the region inaccessible to classical motion ($\rho > 2R_c$).

where the exponent is given by

$$\xi^+ = \frac{k_F\rho}{2}\sqrt{1-\frac{\rho^2}{4R_c^2}+\frac{i}{k_F l}} + 2a^+\arcsin\left[\frac{\rho}{2R_c}\left(1+\frac{i}{k_F l}\right)^{-1/2}\right] \quad (12)$$

and, at $k_F l = \infty$, is equal to the action corresponding to the electron transition $\mathbf{r} \longrightarrow \mathbf{r}'$ along the short arc of the cyclotron orbit.

Approximation (11) to the one-electron Green's function is accurate to within terms of the order of $\omega_c/\mathscr{E}_F \sim 1/k_F R_c$ and $\min(l_B, \lambda_F)/\rho$ and has a simple physical interpretation. The common factor in (11), to within the Fermi momentum replaced by its radial component $k_F\sqrt{1-\rho^2/4R_c^2}$, coincides with the preexponential factor in (8). The first term in the square brackets in (11) is associated with the classical electron motion from $\mathbf{r}$ to $\mathbf{r}'$ along the short (S) arc of the cyclotron orbit, while the second term corresponds to the electron motion along the long (L) arc [10]. The factors $1 + \exp(\pm 2\pi i a^+)$ in the denominators are the result of the summation of the probability amplitudes of the $\mathbf{r} \longrightarrow \mathbf{r}'$ transition after electron making n turns (n = 0, 1, 2, …) in the cyclotron orbit. The moduli of these factors are minimal at the energies $\mathscr{E}/\omega_c = n + 1/2$, corresponding to the centers of the collision-broadened Landau levels. Thus, in the region accessible to classical motion, the retarded Green's function (11), in contrast to (8), is the sum of the diverging wave G_S^+ and barrier-reflected converging wave G_L^+. As the magnetic field is decreased, the amplitude of the latter wave exponentially decreases [as $\propto\exp(-R_c/l)$] compared to the former. Therefore, at $l \ll R_c$ and $\rho \ll R_c$, the bending of electron paths caused by the magnetic field can be ignored and (11) reduces to the asymptotic expression (8).

In the region inaccessible to classical motion ($\rho > 2R_c$), into which electrons penetrate owing to the tunneling effect, the probability amplitude falls off exponentially [as $\propto\exp(-\rho^2/4l_B^2)$] with increasing ρ. In this case, the asymptotic behavior of $G^+(\rho; \mathscr{E})$ is well described by the first term in (11).

The localization corrections to the conductivity in classically strong fields ($l \lesssim R_c$) are expressed in terms of the quantity $P(\rho) = W|G^{\pm}(\rho)|^2$, which is proportional to the probability density of an electron being found at the distance ρ from the point of its last collision. The asymptotic expression (8) corresponds to the exponential distribution $P(\rho) = \exp(-\rho/l)/(2\pi\rho l)$ [5, 7], which is valid only in the limit $B \longrightarrow 0$. Approximation (11) is more convenient, because it allows one to calculate $P(\rho)$ in a wide range of magnetic fields, up to $k_F R_c \approx 10$, and of distances $\min(l_B, \lambda_F) < \rho < +\infty$, including the vicinity of the classical turning point $\rho \approx 2R_c$.[3]

Figure 2 shows the $2\pi\rho lP(\rho)$ dependence as calculated from the asymptotic expression (11) for different values of the ratio l/R_c. At $l \ll R_c$, the dominant contribution to $P(\rho)$ is from the electron motion along the short arc of the cyclotron orbit. In this case, in the region $\rho < R_c$, the $2\pi\rho lP(\rho)$ dependence is approximately described by its asymptotic expression in weak-field range, $\propto\exp(-\rho/l)$, but at $\rho > 2R_c$ the exponential falloff becomes sharper, $\propto\exp(-\rho^2/2l_B^2)$. As the ratio l/R_c is increased, the relative contributions to (11) both from the electron motion along the long arcs of cyclotron orbits and from turns in these orbits increase. As a consequence, in $P(\rho)$ terms that are due to the interference of waves that traveled different paths up to the given point appear. The $P(\rho)$ dependence becomes oscillatory in the $0 < \rho < 2R_c$ range, with oscillations being clearly defined even at $l \sim R_c$.

These and some other features of the one-electron Green's function manifest themselves in the behavior of the localization corrections to the transport coefficients in the range of strong magnetic fields, where $\omega_c\tau \sim 1$.

[3] It is worth noting that if the analytic continuation $k_F \longrightarrow k_F(1 + i/k_F l)^{1/2}$ is not carried out, that is, if $k_F l = \infty$, then from (11) we have $G(\rho; \mathscr{E}) \propto \rho^{-1/2}(1-\rho^2/4R_c^2)^{-1/4}$ [10], which is valid only for $\rho \ll 2R_c, l$.

3. THE COOPERON BEYOND THE CLASSICAL DIFFUSION APPROXIMATION

The quantum corrections (5) and (6) to the conductivity are proportional to the cooperon $C(\mathbf{r}, \mathbf{r}')$, which is represented in a diagrammatic notation by a series of fan-shaped diagrams (Fig. 1). Since the system under study is invariant under translations (on the average) in a zero magnetic field, it is convenient to use the momentum representation, in which the summation of fan-shaped diagrams is readily performed and we obtain

$$C(q) = \frac{P(q)}{1-P(q)},$$
$$P(q) = W\sum_{\mathbf{k}} G^{+}_{\mathbf{k}_+} G^{-}_{\mathbf{k}_-} = (s^2 + l^2 q^2)^{-1/2}, \tag{13}$$

where $q = |\mathbf{q}| = |\mathbf{p} + \mathbf{p}'|$, $\mathbf{k}_\pm = \mathbf{k} \pm \mathbf{q}/2$, $s = 1 + \tau/\tau_\varphi$.

In the long-wavelength limit ($ql \ll 1$) and at a long enough phase diffusion time ($\tau \ll \tau_\varphi$), we have $P(q) = (1 + \tau/\tau_\varphi + q^2 D_0 \tau)^{-1}$, where $D_0 = \nu_F^2 \tau/2$ is the classical diffusion coefficient for a two-dimensional electron system; hence, expression (13) has a conventional diffusion approximation form [1]. In the opposite limit, we have $|P(q)| \ll 1$, and for this reason, it is generally believed [7, 9] that the diffusion approximation to the cooperon (13) is invalid beyond the $ql \ll 1$ and $\tau \ll \tau_\varphi$ ranges. Indeed, at $ql \gg 1$, the first several fan-shaped diagrams dominate. These diagrams represent closed paths of a small length $\sim l$, with a small number of collisions. The electron motion along such paths is quasiballistic, rather than diffusive, in character. However, in the general case (with the proviso that $q \ll k_F$ and $\tau_\varphi \mathscr{E}_F \gg 1$), expression (13) also has the form of a diffusion approximation propagator, namely,

$$C(q, \tau_\varphi^{-1}) = \frac{1}{\tau/\tau_\varphi + q^2 D(q, i/\tau_\varphi)\tau}, \tag{14}$$

where $D(q, i/\tau_\varphi)$ is a generalized diffusion coefficient (dependent on wavenumber q and frequency $\omega = i/\tau_\varphi$), calculated in the ladder approximation [18],

$$D(q, i/\tau_\varphi) = \frac{2D_0}{s + \sqrt{s^2 + l^2 q^2}}. \tag{15}$$

This is consistent with a general result [19] according to which the presence in the irreducible four-leg vertex of a diffusion pole such as in (14), with the exact generalized diffusion coefficient, is due to the time reversal invariance and conservation of the number of particles. Therefore, the electron propagation remains diffusive, but becomes nonlocal in character in the q and τ_φ ranges in question. The nonlocality is enhanced with increasing relative contribution to the cooperon from closed electron paths of small lengths, which takes place for large values of q and $1/\tau_\varphi$. The electron motion does cease to be diffusive, but this occurs on atomic spatial and time scales ($q \sim k_F$, $\tau_\varphi \mathscr{E}_F \sim 1$), where electrons obey quantum-mechanical laws. Substituting (15) in (14), we obtain an expression for the cooperon $C(q, \tau_\varphi^{-1})$, which exactly coincides with that used in [5–7]. For this reason, we focus here only on the physical interpretation of the cooperon at large momenta.

In the presence of an external magnetic field, the system ceases to be invariant under translations. In this case, it is more convenient to treat the cooperon in the coordinate representation, in which the following integral equation takes place:[4]

$$C(\mathbf{r}, \mathbf{r}') = P(\mathbf{r}, \mathbf{r}') + \int d\mathbf{r}_1 P(\mathbf{r}, \mathbf{r}_1) C(\mathbf{r}_1, \mathbf{r}'), \tag{16}$$

where the kernel is given by

$$P(\mathbf{r}, \mathbf{r}') = W\langle \mathbf{r}|G^{+}|\mathbf{r}'\rangle\langle \mathbf{r}|G^{-}|\mathbf{r}'\rangle$$
$$= \exp\{-i2\Phi(\mathbf{r}, \mathbf{r}')\} W|G^{\pm}(\rho)|^2. \tag{17}$$

Obviously, the cooperon $C(\mathbf{r}, \mathbf{r}')$ has the same structure; namely, it is the kernel of an integral operator being diagonal in the basis of its eigenfunctions $\Psi_{n, k_y}(\mathbf{r})$, which describe a particle of charge $2e$ moving in the magnetic field B. Its part invariant under translations has the form

$$C(\rho) = \frac{1}{\pi l_B^2} \sum_{n=0}^{+\infty} \frac{P_n}{1-P_n} J_{n,n}(\sqrt{2}\rho),$$
$$P_n = 2\pi \int_0^{+\infty} \rho d\rho J_{n,n}(\sqrt{2}\rho) P(\rho). \tag{18}$$

Here, we have introduced the notation

$$J_{n,n'}(\rho) = \left(\frac{n_{\min}!}{n_{\max}!}\right)^{1/2} \left(\frac{\rho^2}{2l_B^2}\right)^{|n-n'|/2}$$
$$\times \exp\left(-\frac{\rho^2}{4l_B^2}\right) L_{n_{\min}}^{|n-n'|}\left(\frac{\rho^2}{2l_B^2}\right), \tag{19}$$

where $L_n^m(x)$ is a generalized Laguerre polynomial [$L_n(x) = L_n^0(x)$].

Expressions (18) for the cooperon were derived by Kawabata [5] for the case of a weak magnetic field ($\omega_c \tau \ll 1$). However, they remain valid in the range of quantizing magnetic fields ($\omega_c \tau \gg 1$) [11],[5] if the one-particle Green's functions are calculated in the Landau basis. This allows one to investigate the quantum cor-

[4] Here and henceforth, the time dependence of the phase diffusion time τ_φ is not explicitly indicated for the sake of convenience.

[5] Unfortunately, the expression used in [11] for P_n is true only for large quantum numbers, $n \gg 1$.

rections to the conductivity tensor for both weak and strong magnetic fields, up to the quantum limit.

The relation between the cooperon (18) and the diffusion propagator can be easily obtained considering the asymptotic expression for the cooperon in the range of weak magnetic fields, where the coefficients P_n (as may be inferred from the asymptotic behavior of the Laguerre polynomials for $n \gg 1$ [20]) tend to the Fourier transform of the function $P(\rho)$

$$P_n \approx P(q_n) = 2\pi \int_0^{+\infty} \rho d\rho P(\rho) J_0(q_n \rho) = \frac{1}{s + q_n^2 D(q_n)\tau}, \quad (20)$$

calculated at discrete values of the wavenumber $q_n = \sqrt{(4n+2)}/l_B$, where $J_n(x)$ is the Bessel function of order n.

The asymptotic expression (20) is valid with the proviso that $l^2/l_B^2 \ll q_n^2 l_B^2 \ll R_c k_F = 2\mathscr{E}_F/\omega_c$. The first inequality determines the order of smallness of the corrections to (20), which is $\sim l/(l_B^2 q_n)$, while the second inequality determines the lower limit (atomic spatial scale) of the spatial region, $\rho = |\mathbf{r} - \mathbf{r}'| \gg \lambda_F$, in which the cooperon $C(\rho)$ has the form of the diffusion propagator. The second equality in (20) is obtained using (13) and (14), which relate $P(q)$ to $D(q)$, the generalized diffusion coefficient of electrons in a classical magnetic field. The latter coefficient can be calculated independently, by solving the transport equation in the relaxation time approximation. For the two-dimensional system in the magnetic field we consider here, this yields the following result:

$$P(q) = \sum_{n=-\infty}^{+\infty} \frac{J_n^2(qR_c)}{s + in\omega_c\tau}. \quad (21)$$

In classical magnetic fields, expression (21) and the Fourier transform (20), calculated using (11), coincide up to the terms of the order of $\omega_c/\mathscr{E}_F$ and q/k_F. The classical diffusion approximation to the cooperon in a magnetic field is obtained by expanding (20) and (21) in a power series in τ/τ_φ and q^2 and keeping the lowest-order terms. This yields expression (14), in which $D(q)$ is replaced by $D_B = D_0/(1 + \omega_c^2\tau^2)$; hence, this approximation ignores spatial dispersion of the diffusion coefficient and is valid with the proviso that $D_B(4n+2)\tau/l_B^2 \ll 1$.

Thus, in a magnetic field, the cooperon has the form of the diffusion propagator (14) with the generalized diffusion coefficient dependent on the discrete wavenumber $q_n = \sqrt{4n+2}/l_B$, imaginary frequency i/τ_φ, and magnetic field B if, in the series in (18), the terms corresponding to the range $l^2/l_B^2 \ll q_n^2 l_B^2 \ll R_c k_F$ are dominant. As the magnetic field is increased, this range becomes narrower and the cooperon gradually ceases to have the diffusion propagator form. This is certain to be the case in strong magnetic fields $l^2/l_B^2 \sim R_c k_F$ (or $\omega_c\tau \sim 1$), where the asymptotic expression (20) for the coefficients P_n ceases to be true. At a fairly low mobility of charge carriers [or large values of $B_{tr} = c\hbar/(2|e|l^2)$], this occurs well before the onset of the quasi-ballistic propagation regime in the particle–particle channel and is associated with the violation of the time reversal invariance in a magnetic field.

4. QUANTUM CORRECTIONS TO THE LONGITUDINAL AND HALL RESISTIVITIES

An explicit calculation of the parameters Δ_a and Δ_b, which determine the quantum corrections to the longitudinal and Hall resistivities (7), is similar to that performed in [9, 10]. For this reason, we will discuss only the most important points, without going into detail.

Strictly speaking, all orders of multiple scattering, starting from the second, contribute to Δ_a and Δ_b. However, the second-order scattering is insensitive to a change in the magnetic field, because the closed paths described by electrons envelop the zero area [6]. In this case, the corrections are $\delta\rho^{(2)} = O(B^0)$ and $\delta\rho_H^{(2)} = O(B)$ and, hence, they can be included in the longitudinal (ρ_0) and Hall (ρ_{H_0}) resistivities at $B \longrightarrow 0$, respectively. It should be noted that, in strong magnetic fields, this can be done, because expressions (7) for $\delta\rho$ and $\delta\rho_H$ involve no kinematic factors.

When calculating the vector vertices

$$\left\langle \mathbf{r} \middle| V_\pm G^\pm - G^\mp V_\pm \middle| \mathbf{r}' \right\rangle = \pm \exp(-i\Phi \pm i\varphi) V_F K(\rho) \quad (22)$$

(φ is the polar angle of the vector $\mathbf{r} - \mathbf{r}'$), involved in the quantum corrections (6), the noncommutativity of the components of the velocity operator is ultimately ignored in all theoretical studies on the NMR, including the first papers [2, 5, 12, 14]. In terms of classical mechanics, this is equivalent to ignoring the Lorentz force acting on electrons moving in a magnetic field. No wonder that such an approximation only slightly affects quantum corrections to the longitudinal resistivity, but leads to zero corrections to the Hall resistivity. This result was first obtained by Fukuyama [12] and is now widely believed to be a characteristic feature of the manifestation of localization effects in the galvanomagnetic coefficients of disordered systems. Moreover, scaling [21] and self-consistent [22] theories of the Anderson localization predict that the relation $\rho_H = B/enc$ takes place near the mobility threshold on the metal side of the metal–insulator phase transition ($d > 2$).

The function $K(\rho)$ is given by the following exact expression:

$$K(\rho) = \frac{2}{k_F}\frac{\partial}{\partial\rho}\mathrm{Im}G^+(\rho;\mathscr{E}) - i\,\mathrm{sgn}(e)\frac{\rho}{R_c}\mathrm{Re}G^+(\rho;\mathscr{E}), \quad (23)$$

where $G^+(\rho;\mathscr{E})$ is the translation-invariant part of the one-electron Green's function (9). In magnetic fields weak enough for the asymptotic expression (11) for the one-electron Green's function to be valid, its variation along an electron path is predominantly due to rapidly oscillating phase factors $\propto\exp(\pm i\xi)$. In this case, the first term in (23) is proportional to the radial component of the electron velocity at the distance ρ from the point of its last collision $V_r = \sqrt{V_F^2 - \omega_c^2\rho^2/4} = m^{-1}\partial\xi/\partial\rho$. The second term is proportional to the tangential component $V_t = \omega_c\rho/2$, which is due to the Larmor precession of the electron path in the magnetic field. It is this component of the vector vertex that was not taken into account in the papers mentioned above. This component is purely imaginary and depends on the sign of the charge carriers; it leads to nonzero quantum corrections (7) to the Hall resistivity. It is clear that the tangential component in (23) leads to corrections to $\delta\rho$ in (7) of the second order in the small parameter l/R_c in the range of classical magnetic fields.

Further calculations are basically the same as in [9, 10], and we present only the final results:

$$\Delta = \frac{z}{2(\pi k_F l)^2}\sum_{n=0}^{\infty}\frac{P_n}{1-P_n}[P_nA_n - B_{n-1}^{(+)2} - B_n^{(-)2}], \quad (24)$$

where $z = B/B_{tr} = 2l^2/l_B^2$,

$$A_n = 2\pi W\int_0^{+\infty}\rho d\rho J_{n,n}(\sqrt{2}\rho)K^2(\rho),$$
$$B_n^{\pm} = 2\pi W\int_0^{+\infty}\rho d\rho J_{n,n+1}(\sqrt{2}\rho)G^{\pm}(\rho)K(\rho). \quad (25)$$

In principle, these expressions allow one to analyze the localization corrections to the resistivity tensor in the entire range of magnetic fields, from classically weak ($\omega_c\tau \ll 1$) to quantizing ones ($\omega_c\tau \gg 1$). In the latter case, all calculations should be performed in the Landau basis. The results of [9, 10] for $\delta\rho$ follow from (24) and (25) if, in the integrands in (25), one neglects rapidly oscillating terms involving the products $G^{\pm}G^{\pm}$ of one-type Green's functions. This yields the approximate expressions

$$WK^2 \approx 2P(\rho)(1 - i\,\mathrm{sgn}(e)\rho/R_c),$$
$$WG^{\pm}K \approx P(\rho)(1 - i\,\mathrm{sgn}(e)\rho/2R_c), \quad (26)$$

which are true until the asymptotic expression (11) of the one-electron Green's function is determined by the contributions from short arcs of cyclotron orbits. The numerical results presented above (see Fig. 2) show that this is a good approximation to $G^{\pm}(\rho;\mathscr{E})$ if the magnetic field satisfies the condition $l \lesssim 2R_c/3$. Thus, strictly speaking, this inequality gives the upper limit of the region where the corresponding results of [9, 10] are valid. The tangential component of the vector vertex (23) leads to the emergence of a nonzero imaginary part in expression (24) for Δ. This is a new result, which, contrary to popular opinion [3], predicts nonzero localization corrections to the Hall resistivity.

In weak fields $B \ll B_{tr}$, the series in (24) converges rather slowly. In this case, it is sufficient to replace the coefficients A_n and $B_n^{\pm}$ (25) by their asymptotic expressions for $n \gg 1$. Thus, we obtain the following expressions for the corrections to the longitudinal and Hall resistivities:

$$\delta\rho = \frac{z}{2(\pi k_F l)^2}\sum_{n=0}^{+\infty}\frac{P_n}{1-P_n}\left[2P_n^2 - P_{n-1/2}^2\frac{1-sP_{n-1/2}}{1+s+P_{n-1/2}} - P_{n+1/2}^2\frac{1-sP_{n+1/2}}{1+sP_{n+1/2}}\right],$$
$$\delta\rho_H = -\mathrm{sgn}(e)\frac{l}{R_c}\frac{z}{2(\pi k_F l)^2} \times\sum_{n=0}^{+\infty}\frac{P_n}{1-P_n}[2sP_n^4 - P_{n-1/2}^3(1-sP_{n-1/2}) - P_{n+1/2}^3(1-sP_{n+1/2})], \quad (27)$$

where $P_n = P(q_n)$, defined in (13) and (20). The first terms in the square brackets in (24) and (27) are associated with coherent backward scattering, while the second and third terms are due to scattering through arbitrary angles. The first equation in (27) is identical to the corresponding equation derived in [9]. At $B \to 0$, the sum in (27) can be replaced by an integral, which yields asymptotic expressions that are logarithmically dependent on temperature (through $\tau_\varphi \sim T^{-p}$, with p ranging from 1 to 2)

$$\delta\rho = \frac{2}{s+1}\frac{1}{(\pi k_F l)^2}\left[s\ln\frac{s}{s-1} - \ln 2\right],$$
$$\delta\rho_H = -\mathrm{sgn}(e)\frac{l}{R_c(\pi k_F l)^2}\left[(2s-1)\ln\frac{s}{s-1} - 2\right]. \quad (28)$$

In the range of fairly weak magnetic fields ($l \ll l_B \ll l_\varphi, R_c$), the field dependences of the corrections to the longitudinal and Hall resistivities are also logarithmic, $\delta\rho/\rho_0 \sim \delta\rho_H/\rho_{H_0} \propto \ln(l_B^2/l^2)$. In the opposite limit ($l_B \ll l \ll R_c$), they change over to power laws $\delta\rho/\rho_0 \propto B^{-1/2}$

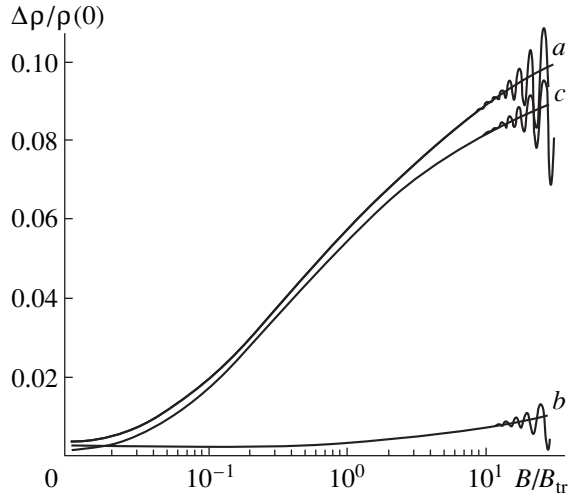

Fig. 3. Negative magnetoresistance $\Delta\rho/\rho(0) = (\rho(B) - \rho(0))/\rho(0)$: (*a*) contribution from coherent backward scattering, (*b*) contribution from scattering through arbitrary angles, and (*c*) total. The curves are calculated from the asymptotic expression (11) for $G^{\pm}(\rho)$ ignoring the contribution from long arcs of cyclotron orbits.

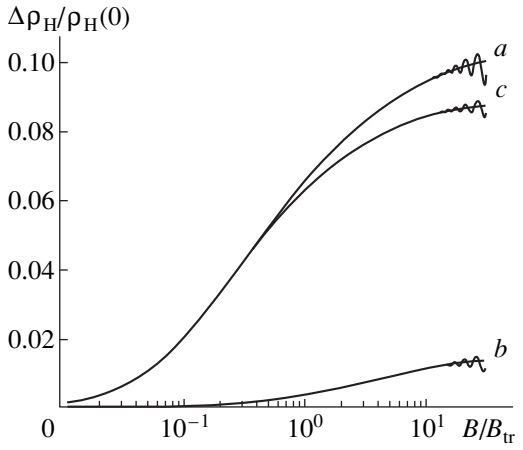

Fig. 4. Same as in Fig. 3 for the Hall resistivity $\Delta\rho_H/\rho_H(0) = (\rho_H(B) - \rho_H(0))/\rho_H(0)$.

[5, 6] and $\delta\rho_H/\rho_{H_0} \propto B^{-3/2}$. The relative values of the quantum corrections to the transport coefficients are of the same order, $(\delta\rho/\rho_0)/|\delta\rho_H/\rho_{H_0}| \sim 1$. The correction $\delta\rho$ is always positive, whereas the sign of $\delta\rho_H$ is opposite to that of charge carriers. In other words, the localization corrections decrease the Hall resistivity in magnitude.

Figures 3 and 4 show numerical calculations of the quantum corrections to the longitudinal and Hall resistivities for $\tau/\tau_\varphi = 10^{-2}$ and $k_F l = 10$, which corresponds to the carrier mobility $\mu \approx 1.5 \times 10^4$ cm^2 V^{-1} s^{-1} if their concentration is $2\pi n = 10^{12}$ cm^{-2}. If the contribution from long arcs to the one-electron Green's functions (11) is neglected, the field dependences of $\Delta\rho/\rho(0)$ and $\Delta\rho_H/\rho_H(0)$ in the $\omega_c\tau < 1$ region only slightly differ from those calculated on the basis of the asymptotic expression (8). In fields higher than those satisfying the condition $\omega_c\tau \approx 0.5$, the longitudinal and Hall resistivities exhibit Shubnikov oscillations, which imposes an upper limit on the validity range of our approximations. In fairly strong fields ($B > B_{tr}$), the field dependences depart from logarithmic ones, but pure power laws $\delta\rho/\rho(0) \propto B^{-1/2}$ and $\delta\rho_H/\rho_H(0) \propto B^{-3/2}$ are not observed, because, for the parameters chosen, they take place when $B/B_{tr} > 10^2$ [8], i.e., far beyond the range of actual fields.[6]

5. DISCUSSION OF RESULTS

It was indicated above that, physically, the localization corrections to the Hall resistivity are due to the procession of electron paths in the magnetic field. Its direction coincides with that of the cyclotron motion of electrons, which leads to an increase in the Hall current or, what is the same, to a decrease of ρ_H in magnitude. The variation of $\delta\rho_H$ with increasing magnetic field is determined by two competing factors: on the one hand, a decrease in the probability of coherent scattering due to magnetic dephasing effect, and on the other, a increase in the Larmor precession frequency.

At first glance, the statement that the localization corrections to the Hall resistivity should be equal to zero (at least, in the first order in $1/k_F l$) is physically well founded (see, e.g., [3]). The point is that the interference effects do not lead to a change in the carrier concentration, while the corresponding quantum corrections to the transport relaxation time cancel each other in the expression for ρ_H. This reasoning is quite correct in the case where the Hall component of the conductivity σ_{yx} has the form following from the classical kinetic equation in a magnetic field [see the first term in (2)]. However, as was first shown in [23], σ_{yx} contains terms for which there is no analog in the classical transport theory. The general structure of these terms was analyzed in detail by Gerhardts [24]. It is easy to verify that, to the first nonvanishing order in the small parameter $\omega_c\tau$, expression (5) for quantum corrections to the Hall conductivity has the same form as the first term on the right-hand side of equation (3.24) in [24].

Thus, in contrast to the longitudinal resistivity, the localization corrections to the Hall resistivity cannot be explained by interference terms in the transport relaxation time [9]. These corrections are proportional to the mean linear velocity of Larmor precession of closed sections of electron paths, $V_L = \langle\omega_c\rho/2\rangle$. We will illustrate this by the example of quantum corrections to the

[6] Estimations show that, in classical fields ($\omega_c\tau < 1$), these field dependences may be observed in perfect heterostructures in which, at a carrier concentration of $2\pi n = 10^{12}$ cm^{-2}, their mobility is as high as $\mu \sim 10^5$–10^6 cm^2 V^{-1} s^{-1}.

Hall resistivity corresponding to Fig. 1a. They can be written as

$$\delta\rho_H^{(a)} = \frac{1}{(\pi k_F l)^2} 2\pi l^2 \sum_{n=3}^{+\infty} \int d^2\mathbf{r} \frac{\omega_c r}{V_F} W_n(r) P(r) = \delta\rho^{(a)} 2\frac{V_L}{V_F}. \quad (29)$$

Here, $W_n(r)$ is the probability density of an electron enduring n collisions and then being found at the distance r from the point of its first collision [7]. A similar expression can also be obtained for $\delta\rho_H^{(b)}$. Naturally, there is no analog for these corrections in the classical transport theory, because in that theory the processes contributing to the transport relaxation time are considered as momentary events. The ratio V_L/V_F in (29) may be thought of as being related to an additional Hall angle, $2V_L/V_F = \tan\theta_{WL}$, which is caused by the Larmor precession of closed electron paths and differs from the classical Hall angle, $\tan\theta = \omega_c l/V_F$. In other words, in the process of multiple scattering, there occurs accumulation of an additional shift of electrons in the direction perpendicular to the current direction.

In our opinion, the results obtained in this paper offer a clearer view of the physical nature of quantum transport phenomena in disordered systems. In particular, they open up possibilities for the theoretical study of these phenomena in the range of quantizing magnetic fields, in which some interesting experimental data were recently obtained [25]. At the same time, they raise a number of problems that remain to be solved. For instance, in order to interpret the experimental data more accurately, one should take a fresh look at the relative contributions from electron–electron interaction and localization to the transport coefficients of two-dimensional disordered systems [3, 15]. Also, the question again arises on the behavior of the Hall coefficient in the vicinity of the metal–insulator phase transition.

ACKNOWLEDGMENTS

The authors would like to thank the members of the Semiconductor Physics Laboratories of the Institute of Metal physics (Ural Division, Russian Academy of Sciences) and of Ural State University for helpful discussions. Thanks are also due to G.M. Min'kov, who acquainted the authors with unpublished Hall resistivity measurements performed by his research group. Special thanks are due to I.V. Gornyĭ for his consultations, which allowed a number of difficulties in this work to be overcome.

This work was supported by the INTAS Foundation, grant no. 99-10-70.

REFERENCES

1. L. P. Gor'kov, A. I. Larkin, and D. E. Khmel'nitskiĭ, Pis'ma Zh. Éksp. Teor. Fiz. **30**, 248 (1979) [JETP Lett. **30**, 228 (1979)].
2. S. Hikami, A. I. Larkin, and Y. Nagaoka, Prog. Theor. Phys. **63**, 707 (1980).
3. B. L. Altshuler, A. G. Aronov, D. E. Khmelnitskii, and A. I. Larkin, in *Quantum Theory of Solids*, Ed. by I. M. Lifshitz (Mir, Moscow, 1982), p. 130.
4. G. Bergman, Phys. Rep. **101**, 1 (1984).
5. A. Kawabata, J. Phys. Soc. Jpn. **53**, 3540 (1984).
6. V. M. Gasparyan and A. Yu. Zyuzin, Fiz. Tverd. Tela (Leningrad) **27**, 1662 (1985) [Sov. Phys. Solid State **27**, 999 (1985)].
7. M. I. Dyakonov, Solid State Commun. **92**, 711 (1994).
8. A. Zduniak, M. I. Dyakonov, and W. Knap, Phys. Rev. B **56**, 1996 (1997).
9. A. P. Dmitriev, I. V. Gornyi, and V. Yu. Kachorovskii, Phys. Rev. B **56**, 9910 (1997).
10. I. V. Gornyĭ, Author's Abstract of Candidate's Dissertation (St. Petersburg, 1998).
11. A. K. Arzhnikov, S. G. Novokshonov, and S. V. Pakhomov, Teor. Mat. Fiz. **94**, 486 (1993).
12. H. Fukuyama, J. Phys. Soc. Jpn. **49**, 644 (1980).
13. B. L. Al'tshuler, A. G. Aronov, A. I. Larkin, and D. E. Khmel'nitskiĭ, Zh. Éksp. Teor. Fiz. **81**, 768 (1981) [Sov. Phys. JETP **54**, 411 (1981)].
14. B. L. Altshuler, D. E. Khmelnitskii, A. I. Larkin, and P. A. Lee, Phys. Rev. B **22**, 5142 (1980).
15. A. Houghton, J. R. Senna, and S. C. Ying, Phys. Rev. B **25**, 2196 (1982).
16. J. M. Ziman, *Principles of the Theory of Solids* (Cambridge, Cambridge Univ. Press, 1972).
17. H. Bateman and A. Erdelyi, *Higher Transcendental Functions* (McGraw-Hill, New York, 1953), Vol. 1.
18. A. G. Groshev and S. G. Novokshonov, Zh. Éksp. Teor. Fiz. **111**, 1787 (1997) [JETP **84**, 978 (1997)].
19. I. M. Suslov, Zh. Éksp. Teor. Fiz. **108**, 1686 (1995) [JETP **81**, 925 (1995)].
20. H. Bateman and A. Erdelyi, *Higher Transcendental Functions* (McGraw-Hill, New York, 1953), Vol. 2.
21. B. Shapiro and E. Abrahams, Phys. Rev. B **24**, 4025 (1981).
22. E. A. Kotov and M. V. Sadovskiĭ, Fiz. Met. Metalloved. **60**, 22 (1985).
23. A. Bastin, C. Leviner, O. Betbeder-Matibet, and P. Nozieres, J. Phys. Chem. Solids **32**, 1811 (1971).
24. R. R. Gerhardts, Z. Phys. B **22**, 327 (1975).
25. S. S. Murzin, Pis'ma Zh. Éksp. Teor. Fiz. **67**, 201 (1998) [JETP Lett. **67**, 216 (1998)].

Translated by Yu. Epifanov

Physics of the Solid State, Vol. 42, No. 7, 2000, pp. 1370–1372. Translated from Fizika Tverdogo Tela, Vol. 42, No. 7, 2000, pp. 1331–1333.

LOW-DIMENSIONAL SYSTEMS AND SURFACE PHYSICS

Initial Ion Velocity in Electron-Stimulated Desorption

S. Yu. Davydov

Ioffe Physicotechnical Institute, Russian Academy of Sciences, Politekhnicheskaya ul. 29, St. Petersburg, 194021 Russia

Received December 21, 1999

Abstract—The effect of electronic-shell repulsion and electron–phonon interaction among atoms of an adsorption complex on the initial ion velocity is considered. *© 2000 MAIK "Nauka/Interperiodica".*

The relaxation model of electron-stimulated desorption (ESD) [1] assumes that a description of the motion of a desorbing ion should take into account the effect of the local substrate field generated by the redistribution of the electronic density after the adsorption bond rupture. It was shown [2] that taking into account short-range repulsion of electronic shells of the ions in an adsorption complex (consisting of ion 1, coupled by an adsorption bond to the metal surface, and ion 2, which interacts directly only with ion 1) considerably affects the energy distribution of the ESD ions. The energy distribution of ESD ions within the "classical" relaxation model [1, 3], which only takes into account the Coulomb interaction of ions with the image force, is strongly asymmetric with the maximum shifted toward lower kinetic energies; the inclusion of repulsion results in an almost bell-shaped distribution and shifts the maximum toward higher energies [2].

The effect of short-range repulsion of electronic shells was taken into account in [2] parametrically, by introducing a nonzero initial velocity v_0 of the desorbing ion. We are going to show here that a nonzero initial ion velocity may arise not only as a result of short-range repulsion, but due to electron–phonon interaction in the adsorption complex as well, and to estimate the magnitude of v_0.

Consider first the short-range repulsion. We assume that at the instant of time $t = 0$ the desorbing ion is acted upon only by the potential

$$V_{\text{rep}}(r) = B\exp[-b(r - r_0)], \tag{1}$$

where r_0 is the equilibrium position of ion 2. Then for the equation of motion of this ion one can write

$$\ddot{r} = bV_{\text{rep}}(r) \tag{2}$$

with the initial conditions $r(0) = r_0$ and $\dot{r}(0) = 0$. Here and in what follows, we use a dimensionless system of units [3] in which all distances are measured in units of the bond length d between the metal and atom (ion) 1 and time is in units of $\tilde{t} = (Md^3/e^2)^{1/2}$ (M is the mass of the desorbing ion and e is the positronic charge). Solutions to this equation are

$$\begin{aligned} r(t) &= r_0 + \frac{2}{b}\ln\cosh\left(\frac{1}{2}bt\sqrt{2B}\right), \\ v(t) &= \sqrt{2B}\tanh\left(\frac{1}{2}bt\sqrt{2B}\right). \end{aligned} \tag{3}$$

It thus follows that the limiting velocity acquired under the action of the short-range potential is $v_0 = \sqrt{2B}$. It is this value that we shall accept for the upper estimate of the initial velocity.

As a specific example, we consider the adsorption of alkali-metal atoms (Li, Na) on a monolayer silicon film deposited on a tungsten or an iridium ribbon [4, 5]. Recalling that, in the Morse potential, whose first term is potential (1), the binding energy is B, the latter quantity can be equated to the desorption energy E_{des}. Because the experiment [6] shows that, for desorption of alkali metals from a monolayer silicon coating on tungsten, E_{des} differs only by one to two tenths of an electron-volt from that for clean tungsten, we accept $E_{\text{des}}(\text{Li}) = 2.98$ and $E_{\text{des}}(\text{Na}) = 2.53$ eV [7]. We thus obtain $v_0(\text{Li}) = 9.05 \times 10^3$ and $v_0(\text{Na}) = 4.56 \times 10^3$ m/s. These values coincide in order of magnitude with the sound velocity in a solid. The effect of recoil processes on the initial velocity is considered in Appendix 1.

We are turning now to another mechanism of the formation of the initial velocity, namely, to the electron–phonon one. We shall consider interaction of a one-electron atom with a metal surface using a Hamiltonian of the form

$$H = H_{\text{m}} + H_{\text{a}} + H_{\text{am}} + H_{\text{ph}}, \tag{4}$$

where

$$H_{\text{m}} = \sum_k \varepsilon_k c_k^+ c_k \tag{5}$$

is the Hamiltonian of the metal,

$$H_{\text{a}} = [\varepsilon_a + \gamma(d - d_0)](a^+ a - n_0) \tag{6}$$

is the adatom Hamiltonian with inclusion of electron–phonon interaction,

$$H_{\text{am}} = g\sum_k (c_k^+ a + \text{h.c.}) \quad (7)$$

is the Hamiltonian describing the adatom interaction with the metal, and, finally,

$$H_{\text{ph}} = (M\omega_0^2/2)(d-d_0)^2 + (M/2)(\dot{d})^2 \quad (8)$$

is the phonon Hamiltonian. Here, ε_k is the metal electron dispersion law; ε_a is the position of the adatom quasilevel; γ is the electron–phonon coupling constant; g is the hybridization constant between the metal and adatom states; M is the desorbing adatom mass; ω_0 is the vibration frequency of the adatom located at a distance d_0 from the metal and having the occupation number n_0; and c_k^+ and a^+ are the operators of electron creation in the metal and at the adatom, respectively. Note that this Hamiltonian was used to describe the electronic and structural rearrangements in an adsorbed layer [8–10] and surface reconstruction of metals [11] and semiconductors [12, 13].

Using Eqs. (5)–(8), one can show [8, 9] that as the adatom filling by electrons changes from n_0 to $n = \langle a^+ a\rangle$, the equilibrium adatom–metal distance changes from d_0 to d, so that

$$d - d_0 = -(\gamma/M\omega_0^2)(n-n_0). \quad (9)$$

Thus, it follows that a decrease of the adatom occupation number should be accompanied by an increase of its distance from the metal, i.e., by outward relaxation. An estimate of the parameter $\zeta = (\gamma/M\omega_0^2)$ made in Appendix 2 shows that $\zeta \cong 2$–4 Å, a far from insignificant figure. It should also be borne in mind that the electron–phonon Hamiltonian (4) is written for small variations of the adatom occupation number, so that directly applying expression (9) to the case of abrupt adatom ionization is generally not valid. It may, however, be conjectured that the sign of the relaxation (outward or inward) is correctly predicted by (9). Note that such a structural rearrangement should occur with a velocity close to the velocity of sound. If this occurs after the bond connecting atoms 1 and 2 with masses $M_{1,2}$ has ruptured, the latter atom acquires a velocity of the order of $(M_2/M_1)v_1$, where v_1 is the velocity with which atom 1 collides with atom 2.

Thus, theoretical estimates show that the initial velocity of an ESD ion is of the order of the sound velocity. It is interesting that in [14] the temperature dependence of the ESD ion yield in the Na–Si/W system was obtained for a reversible desorption mechanism within the relaxation model, i.e., with inclusion not only of the initial velocity v_0 but of the Coulomb forces as well. By fitting this temperature dependence to experiment, the initial velocity of an ESD ion was found to be 1.39×10^3 m/s, which also coincides in order of magnitude with the sound velocity. Thermal vibrations can likewise contribute to the initial impact ejecting ion 2 out of its adsorption fragment [14].

ACKNOWLEDGMENTS

Support of the Federal Program “Surface Atomic Structures” is gratefully acknowledged.

APPENDIX 1

Consider a system consisting of a linear diatomic “molecule” adsorbed on a metal surface. Let atom (ion) 1 closest to the surface be located at point $r = d_0$, and atom (ion) 2 be at point $r = r_0$ (the distance r is measured from the metal surface). Before the system excitation by outer electrons, the interaction of atom 1 with a surface metal atom can be described by the Morse potential V_1 of the form

$$V_1(r) = D\{\exp[-2\alpha(r-d_0)] - 2\exp[-\alpha(r-d_0)]\}.$$

The interaction of atom 1 with atom 2 can be written as

$$V_2(r) = B\left\{\exp[-b(r-r_0)] - 2\exp\left[-\frac{b}{2}(r-r_0)\right]\right\}.$$

After the action of the outer shell electrons has ruptured the bond between atoms 1 and 2, the former atom feels only repulsion from atom 2, i.e., only the first component of the potential $V_2(r)$. Based on the equilibrium condition, one can show that atom 1 transfers to a new equilibrium position d, with

$$\delta d \equiv \frac{d_0 - d}{d_0} = \frac{1}{\alpha d_0}\ln\left(\frac{1+\sqrt{1+4C}}{2}\right),$$

$$C = \frac{bB}{2\alpha D}\exp[-b(r-r_0)],$$

where $r \geq r_0$ is the coordinate of the desorbing atom. For $r \longrightarrow \infty$, atom 1 tends to return to the initial position d_0.

For $C \ll 1$, we obtain $\delta d = C/\alpha d_0$ and $v_0 = \sqrt{2B}\,[1 - (b/2\alpha)C]$. Thus, taking into account the recoil effects reduces the initial velocity. Note that the maximum value $C = bB/2\alpha D$ may be anything but small in the case of a surface molecule, where the binding energy of atoms 1 and 2 considerably exceeds that of atom 1 with the metal ($B \gg D$).

APPENDIX 2

In [15], it was shown how one can calculate the $\zeta = (\gamma/M\omega_0^2)$ parameter, which is the coefficient of proportionality in (9), within Harrison’s model of bonding orbitals [16]. Recalling that $M\omega_0^2 = k$, where k is a force constant describing the response to a change in the

bond length between an atom of the substrate and a silicon atom, we obtain

$$\zeta = \beta^2/k^2, \quad \beta = -(s/d)\alpha_c V_2,$$
$$k = -2s^2\alpha_c V_2 d^{-2}(2n/s - 2 + \alpha_c^2).$$

Here, V_2 is the covalent bound energy, α_c is the covalency, $s = 7/2$, and $n = 4$ [17]. The calculations were carried out for silicon atoms adsorbed on tungsten and iridium. Two cases were considered, namely, of the substrate atom d orbital connected (a) with the silicon-atom p orbital and (b) with the silicon sp^3 orbital. The values obtained for the Si/W system are as follows: (a) $\zeta = 1.46$ and (b) $\zeta = 1.22$ Å. In the Si/Ir case, ζ is (a) 4.25 and (b) 2.36 Å.

REFERENCES

1. V. N. Ageev, O. P. Burmistrova, and Yu. A. Kuznetsov, Usp. Fiz. Nauk **158**, 389 (1989) [Sov. Phys. Usp. **32**, 588 (1989)].
2. S. Yu. Davydov, Fiz. Tverd. Tela (St. Petersburg) **39**, 1679 (1997) [Phys. Solid State **39**, 1498 (1997)].
3. S. Yu. Davydov, Fiz. Tverd. Tela (St. Petersburg) **35**, 2525 (1993) [Phys. Solid State **35**, 1251 (1993)].
4. V. N. Ageev, A. M. Magomedov, and B. V. Yakshinskiĭ, Fiz. Tverd. Tela (Leningrad) **33**, 158 (1991) [Sov. Phys. Solid State **33**, 91 (1991)].
5. V. N. Ageev and B. V. Yakshinskiĭ, Fiz. Tverd. Tela (St. Petersburg) **37**, 483 (1995) [Phys. Solid State **37**, 261 (1995)].
6. É. G. Nazarov and U.Kh. Rasulev, *Nonstationary Processes of Surface Ionization* (Fan, Tashkent, 1991).
7. V. N. Ageev, O. P. Burmistrova, A. M. Magomedov, and B. V. Yakshinskiĭ, Fiz. Tverd. Tela (Leningrad) **32**, 801 (1990) [Sov. Phys. Solid State **32**, 472 (1990)].
8. V. E. Kravtsov and A. G. Mal'shukov, Zh. Éksp. Teor. Fiz. **75**, 691 (1978) [Sov. Phys. JETP **48**, 348 (1978)].
9. S. Yu. Davydov, Fiz. Tverd. Tela (Leningrad) **21**, 2283 (1979) [Sov. Phys. Solid State **21**, 1314 (1979)].
10. A. I. Volokitin and A. A. Karpushin, Fiz. Tverd. Tela (Leningrad) **21**, 3576 (1979) [Sov. Phys. Solid State **21**, 2064 (1979)].
11. L. A. Bol'shov and M. S. Veshchunov, Poverkhnost', No. 1, 35 (1982).
12. L. A. Bol'shov and M. S. Veshchunov, Zh. Éksp. Teor. Fiz. **90**, 569 (1986) [Sov. Phys. JETP **63**, 331 (1986)].
13. L. A. Bol'shov and M. S. Veshchunov, Poverkhnost', No. 7, 5 (1989).
14. S. Yu. Davydov, Zh. Tekh. Fiz. **67** (11), 77 (1997) [Tech. Phys. **42**, 1312 (1997)].
15. S. Yu. Davydov and E. I. Leonov, Fiz. Nizk. Temp. **15**, 536 (1989) [Sov. J. Low Temp. Phys. **15**, 302 (1989)].
16. W. A. Harrison, *Electronic Structure and the Properties of Solids: The Physics of the Chemical Bond* (Freeman, San Francisco, 1980; Mir, Moscow, 1983), Vol. 2.
17. W. A. Harrison, Phys. Rev. B **34**, 2787 (1986).

Translated by G. Skrebtsov

Physics of the Solid State, Vol. 42, No. 7, 2000, pp. 1373–1379. Translated from Fizika Tverdogo Tela, Vol. 42, No. 7, 2000, pp. 1334–1340.

LOW-DIMENSIONAL SYSTEMS AND SURFACE PHYSICS

The Linewidth of Surface States of Simple Metals

V. M. Silkin and E. V. Chulkov

Departamento de Física de Materiales, Facultad de Quimica, Universidad del País Vasco/Fuskal Herrico Unibertsitatea, Apdo. 1072 20018 San Sebastian/Donostia, Basque Country, Spain

Institute of Strength Physics and Materials Science, Siberian Division, Russian Academy of Sciences, Akademicheskiĭ pr. 8, Tomsk, 634021 Russia

e-mail: waxslavs@sqox01.sq.ehu.es

Received January 11, 2000

Abstract—The linewidths (inverse lifetimes) Γ_{e-e} of Be(0001) and Mg(0001) surface electronic states are calculated as the projection of the imaginary part of the self-energy operator of a quasiparticle onto the state. The screened Coulomb interaction is calculated using a model potential, which takes into account the energy gap in the band structure and a surface state located in this gap. The wave functions and energies of electron states are calculated by a self-consistent film pseudopotential method. It is shown that Γ_{e-e} essentially depends on the position of the surface state in the Brillouin zone. The difference between the calculated values of Γ_{e-e} and those obtained in a homogeneous electron gas model is shown to be basically due to transitions from surface bands.

INTRODUCTION

Angle-resolved photoemission spectroscopy (ARPES) is widely used for studying various properties of solids [1]. From the energy positions of peaks in spectra obtained by this method, one can directly determine the three-dimensional energy band structure of bulk materials, as well as the surface band dispersion. In addition, photoemission spectra provide a great deal of information about multi-body effects in the electron system. For instance, an experimentally measured linewidth Γ_{exp} of surface states contains contributions from inelastic electron–electron scattering, electron–phonon interaction, and electron scattering by crystal structure defects and impurities [1–8]. Also, the results depend on the instrumental resolution [8] and experimental conditions. Therefore, the experimentally measured linewidths are determined by a variety of factors. Investigating the influence of these factors on measured spectra is of great importance. Recently, some experimental papers have been published [5–7] in which the effect of surface imperfections and temperature on the linewidths was studied. For copper, the contributions from electron–phonon interaction and electron scattering by defects to the linewidth of surface states were determined [5–7], which allowed one to find the surface state linewidth Γ_{e-e} due to inelastic electron–electron interaction. A comparison of these experimental values and the results obtained in a homogeneous electron gas (HEG) model in the framework of the Fermi liquid theory by Landau [9] showed that, in spite of the precision measurements, the experimental values of Γ_{e-e} of Cu(111) surface states were 4–6 times higher than the theoretical value [5–7]. Similar discordances were also observed for surfaces of other noble [10, 11], as well as simple, metals. For example, for a Be(0001) surface state at the center of the Brillouin zone, the experimental linewidths are 350–440 meV at room temperature [12–14]. Using the temperature dependence of the linewidth Γ_{exp} presented in [13], and assuming that the contribution from defects is similar to that in the case of the Cu(111) surface [6], one may evaluate the Γ_{e-e} for a Be(0001) surface state at the $\bar{\Gamma}$ point to obtain a value of about 300 meV. As with copper, this value is significantly higher than a theoretical value of Γ_{e-e} = 92 meV obtained in the HEG model [9] for the parameter r_s = 1.87 corresponding to bulk beryllium. For another simple metal, Mg, ARPES measurements of the (0001) surface state linewidth at the $\bar{\Gamma}$ point gave values of about 200 [15] and about 500 meV [16], which greatly differ from each other and are much higher than Γ_{e-e} = 60 meV, obtained in the HEG model.

This raises the question of whether the discordance is due to the measurement accuracy not being enough or to a weakness of the theory. It is possible that, an extra damping mechanism, such as that considered in [7], operates in this case. (In [7], an additional broadening of the surface state line is attributed to electron scattering by a particular kind of defects that cannot be detected by the low-energy electron diffraction method). In [9], calculations were performed in the framework of the HEG model, which does not take into account the energy band structure of the metal and the surface effects. In this model, in the vicinity of the Fermi level E_F, the linewidth Γ_{e-e} of a quasiparticle associated with electron–electron interaction is proportional to the squared deviation of the quasiparticle

energy E from E_F,

$$\Gamma_{e-e} = \Gamma_0(E - E_F)^2, \quad (1)$$

where Γ_0 is a parameter, which depends only on the electron gas density of the metal in question [3] (the linewidth Γ_{e-e} is related to the lifetime τ of a quasiparticle by the Heisenberg relation $\Gamma_{e-e}\tau = 1$ a.u. = 660 meV fs).

In this paper, we calculate the natural linewidth Γ_{e-e} of surface states with due account of the three-dimensional atomic structure of the crystal. The method employed here is a generalization of that used in [17] for calculating the linewidth of the states of the image potential. These states are located predominantly outside the crystal [18, 19]. Therefore, the calculation of the linewidth of these states in the quasi-homogeneous approximation is justified. Compared to the image states, the surface states overlap with bulk electron states much more generously and, hence, the surface roughness should affect the linewidths of the surface states more strongly. We calculate the initial and final states of quasiparticles by a self-consistent film pseudopotential method, while the screened Coulomb interaction is calculated as in [17]. Using this approach, we find the natural linewidth Γ_{e-e} of Be(0001) and Mg(0001) surface states. As is well known, the electronic structure of Mg is adequately described in terms of the approximation of nearly free electrons. The pseudopotential of magnesium is fairly weak, and its energy band structure has narrow gaps [20]. Mg(0001) surface electron states are weakly localized near the surface atomic layer and extend deep into the metal [21, 22]. In contrast, the energy band structure of Be differs essentially from that of free electrons. For instance, in bulk beryllium, the density of states at the Fermi level is very low and, in this respect, Be is more like a semiconductor than a metal [23]. The dissimilarity of beryllium from typical nontransition metals is due to its strong ionic pseudopotential. The surface electronic structure of beryllium is characterized by wide energy gaps near the Fermi level, within which well-defined surface states are localized [12, 22–25]. Therefore, using these two *s–p* metals as an example, one may investigate two extreme cases of the influence of the energy band structure and of the surface on the lifetime of surface states.

1. CALCULATION TECHNIQUE

The natural linewidth Γ_{e-e}, which is equal to the reciprocal of the lifetime τ of a quasiparticle (hole, in our case) in a state characterized by wave vector $\bar{\mathbf{q}}$, energy $E_{0\bar{\mathbf{q}}}$, and wave function $\Psi_{0\bar{\mathbf{q}}}(\mathbf{r})$, is determined as the projection of the imaginary part of the self-energy operator Σ of a quasiparticle onto the state,

$$\Gamma_{e-e} = \tau^{-1} = -2\int d\mathbf{r}\int d\mathbf{r}'\Psi^*_{0\bar{\mathbf{q}}}(\mathbf{r})\mathrm{Im}\Sigma(\mathbf{r}, \mathbf{r}'; E_{0\bar{\mathbf{q}}})\Psi_{0\bar{\mathbf{q}}}(\mathbf{r}'). \quad (2)$$

Here and henceforth, we use the standard notation in which two-dimensional vectors are marked with an overscribed bar, $\mathbf{G} = \{\bar{\mathbf{G}}, G_z\}$, and also, the atomic units are used in which $e^2 = \hbar = m_e = 1$. The self-energy operator Σ is calculated in the GW approximation [26], in which only the first-order term is retained in the expansion of Σ in powers of the screened Coulomb potential W. Replacing the Green's function G by its zero-order approximation (Green's function for the system of "noninteracting" particles), $\mathrm{Im}\Sigma$ is easily obtained to be

$$\mathrm{Im}\Sigma(\mathbf{r}, \mathbf{r}'; E_{0\bar{\mathbf{q}}}) = \sum_{E_{0\bar{\mathbf{q}}} < E_{n\bar{\mathbf{k}}} < E_F} \Psi^*_{n\bar{\mathbf{k}}}(\mathbf{r}')\mathrm{Im}W(\mathbf{r}, \mathbf{r}'; (E_{n\bar{\mathbf{k}}} - E_{0\bar{\mathbf{q}}}))\Psi_{n\bar{\mathbf{k}}}(\mathbf{r}), \quad (3)$$

where the summation is carried out over all states characterized by wave functions $\Psi_{n\bar{\mathbf{k}}}(\mathbf{r})$ and energies $E_{n\bar{\mathbf{k}}}$ in the range from the energy $E_{0\bar{\mathbf{q}}}$ to the Fermi energy E_F. The screened Coulomb potential $W(\mathbf{r}, \mathbf{r}'; E)$ is given by

$$W(\mathbf{r}, \mathbf{r}'; E) = \int d\mathbf{r}''\varepsilon^{-1}(\mathbf{r}, \mathbf{r}''; E)V(\mathbf{r}'' - \mathbf{r}'). \quad (4)$$

Here, $\varepsilon^{-1}(\mathbf{r}, \mathbf{r}''; E)$ is the inverse dielectric function and $V(\mathbf{r}'' - \mathbf{r}')$ is the Coulomb potential. In the random phase approximation, ε^{-1} and the response function χ are related by an equation, which can be symbolically written as

$$\varepsilon^{-1} = 1 + V\chi. \quad (5)$$

Thus, in order to calculate the linewidth Γ_{e-e} by formula (2), we need to find the wave functions and energies of the states and the dielectric function ε. These quantities are calculated in the model of thin films, which are regularly arranged one above another parallel to the surface under study and separated by equal vacuum gaps. The number of atomic layers is taken to be 20 and 26 for Be(0001) and Mg(0001), respectively. The origin of coordinates is at the center of a film, with the z axis being normal to the surface.

The wave functions and energies of the initial and final states are calculated by the self-consistent pseudopotential method. The exchange-correlation potential is written in the local-density approximation [27, 28]. The nonlocal and norm preserving pseudopotentials of beryllium and magnesium are constructed according to [29, 30]. In the expansion of the wave functions

$$\Psi_{n\bar{\mathbf{k}}}(\mathbf{r}) = \frac{1}{\sqrt{\Omega}}\sum_{\mathbf{G}} c_{n\bar{\mathbf{k}}}(\mathbf{G})\exp(i(\bar{\mathbf{k}}\bar{\mathbf{r}} + \mathbf{G}\mathbf{r})) \quad (6)$$

we keep all plane waves with energies up to 15 Ry for Be and 5 Ry for Mg. In (6), Ω is the crystal volume and $\mathbf{G}$ is a reciprocal lattice vector.

An *ab initio* calculation of the screened Coulomb potential W for a surface with due account of the three-dimensional atomic crystal structure is a very labor intensive computational problem. For this reason, we calculate W by a method proposed in [17], using a one-dimensional model potential [31, 32]. This potential reproduces the energy gap at the $\bar{\Gamma}$ point of the surface Brillouin zone and the proper binding energies of the surface state and of the first image state and allows one to adequately describe the dependence of the screened Coulomb potential W on the coordinate z. Ignoring the x and y dependences in calculating W does not significantly affect the calculated linewidths because, as was demonstrated in [17], Γ_{e-e} does not depend critically on the form of approximations to W. Thus, we write W as a Fourier series

$$W(\mathbf{r}, \mathbf{r}'; E) = \frac{1}{L^2}\sum_{\bar{\mathbf{q}}} W(z, z', \bar{\mathbf{q}}; E)\exp(i\bar{\mathbf{q}}(\bar{\mathbf{r}} - \bar{\mathbf{r}}')), \quad (7)$$

where L is the normalization length and $\bar{\mathbf{q}}$ is a two-dimensional wave vector. Similar Fourier series are also written for V and χ, and we obtain the following expression for $W(z, z'; \bar{\mathbf{q}}; 0)$:

$$\begin{aligned}\mathrm{Im}W(z, z'; \bar{\mathbf{q}}; E) &= \int dz_1 \int dz_2 V(z, z_1; \bar{\mathbf{q}}) \\ &\times \mathrm{Im}\chi(z_1, z_2; \bar{\mathbf{q}}; E) V(z_2, z'; \bar{\mathbf{q}}).\end{aligned} \quad (8)$$

Here, $V(z, z'; \bar{\mathbf{q}})$ and $\chi(z, z'; \bar{\mathbf{q}}; E)$ are the two-dimensional Fourier transforms of the Coulomb potential and response function, respectively. In the random phase approximation, $\chi(z, z'; \bar{\mathbf{q}})$ obeys the integral equation

$$\begin{aligned}\chi(z, z'; \bar{\mathbf{q}}; E) &= \chi^0(z, z'; \bar{\mathbf{q}}; E) + \int dz_1 \\ &\times \int dz_2 \chi^0(z, z_1; \bar{\mathbf{q}}; E) V(z_1, z_2; \bar{\mathbf{q}}) \chi(z_2, z'; \bar{\mathbf{q}}; E),\end{aligned} \quad (9)$$

where $\chi^0(z, z'; \bar{\mathbf{q}}; E)$ is the response function of "non-interacting" particles. We use the following expression for this function [33]:

$$\begin{aligned}&\chi^0(z, z'; \bar{\mathbf{q}}; E) \\ &= \sum_{l=1}^{E_F}\sum_{l'=1}^{\infty} E_{ll'}(\bar{\mathbf{q}}; E)\varphi_l(z)\varphi_{l'}(z)\varphi_l(z')\varphi_{l'}(z'),\end{aligned} \quad (10)$$

where

$$F_{ll'}(\bar{\mathbf{q}}; E) = -\frac{1}{L^2} f_{\bar{\mathbf{Q}}, l}\left\{\frac{1}{\bar{\mathbf{q}}\bar{\mathbf{Q}} + \bar{\mathbf{q}}^2/2 - \varepsilon_l + \varepsilon_{l'} + E + i\eta} + \frac{1}{\bar{\mathbf{q}}\bar{\mathbf{Q}} + \bar{\mathbf{q}}^2/2 - \varepsilon_l + \varepsilon_{l'} - E - i\eta}\right\}$$

and

$$f_{\bar{\mathbf{Q}}, l} = 2\theta\left(E_F - \varepsilon_l - \frac{\bar{\mathbf{Q}}^2}{2}\right).$$

Here, η is an infinitely small parameter, θ is the Heaviside function, and $\bar{\mathbf{Q}}$ is a two-dimensional reciprocal lattice vector. The wave functions $\varphi_l(z)$ and energies ε_l in (10) are found by solving the Schrödinger equation with a one-dimensional model potential [31, 32] constructed for the films used in calculations. When calculating W, we use the double Fourier transformation

$$\begin{aligned}W(z, z', \bar{\mathbf{q}}; E) &= \sum_{g, g'} W^c_{gg'}(\bar{\mathbf{q}}; E)\cos(gz)\cos(g'z') \\ &+ \sum_{g, g' \neq 0} W^s_{gg'}(\bar{\mathbf{q}}; E)\sin(gz)\sin(g'z').\end{aligned} \quad (11)$$

Here, $-T/2 < z, z' < T/2$; $g = 2\pi n/T$ ($n = 0, 1, 2, 3, \ldots$ for cosine transformations and $n = 1, 2, 3, \ldots$ for sine transformations); and T is the length of the unit cell along the z axis.

Using the approximations and expansions mentioned above and converting the sum in (3) to an integral, we perform the summation of (2) over a set of points of the Brillouin zone and arrive at the following expression for Γ_{e-e}:

$$\begin{aligned}\Gamma_{e-e} &= \frac{1}{2S}\frac{1}{N_{\mathbf{R}}}\sum_{\bar{\mathbf{k}}}\sum_{E_{0\bar{\mathbf{q}}} \le E_{n\bar{\mathbf{k}}} \le E_F} w_n(\bar{\mathbf{k}}) \\ &\times \sum_{\mathbf{R}}\sum_{\bar{\mathbf{G}}_A}\left\{\sum_{g, g'} W^c_{gg'}(\bar{\mathbf{q}} - \mathbf{R}\bar{\mathbf{k}} + \bar{\mathbf{G}}_A; E_{0\bar{\mathbf{q}}} - E_{n\bar{\mathbf{k}}})\right. \\ &\times B^+_{n0}(\bar{\mathbf{q}}, \mathbf{R}\bar{\mathbf{k}}; \bar{\mathbf{G}}_A, g) B^+_{n0}(\bar{\mathbf{q}}, \mathbf{R}\bar{\mathbf{k}}; \bar{\mathbf{G}}_A, g') \\ &+ \sum_{g, g' \neq 0} W^s_{gg'}(\bar{\mathbf{q}} - \mathbf{R}\bar{\mathbf{k}} + \bar{\mathbf{G}}_A; E_{0\bar{\mathbf{q}}} - E_{n\bar{\mathbf{k}}}) \\ &\left.\times B^-_{n0}(\bar{\mathbf{q}}, \mathbf{R}\bar{\mathbf{k}}; \bar{\mathbf{G}}_A, g) B^-_{n0}(\bar{\mathbf{q}}, \mathbf{R}\bar{\mathbf{k}}; \bar{\mathbf{G}}_A, g')\right\},\end{aligned} \quad (12)$$

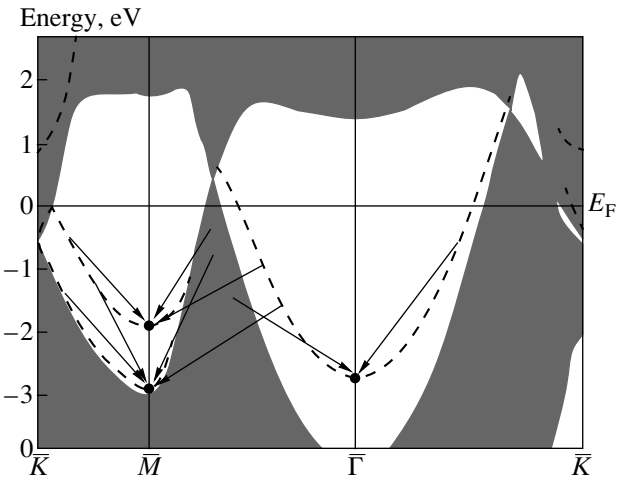

Fig. 1. Electronic structure of the Be(0001) surface. The shaded regions are the projection of bulk states. Surface and resonant states are indicated by dashed lines. Arrows symbolically indicate possible transitions that make a significant contribution to the surface state damping at the $\bar{\Gamma}$ and $\bar{M}$ points.

where we have introduced the notation

$$B^{\pm}_{n0}(\bar{\mathbf{q}}, \mathbf{R}\bar{\mathbf{k}}; \bar{\mathbf{G}}_A, g) = \sum_{\mathbf{G}} c_{n\bar{\mathbf{k}}}(\mathbf{G})[c_{0\bar{\mathbf{q}}}(\mathbf{R}\bar{\mathbf{G}} + \bar{\mathbf{G}}_A, G_z + g) \pm c_{0\bar{\mathbf{q}}}(\mathbf{R}\bar{\mathbf{G}} + \bar{\mathbf{G}}_A, G_z - g)]. \quad (13)$$

In (12), the summation is performed only over an irreducible part of the surface Brillouin zone, with $\bar{\mathbf{k}}$ running over an 18×18 set of points [34]; S is the area of a surface unit cell; $N_{\mathbf{R}}$ is the number of elements $\mathbf{R}$ of the point symmetry group; and $w_n(\bar{\mathbf{k}})$ are the weight factors of the Brillouin zone points, normalized to $N/2$, where N is the number of electrons in a unit cell. In the energy range under consideration, the matrix elements $W^c_{gg'}(\bar{\mathbf{k}}, E)$ and $W^s_{gg'}(\bar{\mathbf{k}}, E)$ rapidly decrease as the vector $\bar{\mathbf{k}}$ increases in magnitude. Therefore, in the sum over the two-dimensional reciprocal lattice vectors $\bar{\mathbf{G}}_A$ in (12), one may keep only several vectors of the smallest magnitude. In the sum over g, terms are kept up to $g^2_{\max} = 5$ Ry for Mg and $g^2_{\max} = 7$ Ry for Be, which corresponds to matrices W^c and W^s of rank 70. The results remain unchanged with increasing rank of the matrices. In (13), the expansion coefficients $c_{n\bar{\mathbf{k}}}(\mathbf{G})$ corresponding to vectors $\mathbf{G}$ of smallest magnitude are dominant and there is no need to keep all the $\mathbf{G}$ for which the energy spectrum is calculated. Checking the calculations shows that it is enough to keep about ~500 different $\mathbf{G}$ in (13) for the results to converge.

2. RESULTS AND DISCUSSION

Figure 1 shows the electronic structure of the Be(0001) surface calculated by the pseudopotential method. It is seen that, in the vicinity of the Fermi level, there are wide energy gaps, in which surface states are localized. The wave functions of the surface state at the $\bar{\Gamma}$ point and of the upper surface state at the $\bar{M}$ point are strongly localized near the surface layer and only slightly penetrate into the bulk of the crystal [22]. The lower surface state at the $\bar{M}$ point has a much less pronounced surface character; the charge density is maximal near the third surface atomic layer [22]. In the figure, the arrows symbolically indicate possible electron transitions involving the surface states at the $\bar{\Gamma}$ and $\bar{M}$ points. For example, the linewidth of the state at the $\bar{\Gamma}$ point is determined fundamentally by electron transitions from bulk states and by intraband transitions from this surface state. The contribution to the linewidth of this state from transitions from the surface states near the $\bar{M}$ point does not exceed 2% of the calculated total linewidth and will not be considered in what follows. A negligibly small contribution is also made to the linewidth of the upper surface state at the $\bar{M}$ point from the lower surface state band. For Be(0001), the linewidth of the surface state at the $\bar{\Gamma}$ point calculated by the method described in the previous section is obtained to be 315 meV. For the upper and lower surface states at the $\bar{M}$ point, the calculated values of Γ_{e-e} are 95 and 110 meV, respectively. In order to investigate the dependence of the linewidth of states on their binding energy, similar calculations of Γ_{e-e} are performed for the surface states at a number of $\bar{\mathbf{k}}$ points along the symmetry directions $\bar{\Gamma}\bar{K}$, $\bar{\Gamma}\bar{M}$, and $\bar{M}\bar{K}$. From Fig. 1, it is seen that the surface state band near the $\bar{\Gamma}$ point, as well as the upper state band near the $\bar{M}$ point, extends up to the Fermi level and above. This allows one to investigate the behavior of the calculated linewidth as the Fermi level is approached. It was shown in [22] that, as one moves across the energy gaps, the spatial charge density distribution in all three surface states changes only slightly. In this case, the change in the calculated values of Γ_{e-e} with variations in the energy of the state is determined fundamentally by the phase space accessible for damping. Figure 2 presents the energy dependence of the linewidths of the three surface states calculated for different $\bar{\mathbf{k}}$ vectors (and, hence, for different binding energies). The experimental values of the linewidth of the surface state at the $\bar{\Gamma}$ point are also indicated in the figure. It is seen that the calculated linewidth for this point agrees with the experimental data. As was noted above, subtracting the contributions due to electron–phonon interaction and surface defects from the experimental values Γ_{exp} will lead to some decrease in the latter, and the agreement with the calculations will become even better. It is evident from Fig. 2 that, at the same energy, the Γ_{e-e} for different states differ greatly in value, by a factor of two or three for binding energies higher than about 0.6 eV. By comparison, Fig. 2 also shows the $\Gamma_{e-e}(E)$ dependences calculated in

the HEG model [9] for the value of the parameter r_s corresponding to Be. It is seen that, for two surface states, the calculated Γ_{e-e} values are two or three times as large as the HEG values at the same energies. At the same time, the linewidth of the lower state at the $\bar{M}$ point is close to that calculated in the HEG model.

To elucidate the reason for this difference, in Fig. 2a, we present the energy dependences of the contributions to the linewidth of the surface state near the $\bar{\Gamma}$ point from bulk states and from intraband transitions from this surface state. It is seen that, for this state, the dominant contribution (as large as 75% of the line broadening) is from intraband transitions from this surface state. At the same time, the contribution from bulk states is close to its value in the HEG model [9]. Approximating the calculated $\Gamma_{e-e}(E)$ dependence by the power law

$$\Gamma_{e-e} = \beta(E - E_F)^{\alpha} \qquad (14)$$

gives $\alpha \approx 1.95$, which is close to the value 2 obtained for the exponent in the HEG model.

Figures 2b and 2c show analogous energy dependences of the linewidth of the upper and lower surface states near the $\bar{M}$ point, respectively. In contrast to the state near the $\bar{\Gamma}$ point, the linewidth of these surface states is dominated by several contributions that are comparable in value. For the upper state, three contributions are dominant: the bulk contribution, the one from the state near the $\bar{\Gamma}$ point, and the one due to intraband transitions from the closest state to the surface. For the lower state, there is also an additional contribution from transitions from the upper surface state near the $\bar{M}$ point. The energy dependence of the linewidth $\Gamma_{e-e}(E)$ of these states, as well as that of the surface state at the $\bar{\Gamma}$ point, is closely approximated by the power law (14) with an exponent α close to 2. However, for these surface states, in contrast to the state at the $\bar{\Gamma}$ point, the contributions due to transitions from bulk states are noticeably smaller than those obtained in the HEG model [9]. For the lower state, this contribution is dominant, because this state has a less pronounced surface character [22].

For the Mg(0001) surface, the variation of the linewidth of surface states with the point in the Brillouin zone is different. Figure 3 shows the electronic structure for this surface near the Fermi level [22]. It is seen that there is a single surface state in each of the narrow energy gaps in the vicinity of the $\bar{\Gamma}$ and $\bar{M}$ points. The energy dependences of Γ_{e-e} of these surface states are presented in Fig. 4. From this figure, it is seen that, for this surface, the Γ_{e-e} of the surface states differ from each other only slightly in the same energy range and differ from their values in the HEG model much less than in the case of beryllium [9]. This figure also shows the energy dependences of different contributions to the linewidth. It is seen that, in contrast to the case of Be,

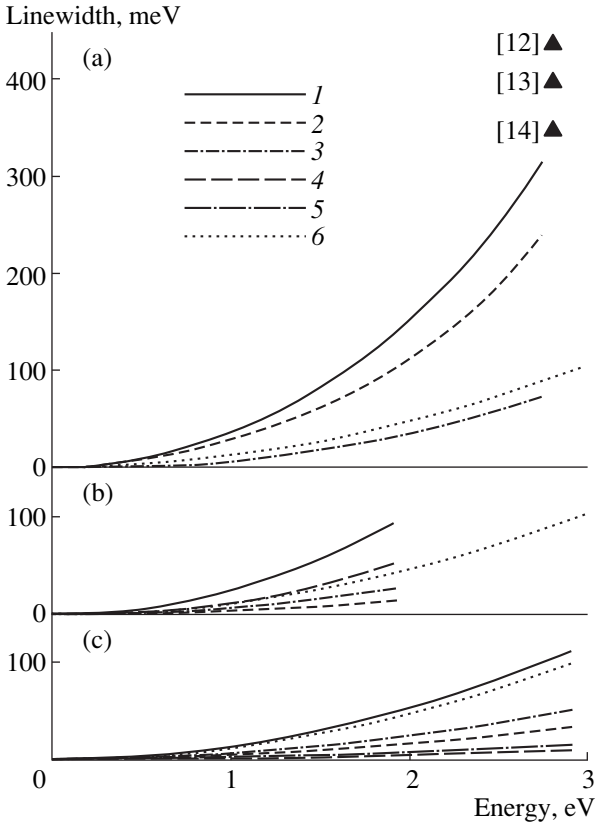

Fig. 2. Dependence of the linewidth of Be(0001) surface states on the binding energy for (a) the state at the $\bar{\Gamma}$ point, (b) the upper and (c) lower states at the $\bar{M}$ point: (*1*) the linewidth Γ_{e-e}; (*2*, *3*) the contributions to Γ_{e-e} due to transitions from the surface state band at the $\bar{\Gamma}$ point and due to interband transitions from bulk states, respectively; (*4*) the contributions to Γ_{e-e} due to transitions from the upper surface state band at the $\bar{M}$ point; (*5*) the contribution to Γ_{e-e} due to intraband transitions from the lower surface state band at the $\bar{M}$ point; and (*6*) the linewidth Γ_{e-e} in the HEG model [9]. Triangles are experimental values of the surface state linewidth at the $\bar{\Gamma}$ point [12–14].

the linewidth of these states is dominated by the bulk contribution. For both states, the contributions from the transitions from surface states are virtually equal in value. As in the case of Be(0001), the bulk contribution to Γ_{e-e} of the surface state at the $\bar{\Gamma}$ point is close to its value obtained in the HEG model for the parameter r_s = 2.65, corresponding to magnesium. The values of Γ_{exp} obtained for the surface state at the $\bar{\Gamma}$ point from the experimental photoemission spectra, Γ_{exp} ~200 [15] and ~500 meV [16], are significantly larger than Γ_{e-e} = 92 meV, calculated in this paper, and than Γ_{e-e} = 60 meV, given by the HEG model. Taking into account our results for the Be(0001) surface and the dramatic discordance between the experimental data, we believe that the principal causes of this disagreement between the theory and experiment are inappropriate experi-

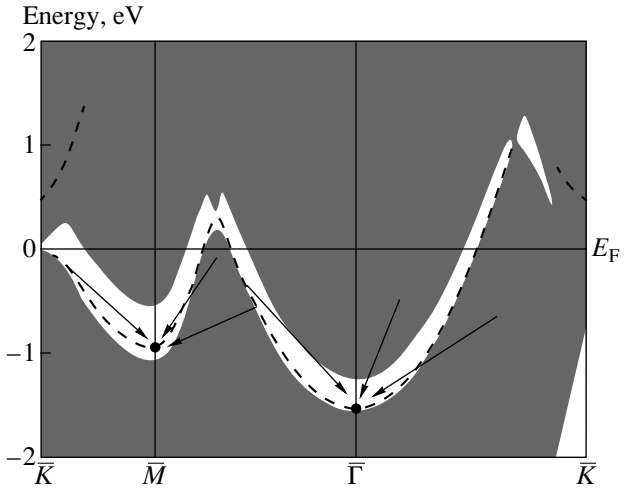

Fig. 3. Same as in Fig. 1, for the Mg(0001) surface.

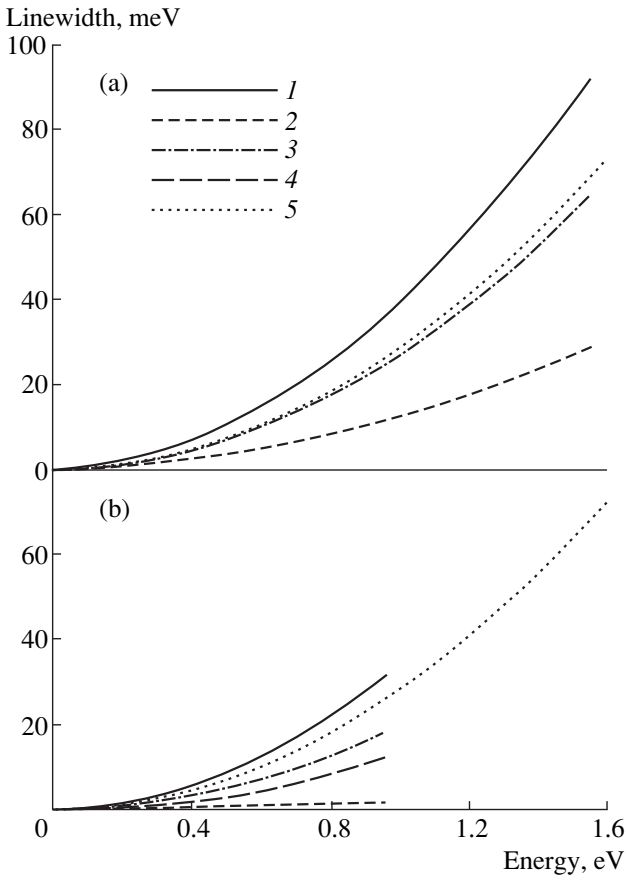

Fig. 4. Dependence of the linewidth of Mg(0001) surface states on the binding energy for the states (a) near the $\bar{\Gamma}$ point and (b) near the $\bar{M}$ point: (*1*) the linewidth Γ_{e-e}; (*2*, *3*) the contributions to Γ_{e-e} due to transitions from the surface state band at the $\bar{\Gamma}$ point and due to interband transitions from bulk states, respectively; (*4*) the contributions to Γ_{e-e} due to intraband transitions from the surface state band at the $\bar{M}$ point; and (*5*) the linewidth Γ_{e-e} in the HEG model [9].

mental conditions and the fact that the experimental values Γ_{exp} were strongly affected by the line broadening due to electron–phonon interaction and surface defects. For this reason, it would be desirable to conduct photoemission spectrum measurements for this surface using advanced sample preparation techniques.

Thus, the calculations performed for the Be(0001) and Mg(0001) surfaces demonstrated that the transitions from surface state bands play an important role in the formation of the linewidth of these states. For both surfaces, the major part of the difference between the linewidths calculated in this paper and those obtained in the HEG model [9] is due to these transitions. For surface states situated in wide energy gaps, the contribution from surface state bands increases the calculated values of Γ_{e-e} by a factor of two or three. In the case of the Be(0001) surface state at the $\bar{\Gamma}$ point, the inclusion of this contribution allows one to obtain a Γ_{e-e} value that agrees well with the recent experimental data [5–7] and thus clears the discordance between the theory and experiment. For the Mg(0001) surface, the band structure effects are much weaker, and the calculated linewidths of surface states are much less divergent from their respective values given by the HEG model. For both surfaces in question, the linewidths of surface states vary as the square of energy, with coefficients of proportionality differing from those in the HEG model and depending on the surface and the type of the surface state.

ACKNOWLEDGMENTS

The authors are grateful to É. Zarata for some computations.

This work was supported in part by the Department of Education of the Basque Country (Spain).

REFERENCES

1. S. D. Kevan, Phys. Rev. Lett. **50**, 526 (1983).
2. J. Tersoff and S. D. Kevan, Phys. Rev. B **28**, 4267 (1983).
3. N. V. Smith, Comments Condens. Matter Phys. **15**, 263 (1992).
4. *Angle-Resolved Photoemission. Theory and Current Applications*, Ed. by S. D. Kevan (Elsevier, Amsterdam, 1992).
5. B. A. McDougall, T. Balasubramanian, and E. Jensen, Phys. Rev. B **51**, 13891 (1995).
6. F. Theilmann, R. Matzdorf, G. Meister, and A. Goldmann, Phys. Rev. B **56**, 3632 (1997).
7. A. Goldmann, R. Matzdorf, and F. Theilmann, Surf. Sci. **414**, L932 (1998).
8. R. Matzdorf, Surf. Sci. Rep. **30**, 153 (1998).
9. J. J. Quinn, Phys. Rev. **126**, 1453 (1962).
10. S. LaShell, B. A. McDougall, and E. Jensen, Phys. Rev. Lett. **77**, 3419 (1996).
11. J. Li, W.-D. Schneider, R. Berndt, *et al.*, Phys. Rev. Lett. **81**, 4464 (1998).

12. R. A. Bartynski, E. Jensen, T. Gustafsson, and E. W. Plummer, Phys. Rev. B **32**, 1921 (1985).
13. T. Balasubramanian, E. Jensen, X. L. Wu, and S. L. Hulbert, Phys. Rev. B **57**, R6866 (1998).
14. R. Matzdorf, A. Gerlach, F. Theilmann, *et al.*, Appl. Phys. B **68**, 393 (1999).
15. U. O. Karlsson, G. V. Hansson, P. E. S. Persson, and S. A. Flodström, Phys. Rev. B **26**, 1852 (1982).
16. R. A. Bartynski, R. H. Gaylord, T. Gustafsson, and E. W. Plummer, Phys. Rev. B **33**, 3644 (1986).
17. E. V. Chulkov, I. Sarria, V. M. Silkin, *et al.*, Phys. Rev. Lett. **80**, 4947 (1998).
18. P. M. Echenique and J. B. Pendry, J. Phys. C **11**, 2065 (1978).
19. P. M. Echenique and J. B. Pendry, Prog. Surf. Sci. **32**, 111 (1989).
20. D. A. Papaconstantopoulos, *Handbook of the Band Structure of Elemental Solids* (Plenum, New York, 1986).
21. E. V. Chulkov and V. M. Silkin, Solid State Commun. **58**, 273 (1986).
22. E. V. Chulkov, V. M. Silkin, and E. N. Shirykalov, Surf. Sci. **188**, 287 (1987).
23. E. W. Plummer and J. B. Hannon, Prog. Surf. Sci. **46**, 149 (1994).
24. V. M. Silkin and E. V. Chulkov, Fiz. Tverd. Tela (St. Petersburg) **37**, 2795 (1995) [Phys. Solid State **37**, 1540 (1995)].
25. Ph. Hofmann, R. Stumpf, V. M. Silkin, *et al.*, Surf. Sci. **355**, L278 (1996).
26. L. Hedin and S. Lundqvist, Solid State Phys. **23**, 1 (1969).
27. W. Kohn and L. J. Sham, Phys. Rev. A **140**, 1133 (1965).
28. L. Hedin and B. I. Lundqvist, J. Phys. C **4**, 2064 (1971).
29. V. M. Silkin, E. V. Chulkov, I. Yu. Sklyadneva, and V. E. Panin, Izv. Vyssh. Uchebn. Zaved. Fiz. **9**, 56 (1984).
30. E. V. Chulkov, V. M. Silkin, and E. N. Shirykalov, Fiz. Met. Metalloved. **64**, 213 (1987).
31. E. V. Chulkov, V. M. Silkin, and P. M. Echenique, Surf. Sci. **391**, L1217 (1997).
32. E. V. Chulkov, V. M. Silkin, and P. M. Echenique, Surf. Sci. **437**, 330 (1999).
33. A. G. Eguiluz, Phys. Rev. Lett. **51**, 1907 (1983).
34. H. J. Monkhorst and J. D. Pack, Phys. Rev. B **13**, 5188 (1976).

Translated by Yu. Epifanov